

MARCH 2020

AJNR

VOLUME 41 • PP 369–550

AJNR

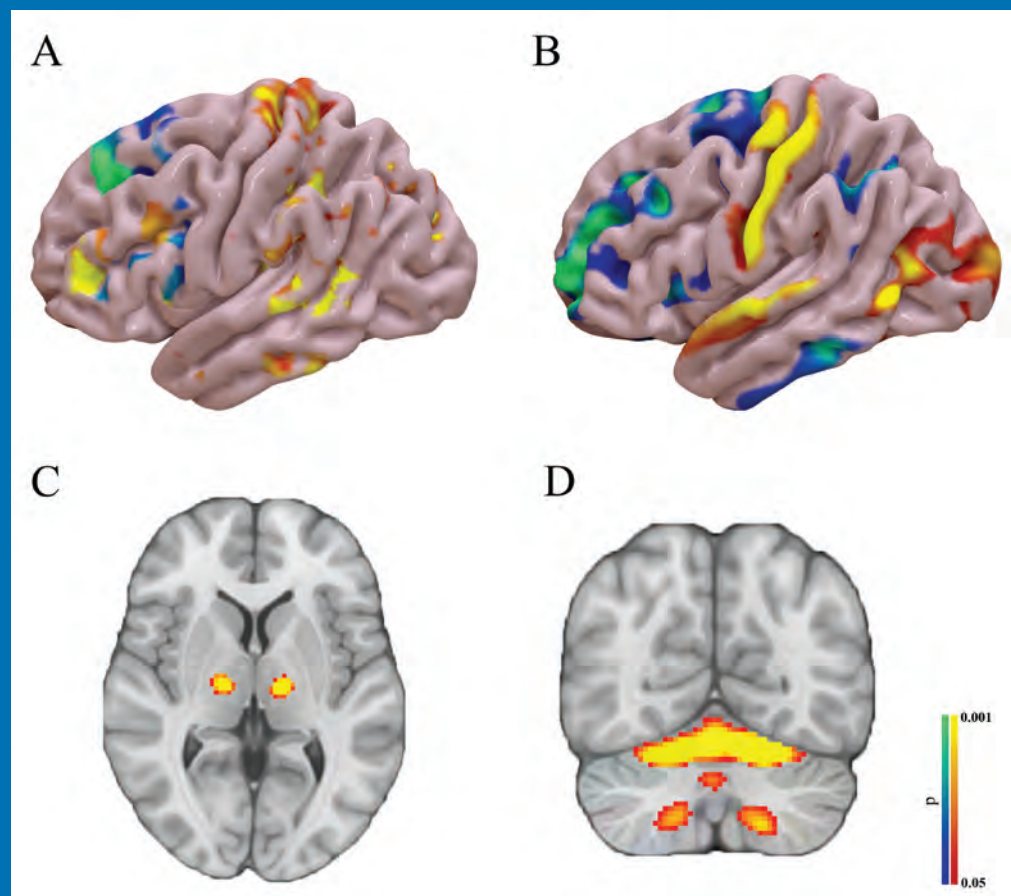
AMERICAN JOURNAL OF NEURORADIOLOGY

MARCH 2020
VOLUME 41
NUMBER 3
WWW.AJNR.ORG

THE JOURNAL OF DIAGNOSTIC AND
INTERVENTIONAL NEURORADIOLOGY

Connectivity patterns in DBS of the GPI for generalized dystonia
AI in the management of intracranial aneurysms
Evaluation of MR imaging grading systems in patients with suspected
nasopharyngeal carcinoma

Official Journal ASNR • ASFNR • ASHNR • ASPNR • ASSR





ONE AND DONE

INDICATIONS FOR USE:

The WEB Aneurysm Embolization System is indicated for use at the middle cerebral artery (MCA) bifurcation, internal carotid artery (ICA) terminus, anterior communicating artery (AComm) complex, or basilar artery apex for the endovascular treatment of adult patients with saccular, wide neck bifurcation intracranial aneurysms with dome diameter from 3 mm to 10 mm and either neck size 4 mm or greater or the dome-to-neck ratio is greater than 1 and less than 2.

The WEB Aneurysm Embolization System is contraindicated for patients with known bacterial infection that may interfere with or negatively affect the implantation procedure and patients with known hypersensitivity to nickel. For complete indications, contraindications, potential complications, warnings, precautions, and instructions, see instructions for use (IFU provided with the device).

The VIA® Catheter is intended for the introduction of non-liquid interventional devices (such as stents/_ow diverters) and infusion of diagnostic (such as contrast media) or non-liquid therapeutic agents into the neuro, peripheral, and coronary vasculature. The VIA Catheter is contraindicated for use with liquid embolic materials, such as n-butyl 2-cyanoacrylate or ethylene vinyl alcohol & DMSO (dimethyl sulfoxide). The VIA Catheter is contraindicated for use in the pediatric population (<22 yrs of age).

Caution: Federal law restricts these devices to sale by or on the order of a physician.

WEB[®]

Aneurysm Embolization System

MicroVention[®] delivers the first intrasaccular solution for wide neck bifurcation aneurysms.

The **world leader**
and **first**
PMA - approved
device in an
important new
category of
intrasaccular
flow disruptors.

The WEB[®] System is a safe
and effective single-device
solution for treating wide
neck bifurcation aneurysms.



SL Device



SLS Device

Contact a MicroVention sales associate to learn more
about integrating the WEB[®] device into your practice.



MicroVention Worldwide
Innovation Center
35 Enterprise
Aliso Viejo, CA 92656 USA
MicroVention UK Limited
MicroVention Europe, S.A.R.L.
MicroVention Deutschland GmbH
microvention.com

PH +1.714.247.8000

PH +44 (0) 191 258 6777

PH +33 (1) 39 21 77 46

PH +49 211 210 798-0



Simplify the MOC Process



Manage your CME Credits Online

CMEgateway.org

Available to Members of Participating Societies

American Board of Radiology (ABR)
American College of Radiology (ACR)
American Roentgen Ray Society (ARRS)
American Society of Neuroradiology (ASNR)
Commission on Accreditation of Medical
Physics Educational Programs, Inc. (CAMPEP)
Radiological Society of North America (RSNA)
Society of Interventional Radiology (SIR)
SNM
The Society for Pediatric Radiology (SPR)

It's Easy and Free!

Log on to CME Gateway to:

- View or print reports of your CME credits from multiple societies from a single access point.
- Print an aggregated report or certificate from each participating organization.
- Link to SAMs and other tools to help with maintenance of certification.

American Board of Radiology (ABR) participation!

By activating ABR in your organizational profile, your MOC-fulfilling CME and SAM credits can be transferred to your own personalized database on the ABR Web site.

Sign Up Today!

go to CMEgateway.org

AJNR

AMERICAN JOURNAL OF NEURORADIOLOGY

MARCH 2020
VOLUME 41
NUMBER 3
WWW.AJNR.ORG

Publication Preview at www.ajnr.org features articles released in advance of print. Visit www.ajnrblog.org to comment on AJNR content and chat with colleagues and AJNR's News Digest at <http://ajnrdigest.org> to read the stories behind the latest research in neuroimaging.

369 **PERSPECTIVES** *M.J. Baumann*

EDITORIAL



370 **Neuroradiology Fellowship Requirements: Updates in 2019**
T.A. Kennedy, et al.

REVIEW ARTICLES



373 **Artificial Intelligence in the Management of Intracranial Aneurysms: Current Status and Future Perspectives** *Z. Shi, et al.*

ADULT BRAIN



380 **Carotid Vessel Wall Imaging on CTA** *H. Baradaran, et al.*

EXTRACRANIAL VASCULAR

GENERAL CONTENTS



387 **Reduction of Radiation Dose and Scanning Time While Preserving Diagnostic Yield: A Comparison of Battery-Powered and Manual Bone Biopsy Systems** *S. Kihira, et al.*

PATIENT SAFETY INTERVENTIONAL



393 **Nephrogenic Systemic Fibrosis Risk Assessment and Skin Biopsy Quantification in Patients with Renal Disease following Gadobenate Contrast Administration** *E. Kanal, et al.*

PATIENT SAFETY



400 **Imaging-Based Algorithm for the Local Grading of Glioma**
E.D.H. Gates, et al.

ADULT BRAIN



408 **Performance of Standardized Relative CBV for Quantifying Regional Histologic Tumor Burden in Recurrent High-Grade Glioma: Comparison against Normalized Relative CBV Using Image-Localized Stereotactic Biopsies** *J.M. Hoxworth, et al.*

ADULT BRAIN FUNCTIONAL



416 **Correction of Motion Artifacts Using a Multiscale Fully Convolutional Neural Network** *K. Sommer, et al.*

ADULT BRAIN



424 **Clinical Experience of 1-Minute Brain MRI Using a Multicontrast EPI Sequence in a Different Scan Environment** *K.H. Ryu, et al.*

ADULT BRAIN



430 **High Intravascular Signal Arterial Transit Time Artifacts Have Negligible Effects on Cerebral Blood Flow and Cerebrovascular Reserve Capacity Measurement Using Single Postlabel Delay Arterial Spin-Labeling in Patients with Moyamoya Disease** *M. Fahlström, et al.*

ADULT BRAIN FUNCTIONAL

AJNR (Am J Neuroradiol ISSN 0195–6108) is a journal published monthly, owned and published by the American Society of Neuroradiology (ASNR), 800 Enterprise Drive, Suite 205, Oak Brook, IL 60523. Annual dues for the ASNR include approximately 21% for a journal subscription. The journal is printed by Cadmus Journal Services, 5457 Twin Knolls Road, Suite 200, Columbia, MD 21045; Periodicals postage paid at Oak Brook, IL and additional mailing offices. Printed in the U.S.A. POSTMASTER: Please send address changes to American Journal of Neuroradiology, P.O. Box 3000, Denville, NJ 07834, U.S.A. Subscription rates: nonmember \$410 (\$480 foreign) print and online, \$320 online only; institutions \$470 (\$540 foreign) print and basic online, \$935 (\$1000 foreign) print and extended online, \$380 online only (basic), \$825 online only (extended); single copies are \$35 each (\$40 foreign). Indexed by PubMed/MEDLINE, BIOSIS Previews, Current Contents (Clinical Medicine and Life Sciences), EMBASE, Google Scholar, HighWire Press, Q-Sensei, RefSeek, Science Citation Index, SCI Expanded, Meta/CZI, ReadCube, and Semantic Scholar. Copyright © American Society of Neuroradiology.

	437	Follow-Up MRI for Small Brain AVMs Treated by Radiosurgery: Is Gadolinium Really Necessary? <i>X. Leclerc, et al.</i>	ADULT BRAIN
☰	446	Vessel Wall MRI Enhancement in Noninflammatory Cerebral Amyloid Angiopathy <i>Q. Hao, et al.</i>	ADULT BRAIN
☰	449	Reduced Global Efficiency and Random Network Features in Patients with Relapsing-Remitting Multiple Sclerosis with Cognitive Impairment <i>R. Hawkins, et al.</i>	ADULT BRAIN
🖋️	456	SWAN-Venule: An Optimized MRI Technique to Detect the Central Vein Sign in MS Plaques <i>M.I. Gaitán, et al.</i>	ADULT BRAIN
🔑	461	Ratio of T1-Weighted to T2-Weighted Signal Intensity as a Measure of Tissue Integrity: Comparison with Magnetization Transfer Ratio in Patients with Multiple Sclerosis <i>D. Pareto, et al.</i>	ADULT BRAIN
	464	Endovascular Thrombectomy of Calcified Emboli in Acute Ischemic Stroke: A Multicenter Study <i>C.J. Maurer, et al.</i>	INTERVENTIONAL
🔑	469	Comparison of Aspiration versus Stent Retriever Thrombectomy as the Preferred Strategy for Patients with Acute Terminal Internal Carotid Artery Occlusion: A Propensity Score Matching Analysis <i>P.F. Xing, et al.</i>	INTERVENTIONAL
	477	Access-Site Complications in Mechanical Thrombectomy for Acute Ischemic Stroke: A Review of Prospective Trials <i>S.Z. Shapiro, et al.</i>	INTERVENTIONAL
☰	482	Implications of the Collar Sign in Incompletely Occluded Aneurysms after Pipeline Embolization Device Implantation: A Follow-Up Study <i>S. Gomez-Paz, et al.</i>	INTERVENTIONAL
	486	Commentary The Collar Sign in Pipeline Embolization Device–Treated Aneurysms <i>C.J. Moran</i>	INTERVENTIONAL
🔑 ☰ 🔍	488	Large Neck and Strong Ostium Inflow as the Potential Causes for Delayed Occlusion of Unruptured Sidewall Intracranial Aneurysms Treated by Flow Diverter <i>T. Su, et al.</i>	INTERVENTIONAL
	495	Contrast Enhancement of Intracranial Aneurysms on 3T 3D Black-Blood MRI and Its Relationship to Aneurysm Recurrence following Endovascular Treatment <i>S. Elsheikh, et al.</i>	INTERVENTIONAL
☰ 🔍	501	Gadolinium Enhancement of the Aneurysm Wall in Extracranial Carotid Artery Aneurysms <i>C.J.H.C.M. van Laarhoven, et al.</i>	EXTRACRANIAL VASCULAR
☰ 🔍	508	Functional and Structural Connectivity Patterns Associated with Clinical Outcomes in Deep Brain Stimulation of the Globus Pallidus Internus for Generalized Dystonia <i>L. Okromelidze, et al.</i>	FUNCTIONAL
★ 🔑 ☰ 🔍	515	Early Detection of Cancer: Evaluation of MR Imaging Grading Systems in Patients with Suspected Nasopharyngeal Carcinoma <i>A.D. King, et al.</i>	HEAD & NECK
★	522	4D–Dynamic Contrast-Enhanced MRI for Preoperative Localization in Patients with Primary Hyperparathyroidism <i>J.L. Becker, et al.</i>	HEAD & NECK
🔑	529	Value of Endolymphatic Hydrops and Perilymph Signal Intensity in Suspected Ménière Disease <i>J.M. van Steekelenburg, et al.</i>	HEAD & NECK
	535	Fractional Flow on TOF-MRA as a Measure of Stroke Risk in Children with Intracranial Arterial Stenosis <i>A.Y. Ibrahim, et al.</i>	PEDIATRICS
☰	542	Is Low-Grade Intraventricular Hemorrhage in Very Preterm Infants an Innocent Condition? Structural and Functional Evaluation of the Brain Reveals Regional Neurodevelopmental Abnormalities <i>M.I. Argyropoulou, et al.</i>	PEDIATRICS
☰ 🔍 🎥	548	Lumbar Puncture: Creation and Resident Acceptance of a Low-Cost, Durable, Reusable Fluoroscopic Phantom with a Fluid-Filled Spinal Canal for Training at an Academic Program <i>D.J. Lerner, et al.</i>	SPINE INTERVENTIONAL

ONLINE FEATURES

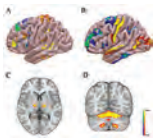
LETTERS

- E10 **Neuronavigation in the Identification and Presurgical Planning of Cortical Focal Dysplasia** *C.J. Valencia-Calderón*
- E12 **Reply** *R. Guerrini, et al.*
-  E13 **Time to Refocus the Target in Stroke Therapy Again?** *K.-O. Lövblad*
- E14 **The Possible Role of Elastic Properties of the Brain and Optic Nerve Sheath in the Development of Spaceflight-Associated Neuro-Ocular Syndrome** *P. Wostyn, et al.*
- E16 **Reply** *D.R. Roberts, et al.*
- E17 **Stroke-Like Episodes in m.3243A ≥ G Carriers Need to be Monitored by MRI Starting with the Onset of Clinical Manifestations** *J. Finsterer*

BOOK REVIEWS

R.M. Quencer, Section Editor

Please visit www.ajnrblog.org to read and comment on Book Reviews.



Group-level structural connectivity results showing cortical connections (A) positively (red) and negatively (blue) correlated with improvement in the UDRS score. Resting-state functional connectivity results show cortical (B), subcortical (C), and cerebellar (D) connectivity profiles correlated with improvement.



Indicates Editor's Choices selection



Indicates Fellows' Journal Club selection



Indicates open access to non-subscribers at www.ajnr.org



Indicates article with supplemental on-line table



Indicates article with supplemental on-line photo



Indicates article with supplemental on-line video



Evidence-Based Medicine Level 1



Evidence-Based Medicine Level 2

EDITOR-IN-CHIEF

Jeffrey S. Ross, MD

Professor of Radiology, Department of Radiology,
Mayo Clinic College of Medicine, Phoenix, AZ

SENIOR EDITORS

Harry J. Cloft, MD, PhD

Professor of Radiology and Neurosurgery,
Department of Radiology, Mayo Clinic College of
Medicine, Rochester, MN

Christopher G. Filippi, MD

Professor and Vice Chair of Biomedical and
Translational Science,
Donald and Barbara Zucker School of Medicine at
Hofstra/Northwell,
Lenox Hill Hospital and Greenwich Village
Healthplex, New York, NY

Thierry A.G.M. Huisman, MD

Radiologist-in-Chief, Texas Children's Hospital,
Houston, TX

Yvonne W. Lui, MD

Associate Professor of Radiology,
Chief of Neuroradiology,
New York University School of Medicine,
New York, NY

C.D. Phillips, MD, FACR

Professor of Radiology, Weill Cornell Medical
College, Director of Head and Neck Imaging,
New York-Presbyterian Hospital, New York, NY

Lubdhra M. Shah, MD, MS

Professor of Radiology and Director of Spine
Imaging, University of Utah Department of
Radiology and Imaging Sciences, Salt Lake City, UT

Charles M. Strother, MD

Professor of Radiology, Emeritus, University of
Wisconsin, Madison, WI

STATISTICAL SENIOR EDITOR

Bryan A. Comstock, MS

Senior Biostatistician,
Department of Biostatistics,
University of Washington, Seattle, WA

ARTIFICIAL INTELLIGENCE DEPUTY EDITOR

Peter D. Chang, MD

Assistant Professor-in-Residence,
Departments of Radiological Sciences,
Computer Sciences, and Pathology,
Director, Center for Artificial Intelligence in
Diagnostic Medicine (CAIDM),
University of California, Irvine, Irvine, CA

EDITORIAL BOARD

Ashley H. Aiken, *Atlanta, GA*
Lea M. Alhilali, *Phoenix, AZ*
Kubilay Aydin, *Istanbul, Turkey*
John D. Barr, *Dallas, TX*
Ari Blitz, *Baltimore, MD*
Barton F. Branstetter IV, *Pittsburgh, PA*
Jonathan L. Brisman, *Lake Success, NY*
Keith Cauley, *Danville, PA*
James Y. Chen, *San Diego, CA*
Asim F. Choudhri, *Memphis, TN*
Daniel Chow, *Irvine, CA*
J. Matthew Debnam, *Houston, TX*
Seena Dehkharghani, *New York, NY*
Yonghong Ding, *Rochester, MN*
Clifford J. Eskey, *Hanover, NH*
Saeed Fakhraan, *Phoenix, AZ*
Massimo Filippi, *Milan, Italy*
Nils D. Forkert, *Calgary, Alberta, Canada*
Wende N. Gibbs, *Phoenix, AZ*
Christine M. Glastonbury, *San Francisco, CA*
John L. Go, *Los Angeles, CA*
Philipp Göltz, *Erlangen, Germany*
Allison Grayev, *Madison, WI*
Brent Griffith, *Detroit, MI*
Ajay Gupta, *New York, NY*
Rakesh Kumar Gupta, *Haryana, India*
Lothi Hacein-Bey, *Sacramento, CA*
Christopher P. Hess, *San Francisco, CA*
Andrei Holodny, *New York, NY*
Benjamin Huang, *Chapel Hill, NC*
Mahesh V. Jayaraman, *Providence, RI*
Valerie Jewells, *Chapel Hill, NC*
Christof Karmonik, *Houston, TX*
Timothy J. Kaufmann, *Rochester, MN*
Hillary R. Kelly, *Boston, MA*
Toshibumi Kinoshita, *Akita, Japan*
Kenneth F. Layton, *Dallas, TX*
Alexander Lerner, *Los Angeles, CA*
Michael Lev, *Boston, MA*
Karl-Olof Lovblad, *Geneva, Switzerland*
Franklin A. Marden, *Chicago, IL*
Joseph C. McGowan, *Merion Station, PA*
Stephan Meckel, *Freiburg, Germany*
Christopher J. Moran, *St. Louis, MO*
Takahisa Mori, *Kamakura City, Japan*
Suresh Mukherji, *Ann Arbor, MI*
Alexander J. Nemeth, *Chicago, IL*
Renato Hoffmann Nunes, *Sao Paulo, Brazil*
Sasan Partovi, *Cleveland, OH*
Laurent Pierot, *Reims, France*
Jay J. Pillai, *Baltimore, MD*
Whitney B. Pope, *Los Angeles, CA*
Joana Ramalho, *Lisbon, Portugal*

Otto Rapalino, *Boston, MA*
Álex Rovira-Cañellas, *Barcelona, Spain*
Paul M. Ruggieri, *Cleveland, OH*
Amit M. Saindane, *Atlanta, GA*
Maksim Shapiro, *New York, NY*
Timothy Shepherd, *New York, NY*
Mark S. Shiroishi, *Los Angeles, CA*
Bruno P. Soares, *Baltimore, MD*
Maria Vittoria Spampinato, *Charleston, SC*
Khin Khin Tha, *Sapporo, Hokkaido, Japan*
Krishnamoorthy Thamburaj, *Hershey, PA*
Cheng Hong Toh, *Taipei, Taiwan*
Aquila S. Turk, *Greenville, SC*
Anja G. van der Kolk, *Utrecht, the Netherlands*
Willem Jan van Rooij, *Tilburg, Netherlands*
Arastoo Vossough, *Philadelphia, PA*
Elysa Widjaja, *Toronto, Ontario, Canada*
Max Wintermark, *Stanford, CA*
Ronald L. Wolf, *Philadelphia, PA*
Kei Yamada, *Kyoto, Japan*
Carlos Zamora, *Chapel Hill, NC*
Vahe M. Zohrabian, *New Haven, CT*

EDITORIAL FELLOW

Hediyeh Baradaran, *Salt Lake City, UT*

SPECIAL CONSULTANTS TO THE EDITOR

AJNR Blog Editor

Neil Lall, *Denver, CO*

Case of the Month Editor

Nicholas Stence, *Aurora, CO*

Case of the Week Editors

Juan Pablo Cruz, *Santiago, Chile*

Sapna Rawal, *Toronto, Ontario, Canada*

Classic Case Editor

Sandy Cheng-Yu Chen, *Taipei, Taiwan*

Health Care and Socioeconomics Editor

Pina C. Sanelli, *New York, NY*

Physics Editor

Greg Zaharchuk, *Stanford, CA*

Podcast Editor

Wende N. Gibbs, *Phoenix, AZ*

Twitter Editor

Roger Jordan, *Houston, TX*

Official Journal:

American Society of Neuroradiology
American Society of Functional Neuroradiology
American Society of Head and Neck Radiology
American Society of Pediatric Neuroradiology
American Society of Spine Radiology

Founding Editor
Juan M. Taveras

Editors Emeriti
Mauricio Castillo, Robert I. Grossman,
Michael S. Huckman, Robert M. Quencer

Managing Editor
Karen Halm
Assistant Managing Editor
Laura Wilhelm
Editorial Assistant
Margaret B. Sabato
Executive Director, ASNR
Mary Beth Hepp

AJNR *go green*

***AJNR* urges American Society of Neuroradiology members to reduce their environmental footprint by voluntarily suspending their print subscription.**

The savings in paper, printing, transportation, and postage directly fund new electronic enhancements and expanded content.

The digital edition of *AJNR* presents the print version in its entirety, along with extra features including:

- Publication Preview
- Case Collection
- Podcasts
- The *AJNR* News Digest
- The *AJNR* Blog

It also reaches subscribers much faster than print. An electronic table of contents will be sent directly to your mailbox to notify you as soon as it publishes.

Readers can search, reference, and bookmark current and archived content 24 hours a day on www.ajnr.org.

ASNR members who wish to opt out of print can do so by using the *AJNR* Go Green link on the *AJNR* Website (<http://www.ajnr.org/content/subscriber-help-and-services>). Just type your name in the email form to stop print and spare our ecosystem.

Introducing
Eclipse 2L
DUAL LUMEN BALLOON CATHETER



Balt's Access Portfolio Delivers Unique Solutions



Visit www.balt-usa.com to learn more



Title: St. Peter's Basilica Dome, Vatican City, Rome. The tallest dome in the world, it rises to a height of 448 feet.
Marlene Julie Baumann, MD, Geisinger Health System, Danville, Pennsylvania



Neuroradiology Fellowship Requirements: Updates in 2019

T.A. Kennedy and J. Anderson

The revised Accreditation Council for Graduate Medical Education (ACGME)-accredited Neuroradiology Fellowship Requirements were recently implemented in July 2019. The revision process was facilitated by a task force that was coordinated by the American Society of Neuroradiology (ASNR). The most notable changes made since the prior requirements were last revised in 2007 primarily affect the number of required procedures, the academic support defined for the program director, and modifications to the curriculum. The new requirements allow fellows to fulfill the foundational expectations for the neuroradiology fellowship and encourage programs to maintain some flexibility to teach individual specialty areas of clinical excellence.

The ACGME is a national organization that establishes accreditation guidelines for many graduate medical programs in the United States, including the Neuroradiology Fellowship Program, which is sponsored by the ASNR. The ACGME periodically and systematically reviews these requirements for each specialty program, making revisions every 10–12 years based on input of the sponsoring specialty society, which are intended to incorporate current and anticipated changes in medical practice.

The Neuroradiology Fellowship Requirements were initially established in 1990 and were last fully revised in 2007.¹ The updated Neuroradiology Fellowship Requirements, which incorporated the recently approved Common Program Requirements (CPRs), were approved by the ACGME in February 2019 and went into effect July 1, 2019.² In this Editorial, the Neuroradiology Fellowship Requirements revision process is discussed as well as the key changes from the prior requirements.

The ASNR Committee Process

An ACGME Requirement Revision Task Force was created with direction from the ASNR Fellowship Directors Committee to generate a list of recommendations to be submitted on behalf of the ASNR to the ACGME Radiology Review Committee to address any programmatic and curricular changes in the ACGME Neuroradiology Fellowship Requirements. The task force consisted of Fellowship Directors, ASNR Executive Committee members, and Young Professional Section members, with a concerted effort to create a group that represented a diversity of programs of different sizes, geography, and specialty areas of excellence across the country. In addition, feedback and input were solicited from subspecialty society leadership from the American Society of Head and Neck Radiology, American Society of Spine Radiology, American Society of Functional Neuroradiology, American Society of Pediatric Neuroradiology, and the Society of Neurointerventional Surgery.

The major revision update happened to coincide with the ACGME review and update of the underlying Common Program Requirements (CPR). These CPRs are the elements of the program requirements that are common to all specialties or, in this case, to the subspecialties. These also provide the framework for any specialty or subspecialty requirements. Thus, elements in the 2019 updated Neuroradiology Fellowship Requirements also include items that were not a result of the process described above but rather due to inclusion by the recommendation of the ACGME CPR revision task force.

Key Changes in the 2019 Updated Requirements

The revision task force began its process on the basis of the understanding that there are fundamental core standards that all ACGME-accredited Neuroradiology Fellowship programs should meet so that any fellow graduating from an accredited program should possess a core set of uniform skills necessary to practice neuroradiology. There is also acknowledgment that neuroradiology programs may individually have certain content areas of expertise. The new requirements allow programs some flexibility to meet core standards but, in so doing, provide an opportunity for programs to have flexibility to offer unique experiences to their trainees.

A number of modifications to the Neuroradiology Fellowship Requirements have been made to reflect contemporary clinical practice guidelines that are different from what they were in 2007. The new requirements address shifting expectations related to neuroangiography, redefine the fellowship curriculum, and outline support for fellowship program directors.

Program Director. To acknowledge the substantial time commitment of the Fellowship Program Director (PD) to administer the neuroradiology training program, changes have been made to provide protected academic time to the Fellowship PD based on a sliding scale. As part of the new requirements, the PD should have protected administrative time and should be granted a minimum of 0.1 full-time equivalent (FTE) for a program with 1–5 fellows and 0.2 FTE for a program with more than 5 fellows (II.A.2.a).² Note that these requirements are based on the approved complement and not on the actual number of fellows enrolled, a subtle-but-important distinction to understand. This protected administrative time was not specified in the prior version. A similar requirement has been incorporated in the core Diagnostic Radiology Residency Requirements as well as within the Interventional Radiology Residency Requirements. In addition, as a prerequisite, PDs should have 3 years of clinical experience and be subspecialty certified (II.A.3).² A summary of the Program Director, Program Coordinator, and Program Faculty requirements is listed in Table 1.

Patient Care and Procedural Skills. Meaningful changes were made to the Patient Care and Procedural Skills section of the requirements. Fellows are now required to interpret a minimum of 3000 total examinations, of which, at least 1500 should be MR imaging studies (IV.B.1.b).(2).(a).(i).² Previously, fellows were

Table 1: Program director, coordinator, and participating faculty requirements

Program Role	Requirements (Minimum)
Program director academic time	1–5 Fellows approved - 0.1 FTE (10%) >6 Fellows approved - 0.2 FTE (20%)
Program director experience	3 Years of clinical experience Subspecialty certification by the American Board of Radiology
Program coordinator	The program coordinator must be provided with adequate time and support, depending on the size of the program
Participating faculty	Minimum of 2 neuroradiology faculty (including the PD) Faculty should spend 80% of time practicing neuroradiology Ratio of at least 1 neuroradiologist for every 2 fellows

Table 2: Required procedures/diagnostic examinations interpreted

Procedures/Studies	No. of Studies (Minimum)	Specifics
Total diagnostic examinations interpreted	3000	Of which at least 1500 should be MR imaging
Vascular imaging interpretation	250	Including CTA, CTV, MRA, MRV, Doppler sonography, and catheter-based angiography
Image-guided invasive procedures performed ^a	100	Which may include LP, myelography, advanced spine procedures, catheter-based angiography, and head and neck biopsies

Note:—LP indicates lumbar puncture.

^a Must demonstrate competence in spinal access.

required to interpret 1500 CT examinations and 1500 MR imaging examinations.¹ While the total number of examinations interpreted has not changed since the prior requirements, the new phrasing allows fellows the opportunity to interpret more advanced MR imaging examinations than previously required. This change allows fellows to concentrate more on complex MRIs than on CTs, to account for CT experience that was likely already gained in residency.

Catheter-Based Angiography and Imaging-Guided Procedures in the New Requirements. Notable changes were made to the catheter-based angiography requirement in 2 sections: Patient Care and Procedural Skills and within the Curriculum section. Fellows are required to interpret a total of 250 vascular studies, which may include a combination of CTA, CTV, MRA, MRV, Doppler sonography, and catheter-based angiography ([IV.B.1.b].[2].[a].[ii]).² Previously, this requirement was met by CTA and MRA alone. Incorporating catheter-based angiography into the interpretive vascular curriculum emphasizes the importance of vascular imaging interpretation rather than the skills needed to perform catheter-based angiography. In addition, within the Curriculum section, it is emphasized that fellows must interpret both noninvasive and invasive neuroangiography. The required rotation length was also decreased from a 6-week minimum to a 4-week rotation or equivalent (IV.C.7.a).² Fellows are encouraged to participate in catheter-based angiography and to understand the pre- and postprocedural care of these patients.

The procedural requirements were also modified in the updated requirements. While the total number of procedures required has not changed and remains 100 procedures, there is now greater flexibility given to programs to fill this requirement, which may include a combination of DSA, lumbar puncture, myelography, advanced spine procedures, and head and neck biopsies ([IV.B.1.b].[2].[a].[iii]).² Spinal access is the one procedure

Table 3: Curriculum summary

Curriculum: Specialty Area of Concentration	Time/Equivalent Experience (Minimum)
Vascular	4 Weeks or equivalent longitudinal experience
Spine	4 Weeks or equivalent longitudinal experience
Head and neck	4 Weeks or equivalent longitudinal experience
Pediatric neuroradiology	4 Weeks or equivalent longitudinal experience
Brain	Remaining time

Table 4: Eligibility for US/Canadian candidates

Eligibility
ACGME-accredited residency
AOA-approved residency program
ACGME International (ACGME-I) Advanced Specialty Accreditation
Royal College of Physicians and Surgeons of Canada
College of Family Physicians of Canada-accredited residency program located in Canada

Note:—AOA indicates American Osteopathic Association.

Table 5: Alternate pathway for fellowship eligibility^a

Candidates Must Meet the Following:
Complete a residency in the core specialty outside the US/Canada
Demonstrate exceptional clinical excellence compared with peers
Demonstrate excellence in research, scholarship, or leadership
Verification of ECFMG status
Evaluation of performance by the CCC within 12 weeks of matriculation

Note:—ECFMG indicates Educational Commission for Foreign Medical Graduates; CCC, Clinical Competency Committee.

^a Fellowship may not lead to certification from American Board of Medical Specialties or AOA certifying boards.

in which fellows are required to demonstrate competence, but the requirements do not specify the number of procedures needed to establish competence ([IV.B.1.b].[2].[b]).² This number will be

Table 6: Duty hours

Duty Hours	Comments
80 Hours per week	Averaged for 4 weeks Includes all in-house clinical and educational activities Includes moonlighting Includes at-home call Clinical work done from home
8 Hours off between clinical work and education periods Minimum of 1 day in 7 free of clinical work and required education	Averaged for 4 weeks At-home call cannot be assigned on these free days Applies to moonlighting
Cannot exceed 24 hours of continued scheduled clinical service Must have 14 hours free of clinical work and education following 24 hours of in-house call Night float: fellows must not be scheduled for shifts greater than every third night	Averaged for 4 weeks

variable depending on the previous experience of the fellow gained in residency training. A summary of procedure requirements is listed in Table 2.

The specific requirement regarding the performance of 50 catheter-based angiographies from the prior version was removed from the updated document. The new requirements reflect the current sentiment among many programs around the country that diagnostic neuroradiology fellows are not performing diagnostic angiographies after fellowship. Many program directors and fellows felt that this requirement did not reflect current practice expectations. The new phrasing regarding the procedure requirement emphasizes the importance of patient evaluation and the consent process rather than learning any one specific type of procedure. This flexibility allows individual fellowship programs to distinguish themselves as centers of excellence regarding learning specific types of neuroradiology-related procedures.

While the field of neuroangiography has changed during the past 10 years, with greater involvement from neurosurgery, neurology, vascular surgery, and interventional radiology, there are a number of centers around the country that have neuro-radiology-trained Neuroendovascular specialists and would like their fellows to be eligible to apply for a dedicated Neuroendovascular Fellowship. The updated requirements will allow those programs the ability to still achieve this goal.

A point that must be emphasized is that the removal of the required number of catheter-based angiographies performed does not indicate any intent to minimize the value of performing catheter-based angiography as a learning endeavor. Many still believe that being part of the angiography team and performing these procedures strengthens the knowledge of the procedure, the indications, risks and benefits, as well as interpretation of both angiography studies and noninvasive angiography. Thus, programs that provide the opportunity to perform and immerse the fellow in the training are encouraged to continue. The changes allow one to provide this experience without the concern for accreditation issues due to the lower volume of cases.

Curriculum. No major changes were made to the length of time that fellows should spend on pediatric, head and neck, and spine rotations, each specifying a 4-week or equivalent longitudinal experience. There was a change to the vascular requirement, which changed from a 6- to 4-week block to align with the other specialty areas (Table 3). While no specific rotation length was allocated to advanced imaging, fellows must document their exposure to MR spectroscopy and fMRI (IV.C.9).²

Fellow Eligibility. As in the past, individuals interested in applying for an ACGME-accredited Neuroradiology Fellowship must have completed an approved residency training program in the United States or Canada as outlined in Table 4. An alternate pathway for fellowship matriculation is possible, which is outlined in Table 5.

Duty Hours. Duty hours were incorporated within the previous requirements without significant changes. Fellows are responsible for documenting clinical and educational work hours and maintaining a maximum of 80 hours worked per week, when averaged for 4 weeks. Additional specifications related to time off between shifts, moonlighting, in-house call, and home call are listed in Table 6.

Summary

The ACGME Neuroradiology Fellowship Requirements have been updated to reflect current trends in neuroradiology practice. The new requirements allow fellows to fulfill the foundational expectations for the Neuroradiology Fellowship and allow programs to maintain some flexibility to focus on teaching specialty areas of clinical excellence.

REFERENCES

1. The ACGME Program Requirements for Graduate Medical Education in Neuroradiology Revised. July 2007. Accessed January 24, 2017
2. The ACGME Program Requirements for Graduate Medical Education in Neuroradiology Revised. July 2019. https://www.acgme.org/Portals/0/PFAssets/ProgramRequirements/423_Neuroradiology_2019.pdf?ver=2019-03-20-145727-847. Accessed December 1, 2019

Artificial Intelligence in the Management of Intracranial Aneurysms: Current Status and Future Perspectives

Z. Shi, B. Hu, U.J. Schoepf, R.H. Savage, D.M. Dargis, C.W. Pan, X.L. Li, Q.Q. Ni, G.M. Lu, and L.J. Zhang



ABSTRACT

SUMMARY: Intracranial aneurysms with subarachnoid hemorrhage lead to high morbidity and mortality. It is of critical importance to detect aneurysms, identify risk factors of rupture, and predict treatment response of aneurysms to guide clinical interventions. Artificial intelligence has received worldwide attention for its impressive performance in image-based tasks. Artificial intelligence serves as an adjunct to physicians in a series of clinical settings, which substantially improves diagnostic accuracy while reducing physicians' workload. Computer-assisted diagnosis systems of aneurysms based on MRA and CTA using deep learning have been evaluated, and excellent performances have been reported. Artificial intelligence has also been used in automated morphologic calculation, rupture risk stratification, and outcomes prediction with the implementation of machine learning methods, which have exhibited incremental value. This review summarizes current advances of artificial intelligence in the management of aneurysms, including detection and prediction. The challenges and future directions of clinical implementations of artificial intelligence are briefly discussed.

ABBREVIATIONS: AI = artificial intelligence; AUC = area under the curve; CAD = computer-assisted diagnostics; DL = deep learning; FP = false-positive; ML = machine learning; SVM = support vector machines

Unruptured intracranial aneurysm remains a major public health concern affecting about 3%–7% of the general population.^{1,2} CTA and MRA are the preferred techniques to identify aneurysms. A steadily increasing number of radiologic examinations are performed for neurologic diagnoses, which require human expertise in image interpretation. However, experienced radiologists are in a relative shortage due to an ever-increasing demand for imaging studies.³ The excess workload imposed on physicians requires them to interpret 1 image every 3–4 seconds within work hours. As a result, uncertainty and inevitable errors when making diagnoses and decisions may arise.⁴

As the most common cause of nontraumatic SAH, aneurysms are responsible for 85% of SAH cases. The overall annual rupture risk is 0.95% and is associated with a high risk of morbidity and mortality.⁵ Endovascular and surgical treatments have a 3%–10% risk of stroke or death and may not permanently eliminate the propensity for rupture.⁶ Therefore, recognition of risk factors and construction of prediction models related to aneurysm initiation, growth, rupture, and assessment of intervention have been popular areas of investigation. However, the management of aneurysms is associated with multiple challenges in all aspects of clinical practice, which cannot be overcome easily by conventional methodology.

Artificial intelligence (AI) describes the development of computer algorithms that simulate human intelligence, which includes learning, reasoning, and self-correction. Brilliant progress has been made that allows machines to automatically interpret complicated data as part of routine clinical care.⁷ AI is also expected to satisfy the clinician's need for higher accuracy and better efficacy at all stages of aneurysm management. This review summarizes current applications of AI in the various phases (Fig 1) of intracranial aneurysm management, which facilitates optimized workflows and adds benefit to patient care. In addition, this review discusses the future challenges and directions of AI-based management of aneurysm.

Received September 30, 2019; accepted after revision December 16.

From the Department of Medical Imaging (Z.S., B.H., Q.Q.N., G.M.L., L.J.Z.), Jinling Hospital, Medical School of Nanjing University, Nanjing, Jiangsu, China; Division of Cardiovascular Imaging (U.J.S., R.H.S., D.M.D.), Department of Radiology and Radiological Science, Medical University of South Carolina, Charleston, South Carolina; DeepWise AI Lab (C.W.P., X.L.L.), Beijing, China; and Peng Cheng Laboratory (X.L.L.), Vanke Cloud City Phase I, Nanshan District, Shenzhen, Guangdong, China.

This work was supported by the National Key Research and Development Program of China (2017YFC0113400 for L.J.Z.) and Key Projects of the National Natural Science Foundation of China (81830057 for L.J.Z.).

Please address correspondence to Long Jiang Zhang, MD, PhD, Department of Medical Imaging, Jinling Hospital, Medical School of Nanjing University, Nanjing, Jiangsu, 210002, China; e-mail: kevinzhj@163.com

 Indicates open access to non-subscribers at www.ajnr.org

 Indicates article with supplemental on-line table.

<http://dx.doi.org/10.3174/ajnr.A6468>

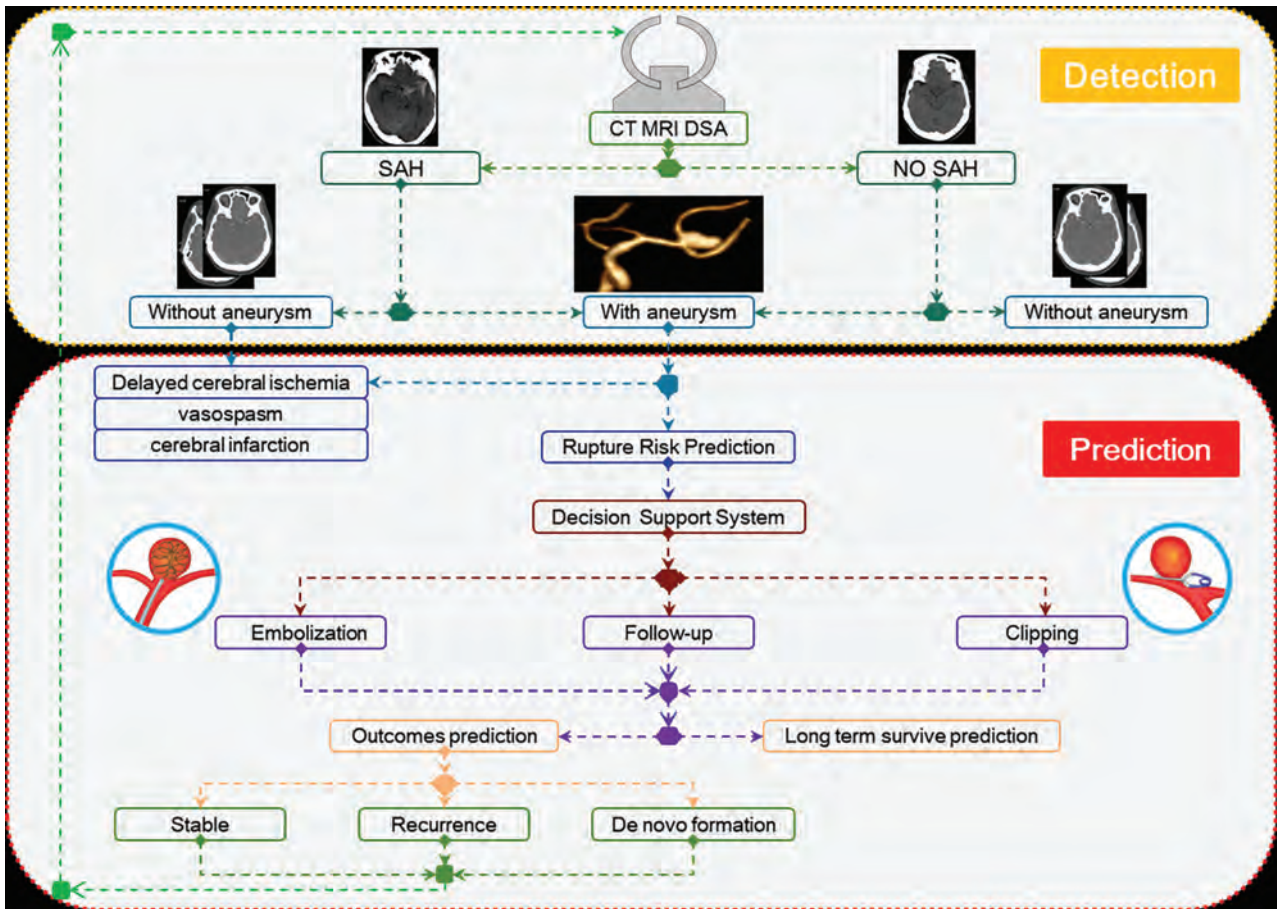


FIG 1. Various phases of intracranial aneurysm management. They include the procedures of detection and prediction.

Brief Overview of AI

AI can perform tasks with humanlike intelligence such as pattern recognition, object identification, and problem resolution. AI can make autonomous decisions based on the data collected for training. Similarly, in the realm of medicine, AI can identify a likely diagnosis and select a suitable treatment based on health records or imaging information without any explicit programming. Machine learning (ML) endows AI with the ability to learn and train models to extract and memorize features and related parameters. There are 3 types of ML: supervised (training with specific labels or annotations), unsupervised (training without specific labels and the algorithm clusters data to reveal underlying patterns), and semi- or weakly supervised learning (training with both labeled and unlabeled data to reduce the annotation burden).⁸

Deep learning (DL) is a subset of machine learning that is end-to-end ML in which it receives input and learns its salient features without explicit examples.⁹ There are 2 key requirements for ML: 1) Data are relevant and detailed enough for answering the clinical questions; and 2) a computational ML technique is appropriate for the type, amount, and complexity of the available data. Finally, it is necessary to further validate the usefulness of ML models in real-world practice.¹⁰

Traditional ML algorithms predefine engineered features that can describe the patterns inherent in regions of interest with explicit parameters based on expert knowledge. Support vector machines (SVM) and random forests are classic ML techniques.

These algorithms have been successfully used in AI studies.^{11,12} Compared with traditional ML algorithms, DL uses an artificial neural network that extracts features from images automatically to create its own filters, called feature maps (independent of human input) and memorizes visual patterns with highest frequency. There are convolution layers, pooling layers, fully connected layers, and normalization layers; the pooling reduces the number of parameters and reduces overfitting. Once a final output is made that is compared with ground truth, the model will reweight the inputs until the best performance is reached, which can be repeated many times (called epochs). For feature-extraction and selection, DL algorithms do not need to predefine features, and the feature representations can be directly learned by navigating the data space. Most DL networks fundamentally build on some basic and similar neural network blocks or layers based on DL attempts to model high-level abstractions.¹³ Therefore, the extracted complex features are then fed through the last layer of the network for the target, such as classification or prediction. Convolutional neural networks are typical types of DL architecture, which consist of characteristic layers of convolutional operations on the input images to extract abstract features.¹³

Computer-Assisted Diagnosis of Aneurysms

CTA and TOF-MRA are widely available techniques for detection. However, very small aneurysms are often missed.¹⁴ Computer-assisted diagnostics (CAD) acts principally as an internal second

opinion and improves reading accuracy of physicians.^{15,16} Algorithms have been devised for automatic detections based on MRA/CTA studies using conventional-style and DL methods (On-line Table).

Conventional-Style CAD Systems. The conventional-style CAD systems were based on presupplied characteristics or imaging features, such as vessel curvature, thresholding, or a region-growing algorithm.¹⁷ The first CAD system geared toward aneurysms reported in the literature was developed by Arimura et al,¹⁸ in 2004, which consisted of multiple gray-level thresholding techniques. It showed 100% sensitivity with 2.4 false-positives (FPs) per patient based on a leave-one-out-by-patient test method. In subsequent validation studies, Hirai et al¹⁹ and Kakeda et al²⁰ found that the sensitivity was 100% and 84%, respectively. However, this algorithm was not fully automated, nor could it detect small or fusiform type of aneurysms. In addition, the aneurysms in these studies were not verified by DSA as an outside reference standard. By using DSA as the reference, Yang et al¹⁷ developed a more automated CAD algorithm by combining 2 complementary techniques: 1) automatic intracranial artery segmentation and 2) detection of points of interest from the segmented vessels. They achieved a sensitivity of 95% with up to 9 additional FP detection marks. However, the sensitivity was lower for small aneurysms (<5 mm). The conventional-style CAD schemes relied on a similar rules-based approach in which prior domain knowledge was incorporated into hand-crafted features before using ML techniques as a classifier. The major limitation is that many false-positive results are found in bending or branching portions of vessels. Multiple methods have been proposed such as an ellipsoid convex enhancement filter to selectively enhance aneurysms while reducing FPs, but the number of FPs remains high.²¹

Deep Learning CAD Systems. More recently, DL-based CAD systems have been developed for aneurysm detection on the basis of MRA.²²⁻²⁴ For example, Nakao et al²² used a 2D convolutional neural network to detect aneurysms and reported a sensitivity of >90% in a single-center study. Similarly, an open-source neural network has also been applied by using 2D MIPs or original image data.^{23,24} However, generalization of these studies requires further validation. The work by Ueda et al²⁵ subsequently improved the sophistication of a DL methodology with a sensitivity of 91% and 93% for the internal and external test datasets, respectively. The external dataset contained images from 4 separate institutions under different environments and MR imaging unit manufacturers, configurations, and field strengths; this feature highlights the rigor and general applicability of the model. However, the study did not have any cases negative for aneurysms. Furthermore, only 74 aneurysms and studies exclusively acquired on Siemens imaging systems were integrated in the external test dataset. Additionally, a high rate of FPs may potentially reduce the enthusiasm of radiologists for the use of this system if distinguishing true-positive aneurysms from FPs becomes too menial.

CTA images have been studied by combining a neural network segmentation model (the HeadXNet model) to augment diagnostic performance in the detection of aneurysms.²⁶ In this study, the clinicians showed significant increases in sensitivity, accuracy, and interrater agreement when they were augmented with the model. However, the lack of a reference standard and external data verification, as well as the focus only on nonruptured aneurysms of >3 mm, limited the generalization and further application of the model.

With respect to the detection of aneurysms, there is a general notion that CAD algorithms have the potential to shorten reading times and increase radiologists' performances in the laboratory and clinical environment.²⁷ Additionally, an AI program of aneurysms may benefit patients who undergo CTA as part of an acute ischemic stroke work-up because it may decrease the likelihood of an incidental aneurysm being undetected. However, to our knowledge, most studies presented so far lack an external reference standard for validation, such as DSA, so further studies are warranted.

AI in the Prediction of Intracranial Aneurysm Rupture Risk

Automated Morphologic Analysis. Identifying the high-risk morphologic features of saccular aneurysms is very important for rupture-risk stratification and treatment decision. Aneurysm size and shape are regarded as the most important criteria.⁵ In clinical practice, the size is routinely measured manually by physicians on 2D/3D projections. However, manual measurements have inherent limitations of subjectivity and inconsistency, which cause intra- and interobserver variations²⁸ and cannot capture the complex geometric features of aneurysms.²⁹ Researchers have introduced several computerized procedures to make morphology assessment more objective and consistent.³⁰⁻³² The detection of the neck plane is the key point for multiple subsequent operations. Larrabide et al³⁰ deterministically identified the aneurysm neck based on the topology analysis of the vasculature skeleton and the concepts of deformable cylinders. They can automatically isolate the sac of an aneurysm, reduce interobserver variability, and avoid the bias between the observers. Automatically derived geometric indices were often large, irrespective of segmentation method or operators.³¹

For rapid assessment in the clinical setting, Xiang et al³² devised an image-based vascular analysis toolkit named AView (<https://www.eng.buffalo.edu/Research/Hemo/AView.html>) to perform automatic computation of morphologic parameters. AView provided a relatively accurate measurement with an average size error of 0.56% and volume error of 2.1% morphologically.³³ This toolkit also enabled increased consistency in morphologic measurement among operators by 62% in size and 82% in neck diameter measurements, which could help potentially avoid inappropriate clinical decisions. In the real-world scenario, Rajabzadeh-Oghaz et al,³⁴ from the same group, tested the algorithm on 39 aneurysms and found that the computer-assisted 3D approach can lead to a more accurate and consistent determination of aneurysm size and neck diameter. Besides, DL methods such as the convolutional neural network model developed by Stember et al²³ can also be used to automatically analyze morphologic indices. However, there is much work to be done before routine clinical application of these technologies is realized.

Automated Calculation of Hemodynamics. Hemodynamics is currently deemed as an important factor for aneurysm formation and rupture risk.³⁵ Modern imaging modalities are adequate for the application of computational fluid dynamics modeling. However, complex procedures are time-consuming and demand substantial human interaction, resulting in limited application in real-time clinical practice, which requires automated tools to execute analysis. Seo et al³⁶ developed a highly automated method to execute a computational process with direct use of a voxelized contrast information from 3D angiograms to construct a level-set-based computational “mask” for a hemodynamic simulation. By testing the method in 7 patient-specific cases against the results of manual evaluation by an experienced neurosurgeon, they found that their proposed algorithm was capable of identifying the lesion and connected vessels for various types of aneurysms. The simulation results presented by the algorithm, which include the values and distribution of wall shear stress, were in line with previous computational studies.³⁷ However, this study was only hypothesis-generating and requires further refinement and validation. Considering that hemodynamic parameters are critical for the development and rupture risk, such approaches bode rather well for clinical utility due to their automation and diminishing need for human interaction.

AI-Based Prediction of Rupture Risk. An increasing number of unruptured aneurysms are detected with the growing use of advanced imaging techniques. However, we are now confronted with the dilemma of making clinical decisions regarding treatment of unruptured aneurysms, because the risk of treatment-related fatality is relatively high, while the rupture risk is low.^{5,6} Predicting rupture risk of aneurysms is challenging and ML is expected to mitigate this problem. Liu et al³⁸ adopted 17 parameters as inputs to a 2-layer feed-forward artificial neural network aimed at predicting the rupture status of anterior communicating artery aneurysms and found an excellent performance. However, this study included only 1 single-center population and used an imbalanced number of samples between ruptured ($n = 540$) and unruptured aneurysms ($n = 54$). The instability of aneurysms is considered a rupture risk. With this knowledge, Liu et al³⁹ applied radiomics tools to extract morphologic features to predict stability and found that flatness was the most important parameter; the area under the curve (AUC) in the testing set reached 0.729 when only flatness was used to predict aneurysm stability, implying the usefulness of radiomics-derived morphologic features for aneurysm rupture risk.

With the introduction of ML methods, it is interesting to understand the distinctive performances of different ML statistical learning approaches. Detmer et al⁴⁰ and Silva et al⁴¹ worked at predicting aneurysm rupture status. They trained several ML methods, including SVM and random forests classifiers. Detmer et al found that multilayer perceptron had the best performance with an AUC of 0.826 (95% CI, 0.768, 0.883) in the test set; important variables included aneurysm location, mean surface curvature, and maximum flow velocity. Silva et al found random forests to have the best performance. In their work, aneurysm location and size were the 2

features that contributed most significantly to the efficacy of the model. This difference may contribute to the uniqueness of input variants and candidate ML methods.

AI in the Prediction of Aneurysm Complications

Prediction of Complications of SAH. Delayed cerebral ischemia, vasospasm, and cerebral infarction are among the complications of aneurysm rupture; several studies have explored the applications of ML methods to predict at least one of them. Dumont et al⁴² developed a proof-of-concept artificial neural network prediction model of symptomatic cerebral vasospasm and found the artificial neural network-based model had a better predictive value (AUC of 0.960) than 2 multiple logistic regression models (AUC = 0.933 and 0.897) developed by Adams et al⁴³ and Qureshi et al,⁴⁴ respectively. Further validation provided an excellent performance in a markedly distinct geographic population setting of southern Arizona with a prospective use of the artificial neural network predictive model.⁴⁵ However, the artificial neural network did not incorporate the timing of symptomatic cerebral vasospasm onset and was not validated in a larger-scale population. Another study had similar findings: ML methods (SVM, random forests, and multilayer perceptron) have a higher performance than logistic regression models in the prediction of delayed cerebral ischemia.⁴⁶

Multiple-task AI has also been studied. Tanioka et al⁴⁷ used random forests to construct early prediction models of delayed cerebral ischemia, angiographic vasospasm, and cerebral infarction development with clinical variables and matricellular proteins at post-onset days 1–3. Three such proteins have been reported to be relevant to delayed cerebral ischemia: osteopontin, periostin, and galectin-3. The prediction accuracies of the 3 conditions were 95.1%, 78.1%, and 83.8%, respectively. The random forest models found that osteopontin and galectin-3 were among the top 3 most important variables. These novel studies in the assessment of complications of aneurysms have demonstrated excellent performances using ML methods.

Another interesting application is the use of clinical data and CT perfusion from hospital admissions⁴⁸ to predict outcomes of aneurysmal SAH. A random forest model was trained to predict dichotomized mRS (≤ 2 and > 2), and the accuracy was 84.4% in the training folds and 70.9% in the validation folds. However, this study had a small population size and therefore cannot be introduced into clinical practice to practically benefit those who have SAH.

Prediction of Treatment Outcomes. Besides aneurysmal SAH, the outcomes of aneurysm treatment have also been explored by ML. For example, the flow diverter has emerged in recent years as one of the endovascular treatments of aneurysms and is particularly suitable for treating wide-neck and intractable aneurysms with unusual morphologies. However, 25% of treated patients are at high risk for thromboembolism formation and aneurysm rerupture.⁴⁹ Paliwal et al¹¹ compared 4 supervised ML algorithms (logistic regression, SVM, K-nearest neighbor, and neural networks) to predict 6-month outcomes of flow diverter-treated aneurysms and found that neural network (AUC = 0.967) performed the best during training; G-SVM (Gaussian-SVM) and neural network had 90%

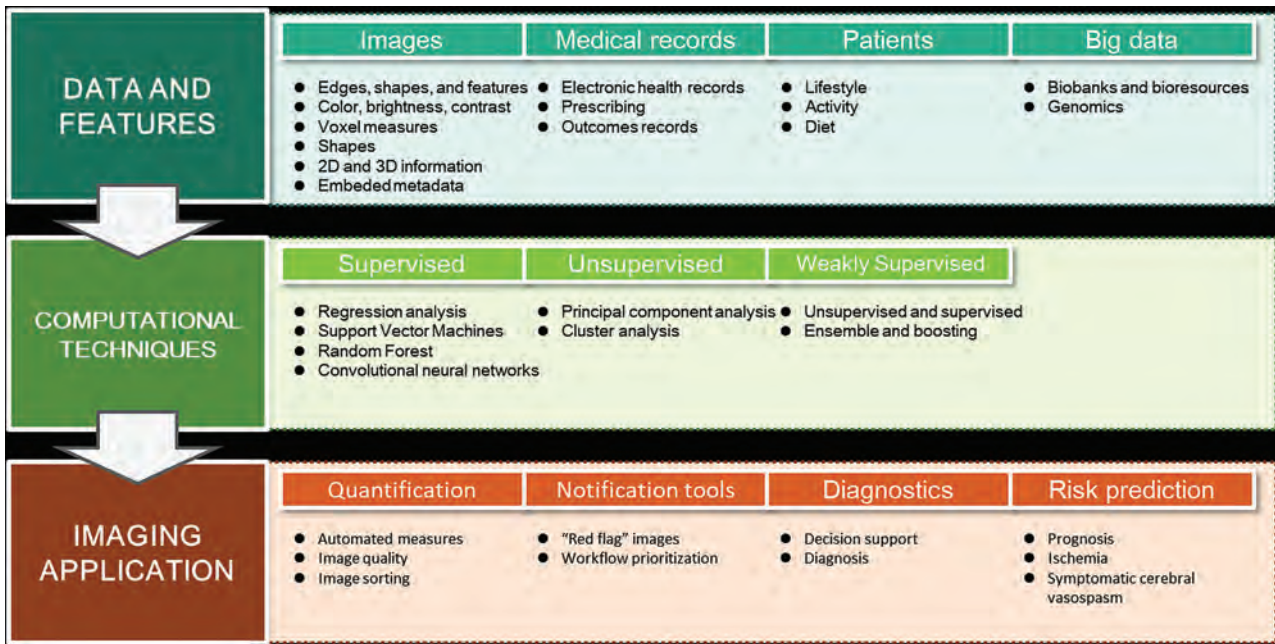


FIG 2. The starting point is high quality data—imaging findings are best contextualized with patients, medical records, and “big data.” Computational methods may be supervised, unsupervised, or combined. Imaging applications include quantification, notification tools, and diagnostic and risk predictions. Adapted with permission from Dey et al¹⁰ with partial revisions.

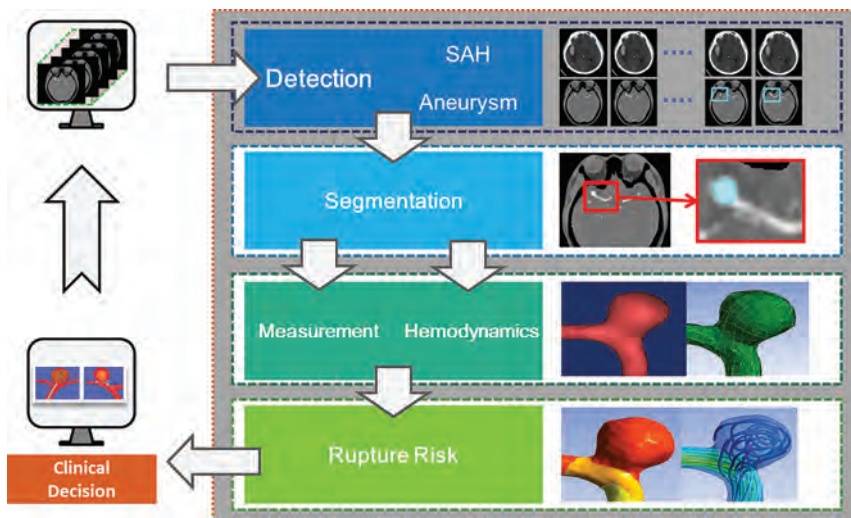


FIG 3. An ideal auto system for intelligent management of intracranial aneurysms. This auto AI system includes the episodes of aneurysm ranging from the detection of SAH and aneurysms to the automatic computation of hemodynamics, dimension index, and clinical decision system.

prediction accuracies in the testing cohort. Although a major concern is the absence of an external validation, it is imperative to develop models that help clinicians choose flow-diverter placement in the appropriate patients.

Limitations and Challenges of AI on Aneurysms

Many investigators have endeavored to develop more intelligent and automated methods to improve the process and streamline the management of aneurysms in clinical practice. Complete management of aneurysms includes detection, rupture risk,

complications prediction, treatment strategies selection, and risk of recurrence evaluation. AI has been involved in almost all consecutive steps; however, the results are not entirely satisfactory and have some limitations and challenges. First, a systematic review showed no better performance of ML compared with traditional logistic regression in predicting adverse clinical outcomes.⁵⁰ Model validation procedures are often not conducted or well-interpreted; thus, a fair comparison in the domain of real-world case studies is still urgently needed. Second, even though DL methods showed promising potential, there remains considerable debate about the time required to train DL.⁵¹ Cost-effectiveness assessment of the high expense of imaging data storage and use of graphics processing units should also

be considered. In addition, stakeholders may be responsible for undertaking cost-effectiveness analyses to determine the impact on health care economics, which requires large-scale feasibility studies to evaluate whether unintended consequences may be incurred following the widespread implementation of AI methods.^{52,53} Third, current datasets used for training and validation in aneurysm studies are often small, frequently from only 1 institution, and usually lack external validation within different populations, imaging devices, platforms, and institutions, resulting in algorithm overfitting.

Future Perspectives of AI in Intracranial Aneurysms

AI should have a great potential in the management of aneurysms in the future. Potential imaging-based AI applications (Fig 2) mainly contain 4 aspects: quantification, notification tools, diagnostics, and risk prediction for therapy.⁸ For aneurysm management, there are various opportunities for AI, including the following: 1) an automated and reliable prescreening triage system to allow radiologists and emergency physicians to shift their focus to patients at higher risk for adverse events; 2) automated detection and intelligent outcome prediction; 3) subsequent prediction of treatment strategies such as clipping, embolization, or follow-up; and 4) automated and intelligent detection of de novo aneurysm formation or recurrence after treatment and the prediction of rerupture risk.

Researchers should intensify their efforts toward the development of advanced DL algorithms to resolve complex problems, such as extracting information on inflammation of vessel walls from high-resolution vessel wall MR imaging, which has been a nascent area of research in recent years. Additionally, AI tools that can perform multiple tasks, instead of those directed at an isolated problem, are in need. Examples include algorithms that can automatically detect and classify the whole variety of cerebrovascular diseases, including multiple entities like aneurysms, AVMs, and Moyamoya disease. Advanced network structures such as convolutional residual networks, active learning, one-shot learning, and generative adversarial networks may help settle these issues.⁵⁴ These areas are newly emerging and require further investigation.

In our perspective, a successful AI tool for aneurysms is expected to be an integrated toolkit that can intelligently and simultaneously navigate multiple tasks, ranging from detection to prediction (Fig 3). In future work, comprehensive multimodality imaging is worth investigating and is expected to learn and exploit feature representation of images more effectively. In addition, human-in-the-loop AI solutions are quickly emerging concepts toward clinical implementation, which can improve the expert-model performance and act as a gatekeeper for clinical decisions.

Most recently published AI studies have not delineated robust validations of clinical performance and generalizability, including in the area of intracranial aneurysms. Kim et al⁵⁵ recommended 4 criteria for validating the clinical performance of AI algorithms in real-world practice; 1) the external validation must be obtained; 2) using a diagnostic cohort study; 3) arise from multiple institutions; and 4) be performed in a prospective manner. A successful AI tool for aneurysm management must be completely reliable in distinguishing true-positive cases with high confidence, which requires an exceedingly high number of annotated imaging studies, before we can expect widespread implementation in real-world practice.

CONCLUSIONS

Recent evidence shows that AI, especially deep learning, is rapidly becoming a promising aid in the management of aneurysm. AI is capable of detecting and evaluating rupture risk, triaging clinical therapy strategies, and predicting treatment outcomes. Although we have not quite yet reached the threshold needed for routine clinical application, we believe

that AI is capable of solving these issues in a patient-centric manner but will require advancing network structures and more sophisticated validation processes.

Disclosures: Zhao Shi—RELATED: Grant: Key Projects of the National Natural Science Foundation of China (81830057 for L.J.Z.)* U. Joseph Schoepf—UNRELATED: Other: Dr Schoepf has received institutional research support and/or honoraria for speaking and consulting from Astellas Pharma, Bayer, Bracco, Elucid Biomed, GE Healthcare, Guerbet, HeartFlow, and Siemens.* Xiuli Li—RELATED: Key Projects of the National Natural Science Foundation of China (81830057 for L.J.Z.)* Long Jiang Zhang—RELATED: Grant: National Key Research and Development Program of China; Key Projects of the National Natural Science Foundation of China, Comments: This work was supported by the National Key Research and Development Program of China (2017YFC0113400 for L.J.Z.) and Key Projects of the National Natural Science Foundation of China (81830057 for L.J.Z.)* *Money paid to the institution.

REFERENCES

1. Vlak MH, Algra A, Brandenburg R, et al. **Prevalence of unruptured intracranial aneurysms, with emphasis on sex, age, comorbidity, country, and time period: a systematic review and meta-analysis.** *Lancet Neurol* 2011;10:626–36 CrossRef Medline
2. Li MH, Chen SW, Li YD, et al. **Prevalence of unruptured cerebral aneurysms in Chinese adults aged 35 to 75 years: a cross-sectional study.** *Ann Intern Med* 2013;159:514–21 CrossRef Medline
3. Boland GW, Guimaraes AS, Mueller PR. **The radiologist's conundrum: benefits and costs of increasing CT capacity and utilization.** *Eur Radiol* 2009;19:9–11 CrossRef Medline
4. McDonald RJ, Schwartz KM, Eckel LJ, et al. **The effects of changes in utilization and technological advancements of cross sectional imaging on radiologist workload.** *Acad Radiol* 2015;22:1191–98 CrossRef Medline
5. Morita A, Kirino T, Hashi K, et al; UCAS Japan Investigators. **The natural course of unruptured cerebral aneurysms in a Japanese cohort.** *N Engl J Med* 2012;366:2474–82 CrossRef Medline
6. Naggara ON, Lecler A, Oppenheim C, et al. **Endovascular treatment of intracranial unruptured aneurysms: a systematic review of the literature on safety with emphasis on subgroup analyses.** *Radiology* 2012;263:828–35 CrossRef Medline
7. He J, Baxter SL, Xu J, et al. **The practical implementation of artificial intelligence technologies in medicine.** *Nat Med* 2019;25:30–36 CrossRef Medline
8. Zhou ZH. **A brief introduction to weakly supervised learning.** *Natl Sci Rev* 2018;5:45–53 CrossRef
9. LeCun Y, Bengio Y, Hinton G. **Deep learning.** *Nature* 2015;521:436–44 CrossRef Medline
10. Dey D, Slomka PJ, Leeson P, et al. **Artificial intelligence in cardiovascular imaging: JACC state-of-the-art review.** *J Am Coll Cardiol* 2019;73:1317–35 CrossRef Medline
11. Paliwal N, Jaiswal P, Tutino VM, et al. **Outcome prediction of intracranial aneurysm treatment by flow diverters using machine learning.** *Neurosurg Focus* 2018;45:E7 CrossRef Medline
12. Varble N, Tutino VM, Yu J, et al. **Shared and distinct rupture discriminants of small and large intracranial aneurysms.** *Stroke* 2018;49:856–64 CrossRef Medline
13. Litjens G, Kooi T, Bejnordi BE, et al. **A survey on deep learning in medical image analysis.** *Med Image Anal* 2017;42:60–88 CrossRef Medline
14. Bechan RS, van Rooij SB, Sprengers ME, et al. **CT angiography versus 3D rotational angiography in patients with subarachnoid hemorrhage.** *Neuroradiology* 2015;57:1239–46 CrossRef Medline
15. Schalekamp S, van Ginneken B, Koedam E, et al. **Computer-aided detection improves detection of pulmonary nodules in chest radiographs beyond the support by bone-suppressed images.** *Radiology* 2014;272:252–61 CrossRef Medline
16. De Fauw J, Ledsam JR, Romera-Paredes B, et al. **Clinically applicable deep learning for diagnosis and referral in retinal disease.** *Nat Med* 2018;24:1342–50 CrossRef Medline

17. Yang X, Blezek DJ, Cheng LTE, et al. **Computer-aided detection of intracranial aneurysms in MR angiography.** *J Digit Imaging* 2011;24:86–95 CrossRef Medline
18. Arimura H, Li Q, Korogi Y, et al. **Automated computerized scheme for detection of unruptured intracranial aneurysms in three dimensional magnetic resonance angiography.** *Acad Radiol* 2004;11:1093–1104 CrossRef Medline
19. Hirai T, Korogi Y, Arimura H, et al. **Intracranial aneurysms at MR angiography: effect of computer-aided diagnosis on radiologists' detection performance.** *Radiology* 2005;237:605–10 CrossRef Medline
20. Kakeda S, Korogi Y, Arimura H, et al. **Diagnostic accuracy and reading time to detect intracranial aneurysms on MR angiography using a computer-aided diagnosis system.** *AJR Am J Roentgenol* 2008;190:459–65 CrossRef Medline
21. Jin Z, Arimura H, Kakeda S, et al. **An ellipsoid convex enhancement filter for detection of asymptomatic intracranial aneurysm candidates in CAD frameworks.** *Med Phys* 2016;43:951–60 CrossRef Medline
22. Nakao T, Hanaoka S, Nomura Y, et al. **Deep neural network-based computer-assisted detection of cerebral aneurysms in MR angiography.** *J Magn Reson Imaging* 2018;47:948–53 CrossRef Medline
23. Stember JN, Chang P, Stember DM, et al. **Convolutional neural networks for the detection and measurement of cerebral aneurysms on magnetic resonance angiography.** *J Digit Imaging* 2019;32:808–15 CrossRef Medline
24. Sichtermann T, Faron A, Sijben R, et al. **Deep learning-based detection of intracranial aneurysms in 3D TOF-MRA.** *AJNR Am J Neuroradiol* 2019;40:25–32 CrossRef Medline
25. Ueda D, Yamamoto A, Nishimori M, et al. **Deep learning for MR angiography: Automated detection of cerebral aneurysms.** *Radiology* 2019;290:187–94 CrossRef Medline
26. Park A, Chute C, Rajpurkar P, et al. **Deep learning-assisted diagnosis of cerebral aneurysms using the HeadXNet model.** *JAMA Netw Open* 2019;2:e195600 CrossRef Medline
27. Miki S, Hayashi N, Masutani Y, et al. **Computer-assisted detection of cerebral aneurysms in MR angiography in a routine image-reading environment: effects on diagnosis by radiologists.** *AJNR Am J Neuroradiol* 2016;37:1038–43 CrossRef Medline
28. Maldaner N, Stienen MN, Bijlenga P, et al. **Interrater agreement in the radiologic characterization of ruptured intracranial aneurysms based on computed tomography angiography.** *World Neurosurg* 2017;103:876–82 CrossRef Medline
29. Suh SH, Cloft HJ, Huston J, et al. **Interobserver variability of aneurysm morphology: discrimination of the daughter sac.** *J Neurointerv Surg* 2016;8:38–41 CrossRef Medline
30. Larrabide I, Cruz Villa-Urriol M, Cárdenas R, et al. **Three-dimensional morphological analysis of intracranial aneurysms: a fully automated method for aneurysm sac isolation and quantification.** *Med Phys* 2011;38:2439–49 CrossRef Medline
31. Piccinelli M, Steinman DA, Hoi Y, et al. **Automatic neck plane detection and 3D geometric characterization of aneurysmal sacs.** *Ann Biomed Eng* 2012;40:2188–2211 CrossRef Medline
32. Xiang J, Antiga L, Varble N, et al. **AView: An image-based clinical computational tool for intracranial aneurysm flow visualization and clinical management.** *Ann Biomed Eng* 2016;44:1085–96 CrossRef Medline
33. Rajabzadeh-Oghaz H, Varble N, Davies JM, et al. **Computer-assisted adjuncts for aneurysmal morphology assessment: toward more precise and accurate approaches.** *Proc SPIE Int Soc Opt Eng* 2017;10134 CrossRef Medline
34. Rajabzadeh-Oghaz H, Varble N, Shallwani H, et al. **Computer-assisted 3D morphology evaluation of intracranial aneurysms.** *World Neurosurg* 2018;119:e541–50 CrossRef Medline
35. Can A, Du R. **Association of hemodynamic factors with intracranial aneurysm formation and rupture: systematic review and meta-analysis.** *Neurosurgery* 2016;78:510–20 CrossRef Medline
36. Seo JH, Eslami P, Caplan J, et al. **A highly automated computational method for modeling of intracranial aneurysm hemodynamics.** *Front Physiol* 2018;9:681 CrossRef Medline
37. Cebral JR, Vazquez M, Sforza DM, et al. **Analysis of hemodynamics and wall mechanics at sites of cerebral aneurysm rupture.** *J Neurointerv Surg* 2015;7:530–36 CrossRef Medline
38. Liu J, Chen Y, Lan L, et al. **Prediction of rupture risk in anterior communicating artery aneurysms with a feed-forward artificial neural network.** *Eur Radiology* 2018;28:3268–75 CrossRef Medline
39. Liu Q, Jiang P, Jiang Y, et al. **Prediction of aneurysm stability using a machine learning model based on PyRadiomics-derived morphological features.** *Stroke* 2019;50:2314–21 CrossRef Medline
40. Detmer FJ, Lücke D, Mut F, et al. **Comparison of statistical learning approaches for cerebral aneurysm rupture assessment.** *Int J Comput Assist Radiology Surg* 2019;15:141–50 CrossRef Medline
41. Silva MA, Patel J, Kavouridis V, et al. **Machine learning models can detect aneurysm rupture and identify clinical features associated with rupture.** *World Neurosurg* 2019;131:e46–51 CrossRef Medline
42. Dumont TM, Rughani AI, Tranmer BI. **Prediction of symptomatic cerebral vasospasm after aneurysmal subarachnoid hemorrhage with an artificial neural network: feasibility and comparison with logistic regression models.** *World Neurosurg* 2011;75:57–63 CrossRef Medline
43. Adams HP Jr, Kassell NF, Torner JC, et al. **Predicting cerebral ischemia after aneurysmal subarachnoid hemorrhage: influences of clinical condition, CT results, and antifibrinolytic therapy: a report of the cooperative aneurysm study.** *Neurology* 1987;37:1586–91 CrossRef Medline
44. Qureshi AI, Sung GY, Razumovsky AY, et al. **Early identification of patients at risk for symptomatic vasospasm after aneurysmal subarachnoid hemorrhage.** *Crit Care Med* 2000;28:984–90 CrossRef Medline
45. Dumont TM. **Prospective assessment of a symptomatic cerebral vasospasm predictive neural network model.** *World Neurosurg* 2016;94:126–30 CrossRef Medline
46. Ramos LA, van der Steen WE, Sales Barros R, et al. **Machine learning improves prediction of delayed cerebral ischemia in patients with subarachnoid hemorrhage.** *J Neurointerv Surg* 2019;11:497–502 CrossRef Medline
47. Tanioka S, Ishida F, Nakano F, et al. **Machine learning analysis of matricellular proteins and clinical variables for early prediction of delayed cerebral ischemia after aneurysmal subarachnoid hemorrhage.** *Mol Neurobiol* 2019;56:7128–35 CrossRef Medline
48. Rubbert C, Patil KR, Beseoglu K, et al. **Prediction of outcome after aneurysmal subarachnoid haemorrhage using data from patient admission.** *Eur Radiol* 2018;28:4949–58 CrossRef Medline
49. Brinjikji W, Murad MH, Lanzino G, et al. **Endovascular treatment of intracranial aneurysms with flow diverters: a meta-analysis.** *Stroke* 2013;44:442–47 CrossRef Medline
50. Christodoulou E, Ma J, Collins GS, et al. **A systematic review shows no performance benefit of machine learning over logistic regression for clinical prediction models.** *J Clin Epidemiol* 2019;110:12–22 CrossRef Medline
51. Lee JG, Jun S, Cho YW, et al. **Deep learning in medical imaging: general overview.** *Korean J Radiology* 2017;18:570–84 CrossRef Medline
52. Retson TA, Besser AH, Sall S, et al. **Machine learning and deep neural networks in thoracic and cardiovascular imaging.** *J Thorac Imaging* 2019;34:192–201 CrossRef Medline
53. Morris MA, Saboury B, Burkett B, et al. **Reinventing radiology: big data and the future of medical imaging.** *J Thorac Imaging* 2018;33:4–16 CrossRef Medline
54. Hesamian MH, Jia W, He X, et al. **Deep learning techniques for medical image segmentation: achievements and challenges.** *J Digit Imaging* 2019;32:582–96 CrossRef Medline
55. Kim DW, Jang HY, Kim KW, et al. **Design characteristics of studies reporting the performance of artificial intelligence algorithms for diagnostic analysis of medical images: results from recently published papers.** *Korean J Radiol* 2019;20:405–10 CrossRef Medline

Carotid Vessel Wall Imaging on CTA

 H. Baradaran and  A. Gupta



ABSTRACT

SUMMARY: Vessel wall imaging has been increasingly used to characterize plaque beyond luminal narrowing to identify patients who may be at the highest risk of cerebrovascular ischemia. Although detailed plaque information can be obtained from many imaging modalities, CTA is particularly appealing for carotid plaque imaging due to its relatively low cost, wide availability, operator independence, and ability to discern high-risk features. The present Review Article describes the current understanding of plaque characteristics on CTA by describing commonly encountered plaque features, including calcified and soft plaque, surface irregularities, neovascularization, and inflammation. The goal of this Review Article was to provide a more robust understanding of clinically relevant plaque features detectable on routine CTA of the carotid arteries.

ABBREVIATIONS: IPH = intraplaque hemorrhage; LRNC = lipid-rich necrotic core

Recent advances in vessel wall imaging have spurred a paradigm shift in the evaluation of carotid plaque. Despite decades of using a degree of luminal stenosis as the primary determinant of treatment for patients with carotid artery stenosis, there has been a recent trend toward adopting advanced imaging techniques to provide a more complete plaque evaluation for more accurate risk assessment. Much of the literature of vessel wall imaging has centered on MR imaging because of its impressive contrast resolution and high sensitivity for identifying high-risk plaque features.^{1,2} In addition to MR imaging, contrast-enhanced sonography is also a powerful tool for evaluating carotid plaque vulnerability.³⁻⁵ CTA is often overlooked as a method for providing detailed evaluation of plaque characteristics, and it has certain benefits in terms of accessibility and ease of use in clinical workflow not present with multisequence MR imaging characterization of carotid plaque. Although CTA does not have the same prospective evidence as MR imaging and ultrasound for predicting future cerebrovascular disease,

CTA does provide valuable information regarding plaque characteristics that should not be ignored.

CTA of the head and neck is a commonly acquired examination to evaluate vessel patency in the setting of cerebrovascular ischemia, especially in the work-up of acute ischemic infarction. In addition to providing accurate information regarding the degree of luminal stenosis, CTA examinations can also provide rich detail regarding plaque morphology and features, given their superb spatial resolution. While identifying thrombosis and the degree of stenosis on CTA is necessary in selecting patients for intervention, other plaque features evident on CTA are also valuable in determining the risk of stroke or TIA and in aiding management decisions. In this review, we will describe technical considerations when performing CTA and then provide detailed descriptions of individual plaque characteristics that can be evaluated on CTA. For each plaque feature, we will summarize the existing literature, associating each feature with stroke risk. We will also include practical considerations and comparisons with other imaging modalities.

Clinical Background

Extracranial atherosclerosis is an important contributor to stroke, accounting for 15%–20% of all ischemic strokes.^{6,7} With improvement in medical management for treating patients with carotid artery stenosis, the annual risk of stroke has decreased in asymptomatic patients to ~1%,⁸ which has made the need to appropriately risk-stratify patients even more critical. Traditionally, imaging risk assessment has been based on the degree of arterial narrowing as measured by the NASCET criteria, which have been used as the basis for randomized

Received September 5, 2019; accepted after revision December 17.

From the Department of Radiology (H.B.), University of Utah, Salt Lake City, Utah; and Department of Radiology (A.G.), Weill Cornell Medicine, New York, New York.

Hediyeh Baradaran is supported by a grant from the Association of University Radiologists—GE Radiology Research Academic Fellowship Award. Ajay Gupta is supported, in part, by National Institutes of Health grants R01HL144541 and R21HL145427.

Please address correspondence to Hediyeh Baradaran, MD, Department of Radiology, University of Utah, 30N 1900 E, Room #1A71, Salt Lake City, UT 84135; e-mail: hediyeh.baradaran@hsc.utah.edu

 Indicates open access to non-subscribers at www.ajnr.org

<http://dx.doi.org/10.3174/ajnr.A6403>

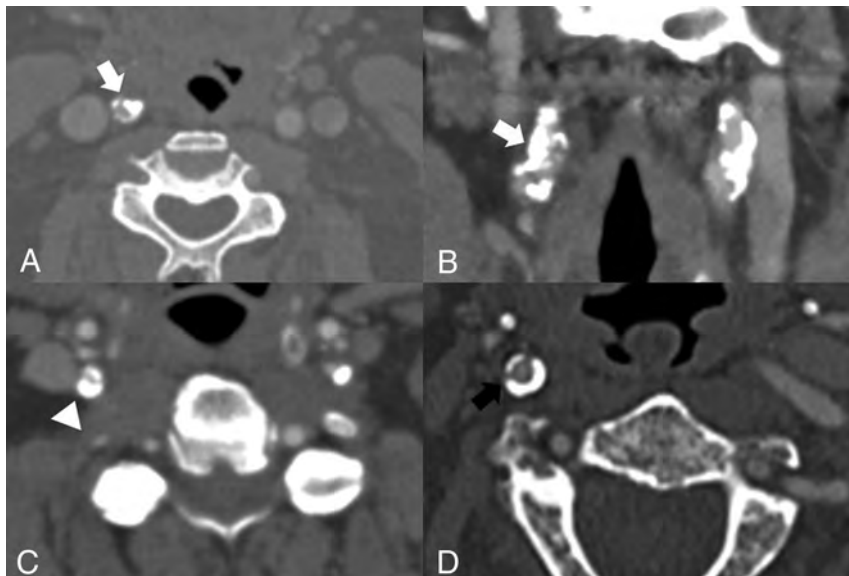


FIG 1. Examples of densely calcified plaques. A and B, A 73-year-old asymptomatic man with a densely calcific plaque resulting in 70% stenosis of the proximal right ICA by the NASCET criteria (white arrows). Note the relative lack of soft or fibrofatty plaque. C, A 50-year-old man presenting with right-sided weakness found to have left MCA vascular territory infarction and with incidental note of severe (approximately 80%) stenosis of the proximal right ICA secondary to a densely calcified plaque (arrowhead). Note the presence of a calcified plaque in the left ICA. Additional plaque was noted more proximally in the left ICA (not shown). D, An asymptomatic 81-year-old man found to have circumferential densely calcified plaque around his proximal right ICA (black arrow), with approximately 40% stenosis by the NASCET criteria.

clinical trials and for many stroke classification schemes.⁹⁻¹⁵ Recently, our understanding of the contributions of plaque features to cerebrovascular ischemia has altered how we evaluate carotid plaque. Infarctions secondary to carotid disease are thought to be caused by not only the flow-reduction from stenotic plaque but also artery-to-artery emboli occurring after fibrous cap rupture.¹⁶ We have learned that the degree of luminal stenosis does not necessarily correlate with the volume of plaque,¹⁷⁻¹⁹ that many plaque features besides luminal stenosis can directly contribute to ischemia, and that these high-risk features can lead to ischemic symptoms regardless of the degree of stenosis.²⁰⁻²³ The disconnect between stenosis severity and stroke risk is an area of active investigation, especially in plaques causing <50% stenosis, which are increasingly being considered as a potential cause of embolic strokes that are otherwise of uncertain etiology.²⁴⁻²⁶

Because of these recent gains in understanding, our attention is being turned to the carotid plaque itself rather than the lumen alone. The American Heart Association has rigorously defined carotid plaque on histopathology, ranging from type I, the most stable, up to type VI, the most vulnerable.²⁷ When performing any type of plaque imaging, we seek to identify imaging correlates to these plaque features. Although 3T MR imaging is often favored when evaluating high-risk carotid plaque, many easily identifiable plaque features can be depicted on CTA and have been histopathologically validated as markers of high-risk plaque.²⁸⁻³²

Technique

CTA is one of the most commonly acquired imaging examinations to accurately evaluate the degree of luminal narrowing. It

has a very high sensitivity (98%), positive predictive value (93%), and inter-operator reliability in evaluating vessel patency and luminal narrowing compared with DSA.³³ One benefit of using CTA for plaque evaluation is the relative standardization of the imaging technique across platforms and institutions.

There are 2 main CT techniques for evaluating plaque characteristics: the more commonly encountered MDCTA and the newer dual-source CT. CTAs are generally acquired after the intravenous administration of nonionic iodinated contrast through a peripheral IV using a power injector with a 4-mL/s flow rate and often using bolus-tracking software. Helical mode CT scanning is then generally performed with a multi-detector scanner (at least 16-detector row but ideally ≥ 64 -detector row) from the aortic arch to the C1 ring with submillimeter (frequently 0.625-mm) resolution. Multiplanar reconstructions in all planes are performed to fully evaluate the vessels and to properly account for inherent vessel tortuosity. MDCTA

of the carotid arteries can be rapidly acquired and is frequently used when screening patients presenting with cerebrovascular ischemic symptoms in the acute setting. For the plaque features described in this article, no postprocessing is necessary, allowing relatively rapid interpretation. Despite these clear benefits, the 2 main limitations for CTA are radiation exposure and the need to inject intravenous iodinated contrast. Another drawback to traditional MDCTA is the difficulty in differentiating calcified plaque from luminal contrast material due to their similar attenuation values. Additional considerations are that compared with ultrasound, CTA examinations are less cost-effective and are limited in the evaluation of vessel hemodynamics.

Dual-source CT can also be used when evaluating carotid plaque on CTA. Dual-source CT uses 2 different sources of x-rays at different kilovolts. By means of postprocessing software taking <10 minutes, features of specific densities such as calcified plaque or bone can be accurately segmented or subtracted to allow differentiation between the luminal iodinated contrast and adjacent calcified plaque. While this method has been increasingly studied,³⁴ it is not as commonly available and used in acute settings.

Relatively Lower Risk Features

Plaque Calcification. The most commonly encountered lower risk feature of plaque is calcification. Plaque calcification is defined as a plaque with a Hounsfield unit $> \sim 130$ (Fig 1 and Table). Plaque calcification is most often detected visually on CTA by increasing the window width, though discriminating between calcified plaque and luminal contrast can sometimes be difficult. Calcified plaques, when detected on sonography, have

Standard definitions of plaque features

Plaque Characteristic	Imaging Definition	Histopathologic Correlate
Calcified plaque	Plaque with increased attenuation of >130 HU	Plaque calcification
Soft plaque	Low-attenuation plaque, around 40–50 HU	Intraplaque hemorrhage and lipid-rich necrotic core
Plaque ulceration	Extension of contrast material beyond the vascular lumen of the plaque, usually of at least 1 mm	Plaque surface irregularity and ulceration
Total plaque thickness	Linear measurement of greatest axial dimension of plaque	Plaque thickness
Carotid plaque enhancement	Enhancement of plaque after administration of contrast	Plaque neovascularity

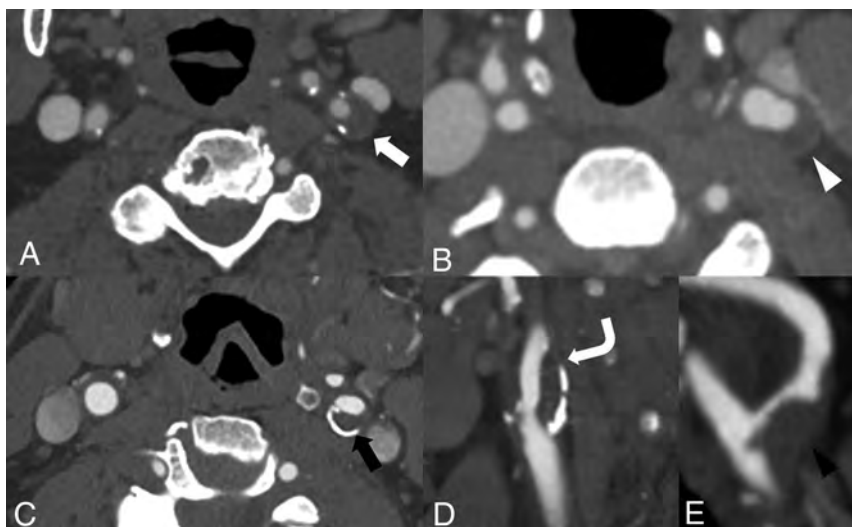


FIG 2. Soft plaque. *A*, 68-year-old man with a left-sided visual deficit found to have a large predominantly soft plaque (*white arrow*) in the proximal left ICA without significant stenosis by the NASCET criteria. *B*, A 74-year-old woman with right-sided weakness with a predominantly soft plaque (*white arrowhead*) at the left carotid bifurcation and proximal left ICA, again without significant stenosis by the NASCET criteria. *C*, An 82-year-old man with a large soft plaque with peripheral calcifications (*black arrow*) in the proximal left ICA with <50% stenosis by the NASCET criteria. *D*, Sagittal reconstruction of the same patient as in *C* demonstrates a large soft plaque component (*curved arrow*) extending throughout the proximal left ICA. *E*, Sagittal reconstruction demonstrates a large, irregular soft plaque narrowing the proximal right ICA (*black arrowhead*) of a 71-year-old man.

been found to be less frequently associated with ischemic events than noncalcified plaques.³⁵ A systematic review and meta-analysis of 7 studies found a negative association between the presence of calcified plaque on CTA and downstream cerebrovascular ischemic symptoms,³⁶ indicating that calcified plaques are less frequently associated with cerebrovascular ischemia. An additional systematic review also found that symptomatic plaques had less calcification than asymptomatic carotid plaques.³⁷ Additionally, some studies have found that the ratio or thickness of calcified plaque is important. One study has shown that if >45% of the plaque is calcified, the patient is more likely to be asymptomatic.³⁸ Furthermore, other studies have shown that each 1-mm increase in calcified plaque decreased the odds of having had a prior ipsilateral stroke or TIA and that those with densely calcified plaques were less likely to have symptomatic disease.^{20,21}

The lack of association between densely calcified plaque and ipsilateral stroke risk is not fully understood. Calcified plaques may decrease the fibrous cap inflammation and, in doing so, provide additional mechanical stability to the plaque surface. These features may prevent thrombus aggregation, thereby decreasing

the likelihood of emboli originating from the plaque.³⁹ Most interesting, one study found that patients on statins were more likely to develop calcified plaques than those not on statins.⁴⁰ Although we frequently encounter densely calcified plaques, which may cause a significant degree of luminal narrowing, the presence and degree of calcification may confer relatively less risk than noncalcified plaque.

Relatively Higher Risk Features

Soft Plaque. The most common high-risk feature of plaque is the so-called “soft” or “fibrofatty” plaque, which reflects a combination of intraplaque hemorrhage (IPH), lipid-rich necrotic core (LRNC), and fibrous elements. IPH and LRNC are 2 plaque features strongly associated with plaque vulnerability and an increased risk of stroke.^{35,41–43} Soft plaque is plaque with a low attenuation, with a median attenuation of around 40–50 HU but ranging around 16–90 HU (Fig 2 and Table). Soft plaque can be seen alone or in association with calcified plaque. When soft plaque is present on the luminal border with surrounding, peripheral calcification, it is thought to be a marker of high risk and is strongly associated with IPH on MR imaging.⁴⁴ It can be difficult to differentiate IPH and LRNC when evaluating plaque visually on CTA, but IPH is thought to have lower Hounsfield units^{32,45,46} than LRNC and fibrous elements with a mean Hounsfield units of 18 compared with LRNC (mean, 63 HU) and fibrous tissue (mean, 93 HU).⁴⁷ In clinical practice, these small differences in Hounsfield units are challenging to detect accurately. Soft plaque, whether it represents IPH or LRNC, is itself a high-risk feature of plaque, so accurate discrimination between exact histologic elements in the plaque may not be essential in acknowledging the increased risk. There is high interobserver agreement in identifying large plaque hemorrhage or areas of low-density lipid cores on CTA.^{29,46} A systematic review and meta-analysis of 6 studies with >1800 arteries found that having soft plaque increases the risk of ipsilateral cerebrovascular ischemia by almost 3 times, regardless of the degree of carotid stenosis.³⁶ As opposed to calcified

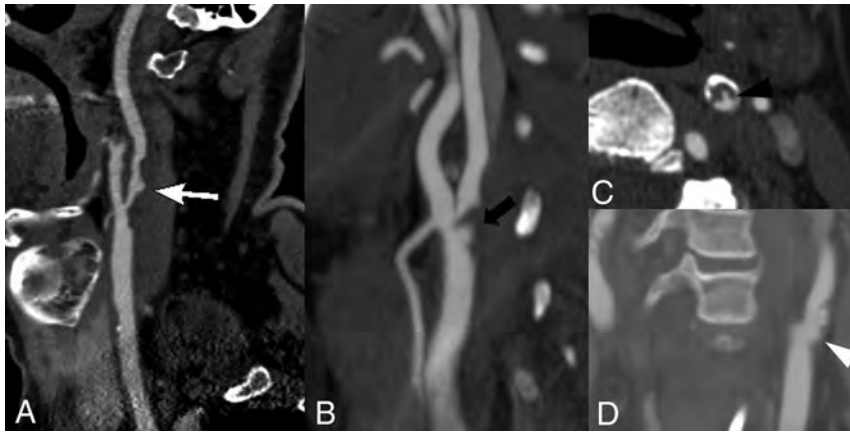


FIG 3. Plaque surface morphology and ulceration. *A*, A 69-year-old woman with a large soft plaque with an irregular surface and focal plaque ulceration (*white arrow*) with the plaque narrowing the proximal left ICA. *B*, A 62-year-old man with focal soft plaque at the right carotid bifurcation and proximal ICA with a large plaque ulceration (*black arrow*). *C*, A 73-year-old man with a predominant soft plaque with peripheral calcification narrowing the left ICA with focal plaque ulceration (*black arrowhead*) extending into the soft plaque. *D*, A 67-year-old woman with irregular, ulcerated plaque (*white arrowhead*) best seen on the coronal reconstruction. There is no significant associated luminal narrowing with this irregular, ulcerated plaque.

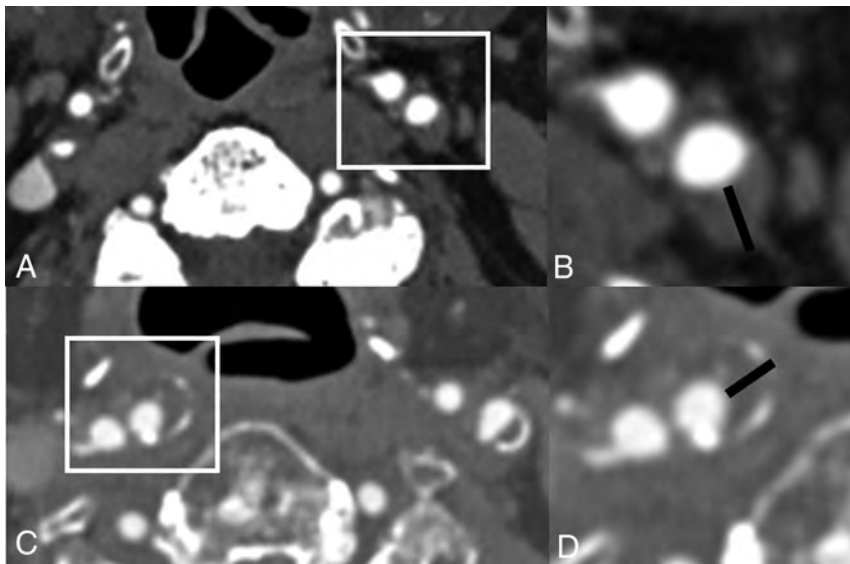


FIG 4. Plaque thickness measurements. *A* and *B*, A 78-year-old man with predominantly soft plaque without significant narrowing of the proximal left ICA, however, with a large soft plaque component measuring up to 5mm in thickness. Despite the lack of significant narrowing, the thickness of the plaque increases the risk of ipsilateral cerebrovascular ischemia. *C* and *D*, An 84-year-old man with a large predominantly soft plaque with peripheral calcifications without significant stenosis by the NASCET criteria but with total plaque thickness of 4mm, again increasing the risk despite the lack of significant stenosis.

plaque, having an increased soft plaque thickness or an increased ratio of soft plaque increases the risk of ipsilateral cerebrovascular ischemia.^{20,21,28}

Overall Plaque Thickness. Beyond individual plaque components, the overall thickness of carotid artery plaque, which is easily quantifiable on CTA, is associated with plaque vulnerability. A simple linear measurement of the greatest plaque

thickness can be a strong discriminator in identifying high-risk plaque (Fig 3), even better than the degree of stenosis.⁴⁸ Studies have shown that greater overall plaque thickness is associated with cerebrovascular ischemic symptoms, even in patients with strokes of an undetermined source.⁴⁸⁻⁵¹ While an exact threshold of total plaque thickness to determine increased plaque vulnerability has not been established, it may be in the 2.5- to 3-mm thickness range.⁴⁸⁻⁵⁰ This association between increasing plaque thickness and increased cerebrovascular ischemia remains, regardless of the degree of luminal narrowing.

Plaque Surface Morphology. Plaque surface irregularity is an important high-risk feature to identify because plaque rupture leading to thromboembolism is considered a critical step in the development of thromboembolic stroke.^{16,52} Plaque ulceration on any imaging technique is strongly associated with ischemic strokes, with hazard ratios ranging from 1.2 to 7.7.⁵³⁻⁵⁸ CTA can accurately differentiate smooth, irregular, and ulcerated surfaces and can detect ulceration with high accuracy (specificity, 99%; sensitivity, 94%).⁵⁹ Plaque ulceration on CT is described somewhat variably across studies but, in general, involves extension of contrast material beyond the vascular lumen of the plaque, usually of at least 1 mm. Sagittal and coronal reformations can be very helpful in assessing plaque ulceration (Fig 4). A systematic review and meta-analysis of 2883 arteries found that the presence of plaque ulceration increased the likelihood of ipsilateral cerebrovascular ischemia 2.2 times.³⁶ One of the limitations in evaluating plaque ulceration is the similarity of the attenuation of calcified plaque and luminal contrast material, which can make the detection of ulceration difficult.

Plaque ulceration is thought to increase the risk of ischemia because the ulceration exposes the inner plaque components to the flowing blood within the vessel, increasing the probability of thromboembolic events. In addition to being a high-risk feature, plaque ulceration is also associated with an increased degree of stenosis,⁶⁰ increased lipid and overall plaque volume,⁶¹ and decreased volume of plaque calcifications.⁶²

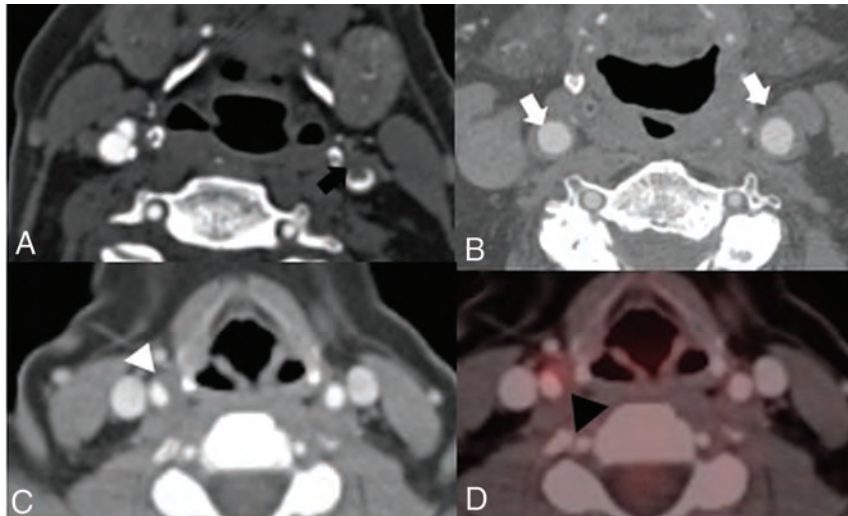


FIG 5. Plaque inflammation. *A*, An 81-year-old man presenting with left MCA territory infarction with a large soft plaque (*black arrow*) in the distal left common carotid artery with associated intraluminal thrombus. *B*, A 67-year-old man with diffuse inflammatory thickening of the distal common carotid artery walls (*white arrows*). *C* and *D*, A 54-year-old woman with mucinous cystadenoma who had a contrast-enhanced PET/CT demonstrating a large eccentric soft plaque in the distal right common carotid artery (*white arrowhead*) with associated increased FDG avidity with a maximum standard uptake value of 6.3 (*black arrowhead*).

Neovascularization and Inflammation. Another feature indicating plaque vulnerability is inflammation and intraplaque neovascularization (Fig 5). Histopathologic studies have found an association between macrophage infiltration, plaque rupture, and ischemic symptoms⁶³ and have confirmed that inflammatory cells accumulate with plaques.⁶⁴ Additionally, studies have shown that neovessels can be seen in carotid plaques, are associated with the degree of inflammation, and increase the risk of IPH.^{65,66} Translating this histopathologic understanding into detectable findings on routine CTA is not as straightforward. One of the imaging correlates to plaque neovascularity and inflammation is carotid plaque enhancement, which has been shown to be associated histologically with neovascularization on CTA⁶⁷ and MR imaging.⁶⁸ Adventitial vasa vasorum and intraplaque neovascularization are known high-risk markers for carotid plaque inflammation and can be detected on contrast-enhanced ultrasound.³⁻⁵ Additionally, arterial wall enhancement has been shown to be associated with symptomatology.^{69,70} The difficulty in evaluating this feature routinely on CTA is that obtaining both pre- and postcontrast imaging of the carotid artery on CT is rarely performed in standard clinical practice. Other studies have shown that increased attenuation in the perivascular fat around the carotid arteries, indicative of surrounding inflammation, is associated with cerebrovascular ischemic symptoms.⁷¹ In general, plaque inflammation is likely best detected using other imaging modalities, including molecular imaging studies⁷² and contrast-enhanced ultrasound,³⁻⁵ with a more limited role for routine CTA.

Future Directions

While there is strong evidence that the presence of specific plaque characteristics on routine CTA imaging is associated with

increased recent cerebrovascular ischemic symptoms, including in patients with strokes, that would otherwise be classified as “cryptogenic,” there are limited prospective data using CTA in asymptomatic individuals who are then followed across time to a first-time cerebrovascular ischemic event. Many prospective studies on histopathologically verified high-risk features on MR imaging and ultrasound plaque have been performed or are being performed⁷³⁻⁷⁵ and have shown an increased risk of future or recurrent cerebrovascular ischemia, but similar prospective studies have not been performed using CTA as the primary imaging technique. Prospective studies with standardized protocols and plaque characteristic definitions to determine the predictive abilities of these plaque features on CTA are certainly warranted. Future studies should also more fully evaluate the role of CTA in monitoring the

response of plaque characteristics to medical therapy, especially in light of various novel treatments that allow significant intensification of medical therapy as a potential alternative to revascularization procedures.

CONCLUSIONS

Routine CTA can provide a detailed assessment of plaque vulnerability, beyond the standard degree of luminal stenosis. Many plaque features can be assessed on routinely acquired CTA examinations without additional postprocessing or excessive delay in interpretation. There is strong evidence showing an association with the described plaque features and cerebrovascular ischemic symptoms. Accurate recognition of these plaque features may assist in appropriate risk stratification.

Disclosures: Hediye Baradaran—*RELATED: Grant:* Association of University Radiologists—GE Radiology Research Academic Fellowship. Money paid to the institution.

REFERENCES

1. Saba L, Yuan C, Hatsukami TS, et al; Vessel Wall Imaging Study Group of the American Society of Neuroradiology. **Carotid artery wall imaging: perspective and guidelines from the ASNRS Vessel Wall Imaging Study Group and Expert Consensus Recommendations of the American Society of Neuroradiology.** *AJNR Am J Neuroradiol* 2018;39:E9–31 CrossRef Medline
2. Brinjikji W, Huston J, Rabinstein AA, et al. **Contemporary carotid imaging: from degree of stenosis to plaque vulnerability.** *J Neurosurg* 2016;124:27–42 CrossRef Medline
3. Staub D, Partovi S, Schinkel AF, et al. **Correlation of carotid artery atherosclerotic lesion echogenicity and severity at standard US with intraplaque neovascularization detected at contrast-enhanced US.** *Radiology* 2011;258:618–26 CrossRef Medline

4. Staub D, Partovi S, Imfeld S, et al. **Novel applications of contrast-enhanced ultrasound imaging in vascular medicine.** *Vasa* 2013; 42:17–31 CrossRef Medline
5. Partovi S, Loebe M, Aschwanden M, et al. **Contrast-enhanced ultrasound for assessing carotid atherosclerotic plaque lesions.** *AJR Am J Roentgenol* 2012;198:W13–19 CrossRef Medline
6. Sacco RL, Kargman DE, Gu Q, et al. **Race-ethnicity and determinants of intracranial atherosclerotic cerebral infarction.** *Stroke* 1995;26:14–20 CrossRef Medline
7. Wityk RJ, Lehman D, Klag M, et al. **Race and sex differences in the distribution of cerebral atherosclerosis.** *Stroke* 1996;27:1974–80 CrossRef Medline
8. Raman G, Moororthy D, Hadar N, et al. **Management strategies for asymptomatic carotid stenosis: a systematic review and meta-analysis.** *Ann Intern Med* 2013;158:676–85 CrossRef Medline
9. Adams HP, Bendixen BH, Kappelle LJ, et al. **Classification of subtype of acute ischemic stroke: definitions for use in a multicenter clinical trial—Toast. Trial of Org 10172 in Acute Stroke Treatment.** *Stroke* 1993;24:35–41 CrossRef Medline
10. Barnett H, Taylor D, Eliasziw M, et al. **Benefit of carotid endarterectomy in patients with symptomatic moderate or severe stenosis.** *N Engl J Med* 1998;339:1415–25 CrossRef Medline
11. **Randomised trial of endarterectomy for recently symptomatic carotid stenosis: final results of the MRC European Carotid Surgery Trial (ECST).** *Lancet* 1998;351:1379–87 Medline
12. Halliday A, Mansfield A, Marro J, et al; MRC Asymptomatic Carotid Surgery Trial (ACST) Collaborative Group. **Prevention of disabling and fatal strokes by successful carotid endarterectomy in patients without recent neurological symptoms: randomised controlled trial.** *Lancet* 2004;363:1491–1502 CrossRef Medline
13. Hobson R, Weiss D, Fields W, et al. **Efficacy of carotid endarterectomy for asymptomatic carotid stenosis.** *N Engl J Med* 1993;328: 221–27 CrossRef Medline
14. Walker LJ, Ismail A, McMeekin W, et al. **Computed tomography angiography for the evaluation of carotid atherosclerotic plaque: correlation with histopathology of endarterectomy specimens.** *Stroke* 2002;33:977–81 CrossRef Medline
15. Barnett HJ, Taylor DW, Haynes RB, et al; North American Symptomatic Carotid Endarterectomy Trial Collaborators. **Beneficial effect of carotid endarterectomy in symptomatic patients with high-grade carotid stenosis.** *N Engl J Med* 1991;325:445–53 CrossRef Medline
16. Caplan LR, Hennerici M. **Impaired clearance of emboli (washout) is an important link between hypoperfusion, embolism, and ischemic stroke.** *Arch Neurol* 1998;55:1475–82 CrossRef Medline
17. Mono ML, Karameshev A, Slotboom J, et al. **Plaque characteristics of asymptomatic carotid stenosis and risk of stroke.** *Cerebrovasc Dis* 2012;34:343–50 CrossRef Medline
18. Rozie S, De Weert T, De Monyé C, et al. **Atherosclerotic plaque volume and composition in symptomatic carotid arteries assessed with multidetector CT angiography; relationship with severity of stenosis and cardiovascular risk factors.** *Eur Radiol* 2009;19:2294–301 CrossRef Medline
19. Saam T, Yuan C, Chu B, et al. **Predictors of carotid atherosclerotic plaque progression as measured by noninvasive magnetic resonance imaging.** *Atherosclerosis* 2007;194:e34–42 CrossRef Medline
20. Gupta A, Baradaran H, Kamel H, et al. **Evaluation of computed tomography angiography plaque thickness measurements in high-grade carotid artery stenosis.** *Stroke* 2014;45:740–45 CrossRef Medline
21. Gupta A, Mtui EE, Baradaran H, et al. **CT angiographic features of symptom-producing plaque in moderate-grade carotid artery stenosis.** *AJNR Am J Neuroradiol* 2015;36:349–54 CrossRef Medline
22. Saba L, Montisci R, Sanfilippo R, et al. **Multidetector row CT of the brain and carotid artery: a correlative analysis.** *Clin Radiol* 2009; 64:767–78 CrossRef Medline
23. Ota H, Yu W, Underhill HR, et al. **Hemorrhage and large lipid-rich necrotic cores are independently associated with thin or ruptured fibrous caps: an in vivo 3T MRI study.** *Arterioscler Thromb Vasc Biol* 2009;29:1696–701 CrossRef Medline
24. Gupta A, Gialdini G, Lerario MP, et al. **Magnetic resonance angiography detection of abnormal carotid artery plaque in patients with cryptogenic stroke.** *J Am Heart Assoc* 2015;4:e002012 CrossRef Medline
25. Gupta A, Gialdini G, Giambone AE, et al. **Association between non-stenosing carotid artery plaque on MR angiography and acute ischemic stroke.** *JACC Cardiovasc Imaging* 2016;9:1228–29 CrossRef Medline
26. Kamel H, Merkler AE, Iadecola C, et al. **Tailoring the approach to embolic stroke of undetermined source: a review.** *JAMA Neurol* 2019;76:855–61 CrossRef Medline
27. Sarty HC, Chandler AB, Dinsmore RE, et al. **A definition of advanced types of atherosclerotic lesions and a histological classification of atherosclerosis: a report from the Committee on Vascular Lesions of the Council on Arteriosclerosis, American Heart Association.** *Circulation* 1995;92:1355–74 CrossRef Medline
28. Trelles M, Eberhardt K, Buchholz M, et al. **CTA for screening of complicated atherosclerotic carotid plaque: American Heart Association type VI lesions as defined by MRI.** *AJNR Am J Neuroradiol* 2013;34:2331–37 CrossRef Medline
29. Wintermark M, Jawadi SS, Rapp JH, et al. **High-resolution CT imaging of carotid artery atherosclerotic plaques.** *AJNR Am J Neuroradiol* 2008;29:875–82 CrossRef Medline
30. Gupta A, Baradaran H, Mtui EE, et al. **Detection of symptomatic carotid plaque using source data from MR and CT angiography: a correlative study.** *Cerebrovasc Dis* 2015;39:151–61 CrossRef Medline
31. Oliver TB, Lammie GA, Wright AR, et al. **Atherosclerotic plaque at the carotid bifurcation: CT angiographic appearance with histopathologic correlation.** *AJNR Am J Neuroradiol* 1999;20:897–901 Medline
32. de Weert TT, Ouhlous M, Meijering E, et al. **In vivo characterization and quantification of atherosclerotic carotid plaque components with multidetector computed tomography and histopathological correlation.** *Arterioscler Thromb Vasc Biol* 2006;26:2366–72 CrossRef Medline
33. Bash S, Villablanca JP, Jahan R, et al. **Intracranial vascular stenosis and occlusive disease: evaluation with CT angiography, MR angiography, and digital subtraction angiography.** *AJNR Am J Neuroradiol* 2005;26:1012–21 CrossRef Medline
34. Das M, Braunschweig T, Mühlenbruch G, et al. **Carotid plaque analysis: comparison of dual-source computed tomography (CT) findings and histopathological correlation.** *Eur J Vasc Endovasc Surg* 2009;38:14–19 CrossRef Medline
35. Gupta A, Kesavabhotla K, Baradaran H, et al. **Plaque echolucency and stroke risk in asymptomatic carotid stenosis: a systematic review and meta-analysis.** *Stroke* 2015;46:91–97 CrossRef Medline
36. Baradaran H, Al-Dasuqi K, Knight-Greenfield A, et al. **Association between carotid plaque features on CTA and cerebrovascular ischemia: a systematic review and meta-analysis.** *AJNR Am J Neuroradiol* 2017;38:2321–26 CrossRef Medline
37. Kwee R. **Systematic review on the association between calcification in carotid plaques and clinical ischemic symptoms.** *J Vasc Surg* 2010;51:1015–25 CrossRef Medline
38. Nandalur KR, Hardie AD, Raghavan P, et al. **Composition of the stable carotid plaque.** *Stroke* 2007;38:935–40 CrossRef Medline
39. Shaalan WE, Cheng H, Gewertz B, et al. **Degree of carotid plaque calcification in relation to symptomatic outcome and plaque inflammation.** *J Vasc Surg* 2004;40:262–69 CrossRef Medline
40. Adraktas DD, Tong E, Furtado AD, et al. **Evolution of CT imaging features of carotid atherosclerotic plaques in a 1-year prospective cohort study.** *J Neuroimaging* 2014;24:1–6 CrossRef Medline
41. Gupta A, Baradaran H, Schweitzer AD, et al. **Carotid plaque MRI and stroke risk.** *Stroke* 2013;44:3071–77 CrossRef Medline
42. Golemati S, Tegos TJ, Sassano A, et al. **Echogenicity of b-mode sonographic images of the carotid artery: work in progress.** *J Ultrasound Med* 2004;23:659–69 CrossRef Medline

43. Saam T, Hetterich H, Hoffmann V, et al. **Meta-analysis and systematic review of the predictive value of carotid plaque hemorrhage on cerebrovascular events by magnetic resonance imaging.** *J Am Coll Cardiol* 2013;62:1081–91 CrossRef Medline
44. Eisenmenger LB, Aldred BW, Kim SE, et al. **Prediction of carotid intraplaque hemorrhage using adventitial calcification and plaque thickness on CTA.** *AJNR Am J Neuroradiol* 2016;37:1496–1503 CrossRef Medline
45. Ajduk M, Bulimbasic S, Pavic L, et al. **Comparison of multidetector-row computed tomography and duplex Doppler ultrasonography in detecting atherosclerotic carotid plaques complicated with intraplaque hemorrhage.** *Coll Antropol* 2013;37:213–19 Medline
46. Ajduk M, Pavić L, Bulimbasić S, et al. **Multidetector-row computed tomography in evaluation of atherosclerotic carotid plaques complicated with intraplaque hemorrhage.** *Ann Vasc Surg* 2009;23:186–93 CrossRef Medline
47. Saba L, Francone M, Bassareo PP, et al. **CT attenuation analysis of carotid intraplaque hemorrhage.** *AJNR Am J Neuroradiol* 2018;39:131–37 CrossRef Medline
48. Zhao X, Hippe Daniel S, Li R, et al; CARE-II Study Collaborators. **Prevalence and characteristics of carotid artery high-risk atherosclerotic plaques in Chinese patients with cerebrovascular symptoms: a Chinese atherosclerosis risk evaluation II study.** *J Am Heart Assoc* 2017;6:e005831 CrossRef Medline
49. Coutinho JM, Derkatch S, Potvin ARJ, et al. **Nonstenotic carotid plaque on CT angiography in patients with cryptogenic stroke.** *Neurology* 2016;87:665–72 CrossRef Medline
50. McLaughlin MS, Hinckley PJ, Treiman SM, et al. **Optimal prediction of carotid intraplaque hemorrhage using clinical and lumen imaging markers.** *AJNR Am J Neuroradiol* 2015;36:2360–66 CrossRef Medline
51. Magge R, Lau BC, Soares BP, et al. **Clinical risk factors and CT imaging features of carotid atherosclerotic plaques as predictors of new incident carotid ischemic stroke: a retrospective cohort study.** *AJNR Am J Neuroradiol* 2013;34:402–09 CrossRef Medline
52. Virmani R, Ladich ER, Burke AP, et al. **Histopathology of carotid atherosclerotic disease.** *Neurosurgery* 2006;59:S213–27 CrossRef
53. Eliasziw M, Streifler JY, Fox AJ, et al. **Significance of plaque ulceration in symptomatic patients with high-grade carotid stenosis: North American Symptomatic Carotid Endarterectomy trial.** *Stroke* 1994;25:304–08 CrossRef Medline
54. Handa N, Matsumoto M, Maeda H, et al. **Ischemic stroke events and carotid atherosclerosis.** *Stroke* 1995;26:1781–86 CrossRef Medline
55. Rothwell PM, Gibson R, Warlow CP. **Interrelation between plaque surface morphology and degree of stenosis on carotid angiograms and the risk of ischemic stroke in patients with symptomatic carotid stenosis.** *Stroke* 2000;31:615–21 CrossRef Medline
56. Rothwell PM, Mehta Z, Howard SC, et al. **From subgroups to individuals: general principles and the example of carotid endarterectomy.** *Lancet* 2005;365:256–65 CrossRef Medline
57. Prabhakaran S, Rundek T, Ramas R, et al. **Carotid plaque surface irregularity predicts ischemic stroke.** *Stroke* 2006;37:2696–701 CrossRef Medline
58. Kuk M, Wannarong T, Beletsky V, et al. **Volume of carotid artery ulceration as a predictor of cardiovascular events.** *Stroke* 2014;45:1437–41 CrossRef Medline
59. Saba L, Caddeo G, Sanfilippo R, et al. **Efficacy and sensitivity of axial scans and different reconstruction methods in the study of the ulcerated carotid plaque using multidetector-row CT angiography: comparison with surgical results.** *AJNR Am J Neuroradiol* 2007;28:716–23 CrossRef Medline
60. Saba L, Caddeo G, Sanfilippo R, et al. **CT and ultrasound in the study of ulcerated carotid plaque compared with surgical results: potentialities and advantages of multidetector row CT angiography.** *AJNR Am J Neuroradiol* 2007;28:1061–66 CrossRef Medline
61. Saba L, Sanfilippo R, Sanna S, et al. **Association between carotid artery plaque volume, composition, and ulceration: a retrospective assessment with MDCT.** *AJR Am J Roentgenol* 2012;199:151–56 CrossRef Medline
62. Homburg PJ, Rozie S, van Gils MJ, et al. **Association between carotid artery plaque ulceration and plaque composition evaluated with multidetector CT angiography.** *Stroke* 2011;42:367–72 CrossRef Medline
63. Yuan XM, Ward LJ, Forssell C, et al. **Carotid atheroma from men has significantly higher levels of inflammation and iron metabolism enabled by macrophages.** *Stroke* 2018;49:419–25 CrossRef Medline
64. Moulton KS, Vakili K, Zurakowski D, et al. **Inhibition of plaque neovascularization reduces macrophage accumulation and progression of advanced atherosclerosis.** *Proc Natl Acad Sci USA* 2003;100:4736–41 CrossRef Medline
65. Virmani R, Kolodgie FD, Burke AP, et al. **Atherosclerotic plaque progression and vulnerability to rupture.** *Arterioscler Thromb Vasc Biol* 2005;25:2054–61 CrossRef Medline
66. McCarthy MJ, Loftus IM, Thompson MM, et al. **Angiogenesis and the atherosclerotic carotid plaque: an association between symptomatology and plaque morphology.** *J Vasc Surg* 1999;30:261–68 CrossRef Medline
67. Saba L, Lai ML, Montisci R, et al. **Association between carotid plaque enhancement shown by multidetector CT angiography and histologically validated microvessel density.** *Eur Radiol* 2012;22:2237–45 CrossRef Medline
68. Qiao Y, Etesami M, Astor BC, et al. **Carotid plaque neovascularization and hemorrhage detected by MR imaging are associated with recent cerebrovascular ischemic events.** *AJNR Am J Neuroradiol* 2012;33:755–60 CrossRef Medline
69. Romero JM, Babiarz LS, Forero NP, et al. **Arterial wall enhancement overlying carotid plaque on CT angiography correlates with symptoms in patients with high grade stenosis.** *Stroke* 2009;40:1894–96 CrossRef Medline
70. Romero JM, Pizzolato R, Atkinson W, et al. **Vasa vasorum enhancement on computerized tomographic angiography correlates with symptomatic patients with 50% to 70% carotid artery stenosis.** *Stroke* 2013;44:3344–49 CrossRef Medline
71. Baradaran H, Myneni PK, Patel P, et al. **Association between carotid artery perivascular fat density and cerebrovascular ischemic events.** *J Am Heart Assoc* 2018;7:e010383 CrossRef Medline
72. Chaker S, Al-Dasuqi K, Baradaran H, et al. **Carotid plaque positron emission tomography imaging and cerebral ischemic disease: a systematic review and meta-analysis.** *Stroke* 2019;50:2072–79 CrossRef Medline
73. Zhao XQ, Hatsukami TS, Hippe DS, et al; AIM-HIGH Carotid MRI Sub-Study Investigators. **Clinical factors associated with high-risk carotid plaque features as assessed by magnetic resonance imaging in patients with established vascular disease (from the AIM-HIGH study).** *Am J Cardiol* 2014;114:1412–19 CrossRef Medline
74. van Dijk AC, Truijman M, Hussain B, et al. **Intraplaque hemorrhage and the plaque surface in carotid atherosclerosis: the Plaque At Risk Study (PARISK).** *AJNR Am J Neuroradiol* 2015;36:2127–33 CrossRef Medline
75. Zavodni AE, Wasserman BA, McClelland RL, et al. **Carotid artery plaque morphology and composition in relation to incident cardiovascular events: the multi-ethnic study of atherosclerosis (MESA).** *Radiology* 2014;271:381–89 CrossRef Medline

Reduction of Radiation Dose and Scanning Time While Preserving Diagnostic Yield: A Comparison of Battery-Powered and Manual Bone Biopsy Systems

S. Kihira, C. Koo, A. Lee, A. Aggarwal, P. Pawha, and A. Doshi



ABSTRACT

BACKGROUND AND PURPOSE: There is scarcity of data on the comparative efficacy between bone biopsy drill systems across various types of bone lesions. Our aim was to investigate differences in diagnostic yield, scanning time, and radiation dose between manual and battery-powered bone biopsy systems in CT-guided biopsies of lytic, sclerotic, and infectious bone lesions.

MATERIALS AND METHODS: This was a retrospective single-center institutional review board–approved study. A total of 585 CT-guided core needle biopsies were performed at 1 institution from May 2010 to February 2019. Classification of bone lesions, location, bone biopsy system, suspected origin of primary disease, final pathologic diagnosis, diagnostic yield, presence of crush artifacts, radiation dose, and scanning times were collected. For the battery-powered system, OnControl was used. For the manual drill system, Bonoptoy, Osteosite, and Laurane drill systems were used. Comparisons in lytic and sclerotic lesions and suspected discitis/osteomyelitis were made using the Fisher exact test. Subgroup analysis of the drill systems for scanning time and radiation dose was performed by 1-way ANOVA.

RESULTS: Our patient cohorts consisted of a total of 585 patients with 422 lytic, 110 sclerotic, and 53 suspected infectious lesions. The mean age was 62 ± 13 years with a male/female ratio of 305:280 for all lesions. The diagnostic yield was 85.5% (362/422) for lytic, 82.7% (91/110) for sclerotic, 50.9% (27/53) for infectious lesions, and 82.1% (480/585) for all lesions. No statistical difference was found when comparing diagnostic yields of powered drills with the manual systems for lytic, sclerotic, and infectious lesions. However, in a subgroup analysis, radiation dose and scanning time were significantly lower for powered drill compared with manual drill systems in lytic ($P = .001$ for both) and sclerotic lesions ($P = .028$ and $P = .012$, respectively). No significant differences were seen between the drill systems for suspected infectious lesions.

CONCLUSIONS: Our findings demonstrate that there was no statistically significant difference in diagnostic yield when comparing battery-powered and manual bone biopsy systems for CT-guided bone biopsies; however, the use of the power drill system resulted in significantly reduced scanning time and radiation dose in lytic and sclerotic lesions.

Image-guided percutaneous bone biopsies have become the preferred method of acquiring tissue biopsies from bone lesions. The procedure is noninvasive and generally well-tolerated, with lower complication rates compared with open biopsies.¹⁻⁵ Bone lesions can vary greatly in density and location, which can affect the choice of biopsy equipment used. Drill systems can be categorized into either manual or battery-powered systems. In a manual

drill system, a needle is manually rotated to reach the desired depth of the lesion. Manual biopsy has been shown to have low complication rates and good diagnostic yield, ranging from 66% to 98%.^{3,5-7} In 2007, a reusable lithium battery–powered drill device, OnControl (Vidacare, Shavano Park, Texas), was approved as an alternative without the need for a manual drill system. Prior comparative studies of drill performance in high-density bone lesions have shown that the battery-powered drill may offer greater ease of use with higher diagnostic yield.⁸⁻¹⁰

However, there is scarcity of data when it comes to assessing the comparative efficacy of these drill systems in lytic and suspected infectious lesions. In lytic lesions, prior studies have shown the diagnostic yield ranging from 70% to 96%;^{3,11,12} however, these studies have predominantly assessed the manual drill systems. One prior study¹³ reported the diagnostic yield and radiation dose for battery-powered drill systems, however, without comparison with manual systems. No prior studies have

Received October 23, 2019; accepted after revision January 11, 2020.

From the Department of Radiology, Icahn School of Medicine at Mount Sinai, New York, New York.

Paper previously presented as Oral Presentation No. 19005412 at: Annual Meeting of the Radiological Society of North America, December 1–6, 2019; Chicago, Illinois.

Please address correspondence to Amish Doshi, MD, Department of Radiology/Neuroradiology, Icahn School of Medicine at Mount Sinai, Mount Sinai Hospital, One Gustave Levy Place, NY, NY 10029; e-mail: amish.doshi@mountsinai.org

Indicates article with supplemental on-line tables.

<http://dx.doi.org/10.3174/ajnr.A6428>

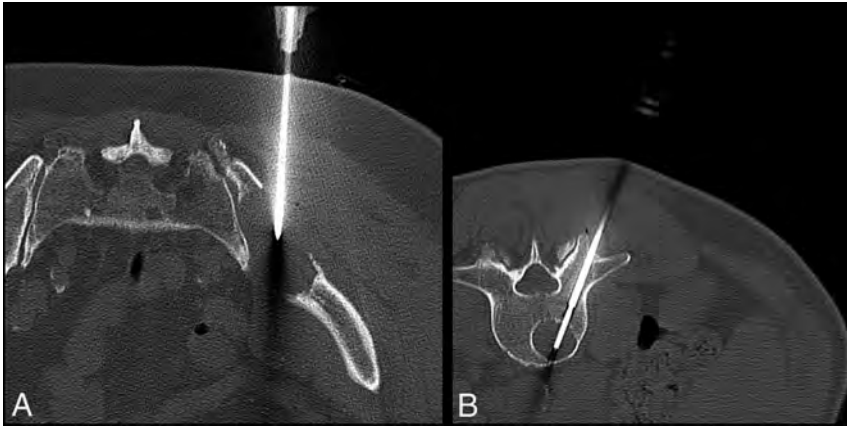


FIG 1. Bone biopsy of lytic bone lesions with manual and battery-powered drills. *A*, A 74-year-old man with multiple myeloma undergoing CT-guided biopsy of a right iliac lytic lesion with the Osteo-site manual system. CT image shows placement of the needle into the right iliac lytic lesion. *B*, A 58-year-old man with multiple myeloma undergoing CT-guided biopsy of a lytic L3 lesion with the OnControl battery-powered system. CT image shows placement of needle into the L3 vertebral body.

compared the performance of battery-powered with manual drill systems in lytic lesions. In sclerotic lesions, studies have shown that the battery-powered drill system has higher diagnostic yield but with varying differences in procedural times compared with the manual systems.^{5,14} In suspected discitis/osteomyelitis, a prior small-scale study ($n = 41$)¹⁵ showed a significantly shorter median duration of conscious sedation with battery-powered systems compared with manual systems, without significant differences in diagnostic yield.

In this study, we investigated differences in diagnostic yield, scanning time, and radiation dose between manual and battery-powered drill systems in 3 different lesion classes: lytic, sclerotic, and suspected infectious lesions.

MATERIALS AND METHODS

Study Population

This was a single-center retrospective study, which was approved by the local institutional review board, with a waiver of informed consent. From May 2010 to February 2019, a total of 1767 CT-guided bone biopsies were performed at our institution in a total of 1454 patients (difference accounting for multiple biopsy cases in 313 patients). Patients were included under the following circumstances: 1) They had pathology reports, 2) had clear documentation and/or hub visualization of the bone drill system, and 3) bone biopsy performed by the 2 fellowship-trained neuroradiologists (6 and 10 years of experience) and 2 fellowship-trained musculoskeletal radiologists (8 and 9 years of experience) chosen on the basis of the highest number of cases at our institution, to reduce operator dependence. These criteria yielded a cohort of 751 patients. Cases with only fine-needle aspiration were excluded from the study. We excluded 72 patients with lesions containing mixed lytic and sclerotic components because these lesions were qualitatively difficult to categorize and the sample size was too small for analysis after further subdivision into predominantly lytic, sclerotic, or

ambiguous. Our final cohort included 585 cases with 422 lytic, 110 sclerotic, and 53 infectious lesions.

Procedure

All CT-guided spine biopsies were performed on a 40-section CT scanner (Somatom Definition AS; Siemens, Erlangen, Germany) in the helical mode. Patients all underwent a standard course for these biopsies similar to that in a prior study.¹⁶ A Fast Find Grid (Webb Medical, Philadelphia, Pennsylvania) was placed over the general biopsy site for localization. A scout was obtained using a standard biopsy protocol (initial scout at 120 kV[peak] and 60 mAs with subsequent scans at 120 kVp and 220 mAs) for all cases. Skin was prepped and draped in normal sterile fashion. One percent lid-

ocaine was infiltrated into tissues for local and deep anesthesia. For the battery-powered system, OnControl was used with a coaxial 13-ga biopsy needle. For the manual drill system, Bonopt (AprioMed, Londonderry, New Hampshire), Osteo-site (Cook, Bloomington, Indiana), and Madison (Laurane Medical; Westbrook, Connecticut) drill systems were used with a coaxial biopsy needle ranging from 11 to 14 ga. The biopsy needle was advanced into the lesion with conventional CT guidance, and images were obtained after each needle advancement (Fig 1). CT fluoroscopy cases were not included in this study. Once the needle was confirmed within the lesion, CT scans were obtained after each biopsy pass. In each patient, 1 final postbiopsy scan was obtained after the needle was removed to assess postprocedural complications.

Data Collection

Classification of bone lesions, location, bone biopsy system, radiation dose, and scanning times were collected from our PACS reporting system. The attenuation of each sclerotic bone lesion and adjacent normal trabecular bone was obtained and averaged over 3 consecutive slices by a senior radiology resident (A.L.) with the requirement that the slices should be at least be 250 HU and twice that of the adjacent normal trabecular bone. Suspected radiologic disease, final pathology diagnosis, diagnostic yield, and the presence of crush artifacts were collected from the clinical notes and pathology reports from our Electronic Medical Records system. Diagnostic yield, the presence of crush artifacts, radiation dose, and scanning time were collected independently and blinded to the drill system used. Diagnostic yield was defined as the number of diagnostic biopsies divided by the total number of biopsies. A biopsy was considered diagnostic when a distinct pathologic diagnosis could be rendered from the surgical pathology, which explained the lesion clinically and through imaging, as defined in multiple past studies.^{3,5,16,17} Surgical pathology was the only source of diagnostic yield for infection, and microbiology results were not used in this study. CT scanning time and radiation dose were assessed

Table 1: Demographic characteristics of patients undergoing bone biopsies^a

	Total	Manual	Battery-Powered	P Value
No.	585	314	271	
Age (mean ± SD)	62 ± 13	62 ± 13	61 ± 12	.541
Sex (M/F)	305:280	173:141	132:139	.135
Suspected origin of primary disease				.103
Bone ^b	41.7 (244)	38.9 (122)	45 (122)	
Prostate	3.8 (22)	4.5 (14)	3.0 (8)	
Breast	10.4 (61)	11.5 (36)	9.2 (25)	
Lung	2.9 (17)	4.8 (15)	0.7 (2)	
Kidney	0.7 (4)	1.0 (3)	0.4 (1)	
Systemic ^c	0.7 (4)	1.0 (3)	0.4 (1)	
Liver	0.3 (2)	0.6 (2)	0 (0)	
Bladder	1.7 (10)	1.6 (5)	1.8 (5)	
Miscellaneous ^d	8.5 (50)	9.2 (29)	7.7 (21)	
Unestablished/unknown ^e	27 (158)	24.8 (78)	29.5 (80)	
Blood	2.2 (13)	2.2 (7)	2.2 (6)	
Location of bone lesion				.16
Vertebral column	47.0 (275)	45.2 (142)	49.1 (133)	
Cervical	0.6 (4)	0.1 (4)	0 (0)	
Thoracic	17.9 (105)	16.2 (51)	19.9 (54)	
Lumbar	17.3 (101)	17.5 (55)	17.0 (46)	
Sacral	11.1 (65)	10.2 (32)	12.2 (33)	
Pelvis	36.9 (216)	39.5 (124)	33.9 (92)	
Extremity	8.4 (49)	10.5 (33)	5.9 (16)	
Miscellaneous ^f	0.5 (3)	0.6 (2)	0.4 (1)	
Disc	7.2 (42)	4.1 (13)	10.7 (29)	

^a Values for frequency of suspected origin of primary disease and lesion location represent percentages followed by total number of cases in parentheses.

^b Primary bone lesions include suspected multiple myeloma from laboratory testing.

^c Predominantly sarcoidosis.

^d Includes thyroid, salivary gland, vulvar, tongue, melanoma, and anal cancers.

^e Includes all cases without known malignancy or suspected primary bone lesion.

^f Includes sternum, ribs, clavicle, scapula, calvaria, and tarsal bones.

from the radiology images, radiology reports, and clinical notes. Scanning time was defined as the interval CT imaging time from the first scout image to the final postbiopsy scan.

Statistical Analysis

The SPSS statistical package for Windows, Version 25 (IBM, Armonk, New York) was used for statistical computations. A 1-sided Fisher exact test was performed for comparison of diagnostic yields among drill systems in lytic and sclerotic lesions and suspected discitis/osteomyelitis. These were further subgrouped in a layered analysis to assess whether there was a statistically significant difference in drill performance affected by sex, lesion location, and suspected origin of the primary disease. Subgroup analysis of the drill systems for radiation dose and procedural time was made by 1-way ANOVA. A separate analysis was performed for sclerotic lesions to assess the effect of density on diagnostic yield using 1-way ANOVA.

RESULTS

Clinical Characteristics of the Patient Population

Our patient cohorts consisted of 585 cases with 422 lytic, 110 sclerotic, and 53 suspected infectious lesions. There were 314 patients in total with manual drill systems and 271 patients in total with the powered drill system (Table 1). The mean age was 62 ± 13 years with a median of 61 years with a male/female ratio of 305:280 for all lesions. Approximately 47.0% (275/585) of the lesions were located in the vertebral column; 36.9% (216/585), in

the pelvic bones; and 8.4% (49/585), in the long bones such as the humerus, femur, and tibia. At the biopsy, 41.7% of bone lesions were suspected of being primary bone lesions. This predominantly included multiple myeloma based on previous laboratory work-up. Additional suspected origins of metastasis included breast (10.4%), prostate (3.8%), lung (2.9%), and bladder (1.7%). Furthermore, 27% of lesions had no definite site or suspicion of malignancy at the time of biopsy. Subgroup analysis revealed no statistical difference ($P < .05$) among patients between the drill systems when comparing age, sex, suspected origin of primary disease, and lesion location (Table 1).

The final pathologic diagnosis revealed 27.2% of cases with metastasis and 22.2% of cases with primary bone malignancy (Fig 2).

Comparison of Drill Systems in Lytic Lesions

A total of 422 lytic lesions included 241 cases with manual drills and 181 cases with the battery-power drill systems. No statistical difference was noted among the suspected origins of primary disease or lesion location ($P = .063$ and $P = .316$, respectively) (On-line Table 1). Diagnostic yields of the manual and powered drill systems were 83.4% and 89.0%, respectively (Table 2). Crush artifacts were present in 5% and 7.7% of manual and battery-powered drills, respectively. No statistically significant difference in diagnostic yield or crush artifacts was noted between the drill systems. However, radiation dose and scanning time were significantly lower for the battery-powered drill compared with the manual drill ($P = .001$ for both). The mean radiation doses for the manual and powered drills were 845 mGy × cm² and 657 mGy × cm², respectively. The mean scanning time for manual and powered drills was 42 and 35 minutes, respectively.

Comparison of Drill Systems in Sclerotic Lesions

A total of 110 patients had sclerotic lesions, with 55 undergoing manual drill biopsies and 55 undergoing battery-powered drill biopsies. No statistical difference was noted among the suspected origins of primary disease or lesion location ($P = .691$ and $P = .355$) (On-line Table 2). The diagnostic yields of the manual and powered drill systems were 76.4% and 89.1%, respectively, and crush artifacts were present in 7.3% for both systems (Table 2). No statistically significant difference was noted among diagnostic yields or crush artifacts between the drill systems. Radiation dose and scanning time were significantly lower for the battery-powered drill compared with the manual drill ($P = .028$ and $P = .012$, respectively). The mean radiation doses were 1061 mGy × cm² and 804 mGy × cm², respectively. The mean scanning times for manual and powered drills were 44 and 37 minutes, respectively.

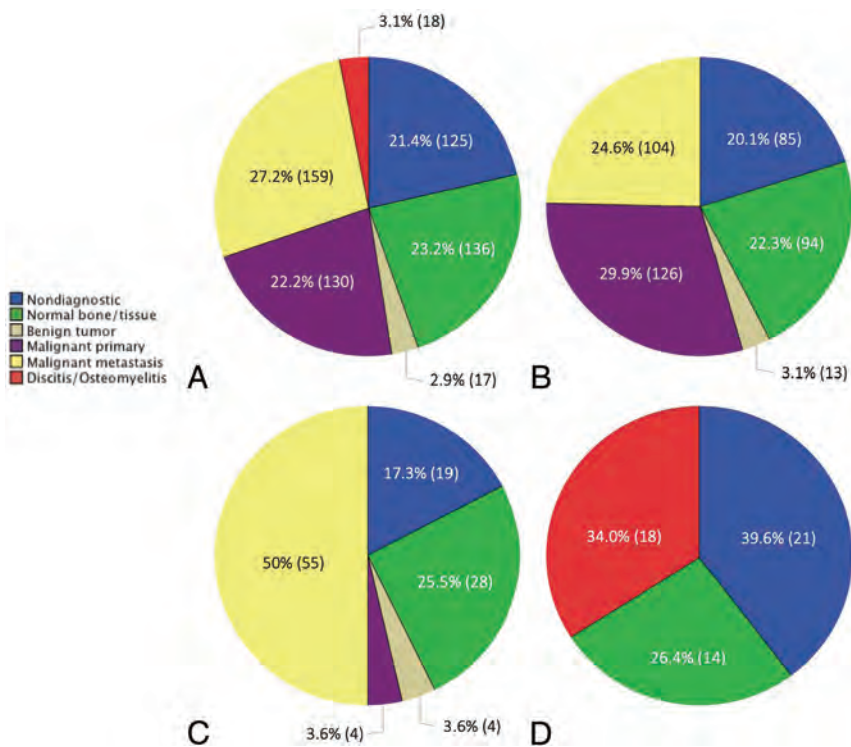


FIG 2. Breakdown of the final pathology diagnosis in various bone lesion classes: all bone lesions (A), lytic lesions (B), sclerotic lesions (C), and suspected infectious lesions (D).

Table 2: Comparative performance of the drill systems in various lesion classifications^a

	Diagnostic Yield	Crush Artifacts	Radiation Dose (mGy × cm ²)	Scanning Time (min)
Lytic lesions				
Manual	83.4 (201/241)	5 (12/241)	845	42
Battery-powered	89.0 (161/181)	7.7 (14/181)	657	35
P value	.069	.168	.001 ^b	.001 ^b
Sclerotic lesions				
Manual	76.4 (42/55)	7.3 (4/55)	1061	44
Battery-powered	89.1 (49/55)	7.3 (4/55)	804	37
P value	.064	1	.028 ^b	.012 ^b
Infectious lesions				
Manual	50.0 (9/18)	11.1 (2/18)	1113	46
Battery-powered	51.4 (18/35)	0 (0/35)	811	39
P value	.576	.111	.155	.128
All lesions				
Manual	80.3 (252/314)	5.7 (18/314)	900	43
Battery-powered	84.1 (228/271)	6.6 (18/271)	704	36
P value	.538	.387	.001 ^b	.001 ^b

^aPercentage followed by the number of cases/total number of cases in parentheses for diagnostic yield and crush artifacts. Mean values are listed for radiation dose and scanning time.

^bSignificant P value (P < .05).

The mean density of sclerotic lesions was 663 HU, with a median density of 649 HU, ranging from 251 to 1412 HU (On-line Table 2). Average densities of sclerotic lesions in the manual and battery-powered system cohorts were 641 HU and 682 HU, respectively, without a statistically significant difference. In a subgroup analysis of biopsies, in manual drill systems, there was no significant difference found in performance based on density in sclerotic lesions. However, in the battery-powered drill system, there was a significantly longer average scanning time for

sclerotic lesions of >700 HU compared with sclerotic lesions below 700 HU (P = .026), with a scanning time of 41 minutes compared with 35 minutes, respectively (Table 3). Additionally, there were higher crush artifacts with sclerotic lesions of >700 HU compared with lower density sclerotic lesions (P = .025), with crush artifacts present in 20% (4/20) and 0% (0/28), respectively. No statistically significant difference was noted for diagnostic yield or radiation dose based on density in the battery-powered drill system.

Comparison of Drill Systems in Suspected Infectious Lesions

A total of 53 patients had suspected discitis/osteomyelitis, with 18 manual drill biopsies and 35 battery-powered drill biopsies. No statistical difference was noted among the lesion locations. Diagnostic yields of the manual and powered drill systems were 50.0% and 51.4%, respectively, and crush artifacts were present in 11.1% and 0%, respectively (Table 2). No statistically significant differences were noted for diagnostic yield, crush artifacts, scanning time, or radiation dose between the drill systems. On the final pathology report, 34.0% were found to have the diagnosis of discitis/osteomyelitis (Fig 2).

DISCUSSION

In our study, we compared the differences in efficacy between manual and battery-powered drill systems in various lesion classes by assessing the diagnostic yield, radiation dose, and scanning time. To our knowledge, this is the first combined, large-scale study assessing comparative performances of drill systems in various bone lesion classes. In our study, we showed that there was a significant decrease in radiation dose and scanning time

when using a battery-powered drill compared with a manual system in lytic and sclerotic bone lesions. Most interesting, there were no statistically significant differences in diagnostic yield or crush artifacts in any class of bone lesion, though the diagnostic yield was generally higher with the use of a battery-powered drill system.

Although there are few prior data on the comparative efficacy of these drill systems in lytic and suspected infectious lesions, Cohen et al⁵ reported a significantly higher diagnostic yield for

Table 3: Comparative performance of drill systems in sclerotic lesions based on density^a

Density (HU)	Diagnostic Yield	Crush Artifacts	Radiation Dose (mGy × cm ²)	Scanning Time (min)
Manual				
250–700	88.5 (23/26)	3.8 (1/26)	1044	45.1
>700	85.7 (12/14)	2.1 (3/14)	1317	46.1
P value	.583	.115	.3	.862
Battery-powered				
250–700	89.3 (25/28)	0 (0/28)	889	34.6
>700	85 (17/20)	20 (4/20)	752	41
P value	.562	.025 ^b	.38	.026 ^b

^aPercentage followed by number of cases/total number of cases in parentheses for diagnostic yield and crush artifacts. Mean values are listed for radiation dose and scanning time.

^bSignificant P value ($P < .05$).

battery-powered systems compared with manual drill systems in sclerotic lesions ($P = .047$), with diagnostic yields of 73% and 55.9%, respectively. In our study, although diagnostic yield was generally higher for the battery-powered drill system compared with manual systems, with diagnostic yields of 89.1% and 76.4%, respectively, the difference was not statistically significant. Of note, the diagnostic yield reported in our study for manual systems is in keeping with most prior studies reporting approximately 75%.^{18,19}

The diagnostic yield of a bone biopsy has been shown, in the past, to be inversely associated with the density of a bone lesion.^{18,20,21} This finding is explained by increased trabecular bone density associated with increased bone tissue stiffness and lowered diagnostic yield.²² It was observed in our study because the diagnostic yield was higher for lytic lesions compared with sclerotic lesions, regardless of the bone biopsy system used. In sclerotic lesions, we further observed that there was a decrease in diagnostic yield, with higher density lesions of >700 HU. We used the density cutoff of 700 HU in keeping with Chang et al²³ reporting difficulty with biopsies of densely sclerotic lesions of >700 HU and Chang et al¹⁴ demonstrating differences in diagnostic yield at this threshold. Although there was no statistically significant difference in diagnostic yield at this threshold in our study, most interesting, for the battery-powered drill system, there was significantly shorter scanning time and a lower prevalence of crush artifacts for lower density sclerotic lesions. Anecdotally, this outcome is likely due to the increased difficulty in drilling into denser lesions; furthermore, increased crush artifacts have been shown to be associated with biopsies of higher density lesions in the past.^{3,5}

A multitude of factors can affect the diagnostic yield independent of operator control. These include the histologic architecture of the bone lesion, nonspecific pathology of the biopsy specimen, and the presence of necrosis or crush artifacts, which can render the sample nondiagnostic. In our study, we show that the choice of a bone biopsy system does not significantly impact diagnostic yield, regardless of the bone lesion classification; however, it can impact the radiation dose and overall scanning time. Although many other factors dictate the choice of a bone biopsy system not assessed in this study, such as operator preference, availability, and cost, understanding the difference in efficacy is clinically significant and beneficial to patient care.

Of note, prior studies have shown that location^{1,24} and primary origin of disease^{20,25} of the bone lesions can affect the diagnostic yield. For example, Hau et al¹ reported a lower diagnostic yield for vertebral lesions compared with lesions in the pelvis or extremity. Tsukushi et al²⁵ showed that there was a higher diagnostic yield for metastatic bone lesions compared with primary bone tumors. In our study, these factors did not significantly impact the comparative performance between the bone biopsy

systems because there were no significant differences in the distribution of lesion location or primary origin of disease between the cohorts.

There are several limitations to our study. First, it was retrospective. A prospective study would facilitate obtaining an equivalent number of cases for each drill system. Furthermore, because the patients were not randomized by drill systems, an inherent bias in drill system selection by the operator cannot be excluded. Additionally, although this study took place at a single institution, the study spanned 9 years, and with technological advancements and software upgrades, there was likely a progressive decrease in scanning time and radiation dose. This factor would likely result in overestimating the actual reduction in scanning time and radiation dose for the battery-powered drill system, which was introduced 2 years after the start of the study at our institution and was used increasingly more frequently in recent years compared with the manual system. However, neither scanner nor scanning parameters were changed during the study.

Additionally, we acknowledge that there can be operator variability in drill performances. We attempted to reduce this by limiting the study to cases performed by only 2 neuroradiologists and 2 musculoskeletal radiologists. Limiting the operator number also ensured that the drill was used in most cases, though not in every case, which is a considerable limitation. Another limitation is the incongruity between scanning time and procedural time. Although scanning time was used as a surrogate for procedural time in this study, we acknowledge that there is likely a delay in the start of the procedure after the initial scan and between the end of procedure and the postbiopsy scan. Finally, only 1 attending radiologist and pathologist determined lesion classification and pathology diagnosis, respectively. We acknowledge that having multiple readers would improve the accuracy and reliability of this study.

CONCLUSIONS

We demonstrated that there was no statistically significant difference in diagnostic yield when comparing battery-powered with manual bone biopsy systems for CT-guided bone biopsies. However, the use of the power drill system resulted in a significantly reduced radiation dose and scanning time in lytic and sclerotic lesions, without significant differences in suspected infectious lesions.

REFERENCES

1. Hau MA, Kim JI, Kattapuram S, et al. **Accuracy of CT-guided biopsies in 359 patients with musculoskeletal lesions.** *Skeletal Radiol* 2002;31:349–53 CrossRef Medline
2. Yao L, Nelson SD, Seeger LL, et al. **Primary musculoskeletal neoplasms: effectiveness of core-needle biopsy.** *Radiology* 1999;212:682–86 CrossRef Medline
3. Wu JS, Goldsmith JD, Horwich PJ, et al. **Bone and soft-tissue lesions: what factors affect diagnostic yield of image-guided core-needle biopsy?** *Radiology* 2008;248:962–70 CrossRef Medline
4. Anderson JM, Murchison J, Patel D. **CT-guided lung biopsy: factors influencing diagnostic yield and complication rate.** *Clin Radiol* 2003;58:791–97 CrossRef Medline
5. Cohen MG, McMahan CJ, Kung JW, et al. **Comparison of battery-powered and manual bone biopsy systems for core needle biopsy of sclerotic bone lesions.** *AJR Am J Roentgenol* 2016;206:W83–86 CrossRef Medline
6. Li Y, Du Y, Luo TY, et al. **Factors influencing diagnostic yield of CT-guided percutaneous core needle biopsy for bone lesions.** *Clin Radiol* 2014;69:e43–47 CrossRef Medline
7. Vieillard MH, Boutry N, Chastanet P, et al. **Contribution of percutaneous biopsy to the definite diagnosis in patients with suspected bone tumor.** *Joint Bone Spine* 2005;72:53–60 CrossRef Medline
8. Miller LJ, Philbeck TE, Montez DF, et al. **Powered bone marrow biopsy procedures produce larger core specimens, with less pain, in less time than with standard manual devices.** *Hematol Rep* 2011;3:e8 CrossRef Medline
9. Berenson JR, Yellin O, Blumenstein B, et al. **Using a powered bone marrow biopsy system results in shorter procedures, causes less residual pain to adult patients, and yields larger specimens.** *Diagn Pathol* 2011;6:23 CrossRef Medline
10. Reed LJ, Raghupathy R, Strakhan M, et al. **The OnControl bone marrow biopsy technique is superior to the standard manual technique for hematologists-in-training: a prospective, randomized comparison.** *Hematol Rep* 2011;3:e21 CrossRef Medline
11. Maciel MJ, Tyng CJ, Barbosa P, et al. **Computed tomography-guided percutaneous biopsy of bone lesions: rate of diagnostic success and complications.** *Radiology Bras* 2014;47:269–74 CrossRef Medline
12. Wiesner EL, Hillen TJ, Long J, et al. **Percutaneous CT-guided biopsies of the cervical spine: technique, histopathologic and microbiologic yield, and safety at a single academic institution.** *AJNR Am J Neuroradiol* 2018;39:981–85 CrossRef Medline
13. Wallace AN, McWilliams SR, Wallace A, et al. **Drill-assisted biopsy of the axial and appendicular skeleton: safety, technical success, and diagnostic efficacy.** *J Vasc Interv Radiol* 2016;27:1618–22 CrossRef Medline
14. Chang IY, Ilaslan H, Sundaram M, et al. **CT-guided percutaneous biopsy of sclerotic bone lesions: diagnostic outcomes.** *Skeletal Radiol* 2018;47:661–69 CrossRef Medline
15. Wallace AN, Pacheco RA, Vyhmeister R, et al. **Fluoroscopy-guided intervertebral disc biopsy with a coaxial drill system.** *Skeletal Radiol* 2016;45:273–78 CrossRef Medline
16. Shpilberg KA, Delman BN, Tanenbaum LN, et al. **Radiation dose reduction in CT-guided spine biopsies does not reduce diagnostic yield.** *AJNR Am J Neuroradiol* 2014;35:2243–47 CrossRef Medline
17. Didolkar MM, Anderson ME, Hochman MG, et al. **Image guided core needle biopsy of musculoskeletal lesions: are nondiagnostic results clinically useful?** *Clin Orthop Relat Res* 2013;471:3601–09 CrossRef Medline
18. Holmes MG, Foss E, Joseph G, et al. **CT-guided bone biopsies in metastatic castration-resistant prostate cancer: factors predictive of maximum tumor yield.** *J Vasc Interv Radiol* 2017;28:1073–81.e1 CrossRef Medline
19. McKay RR, Zukotynski KA, Werner L, et al. **Imaging, procedural and clinical variables associated with tumor yield on bone biopsy in metastatic castration-resistant prostate cancer.** *Prostate Cancer Prostatic Dis* 2014;17:325–31 CrossRef Medline
20. Omura MC, Motamedi K, UyBico S, et al. **Revisiting CT-guided percutaneous core needle biopsy of musculoskeletal lesions: contributors to biopsy success.** *AJR Am J Roentgenol* 2011;197:457–61 CrossRef Medline
21. Duda SH, Johst U, Krahmer K, et al. **Technique and results of CT-guided percutaneous bone biopsy [in German].** *Orthopade* 2001;30:545–50 CrossRef Medline
22. Mulder L, Koolstra JH, den Toonder JMJ, et al. **Intrabone distribution of tissue stiffness and mineralization in developing trabecular bone.** *Bone* 2007;41:256–65 CrossRef Medline
23. Chang CY, Simeone FJ, Huang AJ. **Battery-powered bone drill: caution needed in densely blastic lesions.** *Skeletal Radiol* 2015;44:1845–48 CrossRef Medline
24. Puri A, Shingade VU, Agarwal MG, et al. **CT-guided percutaneous core needle biopsy in deep seated musculoskeletal lesions: a prospective study of 128 cases.** *Skeletal Radiol* 2006;35:138–43 CrossRef Medline
25. Tsukushi S, Katagiri H, Nakashima H, et al. **Application and utility of computed tomography-guided needle biopsy with musculoskeletal lesions.** *J Orthop Sci* 2004;9:122–25 CrossRef Medline

Nephrogenic Systemic Fibrosis Risk Assessment and Skin Biopsy Quantification in Patients with Renal Disease following Gadobenate Contrast Administration

E. Kanal, T.J. Patton, I. Krefting, and C. Wang



ABSTRACT

BACKGROUND AND PURPOSE: Nephrogenic systemic fibrosis following administration of intravenous gadobenate during MR imaging is rare. This study aimed to analyze any nephrogenic systemic fibrosis–related risks and quantify skin gadolinium levels in patients with impaired renal function but without nephrogenic systemic fibrosis who had received gadobenate.

MATERIALS AND METHODS: In this retrospective study with a prospective skin biopsy phase, patients with estimated glomerular filtration rates of <60 mL/min/1.73 m² undergoing contrast-enhanced MR imaging from July 2007 through June 2014 were screened for nephrogenic systemic fibrosis using a questionnaire. This was highly sensitive but not specific and reliably excluded nephrogenic systemic fibrosis if responses to at least 6 of the 8 questions were negative. If no nephrogenic systemic fibrosis was detected, a skin biopsy was requested.

RESULTS: Of 2914 patients who met these criteria, 1988 were excluded for various reasons. Of the remaining 926 patients, 860 were screened negative for nephrogenic systemic fibrosis. Of these, 17 (2%) had estimated glomerular filtration rates of <15 mL/min/1.73 m², 51 (6%) had levels of $15 < 30$ mL/min/1.73 m², 234 (27%) had levels of $30 < 45$ mL/min/1.73 m², and 534 (62%) had levels of $45 < 60$ mL/min/1.73 m². Of the 66 who were not cleared of nephrogenic systemic fibrosis by the questionnaire, 6 patients were evaluated by a dermatologist and confirmed not to have nephrogenic systemic fibrosis (no biopsy required).

CONCLUSIONS: A diagnosis of nephrogenic systemic fibrosis was excluded in 860 patients with impaired renal function who were followed up and received gadobenate during MR imaging. In 14 such patients who underwent at least 1 gadobenate-enhanced MR imaging examination and did not have nephrogenic systemic fibrosis, gadolinium levels in the skin were exceedingly low.

ABBREVIATIONS: eGFR = estimated glomerular filtration rate; GBCA = gadolinium-based contrast agents; ICP-MS = inductively coupled plasma mass spectrometry; NSF = nephrogenic systemic fibrosis

While the relative nephrogenic systemic fibrosis (NSF)–related safety of at least some of the macrocyclic agents has been established, there do not seem to be any confirmed cases of NSF following the prior unconfounded administration of the linear gadolinium-based contrast agent gadobenate.¹ Since gadolinium-based contrast agents (GBCA) received regulatory approval in 1988, >450 million doses have been administered

worldwide.¹ While GBCA have a favorable pharmacologic safety profile, evidence of long-term retention in human tissues and occurrence of NSF in some patients with severely compromised renal function have raised concerns.^{2,3}

The connection between gadolinium exposure and NSF was recognized by Grobner,⁴ in 2006. Gadolinium levels are elevated in the biopsies of skin lesions in patients with NSF.^{3,5–8} In 2014, Kanda et al⁹ noted retention of gadolinium in the brain parenchyma of patients with normal renal function following repeat gadolinium-enhanced MRIs. Gadolinium has also been detected in the skin, bones, and livers of patients with normal renal function following repeat MRIs with commercially available GBCA.

The theory of transmetallation has been quoted as a rationale for patients receiving GBCA and developing NSF. Also known as the dechelation or dissociation theory, this theory recognizes the notable differences in the comparative bond strength and kinetics of dissociation of the bonds between the gadolinium ion and ligand molecules used in GBCA. The kinetics of the dissociation

Received October 24, 2019; accepted after revision December 18.

Departments of Radiology (E.K.) and Dermatology (T.J.P.), University of Pittsburgh Medical Center and University of Pittsburgh, Pittsburgh, Pennsylvania; Division of Medical Imaging and Radiation Medicine (I.K.); and Office of Pharmacovigilance and Epidemiology (C.W.), US Food and Drug Administration, Silver Spring, Maryland.

Dr Wang is currently with Ascentage Pharma Group, Rockville, Maryland.

This work was funded, in part, by FDA Cooperative Agreement U01 FD004713.

Please address correspondence to Ira Krefting, MD, US Food and Drug Administration, 10903 New Hampshire Ave, Building 22, Room 5402, Silver Spring, MD 20993; e-mail: Ira.Krefting@fda.hhs.gov

Indicates open access to non-subscribers at www.ajnr.org

<http://dx.doi.org/10.3174/ajnr.A6448>

strength of these bonds among the linear GBCA in general is faster than that for the macrocyclic GBCA, suggesting that dissociation of the gadolinium ion from its ligand molecule would be greater for linear and especially nonionic linear agents than for macrocyclic agents. Precisely such results have been shown *in vivo*.¹⁰⁻²²

Only low single-digit numbers of cases of NSF have been seen following unconfounded administration of macrocyclic GBCA. As discussed at the December 8, 2009, FDA Advisory Committee,¹ there are several hundred confirmed cases of NSF following unconfounded administration of the linear nonionic gadolinium-based contrast agent, gadodiamide, with several dozen following unconfounded administration of the other linear nonionic gadolinium-based contrast agent, gadoversetamide.

However, the ability of this theory alone to explain clinical observations is called into question with roughly 100 cases of NSF following unconfounded administration of the linear ionic agent gadopentetate, yet zero or 1 possibly case following unconfounded administration of the linear ionic agent gadobenate.^{23,24} These differences cannot be ascribed to the relative market share differences alone.²⁵

The lack of clarity as to causation is compounded by the concern that perhaps NSF might actually represent one extreme on a spectrum of gadolinium-related issues. In other words, there is a concern that a so-called “subclinical NSF” might exist in which some changes may be histologically present but not clinically manifest at lower total exposure levels to various GBCA.

To that end, Phase I of our study was designed to evaluate the incidence of NSF following administration of gadobenate in patients with chronic renal disease who would be expected to be at the highest risk for NSF. Phase II involved measuring gadolinium levels in the skin of patients with impaired renal function who did not have NSF but had undergone at least 1 contrast-enhanced MR imaging study with gadobenate.

This study was performed to attempt to further analyze and quantify any NSF-related risks associated with this linear GBCA.

MATERIALS AND METHODS

Phase I

As part of a clinical quality-assurance project initiated in 2007 at the University of Pittsburgh Medical Center, we recorded data for all clinical patients with impaired renal function (defined as estimated glomerular filtration rate [eGFR] values of <60 mL/min/1.73 m²) who underwent clinically requested contrast-enhanced MR imaging examinations following a clinical benefit-risk assessment in which the outcome was to proceed with the examination.

For this project, all patients who were identified as having at least moderate chronic kidney disease who underwent clinically indicated contrast-enhanced MR imaging with gadobenate were identified from our clinical quality-assurance data base noted above from July 2007 through June 2014 (inclusive). Institutional review board approval for this study was granted in addition to the ongoing clinical quality-assurance project approval and oversight noted above. For each patient with impaired renal function, contemporaneous recording was made of the patient's name and identification number, weight, the administered MR imaging

contrast agent name and dose, and the most recently available eGFR value. A neutral third party reviewed this list of clinical patients and compared it against the medical record data base of deceased patients in the health care system. After we excluded patients identified as deceased, the contact information for the remaining patients was procured from medical records, and attempts were made by the neutral third party to contact each of these patients for NSF-screening purposes. The order in which the patients were contacted was such that the first patients to be contacted were those with the lowest eGFR level at time of gadobenate administration. Because mortality was expected to be highest among those with the greatest levels of impairment of renal function, we opted to begin with those patients to successfully screen as many as possible in the earliest stages of this study.

Using the screening criteria established by Lima et al,²⁶ we verbally screened all contacted patients with an 8-question questionnaire that focused on cutaneous and musculoskeletal manifestations of NSF. Lima et al had demonstrated that affirmative responses to ≥ 3 of the 8 closed-ended (yes/no) questions yielded a 90% sensitivity and 70% specificity for NSF. On the basis of differences in proposed prevalence values, this outcome yielded a positive predictive value for this questionnaire that ranged from a somewhat disappointing 0.3% to 39.7%, but, at the same time, a negative predictive value, which ranged from 97% to $>99\%$. Therefore, a negative response to this questionnaire was thought to reliably exclude a diagnosis of NSF, whereas a positive response to at least 3 of the questions posed in this questionnaire was deemed worthy of further investigation because specificity and positive predictive values were insufficient for conclusive diagnoses based on the questionnaire alone.

During the execution of Phase I of this study, patients who were screened as negative for NSF were asked if they would permit us to contact them at a later date for possible inclusion in a research study. Only those who responded in the affirmative were advanced to Phase II of this study.

Phase II

After the conclusion of Phase I of this study, all patients who screened negative for NSF and who gave permission for future contact were again contacted and recruited to be possible participants in Phase II of this study. These patients had impaired renal function and had undergone at least 1 MR imaging examination enhanced with intravenously administered gadobenate. Study participation entailed undergoing a purely research-generated punch deep skin biopsy of the lateral thigh. These biopsies were then analyzed using inductively coupled plasma mass spectrometry (ICP-MS) for gadolinium-level quantification in Dr Whitney High's laboratory (Department of Dermatology & Dermatopathology, University of Colorado School of Medicine). The ICP-MS methodology is outlined in a previous publication by High et al,⁷ from 2007, which reported gadolinium levels in the skin of patients with NSF; this methodology has not changed.

RESULTS

Phase I

A total of 2914 patients were identified who had eGFR values of <60 mL/min/1.73 m² and who underwent at least 1 contrast-

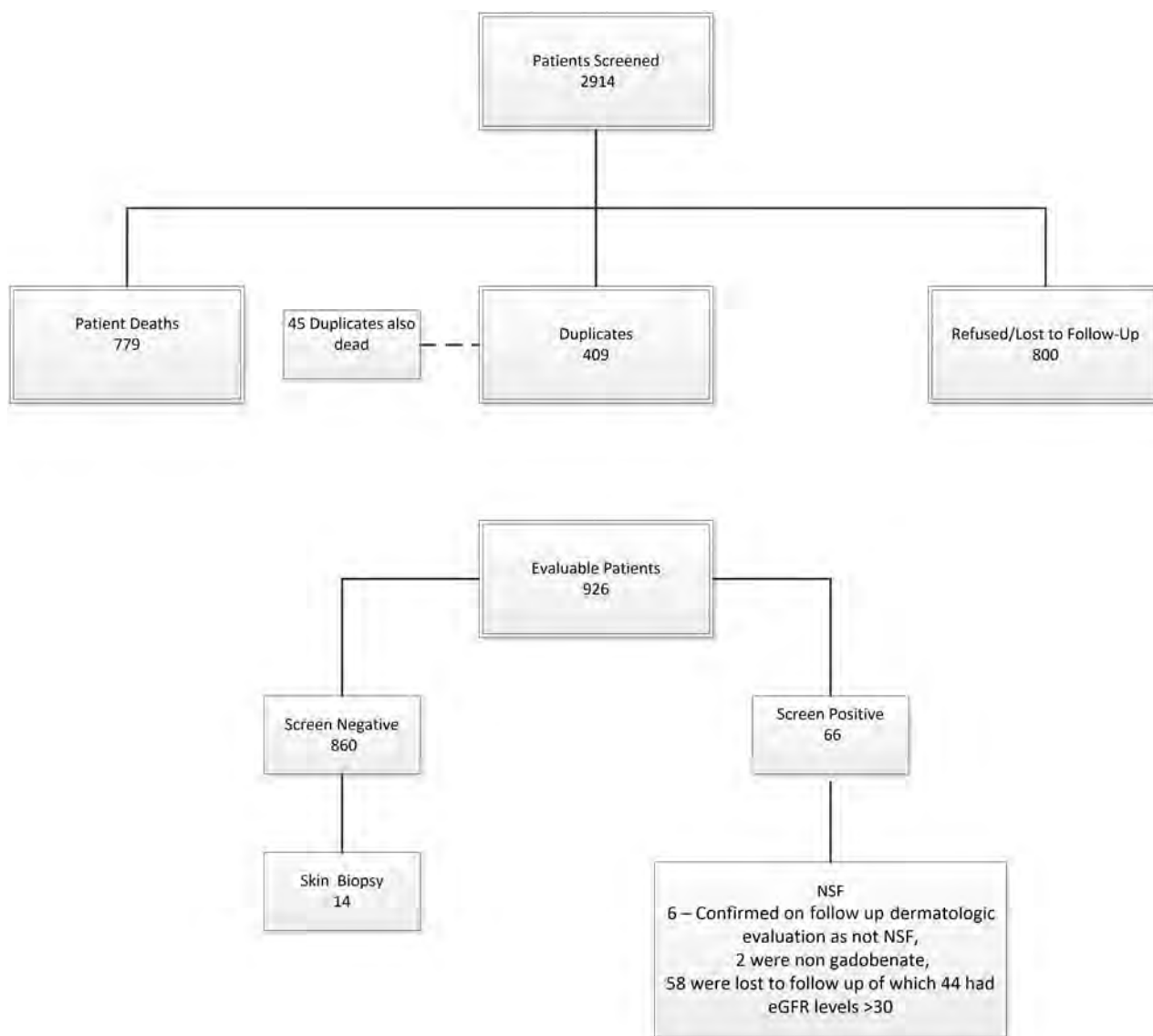


FIG 1. Patient selection.

Table 1: Dose distribution of 926 patients

Dose (Full Dose = 0.1 mMol/kg)	
Patients receiving gadobenate	
1	Double
3	1.5
334	Full
15	0.75
554	0.5
17	0.25
Other GBCA	
1 gadoxetate	
1 gadobutrol	

enhanced MR imaging examination with gadobenate (Fig 1). Of these, 1988 were excluded due to death (779), duplicates (409, deceased patient duplicates numbered 45 of these 409), or patients who refused contact/cooperation or were lost to follow-up (800). Of the remaining 926 patients (Table 1), all except 66 screened negative for NSF. Of the 66 who had responded yes to ≥ 3 questions in the NSF screening questionnaire, 6 patients were

seen and evaluated by a dermatologist and were confirmed to have another diagnosis and not NSF (no biopsy required), 19 lived too far away/could not return for follow-up at our institution, 10 refused follow-up care, 24 did not return multiple (at least 3) separate calls/messages, 3 had dementia/were in nursing home facilities, 2 had died, and 2 had received nongadobenate gadolinium-based contrast agents (1 gadoxetate, 1 gadobutrol).

Of the 860 patients screened as not having NSF, 17 (2%) had eGFR levels of < 15 mL/min/1.73 m², 51 (6%) had eGFR levels of $15 < 30$ mL/min/1.73 m², 234 (27%) had eGFR levels of $30 < 45$ mL/min/1.73 m², 534 (62%) had eGFR levels of $45 < 60$ mL/min/1.73 m², and 24 (3%) had no concurrent eGFR data available or had eGFR levels of > 60 but did have a history of known renal disease. There were no cases of NSF identified either in the screening process using the questionnaire or among those examined directly by the dermatologist and who had responded yes to ≥ 3 questions on the screening questionnaire. In 4 patients, there were nonspecific findings that did not require biopsy (1 of these 4 had undergone an

unrelated clinical biopsy of her lower leg with nonspecific findings that were not consistent with NSF; in another, there was dyspigmentation of the skin consistent with postinflammatory pigment changes secondary to trauma; and one had induration of the distal lower extremities consistent with lipodermatosclerosis.

Of the 66 patients who had responded positively to ≥ 3 questions, 2 had received other GBCA (1 gadoxetate, 1 gadobutrol) and 2 patients were found to have had eGFR levels exceeding 59 at time of administration and were thus excluded from further analysis. Of the remaining 62 patients, 6 (10%) had eGFR levels of < 15 mL/min/1.73 m², 11 (18%) had eGFR levels of $15 < 30$ mL/min/1.73 m², 19 (31%) had eGFR levels of $30 < 45$ mL/min/1.73 m², and 25 (40%) had eGFR levels of $45 < 60$ mL/min/1.73 m². One patient with known renal disease did not have an eGFR before GBCA administration and was excluded from the tally.

Of the 6 patients who had responded positively to ≥ 3 questions and who were examined by a dermatologist, one (17%) had eGFR levels of < 15 mL/min/1.73 m², none (0%) had eGFR levels of $15 < 30$ mL/min/1.73 m², one (17%) had eGFR levels of $30 < 45$ mL/min/1.73 m², and 4 patients (67%) had eGFR levels of $45 < 60$ mL/min/1.73 m².

Phase II

A total of 14 patients with renal impairment who screened negative for NSF on the screening questionnaire consented to participate in this phase of the study and successfully underwent an elective research-motivated deep skin punch biopsy and gadolinium-level quantification using ICP-MS (Fig 2). The measured eGFR values for these 14 research subjects ranged from 26 to 59 mL/min/1.73 m². The measured gadolinium values in the skin biopsies of these patients ranged from < 0.05 to 1.1 $\mu\text{g/g}$ (Table 2). These values were all judged to be consistent with background values for this laboratory and were distinctly lower than gadolinium levels typically measured in this lab for skin biopsies of patients with NSF in whom skin-sample gadolinium levels ranged from 4.8 to 106 $\mu\text{g/g}$.

DISCUSSION

The transmetallation theory has been broadly cited to explain how NSF develops and the mechanism for potential safety issues associated with retained/residual gadolinium following clinical gadolinium administration. However, the transmetallation theory itself does not sufficiently explain the relative incidence of NSF. Certain inconsistencies seem to be present if we seek to explain the NSF incidence on the basis of the transmetallation theory alone. For example, gadopentetate and gadobenate are both linear ionic gadolinium-based contrast agents, yet there is a large difference in the number of cases of NSF associated with their prior unconfounded administration that cannot be explained by relative market share differences.²⁵

The lack of clarity as to causation is compounded by the concern that perhaps NSF might actually represent one extreme on a spectrum of gadolinium-related issues. In other words, there is a concern that a so-called subclinical NSF might exist in which

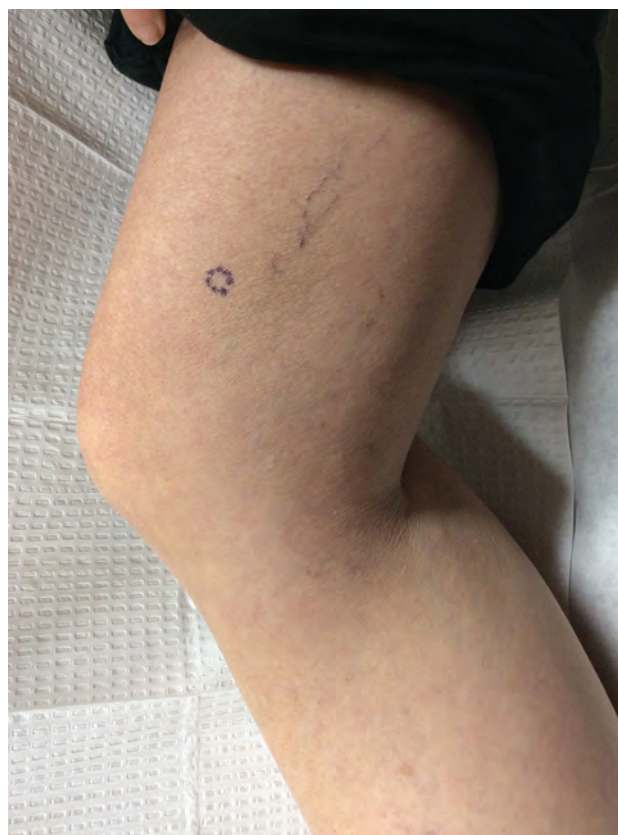


FIG 2. Location marked is representative of the biopsy location on each of the 14 research subjects studied.

Table 2: Subject biopsy details, including gadolinium level and number of prior MRIs

Subject No.	Biopsy Weight (mg)	Gadolinium ($\mu\text{g/g}$)	eGFR	No. Prior MR Imagings
1	1.158	< 0.05	39	1
2	0.638	0.57	33	3
3	0.802	0.15	26	3
4	0.72	0.11	49	3
5	2.505	0.27	52	8
6	0.748	< 0.05	33	1
7	1.213	0.14	50	2
8	1.064	0.08	51	2
9	0.46	0.06	37	9
10	1.07	0.33	40	2
11	0.74	0.10	59	2
12	0.70	0.08	46	2
13	0.52	0.28	53	3
14	0.29	1.1	53	1

some changes may be histologically present but not clinically manifest at lower total exposure levels to various GBCA.

This study was undertaken in an effort to further analyze and quantify the NSF risk associated with gadobenate administration, specifically to the population deemed to be at highest risk for this disease, namely, those with significant renal disease. The findings of this study, revealing no cases of NSF associated with the administration of gadobenate to patients with significant, serious, or end-stage renal disease support those of other publications describing the observed NSF incidence in this specific patient population.²⁷⁻³⁰

Table 3: Gadolinium deposition in skin samples from patients with NSF (adapted from Roberts et al³⁴)

Lead Author	No. of Patients with NSF	Range of Gadolinium Levels (µg/g)	No. of Controls	Range of Gadolinium Levels (µg/g)	Comment
					Inductively Coupled Mass Spectrometry (ICP-MS) Techniques
High et al ⁷	5	4.8–106	1	0	Limits of detection not provided
Khurana et al ³⁵	6	57.2–717.8	2 Infant Foreskin	0.0 (reported as ppm)	3-5 Gadolinium MRIs 1 MS patient marginal renal function
			2 Multiple Sclerosis Patients	0.1	
			Scleroderma Patient	0.2	
Christensen et al ³⁶	13	Affected skin 6.3–348.7	13	2 – 0.1	2 with previous GBCA administration
		Unaffected skin 0.6–68.2		¶ below detectable range	
Roberts et al ³⁴	1?	14.5			61 GBCA MRIs, eGFR >59 mL/min/1.73 m ²

Note:—? indicates NSF diagnosis was not confirmed.

With gadolinium having been reported in the skin of patients with NSF (Table 3),^{5,31} it is interesting to note the lack of elevation of gadolinium levels in the 14 subjects with significant renal disease who had previously undergone at least 1 contrast-enhanced MR imaging examination with gadobenate.

It remains unclear whether the presence of gadolinium in NSF skin lesions is etiologically related, secondary, or incidental in nature, and this lack of clarity provides further evidence of differences between patients with NSF with renal disease relative to those with significant renal disease who had undergone gadobenate-enhanced MR imaging but did not have clinical NSF.

Limitations

The study is limited in that there are several patients who had responded “yes” to ≥3 screening questions about whom there is no follow-up information available due to patient refusals, death, lack of access to follow-up, and so forth. However, the data remain quite reassuring insofar as most patients in this study with significant renal disease who had undergone a gadobenate-enhanced MR imaging examination were able to be successfully screened, and no cases of NSF were found. Another limitation of the examination is that the vast majority of those with significant renal disease in this study who did receive gadobenate received a half-dose and not a full dose. However, this specific gadolinium-based contrast agent has a high relaxivity, and several publications have already documented the favorable diagnostic sensitivities of partial-dose gadobenate relative to studies performed following full doses of several of the other lower relaxivity GBCA used for neuroradiologic imaging.^{32,33} Thus, from a clinical point of view, partial-dose administration of this agent may well be an appropriate diagnostic comparator against a full dose of lower relaxivity agents, with the added benefit of having administered to the patient proportionally fewer gadolinium ions by so doing.

The gadolinium levels were obtained after the patient volunteered for the study and therefore at various times following

the last gadolinium contrast MR imaging, the date of which was not available to the study team. We, therefore, view these levels as a “snapshot” at an indeterminate time from the last administration.

Gadolinium levels should be considered either negligible or large; exact quantitation, given the small mass of the skin biopsy, may not be achievable. The small mass of the skin biopsies introduces the possibility of contamination during multiple processing procedures to determine gadolinium levels such as the following:

- Metal in the punch biopsy device
- Metal in the forceps
- Non-reagent grade chemicals used in the processing procedures
- Contamination from the microtomes
- Contamination from the water baths.

Consistent with other similar reports, in our study of 860 patients with varying levels of impaired renal function (defined as <60 mL/min/1.73 m²) who underwent clinically indicated MR imaging examinations with gadobenate, subsequent screening failed to reveal any cases of nephrogenic systemic fibrosis. In comparison with previous publications, we screened patients with a uniform, previously validated questionnaire and performed skin biopsies. Previous studies also faced the methodologic difficulty of accounting for drop-out and deceased patients. Gadolinium-level quantification by ICP-MS of deep skin punch biopsies of 14 research subjects with impaired renal function who did not have clinical signs or symptoms of NSF and who had previously undergone at least 1 contrast-enhanced MR imaging examination with gadobenate failed to reveal any measurable elevation of skin gadolinium levels beyond that found in healthy controls.

CONCLUSIONS

No evidence of NSF was found in 860 patients with moderate or worse chronic kidney disease for whom follow-up was available

and who had received (predominantly half dose) gadobenate for clinical MR imaging examinations. Additionally, in 14 patients with impaired renal function who underwent at least 1 gadobenate-enhanced MR imaging examination and who did not have clinical NSF, ICP-MS determined that gadolinium levels in the skin were exceedingly low and were considered essentially at background levels without evidence of abnormal gadolinium accumulation. Implications for patient care are that NSF was not identified in patients with renal disease undergoing predominantly half-dose gadobenate contrast MR imaging and that gadolinium skin retention is minimal in these patients.

ACKNOWLEDGMENT

The authors wish to thank Dr Whitney High for his assistance in testing skin samplings for gadolinium.

Disclosures: Emanuel Kanal—UNRELATED: Consultancy: Bracco Diagnostics, GE Healthcare, Guerbet, Comments: MR imaging safety consulting.

REFERENCES

- Balzer T. **Presence of Gadolinium (Gd) in the Brain and Body: Presentation to the Medical Imaging Drugs Advisory Committee**, September 8, 2017. FDA. Silver Spring, Md: U.S. Food and Drug Administration. <https://www.fda.gov/media/107670/download>. Accessed February 5, 2020
- McDonald RJ, Levine D, Weinreb J, et al. **Gadolinium retention: a research roadmap from the 2018 NIH/ACR/RSNA Workshop on Gadolinium Chelates**. *Radiology* 2018;289:517–34 CrossRef Medline
- Boyd AS, Zic JA, Abraham JL. **Gadolinium deposition in nephrogenic fibrosing dermopathy**. *J Am Acad Dermatol* 2007;56:27–30 CrossRef Medline
- Grobner T. **Gadolinium: a specific trigger for the development of nephrogenic fibrosing dermopathy and nephrogenic systemic fibrosis?** *Nephrol Dial Transplant* 2006;21:1104–08 CrossRef Medline
- Birka M, Wentker KS, Lusmoller E, et al. **Diagnosis of nephrogenic systemic fibrosis by means of elemental bioimaging and speciation analysis**. *Anal Chem* 2015;87:3321–28 CrossRef Medline
- High WA, Ayers RA, Chandler J, et al. **Gadolinium is detectable within the tissue of patients with nephrogenic systemic fibrosis**. *J Am Acad Dermatol* 2007;56:21–26 CrossRef Medline
- High WA, Ayers RA, Cowper SE. **Gadolinium is quantifiable within the tissue of patients with nephrogenic systemic fibrosis**. *J Am Acad Dermatol* 2007;56:710–12 CrossRef Medline
- Grobner T, Prischl FC. **Gadolinium and nephrogenic systemic fibrosis**. *Kidney Int* 2007;72:260–64 CrossRef Medline
- Kanda T, Ishii K, Kawaguchi H, et al. **High signal intensity in the dentate nucleus and globus pallidus on unenhanced T1-weighted MR images: relationship with increasing cumulative dose of a gadolinium-based contrast material**. *Radiology* 2014;270:834–41 CrossRef Medline
- Kanda T, Osawa M, Oba H, et al. **High signal intensity in dentate nucleus on unenhanced T1-weighted MR images: association with linear versus macrocyclic gadolinium chelate administration**. *Radiology* 2015;275:803–09 CrossRef Medline
- Boyken J, Frenzel T, Lohrke J, et al. **Gadolinium accumulation in the deep cerebellar nuclei and globus pallidus after exposure to linear but not macrocyclic gadolinium-based contrast agents in a retrospective pig study with high similarity to clinical conditions**. *Invest Radiol* 2018;53:278–85 CrossRef Medline
- Jost G, Lenhard DC, Sieber MA, et al. **Signal increase on unenhanced T1-weighted images in the rat brain after repeated, extended doses of gadolinium-based contrast agents: comparison of linear and macrocyclic agents**. *Invest Radiol* 2016;51:83–89 CrossRef Medline
- Lohrke J, Frisk AL, Frenzel T, et al. **Histology and gadolinium distribution in the rodent brain after the administration of cumulative high doses of linear and macrocyclic gadolinium-based contrast agents**. *Invest Radiol* 2017;52:324–33 CrossRef Medline
- Kartamihardja AA, Nakajima T, Kameo S, et al. **Distribution and clearance of retained gadolinium in the brain: differences between linear and macrocyclic gadolinium-based contrast agents in a mouse model**. *Br J Radiol* 2016;89:20160509 CrossRef Medline
- McDonald RJ, McDonald JS, Dai D, et al. **Comparison of gadolinium concentrations within multiple rat organs after intravenous administration of linear versus macrocyclic gadolinium chelates**. *Radiology* 2017;285:536–45 CrossRef Medline
- Moser FG, Watterson CT, Weiss S, et al. **High signal intensity in the dentate nucleus and globus pallidus on unenhanced T1-weighted MR images: comparison between gadobutrol and linear gadolinium-based contrast agents**. *AJNR Am J Neuroradiol* 2018;39:421–26 CrossRef Medline
- Radbruch A, Weberling LD, Kieslich PJ, et al. **Intraindividual analysis of signal intensity changes in the dentate nucleus after consecutive serial applications of linear and macrocyclic gadolinium-based contrast agents**. *Invest Radiol* 2016;51:683–90 CrossRef Medline
- Rasschaert M, Emerit A, Fretellier N, et al. **Gadolinium retention, brain T1 hyperintensity, and endogenous metals: a comparative study of macrocyclic versus linear gadolinium chelates in renally sensitized rats**. *Invest Radiol* 2018;53:328–37 CrossRef Medline
- Robert P, Lehericy S, Grand S, et al. **T1-weighted hypersignal in the deep cerebellar nuclei after repeated administrations of gadolinium-based contrast agents in healthy rats: difference between linear and macrocyclic agents**. *Invest Radiol* 2015;50:473–80 CrossRef Medline
- Runge VM. **Macrocyclic versus linear gadolinium chelates**. *Invest Radiol* 2015;50:811 CrossRef Medline
- Runge VM. **Commentary on T1-weighted hypersignal in the deep cerebellar nuclei after repeated administrations of gadolinium-based contrast agents in healthy rats: difference between linear and macrocyclic agents**. *Invest Radiol* 2015;50:481–82 CrossRef Medline
- Schmitt-Willich H. **Stability of linear and macrocyclic gadolinium-based contrast agents**. *Br J Radiol* 2007;80:581–82 CrossRef Medline
- Edwards BJ, Laumann AE, Nardone B, et al. **Advancing pharmacovigilance through academic-legal collaboration: the case of gadolinium-based contrast agents and nephrogenic systemic fibrosis: a Research on Adverse Drug Events and Reports (RADAR) report**. *Br J Radiol* 2014;87:20140307 CrossRef Medline
- Lohani S, Golenbiewski J, Swami A, et al. **A unique case of nephrogenic systemic fibrosis from gadolinium exposure in a patient with normal eGFR**. *BMJ Case Rep* 2017;2017 CrossRef Medline
- FDA. **Meeting Materials Cardiovascular and Renal Drugs Advisory Committee**. March 19, 2009. Adelphi, Maryland. <https://www.federalregister.gov/documents/2009/02/13/E9-3089/cardiovascular-and-renal-drugs-advisory-committee-notice-of-meeting>. Accessed February 5, 2020
- Lima XT, Alora-Palli MB, Kimball AB, et al. **Validation of a screening instrument for nephrogenic systemic fibrosis**. *Arthritis Care Res (Hoboken)* 2013;65:637–42 CrossRef Medline
- Bryant BJ, Im K, Broome DR. **Evaluation of the incidence of nephrogenic systemic fibrosis in patients with moderate renal insufficiency administered gadobenate dimeglumine for MRI**. *Clin Radiol* 2009;64:706–13 CrossRef Medline
- Nandwana SB, Moreno CC, Osipow MT, et al. **Gadobenate dimeglumine administration and nephrogenic systemic fibrosis: is there a real risk in patients with impaired renal function?** *Radiology* 2015;276:741–47 CrossRef Medline
- Soulez G, Bloomgarden DC, Rofsky NM, et al. **Prospective cohort study of nephrogenic systemic fibrosis in patients with stage 3–5 chronic kidney disease undergoing MRI with injected gadobenate dimeglumine or gadoteridol**. *AJR Am J Roentgenol* 2015;205:469–78 CrossRef Medline

30. Bruce R, Wentland AL, Haemel AK, et al. **Incidence of nephrogenic systemic fibrosis using gadobenate dimeglumine in 1423 patients with renal insufficiency compared with gadodiamide.** *Invest Radiol* 2016;51:701–05 CrossRef Medline
31. Roberts DR, Chatterjee AR. **The critical need for pediatric and juvenile animal research addressing gadolinium retention in the developing body.** *Invest Radiol* 2019;54:72–75 CrossRef Medline
32. Vaneckova M, Herman M, Smith MP, et al. **The benefits of high relaxivity for brain tumor imaging: results of a multicenter intra-individual crossover comparison of gadobenate dimeglumine with gadoterate meglumine (the BENEFIT Study).** *AJNR Am J Neuroradiol* 2015;36:1589–98 CrossRef Medline
33. Khouri Chalouhi K, Papini GD, Bandirali M, et al. **Less is better? Intra-individual and inter-individual comparison between 0.075 mmol/kg of gadobenate dimeglumine and 0.1 mmol/kg of gadoterate meglumine for cranial MRI.** *Eur J Radiol* 2014;83:1245–49 CrossRef Medline
34. Roberts DR, Lindhorst SM, Welsh CT, et al. **High levels of gadolinium deposition in the skin of a patient with normal renal function.** *Invest Radiol* 2016;51:280–89 CrossRef Medline
35. Khurana A, Greene JF Jr, High WA. **Quantification of gadolinium in nephrogenic systemic fibrosis: re-examination of a reported cohort with analysis of clinical factors.** *J Am Acad Dermatol* 2008;59:218–24 CrossRef Medline
36. Christensen KN, Lee CU, Hanley MM, et al. **Quantification of gadolinium in fresh skin and serum samples from patients with nephrogenic systemic fibrosis.** *J Am Acad Dermatol* 2011;64:91–96 CrossRef Medline

Imaging-Based Algorithm for the Local Grading of Glioma

 E.D.H. Gates,  J.S. Lin,  J.S. Weinberg,  S.S. Prabhu,  J. Hamilton,  J.D. Hazle,  G.N. Fuller,  V. Baladandayuthapani,  D.T. Fuentes, and  D. Schellingerhout



ABSTRACT

BACKGROUND AND PURPOSE: Gliomas are highly heterogeneous tumors, and optimal treatment depends on identifying and locating the highest grade disease present. Imaging techniques for doing so are generally not validated against the histopathologic criterion standard. The purpose of this work was to estimate the local glioma grade using a machine learning model trained on preoperative image data and spatially specific tumor samples. The value of imaging in patients with brain tumor can be enhanced if pathologic data can be estimated from imaging input using predictive models.

MATERIALS AND METHODS: Patients with gliomas were enrolled in a prospective clinical imaging trial between 2013 and 2016. MR imaging was performed with anatomic, diffusion, permeability, and perfusion sequences, followed by image-guided stereotactic biopsy before resection. An imaging description was developed for each biopsy, and multiclass machine learning models were built to predict the World Health Organization grade. Models were assessed on classification accuracy, Cohen κ , precision, and recall.

RESULTS: Twenty-three patients (with 7/9/7 grade II/III/IV gliomas) had analyzable imaging-pathologic pairs, yielding 52 biopsy sites. The random forest method was the best algorithm tested. Tumor grade was predicted at 96% accuracy ($\kappa = 0.93$) using 4 inputs (T2, ADC, CBV, and transfer constant from dynamic contrast-enhanced imaging). By means of the conventional imaging only, the overall accuracy decreased (89% overall, $\kappa = 0.79$) and 43% of high-grade samples were misclassified as lower-grade disease.

CONCLUSIONS: We found that local pathologic grade can be predicted with a high accuracy using clinical imaging data. Advanced imaging data improved this accuracy, adding value to conventional imaging. Confirmatory imaging trials are justified.

ABBREVIATIONS: DCE = dynamic contrast-enhanced; K^{trans} = transfer constant from dynamic contrast-enhanced imaging; NAWM = normal-appearing white matter; ROC = receiver operating characteristic; TIC = T1 post-gadolinium; WHO = World Health Organization; IDH = *Isocitrate dehydrogenase*

Gliomas are the most common central nervous system malignancy. They are graded according to the World Health Organization (WHO) grading scale, which represents the overall malignant potential of the tumor.¹ The difference in prognosis for gliomas varies with grade, from 5–12 years (WHO II) to

<14 months (WHO IV),^{2–4} and nearly all treatment decisions rest critically on the grade of the disease.

In routine clinical care, the overall grade of a tumor is assigned as the highest grade found in ≥ 1 small biopsy sample. Thus, it is crucial that these samples represent the highest grade present within the tumor so that patients with high-grade disease are not “undergraded.” Several studies have highlighted the intratumoral heterogeneity of gliomas,^{5,6} which makes sampling the highest grade areas of the tumor a challenging task. The problem of undergrading can occur in as high as 30% of cases.⁷

Received October 22, 2019; accepted after revision December 16.

From the Departments of Imaging Physics (E.D.H.G., J.S.L., J.D.H., D.T.F.), Neurosurgery (J.S.W., S.S.P.), Pathology (G.N.F.), Neuroradiology (D.S.), and Cancer Systems Imaging (D.S.), University of Texas MD Anderson Cancer Center, Houston, Texas; University of Texas MD Anderson Cancer Center UTHealth Graduate School of Biomedical Sciences (E.D.H.G.), Houston, Texas; Baylor College of Medicine (J.S.L.), Houston, Texas; Department of Bioengineering (J.S.L.), Rice University, Houston, Texas; Radiology Partners (J.H.), Houston, Texas; and Department of Computational Medicine and Bioinformatics (V.B.), University of Michigan School of Public Health, Ann Arbor, Michigan.

This work was supported by the National Institutes of Health and National Cancer Institute grants R01-CA194391 and R01-CA160736 and the Cancer Center Support Grant P30 CA016672 (Biostatistics Shared Resource) to V.B. Partial support for this study was provided by the Dunn Chair funds (to Dr Bill Murphy), the MD Anderson Cancer Center Internal Research Grant and Clinical Research Support mechanisms for physician-sponsored clinical trials, and the Greenspun neurosurgical research fund.

Please address correspondence to Dawid Schellingerhout, MD, Neuroradiology and Cancer Systems Imaging, University of Texas MD Anderson Cancer Center, 1400 Pressler St, Unit 1482, Houston, TX 77030; e-mail: Dawid.Schellingerhout@mdanderson.org

 Indicates open access to non-subscribers at www.ajnr.org

 Indicates article with supplemental on-line appendix and tables.

 Indicates article with supplemental on-line photo.

<http://dx.doi.org/10.3174/ajnr.A6405>

There is a gap in our knowledge regarding the use of imaging to identify the highest grade portions of gliomas on the local scale. In this study, we sought to measure the strength of imaging correlations with WHO grade on a per-biopsy level. Our goal was to estimate the WHO pathologic grade based on imaging data input.

Our study is characterized by the use of the latest imaging technologies, state-of-the-art surgical and neuropathologic techniques, and very close spatial imaging-pathologic correlations. We found that imaging data can predict tumor grade to clinically useful accuracies and that advanced imaging (perfusion, permeability, and diffusion) adds value to conventional imaging and improves the accuracy of grade estimates.

MATERIALS AND METHODS

Patients

Data were acquired in a prospective clinical imaging trial (clinicaltrials.gov, NCT03458676), for which this article serves as an interim report. The study was approved by the University of Texas MD Anderson Cancer Center institutional review board, complied with all Health Insurance Portability and Accountability Act regulations, and required informed consent of each participant. We recruited from the pool of previously untreated adult patients with gliomas scheduled for surgical resection in the neurosurgical service at our institution. Patients for whom MR imaging or intravenous contrast was contraindicated were excluded from the study. We previously reported a study estimating the cellular proliferation marker Ki-67 in this same patient population.⁸ The current study is based on a separate analysis using a different histologic outcome measure, tumor grade.

Biopsy Sites: Selection and Pathology Analysis

Biopsy target locations were planned before the operation and used either conventional (areas of contrast enhancement) or advanced imaging features (high CBV and/or the transfer constant from dynamic contrast enhanced imaging [K^{trans}] and/or low ADC) to locate sites of suspected high-grade disease. At least 2 biopsy sites were prospectively located before an operation. Biopsy sites were subject to surgeon approval and could be modified as surgically dictated, provided that the altered coordinates were documented. During craniotomy, a neurosurgeon collected ≥ 1 biopsy using a stereotactic technique before starting resection. As the samples were collected, coordinates of the sampling location were recorded using neuronavigation software (“iPlan”, Brainlab, Munich, Germany). This allowed precise, unambiguous identification of the sampling location on the preoperative imaging.⁹ Tissue specimens were sectioned and stained using H&E. A board-certified neuropathologist graded each sample independently according to the WHO criteria while blinded to the imaging data.

Although our patients were evenly distributed among final WHO grades II–IV and biopsies were targeted toward areas of increased malignancy, we ultimately collected relatively few high-grade samples. For statistical reasons, we further grouped our samples into 3 categories: normal tissue; lower grade, composed of grade II samples; and higher grade, consisting of grouped grades III and IV samples. *Isocitrate dehydrogenase (IDH)* mutation status was not considered when grouping samples into lower- and higher-grade groups.

Imaging

All patients were scanned on a Signa HDxt or Discovery MR750 3T (GE Healthcare, Milwaukee, Wisconsin) clinical scanner using an 8-channel head coil. We collected conventional anatomic MR imaging sequences such as T1-weighted, T1-postgadolinium (T1C), T2-weighted, susceptibility-weighted angiography (SWAN) and T2 FLAIR, as well as advanced diffusion-weighted (DWI/DTI), DSC, and dynamic contrast-enhanced (DCE) sequences. The advanced imaging series were processed into parametric or pharmacokinetic maps using the Advantage Workstation (Version 4.5; GE Healthcare) and NordicICE (NordicNeuroLab, Bergen, Norway). Specific acquisition parameters are given in On-line Tables 1 and 2.

Diffusion-weighted images (4 b-values from 0 to 2000) were processed to maps of ADCs and exponential ADC and diffusion tensor imaging (27 encoding directions) provided maps of fractional anisotropy. DSC and DCE imaging used separate boluses of 0.1 mmol/kg of gadolinium contrast at 5 mL per second. The DCE bolus served as a preload for DSC imaging and was used for T1 postcontrast imaging. DCE time-series were processed into transfer constants and voxel fractions (K^{trans} , k_{ep} , v_p , v_e). We also computed slopes (wash-in, wash-out), TTP, peak enhancement, and curve area voxelwise from the time-series. DSC data were similarly processed into maps of relative CBF and CBV, delay time and MTT, and leakage parameter with a cutoff of 0.01. We did not apply motion correction or spatial or temporal smoothing to DSC or DCE time-series before processing.

Brain-extracted images were coregistered using rigid (6 *df*), followed by affine (12 *df*) mutual information–based registration.¹⁰ The T2-weighted image was used as the reference for each patient. Anatomic images were normalized using ROIs manually placed in CSF, deep GM, or normal-appearing white matter (NAWM). Each image was linearly scaled so that the darkest and brightest ROIs had mean intensities of 0 and 1, respectively. For example, each patient’s T2-weighted image was independently scaled to have a mean WM intensity of 0 and CSF intensity of 1. We found that this scaling greatly reduced interpatient variability.¹¹ DWI, DTI, DSC, and DCE quantitative parameters were used without normalization.

We recorded the average intensity in a 5-mm diameter spheric VOI centered on the biopsy coordinates for each sample. Ultimately, each sample had 23 imaging values associated with it (On-line Table 3), one for each imaging parameter. We also selected coordinates mirrored across the midline contralateral to each biopsy in NAWM to represent normal tissue. An oncologic neuroradiologist reviewed these placements to ensure that they were completely in NAWM. Corresponding imaging values were extracted for these “virtual biopsy” sites to serve as controls for tumor biopsies.

These contralateral virtual biopsies are intended to help the model discern the imaging features of normal brain versus tumor, and omitting these might yield a model good only for distinguishing grades from one another, but failing to distinguish normal brain from tumor (On-line Table 4). The ability to distinguish normal brain from tumor and various local grades from one another stands as equally desirable for clinical applications. Clearly, the best solution would be to acquire real,

histologically normal samples from peritumoral and normal brain regions, but ethical constraints prohibited us.

Modeling of Image Features to Predict Tumor Grade

Modeling and analysis were implemented using R, Version 3.4.2.¹² We used random forest,¹³ support vector machine, and neural network classifiers for prediction of multiclass output of tumor grade (normal, lower-grade, higher-grade). The results of all models are given in On-line Table 5, and descriptions of model parameters are given in On-line Table 6. Although deep convolutional networks are powerful models for image-based prediction tasks, we elected not to use one in this case. The strength of this dataset is in the spatial specificity of the tissue samples, which means our training data are only the very small region around each sampling location. This is generally incompatible with convolutional networks, which require either large segmented regions or whole-image classifications for training. Our models were assessed using five-fold cross-validation, with the proportion of samples of each grade maintained between each fold. The classifier performance was measured using the average classification accuracy of the model over the testing set (20% of biopsy data not used for model training) and the Cohen κ .¹⁴ The κ metric measures the accuracy relative to the expected agreement based on random guessing. Similarly to

overall accuracy, $\kappa = 1$ for perfect classification. However, unlike accuracy, $\kappa = 0$ means that the classifier is no better than chance, even though some samples may be correctly classified (for an observed proportion of agreement p_{obs} and expected agreement p_{exp} : $\kappa = \frac{p_{obs} - p_{exp}}{1 - p_{exp}}$).

We focused our presentation on the results of our best-performing approach, the random forest. Performance of other models tested is listed in On-line Table 5. We found that an accurate model could be made using only 1 imaging parameter from each family of sequences. In each fold of cross-validation, we selected the best predictor from each family and used that reduced 4-variable set to make predictions on the testing set. We also aggregated the dominant imaging predictors into a single fixed variable set and repeated the cross-validation to estimate the performance of this final fixed model. Finally, we repeated the variable selection and cross-validation using conventional imaging only to investigate the benefit of diffusion, perfusion, and permeability imaging.

The primary benefit in predicting sample grades is localizing areas of high-grade disease. We further analyzed the ability of the classifier to separate the higher-grade samples from the pooled normal and lower-grade samples using receiver operating characteristic (ROC) and precision recall curves.

RESULTS

Patients

Thirty-one patients were initially recruited; surgical complexity prohibited tissue harvest in 5 cases. Among the 26 patients with successful tissue harvest, a total of 64 biopsies were collected. Additional patient exclusion occurred due to missing DCE imaging (1 patient, 3 biopsies) and missing histologic values due to lack of analyzable tissue (2 patients, 4 total biopsies). Further exclusion of biopsies occurred due to poor VOI placement ($n = 3$ biopsies), insufficient quality of tissue for pathologic analysis ($n = 1$), and missing grades ($n = 1$). This left 23 patients, including 7 patients with grade II, 9 with grade III, and 7 with grade IV gliomas (final clinical grade) for use in the final analysis, with 52 real biopsies and 52 paired virtual biopsies. When a biopsy site was excluded, its corresponding imputed virtual biopsy site was also excluded. Full details of sample exclusions are given in the On-line Figure.

Among the 23 patients used in the final analysis, 11 (25 samples) had *IDH* wild-type tumors and the remainder (12 patients, 27 samples) had *IDH*-mutant tumors. *MGMT* promoter methylation was present in 21/23, and 1p/19q codeletion, in 9/23.

Pathology and Imaging Analysis

Samples were graded II–IV using the WHO criteria on a per-biopsy basis (ie, only features of that particular

Table 1: Enhancement status—the overall enhancement characteristics of each tumor separated by clinical WHO grade on a patient-by-patient basis^a

Tumor Type	Patient Clinical Grade		
	II	III	IV
Enhancing	0	1	6
Nonenhancing	7	8	1

^a As expected, grade II gliomas are nonenhancing and grade IV gliomas are almost all enhancing.

Table 2: Enhancement status—tabulates which samples were collected from enhancing-versus-nonenhancing regions^a

Tumor Type	Sampling Region	Sample Grade (52 Total)				
		Normal	II	II/III	III	IV
Enhancing tumor	Enhancing volume	0	4	0	2	3
	Nonenhancing volume	1	4	1	0	2
Nonenhancing tumor	Nonenhancing volume	2	31	2	0	0

^a In this table, the grade represents the individual grade of the sample, on a sample-by-sample basis, which is not necessarily equal to the patient's clinical grade. For enhancing tumors, about half the samples were collected from the enhancing portion of the tumor.

Table 3: Model accuracy—accuracy for random forest models trained on conventional (anatomic imaging) and conventional-plus-advanced (diffusion, perfusion, permeability) imaging^a

Metric	Variables	Conventional	Conventional-Plus-Advanced
Accuracy	All Variables	0.904	0.952
	RF Rank	0.875	0.933
κ	RF (fixed variables)	0.885 (T2, TIC, FLAIR, T1)	0.962 (T2, ADC, CBV, κ^{trans})
	All Variables	0.822	0.912
	RF Rank	0.768	0.877
	RF (fixed variables)	0.788	0.930

Note:—RF indicates random forest.

^a Performance using all 23 variables is compared with the performance averaged over 5 folds of cross-validation as well as the results using a fixed-variable subset. The Cohen κ is larger for more accurate models but is scaled so that a no-information classifier would have κ equal to zero.

Table 4: Model predictions by sample grade—confusion matrix for the random forest model trained on 4 fixed variables^a

Predicted	Reference			Total
	Normal	Lower	Higher	
Conventional plus advanced				
Normal	53	1	0	54
Lower	2	41	1	43
Higher	0	0	6	7
Total	<i>n</i> = 55	<i>n</i> = 42	<i>n</i> = 7	104
Conventional only				
Normal	52	5	0	57
Lower	3	36	3	42
Higher	0	1	4	5
Total	<i>n</i> = 55	<i>n</i> = 42	<i>n</i> = 7	104

^a A perfect classifier would have all entries along the main diagonal. The random forest using conventional-plus-advanced imaging had 96.2% (100/104) overall accuracy with $\kappa = 0.930$, whereas the random forest using only conventional imaging had 88.5% (92/104) accuracy with $\kappa = 0.788$. The conventional-only classifier also misclassified 43% (3/7) of high-grade samples.

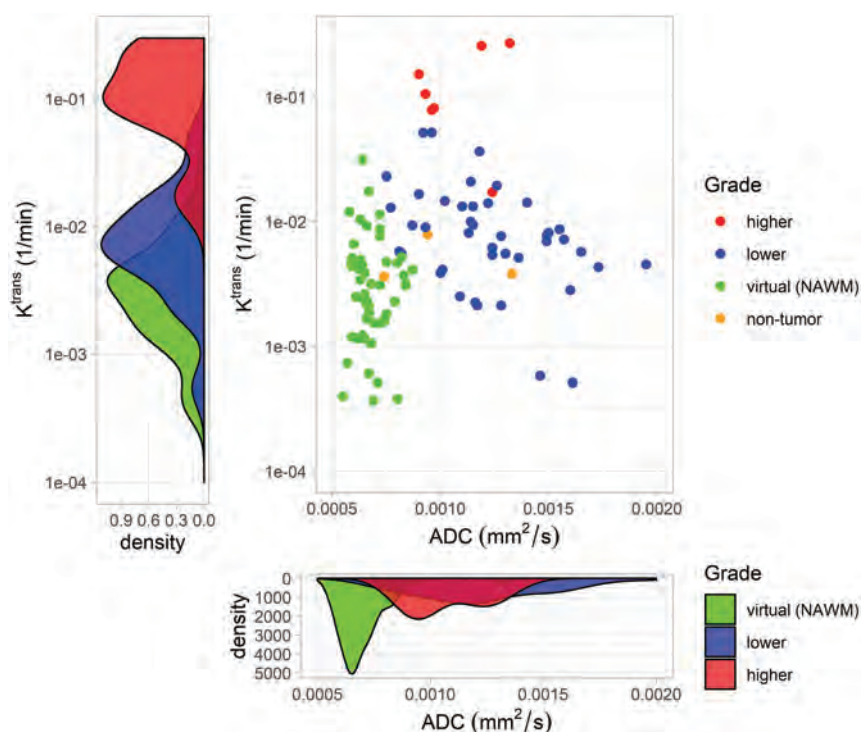


FIG 1. Synergistic properties of imaging sequences with “orthogonal” information. Two representatives of the variable inputs used to generate the grade map seen in Fig 3 are shown. The scatterplot shows the ADC (square millimeters/second) from DWI and K^{trans} (minute⁻¹) from DCE for normal, lower-grade, and higher-grade samples. The normal samples are further identified as being either virtual biopsies in NAWM or nontumor real tissue samples as designated by a pathologist. Each imaging parameter roughly separates 2 of the classes as seen by histograms. Combined, they form 3 distinct clusters that are identified by the random forest. K^{trans} alone distinguishes lower- and higher-grade samples but does not differentiate lower-grade tumor samples from those of healthy controls, as shown by the degree of overlap in the left density plot. However, the ADC from diffusion-weighted imaging separates these healthy controls from tumor samples but differs little among different grades (lower density plot). Combining these successfully identifies all 3 sample grades (normal, lower-grade, and higher-grade) simultaneously. This separation is further increased by adding CBV and T2-weighted signal intensity.

biopsy as judged on H&E staining were used to assign a grade to that biopsy). Note that this research methodology is at variance with the clinical practice of assigning a clinical grade corresponding to the maximum local grade found to a patient. The per-

biopsy local grading used in this article is different from the conventional per-patient clinical grading. Some biopsy samples were graded II/III as an intermediate between grades II and III, due to our pathologist’s clinical assessment that their malignant potential exceeded that of regular grade II samples.¹⁵ Of the 52 real biopsies, 3 were normal brain, 39 grade II, 3 grade II/III, 2 grade III, and 5 grade IV. The lack of grade I disease is expected in a nonpediatric population. For the final analysis, we had 55 biopsies with normal results (3 real and 52 virtual), 42 lower-grade samples, and 7 higher-grade samples.

Among the 23 patients, nearly all the grade IV tumors were contrast-enhancing and nearly all of the grade II and III tumors were nonenhancing (see Table 1 for specifics). We collected both lower- and higher-grade samples in regions of contrast enhancement. Five of 7 higher-grade samples and 4 of 42 lower-grade samples were collected from the enhancing volume of an enhancing tumor. Table 2 lists the number of samples of each grade taken from regions of enhancement. This table shows that while enhancement is a good surrogate for local grade, it does not perfectly discriminate.

For 5 biopsies among 2 patients, missing susceptibility-weighted angiography imaging values were imputed as the median values among the corresponding real (*n* = 46) or virtual biopsies (*n* = 47). All imaging sequences were available for the remaining patients.

Modeling Results

We trained a random forest model to predict the grade of individual samples using imaging values. We chose to use the random forest because it had the best average performance and provides some resistance to overfitting.¹³

Because many of the 23 parameters, especially those from the same family of imaging sequences, contain mostly redundant information, we used only the top predictor from each family for predictive modeling. We repeated this procedure for each fold of cross-validation (On-line Table 7) and

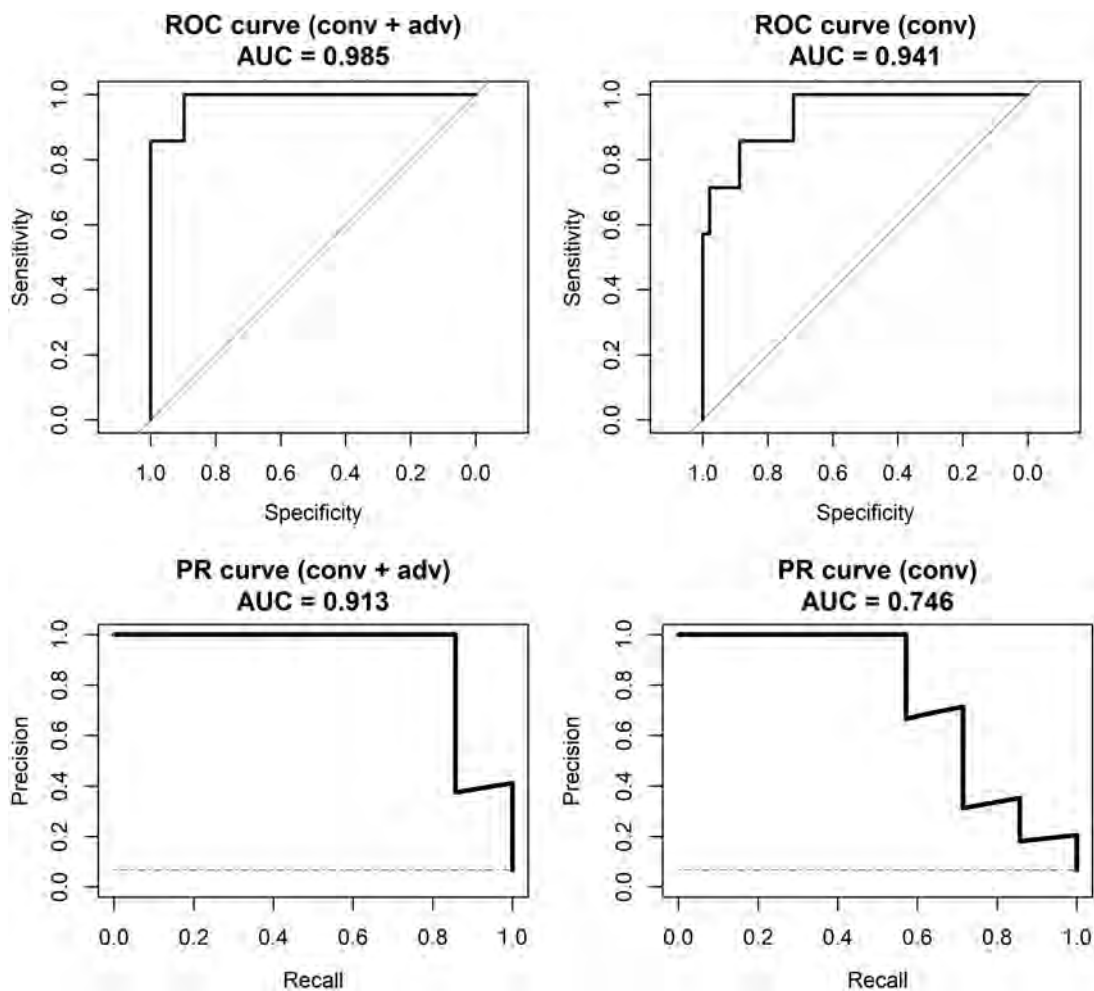


FIG 2. ROC and precision-recall (PR) curves for distinguishing high-grade samples versus normal tissue and low-grade disease samples. Plots in the left columns are based on the predictions from the random forest model using conventional and advanced imaging, whereas plots on the right are based on models using conventional imaging only. Although the area under the ROC curves is similar, the area under the PR curve is much smaller for conventional imaging only. The *diagonal lines* on the ROC curves and *horizontal dashed lines* on PR curves show the performance of a no-information or random classifier. Conv indicates conventional; adv, advanced; AUC, area under the curve.

selected the final 4-variable predictor set on the basis of consensus. This 4-variable set was T2, ADC, CBV, and K^{trans} .

With these 4 inputs, the random forest correctly classified the grade of individual samples with 96% accuracy (Cohen $\kappa = 0.930$) as shown in Table 3. Furthermore, none of the high-grade biopsies were classified as normal brain or vice versa (Table 4). The positive predictive value for high-grade disease is 1.0 (all predictions of high-grade are correct), and the negative predictive value is 0.990. Fig 1 intuitively shows how the combination of imaging from different families like diffusion and DCE are able to separate samples of different grades. The random forest leverages this type of separation to classify unknown samples. The normal, lower-, and higher-grade samples separate even more with the addition of conventional (T2) and perfusion (CBV) imaging.

By means of conventional imaging only (T2, T1C, FLAIR, T1), the model still managed to achieve 88.5% accuracy ($\kappa = 0.788$), but the error rate for high-grade samples was $>40\%$ (Table 4). In other words, the conventional imaging was generally unable to differentiate high-grade disease from low-grade disease using only anatomic MR imaging sequences. This issue highlights

the importance of advanced and functional imaging in determining the grade of individual samples. For reference, a classifier with no information would achieve 53% accuracy by classifying every sample as normal, the most frequent class.

While our patient population is fairly well-distributed among clinical WHO grades II, III, and IV, the higher-grade samples represent a minority in the sample population. To analyze the ability of the model to specifically identify higher-grade disease in light of this class imbalance, we analyzed the ROC and precision-recall curves for the final models. Specifically, we used the estimated probability of each model that a given sample was higher-grade (WHO grade III or IV) disease to create a binary output. The areas under the ROC curves were very high for both conventional and conventional-plus-advanced models at 0.94 and 0.99, respectively (Fig 2). However, the area under the precision-recall curve was considerably lower for the conventional-only model at 0.75 versus 0.91 for the conventional-plus-advanced model. The decreased precision or positive predictive value reiterates the difficulty for the conventional-only model in identifying higher-grade disease.

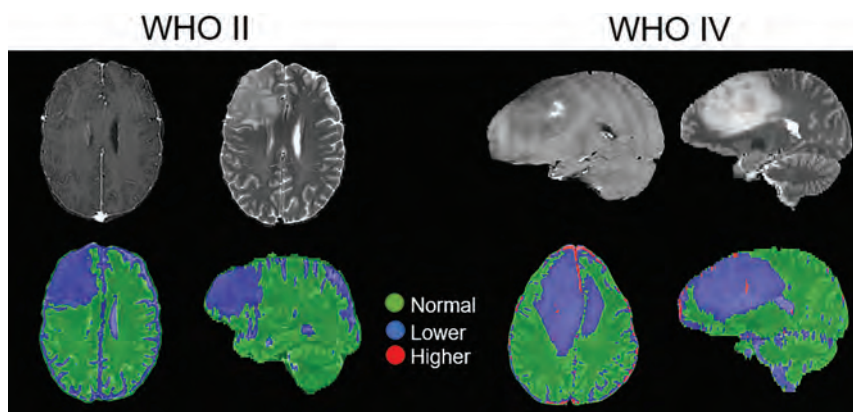


FIG 3. A clinically relevant map of the predicted tumor grade using the highest probability grade and smoothed by a median filter (2-voxel radius) superimposed on a T2-weighted image. Green, blue, and red correspond to predicted normal tissue and lower-grade and higher-grade disease, respectively. Shown on the left is a WHO grade II oligodendroglioma with a T2-weighted image for reference, and on the right is a WHO grade IV glioblastoma with a T1 postcontrast image for reference (*upper part*). The classifier identifies the oligodendroglioma as containing only lower-grade disease, while the glioblastoma has a central region of higher grade near the enhancing-focus disease surrounded by lower-grade disease. Areas of normal brain falsely identified as tumor (ie, sulcus) are unlikely to confuse a clinician.

Virtual biopsy regions in contralateral normal-appearing white matter constituted a majority of the normal tissue class and half of the overall training data. To ensure that this did not unnecessarily bias the model against normal samples in the peritumoral region, we re-trained the model using only the real biopsy samples and found that the model retained a high overall accuracy (>90%) and 86% sensitivity to high-grade disease. More details are provided in On-line Table 4.

DISCUSSION

We found the following: 1) imaging could be used to predict the WHO grade in glioma to clinically useful accuracies using a random forest model, 2) advanced imaging (diffusion, perfusion, and permeability) outperformed conventional anatomic imaging alone, 3) the best anatomic imaging sequences for estimating grade were T2-weighted, FLAIR, and T1-weighted both pre- and postcontrast, 4) the best overall imaging sequences for estimating grade were T2-weighted, ADC, CBV from DSC, and K^{trans} , and 5) the algorithm developed could be used to derive graphic grade maps to visually present the information for imaging guidance.

Image-guided brain tissue sampling is costly and technically demanding. Furthermore, imaging technology development is rapid, meaning the literature on tissue correlations between modern imaging sequences and neuropathologic techniques is continually evolving.¹⁶⁻¹⁹ Previous studies include predicting likely areas of infiltrative tumor and recurrence in glioblastoma using support vector machines and MR imaging.²⁰ However, the authors acknowledged that a limitation of their work was the lack of histopathologic validation. Indeed, many studies correlating image-based metrics with glioma grades are limited by this heterogeneity and lack of local histologic validation.^{19,21,22} In other work, Barajas et al²³ demonstrated that pathologic features of aggressiveness correlated with increased relative CBV and decreased relative ADC. Other recent work using hand-crafted

image features or neural networks to predict *IDH*-mutation status or glioma grade shows good overall accuracy but only evaluates the tumor as a whole and provides no regional information.^{24,25}

We constructed a random forest model using imaging inputs to predict the individual WHO grade of brain biopsies with reasonable success. The ranking of imaging input also demonstrates which imaging sequences were most valuable in predicting clinical information. Our work agrees with the literature showing that perfusion, K^{trans} ,²⁶ and ADC can all distinguish low- and high-grade tumors.^{27,28} CBV has also been shown to better differentiate tumor grades compared with conventional MR imaging.^{19,29,30}

Our best cross-validated model for predicting tumor grade was extrapolated voxelwise across the whole-brain volume. This extrapolation provided a map of normal, lower-grade, and higher-grade disease for each patient using only a small number of imaging inputs (Fig 3). For the high-grade glioblastoma case shown, we can see a central region of high-grade disease surrounded primarily by low-grade disease. Indeed, one of the biopsies from this patient near the tumor periphery was graded as WHO grade II, while another sample near the center of the tumor was graded as WHO grade IV.

Maps generated with these models contain some obvious errors (higher-grade assignment in the sulci and sinuses). A skilled clinician using such maps should not find such errors confusing and would be able to recognize these as artifacts of processing. Our future work will remove these spurious signals. While voxelwise validation of maps is impractical, the predictive accuracy at known biopsy sites is sufficient justification for use as a clinical tool to guide procedures like biopsies. While we see qualitative agreement between predicted regions of high-grade disease and contrast enhancement, which is the clinical standard for targeting biopsies, in our data, the contrast-enhanced T1 was not sufficient to discriminate between all high- and low-grade samples. This result suggests that the predictive models may be able to identify high-grade disease outside the enhancing volume.

As of 2016, the WHO classification of gliomas heavily incorporates genetic and molecular factors.¹ Factors like *IDH1* mutation and *MGMT* promoter methylation are known to be highly prognostic.³¹ However, many of these prognostic factors, particularly *IDH1* mutation, are homogeneously expressed throughout the tumor. Thus, there is no risk of undersampling *IDH1* mutation status with clinical biopsy. Our work focuses on the heterogeneous tissue characteristics that are at risk for undersampling, hence, our categorization of lower- and higher-grade samples based on histologic grading.

Limitations

Although our patients were evenly distributed among final WHO grades II–IV and biopsies were targeted toward areas of increased malignancy, we collected relatively few high-grade samples. In our final analysis, we combined WHO grade III and IV samples into a higher-grade category as an attempt to balance our dataset. This feature removes the ability to predict grade III versus IV but still allows us to separate high-grade from low-grade disease. The lack of high-grade samples also highlights the potential for undergrading high-grade tumors using a single biopsy sample. Future trials and larger datasets would allow finer distinctions like these.

The use of virtual biopsies in contralateral NAWM is a limitation, and while we would clearly prefer to have normal histologic samples and imaging parameters sufficient to balance out our tumor histology data, we faced ethical constraints. We chose contralateral regions because in the absence of true histologic validation, they had the highest likelihood of truly being normal. There very likely is tumor-infiltrated brain that appears normal on imaging and the opposite case of imaging of abnormal brain that actually is nontumoral; but reliably characterizing these cases will require a much greater number of well-chosen biopsies, something we would like to address in future work, using our current data as a springboard.

Future Work

In addition to improved discriminatory ability among sample grades, we believe that “grade maps” like Fig 3 could provide a useful tool for surgical guidance. Such maps could help surgeons identify areas of highest grade²⁰ or identify as eloquent that only containing low-grade disease and could be less aggressively treated to avoid neurologic deficits. These models could also be used to help plan biopsies⁷ or radiation therapy, specifically by developing probability maps for tumor presence or severity,^{32,33} especially in the peritumoral brain zone.³⁴ Prospective evaluation of the derived models in further imaging and surgical trials is justified, along with further imaging-directed biopsy trials to refine our results even more in the peritumoral area.

CONCLUSIONS

Individual biopsy grades can be predicted to useful accuracies using noninvasive MR imaging. Advanced imaging (diffusion, perfusion, and permeability) improves predictive results over conventional imaging alone.

Disclosures: Evan D. H. Gates—RELATED: a training fellowship from the Gulf Coast Consortia, the National Library of Medicine Training Program in Biomedical Informatics and Data Science (T15LM007093). A scholarship from the American Legion Auxiliary. Jonathan S. Lin—RELATED: the Baylor College of Medicine Medical Scientist Training Program and the Cullen Trust for Higher Education Physician/Scientist Fellowship Programs for the duration of this research.

REFERENCES

1. Louis DN, Perry A, Reifenberger G, et al. **The 2016 World Health Organization Classification of Tumors of the Central Nervous System: a summary.** *Acta Neuropathol* 2016;131:803–20 CrossRef Medline
2. Stupp R, Mason WP, Van Den Bent MJ, et al; National Cancer Institute of Canada Clinical Trials Group. **Radiotherapy plus**

- concomitant and adjuvant temozolomide for glioblastoma.** *N Engl J Med* 2005;352:987–96 CrossRef Medline
3. Okamoto Y, Di Patre PL, Burkhard C, et al. **Population-based study on incidence, survival rates, and genetic alterations of low-grade diffuse astrocytomas and oligodendrogliomas.** *Acta Neuropathol* 2004;108:49–56 CrossRef Medline
4. Ohgaki H, Kleihues P. **Epidemiology and etiology of gliomas.** *Acta Neuropathol* 2005;109:93–108 CrossRef Medline
5. Parker NR, Khong P, Parkinson JF, et al. **Molecular heterogeneity in glioblastoma: potential clinical implications.** *Front Oncol* 2015;5:55 CrossRef Medline
6. Aum DJ, Kim DH, Beaumont TL, et al. **Molecular and cellular heterogeneity: the hallmark of glioblastoma.** *Neurosurg Focus* 2014;37:E11 CrossRef Medline
7. Jackson RJ, Fuller GN, Abi-Said D, et al. **Limitations of stereotactic biopsy in the initial management of gliomas.** *Neuro Oncol* 2001;3:193–200 CrossRef Medline
8. Gates EDH, Lin JS, Weinberg JS, et al. **Guiding the first biopsy in glioma patients using estimated Ki67 maps derived from magnetic resonance imaging: conventional versus advanced imaging.** *Neuro Oncol* 2019;21:527–36 CrossRef
9. Ringel F, Ingerl D, Ott S, et al. **VarioGuide: a new frameless image-guided stereotactic system: accuracy study and clinical assessment.** *Oper Neurosurg* 2009;64(5 Suppl 2):365–71 CrossRef Medline
10. Avants BB, Tustison NJ, Song G, et al. **A reproducible evaluation of ANTs similarity metric performance in brain image registration.** *Neuroimage* 2011;54:2033–44 CrossRef Medline
11. Leung KK, Clarkson MJ, Bartlett JW, et al.; Alzheimer’s Disease Neuroimaging Initiative. **Robust atrophy rate measurement in Alzheimer’s disease using multi-site serial MRI: tissue-specific intensity normalization and parameter selection.** *Neuroimage* 2010;50:516–23 CrossRef Medline
12. R Core Team. *R: A Language and Environment for Statistical Computing.* Vienna: R Foundation for Statistical Computing; 2019 <https://www.R-project.org/>
13. Breiman L. **Random forests.** *Mach Learn* 2001;45:5–32 CrossRef
14. Cohen J. **A coefficient of agreement for nominal scales.** *Educational and Psychological Measurement* 1960;20:37–46 CrossRef
15. Pedeutour-Braccini Z, Burel-Vandenbos F, Gozé C, et al. **Microfoci of malignant progression in diffuse low-grade gliomas: towards the creation of an intermediate grade in glioma classification?** *Virchows Arch* 2015;466:433–44 CrossRef Medline
16. Zhao M, Guo LL, Huang N, et al. **Quantitative analysis of permeability for glioma grading using dynamic contrast enhanced magnetic resonance imaging.** *Oncol Lett* 2017;14:5418–26 CrossRef Medline
17. Prah MA, Al-Gizawiy MM, Mueller WM, et al. **Spatial discrimination of glioblastoma and treatment effect with histologically-validated perfusion and diffusion magnetic resonance imaging metrics.** *J Neurooncol* 2018;136:13–21 CrossRef Medline
18. Hu LS, Ning S, Eschbacher JM, et al. **Multi-parametric MRI and texture analysis to visualize spatial histologic heterogeneity and tumor extent in glioblastoma.** *PLoS One* 2015;10:e0141506 CrossRef Medline
19. Law M, Yang S, Wang H, et al. **Glioma grading: sensitivity, specificity, and predictive values of perfusion MR imaging and proton MR spectroscopic imaging compared with conventional MR imaging.** *AJNR Am J Neuroradiol* 2003;24:1989–98 Medline
20. Akbari H, Macyszyn L, Da X, et al. **Imaging surrogates of infiltration obtained via multiparametric imaging pattern analysis predict subsequent location of recurrence of glioblastoma.** *Neurosurg* 2016;78:572–80 CrossRef Medline
21. Miloushev VZ, Chow DS, Filippi CG. **Meta-analysis of diffusion metrics for the prediction of tumor grade in gliomas.** *AJNR Am J Neuroradiol* 2015;36:302–08 CrossRef Medline
22. Jakab A, Molnár P, Emri M, et al. **Glioma grade assessment by using histogram analysis of diffusion tensor imaging-derived maps.** *Neuroradiology* 2011;53:483–91 CrossRef Medline

23. Barajas RF Jr, Hodgson JG, Chang JS, et al. **Glioblastoma multi-forme regional genetic and cellular expression patterns: influence on anatomic and physiologic MR imaging.** *Radiology* 2010;254:564–76 CrossRef Medline
24. Zhang X, Yan LF, Hu YC, et al. **Optimizing a machine learning based glioma grading system using multi-parametric MRI histogram and texture features.** *Oncotarget* 2017;8:47816–30 CrossRef Medline
25. Chang K, Bai HX, Zhou H, et al. **Residual convolutional neural network for the determination of IDH status in low- and high-grade gliomas from MR imaging.** *Clin Cancer Res* 2018;24:1073–81 CrossRef Medline
26. Law M, Yang S, Babb JS, et al. **Comparison of cerebral blood volume and vascular permeability from dynamic susceptibility contrast-enhanced perfusion MR imaging with glioma grade.** *AJNR Am J Neuroradiol* 2004;25:746–55 Medline
27. Sugahara T, Korogi Y, Kochi M, et al. **Usefulness of diffusion-weighted MRI with echo-planar technique in the evaluation of cellularity in gliomas.** *J Magn Reson Imaging* 1999;9:53–60 CrossRef Medline
28. Lee S, Choi SH, Ryoo I, et al. **Evaluation of the microenvironmental heterogeneity in high-grade gliomas with IDH1/2 gene mutation using histogram analysis of diffusion-weighted imaging and dynamic-susceptibility contrast perfusion imaging.** *J Neurooncol* 2015;121:141–50 CrossRef Medline
29. Yan H, Parsons DW, Jin G, et al. **IDH1 and IDH2 mutations in gliomas.** *N Engl J Med* 2009;360:765–73 CrossRef Medline
30. Noguchi T, Yoshiura T, Hiwatashi A, et al. **Perfusion imaging of brain tumors using arterial spin-labeling: correlation with histopathologic vascular density.** *AJNR Am J Neuroradiol* 2008;29:688–93 CrossRef Medline
31. Hartmann C, Hentschel B, Wick W, et al. **Patients with IDH1 wild type anaplastic astrocytomas exhibit worse prognosis than IDH1-mutated glioblastomas, and IDH1 mutation status accounts for the unfavorable prognostic effect of higher age: implications for classification of gliomas.** *Acta Neuropathol* 2010;120:707–18 CrossRef Medline
32. Shah V, Turkbey B, Mani H, et al. **Decision support system for localizing prostate cancer based on multiparametric magnetic resonance imaging.** *Med Phys* 2012;39:4093–103 CrossRef Medline
33. Durst CR, Raghavan P, Shaffrey ME, et al. **Multimodal MR imaging model to predict tumor infiltration in patients with gliomas.** *Neuroradiology* 2014;56:107–15 CrossRef Medline
34. Lemee JM, Clavreul A, Menei P. **Intratumoral heterogeneity in glioblastoma: don't forget the peritumoral brain zone.** *Neuro Oncol* 2015;17:1322–32 CrossRef Medline

Performance of Standardized Relative CBV for Quantifying Regional Histologic Tumor Burden in Recurrent High-Grade Glioma: Comparison against Normalized Relative CBV Using Image-Localized Stereotactic Biopsies

J.M. Hoxworth, J.M. Eschbacher, A.C. Gonzales, K.W. Singleton, G.D. Leon, K.A. Smith, A.M. Stokes, Y. Zhou, G.L. Mazza, A.B. Porter, M.M. Mrugala, R.S. Zimmerman, B.R. Bendok, D.P. Patra, C. Krishna, J.L. Boxerman, L.C. Baxter, K.R. Swanson, C.C. Quarles, K.M. Schmainda, and L.S. Hu



ABSTRACT

BACKGROUND AND PURPOSE: Perfusion MR imaging measures of relative CBV can distinguish recurrent tumor from posttreatment radiation effects in high-grade gliomas. Currently, relative CBV measurement requires normalization based on user-defined reference tissues. A recently proposed method of relative CBV standardization eliminates the need for user input. This study compares the predictive performance of relative CBV standardization against relative CBV normalization for quantifying recurrent tumor burden in high-grade gliomas relative to posttreatment radiation effects.

MATERIALS AND METHODS: We recruited 38 previously treated patients with high-grade gliomas (World Health Organization grades III or IV) undergoing surgical re-resection for new contrast-enhancing lesions concerning for recurrent tumor versus post-treatment radiation effects. We recovered 112 image-localized biopsies and quantified the percentage of histologic tumor content versus posttreatment radiation effects for each sample. We measured spatially matched normalized and standardized relative CBV metrics (mean, median) and fractional tumor burden for each biopsy. We compared relative CBV performance to predict tumor content, including the Pearson correlation (r), against histologic tumor content (0%–100%) and the receiver operating characteristic area under the curve for predicting high-versus-low tumor content using binary histologic cutoffs ($\geq 50\%$; $\geq 80\%$ tumor).

RESULTS: Across relative CBV metrics, fractional tumor burden showed the highest correlations with tumor content (0%–100%) for normalized ($r = 0.63$, $P < .001$) and standardized ($r = 0.66$, $P < .001$) values. With binary cutoffs (ie, $\geq 50\%$; $\geq 80\%$ tumor), predictive accuracies were similar for both standardized and normalized metrics and across relative CBV metrics. Median relative CBV achieved the highest area under the curve (normalized = 0.87, standardized = 0.86) for predicting $\geq 50\%$ tumor, while fractional tumor burden achieved the highest area under the curve (normalized = 0.77, standardized = 0.80) for predicting $\geq 80\%$ tumor.

CONCLUSIONS: Standardization of relative CBV achieves similar performance compared with normalized relative CBV and offers an important step toward workflow optimization and consensus methodology.

ABBREVIATIONS: AUC = area under the curve; FTB = fractional tumor burden; GBM = glioblastoma multiforme; NAWM = normal-appearing white matter; PTRE = posttreatment radiation effects; rCBV = relative CBV; ROC = receiver operating characteristic

Conventional contrast-enhanced MR imaging guides response assessment for essentially all patients with high-grade gliomas and clinical trials worldwide. Despite this widespread use,

diagnostic challenges remain. In particular, nontumoral post-treatment radiation effects (PTRE), namely pseudoprogression

Received September 30, 2019; accepted after revision December 23.

From the Departments of Radiology (J.M.H., Y.Z., L.S.H.), Psychiatry and Psychology (A.C.G.), Neuro-Oncology (A.B.P., M.M.M.), Neurosurgery (R.S.Z., C.K.), and Precision Neurotherapeutics Lab (K.W.S., G.D.L., B.R.B., K.R.S.), Mayo Clinic in Arizona, Phoenix, Arizona; Departments of Pathology (J.M.E.), Neurosurgery (K.A.S.), Neurobiology (C.C.Q.), and Keller Center for Imaging Innovation (A.M.S.), Barrow Neurological Institute, Phoenix, Arizona; Department of Health Sciences Research (G.L.M.), Division of Biomedical Statistics and Informatics, Mayo Clinic Scottsdale, Scottsdale, Arizona; Departments of Neurosurgery (D.P.P.) and Neuropsychology (L.C.B.), Mayo Clinic Hospital, Phoenix, Arizona; Department of Diagnostic Imaging (J.L.B.), Rhode Island Hospital, Providence, Rhode Island; and Department of Radiology (K.M.S.), Medical College of Wisconsin, Milwaukee, Wisconsin.

This work was supported by grants NS082609 (NIH), CA221938 (NIH), CA220378 (NIH), CA158079 (NIH), Mayo Clinic Foundation, James S. McDonnell Foundation, Ben and Catherine Ivy Foundation, and the Arizona Biomedical Research Commission (ABRC).

Please address correspondence to Leland S. Hu, MD, Department of Radiology, Mayo Clinic, 5777 E. Mayo Blvd, Phoenix, AZ 85054; e-mail: Hu.Leland@Mayo.Edu

Indicates open access to non-subscribers at www.ajnr.org

Indicates article with supplemental on-line table.

Indicates article with supplemental on-line photos.

<http://dx.doi.org/10.3174/ajnr.A6486>

and radiation necrosis, can exactly mimic tumor recurrence on contrast-enhanced MR imaging.¹⁻⁴ While tumor recurrence signals treatment failure, PTRE represents a positive response to treatment with a good prognosis. This distinction can be further complicated by the histologic admixture between tumor and PTRE, which can impact both diagnosis and prognostication, depending on the relative histologic burden of each entity.⁵⁻⁸ In the case of surgical biopsy, regional heterogeneity and resulting sampling errors can negatively affect the diagnostic confirmation of tumor versus PTRE, as well as the adequacy of tumor content for molecular and genomic profiling.⁹ These issues underscore the importance of improving image-based response assessment, particularly in the context of intratumoral heterogeneity.

During the past decade, DSC-MR imaging has emerged as a clinically valuable and accessible tool to distinguish tumor recurrence from PTRE.¹⁰ A continually expanding body of literature has shown how DSC-MR imaging measures of relative cerebral blood volume (rCBV) are significantly higher in tumor compared with PTRE.^{1,10-14} These studies have spurred the development of proposed guidelines for interpretation and have helped promote clinical adoption and accessibility across an increasing number of clinical practices.¹⁵ At the same time, this expansion has brought to light issues of interinstitutional variability in DSC-MR imaging methodology, which can affect how rCBV is clinically measured and interpreted.^{10,16,17} This variability has motivated the effort to develop consensus recommendations on DSC-MR imaging acquisition and postprocessing that can help standardize clinical practice across institutions.¹⁵

Of the various methodologic factors that can impact rCBV measurement (eg, software modeling,^{18,19} preload dose,^{16,17,20,21} pulse sequence parameters^{16,17}), the process of rCBV normalization is arguably the most fundamental.²²⁻²⁴ While quantitative measurements of rCBV are not possible given the poor reliability of arterial input functions on DSC-MR imaging and unknown voxelwise contrast agent T2* relaxivity, rCBV normalization provides a means of semiquantification against internal reference tissue in each patient. By convention, users define ROIs within the contralateral normal-appearing white matter (NAWM) and/or normal gray matter.^{13,20} These user-defined inputs are susceptible to variability (eg, size and location of ROIs, vascularity of selected reference tissues), which can lead to substantial variability in rCBV measurements.²⁰ The technique of standardization has been proposed to eliminate the need for user-defined input and thereby reduce rCBV variabilities.²² This process transforms rCBV maps to a standardized intensity scale, without the need for reference ROIs, and has been shown to increase the consistency in rCBV measurements across time and patients.²³

While standardized rCBV thresholds have also been proposed to distinguish tumor from PTRE, these have not been prospectively evaluated.¹¹ The use of standardized rCBV is currently not widely accepted due, in part, to a need for tissue-validation studies. To address this issue, we undertook this study and hypothesized that standardized rCBV values will demonstrate similar, if not better, predictive performance in distinguishing tumor from PTRE compared with normalized rCBV. Thus, this study will compare the predictive accuracy of standardized and normalized rCBV values using a dataset of image-localized biopsies and

coregistered DSC-MR imaging perfusion maps in a cohort of patients with recurrent high-grade gliomas, to distinguish and quantify the spatial heterogeneity of tumor recurrence relative to PTRE.

MATERIALS AND METHODS

Patients

We prospectively recruited previously treated (surgery, chemoradiation therapy) patients with World Health Organization grades III and IV primary high-grade gliomas, undergoing preoperative imaging for surgical re-resection of newly developed contrast-enhancing lesions identified on surveillance MR imaging. Recruitment was from 2007 to 2018. Patients were recruited from 2 institutions (Mayo Clinic and Barrow Neurological Institute). We included patients who previously underwent standard adjuvant chemoradiation therapy per the Stupp protocol.²⁵ All our patients were diagnosed on the basis of clinical standards at the time of enrollment. We also recorded the molecular status for *isocitrate dehydrogenase (IDH) 1/2* mutations and the codeletion status of 1p/19q for those patients clinically diagnosed on the basis of the revised 2016 World Health Organization classification criteria.²⁶ The institutional review boards of each institution approved our study, and written and informed consent was obtained from each subject.

MR Imaging Protocol, Parametric Maps, and Image Coregistration

Conventional MR Imaging and Acquisition Conditions. We acquired 3T MR imaging (Sigma HDx, GE Healthcare, Milwaukee, Wisconsin; Ingenia, Philips Healthcare, Best, Netherlands; Magnetom Skyra, Siemens, Erlangen Germany) within 1 day before stereotactic surgery. Conventional MR imaging and advanced MR imaging parameters have been detailed previously.²⁷ Briefly, we acquired precontrast and postcontrast T1-weighted echo-spoiled gradient-echo inversion-recovery images (TI/TR/TE = 300/6.8/2.8 ms; matrix = 320 × 224; FOV = 26 cm; thickness = 2 mm). We acquired postcontrast T1-weighted images after completing DSC perfusion MR imaging following a total Gd-DTPA dosage of 0.15 mmol/kg as previously described.^{5,13,20,27-29}

Preoperative DSC-MR Imaging Protocol. We used a 3T MR imaging system for all patients. After antecubital fossa or forearm intravenous catheter placement, we administered 0.1 mmol/kg of Gd-DTPA contrast agent (gadodiamide or gadobenate dimeglumine) preload dose 6 minutes before the DSC-MR imaging acquisition to minimize T1-weighted leakage effects.^{20,21,30,31} During the DSC-MR imaging acquisition, we administered a 0.05-mmol/kg bolus at 3–5 mL/s. The DSC-MR imaging sequence parameters were the following: gradient-echo EPI with TR/TE/flip angle = 1500–2000 ms/20 ms/60°; FOV = 24 × 24 cm; matrix = 128 × 128; NEX = one; 5-mm sections; no interslice gap. These parameters yielded an in-plane spatial resolution of 1.8 × 1.8 mm and voxel volumes of 16 mm³. The total Gd-DTPA dose was 0.15 mmol/kg of body weight.

rCBV and Fractional Tumor Burden Map Generation

Overview of Image Segmentation, Coregistration, and Parametric Map Generation. For each patient, we used IB RadTech (Version 2.0.1259; Imaging Biometrics, Elm Grove, Wisconsin) to perform the following: 1) segment all T1-weighted postcontrast enhancing lesion voxels; 2) generate both normalized rCBV and standardized rCBV maps; 3) coregister all rCBV maps to respective T1-weighted postcontrast images; and 4) perform rCBV thresholding to generate separate fractional tumor burden (FTB) maps from the respective normalized and standardized rCBV maps. (Note because absolute rCBV values are not determined, the map is a relative CBV map; ie, the values are interpreted relative to other values throughout the brain in a given patient.) IB RadTech automates the previously described manual functions that were detailed for FTB map generation.⁵ Voxelwise rCBV was calculated on the basis of well-established methods.^{20,21,30} In short, after excluding the first 4 time points of each DSC-MR imaging series to reach a steady-state, we normalized the signal intensity-to-baseline and converted the dynamic series to change the relaxation rate across time [$\Delta R2^*(t)$] for the entire brain. We generated rCBV maps by integrating the area under the $\Delta R2^*(t)$ curve, ending at the time point 40 seconds after the nadir signal intensity of the first-pass bolus. All rCBV values were corrected for residual T1-/T2-/T2*-weighted leakage effects using the well-established Boxerman-Schminda-Weisskoff algorithm.^{20,21,30}

Normalized rCBV and FTB Maps. We generated normalized rCBV and normalized FTB maps using IB RadTech, based on a previously published workflow,⁵ which we also summarize in On-line Fig 1. The generation of normalized rCBV required a user to manually select 5×5 mm ROIs from the contralateral NAWM. To reduce the potential for user-associated variability, we developed criteria to guide the selection of uniform ROI locations within the frontal and parietal lobes, which are illustrated in On-line Fig 1.^{5,13,20} These ROI locations were chosen specifically to help minimize potential volume averaging from adjacent cortical/deep gray matter, adjacent ventricles, and adjacent large surface vessels along the cortex. All NAWM ROIs were selected by a single board-certified neuroradiologist (L.S.H.) with >15 years of experience. For normalized FTB, we used the normalized rCBV threshold of 1.0 (tumor > 1.0; PTRE \leq 1.0), which has previously been established through image-localized biopsy and spatially matched histopathologic correlation.^{5,13,20} FTB is defined as the percentage of tumor voxels within a region with rCBV > 1.0 (On-line Fig 2). To assess potential user-dependent variability, we assigned another board-certified neuroradiologist (J.M.H.), also with >15 years of experience, to separately guide placement of NAWM ROIs, which were used to generate a separate set of normalized rCBV and normalized FTB maps. We used these data to assess interrater reliability and evaluate potential differences in predictive accuracy, which are presented in (On-line Table).

Standardized rCBV and FTB Maps. Standardized rCBV maps were generated in IB RadTech on the basis of the previously described algorithm that transforms rCBV intensities to an initial standard scale of 0–50,000.^{11,22,23} This transformation is achieved in 2 steps: a training step that is executed only once and a

transformation step that is executed for each new input rCBV image. The training step was previously performed,²² resulting in a calibration rule (historically referred to as the “standardization step”) in which standard rCBV intensity values [$\mu'_j(L_k)$] for pre-chosen percentile landmarks (L_k) were determined (On-line Fig 2A). Subsequently, each new input rCBV map can be transformed to the standardized space (ie, calibrated) so that the input rCBV intensity histogram is deformed to match the standard histogram. As shown (On-line Fig 2B), this step usually results in a nonlinear intensity transformation for a given image. However, the relationship between tissue intensities is maintained, and intensity comparisons can be made using the standardized images.³² For comparison purposes (to normalized FTB), the standardized values were divided by 3575, the value shown to match an rCBV value of 1. The standardized rCBV value of 3575 was found, in a separate study, to accurately distinguish tumor from treatment effect, which was validated with spatially correlated biopsy tissue and coregistered standardized rCBV values.¹¹ The threshold standardized rCBV of 1.0 was used (tumor > 1.0; PTRE \leq 1.0) to define FTB as the percentage of tumor voxels within a region with rCBV > 1.0.

Acquisition of Surgical Tissue, Criteria for Histologic Diagnosis, and Estimation of Histologic Tumor Fraction

We collected multiple image-localized biopsies for each patient during surgical re-resection of MR imaging enhancing lesions for suspected recurrent disease.^{5,13,20,29} In short, each neurosurgeon collected an average of 2–3 biopsy specimens from spatially distinct regions within different poles of each MR imaging enhancing lesion, following the smallest possible diameter craniotomy to minimize brain shift. Biopsy target locations were based on clinical feasibility (eg, accessibility of the target site, overlying vessels, eloquent brain). The neurosurgeons recorded biopsy locations via screen capture to allow subsequent coregistration with DSC and conventional MR imaging datasets. The neurosurgeon visually validated stereotactic imaging locations with corresponding intracranial anatomic landmarks, such as vascular structures and ventricle margins, before recording specimen locations as previously described.^{27,28} We fixed all surgical tissue specimens in 10% formalin, embedded in paraffin, sectioned (10- μ), and hematoxylin-eosin-stained per standard diagnostic protocol at our institutions. The presence and quantity of recurrent tumor and/or PTRE elements were determined by expert neuropathology review (J.M.E.) as previously described.^{5,7,33} In short, for all submitted surgical tissue, we estimated the tumor burden (ie, tumor content; range, 0%–100%) relative to nonneoplastic features, on the basis of relative fractions of neoplastic features versus treatment effects, as previously described. Areas of tumor and PTRE were marked on each slide, grossly measured, microscopically re-evaluated, and used to determine the percentage of tumor/PTRE for each biopsy specimen. PTRE features included paucicellularity; scattered, rare, or no atypical cells; lack of mitotic figures except in inflammatory cells; preponderance of reactive cells including astrocytes (gemistocytes), microglia, and macrophages; and vascular hyaline fibrosis. Necrosis, often circumscribed in nonneoplastic parenchyma, if present, was considered specific for PTRE. Features of tumor recurrence included cellular sheets and/

Table 1: Patient demographics and distribution of recurrent tumors by pathology and grade

	Total No.	Age (yr)	Men (Total)	Women (Total)
Patient demographics	38	Mean = 49.3, Range = 24–69	19	19
Pathology and grade				
Recurrent ODG (GIII)	3	Mean = 46	2	1
Recurrent astrocytoma (GIII)	2	Mean = 52	1	1
Recurrent GBM (GIV)	33	Mean = 50	16	17

Note:—ODG indicates oligodendroglioma; GIII, WHO Grade III; GIV, WHO Grade IV.

Table 2: Summary of predictive performance for normalized and standardized rCBV metrics

rCBV Metric	Histologic Tumor Content (0%–100%), Pearson Coefficient (P Value)	Tumor Content ≥50%, ROC-AUC (Optimal Threshold)	Tumor Content ≥80%, ROC-AUC (Optimal Threshold)
FTB			
Normalized	$r = 0.63 (<.001)$	0.80 (0.72)	0.77 (0.84)
Standardized	$r = 0.66 (<.001)$	0.82 (0.56)	0.80 (0.64)
Mean rCBV			
Normalized	$r = 0.45 (<.001)$	0.86 (1.558)	0.75 (1.603)
Standardized	$r = 0.53 (<.001)$	0.85 (1.187)	0.78 (1.187)
Median rCBV			
Normalized	$r = 0.48 (<.001)$	0.87 (1.68)	0.77 (1.378)
Standardized	$r = 0.55 (<.001)$	0.86 (1.071)	0.79 (1.10)

or nests of atypical cells often with mitotic figures. If necrosis was present, it was a minor component of the cellular tumor rather than parenchyma. The finding of fewer atypical cells in a linear infiltrative configuration in parenchyma without prominent reactive changes was also classified as recurrence.^{5,7}

Extraction of Regional rCBV Metrics from Image-Localized Biopsy Locations. All FTB and rCBV maps were exported and processed through our image-analysis pipeline, which includes coregistration of all image datasets to a standardized resolution (1.17 × 1.17 × 3 mm) as previously described.^{27,28} We generated 5 × 5 voxel ROIs at the stereotactic coordinates for each biopsy location for feature extraction, and the location of each ROI was verified by expert neuroradiology review (J.M.H. and L.S.H.) at the time of image analysis. We measured FTB and base statistical metrics (eg, mean, mode, SD) from each ROI for both standardized and normalized rCBV maps. This step enabled subsequent statistical analysis between spatially matched rCBV metrics and corresponding histologic quantification of tumor burden for each respective image-localized biopsy specimen.

Statistical Analysis and Predictive Accuracy. We estimated Pearson correlation coefficients (r) between spatially matched rCBV metrics (ie, FTB, mean and median rCBV) and histologic tumor content (range, 1%–100%) from corresponding biopsies for both standardized and normalized maps. We also performed receiver operating characteristic (ROC) analysis and determined the area under the curve (AUC) for standardized and normalized rCBV metrics to predict tumor content for each sample using 2 different histologic thresholds (≥50% tumor, ≥80% tumor). We compared Pearson correlations and the AUC for standardized-versus-normalized rCBV metrics. We defined statistical significance as $P < .05$.

RESULTS

Subject Population and Clinical Data

We recruited a total of 38 patients with recurrent high-grade gliomas undergoing surgical re-resection and collected a total of 134 image-localized biopsy samples. We had to exclude 22 biopsy samples from subsequent image processing and correlative analysis, due to either insufficient biopsy material ($n = 1$), biopsy location near the skull base causing susceptibility artifacts ($n = 1$), biopsy location from nonenhancing parenchyma ($n = 3$), biopsy locations along a thin cystic wall/resection cavity that caused ROI overlap with nonparenchymal CSF-containing structures (eg, fluid-filled cyst, central necrotic core, resection cavity, $n = 8$), biopsy location adjacent to large vessels ($n = 4$), or inadequate coregistration of image datasets with biopsy location ($n = 5$). This exclusion allowed us to include 112 specimens from 38 patients for final analysis.

Thirty-five patients were recruited from Barrow Neurological Institute and scanned on the GE MR imaging system. Two patients were recruited from Barrow Neurological Institute and scanned on the Phillips MR imaging system. One patient was recruited from Mayo Clinic and scanned on the Siemens MR imaging system. We could not identify significant differences in MR imaging image quality or rCBV measurements between scanners or institutions.

All patients had previously undergone standard adjuvant chemotherapy and radiation therapy.²⁵ One patient was recruited twice for 2 separate operations (both for recurrent glioblastoma multiforme [GBM]) that were 8 months apart. The number of biopsies ranged from 1 to 6 per patient. Patient demographics and clinical data are summarized in Table 1. Thirty patients were recruited before 2016 and were clinically/pathologically diagnosed using the World Health Organization criteria before the 2016 recommendations. Thus, *IDH* and 1p/19q codeletion status were unknown in these patients. The remaining 8 patients (all with recurrent GBM) were diagnosed clinically/pathologically using the revised 2016 World Health Organization classification criteria: Five recurrent GBM tumors were *IDH* wild-type, and 3 recurrent GBM tumors were *IDH*-mutant (1p/19q intact).

Predictive Accuracies and Correlations between rCBV-Based Metrics and Histologic Tumor Content

All correlations and predictive accuracies are summarized in Table 2. Pearson correlations with histologic tumor content as a continuous variable (0%–100%) were highest with the FTB metric, showing similar coefficients for normalized FTB ($r = 0.63, P < .001$) and standardized FTB ($r = 0.66, P < .001$). Figure 1 shows 3 separate cases correlating FTB maps with spatially matched histologic tumor content from

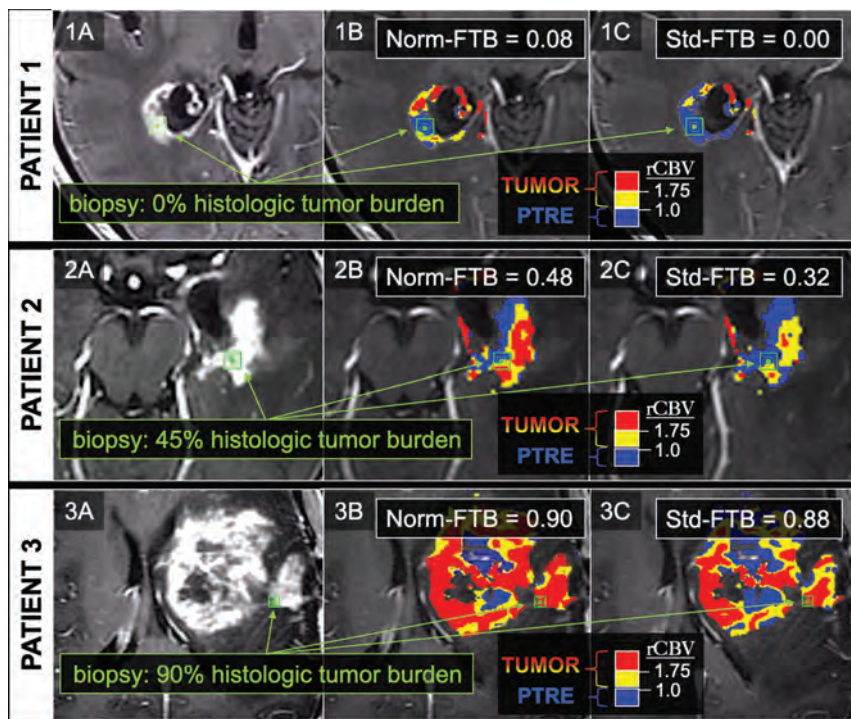


FIG 1. FTB maps in 3 separate biopsy cases correlating with low, medium, and high histologic tumor content. The 3 rows correspond to 3 separate patients and 3 separate biopsy locations, as shown by the *green square ROIs* on the anatomic postcontrast images in the far-left column (1A, 1B, 1C). The middle and far right columns show the biopsy locations (*green square ROIs*) in relation to the normalized (Norm) FTB (1B, 2B, 3B) and standardized (Std) FTB (1C, 2C, 3C) maps. On the FTB maps, blue corresponds to predicted PTRE regions with low $rCBV \leq 1.0$. The yellow ($1.75 \geq rCBV > 1.0$) and red ($rCBV > 1.75$) correspond to predicted tumor regions. For this study, FTB was defined as the percentage of both yellow and red voxels relative to all voxels within an ROI.

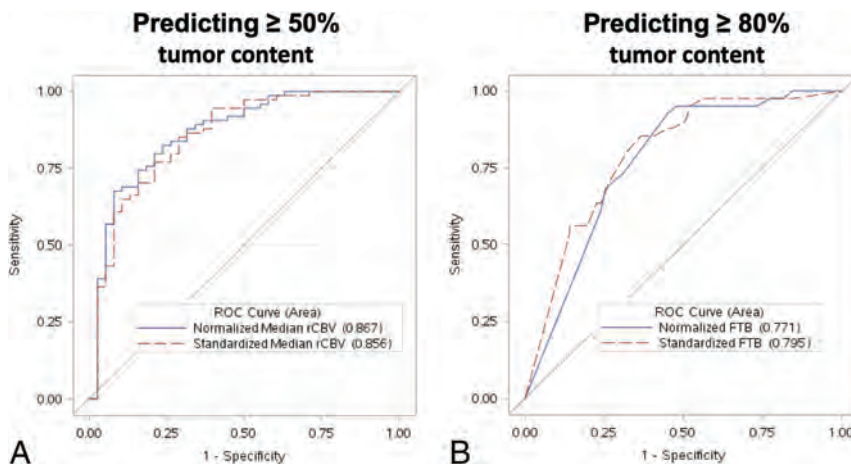


FIG 2. ROC analyses of the top-performing rCBV metrics for predicting $\geq 50\%$ histologic tumor content (A) and $\geq 80\%$ histologic tumor content (B). A, ROC curve for predicting $\geq 50\%$ histologic tumor content using normalized (*blue curve*) and standardized (*red dotted curve*) median rCBV. B, ROC curve for predicting $\geq 80\%$ histologic tumor content using normalized (*blue curve*) and standardized (*red dotted curve*) FTB. The standardized metrics show similar performance compared with corresponding normalized metrics.

corresponding biopsies. As shown in Table 2, correlations among mean and median rCBV were slightly higher for standardized compared with normalized metrics. When we distinguished histologic

tumor content based on binary cutoffs (ie, $\geq 50\%$ tumor, $\geq 80\%$ tumor), predictive accuracies were similar for both standardized and normalized metrics (Table 2). Median rCBV achieved the highest AUC (normalized = 0.87, standardized = 0.86) for predicting at least 50% tumor. Meanwhile, FTB achieved the highest AUC (normalized = 0.77, standardized = 0.80) for predicting at least 80% tumor (Table 2). The ROC analyses are also summarized in Fig 2. The remaining ROC analyses are shown in On-line Figs 3 and 4. We also evaluated interrater reliability by comparing normalized rCBV and normalized FTB metrics from a second user defining NAWM regions. As shown in the On-line Table, the intraclass correlation between the main user and second user-defined normalized FTB and mean and median rCBV equaled 0.89, 0.92, and 0.92, respectively, based on a 2-way model with absolute agreement. These intraclass correlations suggest strong agreement between the 2 users.

DISCUSSION

As a primary goal of this study, we sought to determine the impact of rCBV standardization on predictive accuracy, compared with the conventional method of rCBV normalization. Our data show that standardized rCBV metrics can achieve predictive performance that is similar (if not slightly superior) to that of normalized rCBV. While standardized and normalized rCBV are both reflective of tissue vascular volume fraction, as developed, the standardization method sets values above the 99.8th percentile of each rCBV map to the maximum standardized value.²² This threshold eliminates unrealistic upper bound landmarks computed from spurious signals that might skew the histogram of the pre-standardized image data. Presumably these values correspond to large vessels, either near cortical margins or within large feeding or draining vessels that course through the enhancing lesions themselves. While these vessels potentially skew normalized rCBV to overestimate tumor content,^{5,11} standardized rCBV would be less susceptible to these biases. Nevertheless, we found that tumor standardized rCBV values fell within the middle of the standardized range. Standardization of rCBV also

eliminates user-defined input (ie, normal ROIs), shown to improve inter- and inpatient consistency and repeatability of rCBV compared with manually defined normal ROIs.²³ It is possible that these improvements in variance and reproducibility may help bolster the correlation between standardized rCBV and histologic benchmarks, particularly across a large cohort analysis. Methodology for automatic segmentation of NAWM has recently been reported, demonstrating improvement over manually defined NAWM in the application of tumor grading.³⁴ Future studies would be helpful for comparing such methodology with standardization of rCBV, particularly for differentiating tumor from PTRE in the posttreatment setting. It will also be important to evaluate standardization and normalization methods with evolving consensus recommendations for DSC acquisition, such as with low-flip angle techniques.³⁵

In this study, we spatially matched regional rCBV metrics with regional histologic tumor content, measured in a set of image-localized biopsies from a cohort of patients with recurrent high-grade gliomas. Our results demonstrate that histologic tumor content, at the level of image-localized biopsies, can be predicted by fundamental rCBV metrics such as mean and median rCBV, as well as the FTB metric that reflects the local percentage of voxels with rCBV above/below predetermined thresholds.^{5,11} These thresholds have previously undergone rigorous histopathologic validation,^{5,11} and the FTB metric itself has been shown to correlate strongly with global tumor content as a predictor of overall survival,^{5,11} which can also help to inform clinical decision-making.³⁶ Most interesting, all of the rCBV metrics performed comparably well in distinguishing high-versus-low histologic tumor content when using binary cutoffs (eg, $\geq 50\%$ tumor, $\geq 80\%$ histologic tumor content), though the FTB metric appeared to outperform mean and median rCBV when predicting histologic tumor content as a continuous variable (ie, 0%–100% histologic tumor content) (Table 2).

The underlying reasons for this have been suggested previously but likely relate to the microvascular heterogeneity and broad rCBV variability that can be exhibited by GBM, even among tumor subregions.⁵ These features would make the calculation of mean rCBV susceptible to biases from extremely high or low values, even in a relatively small population of tumor voxels, which could negatively impact the correlation between rCBV magnitude (ie, mean, median rCBV) and variations in histologic tumor proportion. Meanwhile, rCBV magnitude would have less impact on calculation of FTB, except to classify voxels according to minimum threshold requirements. This approach would more purely approximate the volume of histologic tumor content by mitigating influences from varying degrees of tumoral angiogenesis. As an example, a voxel with an rCBV of 1.2 will be classified as tumor in the same manner as another voxel with an rCBV of 12.0. Overall, the use of rCBV, and FTB in particular, offers potential future applications for reducing tissue-sampling errors during surgical biopsy and/or resection of recurrent high-grade gliomas, as well as helping to recover adequate tumor content when molecular profiling is desired.⁹ As an aside, our cohort did not include patients treated with antiangiogenic therapy such as bevacizumab. Bevacizumab has been shown to decrease both microvessel volume and rCBV values, through mechanisms such as pericyte contraction.^{37–39} For the aforementioned

reasons, thresholding metrics such as FTB would likely be relatively less affected by antiangiogenic-induced rCBV alterations, compared with metrics such as mean rCBV, though further studies are likely needed to fully understand the impact on histologic quantification.

With predictive performance aside, the standardization of rCBV offers methodologic advantages that would help to promote clinical adoption and optimize workflow. There have been recent mounting efforts to homogenize DSC-MR imaging acquisition and analysis toward consensus methodology. The current variability in DSC-MR imaging methodology, from one institution to another, has been implicated as a major reason for the wide variability in reported thresholds that guide clinical diagnosis.^{10,16,17} The user-based selection of normal brain structures (for rCBV normalization) represents a fundamental process of rCBV map generation that can impact the variability of rCBV values and thresholds, not only across different institutions but at the same institution and within the same patient across repeat examinations.^{5,20,23}

In our study, the intraclass correlations remained high when comparing 2 users defining NAWM regions. In reality, however, this finding may underestimate interrater reliability because we use a highly specific system of NAWM ROI placement in our practice. It would likely be difficult to replicate this level of agreement across different institutions and in routine practice without investing in expert user training to maintain consistency for this postprocessing step. The adoption of rCBV standardization would eliminate the need for user-based input for normalization, which represents an important step toward consensus methodology. One of the key advantages of standardization is that it can be applied to rCBV maps collected at any field strength and for any vendor. This advantage is supported by the positive results obtained with standardized rCBV maps in several clinical trials (American College of Radiology Imaging Network 6677, American College of Radiology Imaging Network 6684) that were collected at both 1.5T and 3T in a range of scanner vendors and at many different institutions.^{40,41} As explained in the original article on the standardization method,³² standardization calibration files are created for a given protocol. Standardization is therefore robust against slight variations in TE and TR, for example. Furthermore, the fully automated nature of rCBV standardization will also help streamline clinical workflow. By eliminating the need for expert user training, staffing of these user experts, and supervisor oversight (all currently needed for rCBV normalization), the adoption of rCBV standardization (over rCBV normalization) would address potential existing obstacles to integrating DSC-MR imaging in many clinical practices.

We recognize potential limitations to our study. First, image distortions and brain shift following craniotomy could lead to misregistration errors. To compensate, neurosurgeons used small craniotomy sizes to minimize brain shift and also visually validated stereotactic image location with intracranial neuroanatomic landmarks to help correct for random brain shifts. We also used rigid-body coregistration of stereotactic and advanced MR imaging to help reduce possible geometric distortions.^{29,42} Overall, our experience suggests combined

misregistration at approximately 1–2 mm from both brain shift and registration techniques, which is similar to that from previous studies using stereotactic needle biopsy.⁴³ We also acquired DSC-MR imaging data from different MR imaging vendors at 2 different clinical practices. We used identical DSC-MR imaging acquisition parameters but recognize that subtle variability in DSC data could persist. Nonetheless, we also think that this variability could be reflective of the real-world variability that could be encountered in clinical practice and potentially lends strength to the study, given the relatively robust results.

CONCLUSIONS

The standardization of rCBV achieves similar diagnostic accuracy compared with normalized rCBV in diagnosing and quantifying recurrent high-grade glioma tumor burden relative to nontumoral posttreatment radiation effects following standard multimodal therapy. Compared with normalized rCBV, the standardization of rCBV would also eliminate the need for user-based input for normalization (and resulting variabilities in measurement), which represents an important step toward workflow optimization and consensus methodology.

Disclosures: Kris A. Smith—UNRELATED: Payment for Lectures Including Service on Speakers Bureaus: Metabolic Health; Patents (Planned, Pending or Issued): OsteoMed. Richard S. Zimmerman—UNRELATED: Consultancy: NeuroPage, Medtronic. Leslie C. Baxter—RELATED: Grant: National Cancer Institute. Comments: My institution received funding as part of the grant under which this work was performed*; UNRELATED: Employment: Barrow Neurological Institute. Kristin R. Swanson—RELATED: Grant: NS082609, CA221938, CA220378, Mayo Clinic Foundation, James S. McDonnell Foundation, Ivy Foundation, Arizona Biomedical Research Commission*; UNRELATED: Board Membership: James S McDonnell Foundation Scientific Board; Payment for Development of Educational Presentations: multiple patents and applications but no funds. Christopher C. Quarles—RELATED: Grant: National Institutes of Health.* Kathleen M. Schmainda—RELATED: Grant: National Institutes of Health*; UNRELATED: Stock/Stock Options: IQ-AI Ltd, Comments: ownership interest; Other: Imaging Biometrics LLC, Comments: spouse's salary. Leland S. Hu—RELATED: Grant: U01 CA220378, R01 CA221938, R21 NS082609, Mayo Clinic Foundation, Arizona Biomedical Research Commission*; UNRELATED: Patents (Planned, Pending or Issued): multiple patents but no money paid. *Money paid to the institution.

REFERENCES

- Shiroishi MS, Boxerman JL, Pope WB. **Physiologic MRI for assessment of response to therapy and prognosis in glioblastoma.** *Neuro Oncol* 2016;18:467–78 CrossRef Medline
- Brandma D, van den Bent MJ. **Pseudoprogression and pseudoresponse in the treatment of gliomas.** *Curr Opin Neurol* 2009;22:633–38 CrossRef Medline
- Fink J, Born D, Chamberlain MC. **Pseudoprogression: relevance with respect to treatment of high-grade gliomas.** *Curr Treat Options Oncol* 2011;12:240–52 CrossRef Medline
- Clarke JL, Chang S. **Pseudoprogression and pseudoresponse: challenges in brain tumor imaging.** *Curr Neurol Neurosci Rep* 2009;9:241–46 CrossRef Medline
- Hu LS, Eschbacher JM, Heiserman JE, et al. **Reevaluating the imaging definition of tumor progression: perfusion MRI quantifies recurrent glioblastoma tumor fraction, pseudoprogression, and radiation necrosis to predict survival.** *Neuro Oncol* 2012;14:919–30 CrossRef Medline
- Kim JH, Bae Kim Y, Han JH, et al. **Pathologic diagnosis of recurrent glioblastoma: morphologic, immunohistochemical, and molecular analysis of 20 paired cases.** *Am J Surg Pathol* 2012;36:620–28 CrossRef Medline

- Forsyth PA, Kelly PJ, Cascino TL, et al. **Radiation necrosis or glioma recurrence: is computer-assisted stereotactic biopsy useful?** *J Neurosurg* 1995;82:436–44 CrossRef Medline
- Rock JP, Hearnshen D, Scarpace L, et al. **Correlations between magnetic resonance spectroscopy and image-guided histopathology, with special attention to radiation necrosis.** *Neurosurgery* 2002; 51:912–19; discussion 919–20 CrossRef Medline
- Cancer Genome Atlas Research Network. **Comprehensive genomic characterization defines human glioblastoma genes and core pathways.** *Nature* 2008;455:1061–68 CrossRef Medline
- Patel P, Baradaran H, Delgado D, et al. **MR perfusion-weighted imaging in the evaluation of high-grade gliomas after treatment: a systematic review and meta-analysis.** *Neuro Oncol* 2017;19:118–27 CrossRef Medline
- Prah MA, Al-Gizawiy MM, Mueller WM, et al. **Spatial discrimination of glioblastoma and treatment effect with histologically-validated perfusion and diffusion magnetic resonance imaging metrics.** *J Neurooncol* 2018;136:13–21 CrossRef Medline
- Barajas RF, Chang JS, Segal MR Jr, et al. **Differentiation of recurrent glioblastoma multiforme from radiation necrosis after external beam radiation therapy with dynamic susceptibility-weighted contrast-enhanced perfusion MR imaging.** *Radiology* 2009;253:486–96 CrossRef Medline
- Hu LS, Baxter LC, Smith KA, et al. **Relative cerebral blood volume values to differentiate high-grade glioma recurrence from post-treatment radiation effect: direct correlation between image-guided tissue histopathology and localized dynamic susceptibility-weighted contrast-enhanced perfusion MR imaging measurements.** *AJNR Am J Neuroradiol* 2009;30:552–58 CrossRef Medline
- Fatterpekar GM, Galheigo D, Narayana A, et al. **Treatment-related change versus tumor recurrence in high-grade gliomas: a diagnostic conundrum—use of dynamic susceptibility contrast-enhanced (DSC) perfusion MRI.** *AJR Am J Roentgenol* 2012;198:19–26 CrossRef Medline
- Welker K, Boxerman J, Kalnin A, et al; American Society of Functional Neuroradiology MR Perfusion Standards and Practice Subcommittee of the ASFN Clinical Practice Committee. **ASFN recommendations for clinical performance of MR dynamic susceptibility contrast perfusion imaging of the brain.** *AJNR Am J Neuroradiol* 2015;36:E41–51 CrossRef Medline
- Semmineh NB, Bell LC, Stokes AM, et al. **Optimization of acquisition and analysis methods for clinical dynamic susceptibility contrast MRI using a population-based digital reference object.** *AJNR Am J Neuroradiol* 2018;39:1981–88 CrossRef Medline
- Leu K, Boxerman JL, Ellingson BM. **Effects of MRI protocol parameters, preload injection dose, fractionation strategies, and leakage correction algorithms on the fidelity of dynamic-susceptibility contrast MRI estimates of relative cerebral blood volume in gliomas.** *AJNR Am J Neuroradiol* 2017;38:478–84 CrossRef Medline
- Hu LS, Kelm Z, Korfiatis P, et al. **Impact of software modeling on the accuracy of perfusion MRI in glioma.** *AJNR Am J Neuroradiol* 2015;36:2242–49 CrossRef Medline
- Kelm ZS, Korfiatis PD, Lingineni RK, et al. **Variability and accuracy of different software packages for dynamic susceptibility contrast magnetic resonance imaging for distinguishing glioblastoma progression from pseudoprogression.** *J Med Imaging (Bellingham)* 2015;2:026001 CrossRef Medline
- Hu LS, Baxter LC, Pinnaduwa DS, et al. **Optimized preload leakage-correction methods to improve the diagnostic accuracy of dynamic susceptibility-weighted contrast-enhanced perfusion MR imaging in posttreatment gliomas.** *AJNR Am J Neuroradiol* 2010;31:40–48 CrossRef Medline
- Boxerman JL, Schmainda KM, Weisskoff RM. **Relative cerebral blood volume maps corrected for contrast agent extravasation significantly correlate with glioma tumor grade, whereas uncorrected maps do not.** *AJNR Am J Neuroradiol* 2006;27:859–67 Medline
- Bedekar D, Jensen T, Schmainda KM. **Standardization of relative cerebral blood volume (rCBV) image maps for ease of both inter-**

- and inpatient comparisons. *Magn Reson Med* 2010;64:907–13 CrossRef Medline
23. Prah MA, Stufflebeam SM, Paulson ES, et al. **Repeatability of standardized and normalized relative CBV in patients with newly diagnosed glioblastoma.** *AJNR Am J Neuroradiol* 2015;36:1654–61 CrossRef Medline
 24. Smits M, Bendszus M, Collette S, et al. **Repeatability and reproducibility of relative cerebral blood volume measurement of recurrent glioma in a multicentre trial setting.** *Eur J Cancer* 2019;114:89–96 CrossRef Medline
 25. Stupp R, Mason WP, van den Bent MJ, et al; European Organisation for Research and Treatment of Cancer Brain Tumor and Radiotherapy Groups; National Cancer Institute of Canada Clinical Trials Group. **Radiotherapy plus concomitant and adjuvant temozolomide for glioblastoma.** *N Engl J Med* 2005;352:987–96 CrossRef Medline
 26. Louis DN, Perry A, Reifenberger G, et al. **The 2016 World Health Organization Classification of Tumors of the Central Nervous System: a summary.** *Acta Neuropathol* 2016;131:803–20 CrossRef Medline
 27. Hu LS, Ning S, Eschbacher JM, et al. **Multi-parametric MRI and texture analysis to visualize spatial histologic heterogeneity and tumor extent in glioblastoma.** *PLoS One* 2015;10:e0141506 CrossRef Medline
 28. Hu LS, Ning S, Eschbacher JM, et al. **Radiogenomics to characterize regional genetic heterogeneity in glioblastoma.** *Neuro Oncol* 2017;19:128–37 CrossRef Medline
 29. Hu LS, Eschbacher JM, Dueck AC, et al. **Correlations between perfusion MR imaging cerebral blood volume, microvessel quantification, and clinical outcome using stereotactic analysis in recurrent high-grade glioma.** *AJNR Am J Neuroradiol* 2012;33:69–76 CrossRef Medline
 30. Paulson ES, Schmainda KM. **Comparison of dynamic susceptibility-weighted contrast-enhanced MR methods: recommendations for measuring relative cerebral blood volume in brain tumors.** *Radiology* 2008;249:601–13 CrossRef Medline
 31. Kassner A, Annesley DJ, Zhu XP, et al. **Abnormalities of the contrast re-circulation phase in cerebral tumors demonstrated using dynamic susceptibility contrast-enhanced imaging: a possible marker of vascular tortuosity.** *J Magn Reson Imaging* 2000;11:103–13 CrossRef Medline
 32. Nyul LG, Udupa JK. **Approach to standardizing MR image intensity scale.** In: *Proceedings of the SPIE* 1999;3658:595–603 CrossRef
 33. Burger PC, Mahley MS Jr, Dudka L, et al. **The morphologic effects of radiation administered therapeutically for intracranial gliomas: a postmortem study of 25 cases.** *Cancer* 1979;44:1256–72 CrossRef Medline
 34. Bell LC, Stokes AM, Quarles CC. **Analysis of postprocessing steps for residue function dependent dynamic susceptibility contrast (DSC)-MRI biomarkers and their clinical impact on glioma grading for both 1.5 and 3T.** *J Magn Reson Imaging* 2020;51:547–53 CrossRef Medline
 35. Schmainda KM, Prah MA, Hu LS, et al. **Moving toward a consensus DSC-MRI protocol: validation of a low-flip angle single-dose option as a reference standard for brain tumors.** *AJNR Am J Neuroradiol* 2019;40:626–33 CrossRef Medline
 36. Iv M, Liu X, Lavezo J, et al. **Perfusion MRI-based fractional tumor burden differentiates between tumor and treatment effect in recurrent glioblastomas and informs clinical decision-making.** *AJNR Am J Neuroradiol* 2019;40:1649–57 CrossRef Medline
 37. Muruganandham M, Lupu M, Dyke JP, et al. **Preclinical evaluation of tumor microvascular response to a novel antiangiogenic/antitumor agent RO0281501 by dynamic contrast-enhanced MRI at 1.5 T.** *Mol Cancer Ther* 2006;5:1950–57 CrossRef Medline
 38. Wilmes LJ, Pallavicini MG, Fleming LM, et al. **AG-013736, a novel inhibitor of VEGF receptor tyrosine kinases, inhibits breast cancer growth and decreases vascular permeability as detected by dynamic contrast-enhanced magnetic resonance imaging.** *Magn Reson Imaging* 2007;25:319–27 CrossRef Medline
 39. Doblas S, He T, Saunders D, et al. **Glioma morphology and tumor-induced vascular alterations revealed in seven rodent glioma models by in vivo magnetic resonance imaging and angiography.** *J Magn Reson Imaging* 2010;32:267–75 CrossRef Medline
 40. Schmainda KM, Zhang Z, Prah M, et al. **Dynamic susceptibility contrast MRI measures of relative cerebral blood volume as a prognostic marker for overall survival in recurrent glioblastoma: results from the ACRIN 6677/RTOG 0625 multicenter trial.** *Neuro Oncol* 2015;17:1148–56 CrossRef Medline
 41. Gerstner ER, Zhang Z, Fink JR, et al. **ACRIN 6684: Assessment of Tumor Hypoxia in Newly Diagnosed Glioblastoma Using 18F-FMISO PET and MRI.** *Clin Cancer Res* 2016;22:5079–86 CrossRef Medline
 42. Barajas RF, Phillips JJ, Parvataneni R Jr, et al. **Regional variation in histopathologic features of tumor specimens from treatment-naïve glioblastoma correlates with anatomic and physiologic MR imaging.** *Neuro Oncol* 2012;14:942–54 CrossRef Medline
 43. Stadlbauer A, Ganslandt O, Buslei R, et al. **Gliomas: histopathologic evaluation of changes in directionality and magnitude of water diffusion at diffusion-tensor MR imaging.** *Radiology* 2006;240:803–10 CrossRef Medline

Correction of Motion Artifacts Using a Multiscale Fully Convolutional Neural Network

 K. Sommer,  A. Saalbach,  T. Brosch,  C. Hall,  N.M. Cross, and  J.B. Andre



ABSTRACT

BACKGROUND AND PURPOSE: Motion artifacts are a frequent source of image degradation in the clinical application of MR imaging (MRI). Here we implement and validate an MRI motion-artifact correction method using a multiscale fully convolutional neural network.

MATERIALS AND METHODS: The network was trained to identify motion artifacts in axial T2-weighted spin-echo images of the brain. Using an extensive data augmentation scheme and a motion artifact simulation pipeline, we created a synthetic training dataset of 93,600 images based on only 16 artifact-free clinical MRI cases. A blinded reader study using a unique test dataset of 28 additional clinical MRI cases with real patient motion was conducted to evaluate the performance of the network.

RESULTS: Application of the network resulted in notably improved image quality without the loss of morphologic information. For synthetic test data, the average reduction in mean squared error was 41.84%. The blinded reader study on the real-world test data resulted in significant reduction in mean artifact scores across all cases ($P < .03$).

CONCLUSIONS: Retrospective correction of motion artifacts using a multiscale fully convolutional network is promising and may mitigate the substantial motion-related problems in the clinical MRI workflow.

ABBREVIATIONS: FCN = fully convolutional neural network; MSE = mean squared error; SSIM = structural similarity index

Patient motion during MRI examinations results in artifacts that are a frequent source of image degradation in clinical practice, reportedly impacting image quality in 10%–42% of examinations of the brain.^{1,2} Motion artifacts that substantially affect the diagnostic value of an MRI examination may be recognized at the time of image acquisition, resulting in repeat sequences in nearly 20% of all MRI examinations.^{1,3} These repeat sequences incur substantial temporal and financial costs to the radiology department.¹ Because there is no guarantee that a patient will be better able to lie motionless during the repeat sequence, the diagnostic value of the images is often impaired.

The problem of motion has been addressed extensively by the MRI research community, leading to a large number of proposed techniques to reduce or eliminate motion artifacts in MRI.⁴ Among the most widely used methods are prospective^{5,6} and retrospective^{7,8} navigator-based approaches, in which position information is extracted from data acquired using the MRI scanner itself. Most of these methods, however, are limited to a particular imaging situation and/or require additional scan time, which is usually undesirable. One of the most popular techniques for motion correction is the PROPELLER technique, in which rotating strips of several parallel k -space lines are acquired, leading to a strong oversampling of the k -space center.⁹ Although widely used in clinics, it involves an increased acquisition time and can fail to correct for artifacts due to through-plane motion. Finally, iterative “autocorrection” methods that retrospectively suppress motion artifacts without additional information have been presented.^{10,11} Most of these approaches, however, usually produce images with residual artifacts after correction.

On the other hand, deep neural network techniques have recently received much attention due to impressive results in many computer vision tasks.¹² In particular, fully convolutional neural networks (FCNs) have been successfully applied to complex image-to-image translation tasks such as semantic segmentation¹³ or denoising.¹⁴

Received October 10, 2019; accepted after revision January 7, 2020.

From Philips Research, (K.S., A.S., T.B.) Hamburg, Germany; Radiology Solutions (C.H.), Philips, Seattle, Washington; and Department of Radiology (N.M.C., J.B.A.), University of Washington, Seattle, Washington.

The basic concept of this work previously presented at: Joint Annual Meeting of the International Society for Magnetic Resonance in Medicine and the European Society for Magnetic Resonance in Medicine and Biology, June 16–21, 2018; Paris, France (Abstract no. #1175).

Please address correspondence to Karsten Sommer, PhD, Philips GmbH Innovative Technologies, Röntgenstr 24-26, 22335 Hamburg, Germany; e-mail: karsten.sommer@philips.com



Indicates article with supplemental on-line photo.

<http://dx.doi.org/10.3174/ajnr.A6436>

In an early feasibility study, it was demonstrated that FCNs can also be applied to retrospectively correct motion artifacts in MRI.¹⁵ Recently, this approach was used in a work by Duffy et al,¹⁶ which relied on a large dataset and also explored the applicability of other network architectures to address this problem. Here we present an alternative artifact-correction method that relies on a multiscale FCN and includes both translational and rotational motion as well as a variety of complex patient motion profiles throughout the scan. The multiscale network architecture was trained in a residual learning setup, which allowed efficient capture of both high- and low-level artifact features in the input images. To validate our hypothesis that the presented method can significantly reduce the level of motion artifacts in MR brain images, a blinded reader study was conducted in which 2 experienced neuroradiologists visually assessed the degree of motion artifacts in a real-world test dataset of clinical MR brain images before and after correction by the trained network.

MATERIALS AND METHODS

Data Acquisition and Analysis

An institutional review board–approved retrospective Health Insurance Portability and Accountability Act–compliant study was performed, and patient consent was waived. Training of the FCN was accomplished using a dataset with simulated artifacts introduced into in vivo clinical brain image data. To create a dataset representative of images obtained in the clinical routine, we selected 46 scans from consecutive patients undergoing clinically indicated MRI brain examinations from the image archive of the department. Common indications included known or suspected intracranial tumor (primary or metastatic, including follow-up), known or suspected acute ischemic stroke (including follow-up), known or suspected demyelinating disease, dementia, suspected transient ischemic attack, and headache. Findings included acute and subacute ischemic infarcts, metastatic lesions, and microvascular angiopathy, among others. Eight scans (17.4%) did not show any detectable pathology. Patient age ranged from 28 to 89 years (mean age, 58.7 years), with a male/female ratio of 1:1.05.

All image volumes were manually reviewed on a slice-by-slice basis by an experienced neuroradiologist. Annotation of rigid body motion was performed using a previously defined 5-point Likert scale with a range of $S = 0-4$, in which the scores correspond to no ($S = 0$), minimal ($S = 1$), mild ($S = 2$), moderate ($S = 3$), and severe ($S = 4$) artifacts.¹ Of note, scans with $S \geq 3$ are considered marginal in diagnostic quality and should be repeated.¹ In this initial review, a single motion-artifact score was given to each scan/volume (ie, sequence). All scans had been performed at a single institution on 1 of two 3T MRI scanners (both Ingenia; Philips, Best, the Netherlands) and consisted of T2-weighted multislice 2D turbo spin-echo whole-brain sequences. Scan parameters were in the following ranges: TE = 80–100 ms, TR = 3000–5700 ms, flip angle = 90°, echo-train length = 12–21, acquisition matrix size = 400–480 × 280–400, reconstructed image matrix size = 512–560 × 512–560, number of slices = 30–50, slice thickness = 3–5 mm, number of signal averages = 1–2, pixel bandwidth = 142–204 Hz/px, phase FOV = 74%–88%. Only magnitude data were used because the images were

retrieved from the DICOM archive of the imaging department. All retrieved DICOM data were anonymized.

Dataset Generation

All volumes that were deemed artifact-free by the radiologist (18 of 46) were then used to generate the synthetic training and test dataset (16 and 2 volumes, respectively). In each volume, the lower 8 and top 5 slices were discarded to restrict the analysis to clinically relevant parts of the scan, resulting in 312 and 39 slices that were used for generation of the synthetic training and the test dataset, respectively. Artifacts simulating rigid translational and rotational in-plane motion were then introduced into the Fourier-transformed data, in which the parameter ranges were selected to generate a large range of realistic artifact appearances. For each input image, the assumed echo-train length of the turbo spin-echo readout was chosen randomly in the range of 8–32. Similarly, the assumed extent of zero-padding in k -space was chosen randomly in the range of 0–100. Motion trajectories, (ie, translation/rotation vectors as a function of scan time) were generated randomly to simulate the artifacts. The different types of motion trajectories that were used in this study are shown exemplarily in Fig 1. In the “sudden motion” trajectory (top and middle profiles in Fig 1), the subject is assumed to lie still for a large part of the examination, until a swift translation or rotation of the head occurs. The time point of the sudden motion was taken randomly as a fraction of the total scan time in the range of one-third to seven-eighths. In addition, a large range of random motion trajectories was simulated (bottom profile in Fig 1) using a random colored noise generator.¹⁷ The exponent of the power spectral density of the generator was randomly chosen in the range of 1–100 to create both high- and low-frequency motion profiles. To account for possible motion during the “waiting time” in a multislice acquisition sequence (ie, the time that is spent to acquire data from other slices), we added small random shifts to the motion profiles after each assumed acquisition of an interleaf (defined by the echo-train length) in the k -space, as shown in the bottom profile in Fig 1. The maximum magnitude of the motion was chosen randomly in the range of 1–4 px and 0.5°–4.0° for translation and rotation artifacts, respectively. For artifacts due to rotation, the center of rotation was also varied randomly in the range of 0–100 px in each direction.

The synthetic training dataset was generated using 16 of the 18 volumes. For each input image, data augmentation was realized using random translation (0–10 px), random rotation (0°–10°), and random deformation of each input image before insertion of the artifacts. For the latter, 2 random second-order 2D polynomials were used as pixel-shift maps for x - and y -deformation. An artifact-only image was calculated by subtracting the artifact-free reference image from the artifact-corrupted image. For the synthetic training dataset, 300 image pairs (artifact-corrupted and artifact-only images) were created for each input image, resulting in 93,600 image pairs in total. The synthetic test dataset was derived from the 2 remaining volumes and consisted of 11,700 image pairs.

To evaluate the performance of the network on data with artifacts due to actual patient motion, we used the 28 clinical

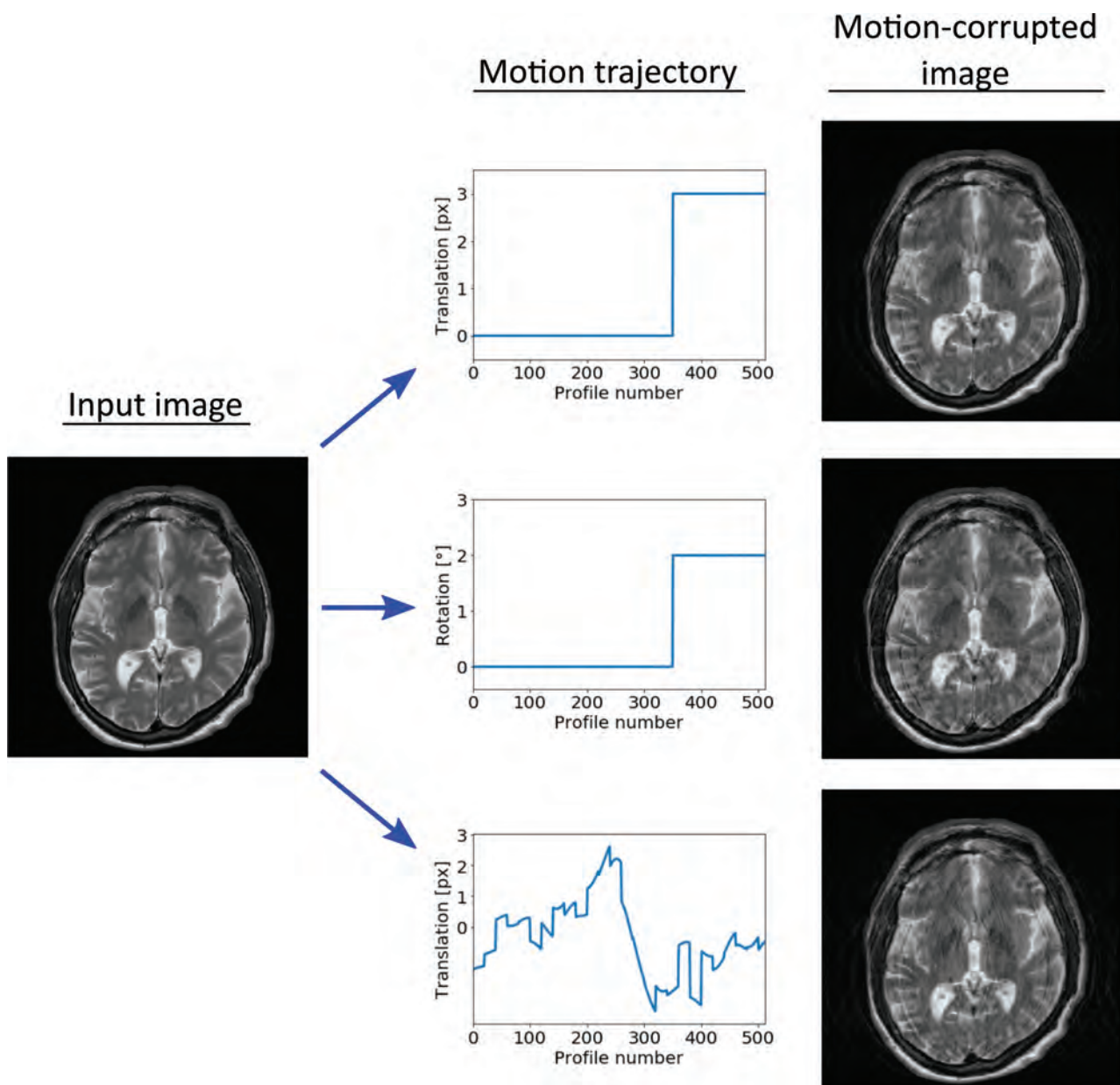


FIG 1. Examples of motion-artifact generation. Examples of different motion trajectories that were used are shown in the central column: sudden translation (*upper*), sudden rotation (*middle*), and random translation (*lower*). The right column shows the corresponding artifact-corrupted output images.

volumes that were initially rated with the score $S = 1-4$ (ie, containing motion artifacts) as a real-world test dataset.

Network Structure, Training, and Evaluation

The network structure used in this study, depicted in Fig 2, was based on a recently proposed architecture called Foveal FCN.¹⁸ In contrast to standard FCN architectures, it involved the processing of the input image at 3 different scales, thereby realizing an efficient extraction of both high- and low-level features with minimal memory requirement. Even for the relatively large input images used in this study ($512-560 \times 512-560$ pixels), a mini-batch size of 32 could be used. The FCN allowed a patch-based processing of the image, which did not affect the overall outcome of the correction. Therefore, the image was divided into

nonoverlapping patches, which were processed in conjunction with larger, but down-sampled patches at the same position (depicted by the different colored boxes in Fig 2). Feature extraction for each patch was performed using 2 layers, each consisting of a convolutional layer, followed by batch normalization, and a rectified linear unit. Larger kernel sizes were used for the convolutional layers in the higher scales to allow larger effective receptive fields. Feature integration was realized using average unpooling and convolutional layers. This patch-based processing allowed processing of input images with variable size.

The network was trained for 50 epochs using stochastic gradient descent, in which the Adam algorithm¹⁹ was used to update the learning rate for each parameter. The mean squared error (MSE) between the artifact estimate of the network and the

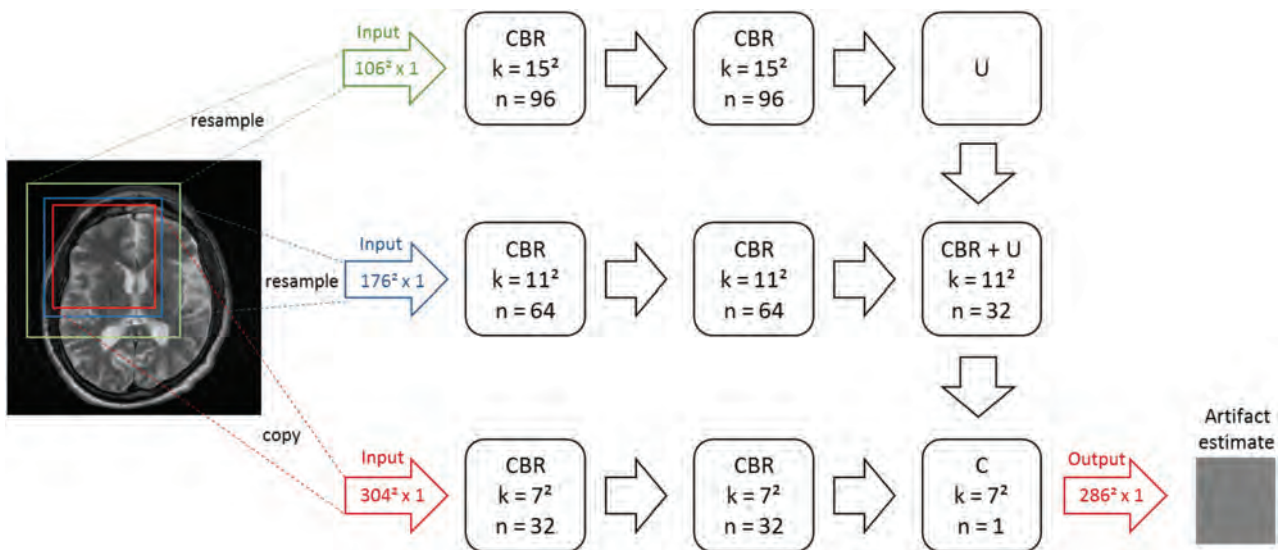


FIG 2. Architecture of the used Foveal fully convolutional neural network. The input image was split into different patches (indicated by *red box*), and each patch was processed in conjunction with larger, down-sampled patches at the same location (*blue and green boxes*). The size of the patches was chosen to account for the loss of border pixels in every convolutional layer. Each feature-extraction path consisted of 2 layers, each comprising a convolutional layer (C), batch normalization (B), and a rectified linear unit (R) activation. Feature integration was realized using average unpooling (U) and convolutional layers. Kernel sizes and the number of channels are denoted as k and n , respectively. The output was the estimate of the motion artifacts by the network for the selected image patch.

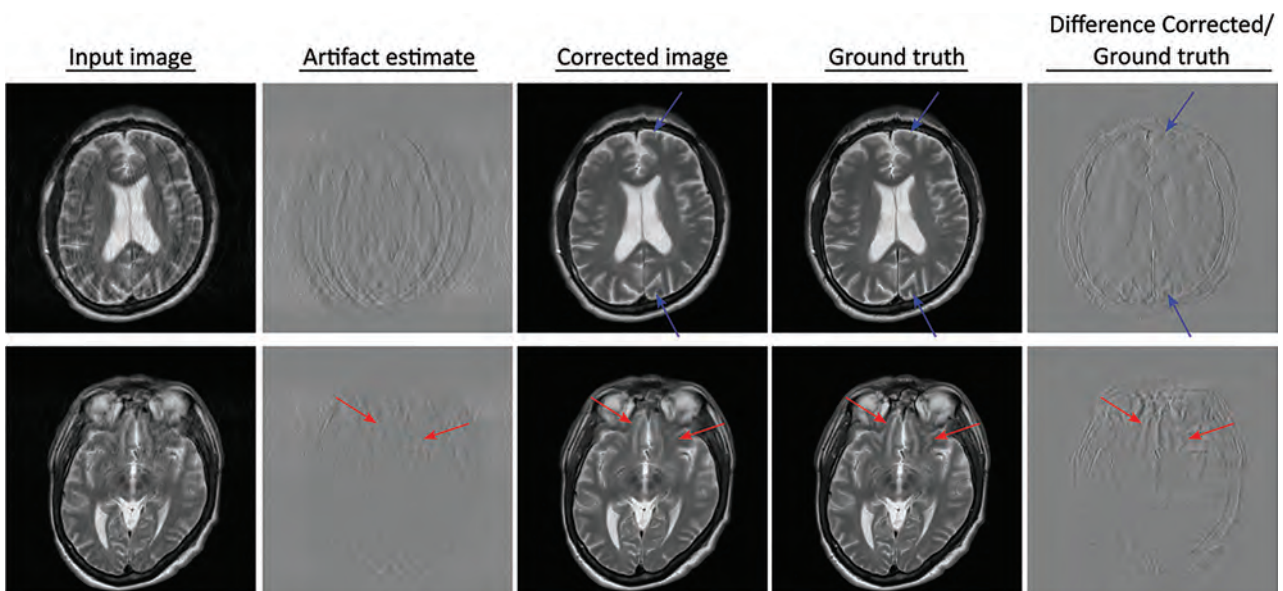


FIG 3. Examples of the performance of the network on the synthetic test dataset containing simulated motion artifacts. *Blue arrows* indicate residual artifacts. *Red arrows* mark regions where slight blurring can be observed in the corrected images compared with the ground truth. The blurred structures cannot be identified in the artifact-estimate image (ie, the network output), indicating that this effect was not introduced by the network.

ground truth was used as a cost function. Training was realized using the Microsoft Cognitive Toolkit (<https://github.com/Microsoft/CNTK>) with a computation time of approximately 6 days on a single Nvidia GTX 1080ti GPU. With the same hardware, inference time for a single slice was about 200 ms.

After training, the network was applied to the synthetic test dataset (with simulated artifacts), which allowed direct visual

comparison with the artifact-free reference image. In addition, quantitative analysis was performed using the MSE and the structural similarity index²⁰ between artifact-corrected and reference images as metrics. Two-sample *t* tests were performed to test whether the network application yielded a significant alteration of these metrics. To evaluate the impact on artifact-free images, the network was also applied to all slices of the 2 test volumes without simulated artifacts.

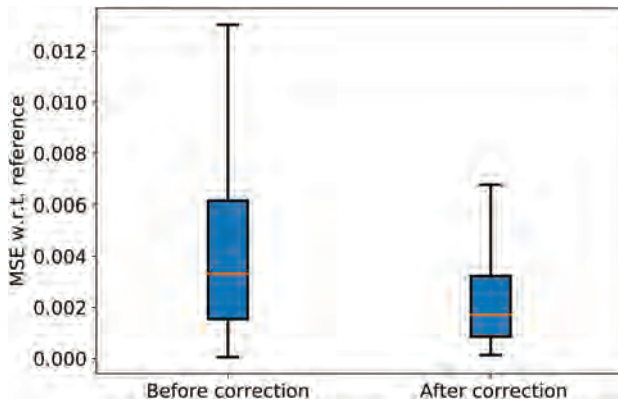


FIG 4. Boxplot of the MSE relative to the reference data before and after the correction. w.r.t. indicates with respect to.

In addition, the trained network was also evaluated on the real-world test dataset. For each section, the artifact estimate of the network was subtracted from the original input image. Because artifact-free reference images were not available for these 28 clinical motion cases, all artifact-corrupted input and artifact-corrected output images (962 in total) were rated on a section-by-section level in a blinded reader study using the 0–4 qualitative scale described previously. The images were shown to 2 board-certified neuroradiologists in random order and did not contain any information regarding origin (ie, before/after correction). A 1-sample *t* test was performed for each artifact score class using a significance level of .05, corresponding to critical values in the range of 1.65–1.75 for the different score classes.

RESULTS

For the synthetic test data, the network-based correction resulted in a reduction of motion artifacts and yielded image data with improved image quality. Figure 3 shows the performance of the network for 2 sample slices from the synthetic test dataset. Only minor residual artifacts can be identified in the corrected images (marked by blue arrows). In some parts of the corrected images, a mild blurring can be observed compared with the ground truth images (marked by red arrows). This is confirmed by inspection of the difference between corrected and ground truth images (rightmost column in Fig 3), where the contours of certain anatomic structures can be discerned. Most important, these structures cannot be identified in the artifact-estimate image (ie, the network output).

The results of the quantitative analysis on the synthetic test dataset are visualized in Fig 4, which reveals a substantial reduction of the MSE due to application of the network. On average, the network-based artifact correction resulted in a reduction of the MSE of 41.84%. Similarly, an average increase of the structural similarity index from 0.863 to 0.924 was observed (ie, the network increased similarity to the ground truth). Both the reduction of MSE and increase of the structural similarity index were confirmed to be statistically significant ($P < .001$ in both cases). For the images without motion artifacts, the structural similarity index was only slightly reduced from 1.0 to 0.99,

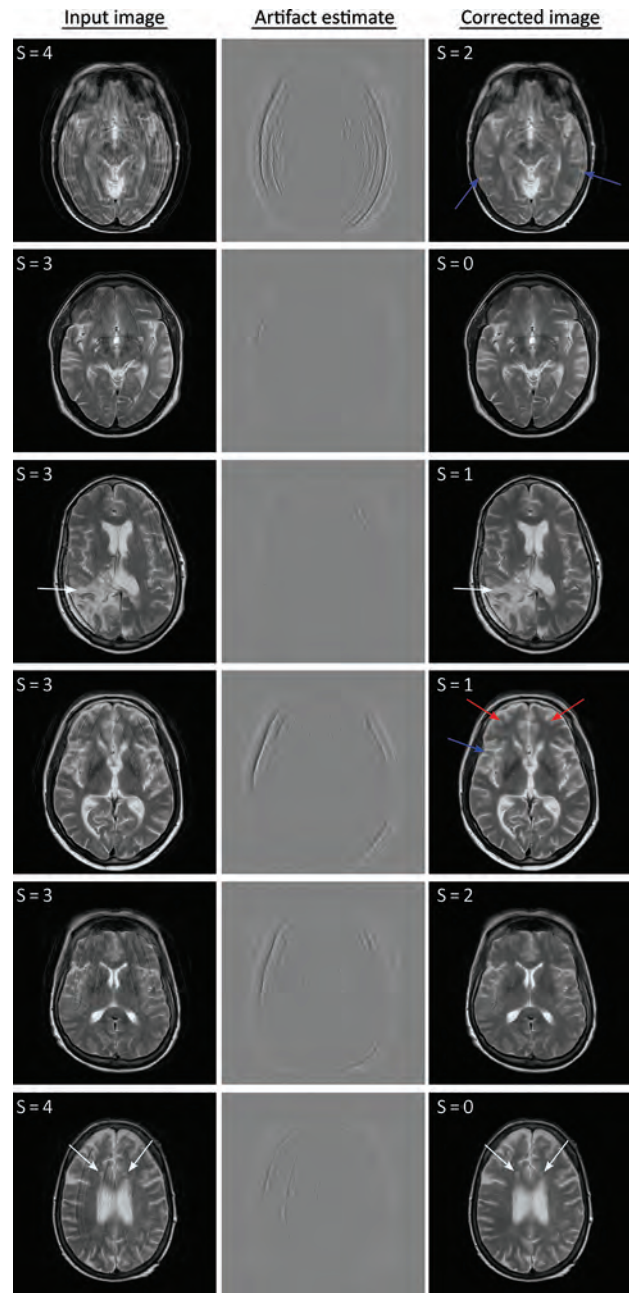


FIG 5. Examples of the performance of the network on real-world test data. Residual artifacts and regions of residual blurring are indicated by *blue and red arrows*, respectively. *White arrows* indicate lesions where the network removed the motion artifacts despite the lack of such structures in the training dataset. The numbers in the top left of the images are the scores given by the neuroradiologist.

suggesting that the modifications by the network were negligible in these cases. The network performance on 2 sample cases that were rated as artifact-free by the radiologists is shown in the Online Figure.

Similar results were obtained for the test dataset with real motion cases, as shown exemplarily in Fig 5. Substantial improvement of image quality was observed for nearly all cases, often with no, or only minor, residual artifacts (marked by blue arrows). Similar to the synthetic test data, minor blurring was

Results of the blinded reader study^a

Artifact Score S before Correction (1 = Minimal, 4 = Severe)	Mean Artifact Score S after Correction	Fraction of Images for Which the Score was Improved by the Correction
S = 1 (minimal; 186/54 images)	0.269/0.221	74.73%/78.57%
S = 2 (mild; 82/110 images)	0.683/0.646	95.12%/98.18%
S = 3 (moderate; 34/40 images)	0.971/1.225	100.00%/97.50%
S = 4 (severe; 17/6 images)	1.588/2.167	100.00%/83.33%

^a In all columns, the pair of numbers refers to the annotations given by readers 1 and 2, respectively.

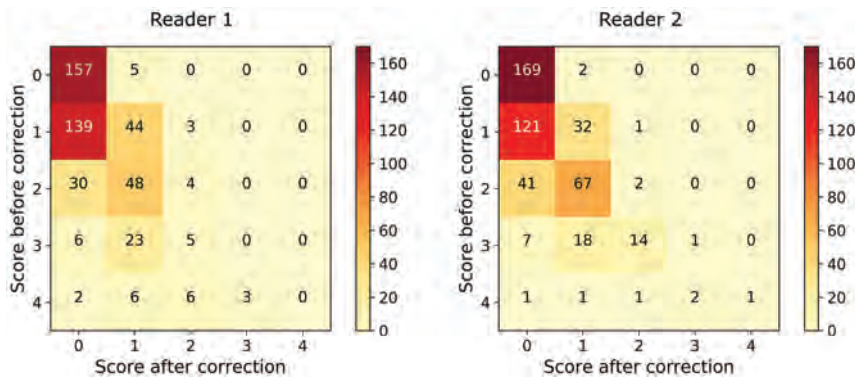


FIG 6. Matrices showing the detailed results of the blinded reader study. Each cell in the matrix indicates the number of images for a particular score pair (before/after correction).

observed in some parts of the images (marked by red arrows), typically in regions with severe artifacts in the input images. Most interesting, the algorithm showed robust performance even for radiologically detectable brain pathologies that were not present in the training dataset, such as the lesions in the third and sixth rows of Fig 5 (marked by white arrows), suggesting that the FCN appropriately targeted the motion artifacts only and left the underlying image data relatively unaltered.

These qualitative findings were confirmed by the results of the blinded reader study. The mean artifact scores for the real-world test dataset before and after the network-based correction are listed in the Table for both readers. Application of the correction resulted in a reduction of the mean artifact score for all artifact levels and both readers. As can be seen from the Table, the total reduction of the mean artifact score was substantially larger for the higher artifact score classes. This reduction was statistically significant for all score classes, as confirmed by the 1-sample *t* tests for the different artifact score classes: $P < .03$ and $t > 3.0$ in all cases. The detailed results of the reader study are shown in Fig 6 in matrix form, where each cell indicates the number of images for a particular score pair (before/after correction). Both matrices are dominated by values on or below the diagonal, again confirming the overall positive impact of the network-based artifact correction. Agreement between both readers was high: Both readers agreed in 74.4% of all images and disagreed by 1/2/3/4 scores in 24.2%/1.2%/0.1%/0.0% of all images. The weighted Cohen κ was $\kappa = 0.82$.

DISCUSSION

The presented network-based motion artifact correction represents a purely retrospective correction technique, requiring only

standard-magnitude images from a traditional DICOM repository (PACS for example), which can be performed at any time after image acquisition. Its artifact-detection and removal capabilities rely on the prior knowledge that has been encoded in the network parameters during training. As a consequence, it does not require additional scan time or data input apart from the magnitude-only MRI. It may, hence, be applied retrospectively to all suitable datasets in an image archive, potentially mitigating artifact-related clinical problems such as difficult radiologic interpretations, reduced workflow efficiency, and increased institutional costs. A fundamental requirement for such applications is the ability of the network to generalize to unseen anatomic and pathologic structures. The successful identification of artifacts in clinical motion cases, even in the presence of pathologies that were not seen during

training (Fig 5), is very promising in this regard.

The real-world applicability of this technique was preliminarily assessed in the clinical reader portion of this study, which suggested that optimal FCN performance (resulting in the highest final image quality) was generally obtained for cases with motion artifacts that were scored as “mild” before correction (scores $S = 1$ or $S = 2$). In many of these cases, the resulting images were considered artifact-free by the blinded radiologists. The small number of cases in which an increased artifact score was given after the correction—8 and 3 of 481 images for readers 1 and 2, respectively—may be attributed to intrareader variability. Direct visual comparison of these images before and after the correction did not reveal an increased artifact level due to the application of the network.

On the other hand, reduction of the mean artifact score was most pronounced for the severe-artifact cases (initial motion scores of 3 and 4), which almost always yielded lower motion scores than those assigned before correction. Of note, the complete removal of all artifacts was not achieved in all of these cases, however, as confirmed by visual inspection (Fig 5). It is currently not clear whether these residual artifacts constitute a fundamental limitation of the presented method or whether further improvements are possible. Given that performance on classic computer vision tasks such as image classification has recently been considerably improved by increasing network depth,^{21,22} more comprehensive training datasets, as well as various other technical developments,^{23,24} it is conceivable that the application of such techniques to the examined problem may yield even lower residual artifact levels. Such developments may be further supported by applying the network to complex input data. Because motion artifacts are typically very prominent in the phase images, separation of artifacts and anatomy may be facilitated. Alternatively,

other loss functions such as L1²⁵ or perceptual loss²⁶ may be explored in this regard. Recently, several works also suggested an adversarial loss to improve the visual appearance of the corrected images.^{16,27} While further research is needed on this topic, we avoided adversarial loss terms in this study due to the potential threat of generating visually pleasing but synthetic structures, which, in the worst case, may be misinterpreted as pathologies.

Compared with the results of the clinical reader study, quantitative analysis of the network performance on synthetic data revealed a somewhat limited reduction of the MSE, in particular in view of the striking visual improvements of image quality as shown in Figs 3 and 5. This discrepancy between visual assessment and MSE may be partially explained by the fact that the correction capability of the network relies mainly on a removal of ghosting artifacts, whereas the corresponding minor reduction in signal intensity of the original anatomic structures is relatively unaffected. While the latter effect has a negligible impact on visual perception, it significantly affects the MSE. This interpretation confirms previous reports of the inadequacy of the MSE for measuring image similarity.^{20,28}

Another potential limitation may be the residual image blurring that could be identified in select cases following filtering, particularly in images that were initially scored as having severe motion artifacts. Arguably correction of this blurring may represent a more difficult image translation task than removal of the typical ghosting artifacts due to motion. Recent works,^{29,30} however, suggest that neural networks may also enable such image deblurring.

Future works should address these current limitations, as well as extend the presented clinical validation to more diverse datasets. In particular, cases with small lesions (eg, intracranial metastases) or anatomic structures that may have an appearance similar to motion artifacts (eg, small vessels) may prove critical. In addition, the performance of the network in case of other MRI contrasts, other anatomies, or additional artifacts, such as signal voids, wrap-around artifacts, or N/2 ghosting,³¹ should be examined in detail.

The presented Foveal FCN offers the potential for retrospective improvement in image quality in examinations with motion during acquisition. Our study suggests that a network-based correction technique is capable of significantly improving image quality in clinical, motion-degraded images. Admittedly, this technique may not yet be capable of completely removing all motion-related artifacts, though implementation of such an FCN may prove a useful asset in the clinical workflow. Radiologists often claim a capacity to “see through” certain types of mild artifacts so that a modest reduction in the degree of artifacts may suffice to enable a reliable interpretation of the images. In addition, the presented method is largely orthogonal to other techniques for motion-artifact reduction such as those based on MRI navigators or external tracking devices. It may be used to correct for residual motion artifacts that often remain even when such techniques are applied.

CONCLUSIONS

This work demonstrates the feasibility of retrospective motion-artifact correction in MRI using a multiscale FCN. The presented

method does not require additional input data apart from magnitude-only MRI and appears to effectively correct for motion artifacts, even in case of unseen pathologies.

ACKNOWLEDGMENTS

The authors would like to thank David R. Haynor for fruitful discussions and proofreading of the article.

Disclosures: Karsten Sommer—UNRELATED: Employment: Philips GmbH Innovative Technologies; Patents (Planned, Pending or Issued): Philips GmbH Innovative Technologies. Axel Saalbach—UNRELATED: Employment: Philips GmbH Innovative Technologies; Patents (Planned, Pending or Issued): Philips GmbH Innovative Technologies; OTHER RELATIONSHIPS: employee of Philips Research Hamburg. Tom Brosch—UNRELATED: Employment: Philips GmbH Innovative Technologies; Patents (Planned, Pending or Issued): Philips GmbH Innovative Technologies. Christopher Hall—UNRELATED: Employment: Philips, Comments: I was a Philips employee when this study was performed; Stock/Stock Options: Philips, Comments: I no longer own Philips shares or options. Jalal B. Andre—UNRELATED: Grants/Grants Pending: Philips Healthcare, Comments: local grant recipient for an unrelated project.* Nathan M. Cross—UNRELATED: Grants/Grants Pending: National Institute of Arthritis and Musculoskeletal and Skin Diseases P30 AR072572, Guerbet GDx-44-010*; Travel/Accommodations/Meeting Expenses Unrelated To Activities Listed: GE Signa Masters Conference, Comments: travel covered by GE to this conference in 2019. *Money paid to the institution.

REFERENCES

1. Andre JB, Bresnahan BW, Mossa-Basha M, et al. **Toward quantifying the prevalence, severity, and cost associated with patient motion during clinical MR examinations.** *J Am Coll Radiology* 2015; 12:689–95 CrossRef Medline
2. Satterthwaite TD, Wolf DH, Loughhead J, et al. **Impact of in-scanner head motion on multiple measures of functional connectivity: relevance for studies of neurodevelopment in youth.** *Neuroimage* 2012; 60:623–32 CrossRef Medline
3. Schreiber-Zinaman J, Rosenkrantz AB. **Frequency and reasons for extra sequences in clinical abdominal MRI examinations.** *Abdom Radiology (NY)* 2017;42:306–11 CrossRef Medline
4. Zaitsev M, Maclaren J, Herbst M. **Motion artifacts in MRI: a complex problem with many partial solutions.** *J Magn Reson Imaging* 2015;42:887–901 CrossRef Medline
5. McConnell MV, Khasgiwala VC, Savord BJ, et al. **Prospective adaptive navigator correction for breath-hold MR coronary angiography.** *Magn Reson Med* 1997;37:148–52 CrossRef Medline
6. Maclaren J, Herbst M, Speck O, et al. **Prospective motion correction in brain imaging: a review.** *Magn Reson Med* 2013;69:621–36 CrossRef Medline
7. Atkinson D, Hill D. **Reconstruction after rotational motion.** *Magn Reson Med* 2003;49:183–87 CrossRef Medline
8. Kochunov P, Lancaster JL, Glahn DC, et al. **Retrospective motion correction protocol for high-resolution anatomical MRI.** *Hum Brain Mapp* 2006;27:957–62 CrossRef Medline
9. Pipe JG. **Motion correction with PROPELLER MRI: application to head motion and free-breathing cardiac imaging.** *Magn Reson Med* 1999;42:963–69 CrossRef Medline
10. McGee KP, Manduca A, Felmlee JP, et al. **Image metric-based correction (autocorrection) of motion effects: analysis of image metrics.** *J Magn Reson Imaging* 2000;11:174–81 CrossRef Medline
11. Loktyushin A, Nickisch H, Pohmann R, et al. **Blind retrospective motion correction of MR images.** *Magn Reson Med* 2013;70:1608–18 CrossRef Medline
12. Krizhevsky A, Sutskever I, Hinton GE. **Imagenet classification with deep convolutional neural networks.** *Adv Neural Inf Process Syst* 2012;1097–1105
13. Long J, Shelhamer E, Darrell T. **Fully convolutional networks for semantic segmentation.** In: *Proceedings of the 2015 IEEE Conference*

- on *Computer Vision and Pattern Recognition*, Boston, Massachusetts. June 7–12, 2015
14. Zhang K, Zuo W, Chen Y, et al. **Beyond a Gaussian denoiser: residual learning of deep CNN for image denoising.** *IEEE Trans Image Process* 2017;26:3142–55 CrossRef Medline
 15. Sommer K, Brosch T, Wiemker R, et al. **Correction of motion artifacts using a multi-resolution fully convolutional neural network.** In: *Proceedings of the Joint Annual Meeting of the International Society for Magnetic Resonance in Medicine and the European Society for Magnetic Resonance in Medicine and Biology*, Paris, France. June 16–18, 2018
 16. Duffy BA, Zhang W, Tang H, et al. **Retrospective correction of motion artifact affected structural MRI images using deep learning of simulated motion.** In: *Proceedings of the 1st Conference on Medical Imaging with Deep Learning (MIDL 2018)*, Amsterdam, the Netherlands. June 4–6, 2018
 17. Kasdi NJ. **Discrete simulation of colored noise and stochastic processes and $1/f$ /sup/ α power law noise generation.** *Proceedings of the IEEE* 1995;83:802–27 CrossRef
 18. Brosch T, Saalbach A. **Foveal fully convolutional nets for multi-organ segmentation.** In: *Medical Imaging 2018: Image Processing: SPIE Proceedings*. Bellingham: Society of Photo-Optical Instrumentation Engineers; 2018
 19. Kingma DP, Ba J. **Adam: a method for stochastic optimization.** In: *Proceedings of the 3rd International Conference for Learning Representations*, San Diego. May 7–9, 2015
 20. Wang Z, Bovik AC, Sheikh HR, et al. **Image quality assessment: from error visibility to structural similarity.** *IEEE Trans Image Process* 2004;13:600–12 CrossRef Medline
 21. Simonyan K, Zisserman A. **Very deep convolutional networks for large-scale image recognition.** *arXiv* 2014;1409:1556
 22. He K, Zhang X, Ren S, et al. **Deep residual learning for image.** In: *Proceedings of the IEEE 2016 Conference on Computer Vision and Pattern Recognition*, Las Vegas, Nevada. June 27–30, 2016
 23. Szegedy C, Liu W, Jia Y, et al. **Going deeper with convolutions.** In: *Proceedings of the IEEE 2015 Conference on Computer Vision and Pattern Recognition*, Boston, Massachusetts. June 7–12, 2015
 24. Huang G, Liu Z, Van Der Maaten L, et al. **Densely connected convolutional networks.** In: *Proceedings of the IEEE 2017 Conference on Computer Vision and Pattern Recognition*, Honolulu, Hawaii. June 21–26, 2017
 25. Zhao H, Gallo O, Frosio I, et al. **Loss functions for image restoration with neural networks.** *IEEE Transactions on Computational Imaging* 2017;3:47–57 CrossRef
 26. Johnson J, Alahi A, Fei-Fei L. **Perceptual losses for real-time style transfer and super-resolution.** In: *Proceedings of the European Conference on Computer Vision*, Amsterdam, the Netherlands, October 11–14, 2016
 27. Latif S, Asim M, Usman M, et al. **Automating motion correction in multishot MRI using generative adversarial networks.** In: *Proceedings of the 32nd Conference on Neural Information Processing Systems*, Montreal, Canada. December 2–8, 2018
 28. Wang Z, Bovik AC. **Mean squared error: love it or leave it? A new look at signal fidelity measures.** *IEEE Signal Processing Magazine* 2009;26:98–117 CrossRef
 29. Svoboda P, Hradis M, Marsik L, et al. **CNN for license plate motion deblurring.** In: *Proceedings of the 2016 IEEE International Conference on Image Processing*, Phoenix, Arizona. September 25–28, 2016
 30. Schuler C, Hirsch M, Harmeling S, et al. **Learning to deblur.** *IEEE Trans Pattern Anal Mach Intell* 2016;38:1439–51 CrossRef Medline
 31. Heiland S. **From A as in aliasing to Z as in zipper: artifacts in MRI.** *Clin Neuroradiol* 2008;18:25–36 CrossRef

Clinical Experience of 1-Minute Brain MRI Using a Multicontrast EPI Sequence in a Different Scan Environment

 K.H. Ryu,  H.J. Baek,  S. Skare,  J.I. Moon,  B.H. Choi,  S.E. Park,  J.Y. Ha,  T.B. Kim,  M.J. Hwang, and  T. Sprenger



ABSTRACT

BACKGROUND AND PURPOSE: The long scan time of MR imaging is a major drawback limiting its clinical use in neuroimaging; therefore, we aimed to investigate the clinical feasibility of a 1-minute full-brain MR imaging using a multicontrast EPI sequence on a different MR imaging scanner than the ones previously reported.

MATERIALS AND METHODS: We retrospectively reviewed the records of 146 patients who underwent a multicontrast EPI sequence, including T1-FLAIR, T2-FLAIR, T2WI, DWI, and T2*WI sequences. Two attending neuroradiologists assessed the image quality of each sequence to compare the multicontrast EPI sequence with routine MR imaging protocols. We used the Wilcoxon signed rank test and McNemar test to compare the 2 MR imaging protocols.

RESULTS: The multicontrast EPI sequence generally showed sufficient image quality of >2 points using a 4-point assessment scale. Regarding image quality and susceptibility artifacts, there was no significant difference between the multicontrast EPI sequence DWI and routine DWI ($P > .05$), attesting to noninferiority of the multicontrast EPI, whereas there were significant differences in the other 4 sequences between the 2 MR imaging protocols.

CONCLUSIONS: The multicontrast EPI sequence showed sufficient image quality for clinical use with a shorter scan time; however, it was limited by inferior image quality and frequent susceptibility artifacts compared with routine brain MR imaging. Therefore, the multicontrast EPI sequence cannot completely replace the routine MR imaging protocol at present; however, it may be a feasible option in specific clinical situations such as screening, time-critical diseases or for use with patients prone to motion.

ABBREVIATIONS: EPIMix = multicontrast EPI sequence; SWAN = susceptibility-weighted angiography

The long scan time of brain MR imaging is a major drawback limiting its clinical use. To shorten the scan time, fast imaging techniques have been introduced.¹⁻⁶ However, most studies have examined specific clinical conditions, thus

only evaluating limited sequences.⁷⁻¹⁵ Another fast technique, synthetic MR imaging, quantitatively approaches the absolute physical properties for single-scan, multiple-contrast generation with a total scan time of 4–5 minutes.^{4-6,16,17} Routine clinical use of synthetic MR imaging is limited because it cannot produce DWI and T2*WI and provide inferior image quality in synthetic T2-FLAIR due to partial volume effects.¹⁸ Following technical advances, some studies have focused on ultrafast MR imaging with 5 essential sequences in patients prone to motion, combining advanced imaging techniques with optimized accelerated versions of commercially available sequences, and the studies showed sufficient image quality for diagnostic use with scan times of 2 minutes 47 seconds and 4 minutes.^{19,20}

Recently, a new 1-minute full brain, multicontrast EPI sequence (EPIMix) was introduced,²¹ which can shorten scan time and generate T1-FLAIR, T2WI, T2-FLAIR, DWI, apparent diffusion coefficient, and T2*WI sequences in 78 seconds. Only 1 study showed comparable diagnostic performance between EPIMix and routine brain MR imaging for clinical use.²² However, the EPIMix studies did not fully evaluate image quality according to individual

Received October 4, 2019; accepted after revision January 2, 2020.

From the Department of Radiology (K.H.R., H.J.B., J.I.M., B.H.C., S.E.P., J.Y.H., T.B.K.), Gyeongsang National University School of Medicine and Gyeongsang National University Changwon Hospital, Changwon, Republic of Korea; Department of Radiology (H.J.B.), Institute of Health Sciences, Gyeongsang National University School of Medicine, Jinju, Republic of Korea; Department of Clinical Neuroscience (S.S., T.S.), Karolinska Institute, Stockholm, Sweden; Department of Neuroradiology (S.S.), Karolinska University Hospital, Stockholm, Sweden; MR Applications and Workflow, GE Healthcare (M.J.H.), Seoul, Republic of Korea; and MR Applied Science Laboratory Europe (T.S.), GE Healthcare Stockholm, Sweden.

Please address correspondence to Hye Jin Baek, MD, PhD, Department of Radiology, Gyeongsang National University School of Medicine and Gyeongsang National University Changwon Hospital, 11 Samjeongja-ro, Seongsan-gu, Changwon 51472, Republic of Korea; e-mail: sartre81@gmail.com

 Indicates open access to non-subscribers at www.ajnr.org

 Indicates article with supplemental on-line table.

 Indicates article with supplemental on-line photos.

<http://dx.doi.org/10.3174/ajnr.A6427>

Acquisition parameters of EPIMix and routine protocols

Imaging Parameter	EPIMix MR Imaging					Routine Brain MR Imaging				
	T1-FLAIR	T2WI	T2-FLAIR	DWI	T2*WI	T1-FLAIR	T2WI	T2-FLAIR	DWI	SWAN
FOV (cm)	24	24	24	24	24	22	22	22	22	22
Section thickness (mm)	5	5	5	5	5	5	5	5	5	1.2
TR (ms)	1300	2447	5818	2447	2542	2400	5175	9000	5417	32.8
TI (ms)	570.2		2751			850		2465		
TE (ms)	19.3	109	115	109	30.5	25.8	119.4	102.7	73.1	22.9
ETL (ms)						5	26	32	1	3
Frequency matrix	180	180	180	180	180	360	512	288	128	288
Phase matrix	180	180	180	180	180	280	512	288	192	260
Flip angle	90°	90°	90°	90°	90°	90°	90°	90°	90°	15°
Bandwidth (kHz)	250	250	250	250	250	50	50	41.67	250	41.67
Parallel imaging acceleration factor							ARC 3	ARC 3	ASSET 2.5	ASSET 2.5
Net scan time (min:sec)	1:12					1:58	2:29	2:25	1:19	2:33
Total scan time (min:sec)	1:28					1:58	2:56	2:49	1:37	2:39

Note:—ARC indicates autocalibrating reconstruction for Cartesian imaging; ASSET, array spatial sensitivity encoding technique; ETL, echo-train length.

sequences, and they acquired images using the same MR imaging scanners at the same institution.^{21,22} Therefore, here, we evaluated the clinical feasibility of EPIMix on a different MR imaging scanner by comparing EPIMix with the routine MR imaging protocol. We hypothesized that EPIMix would be non-inferior to the routine protocol for clinical use with a 10-fold reduction in scan time to obtain the basic 5 sequences.

MATERIALS AND METHODS

Patients

We retrospectively reviewed the database of our institution and identified 146 patients who underwent diagnostic brain MR imaging examinations, including EPIMix and routine protocols with the 5 basic sequences in a single examination session from January 2019 to May 2019. The included patients were 75 men and 71 women (age range, 15–89 years; mean age, 57.2 years). MR imaging examinations were performed for headache (32/146, 21.9%), dizziness or vertigo (29/146, 19.9%), brain metastasis work-up (17/146, 11.6%), follow-up of treated intracranial aneurysm (10/146, 6.8%), weakness of the extremities (7/146, 4.8%), syncope (7/146, 4.8%), brain tumor follow-up (7/146, 4.8%), sensory change (6/146, 4.1%), altered mental status (6/146, 4.1%), parkinsonism (5/146, 3.4%), infarction follow-up (5/146, 3.4%), intracranial hemorrhage (3/146, 2.1%), dysarthria (2/146, 1.4%), and other reasons (10/146, 6.8%).

This study was approved by the institutional review board at Gyeongsang National University Changwon Hospital. The institutional review board determined that patient approval and informed consent were not required due to the retrospective nature of the study.

Imaging Acquisition

MR imaging was performed using a 3T system (Signa Architect; GE Healthcare, Milwaukee, Wisconsin) with a 48-channel head coil. Both the EPIMix and routine MR imaging protocols included 5 basic image contrasts: T1-FLAIR, T2WI, T2-FLAIR, DWI, and susceptibility-weighted angiography (SWAN)/T2*WI. At our institution, we use the ultrafast protocol for clinical purposes in specific clinical situations (such as motion-prone

patients or patients with time-critical disease), and we routinely acquire images using the 2 sets of MR imaging protocols (EPIMix and routine protocols) in such clinical cases.

EPIMix Brain MR Imaging Protocol

The EPIMix pulse sequence was acquired using a Discovery 750w 3T or an Optima 450 1.5T MR imaging system (GE Healthcare) in the original study.²¹ Compared with the initial version of EPIMix,²¹ the present version was improved by reducing the wait time before the T2-FLAIR block, and 2 EPI echoes were applied for DWI and T2-FLAIR to increase the SNR, with the same version as that used in a recent study.²² The present version of EPIMix was optimized for our MR imaging system; therefore, EPIMix was acquired using a section thickness of 5 mm, in-plane acceleration factor of R=3, and section number of 28. The EPIMix protocol is detailed in the Table. It included axial T1-FLAIR, T2WI, T2-FLAIR, DWI, and T2*WI. More detailed technical aspects of EPIMix can be found in a previous study.²¹ The net scan time was 1 minute 12 seconds, and the total scan time was 1 minute 28 seconds.

Routine Brain MR Imaging Protocol

The routine brain MR imaging protocol included 5 basic sequences of axial T1-FLAIR, T2WI, T2-FLAIR, DWI, and SWAN. Details of routine MR imaging protocols can be found in the Table. The net scan time of routine MR imaging was 10 minutes 44 seconds, and the total scan time was 11 minutes 59 seconds.

Image Analysis

All datasets were anonymized with randomization, and 2 readers, blinded to patient information, reviewed all images using a PACS. Two attending neuroradiologists with 9 and 4 years of experience, respectively, performed an independent analysis of both brain MR imaging protocols to evaluate the image quality of EPIMix from a clinical feasibility perspective. On-line Figure 1 shows a representative example of the images obtained with the 2 different MR imaging protocols. For interpretation, each reader first analyzed and assessed all EPIMix sequences. After a 4-week memory-washout period, the readers analyzed and assessed all routine MR imaging sequences. The evaluation included

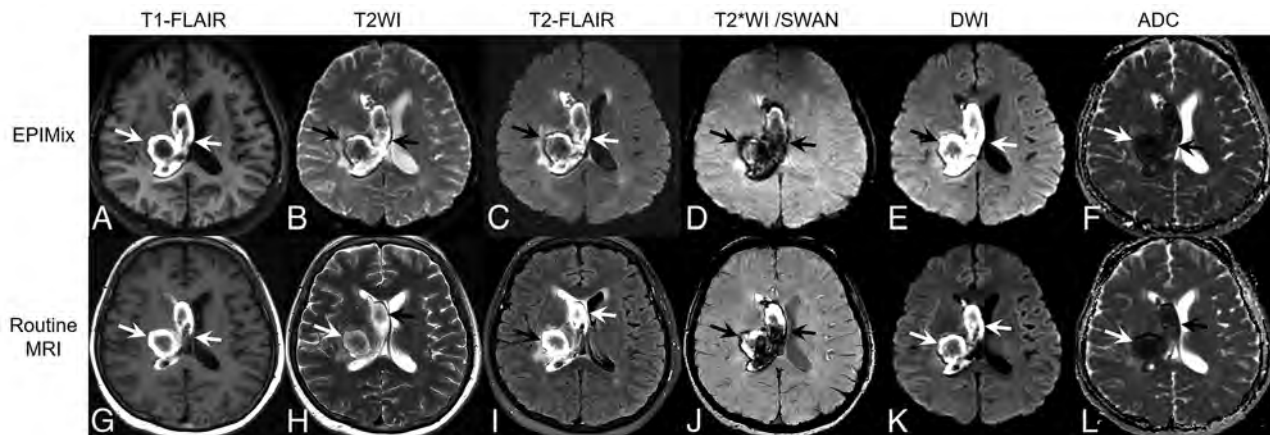


FIG 1. A 59-year-old woman with intracranial hemorrhage. A right thalamic hemorrhage with intraventricular extension to the right lateral ventricle shows mainly hyperintensity on T1-FLAIR (A and G), hyperintensity on T2WI (B and H) and T2-FLAIR (C and I), blooming artifacts on T2*WI (D) and SWAN (J), and diffusion restriction on DWI (E and K) (arrows in each sequence). These findings are well-visualized on both EPIMix MR imaging (A–F) and routine MR imaging (G–L).

assessments of overall image quality, visualization of several anatomic structures, and the severity of artifacts.

For T1-FLAIR, T2WI, and T2-FLAIR, the image quality was rated according to the following 4 criteria: 1, overall image quality; 2, differentiation of gray matter–white matter at the level of the lateral ventricles; 3, demarcation of the basal ganglia at the level of the foramen of Monro; and 4, demarcation of the sulci. For DWI and T2*WI/SWAN, the overall image quality was rated. Each criterion was graded on a Likert scale of 1–4 points:²³ 1, inadequate (not acceptable for diagnostic use); 2, sufficient (acceptable for diagnostic use but with minor issues); 3, good (acceptable for diagnostic use); and 4, excellent (acceptable for diagnostic use).

The severity of artifacts was rated for all sequences according to the following 2 criteria: 1, motion artifacts; 2, susceptibility artifacts. Each criterion was also scored on a 4-point Likert scale, in which²³ images contain the following: 1, severe artifacts (not acceptable for diagnostic use); 2, moderate artifacts (sufficient for diagnostic use but with minor issues); 3, mild artifacts (acceptable for diagnostic use because minor artifacts do not adversely affect diagnostic use); and 4, images do not contain visible artifacts (acceptable for diagnostic use). Then, the readers' ratings were simply dichotomized as follows: 1) image quality assessments, sufficient for clinical use (2 points) versus excellent for clinical use (≥ 3 points); and 2) artifact assessments, severe degree (2 points) versus lesser degree (≥ 3 points) because there was no case assigned 1 point in the image quality assessment.

Statistical Analysis

We assigned numeric values to the image quality assessments. Although we did not directly statistically compare the mean values of the readers' ratings because they did not strictly comprise continuous variables, we decided to present a summary of the readers' ratings for each MR imaging sequence, expressed as mean \pm SD. We used the Wilcoxon signed rank test to compare ordinal variables and the McNemar test to compare dichotomous variables between the 2 MR imaging protocols. We also calculated the disagreement percentage of the image quality between the proposed EPIMix protocol and the routine protocol.

Additionally, we present the interobserver agreement as the percentage agreement. We performed all statistical analyses with statistical software (SPSS, Version 24.0; IBM, Armonk, New York), and we considered *P* values $< .05$ statistically significant.

Data Availability Statement

The anonymized data of this study will be shared on request by any qualified investigator.

RESULTS

Study Population

Of 146 patients, 117 (80.1%) had abnormal MR imaging findings and 29 (19.9%) had findings that were considered normal. There were the following diagnoses: ischemic/hemorrhagic stroke or small-vessel disease (79/146, 54.1%), intracranial neoplasm (9/146, 6.2%), vascular abnormality (9/146, 6.2%), infectious or demyelinating disease (5/146, 3.4%), metabolic or degenerative disorder (4/146, 2.7%), congenital CNS malformation (1/146, 0.7%), and miscellaneous, including trauma or indeterminate condition (10/146, 6.8%).

Image Quality Assessment

The On-line Table provides the mean scores from the 2 readers, the interobserver percentage agreement of the readers' ratings, and disagreement percentages of the dichotomized mean scores for the 5 sequences of the 2 MR imaging protocols. Although the overall image quality of all sequences derived from EPIMix, except for DWI, showed a significant difference ($P < .05$) between the EPIMix and the routine protocols, the EPIMix sequence showed at least sufficient image quality, with an assessment rating of > 2 points on average (Figs 1–3 and On-line Figs 1–2). Among the 5 EPIMix sequences, T2WI had the lowest mean score in the overall image quality assessment. In contrast, the overall quality of EPIMix DWI was not significantly different from that of routine DWI ($P > .05$). EPIMix T1-FLAIR, T2WI, T2-FLAIR, and T2*WI showed significant susceptibility artifacts compared with the corresponding sequences of routine MR imaging ($P < .05$). However, fewer motion artifacts tended

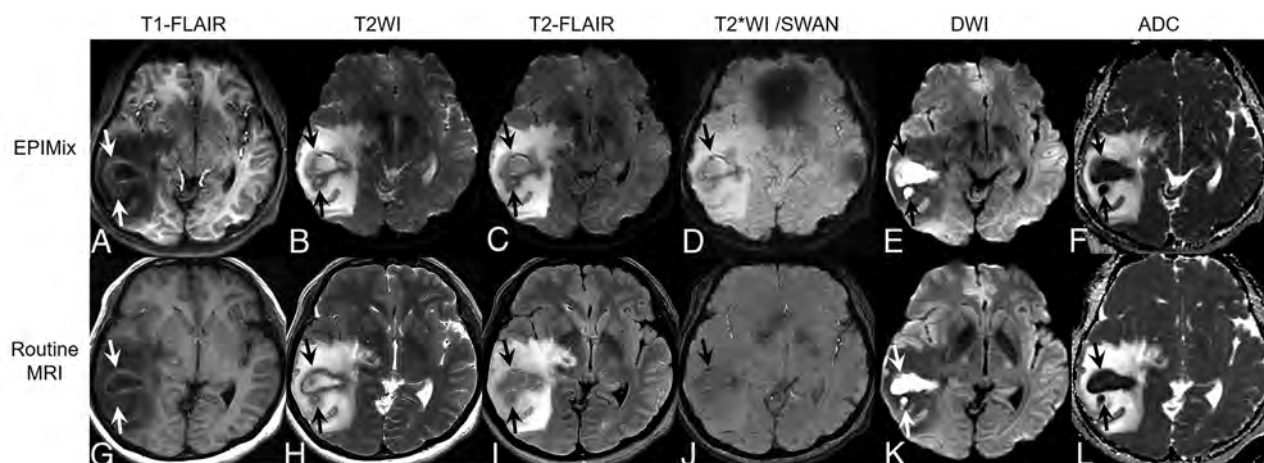


FIG 2. A 48-year-old woman with brain abscesses. There are 2 irregularly shaped masslike lesions with perilesional edema in the right temporal lobe. The internal content shows hypointensity on T1-FLAIR (A and G) and hyperintensity on T2WI (B and H) and T2-FLAIR (C and I) (arrows). The internal content shows diffusion restriction on DWI (E and K) (arrows). There are blooming artifacts on T2*WI (D) and SWAN (J) (arrows). These findings are well-visualized on both EPIMix MR imaging (A–F) and routine MR imaging (G–L).

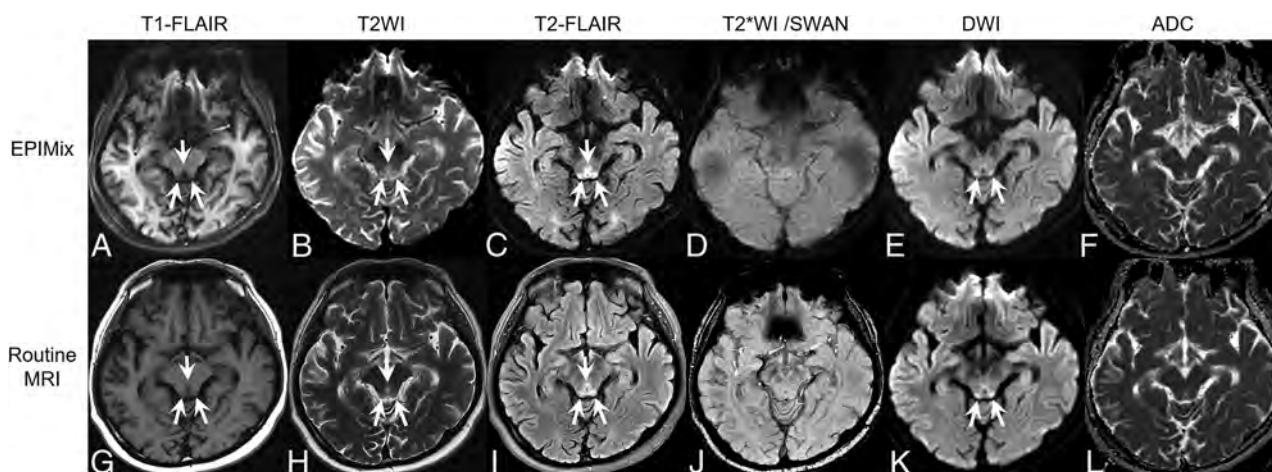


FIG 3. A 52-year-old man with Wernicke encephalopathy. Signal changes in the tectal plate of the midbrain and periaqueductal gray matter showing hypointensity on T1-FLAIR (A and G), hyperintensity on T2WI (B and H) and T2-FLAIR (C and I), and hyperintensity on DWI (E and K) are well-visualized on both EPIMix MR imaging (A–F) and routine MR imaging (G–L) (arrows in each sequence).

to be observed in the EPIMix than in the routine protocol. Additionally, there was no difficulty in detecting small lesions on EPIMix in the enrolled patients (Fig 3).

DISCUSSION

In the current study, we assessed the diagnostic image quality of the EPIMix sequence outside the institution that developed it using a different scan environment and found that the EPIMix protocol had sufficient image quality with fewer motion artifacts with a short scan time of approximately 1 minute. However, the EPIMix protocol was inferior in terms of overall image quality, with more severe susceptibility artifacts than those observed in routine brain MR imaging.

Previous clinical fast brain MR imaging protocol studies have shown comparable image quality and high diagnostic concordance with conventional MR imaging.^{19,20} However, the scan time in those studies varied, ranging from 2 to 10 minutes, being

much longer than that of the present EPIMix protocol.^{14,15,19} To date, the fastest brain MR imaging protocol reported required 1 minute 7 seconds of net scan time; however, the total scan time was 2 minutes 47 seconds due to the prescanning time before each sequence,²⁰ whereas the EPIMix protocol, including all 5 essential sequences, required only a single prescan at the start of the MR imaging examination. Moreover, the EPI readout is more SNR-efficient than the corresponding fast spin-echo readout, and the smaller matrix size can accelerate the EPIMix scan.²¹ On the basis of these advantages, the total EPIMix scan time appears to be the shortest among those of the reported ultrafast protocols.

The EPIMix protocol uses different magnetization preparations combined with 1 of 2 sets of EPI readout trains to directly acquire the weighted contrast in a short scan time of 1 minute.²¹ It also uses a dynamic combination of 11 sequence modules with a unique role in the acquisition to generate a specific image contrast, and 2 EPI readout modules are reused throughout the sequence and are prepended by other modules to form the

desired MR contrasts.²¹ This new 1-minute EPIMix protocol showed diagnostic performance comparable with that of routine brain MR imaging in terms of disease identification and categorization in a previous clinical study;²² however, the authors did not analyze image quality and characteristics on the basis of individual sequences derived from EPIMix.²² From the perspective of feasibility, analyses of the image quality and characteristics of each image sequence are essential to apply EPIMix to clinical use to cover a wide range of patient groups because important image sequences for diagnosis differ depending on pathology. Therefore, we performed image quality analysis for individual image sequences to evaluate the clinical feasibility of EPIMix in various brain pathologies compared with the routine brain MR imaging protocol.

In this study, EPIMix T1-FLAIR showed excellent anatomic delineation, including differentiation of gray matter–white matter, comparable with that of the routine sequence. However, geometric distortion, especially in the skull base and frontal lobe, downgraded the overall image quality of EPIMix T1-FLAIR. Although a higher acceleration factor reduces geometric distortion and T2* blurring on images with increasingly effective image sharpness, the susceptibility artifacts of EPIMix could not be completely overcome and there remained some g-factor-related SNR loss.²¹ Additionally, EPIMix T2-FLAIR showed good overall image quality with good-to-excellent anatomic delineation. Our findings are consistent with those of previous studies that showed image quality and diagnostic performance comparable with that of conventional T2-FLAIR in patients with acute stroke,²⁴ and the contrast-to-noise ratio of EPI-FLAIR was also comparable with that of conventional FLAIR.²⁵ However, EPI T2-FLAIR may be particularly useful in only limited clinical situations in the acute setting because it involves inherently unavoidable susceptibility artifacts. On EPIMix T2WI, the overall image quality and anatomic delineation were far inferior to those of the other EPIMix sequences because T2WI is basically a $b=0$ image. Therefore, it is essential to improve the image quality of T2WI to broaden the clinical use of EPIMix. Furthermore, EPIMix has a well-known limitation of unavoidable geometric distortion and susceptibility artifacts in all sequences, especially in the skull base, frontal lobe, posterior fossa, and brain stem. These artifacts may limit diagnostic performance in these regions and render EPIMix unsuitable for patients undergoing stereotactic surgery or radiation therapy and for postoperative follow-up imaging.²¹

Despite these shortcomings, EPIMix can generate all 5 essential sequences in 1 minute with minimal bore time for the patients. Therefore, the shorter scan time allows EPIMix to be used as a motion-resistant MR imaging protocol in certain clinical situations such as for use with patients prone to motion, pediatric or pregnant patients, or patients with claustrophobia or pain, by decreasing patient anxiety and reducing the need for sedation. It also has superior soft-tissue contrast compared with CT without generating radiation during the examination, and EPIMix DWI has excellent image quality, comparable with that of routine DWI. Therefore, EPIMix can be a useful option in patients with time-critical diseases.

Furthermore, if EPIMix is run at the beginning of an examination, it may also help in the planning of detailed conventional brain MR imaging sequences.

This study has several limitations. First, it was retrospective and may have, therefore, involved unavoidable selection bias. Second, we did not perform quantitative analysis such as of the contrast-to-noise ratio or SNR because the shorter scan time inevitably leads to degraded overall image quality as also reported by previous studies.^{15,19,20} Although the image quality analysis is limited by the reader's subjective judgment, the readers could intuitively perceive the effect of the contrast-to-noise ratio and SNR in the 2 brain MR imaging protocols during the image quality analysis. Third, we could not randomize the acquisition order of EPIMix and routine MR imaging because of the retrospective study design. Fourth, we did not perform a direct comparison between the EPIMix protocol and brain CT in this study. Further comparative studies with head CT would be helpful to confirm the clinical utility of our EPIMix protocol as a proper CT substitute. However, further studies need to be carefully designed because CT involves radiation exposure. Fifth, interobserver agreement between the 2 readers was provided as a percentage agreement because κ statistics provided a paradoxically low value due to an imbalance in the number of concordant and discordant pairs.^{26,27} Last, EPIMix is a noncommercialized sequence under technical development. It is, therefore, challenging to immediately apply it on different MR imaging scanners from multiple vendors.

CONCLUSIONS

The overall EPIMix image quality was sufficient for diagnostic use with fewer motion artifacts. However, EPIMix is limited by its inherent geometric distortion, being particularly problematic in the skull base near the tissue-air boundaries, and has lower resolution compared with fast spin-echo-based series in a routine protocol. Therefore, it cannot completely replace the routine MR imaging protocol at this time; however, it may be a feasible option in specific clinical situations such as screening, time-critical disease, or patients prone to motion. After further development of the improved EPIMix version, future studies with a larger sample size will help expand the clinical indications of EPIMix and validate our results.

Disclosures: Tim Sprenger—UNRELATED: Employment: GE Healthcare, Comments: Tim Sprenger is one of the joint developers of the multicontrast EPI sequences with Professor Skare, and they provided the multicontrast EPI research pulse sequence for this study. However, GE Healthcare had no role in the design of the study, data analyses, or data interpretation.

REFERENCES

1. Heidemann RM, Ozsarlak O, Parizel PM, et al. **A brief review of parallel magnetic resonance imaging.** *Eur Radiol* 2003;13:2323–37 CrossRef Medline
2. Deshmane A, Gulani V, Griswold MA, et al. **Parallel MR imaging.** *J Magn Reson Imaging* 2012;36:55–72 CrossRef Medline
3. Barth M, Breuer F, Koopmans PJ, et al. **Simultaneous multislice (SMS) imaging techniques.** *Magn Reson Med* 2016;75:63–81 CrossRef Medline
4. Warntjes JB, Leinhard OD, West J, et al. **Rapid magnetic resonance quantification on the brain: Optimization for clinical usage.** *Magn Reson Med* 2008;60:320–29 CrossRef Medline
5. Gulani V, Schmitt P, Griswold MA, et al. **Towards a single-sequence neurologic magnetic resonance imaging examination: multiple-**

- contrast images from an IR TrueFISP experiment. *Invest Radiol* 2004;39:767–74 CrossRef Medline
6. Hagiwara A, Warntjes M, Hori M, et al. **SyMRI of the brain: rapid quantification of relaxation rates and proton density, with synthetic MRI, automatic brain segmentation, and myelin measurement.** *Invest Radiol* 2017;52:647–57 CrossRef Medline
 7. Ashley WW Jr, McKinstry RC, Leonard JR, et al. **Use of rapid-sequence magnetic resonance imaging for evaluation of hydrocephalus in children.** *J Neurosurg* 2005;103:124–30 CrossRef Medline
 8. Niederhauser BD, McDonald RJ, Eckel LJ, et al. **Retrospective review of rapid pediatric brain MR imaging at an academic institution including practice trends and factors affecting scan times.** *AJNR Am J Neuroradiol* 2013;34:1836–40 CrossRef Medline
 9. Ryan ME, Jaju A, Ciolino JD, et al. **Rapid MRI evaluation of acute intracranial hemorrhage in pediatric head trauma.** *Neuroradiology* 2016;58:793–99 CrossRef Medline
 10. Wagner MW, Kontzialis M, Seeburg D, et al. **Acute brain imaging in children: can MRI replace CT as a screening tool?** *J Neuroimaging* 2016;26:68–74 CrossRef Medline
 11. Kralik SF, Yasrebi M, Supakul N, et al. **Diagnostic performance of ultrafast brain MRI for evaluation of abusive head trauma.** *AJNR Am J Neuroradiol* 2017;38:807–13 CrossRef Medline
 12. Missios S, Quebada PB, Forero JA, et al. **Quick-brain magnetic resonance imaging for nonhydrocephalus indications.** *J Neurosurg Pediatr* 2008;2:438–44 CrossRef Medline
 13. Penzkofer AK, Pfluger T, Pochmann Y, et al. **MR imaging of the brain in pediatric patients: diagnostic value of HASTE sequences.** *AJR Am J Roentgenol* 2002;179:509–14 CrossRef Medline
 14. U-King-Im JM, Trivedi RA, Graves MJ, et al. **Utility of an ultrafast magnetic resonance imaging protocol in recent and semi-recent strokes.** *J Neurol Neurosurg Psychiatry* 2005;76:1002–05 CrossRef Medline
 15. Nael K, Khan R, Choudhary G, et al. **Six-minute magnetic resonance imaging protocol for evaluation of acute ischemic stroke: pushing the boundaries.** *Stroke* 2014;45:1985–91 CrossRef Medline
 16. Tanenbaum LN, Tsiouris AJ, Johnson AN, et al. **Synthetic MRI for clinical neuroimaging: results of the Magnetic Resonance Image Compilation (MAGiC) prospective, multicenter, multireader trial.** *AJNR Am J Neuroradiol* 2017;38:1103–10 CrossRef Medline
 17. Ryu KH, Baek HJ, Moon JI, et al. **Initial clinical experience of synthetic MRI as a routine neuroimaging protocol in daily practice: a single-center study.** *J Neuroradiol* 2019 Apr 2. [Epub ahead of print] CrossRef Medline
 18. Vargas MI, Boto J, Delatre BM. **Synthetic MR imaging sequence in daily clinical practice.** *AJNR Am J Neuroradiol* 2016;37:E68–E69 CrossRef Medline
 19. Prakkamakul S, Witzel T, Huang S, et al. **Ultrafast brain MRI: clinical deployment and comparison to conventional brain MRI at 3T.** *J Neuroimaging* 2016;26:503–10 CrossRef Medline
 20. Ryu KH, Choi DS, Baek HJ, et al. **Clinical feasibility of 1-min ultrafast brain MRI compared with routine brain MRI using synthetic MRI: a single center pilot study.** *J Neurol* 2019;266:431–39 CrossRef Medline
 21. Skare S, Sprenger T, Norbeck O, et al. **A 1-minute full brain MR exam using a multicontrast EPI sequence.** *Magn Reson Med* 2018;79:3045–54 CrossRef Medline
 22. Delgado AF, Kits A, Bystam J, et al. **Diagnostic performance of a new multicontrast one-minute full brain exam (EPIMix) in neuro-radiology: a prospective study.** *J Magn Reson Imaging* 2019;50:1824–33 CrossRef Medline
 23. Likert R. **A technique for the measurement of attitudes.** *Archives of Psychology* 1932;22:1–55 <https://psycnet.apa.org/record/1933-01885-001>. Accessed July 28, 2019
 24. Meshksar A, Villablanca JP, Khan R, et al. **Role of EPI-FLAIR in patients with acute stroke: a comparative analysis with FLAIR.** *AJNR Am J Neuroradiol* 2014;35:878–83 CrossRef Medline
 25. Korogi Y, Sugahara T, Shigematsu Y, et al. **Ultrafast FLAIR imaging with single-shot echo-planar technique in evaluation of intracranial lesions.** *Comput Med Imaging Graph* 1999;23:119–26 CrossRef Medline
 26. Viera AJ, Garrett JM. **Understanding interobserver agreement: the kappa statistic.** *Fam Med* 2005;37:360–63 Medline
 27. Feinstein AR, Cicchetti DV. **High agreement but low kappa, I: the problems of two paradoxes.** *J Clin Epidemiol* 1990;43:543–49 CrossRef Medline

High Intravascular Signal Arterial Transit Time Artifacts Have Negligible Effects on Cerebral Blood Flow and Cerebrovascular Reserve Capacity Measurement Using Single Postlabel Delay Arterial Spin-Labeling in Patients with Moyamoya Disease

M. Fahlström, A. Lewén, P. Enblad, E.-M. Larsson, and J. Wikström



ABSTRACT

BACKGROUND AND PURPOSE: Arterial spin-labeling-derived CBF values may be affected by arterial transit time artefacts. Thus, our aim was to assess to what extent arterial spin-labeling-derived CBF and cerebrovascular reserve capacity values in major vascular regions are overestimated due to the arterial transit time artifacts in patients with Moyamoya disease.

MATERIALS AND METHODS: Eight patients with Moyamoya disease were included before or after revascularization surgery. CBF maps were acquired using a 3D pseudocontinuous arterial spin-labeling sequence, before and 5, 15, and 25 minutes after an IV acetazolamide injection and were registered to each patient's 3D-T1-weighted images. Vascular regions were defined by spatial normalization to a Montreal Neurological Institute-based vascular regional template. The arterial transit time artifacts were defined as voxels with high signal intensity corresponding to the right tail of the histogram for a given vascular region, with the cutoff selected by visual inspection. Arterial transit time artifact maps were created and applied as masks to exclude arterial transit time artifacts on CBF maps, to create corrected CBF maps. The cerebrovascular reserve capacity was calculated as CBF after acetazolamide injection relative to CBF at baseline for corrected and uncorrected CBF values, respectively.

RESULTS: A total of 16 examinations were analyzed. Arterial transit time artifacts were present mostly in the MCA, whereas the posterior cerebral artery was generally unaffected. The largest differences between corrected and uncorrected CBF and cerebrovascular reserve capacity values, reported as patient group average ratio and percentage point difference, respectively, were 0.978 (95% CI, 0.968–0.988) and 1.8 percentage points (95% CI, 0.3–3.2 percentage points). Both were found in the left MCA, 15 and 5 minutes post-acetazolamide injection, respectively.

CONCLUSIONS: Arterial transit time artifacts have negligible overestimation effects on calculated vascular region-based CBF and cerebrovascular reserve capacity values derived from single-delay 3D pseudocontinuous arterial spin-labeling.

ABBREVIATIONS: ACA = anterior cerebral artery; ACZ = acetazolamide; ASL = arterial spin-labeling; ATT = arterial transit time; ATT_{over} = long arterial transit time where CBF is overestimated; ATT_{under} = very long arterial transit time where CBF is underestimated; CVRC = cerebrovascular reserve capacity; Diff = absolute difference; MMD = Moyamoya disease; PCA = posterior cerebral artery; pCASL = pseudocontinuous arterial spin-labeling; PLD = postlabeling delay; pp = percentage points

Moyamoya disease (MMD) is characterized by stenosis or occlusion at the terminal portions of the ICA, the proximal anterior cerebral arteries (ACAs), or the MCA. Common for

patients with MMD is the presence of abnormal vascular networks in the arterial territories close to the stenotic or occlusive lesion.¹⁻³ Most patients can maintain adequate CBF through compensatory collateral flow, while others experience cerebral ischemia and hemorrhage.^{1,4} The capability of the brain to increase CBF in response to a vasodilatory challenge can be assessed using cerebrovascular reserve capacity (CVRC) estimates, calculated as the maximal percentage increase in CBF after vasodilatory stimulus (commonly IV acetazolamide [ACZ], referred to as the ACZ challenge) relative to baseline.⁴ CVRC can predict the risk of ischemic events in patients with MMD; moreover, CVRC can also provide information on indications for or assessment after cerebral revascularization surgery.^{4,5}

Received September 29, 2019; accepted after revision December 24.

From the Departments of Surgical Sciences (M.F., E.-M.L., J.W.) and Neuroscience (A.L., P.E.), Uppsala University, Uppsala, Sweden.

Please address correspondence to Markus Fahlström, MSc, Department of Surgical Sciences, Uppsala University, Akademiska Sjukhuset, SE 751 85 Uppsala, Sweden; e-mail: Markus.Fahlstrom@radiol.uu.se



Indicates article with supplemental on-line tables.



Indicates article with supplemental on-line photos.

<http://dx.doi.org/10.3174/ajnr.A6411>

Arterial spin-labeling (ASL) is a completely noninvasive and highly repeatable perfusion imaging technique that has demonstrated potential in numerous cerebral disorders.^{3,6,7} With ASL, quantification of CBF is possible using the patient's own blood as a freely diffusible tracer. One inherent limitation with single-delay pseudocontinuous ASL (pCASL) is the dependency on an arterial transit time (ATT; ie, the time for labeled blood to flow from the labeling plane to the tissue of interest), in which arterial transit time should not exceed the user-defined parameter, postlabeling delay (PLD). This limitation is known as the ATT artifact and have 2 different effects on the derived CBF maps, depending on to what extent the blood flow is delayed (ie, the length of the ATT). First, at a very long ATT, in which no blood has reached the imaging volume in time for the readout, derived CBF will be inherently low and underestimated (denoted "ATT_{under}"). Second, the ATT artifacts will appear as bright intravascular signal when the blood has reached the imaging volume but not the capillary bed—that is, it is found in precapillary arterioles, presenting as hyperintense areas in the derived CBF maps, thus overestimating CBF (denoted "ATT_{over}").^{2,7-11} However, the ATT_{over} artifacts have been shown to provide important information about the presence and extent of collateral flow by visual grading in patients with MMD when long ATTs are present through collateral pathways.^{2,3,9} No effort has been made to quantitatively define ATT_{over} artifacts, and their impact on CBF and CVRC calculations in major vascular regions, thus, testing the hypothesis that ATT_{over} has negligible effects on large ROIs.⁸

The aim of this study was to assess to what extent vascular region-based CBF and CVRC are affected by the ATT_{over} artifacts defined by means of histogram analysis.

MATERIALS AND METHODS

Patients

Eight patients with confirmed MMD were included before or after revascularization surgery. This study was performed in accordance with the Declaration of Helsinki and was approved by the local ethics committee. Patients were examined by MR imaging for pre- or postoperative assessment: monitoring the progression of the disease as a decision basis for an operation or postoperative follow-up assessing the surgical outcome, compared with preoperative assessment if available, both performed on a yearly basis or close to the scheduled operation. All patients received an intravenous injection with 1 g or 10 mg/kg of ACZ for adults and children, respectively.

MR Imaging Acquisition

All examinations were performed on an Achieva 3T scanner (Philips Healthcare, Best, the Netherlands) using a 32-channel head coil. High-resolution 3D T1-weighted and 3D T2-weighted FLAIR images were acquired as structural images. A commercially available 3D-pCASL sequence with a gradient and spin-echo readout module was used for acquiring CBF maps with a PLD of 2500 ms. The full set of acquisition parameters for all MR imaging sequences is presented in On-line Table 1. ASL-derived CBF maps were automatically calculated by the scanner according to the model defined by Buxton et al¹² and recommended by Alsop et al.⁸ The standard ACZ challenge protocol included a total of

4 3D-pCASL acquisitions, performed before and 5, 15, and 25 minutes after the ACZ injection. Two examinations deviated from the above-described study protocol. For the first examination (the pilot), a work-in-progress 3D-pCASL sequence with a PLD of 2000 ms was performed before and 5, 10, and 15 minutes after ACZ injection. For the other examination, a work-in-progress 3D-pCASL sequence with a PLD of 2500 ms was performed with the standard ACZ challenge protocol described above. Because only 2 examinations at 10 minutes post-ACZ injections were performed, they were excluded from the statistical analysis.

Vascular Regions and Image Postprocessing

T2-weighted FLAIR images and CBF maps were coregistered to each subject's corresponding T1-weighted images. Gray matter probability maps were segmented from T1-weighted images and coregistered T2-weighted FLAIR images.¹³ Gray matter maps were defined with a partial volume fraction above 75%. A deformation field, defining the transformation from Montreal Neurological Institute template space to subject-specific space for each subject, was derived on the basis of the subject's T1-weighted image and was applied to a standard vascular territory template,^{14,15} including the bilateral ACA, MCA, and posterior cerebral artery (PCA). Each subject-specific vascular territory was masked with the corresponding gray matter map to correct for partial volume effects.¹⁶⁻¹⁸ All processing steps, as described above, were performed using the SPM12 toolbox (<http://www.fil.ion.ucl.ac.uk/spm/software/spm12>).

Arterial Transit Time Artifact Correction

Arterial transit time artifacts (ATT_{over} artifacts) were defined as hyperintense spots and serpiginous regions in the right tail of the corresponding histogram of all vascular territory regions and for all CBF maps, respectively (Figs 1 and 2). The right tail segment corresponding to the ATT_{over} artifacts was selected, including histogram bins from right to left, thus always including the highest CBF values. The cutoff value was selected by visual inspection so that only voxels within the hyperintense spots were included, thus creating binary ATT_{over} maps. Furthermore, for each vascular region, ATT_{over} artifact volume and ATT_{over} artifact ratio (defined as ATT_{over} volume divided by total vascular region volume) were calculated.

CBF and CVRC Calculation

All uncorrected CBF maps were smoothed using a 5-mm Gaussian filter. Corrected CBF maps were created by masking uncorrected, smoothed CBF maps with corresponding ATT_{over} maps, thus excluding voxels defined as ATT_{over} artifacts from the statistical analysis. Corrected and uncorrected CBF values were extracted using previously defined vascular regions, respectively. CVRC values were calculated on the basis of regional CBF, using equation 1 for all post-ACZ-acquired corrected and uncorrected CBF maps, respectively, with corresponding CBF^{0 minute} defining baseline. Furthermore, the absolute difference (Diff) in percentage points between the corrected and uncorrected CVRC was calculated. Super- and subscript will be used to clarify ratios and to distinguish between baseline (0 min) and post-ACZ injection (5 min and so forth), eg, CBF_{Ratio}^{5 min} or CVRC_{Diff}^{5 min} when applicable.

$$1) \quad CVRC = (CBF^{post-ACZ} - CBF^{0 \text{ minute}}) / (CBF^{0 \text{ minute}})$$

Statistical Analysis

For descriptive analysis of ATT_{over} volume and ATT_{over} ratio, mean, maximum value, and 95% CI were calculated. Further-

more, CBF and CVRC comparisons were performed by descriptive analysis of the corrected-to-uncorrected ratio (CBF) or the absolute difference in percentage points (CVRC); thus, the average ratio/difference with 95% CI and maximum/minimum were calculated and analyzed. Descriptive analysis was performed for all vascular regions and baseline and 5, 15, and 25 minutes post-ACZ injection, respectively. A correlation analysis was performed comparing the CBF_{Ratio} with ATT volume using the Pearson correlation coefficient. This was performed using all time point values as 1 large dataset. Derived *P* values are presented as exact values and are 2-sided, and *P* < .05 is considered significant. GraphPad Prism 8 for Mac (GraphPad Software, San Diego, California) was used for statistical analysis and graph design.

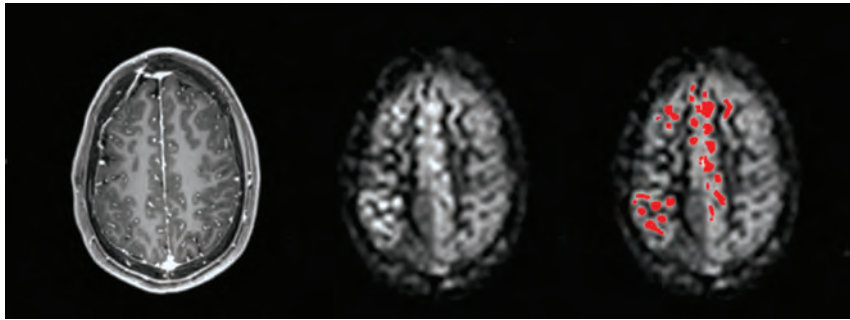


FIG 1. A 3D T1-weighted image with derived CBF maps with and without binary ATT_{over} voxels (red).

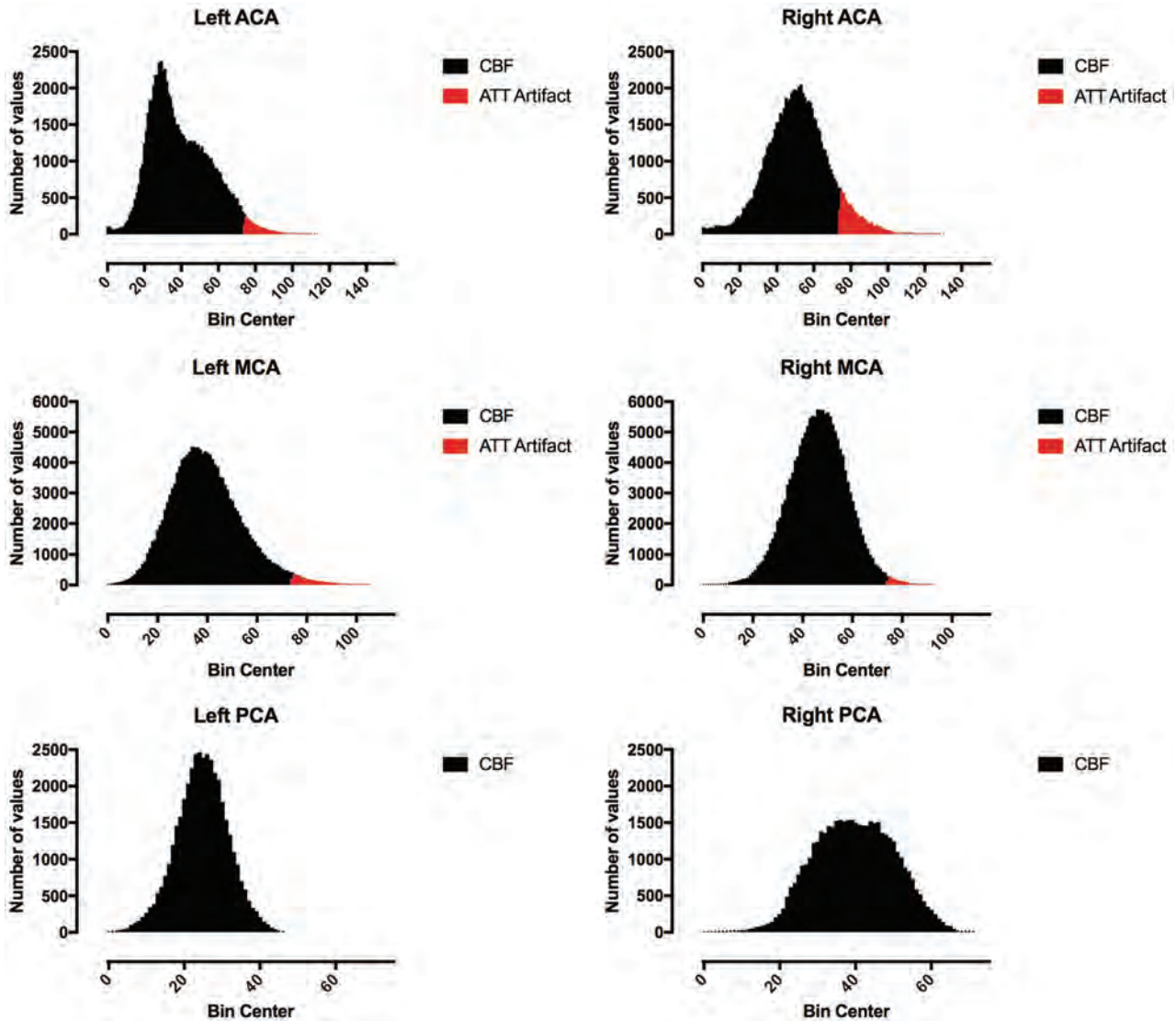


FIG 2. Derived histograms and defined ATT_{over} voxels from the CBF maps presented in Fig 1.

Table 1: Average of derived ratios, minimum/maximum, and 95% CI for CBF_{Ratio}

CBF _{Ratio}	ACA		MCA		PCA	
	Left	Right	Left	Right	Left	Right
Baseline						
Mean	0.989	0.986	0.979	0.980	0.995	0.996
95% CI	0.981–0.995	0.978–0.994	0.971–0.988	0.972–0.987	0.990–1.000	0.992–1.001
Min-max	0.949–1.000	0.942–1.000	0.954–1.000	0.958–0.999	0.961–1.000	0.970–1.000
5 minutes						
Mean	0.991	0.987	0.981	0.978	0.992	0.992
95% CI	0.986–0.991	0.980–0.995	0.975–0.988	0.970–0.986	0.985–0.999	0.985–0.999
Min-max	0.975–0.999	0.955–0.998	0.961–0.998	0.950–0.998	0.956–1.000	0.952–1.000
15 minutes						
Mean	0.990	0.987	0.981	0.979	0.995	0.996
95% CI	0.983–0.997	0.980–0.993	0.973–0.988	0.970–0.987	0.992–0.998	0.993–0.999
Min-max	0.948–0.999	0.957–0.999	0.937–0.998	0.942–0.997	0.980–1.000	0.982–1.000
25 minutes						
Mean	0.989	0.985	0.980	0.978	0.995	0.997
95% CI	0.981–0.998	0.977–0.993	0.970–0.990	0.968–0.988	0.991–0.999	0.994–1.000
Min-max	0.943–1.000	0.960–1.000	0.938–0.996	0.944–0.997	0.976–1.000	0.982–1.000

Note:—Min-max indicates minimum-maximum.

Table 2: Average of derived differences, maximum, and 95% CI for CVRC_{Diff}

CVRC _{Diff} (pp)	ACA		MCA		PCA	
	Left	Right	Left	Right	Left	Right
5 minutes						
Mean	0.7	1.1	1.8	1.7	0.8	1.5
95% CI	0.3–1.0	0.4–1.7	0.3–3.2	0.9–2.6	0.1–1.6	–0.5–3.1
Maximum	2.2	4.2	11.3	5.9	5.2	7.8
15 minutes						
Mean	0.8	1.1	0.9	1.5	0.9	0.8
95% CI	0.3–1.2	0.4–1.7	0.4–1.5	0.6–2.3	–0.2–1.9	–0.2–1.9
Maximum	3.5	4.5	3.1	5.4	6.7	6.8
25 minutes						
Mean	1.0	1.3	1.7	1.5	0.3	0.4
95% CI	0.4–1.7	0.4–2.2	0.5–2.9	0.7–2.3	0.0–0.5	–0.2–1.1
Maximum	4.1	5.5	5.8	4	0.9	3.3

RESULTS

Patients

A total of 16 examinations were performed, which included 9 preoperative and 7 postoperative examinations. Two patients had both pre- and postoperative examinations.

ATT_{over} Volume

A representative example of ATT_{over} artifact definition can be seen in Figs 1 and 2. For all examinations, arranged by post-ACZ injection time points, descriptive statistics for bilateral ACA, MCA, and PCA are presented in On-line Table 2 and On-line Fig 1. The largest ATT_{over} artifact volume was 30.9 cm³ (left MCA at 25 minutes post-ACZ injection). Generally, ATT_{over} artifacts were mostly present in the MCA, while the PCA was mostly unaffected; furthermore, the volumes typically increased from baseline compared with post-ACZ injection.

Comparison of CBF Values

The average CBF_{Ratio} was generally close to 1.0, with a narrow 95% CI, considering all major vascular regions including ACZ challenges, thus suggesting minor differences between corrected and uncorrected CBF. The smallest calculated CBF_{Ratio} was 0.937 (corrected CBF, 51.16 mL/100 g/min, and uncorrected, 54.61 mL/100 g/min in the left MCA at 15 minutes post-ACZ

injection)—that is, the largest difference found between any corrected and uncorrected CBF values was 6.3% (Table 1 and On-line Fig 2). The correlation between the CBF_{Ratio} and ATT volume was negative and strong ($r = -0.85$, $P < .001$, On-line Fig 3).

Comparison of CVRC Values

For all major vascular regions, including ACZ challenges, the calculated average CVRC_{Diff} was small, with a narrow 95% CI (highest CVRC_{Diff} average, 1.8 percentage points [pp]; 95% CI, 0.3–3.2 pp; On-line Fig 4). The

maximum CVRC_{Diff} was 11.3 pp (the corrected CVRC was 46.2% and the uncorrected CVRC was 34.9% in the left MCA at 5 minutes post-ACZ injection, Table 2).

DISCUSSION

This study assessed the extent of the ATT_{over} artifacts, presenting as hyperintense spots on single-delay ASL acquisitions during ACZ challenges in patients with MMD, and the effect of the ATT_{over} artifacts on CBF and CVRC values in major vascular territories. Major findings included the following: In major vascular territories, the ATT_{over} artifacts have negligible effects on derived CBF and CVRC values.

The anterior circulation is predominantly affected in patients with MMD;^{1,4,9} furthermore, no patient in our study had any occlusion affecting the PCA. This finding agrees with the derived distribution of average ATT_{over} volume in the bilateral major vascular territories used in this study.

Comparing corrected and uncorrected CBF values, we found small, negligible differences. Alsop et al⁸ suggested that CBF measurements may still be valid in large ROIs in the presence of ATT_{over} if flow-crushing gradients are not used. The results of this study prove this hypothesis valid for major vascular regions in patients with MMD. Furthermore, because CVRC is an

imperative prognostic factor for assessing and evaluating patients with MMD pre- and postsurgery,^{4,5} assessing how CVRC is affected by the ATT_{over} artifacts is of great importance. We found generally small, negligible percentage point differences between corrected and uncorrected CVRC. The maximum difference was 11.3 pp (corrected CVRC, 46.2%; and uncorrected CVRC, 34.9%). In this case, the difference was found at 5 minutes post-ACZ injection, a time point not commonly used during ACZ challenges and CVRC calculation.^{4,19-24} We also assessed possible correlations between CBF_{Ratio} and ATT_{over} volume and found a strong, significant negative correlation ($r = -0.85, P < .001$). This is expected; as we exclude more pixel values with increasing ATT_{over} volume, the effect on average corrected mean CBF would inherently be larger. However, we do not consider this relationship to be a potential bias.

In a quantitative regional analysis comparing multidelay pulsed ASL with DSC MR imaging, Martin et al²⁵ found a moderate correlation for normalized CBF, which increased slightly after exclusion of ATT_{over} in the MCA region. It is inherently difficult to compare these results with ours because important inconsistencies between the studies exist. The study by Martin et al was primarily designed to compare a multidelay pulsed ASL with DSC MR imaging in patients with unilateral atherosclerotic stenocclusive disease. CBF was normalized to contralateral vascular regions not affected by occlusion, and pulsed ASL has a lower achievable SNR compared with pCASL. Multidelay ASL has been proposed as an imaging technique for patients with MMD, due to mainly 1 advantage: less vulnerability to ATT artifacts. On the other hand, single-delay ASL has signal-to-noise and scan time advantages over multidelay ASL,²⁶ and the results presented here should be considered favorable for single-delay ASL.

We acquired CBF measurements 5, 15, and 25 minutes post-ACZ injection. While the ATT_{over} volume increased post-ACZ injection, there were no pronounced effects on either CBF or CVRC. The increase in ATT_{over} volume is expected, considering the reported increase in MTT derived from perfusion CT post-ACZ injection, especially in regions supplied by occluded vessels.^{4,27} However, Federau et al²¹ showed that ATT estimates based on multidelay ASL-acquired data decreased after injection of ACZ.

The current reference standard for CBF measurements (and thus CVRC) is ^{15}O -water PET.^{9,24} ^{15}O -water PET requires, however, an on-site cyclotron, and the availability is limited.⁹ SPECT is more readily available and is frequently used for MMD evaluation, but with limitations such as poor spatial resolution.^{24,28} In addition, both PET and SPECT imaging are invasive and expose the patient to ionizing radiation.^{2,5,9,23,29} Consequently, assessing the correlation between ASL-derived CBF and CBF derived from PET and SPECT is important, and this has been studied extensively. High correlations have been reported between SPECT (^{123}I -iodoamphetamine and $^{99\text{m}}\text{Tc}$ -hexamethylpropyleneamine oxime) and ASL (different sequences, PLDs, and field strengths).^{5,23,24,30} The dependency of the PLD as a parameter affecting correlation with ^{15}O -water PET has been highlighted by others. Hara et al²⁹ concluded that ASL acquired with a short PLD (1525 ms) showed better correlation with ^{15}O -gas PET in normally perfused areas compared with a long PLD (2525 ms) in patients with MMD. However, in

symptomatic areas, where arterial transit is delayed, correlation increased for a long PLD and was then higher than a short PLD. The importance of the PLD was furthermore highlighted in a study by Inoue et al,⁶ presenting different CVRC values in healthy volunteers depending on the PLD. In a comparative study using simultaneously acquired ASL and ^{15}O -water PET, Fan et al⁹ concluded that long PLDs (4000 ms, compared with our PLD of 2500 ms) are needed to achieve good correlations between relative CBF measurements in patients with MMD.

Another limitation addressed by the authors is the lack of acquired arterial blood samples to enable absolute CBF from kinetic modeling of the PET data. Arterial blood samples were not collected, as stated by the authors, to minimize patient discomfort. Goetti et al³¹ also reported good correlations in children and young adults with MMD between ASL and ^{15}O -water PET; however, data were not acquired simultaneously, with a short PLD of 1500 ms and after normalization to cerebellar CBF-values. Again, no arterial blood samples were collected. This feature is an important limitation with ^{15}O -water PET; quantitative studies require an arterial input function most reliably acquired through continuous arterial sampling.^{32,33} Arterial sampling may not be feasible in patients in poor condition and is not feasible in children with MMD.³³ However, several noninvasive methods can estimate relative CBF in the absence of existing arterial blood sampling.^{33,34} ASL is, by definition, fully noninvasive, with no radiation exposure and greater availability than cyclotron-dependent ^{15}O -water PET. As concluded by other authors, ASL-derived CBF/CVRC has potential in pre-/postoperative assessment in patients with MMD.^{3,5,6,9,24-26,29,31,35-37}

Limitations

In the histogram analysis, the right tail cutoff value defining the ATT_{over} artifacts was selected by visual inspection. A manual approach with only 1 reader is generally considered a limitation due to the dependency on the reader's ability to achieve high specificity. However, the histogram analysis method appeared robust, and the highest CBF values were always included because the selection of the ATT_{over} segment of the histogram was performed from right to left; thus, we do not consider this to confound our results.

Another drawback of our study was that we did not have a sufficient imaging slab to cover the whole brain, including the cerebellum, which has been used for normalization in several publications.^{2,24,29,31} However, cerebellar normalization is not commonly performed, and CVRC is, by definition, a ratio; thus, we do not expect this to affect our results.

Two ACZ challenges were performed with a work-in-progress 3D-pCASL sequence with PLDs of 2000 and 2500 ms, respectively. These examinations were not excluded from this study and were not different from the others in regard to the derived CBF_{Ratio} and $CVRC_{\text{Diff}}$.

In the present study, no effort was made to assess whether the presence of ATT_{under} artifacts would affect our results. Given the theory of ATT artifacts as outlined in the introduction, the presence of ATT_{over} artifacts could indicate that possible surrounding regional hypoperfusion can be a consequence of ATT_{under} artifacts. Still, we are analyzing ratio-based data, and given that both corrected and uncorrected CBF maps would have the same extent

for the ATT_{under} artifacts, we consider this to have a minor impact on our results and conclusions. Moreover, the use of a long PLD in this study will reduce the ATT_{under} artifacts as reported by Hara et al.²⁹

Partial volume effects are caused by the limited spatial resolution in ASL and tend to result in under- and overestimation of CBF in the GM and WM, respectively.^{17,38} We used a simple partial volume correction method, masking all vascular regions with a GM mask. Furthermore, to reduce any registration errors between pre- and post-ACZ ASL acquisitions, we applied a Gaussian filter of 5 mm before ATT_{over} correction.^{5,20,31,35}

We argue that single-delay ASL still has potential for this patient population. We also argue that ASL, in general, should be considered an excellent method for clinical assessment in patients with MMD. ASL allows us to capture the dynamic response⁶ and further explore the clinical implications of the ACZ challenge in patients with MMD. Still, further studies are needed to evaluate single-delay and as well as multidelay ASL as a complete substitute for other, invasive, not readily available, ionizing radiation-based methods.

CONCLUSIONS

ATT_{over} artifacts, defined by means of histogram analysis, have negligible effects on calculated CBF and CVRC derived from single-delay 3D-pCASL while suppressing ATT_{under} using a long PLD. Major vascular regions are large enough for CBF and CVRC to be valid, thus making single-delay 3D-pCASL a valuable tool in pre- and postoperative assessment of patients with MMD.

REFERENCES

1. Kuroda S, Houkin K. **Moyamoya disease: current concepts and future perspectives.** *Lancet Neurol* 2008;7:1056–66 CrossRef Medline
2. Lee S, Yun TJ, Yoo RE, et al. **Monitoring cerebral perfusion changes after revascularization in patients with Moyamoya disease by using arterial spin-labeling MR imaging.** *Radiology* 2018;288:565–72 CrossRef Medline
3. Zaharchuk G, Do HM, Marks MP, et al. **Arterial spin-labeling MRI can identify the presence and intensity of collateral perfusion in patients with Moyamoya disease.** *Stroke* 2011;42:2485–91 CrossRef Medline
4. Vagal AS, Leach JL, Fernandez-Ulloa M, et al. **The acetazolamide challenge: techniques and applications in the evaluation of chronic cerebral ischemia.** *AJNR Am J Neuroradiol* 2009;30:876–84 CrossRef Medline
5. Noguchi T, Kawashima M, Nishihara M, et al. **Noninvasive method for mapping CVR in Moyamoya disease using ASL-MRI.** *Eur J Radiol* 2015;84:1137–43 CrossRef Medline
6. Inoue Y, Tanaka Y, Hata H, et al. **Arterial spin-labeling evaluation of cerebrovascular reactivity to acetazolamide in healthy subjects.** *AJNR Am J Neuroradiol* 2014;35:1111–16 CrossRef Medline
7. Zaharchuk G. **Arterial spin-labeling for acute stroke: practical considerations.** *Transl Stroke Res* 2012;3:228–35 CrossRef Medline
8. Alsop DC, Detre JA, Golay X, et al. **Recommended implementation of arterial spin-labeled perfusion MRI for clinical applications: a consensus of the ISMRM Perfusion Study Group and the European Consortium for ASL in Dementia.** *Magn Reson Med* 2015;73:102–16 CrossRef Medline
9. Fan AP, Guo J, Khalighi MM, et al. **Long-delay arterial spin labeling provides more accurate cerebral blood flow measurements in Moyamoya patients: a simultaneous positron emission tomography/MRI study.** *Stroke* 2017;48:2441–49 CrossRef Medline
10. Mutke MA, Madai VI, von Samson-Himmelstjerna FC, et al. **Clinical evaluation of an arterial-spin-labeling product sequence in stenotic disease of the brain.** *PLoS One* 2014;9:e87143 CrossRef Medline
11. Chng SM, Petersen ET, Zimine I, et al. **Territorial arterial spin labeling in the assessment of collateral circulation: comparison with digital subtraction angiography.** *Stroke* 2008;39:3248–54 CrossRef Medline
12. Buxton RB, Frank LR, Wong EC, et al. **A general kinetic model for quantitative perfusion imaging with arterial spin-labeling.** *Magn Reson Med* 1998;40:383–96 CrossRef Medline
13. Lindig T, Kotikalapudi R, Schweikardt D, et al. **Evaluation of multimodal segmentation based on 3D T1-, T2- and FLAIR-weighted images: the difficulty of choosing.** *Neuroimage* 2018;170:210–21 CrossRef Medline
14. Mutsaerts HJ, van Dalen JW, Heijtel DF, et al. **Cerebral perfusion measurements in elderly with hypertension using arterial-spin labeling.** *PLoS One* 2015;10:e0133717 CrossRef Medline
15. Tatu L, Moulin T, Bogousslavsky J, et al. **Arterial territories of the human brain: cerebral hemispheres.** *Neurology* 1998;50:1699–1708 CrossRef Medline
16. Chen Y, Wang DJ, Detre JA. **Test-retest reliability of arterial spin-labeling with common labeling strategies.** *J Magn Reson Imaging* 2011;33:940–49 CrossRef Medline
17. Petr J, Schramm G, Hofheinz F, et al. **Partial volume correction in arterial spin-labeling using a Look-Locker sequence.** *Magn Reson Med* 2013;70:1535–43 CrossRef Medline
18. Wu WC, Jiang SF, Yang SC, et al. **Pseudocontinuous arterial spin labeling perfusion magnetic resonance imaging: a normative study of reproducibility in the human brain.** *Neuroimage* 2011;56:1244–50 CrossRef Medline
19. Andaluz N, Choutka O, Vagal A, et al. **Patient selection for revascularization procedures in adult Moyamoya disease based on dynamic perfusion computerized tomography with acetazolamide challenge (PCTA).** *Neurosurg Rev* 2010;33:225–32; discussion 232–33 CrossRef Medline
20. Detre JA, Samuels OB, Alsop DC, et al. **Noninvasive magnetic resonance imaging evaluation of cerebral blood flow with acetazolamide challenge in patients with cerebrovascular stenosis.** *J Magn Reson Imaging* 1999;10:870–75 CrossRef Medline
21. Federau C, Christensen S, Zun Z, et al. **Cerebral blood flow, transit time, and apparent diffusion coefficient in Moyamoya disease before and after acetazolamide.** *Neuroradiology* 2017;59:5–12 CrossRef Medline
22. Ni WW, Christen T, Rosenberg J, et al. **Imaging of cerebrovascular reserve and oxygenation in Moyamoya disease.** *J Cereb Blood Flow Metab* 2017;37:1213–22 CrossRef Medline
23. Noguchi T, Kawashima M, Irie H, et al. **Arterial spin-labeling MR imaging in moyamoya disease compared with SPECT imaging.** *Eur J Radiol* 2011;80:e557–62 CrossRef Medline
24. Yun TJ, Paeng JC, Sohn CH, et al. **Monitoring cerebrovascular reactivity through the use of arterial spin labeling in patients with Moyamoya disease.** *Radiology* 2016;278:205–13 CrossRef Medline
25. Martin SZ, Madai VI, von Samson-Himmelstjerna FC, et al. **3D GRASE pulsed arterial spin labeling at multiple inflow times in patients with long arterial transit times: comparison with dynamic susceptibility-weighted contrast-enhanced MRI at 3 Tesla.** *J Cereb Blood Flow Metab* 2015;35:392–401 CrossRef Medline
26. Donahue MJ, Achten E, Cogswell PM, et al. **Consensus statement on current and emerging methods for the diagnosis and evaluation of cerebrovascular disease.** *J Cereb Blood Flow Metab* 2018;38:1391–1417 CrossRef Medline
27. Eskey CJ, Sanelli PC. **Perfusion imaging of cerebrovascular reserve.** *Neuroimaging Clin N Am* 2005;15:367–81, xi CrossRef Medline

28. Lee M, Zaharchuk G, Guzman R, et al. **Quantitative hemodynamic studies in Moyamoya disease: a review.** *Neurosurg Focus* 2009;26:E5 CrossRef Medline
29. Hara S, Tanaka Y, Ueda Y, et al. **Noninvasive evaluation of CBF and perfusion delay of Moyamoya disease using arterial spin-labeling MRI with multiple postlabeling delays: comparison with (15)O-Gas PET and DSC-MRI.** *AJNR Am J Neuroradiol* 2017;38:696–702 CrossRef Medline
30. Sugino T, Mikami T, Miyata K, et al. **Arterial spin-labeling magnetic resonance imaging after revascularization of Moyamoya disease.** *J Stroke Cerebrovasc Dis* 2013;22:811–16 CrossRef Medline
31. Goetti R, Warnock G, Kuhn FP, et al. **Quantitative cerebral perfusion imaging in children and young adults with Moyamoya disease: comparison of arterial spin-labeling-MRI and H(2)[(15)O]-PET.** *AJNR Am J Neuroradiol* 2014;35:1022–28 CrossRef Medline
32. Boellaard R, van Lingen A, van Balen SC, et al. **Characteristics of a new fully programmable blood sampling device for monitoring blood radioactivity during PET.** *Eur J Nucl Med* 2001;28:81–89 CrossRef Medline
33. Koopman T, Yaqub M, Heijtel DF, et al. **Semi-quantitative cerebral blood flow parameters derived from non-invasive [(15)O]H₂O PET studies.** *J Cereb Blood Flow Metab* 2019;39:163–72 CrossRef Medline
34. Khalighi MM, Deller TW, Fan AP, et al. **Image-derived input function estimation on a TOF-enabled PET/MR for cerebral blood flow mapping.** *J Cereb Blood Flow Metab* 2018;38:126–35 CrossRef Medline
35. Blauwblomme T, Lemaitre H, Naggara O, et al. **Cerebral blood flow improvement after indirect revascularization for pediatric Moyamoya disease: a statistical analysis of arterial spin-labeling MRI.** *AJNR Am J Neuroradiol* 2016;37:706–12 CrossRef Medline
36. Wang R, Yu S, Alger JR, et al. **Multi-delay arterial spin labeling perfusion MRI in Moyamoya disease—comparison with CT perfusion imaging.** *Eur Radiol* 2014;24:1135–44 CrossRef Medline
37. Choi HJ, Sohn CH, You SH, et al. **Can arterial spin-labeling with multiple postlabeling delays predict cerebrovascular reserve?** *AJNR Am J Neuroradiol* 2018;39:84–90 CrossRef Medline
38. Ahlgren A, Wirestam R, Lind E, et al. **A linear mixed perfusion model for tissue partial volume correction of perfusion estimates in dynamic susceptibility contrast MRI: impact on absolute quantification, repeatability, and agreement with pseudo-continuous arterial spin labeling.** *Magn Reson Med* 2017;77:2203–14 CrossRef Medline

Follow-Up MRI for Small Brain AVMs Treated by Radiosurgery: Is Gadolinium Really Necessary?

X. Leclerc, O. Guillaud, N. Reys, J. Hodel, O. Outteryck, F. Bala, N. Bricout, M. Bretzner, N. Ramdane, J.-P. Pruvo, L. Hacin-Bey, and G. Kuchcinski

ABSTRACT

BACKGROUND AND PURPOSE: Follow-up MR imaging of brain AVMs currently relies on contrast-enhanced sequences. Noncontrast techniques, including arterial spin-labeling and TOF, may have value in detecting a residual nidus after radiosurgery. The aim of this study was to compare noncontrast with contrast-enhanced MR imaging for the differentiation of residual-versus-obliterated brain AVMs in radiosurgically treated patients.

MATERIALS AND METHODS: Twenty-eight consecutive patients with small brain AVMs (<20 mm) treated by radiosurgery were followed with the same MR imaging protocol. Three neuroradiologists, blinded to the results, independently reviewed the following: 1) postcontrast images alone (4D contrast-enhanced MRA and postcontrast 3D T1 gradient recalled-echo), 2) arterial spin-labeling and TOF images alone, and 3) all MR images combined. The primary end point was the detection of residual brain AVMs using a 5-point scale, with DSA as the reference standard.

RESULTS: The highest interobserver agreement was for arterial spin-labeling/TOF ($\kappa = 0.81$; 95% confidence interval, 0.66–0.93). Regarding brain AVM detection, arterial spin-labeling/TOF had higher sensitivity (sensitivity, 85%; specificity, 100%; 95% CI, 62–97) than contrast-enhanced MR imaging (sensitivity, 55%; specificity, 100%; 95% CI, 27–73) and all MR images combined (sensitivity, 75%; specificity, 100%; 95% CI, 51–91) ($P = .008$). All nidus obliterations on DSA were detected on MR imaging. In 6 patients, a residual brain AVM present on DSA was only detected with arterial spin-labeling/TOF, including 3 based solely on arterial spin-labeling images.

CONCLUSIONS: In this study of radiosurgically treated patients with small brain AVMs, arterial spin-labeling/TOF was found to be superior to gadolinium-enhanced MR imaging in detecting residual AVMs.

ABBREVIATIONS: ASL = arterial spin-labeling; AVS = arteriovenous shunting; BAVM = brain AVM; GRE = gradient recalled-echo; PLD = post label delay

Brain AVMs (BAVMs) are characterized by abnormal communications between the arterial and venous circulations without a normal interposed capillary bed in the form of multiple feeding arteries, an abnormal capillary network (nidus), and enlarged draining veins. The main risk of BAVMs is hemorrhage, which occurs in 2%–4% of patients per year and may

lead to disability or even death.^{1–3} The treatment of BAVMs depends on the clinical presentation (including prior hemorrhage) and size and location of the nidus⁴ and may combine various modalities, including surgery, embolization, and/or radiosurgery. Radiosurgery, which allows progressive vascular obliteration for up to 5 years by radiation-induced obliterative endarteritis, is most often used for small BAVMs in deep or eloquent locations.^{5,6}

DSA is the reference standard to evaluate treatment efficacy at follow-up owing to high spatial resolution and superior temporal resolution relative to MR imaging, allowing differentiation of arterial and venous angiographic phases.⁷ However, DSA is an invasive test, which may result in neurologic and vascular complications.⁸ MR imaging, which is noninvasive, is increasingly used to evaluate treatment effectiveness after radiosurgery. At our institution, time-resolved (4D) contrast MRA and postcontrast 3D T1 gradient recalled-echo (GRE) sequences are routinely used to assess gradual nidus obliteration after radiosurgery. However,

Received September 26, 2019; accepted after revision December 17.

From the Departments of Neuroradiology (X.L., O.G., O.O., F.B., N.B., M.B., J.-P.P., G.K.), Neurosurgery (N. Reys), Neurology (O.O.), Centre Hospitalier Universitaire Lille, Lille, France; Inserm U1171, Degenerative and Vascular Cognitive Disorders (X.L., O.O., J.-P.P., G.K.), University of Lille, Lille, France; Inserm U1189-ONCO-THAI-Image Assisted Laser Therapy for Oncology (N. Reys), University of Lille, Lille, France; Department of Neuroradiology (J.H.), Hôpital Henri Mondor, Créteil, France; EA 2694-Public Health: Epidemiology and Quality of Care (N. Ramdane), University of Lille, Centre Hospitalier Universitaire Lille, Lille, France; and Neuroradiology, Radiology Department (L.H.-B.), University of California Davis School of Medicine, Sacramento, California.

Please address correspondence to Xavier Leclerc, MD, Neuroradiology Department, Hôpital Roger Salengro, Rue Emile Laine, 59037 Lille, France; e-mail: xavier.leclerc@chru-lille.fr

<http://dx.doi.org/10.3174/ajnr.A6404>

the sensitivity and specificity of contrast-enhanced MR images to detect a small nidus remain low, mainly because of inherent limited spatial resolution.^{9,10} Furthermore, serial injections of gadolinium-based contrast agent across time may prove harmful, for various reasons, including deposition in deep gray nuclei.^{11,12}

Studies have shown the usefulness of 3D-TOF and arterial spin-labeling (ASL) for the detection of BAVMs. 3D-TOF is sensitive for detecting BAVMs because faster blood flow within the BAVM causes hypersignal from the inflow effect. However, the detection of small BAVMs can remain challenging.¹³ On the other hand, ASL, which relies on arterial flow proton labeling at the cervical level, allows measuring cerebral blood flow. Following a short (1500–2000 ms) postlabel delay (PLD), brain images are acquired at the time magnetically labeled protons flow into the capillary bed.^{14,15} Labeled protons do not normally reach venous structures, which then appear hypointense due to T1 decay during capillary transit. However, Wolf et al,¹⁶ in 2008, demonstrated the presence of hyperintense signal in the venous structures on ASL maps in patients with BAVM, and Le et al,¹⁷ in 2012, showed that venous ASL signal intensity was the strongest predictor of arteriovenous shunting (AVS) on DSA.

We hypothesized that ASL/TOF is as sensitive as contrast-enhanced MR imaging in detecting either nidus obliteration or residual shunting in patients treated with radiosurgery.

In this study of a cohort of patients with small BAVMs (<20 mm) treated with gamma knife radiosurgery and followed by DSA, we aimed to evaluate the comparative performance levels of noncontrast MR imaging, including ASL and 3D-TOF, and contrast-enhanced MR imaging, including 4D contrast MRA and postcontrast 3D T1 GRE, in assessing nidus obliteration or a residual BAVM.

MATERIALS AND METHODS

Patient Population

This retrospective study was approved by our institutional review board of Lille University. We selected patients with a high likelihood of nidus obliteration or small residual shunting for whom MR imaging is highly challenging. Inclusion criteria were as follows:

- MRI studies obtained on a 3T MR imaging scanner
- Nidus size (maximum diameter) of ≤ 20 mm after radiosurgery
- Last treatment procedure by radiosurgery alone or by embolization and radiosurgery at least 2 years before DSA
- Time interval between DSA and MRI of ≤ 2 months
- No BAVM treatment between DSA and MRI.

From February 2017 to March 2019, forty-seven consecutive patients with small BAVMs underwent follow-up imaging with DSA and 3T MR imaging, including TOF and ASL, after gamma knife radiosurgery. Of those 47 patients, 19 were excluded from this study for the following reasons: a BAVM size of >20 mm in 9 patients, early DSA control after radiosurgery (6 months) in 6 patients, and a long delay between DSA and MR imaging in 4 patients.

Twenty-eight consecutive patients (10 women/18 men; mean age, 41 years; range, 17–65 years) remained in the study. In this cohort, BAVM presentation was intracranial hemorrhage ($n = 20$), seizures ($n = 5$), and incidental discovery ($n = 3$). Radiosurgery alone was used in 13 patients, and embolization followed by radiosurgery, in 15. DSA was performed in all patients after brain MR imaging to confirm BAVM obliteration or to evaluate the size of the residual nidus. The mean time interval between radiosurgery and MR imaging was 4.2 years (range, 2–10 years), and the mean time interval between MR imaging and DSA was 10 days (range, 1–45 days).

Imaging Methods

DSA was performed on a flat panel biplane system (Allura-Clarity; Philips Healthcare, Best, the Netherlands). Selective bilateral carotid and vertebral angiograms with at least 2 orthogonal views (anteroposterior and lateral) and 3D rotational angiography acquired at 3 frames per second with a 1024×1024 matrix size and a 20-cm FOV were obtained. Superselective feeding artery angiography with focused angiographic views was consistently performed if there was uncertainty as to the presence of a residual nidus.

MR imaging examinations were performed on a 3T scanner (Achieva; Philips Healthcare) with a 32-channel head coil. Imaging protocol included the following sequences: DWI ($b = 1000$ s/mm²; TR/TE, 2827/67 ms), axial FLAIR (TR/TE/TI, 11,000/125/2800 ms), axial T2* (TR/TE, 890/16 ms) or SWI (TR/TE, 28/5.6 ms), axial spin-echo T1 (TR/TE, 531/10 ms), 3D-TOF (TR/TE, 25/3.5 ms; FOV, 19 cm; matrix, 472×270 ; section thickness, 1.2 mm; scan time, 5 minutes 39 seconds), 2D pseudocontinuous ASL (TR/TE, 4297/14 ms; FOV, 24 cm; labeling period, 1650 ms followed by a PLD of 2000 ms; section thickness, 5 mm; scan time, 4 minutes 55 seconds), 4D contrast MRA (TR/TE, 3/1.1 ms; FOV, 24 cm; matrix, 240×240 ; temporal resolution, 1.1 second per volume; scan time, 1 minutes 4 seconds), half-brain coverage ipsilateral to the BAVM side, and postcontrast 3D T1 GRE (TR/TE, 7.7/3.7 ms; FOV, 24 cm; matrix, 240×240 ; scan time 3 minutes 43 seconds). Intravenous gadoterate meglumine (Dotarem; Guerbet, Aulnay-sous-Bois, France) was administered at a concentration of 0.1 mmol/kg and a rate of 1.5 mL/s.

Imaging Analysis

DSA examinations were interpreted conjointly by 2 interventional neuroradiologists (N.B., X.L.), each with >8 years of experience. The presence of a residual nidus or early venous drainage was recorded. BAVM nidus maximum diameter, location, and drainage type were recorded. Evidence of a draining vein on the arterial phase of angiograms without a measurable nidus was defined as a residual AVS.

MR images were de-identified and randomly interspersed. Three reviewers, a diagnostic neuroradiologist with 10 years of experience (G.K.), a senior interventional neuroradiologist (F.B.) with 6 years of experience, and a junior neuroradiologist (O.O.) with 3 years of experience, blinded to the clinical data and MR imaging/DSA correlations, independently reviewed MR imaging examinations in random order. MR images were reviewed at 3 separate sessions, each separated by a month. At each review

Table 1: Patient characteristics and imaging findings after gamma knife radiosurgery

Patients			DSA			MRI		
No.	Age (yr)	Sex	Presentation	Location	Drainage	Findings	Contrast MRI	ASL/TOF
1	65	M	Hemorrhage	L temporal	Superficial	AVS	-	+
2	23	F	Hemorrhage	L thalamus	Deep	AVS	-	+
3	17	M	Hemorrhage	L frontal	Mixed	Nidus 13 mm	+	+
4	36	M	Hemorrhage	R frontal	Superficial	AVS	-	-
5	64	M	Hemorrhage	L cerebellar	Deep	O	-	-
6	47	M	Hemorrhage	R frontal	Superficial	AVS	-	+
7	45	F	Hemorrhage	L parietal	Mixed	Nidus 9 mm	+	+
8	35	M	Hemorrhage	R frontal	Deep	Nidus 14 mm	+	+
9	22	F	Incidental	L temporal	Superficial	AVS	-	-
10	47	M	Hemorrhage	R occipital	Deep	O	-	-
11	27	M	Hemorrhage	L occipital	Superficial	AVS	-	+
12	41	M	Seizure	L frontal	Deep	O	-	-
13	52	F	Hemorrhage	L temporal	Deep	Nidus 10 mm	+	+
14	37	F	Incidental	L frontal	Superficial	O	-	-
15	65	F	Hemorrhage	L temporal	Superficial	AVS	-	-
16	30	F	Hemorrhage	R parietal	Superficial	Nidus 18 mm	+	+
17	40	M	Seizure	R frontal	Superficial	Nidus 20 mm	+	+
18	31	M	Seizure	L parietal	Superficial	Nidus 17 mm	+	+
19	33	F	Hemorrhage	L parietal	Deep	Nidus 12 mm	+	+
20	26	F	Hemorrhage	L temporal	Deep	Nidus 8 mm	+	+
21	60	M	Hemorrhage	L parietal	Mixed	Nidus 5 mm	-	+
22	37	M	Hemorrhage	R parietal	Superficial	O	-	-
23	42	F	Hemorrhage	R parietal	Deep	O	-	-
24	50	M	Incidental	R frontal	Superficial	O	-	-
25	23	M	Seizure	L temporal	Superficial	Nidus 11 mm	+	+
26	56	M	Hemorrhage	R frontal	Deep	O	-	-
27	53	M	Hemorrhage	R cerebellar	Mixed	AVS	-	+
28	54	M	Seizure	R frontal	Mixed	Nidus 15 mm	+	+

Note:—+, residual brain arteriovenous malformation; —, nidus obliteration; L, left; R, right; O, occlusion.

session, attention was paid to the presence of hemorrhage, edema, abnormal vessels, and embolization material on FLAIR, T2*, and/or SWI sequences.

At the first review session, only contrast-enhanced MR images (4D contrast MRA and postcontrast 3D T1 GRE) were added to FLAIR and T2*/SWI. The presence of a nidus, abnormal serpiginous vessels, early venous drainage, and radiation-induced contrast enhancement was recorded. Contrast enhancement was interpreted as radiation-related injury when it showed nodular or heterogeneous contrast enhancement on postcontrast 3D T1 GRE at the site of the radiated nidus without an early draining vein on 4D contrast MRA. At the second review session, only non-contrast-enhanced MR images (3D TOF, ASL FLAIR, and T2*/SWI) were assessed. The presence of hypersignal at the site of the nidus and/or within neighboring venous structures was noted. At the time of the third and final review session, all MR images were available for interpretation.

After each case, readers used a 5-point scale to rate the likelihood of a residual AVM without distinction between the nidus and AVS: 1) very unlikely, 2) unlikely, 3) uncertain, 4) likely, and 5) very likely. The 2 noncontrast (ASL and TOF) and the 2 contrast-enhanced (4D contrast-MRA and postcontrast 3D T1 GRE) techniques were interpreted conjointly but rated separately. Cases resulting in disagreement among readers were then jointly reviewed by the 3 readers to reach a consensus. For the statistical analysis, the 5-point scale was reduced to a 3-point scale as follows: negative (1 and 2), uncertain (3), and positive (4 and 5) for the likelihood of a residual AVM.

Statistical Analysis

Data were analyzed using the SAS software package, Release 9.4 (SAS Institute, Cary, North Carolina). Results were presented as numbers and percentages for categorical variables. Sensitivity, specificity, and predictive values were calculated for the 3 readers separately, the consensus results, and the 3 sessions using DSA as the reference standard. Sensitivity and specificity of the consensus data were compared using the McNemar test. Interobserver agreement on the diagnosis for each sequence was assessed using a weighted κ coefficient or a Cohen κ coefficient.¹⁸ The Krippendorff α coefficient was also calculated to measure the agreement among the different observers as a whole. This was interpreted as follows¹⁹: poor agreement for values <0.45, fair to good agreement for values between 0.45 and 0.75, and excellent agreement for values >0.75. κ coefficients within 95% confidence intervals were also calculated. Statistical testing was conducted as the 2-tailed α level of .05.

RESULTS

DSA Findings

Patient characteristics and imaging findings after radiosurgery are presented in Table 1. Of the 28 BAVMs radiosurgically treated, follow-up DSA revealed that 8 were obliterated, 12 had a residual nidus (mean size, 12.5 mm; range, 5–20 mm), and 8 had a residual AVS (nonmeasurable nidus). Venous drainage was superficial in 13 patients, deep in 10 patients, and mixed in 5 patients.

Interobserver Agreement

Interobserver agreement data (κ value, 95% CI) are described in Table 2. The overall agreement was highest at the second session (ASL/TOF) with $\kappa = 0.81$ (95% CI, 0.66–0.93). There were 3 disagreements with ASL: In 2 cases, hypersignal at the site of the nidus was judged too faint to be related to a residual BAVM by reader 2 in one case and by readers 1 and 3 in another case. The third disagreement concerned faint hypersignal considered to represent a residual BAVM by readers 2 and 3, but judged artifactual by reader 1. In 1 case, contrast enhancement on 3D T1 GRE at the site of the nidus was read as a residual BAVM by

readers 2 and 3 and as radiation-induced contrast enhancement by reader 1.

Comparison of All MR Imaging Sequences and DSA

The sensitivity, specificity, positive predictive value, and negative predictive value of MR imaging (all sequences combined) for the detection of residual AVM were respectively 75% (95% CI, 51–91), 100% (95% CI, 63–100), 100% (95% CI, 78–100), and 61.5% (95% CI, 32–86). Individual results are presented in Table 3. In 2 patients, all 3 reviewers reported a BAVM obliteration on MR imaging, whereas DSA demonstrated residual AVS. Of the 6 patients with MR images interpreted as uncertain, DSA revealed residual AVS in 3 patients and nidus obliteration in 3 patients. Fig 1 shows an illustrative example of a residual BAVM demonstrated on both contrast-enhanced MR images and ASL/TOF.

Table 2: Agreement among the 3 readers^a

Readers	First Sitting (Contrast-Enhanced)	Second Sitting (ASL/TOF)	Third Sitting (All Sequences)
1 and 2	0.72 (0.54–0.9)	0.88 (0.72–1)	0.72 (0.53–0.9)
1 and 3	0.67 (0.46–0.88)	0.81 (0.6–1)	0.61 (0.37–0.84)
2 and 3	0.64 (0.42–0.85)	0.84 (0.67–1)	0.80 (0.65–0.96)
Overall agreement	0.59 (0.44–0.77)	0.81 (0.66–0.93)	0.58 (0.42–0.74)

^a Data are κ (95% CI).

Table 3: Sensitivity, specificity, PPV, and NPV of the third sitting (all sequences available)

Readers	Sensitivity (95% CI)	Specificity (95% CI)	PPV (95% CI)	NPV (95% CI)
1	70% (46–88)	100% (63–100)	100% (77–100)	57.1% (29–82)
2	75% (51–91)	93.7% (47–100)	87.5% (70–100)	58.3% (28–84)
3	75% (51–91)	93.7% (47–100)	87.5% (70–100)	58.3% (28–84)
Consensus	75% (51–91)	100% (63–100)	100% (78–100)	61.5% (32–86)

Note:—PPV indicates positive predictive value; NPV, negative predictive value.

Contrast-Enhanced MR Imaging Sequences for the Detection of Residual BAVM

Sensitivity, specificity, positive predictive value, and negative predictive value of contrast MR imaging for the detection of residual BAVMs were respectively 55% (95% CI, 27–73), 100% (95% CI, 63–100), 100% (95%

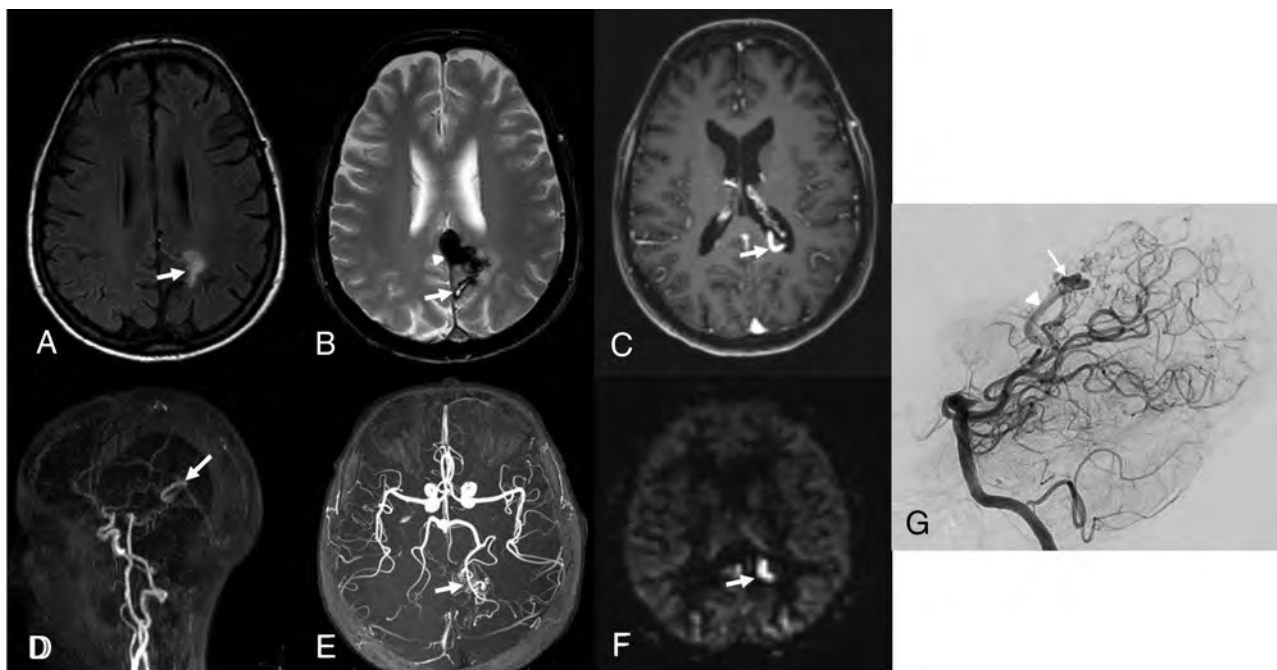


FIG 1. Patient 19. Follow-up MR imaging 2 years after embolization and radiosurgery for a ruptured left parietal brain AVM. A, Axial FLAIR shows hyperintense signal in the left parietal region (arrow) due to radiation injury. B, Axial T2* shows mixed signal intensity related to prior hemorrhage (arrow) posterior to hypointense embolization material (arrowhead). C, Postcontrast 3D T1 GRE axial image shows an enhanced tubular draining vein of a residual BAVM (arrow). D, Sagittal view from 4D contrast MRA with MIP reconstruction shows an early enhanced draining vein on the arterial phase of the angiogram (arrow). E, 3D-TOF with MIP reconstruction shows a residual BAVM (arrow). F, ASL image shows a focal hyperintense signal in the left lateral part of the cingulate gyrus (arrow). G, DSA, lateral view from a vertebral angiogram, confirms a residual nidus (arrow) with deep venous drainage (arrowhead).

CI, 69–100), and 47% (95% CI, 21–69). Individual results are described in Table 4. There were 9 false-negatives of a DSA-proved residual nidus or AVS, which were read as BAVM obliteration on contrast-enhanced MR images. In 5 patients, postcontrast 3D T1 GRE images showed radiation-induced contrast enhancement at the site of the radiosurgically treated nidus, including nodular enhancement (Fig 2) in 3 and linear-like heterogeneous enhancement in 2 (Fig 3). Of the 5 patients, 4 were given a very unlikely or unlikely score (1/5 or 2/5, respectively), and 1, an uncertain score (3/5). In the 5 patients with radiation-induced changes, 4D MRA findings were interpreted as negative, whereas DSA showed a residual BAVM in 3 and nidus obliteration in 2. In 4 other patients, 4D-MRA findings were considered negative, whereas a residual BAVM was demonstrated on postcontrast 3D T1 GRE.

ASL/TOF for the Detection of Residual BAVMs

The sensitivity, specificity, positive predictive value, and negative predictive value of ASL/TOF for the detection of residual BAVMs

were respectively 85% (95% CI, 62–97), 100% (95% CI, 63–100), 100% (95% CI, 80–100), and 73% (95% CI, 39–94). Individual results are described in Table 5. All residual BAVMs detected on ASL/TOF were confirmed on DSA. However, in 3 patients, while ASL/TOF findings were interpreted as negative, residual AVS was demonstrated on DSA. Of those 3 patients, imaging of 1 patient demonstrated faint hypersignal on ASL images at the site of the nidus, considered suggestive of a residual BAVM by all 3 readers; however, the lack of signal abnormality on anatomic MR images prevented the readers, who were blinded to the BAVM location, from detecting the nidus site (Fig 4). Comparison of TOF and ASL ratings showed that all residual BAVMs and nidus obliterations detected on TOF images were correctly classified on ASL images. In 3 patients with negative findings on TOF images, ASL showed the presence of a residual AVS in 2 patients and a 5-mm residual BAVM in 1 patient (Fig 2).

Comparison of Contrast-Enhanced MR Imaging Sequences and ASL/TOF

ASL/TOF demonstrated superior residual BAVM detection compared with contrast-enhanced MR imaging ($P = .008$). In 5 patients with AVS and in 1 with a 5-mm nidus, all shown on DSA, a residual BAVM was only

Table 4: Sensitivity, specificity, PPV, and NPV of the first sitting (only FLAIR, T2*, and contrast-enhanced MR images)

Readers	Sensitivity (95% CI)	Specificity (95% CI)	PPV (95% CI)	NPV (95% CI)
1	55% (31–77)	100% (63–100)	100% (71–100)	47% (23–72)
2	55% (31–77)	100% (63–100)	100% (71–100)	47% (23–72)
3	45% (23–68)	100% (63–100)	100% (66–100)	42% (20–66)
Consensus	55% (27–73)	100% (63–100)	100% (69–100)	47% (21–69)

Note:—PPV indicates positive predictive value; NPV, negative predictive value.

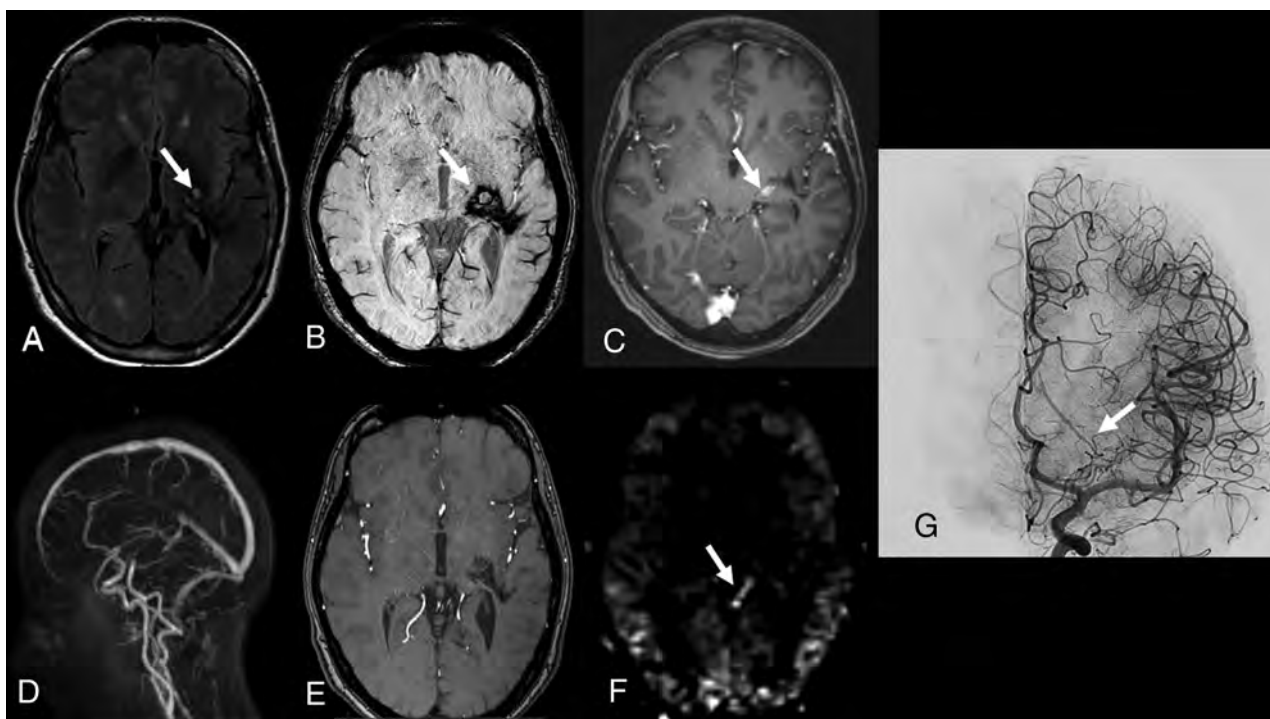


FIG 2. Patient 2. Follow-up MR imaging 7 years after radiosurgery for a ruptured left thalamic brain AVM. A, Axial FLAIR shows slight hypersignal at the site of the radiosurgically treated nidus (arrow). B, SWI shows hypointense hemorrhagic focus in the left deep nuclei (arrow). C, Postcontrast 3D T1 GRE axial image shows nodular contrast enhancement at the nidus site (arrow) due to radio-induced changes. D, Sagittal view from 4D contrast MRA does not show residual BAVM. Source image from 3D-TOF (E) does not demonstrate abnormal signal intensity at the nidus site, whereas the ASL image (F) shows focal tubular hyperintense signal of the deep draining vein (arrow). G, DSA with an anteroposterior intracranial view from a left carotid angiogram confirms the presence of residual AVS without a measurable nidus. Only early draining vein contrast filling is detected on an angiogram (arrow).

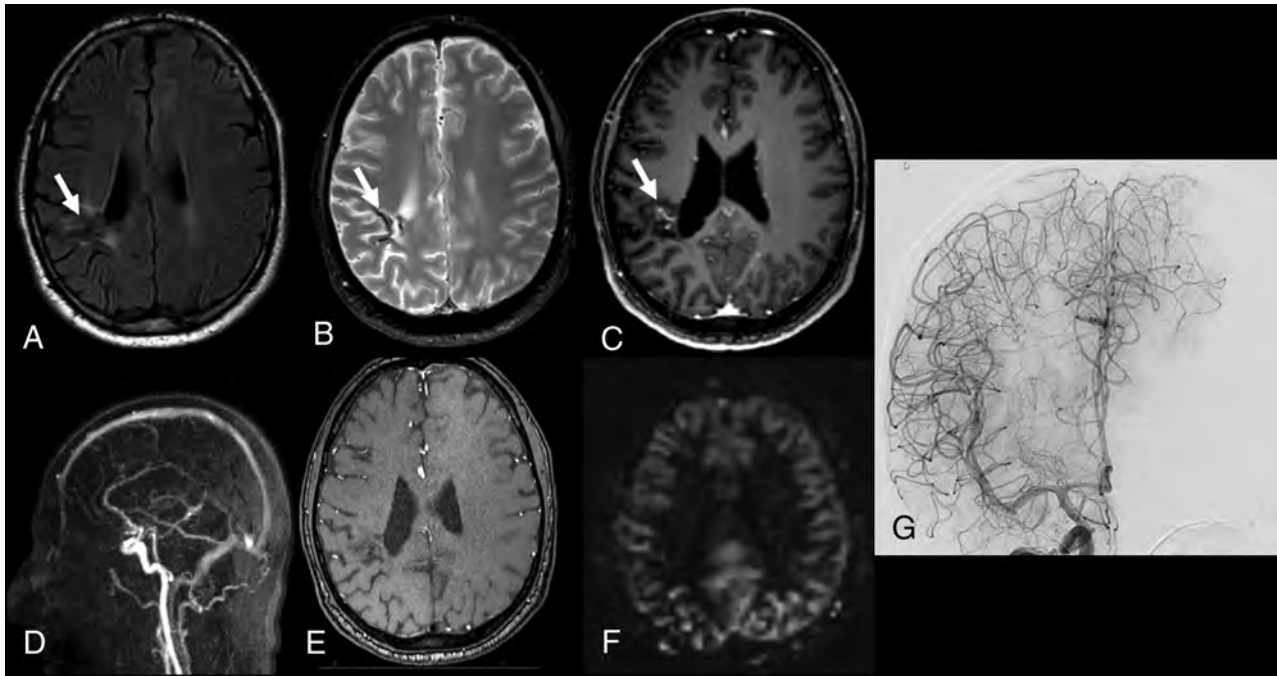


FIG 3. Patient 22. Follow-up MR imaging 4 years after radiosurgery for a ruptured right parietal brain AVM. A, Axial FLAIR shows mixed signal at the site of a radiosurgically treated BAVM (arrow). B, Axial T2* shows subcortical right parietal hypointense signal related to prior hemorrhage (arrow). C, Postcontrast 3D T1 GRE shows linear-like heterogeneous contrast enhancement at the nidus site (arrow) due to radiation injury misinterpreted as a residual BAVM by 2 readers. 4D contrast MRA (D), source image from 3D TOF (E), and ASL (F) do not reveal a residual BAVM. G, DSA with an anteroposterior intracranial view from a right carotid angiogram confirms the absence of a residual BAVM.

Table 5: Sensitivity, specificity, PPV, and NPV of the second sitting (FLAIR, T2*, and ASL/TOF images)

Readers	Sensitivity (95% CI)	Specificity (95% CI)	PPV (95% CI)	NPV (95% CI)
1	85% (62–97)	100% (63–100)	100% (80–100)	72.7% (39–94)
2	85% (62–97)	94.4% (47–100)	87.5% (72–100)	70% (35–93)
3	80% (56–94)	94.1% (47–100)	87.5% (71–100)	63.6% (31–89)
Consensus	85% (62–97)	100% (63–100)	100% (80–100)	73% (39–94)

Note:—PPV indicates positive predictive value; NPV, negative predictive value.

detected on ASL/TOF, while the nidus was considered obliterated on contrast-enhanced MR images (Fig 5). Of the 5 patients with DSA-proved AVS considered occluded on contrast-enhanced MR imaging, ASL showed a residual BAVM in 3. Nine patients were given an uncertain score (3/5) at the first session (contrast-enhanced MR imaging), and 6, patients at the third session (all MR images). With ASL/TOF alone, no uncertain score was given (Fig 6).

DISCUSSION

In this study, noncontrast 3T MR imaging using ASL and 3D-TOF was found to be more sensitive than contrast-enhanced MR imaging for the detection of a residual nidus in patients with small (<20 mm) BAVMs treated by radiosurgery. We found that the clinical value of noncontrast MR images was even better when they were analyzed without postcontrast 3D T1 GRE images, in part owing to confusion between radiation-induced enhancement and residual BAVMs.

To our knowledge, ours is the first study to evaluate the comparative performance of noncontrast MR imaging and

contrast-enhanced MR imaging for the follow-up of patients treated radiosurgically for a small BAVM. ASL and TOF sequences were interpreted conjointly, but the separate ratings of ASL and TOF showed the potential benefit of ASL compared with TOF for detecting a residual BAVM after radiosurgery because a residual

DSA-proved BAVM was only detected on ASL images in 3 patients. A small number of published studies, to date, have discussed the usefulness of ASL in the evaluation of intracranial arteriovenous dural fistulas and/or BAVMs,^{17,20–23} including 2 studies of radiosurgically treated patients with BAVMs.^{21,23} In our study, only patients with small (<20 mm) BAVMs treated by radiosurgery were included. In this highly selective cohort, and although follow-up angiography demonstrated the most evidence of either nidus obliteration or subtle residual AVS, we showed that detection of residual shunting with ASL/TOF was possible with excellent interobserver agreement and superior sensitivity in comparison with contrast-enhanced MR imaging, with a high confidence level and a zero rate of uncertain scores to detect a residual flow on ASL/TOF images.

When the PLD is appropriately obtained, ASL images of a healthy brain do not show any hypersignal in the venous structures because the transit time of labeled arterial protons in the capillary bed is longer than the PLD. Conversely, when AVS is present, rapid passage of labeled protons into the venous compartment results in hypersignal in the nidus and/or the draining

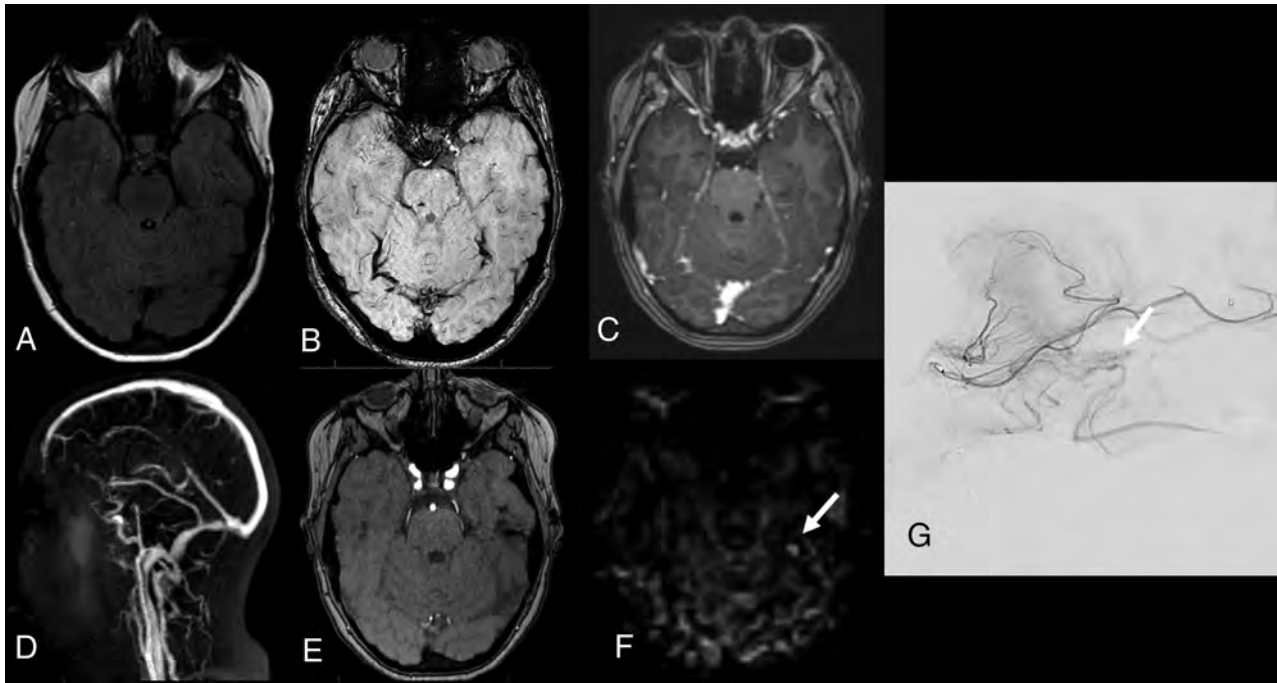


FIG 4. Patient 9. Follow-up MR imaging 6 years after radiosurgery for an unruptured left posterior temporal brain AVM. T1-weighted noncontrast (A), SWI (B), postcontrast 3D T1 GRE (C), 4D contrast-MRA (D), and a source image from 3D-TOF (E) do not show signal abnormality. F, ASL shows faint hyperintense signal (arrow) not interpreted as a residual BAVM by the 3 readers who were blinded to the BAVM location. G, DSA with a sagittal intracranial view from a superselective left temporal artery angiogram shows an early superficial draining vein contrast filling (arrow).

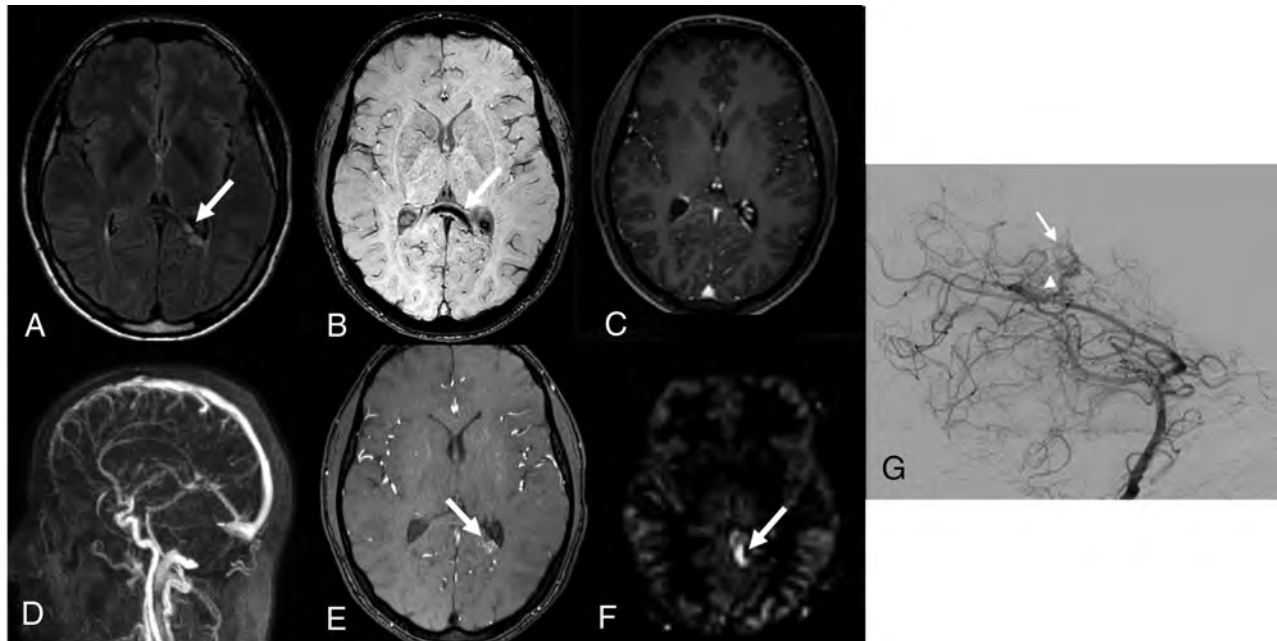


FIG 5. Patient 21. Follow-up MR imaging 2 years after radiosurgery for a ruptured parietal brain AVM adjacent to the corpus callosum. A, Axial FLAIR shows slight hypersignal at the nidus site (arrow). B, T2* image shows hypointense prior hemorrhagic focus in the corpus callosum (arrow). Postcontrast 3D T1 GRE (C) and 4D contrast MRA (D) do not reveal a residual BAVM. E, Source image from 3D-TOF shows a residual 5-mm nidus (arrow). F, ASL image shows focal hyperintense signal of a deep draining vein (arrow). G, DSA, oblique intracranial view from a left vertebral angiogram confirms the presence of a residual nidus (arrow) with an early deep draining vein (arrowhead).

veins. In a study published in 2017, Kodera et al,²³ evaluating 7 patients with BAVMs treated by radiosurgery, showed, in all 7 patients, a correlation between BAVM obliteration on DSA and lack of BAVM detection on ASL images. More recently, Heit

et al,²¹ in a retrospective study including 15 patients with larger BAVM nidus sizes in comparison with our cohort, showed 100% sensitivity and 95% specificity of ASL for the detection of residual BAVMs after radiosurgery. These data suggest a role for ASL in

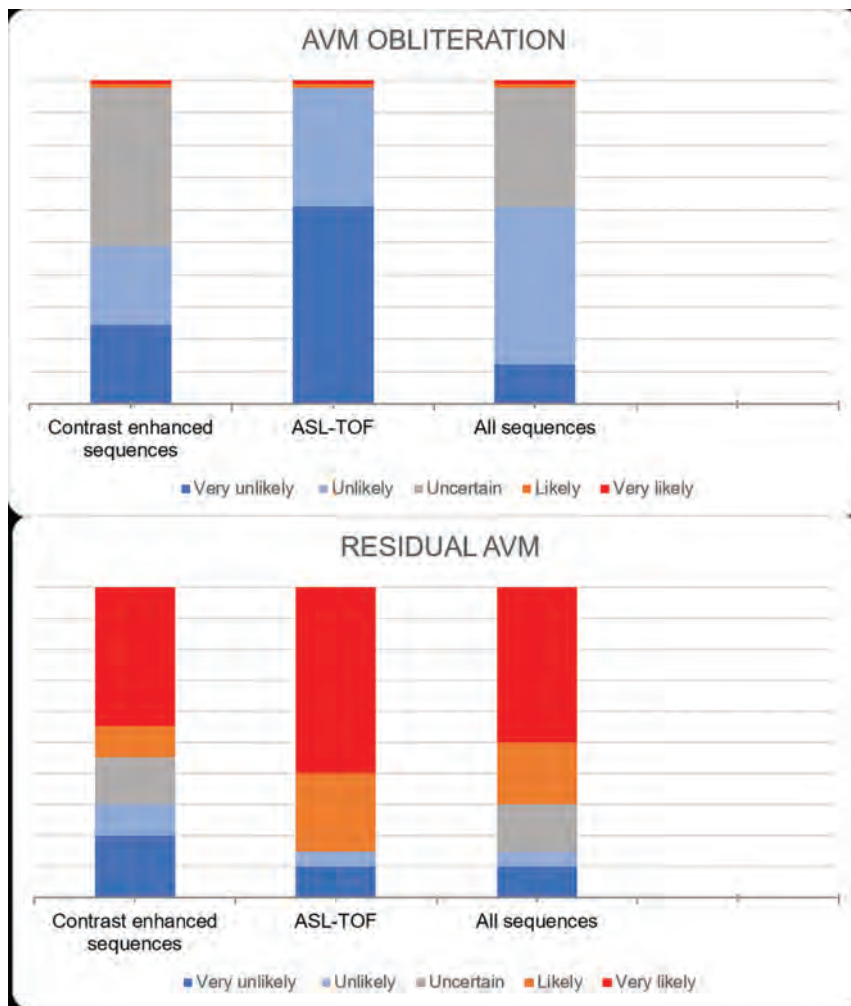


FIG 6. Distribution of the 5-point scale of the 3 sittings in the 28 patients with and without residual brain AVMs on DSA. In the “AVM OBLITERATION” group, reader accuracy and confidence increased with ASL/TOF with zero uncertain scores and more scores of very unlikely. In the “RESIDUAL AVM” group, reader accuracy and confidence increased with ASL/TOF with zero uncertain scores and more scores of very likely.

3T MR imaging protocols to determine the adequate timing for follow-up DSA in treated patients.

In addition, although previous studies have demonstrated the usefulness of 3D-TOF in detecting intracranial arteriovenous shunting or in characterizing BAVMs,¹³ ours is the first study to combine TOF-MRA with ASL for the follow-up of radiosurgically treated patients with BAVMs. Our study also suggests a high interobserver confidence level in detecting residual shunting using combined sequences as opposed to contrast-enhanced MR imaging alone, even though ASL appears to show the highest sensitivity in residual nidus flow detection. The reproducibility of our results may be limited because the spatial resolution of TOF and ASL sequences was optimized in this study by the use of a 3T magnet and 32-channel coil.

The sensitivity of 4D contrast MRA for the detection of residual BAVMs in the present study was lower compared with that reported in a previous study by Soize et al,¹⁰ who followed up a cohort of patients treated by embolization, radiosurgery, and/or surgery. They showed an overall sensitivity of 73% for the

detection of residual BAVMs compared with 55% in the present study. This discrepancy may be explained by the selected patient group in our study, because 8 of the 28 BAVMs were obliterated and 8 had only residual AVS without a measurable nidus.

On postcontrast 3D T1 GRE images, various aspects of radiation-induced contrast enhancement were found in this study that might lead to confusion between a residual BAVM or radiation-induced changes, translating into scores of uncertain in some patients. These radiation-induced imaging changes may be related to various factors, including blood-brain barrier damage due to inflammation, dilated capillary vessels, or neovascularization in the wall of a perinidal cavity with neoangiogenic nodule formation.²⁴ Negative findings on 4D contrast MRA did not provide additional information because they could be related to either radiation-induced imaging changes or a residual BAVM, explained by the limited temporal and spatial resolution inherent to the 4D contrast MRA technique, which hindered the detection of small nidi with decreased flow.

Most important, these preliminary data also suggest that for long-term follow-up of patients with BAVMs treated by radiosurgery, the use of a gadolinium contrast medium may not be systematically required; this possibility could reduce the likelihood of

long-term effects of gadolinium retention, including within deep nuclei.¹¹

Several limitations may be highlighted in our study. First, this is a retrospective, single-center study design and, therefore, subject to a potential selection bias. Prospective randomized studies with properly selected control groups would be useful to support our preliminary data. Second, the small sample size may not easily allow reproducibility, especially considering the low prevalence of small BAVMs. Third, the lack of a control group of patients without BAVMs, who would have been evaluated with both DSA and MR imaging with ASL/TOF, may reduce the statistical power; however, the performance of DSA and the administration of gadolinium contrast in healthy subjects may not have been ethically justifiable. Last, 2D-ASL with a single PLD value was the technique used in this study; there have been recent technical advances with commercially available 3D-ASL sequences, including multi-PLD, that may potentially improve the image quality and robustness of image interpretation.²⁵ Despite these limitations, we believe that our results suggest

that as advanced MR imaging techniques such as ASL become generalized, the systematic use of contrast-enhanced MR images may become unwarranted in clinical routine to guide decision-making about the timing of appropriate DSA follow-up in this group of patients.

CONCLUSIONS

In this study, contrast-enhanced MR images were found to be inferior to noncontrast MR imaging, including TOF and ASL at 3T, in demonstrating a residual nidus for the follow-up of patients with BAVMs treated by radiosurgery. These data suggest that ASL/TOF could be used to decide the appropriate timing for follow-up DSA to confirm AVM obliteration. As a result, sequential injections of gadolinium contrast medium could be avoided, sparing patients the potential risk of gadolinium accumulation, including within deep brain nuclei. Further studies including larger groups of patients are needed to confirm this hypothesis.

Disclosures: Nicolas Bricout—RELATED: Consulting Fee or Honorarium: None.

REFERENCES

1. Arteriovenous Malformation Study Group. **Arteriovenous malformations of the brain in adults.** *N Engl J Med* 1999;340:1812–18 CrossRef Medline
2. Laakso A, Hernesniemi J. **Arteriovenous malformations: epidemiology and clinical presentation.** *Neurosurg Clin N Am* 2012;23:1–6 CrossRef Medline
3. Yamada S, Takagi Y, Nozaki K, et al. **Risk factors for subsequent hemorrhage in patients with cerebral arteriovenous malformations.** *J Neurosurg* 2007;107:965–72 CrossRef Medline
4. van Beijnum J, van der Worp HB, Buis DR, et al. **Treatment of brain arteriovenous malformations: a systematic review and meta-analysis.** *JAMA* 2011;306:2011–19 CrossRef Medline
5. Vlaskou Badra E, Ermiş E, Mordasini P, et al. **Radiosurgery and radiotherapy for arteriovenous malformations: outcome predictors and review of the literature.** *J Neurosurg Sci* 2018;62:490–504 CrossRef Medline
6. Friedman WA, Bova FJ. **Radiosurgery for arteriovenous malformations.** *Neurol Res* 2011;33:803–19 CrossRef Medline
7. Chowdhury AH, Ghose SK, Mohammad QD, et al. **Digital subtraction angiography is superior to magnetic resonance angiography in diagnosis of cerebral arteriovenous malformation.** *Mymensingh Med J MMJ* 2015;24:356–65 Medline
8. Willinsky RA, Taylor SM, terBrugge K, et al. **Neurologic complications of cerebral angiography: prospective analysis of 2,899 procedures and review of the literature.** *Radiology* 2003;227:522–28 CrossRef Medline
9. Hadizadeh DR, von Falkenhausen M, Gieseke J, et al. **Cerebral arteriovenous malformation: Spetzler-Martin classification at sub-second-temporal-resolution four-dimensional MR angiography compared with that at DSA.** *Radiology* 2008;246:205–13 CrossRef Medline
10. Soize S, Bouquigny F, Kadziolka K, et al. **Value of 4D MR angiography at 3T compared with DSA for the follow-up of treated brain arteriovenous malformation.** *AJNR Am J Neuroradiol* 2014;35:1903–09 CrossRef Medline
11. Choi JW, Moon WJ. **Gadolinium deposition in the brain: current updates.** *Korean J Radiology* 2019;20:134–47 CrossRef Medline
12. Adin ME, Kleinberg L, Vaidya D, et al. **Hyperintense dentate nuclei on T1-weighted MRI: relation to repeat gadolinium administration.** *AJNR Am J Neuroradiol* 2015;36:1859–65 CrossRef Medline
13. Buis DR, Bot JC, Barkhof F, et al. **The predictive value of 3D time-of-flight MR angiography in assessment of brain arteriovenous malformation obliteration after radiosurgery.** *AJNR Am J Neuroradiol* 2012;33:232–38 CrossRef Medline
14. Grade M, Hernandez Tamames JA, Pizzini FB, et al. **A neuroradiologist's guide to arterial spin labeling MRI in clinical practice.** *Neuroradiology* 2015;57:1181–202 CrossRef Medline
15. Haller S, Zaharchuk G, Thomas DL, et al. **Arterial spin labeling perfusion of the brain: emerging clinical applications.** *Radiology* 2016;281:337–56 CrossRef Medline
16. Wolf RL, Wang J, Detre JA, et al. **Arteriovenous shunt visualization in arteriovenous malformations with arterial spin-labeling MR imaging.** *AJNR Am J Neuroradiol* 2008;29:681–87 CrossRef Medline
17. Le TT, Fischbein NJ, André JB, et al. **Identification of venous signal on arterial spin labeling improves diagnosis of dural arteriovenous fistulas and small arteriovenous malformations.** *AJNR Am J Neuroradiol* 2012;33:61–68 CrossRef Medline
18. Cohen J. **A coefficient of agreement for nominal scales.** *Educ Psychol Meas* 1960;20:37–46 CrossRef Medline
19. Fleiss JL. **Reliability of measurement.** In: Fleiss JL. *The Design and Analysis of Clinical Experiments.* New York: John Wiley & Sons; 1986:1–32
20. Amukotuwa SA, Marks MP, Zaharchuk G, et al. **Arterial spin-labeling improves detection of intracranial dural arteriovenous fistulas with MRI.** *AJNR Am J Neuroradiol* 2018;39:669–77 CrossRef Medline
21. Heit JJ, Thakur NH, Iv M, et al. **Arterial-spin labeling MRI identifies residual cerebral arteriovenous malformation following stereotactic radiosurgery treatment.** *J Neurosurg* 2019 Jan 15. [Epub ahead of print] CrossRef Medline
22. Hodel J, Leclerc X, Kalsoum E, et al. **Intracranial arteriovenous shunting: detection with arterial spin-labeling and susceptibility-weighted imaging combined.** *AJNR Am J Neuroradiol* 2017;38:71–76 CrossRef Medline
23. Kodera T, Arai Y, Arishima H, et al. **Evaluation of obliteration of arteriovenous malformations after stereotactic radiosurgery with arterial spin labeling MR imaging.** *Br J Neurosurg* 2017;31:641–47 CrossRef Medline
24. Malikova H, Koubska E, Vojtech Z, et al. **Late morphological changes after radiosurgery of brain arteriovenous malformations: an MRI study.** *Acta Neurochir (Wien)* 2016;158:1683–90 CrossRef Medline
25. Johnston ME, Lu K, Maldjian JA, et al. **Multi-TI arterial spin labeling MRI with variable TR and bolus duration for cerebral blood flow and arterial transit time mapping.** *IEEE Trans Med Imaging* 2015;34:1392–402 CrossRef Medline

Vessel Wall MRI Enhancement in Noninflammatory Cerebral Amyloid Angiopathy

Q. Hao, N.M. Tsankova, H. Shoirah, C.P. Kellner, and K. Nael



ABSTRACT

SUMMARY: Cerebral amyloid angiopathy is characterized by deposition of amyloid- β fibrils in the walls of small-to-medium-sized blood vessels. In this retrospective review of 5 patients with histologically confirmed noninflammatory cerebral amyloid angiopathy, high-resolution vessel wall MRI showed arterial wall enhancement in 2 patients (40%). Despite common consensus of equating vessel wall enhancement with inflammation, this report demonstrates that β -amyloid accumulation alone without inflammation can be associated with arterial wall enhancement in a subset of patients.

ABBREVIATIONS: CAA = cerebral amyloid angiopathy; VWMRI = vessel wall MR imaging

Cerebral amyloid angiopathy (CAA) is characterized by deposition of amyloid- β fibrils in the vessel walls of leptomeningeal and cortical arteries, arterioles, and, less often, capillaries and veins of the central nervous system.¹ Histologically, Puchtler alkaline Congo Red stain remains the standard diagnostic method for staining amyloid deposition, which can be seen in the adventitia, tunica media, or all layers of vessel wall.

Along the spectrum of amyloid-deposition-related angiopathies, there are 3 entities: 1) CAA (generally there is an absence of wall inflammation); 2) inflammatory CAA (varying amounts of perivascular inflammation are present, including multinucleated giant cells); and 3) amyloid- β -related angiitis (in which there is destructive vasculitis).² There is often overlap in the clinical presentations of these entities, which may include focal neurologic deficits, cognitive impairment, or seizure related to hemorrhagic or ischemic changes. The clinical diagnosis of CAA relies on clinical history and imaging evidence of microbleeds or lobar hemorrhage that are not explained by other etiologies.¹

High-resolution vessel wall MR imaging (VWMRI) is an emerging technique that is used to assess various vasculopathies, such as atherosclerotic disease, vasculitis, Moyamoya disease, reversible cerebral vasoconstriction syndrome, and dissection.³ While vessel wall enhancement using VWMRI has been reported in the inflammatory variety of amyloid-related angiopathies,^{2,3} very little is known about the VWMRI findings in patients with noninflammatory CAA. We report the VWMRI findings in a patient with histologically confirmed CAA.

Brief Report

A 75-year-old patient with a history of hypertension, diabetes, progressive memory loss, and behavior changes during 6 months presented with worsening of mental status followed by seizures and status epilepticus. The initial neurologic examination revealed impaired attention and language; however, cranial nerves, motor strength, and gait were unremarkable. The patient had fluctuating mental status during the first 3 days and developed a clinical seizure on the fourth day with subsequent nonconvulsive status epilepticus, which was revealed on video-electroencephalography and required multiple antiepileptic agents. MR imaging showed no acute infarction but a few chronic microhemorrhages (Fig 1A) and some white matter changes. Due to the presence of chronic microhemorrhages, the differential diagnosis of vasculitis or amyloid angiopathy was entertained. Conventional angiography showed normal intracranial arteries. VWMRI (3D T1-weighted fast-spin-echo sequence with variable refocusing flip angle acquisition with inherent black-blood effect [sampling perfection with application-optimized contrasts by

Received October 17, 2019; accepted after revision January 9, 2020.

From the Departments of Neurology (Q.H.), Pathology (N.M.T.), Neurosurgery (H.S., C.P.K.), and Radiology (K.N.), Icahn School of Medicine at Mount Sinai, New York, New York; and Department of Radiological Sciences (K.N.), David Geffen School of Medicine, University of California at Los Angeles, Los Angeles, California.

Paper previously presented, in part, at: Annual Meeting of American Society of Neuroradiology, May 18–23, 2019; Boston, Massachusetts.

Please address correspondence to Kambiz Nael, MD, David Geffen School of Medicine at UCLA, Department of Radiological Sciences, 757 Westwood Plaza, Suite 1621D, Los Angeles, CA, 90095-7532; e-mail: kambiznael@gmail.com; @kambiznael



Indicates article with supplemental on-line table.

<http://dx.doi.org/10.3174/ajnr.A6445>

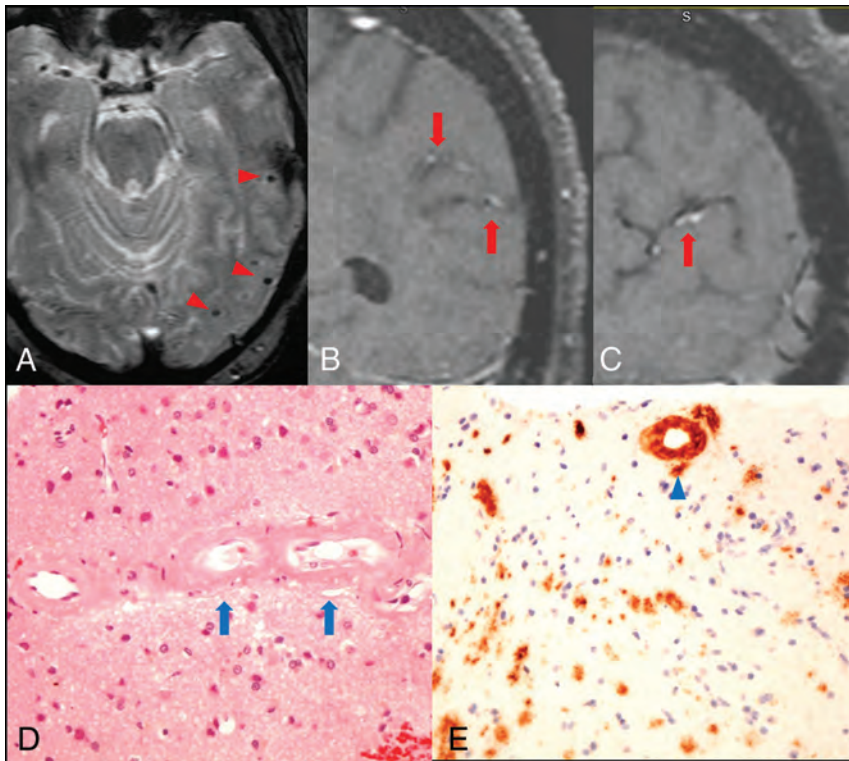


FIG 1. Arterial wall enhancement is associated with amyloid accumulation within the vessel wall. *A*, Gradient-echo image shows microhemorrhages in the left temporal lobe (*red arrowheads*). *B* and *C*, coronal and sagittal views of postcontrast T1-weighted VWMRI show enhancement in the wall of cortical branches of the left middle cerebral artery in the parietal and temporal lobes (*red arrows*). *D*, Hematoxylin-eosin stain of a left temporal lobe sample shows thickened, hyalinized blood vessels containing amorphous eosinophilic material (*blue arrows*) in small- and medium-sized arteries within the leptomeninges and superficial cortical gray matter. *E*, Immunostain for β -amyloid shows amyloid accumulation within the vessel wall (*blue arrowhead*). No inflammatory cells were observed surrounding the vessels.

using different flip angle evolution, SPACE sequence; Siemens, Erlangen, Germany]: FOV, 230 mm; TR/TE, 700/18 ms; matrix, 256 mm²; 144 sections \times 0.9-mm thick; voxels, 0.9 \times 0.9 \times 0.9 mm³) on the eighth day of admission showed arterial wall enhancement along the cortical branches of the left middle cerebral artery in the left parietal and temporal lobes (Fig 1*B*, -*C*). Findings of clinical and laboratory work-ups were negative for CNS infection, systemic vasculitis, or metabolic abnormalities except for elevated blood glucose (340 mg/dL on admission). Biopsy revealed β -amyloid accumulation in the vessel wall without associated inflammation (Fig 1*D*, -*E*).

Following institutional review board approval, we subsequently reviewed digital charts of patients with a histologically proved diagnosis of noninflammatory CAA between August 2010 and February 2019. From a total of 10 patients identified, only 4 patients had adequate imaging for inclusion in this study (no MR imaging, $n = 2$; inadequate MR imaging image quality to assess vessel wall enhancement, $n = 4$). Of these 4 patients, 1 demonstrated arterial wall enhancement similar to that in our report. Clinical and demographic data, imaging findings including VWMRI and the number of microhemor-

rhages, and histopathologic findings are summarized in the On-line Table.

DISCUSSION

Intracranial vessel wall enhancement detected by high-resolution MR imaging has been considered a sign of inflammation and/or vasa vasorum in-growth in patients with atherosclerosis or vasculitis.^{3,4} Although vessel wall enhancement can be expected with vascular inflammatory processes such as primary angiitis of the central nervous system or an inflammatory type of amyloid such as amyloid β -related angiitis, in our report, we show that vessel wall enhancement can also be seen in a subset of patients with noninflammatory CAA (40%). This suggests that β -amyloid accumulation by itself and without inflammation can also result in vessel wall enhancement. This report, to our knowledge, is the first on VWMRI findings in patients with histopathologically proved noninflammatory CAA. An earlier study by De Havenon et al⁵ showed vessel wall enhancement in about 50% of patients with CAA; however, in this study, there was no discrimination between inflammatory and noninflammatory CAA because the patients did not have histopathology to confirm the diagnosis.

One hypothesis or explanation for our findings is potential change and disruption of the blood-brain barrier in CAA. CAA-positive vessels often exhibit morphologic changes such as loss of smooth-muscle cells and vessel wall thickening, which, in turn, can result in increased leakiness and an increased incidence of microbleeds.^{6,7} It is likely that this increased permeability is responsible for wall enhancement in a subset of CAA (despite the absence of inflammation). Most interesting, our patients who exhibited vessel wall enhancement also had numerous microhemorrhages, while those without vessel wall enhancement had none or just a few.

There are several limitations to our study. First, our sample size is very small, precluding any meaningful statistical analysis. Second, there is potential selection bias in this retrospectively collected series. Third, due to the retrospective nature of our study, there may have been variability in our VWMRI sequence parameters. Also, we did not use delay alternating with nutation for tailored excitation (DANTE) preparation to refine our blood suppression. However, we used the best option available to us from our vendors to perform these clinical studies using FDA-approved sequences in a clinical environment. Future prospective radiologic-histologic studies using dedicated VWMRI are needed to better characterize the arterial wall changes in CAA with and

without inflammation, and their role in CAA-related cerebral pathologies.

Disclosures: Kambiz Nael—UNRELATED: Board Membership: Olea Medical, Comments: Medical Advisory Board. Qing Hao—RELATED: Support for Travel to Meetings for the Study or Other Purposes: Icahn School of Medicine at Mount Sinai, Comments: conference support from departmental research fund.

REFERENCES

1. Biffi A, Greenberg SM. **Cerebral amyloid angiopathy: a systematic review.** *J Clin Neurol* 2011;7:1–9 CrossRef Medline
2. Moussaddy A, Levy A, Strbian D, et al. **Inflammatory cerebral amyloid angiopathy, amyloid-beta-related angiitis, and primary angiitis of the central nervous system: similarities and differences.** *Stroke* 2015;46:e210–13 CrossRef Medline
3. Alexander MD, Yuan C, Rutman A, et al. **High-resolution intracranial vessel wall imaging: imaging beyond the lumen.** *J Neurol Neurosurg Psychiatry* 2016;87:589–97 CrossRef Medline
4. Lehman VT, Brinjikji W, Kallmes DF, et al. **Clinical interpretation of high-resolution vessel wall MRI of intracranial arterial diseases.** *Br J Radiol* 2016;89:20160496 CrossRef Medline
5. De Havenon A, Lobo R, Eisenmenger L, et al. **MRI detection of vessel wall inflammation and contrast leakage in cerebral amyloid angiopathy.** In: *Proceedings of the International Stroke Conference*, Houston, TX, Feb 22–24, 2017: WP138
6. Freeze WM, Bacskai BJ, Frosch MP, et al. **Blood-brain barrier leakage and microvascular lesions in cerebral amyloid angiopathy.** *Stroke* 2019;50:328–35 CrossRef Medline
7. Charidimou A, Boulouis G, Gurol ME, et al. **Emerging concepts in sporadic cerebral amyloid angiopathy.** *Brain* 2017;140:1829–50 CrossRef Medline

Reduced Global Efficiency and Random Network Features in Patients with Relapsing-Remitting Multiple Sclerosis with Cognitive Impairment

R. Hawkins, A.S. Shatil, L. Lee, A. Sengupta, L. Zhang, S. Morrow, and R.I. Aviv



ABSTRACT

BACKGROUND AND PURPOSE: Graph theory uses structural similarity to analyze cortical structural connectivity. We used a voxel-based definition of cortical covariance networks to quantify and assess the relationship of network characteristics to cognition in a cohort of patients with relapsing-remitting MS with and without cognitive impairment.

MATERIALS AND METHODS: We compared subject-specific structural gray matter network properties of 18 healthy controls, 25 patients with MS with cognitive impairment, and 55 patients with MS without cognitive impairment. Network parameters were compared, and predictive value for cognition was assessed, adjusting for confounders (sex, education, gray matter volume, network size and degree, and T1 and T2 lesion load). Backward stepwise multivariable regression quantified predictive factors for 5 neurocognitive domain test scores.

RESULTS: Greater path length ($r = -0.28, P < .0057$) and lower normalized path length ($r = 0.36, P < .0004$) demonstrated a correlation with average cognition when comparing healthy controls with patients with MS. Similarly, MS with cognitive impairment demonstrated a correlation between lower normalized path length ($r = 0.40, P < .001$) and reduced average cognition. Increased normalized path length was associated with better performance for processing ($P < .001$), learning ($P < .001$), and executive domain function ($P = .0235$), while reduced path length was associated with better executive ($P = .0031$) and visual domains. Normalized path length improved prediction for processing ($R^2 = 43.6\%$, $G^2 = 20.9$; $P < .0001$) and learning ($R^2 = 40.4\%$, $G^2 = 26.1$; $P < .0001$) over a null model comprising confounders. Similarly, higher normalized path length improved prediction of average z scores ($G^2 = 21.3$; $P < .0001$) and, combined with WM volume, explained 52% of average cognition variance.

CONCLUSIONS: Patients with MS and cognitive impairment demonstrate more random network features and reduced global efficiency, impacting multiple cognitive domains. A model of normalized path length with normal-appearing white matter volume improved average cognitive z score prediction, explaining 52% of variance.

ABBREVIATIONS: C = characteristic clustering coefficient; CI = cognitive impairment; CP = Cognitively preserved; γ = normalized clustering coefficient; HC = healthy controls; L = characteristic path length; λ = normalized path length; NAWM = normal-appearing white matter; RRMS = relapsing-remitting MS

MS is a chronic inflammatory disease of the central nervous system characterized by WM and GM axonal loss and demyelination and associated with whole-brain atrophy.¹ The most commonly described manifestation of MS is physical disability, but cognitive impairment is common and underrecognized.² Historically, WM lesions were considered the primary contributing

factor to impairment; however, WM damage only partly accounts for functional status, and recent studies have shown that structural GM measures are crucial contributors to disease manifestation.^{3,4} A recently introduced method of GM analysis differs from traditional voxel- and surfaced-based methods by taking advantage of graph theory applications and MR imaging to obtain parameters that reflect the structural connectivity of the cortex.⁵

By means of a graph theoretical approach, sets of nodes describe spatial regions of gray matter, either obtained from an atlas⁶ or defined by cubes of voxels,⁵ and the edges describe the

Received March 29, 2019; accepted after revision January 11, 2020.

From the Department of Medical Imaging (R.H., A.S.S., A.S., L.Z.) and Division of Neurology (L.L.), Department of Medicine, Sunnybrook Health Sciences Centre, Toronto, Ontario, Canada; Division of Neurology (S.M.), Lawson Health Research Institute, London Health Sciences Centre, University Hospital, London, Ontario, Canada; Institute of Biomaterials and Biomedical Engineering (R.I.A.), University of Toronto, Toronto, Ontario, Canada; and Department of Radiology (R.I.A.), University of Ottawa, and Division of Neuroradiology, The Ottawa Hospital, Ottawa, Ontario, Canada.

Biostatistician: Dr Liying Zhang

Dr Aviv was supported by a Physicians Services Incorporated Foundation grant No. 16-40.

Please address correspondence to Richard I. Aviv, MBChB, Department of Radiology, University of Ottawa, CPCR Building, Room L2121, Ottawa, ON K1H1M2, Canada; e-mail: raviv@toh.ca; @OttawaRadCME

Indicates article with supplemental on-line table.

<http://dx.doi.org/10.3174/ajnr.A6435>

structural similarity between 2 nodes. Networks defined in this way have been found to exhibit small world properties.⁷ Small world networks are more efficient systems, characterized by higher clustering and similar characteristic path length compared with randomly created networks of the same size and degree of distribution.⁸ In comparison, “regular” networks show both higher clustering and higher characteristic path length than random networks.⁸ The graph theoretical approach supports the axonal tension hypothesis, which theorizes that interconnected areas of the brain are structurally similar due to mutual tension between axons.⁹ Studies have shown that structural networks become disorganized in patients with Alzheimer disease,¹⁰ schizophrenia,¹¹ and diabetes.¹² However, studies applying this approach to patients with MS have shown contradictory results.^{6,13} Rimkus et al¹³ showed that patients with MS have a more random network topology than healthy controls (HC), whereas Tewarie et al⁶ showed that patients with MS have a more regular network topology. This inconsistency may be due to different methods of extracting structural networks and a higher percentage of patients with secondary-progressive MS included in the latter study. Patients with secondary-progressive MS have been shown to undergo different cortical atrophy patterns than patients with relapsing-remitting MS (RRMS),¹⁴ potentially altering the structural gray matter network topology and affecting whole-group analysis. Thus, although graph theoretical approaches have shown promise in other disease processes, methodologic inconsistencies in previous MS studies have prevented meaningful comparison of results.^{6,12,15}

In this study, we used a voxel-based definition of the GM structural covariance networks to determine network characteristics in a cohort of patients with RRMS with (CI) and without cognitive impairment (CP). Using the same method as Rimkus et al,¹³ we sought to determine the association between network parameters and CI. Consistent with a more small world network in normal health and degeneration to a more random network in disease, we hypothesized a higher degree and density in HC compared with patients with MS and a higher degree, density, and normalized (λ) and reduced path length in MS-CP versus MS-CI. We expand on prior reported findings by quantifying the added contribution to a model of CI of network parameters over traditional determinants such as white matter lesion load.

MATERIALS AND METHODS

Patient Cohort

Patients with RRMS were prospectively recruited for this ethics board–approved study from tertiary referral MS clinics and were age- and sex-matched with HC. MS diagnosis was established using the revised McDonald (2017) criteria by a senior MS neurologist (20 years’ experience).¹⁶ Participants’ clinical histories, including age, sex, education level, and disease duration, were recorded. Exclusion criteria were drug/alcohol abuse, relapse or corticosteroid use within the past 3 months, premorbid psychiatric history, head injury (including loss of consciousness), and concurrent morbidity (cerebrovascular disease and MR imaging/gadolinium contraindications, including impaired renal function). Eighty patients with RRMS (55 CP, 25 CI) and 18 healthy controls were recruited.

Neuropsychological Assessment

All participants were assessed for cognitive impairment using the minimal assessment of cognitive function in MS, assessing 5 cognitive domains with 7 tests. These domains include learning and memory (California Verbal Learning Test-II, Brief Visuospatial Test-revised); processing speed and working memory (Paced Auditory Serial Addition, Symbol Digit Modalities Test); executive function (Delis-Kaplan Executive Function System); verbal fluency (Controlled Oral Word Association Test); and visuospatial perception/spatial processing (Judgment of Line Orientation test). Age- and sex-adjusted normative data were used to convert raw test scores to *z* scores.¹⁷ *Z* scores less than -1.5 for a single test defined impairment, and patients impaired on ≥ 2 tests were considered impaired for MS group dichotomization, whereas an average *z* score was also calculated for each patient.

Image Acquisition

MR imaging was performed on a 3T MR imaging system (Magnetom Prisma; Siemens, Erlangen, Germany) with a 20-channel phased array coil. The acquisitions included sagittal volumetric T1 (TR/TE/flip angle, 2300 ms/2.26 ms/9°; number of averages, 1; FOV, 256 mm; section thickness, 1 mm; matrix size, 256 × 256 mm); T2 sampling perfection with application-optimized contrasts by using different flip angle evolution (SPACE sequence; Siemens) (TR/TE, 3200/408 ms; FOV, 230 mm; section thickness, 0.9 mm; matrix, 230 × 230 mm); T2 FLAIR (TR/TE, 500/387 ms; FOV, 230 mm; section thickness, 0.9 mm; matrix, 230 × 230 mm); and phase-sensitive inversion recovery (TR/TE, 2900/9.5 ms; FOV, 220 mm; section thickness, 2 mm; matrix, 220 × 176).

Segmentation and Lesion Measurement

T2 FLAIR images were coregistered to structural T1-weighted images by Statistical Parametric Mapping software, Version 12 (SPM 12; <http://www.fil.ion.ucl.ac.uk/spm/software/spm12>). A neuroradiologist (17 years of experience) used the threshold function in Analyze (Version 12.0; AnalyzeDirect, Overland Park, Kansas) to derive the WM T2-hyperintense and T1-hypointense lesion tracings on T1 and T2 images. Lesion volumes were filled using the SPM SLF Toolbox (<https://github.com/NIC-VICOROB/SLF>) to remove segmentation errors.¹⁸ Lesion-filled T1 images were automatically segmented into cortical GM, WM, and CSF volumes using the SPM12 segmentation tool (<https://neuroimage.usc.edu/brainstorm/Tutorials/SegCAT12>) with the minimum probability of cortical GM set to 70% to correct for GM/WM partial volume effects. The segmentations were inspected visually, and no scan was excluded. GM volumes were realigned with the standard space Montreal Neurological Institute T1 template and resliced into 2 × 2 × 2 mm³ isotropic voxels. Deep GM structure volumes (ie, basal ganglia and thalamus) were segmented using the FMRIB Integrated Registration and Segmentation Tool, Version 5 (<https://fsl.fmrib.ox.ac.uk/fsl/fslwiki/FIRST>).

Gray Matter Network Construction

Network construction was performed using a previously published process available on-line at https://github.com/bettytijms/Single_Subject_Gray_Matter_Networks.⁶ Briefly, realigned and

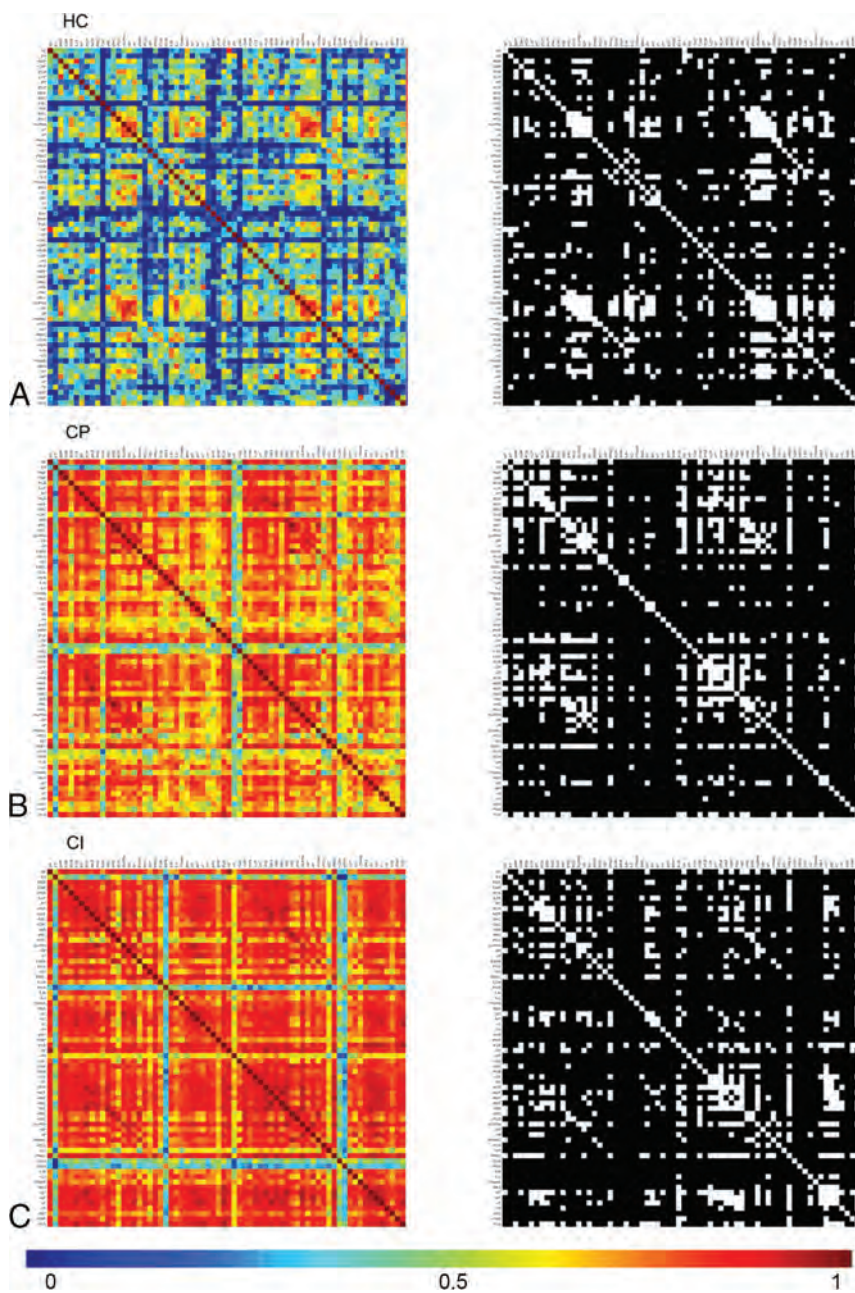


FIGURE. Pearson correlations (edges) between all pairs of GM regions (nodes) for a group of subjects. Here the rows/columns denote the nodes, and the warmer colors represent the greater edge weights/connectivity between the nodes. The colored matrices (*left column*) here show the weighted undirected network, where the edges are associated with the strength of the connection and are undirected (ie, if node *j* is connected to node *k*, then node *k* is also connected to node *j*), resulting in a symmetric connectivity matrix. The black-white matrices are binary undirected networks, where edges are either 0 or 1, indicating the absence or presence of a connection, and they have no directionality. Nodal correlations are proportional to longer path length. MS-CI shows a warmer matrix than MS-CP or HC.

resliced GM segmentations were divided into $3 \times 3 \times 3$ voxel cubes representing the nodes in the structural network. Two nodes were connected by an edge when their Pearson correlation coefficient exceeded a certain threshold. To correct for cortical curvature, we rotated cubes by multiples of 45° and reflected them over all axes to find the maximum correlation coefficient between each pairing (Figure, left column matrices).

The similarity matrices were then binarized using a subject-specific threshold based on permutation testing to ensure a similar chance of including 5% spurious correlations for each patient (Figure, right column matrices).¹³ The resulting unweighted, undirected networks were used to calculate the following network parameters: size, degree, connectivity density, betweenness centrality, characteristic clustering coefficient (*C*), and characteristic path length (*L*). Network measures were calculated using the Brain Connectivity Toolbox (<https://www.nitrc.org/projects/bct/>). Definitions for the network parameters are the following¹⁹—size: total number of nodes present in the network; degree: average number of edges connected to each node divided by the total number of nodes; density: number of edges present in the network divided by the number of possible edges; betweenness centrality: number of shortest paths that pass through a given node; *C*: how many of the nodes are connected to a given node, which are also connected to one another; and *L*: average of smallest number of edges connecting all possible pairs of nodes.

Normalized clustering coefficient (γ) and normalized path length (λ) were calculated by dividing *C* and *L* respectively by *C* and *L*, obtained from averaging over 20 randomized networks of the same size and degree distribution.¹³ The small world coefficient of the network was then calculated by dividing γ/λ . Small world networks have a characteristic clustering coefficient much larger than random networks and a characteristic path length approximately equal to those of random networks. Thus, a small world network can be seen when $\gamma/\lambda > 1$.²⁰

Size, degree, and density are included as potential confounders for more complex network parameters. Characteristic clustering coefficient and path length are included as important descriptors of graph topology and graph connectivity. γ , λ , and small world coefficient are included as quantifiers for randomness and small worldness. The betweenness coefficient is included to determine regional hubs in future analyses.

Table 1: Demographic and clinical characteristics of healthy controls and patients with MS

Characteristics	HC	MS		
		Total Sample	MS-CP	MS-CI
No.	18	80	55	25
Female sex (No.) (%)	13 (72%)	54 (68%)	41 (75%)	13 (52%) ^a
Age (mean) (SD) (yr)	48.7 (7.2)	51.8 (8.6)	52.7 (8.8)	49.7 (7.9)
Education (mean) (SD) (yr)	17.0 (2.9)	15.0 (2.4) ^b	15.2 (2.2)	14.6 (2.7)
Disease duration (mean) (SD) (yr)	NA	15.8 (8.9)	15.7 (8.4)	15.9 (9.9)
EDSS (mean) (SD)	NA	4.3 (2.3)	4.1 (2.4)	4.6 (2.2)
T1 lesion load (mean) (SD)	NA	4.0 (5.6)	2.8 (3.3)	6.7 (8.3) ^c
T2 lesion load (mean) (SD)	NA	15.8 (15.8)	11.8 (11.2)	24.6 (20.5) ^c
Global gray matter volume (mean) (SD)	875.9 (48.9)	748.5 (69.6) ^d	761.2 (65.9)	720.6 (70.8) ^a
NAWM volume (mean) (SD)	616.2 (39.9)	510.9 (101.3) ^d	540.9 (56.3)	444.7 (141.5) ^e
Neurocognitive domain score (mean) (SD)				
Processing	-0.17 (0.74)	-0.90 (0.99) ^e	-0.43 (0.68)	-2.01 (0.65) ^f
Learning	0.12 (0.73)	-0.80 (1.29) ^e	-0.093 (0.76)	-2.35 (0.74) ^f
Executive functioning	0.50 (0.75)	-0.062 (1.12)	0.30 (0.80)	-0.85 (1.32) ^f
Visual	0.98 (0.20)	0.55 (0.91)	0.79 (0.86)	0.010 (0.80) ^f
Language	-0.70 (0.84)	-0.86 (1.05)	-0.56 (0.84)	-1.53 (1.17) ^f
Average z score	0.15 (0.41)	-0.42 (0.80) ^e	-0.003 (0.48)	-1.34 (0.54) ^f

Note:—NA indicates not applicable; EDSS, Expanded Disability Status Scale.

^a Adjusted $P < .05$ (comparison within MS groups is based on cognitive impairment status).

^b Adjusted $P < .05$ (comparison of total sample of MS patients with healthy control).

^c Adjusted $P < .01$ (comparison within MS groups is based on cognitive impairment status).

^d Adjusted $P < .001$ (comparison of total sample of MS patients with healthy control).

^e Adjusted $P < .01$ (comparison of total sample of MS patients with healthy control).

^f Adjusted $P < .001$ (comparison within MS groups is based on cognitive impairment status).

Statistical Analysis

Demographic factors were compared between all patients with MS and HC or between patients with MS-CI and MS-CP using the Wilcoxon rank sum test for continuous variables and the Fisher exact test or χ^2 test for categorical variables as appropriate. Using the ANCOVA with the Fisher least significant difference test correction, we compared the network parameters between groups, accounting for confounding factors including sex, education, global GM volume, NAWM, and factors of size, degree, and density. Confounding factors included sex, education, global gray matter volume, network size and degree, and T1 and T2 lesion loads. To normalize distributions for T1 and T2 lesion loads, we used natural log transformation. Similarly, the associations between each of 9 network parameters and each of 6 neurocognitive domain test scores were tested in patients with MS only. To control for the multiple comparisons, we applied the Benjamini-Hochberg adaptive linear step-up method,²¹ and the adjusted P value $< .05$ was considered statistically significant. Partial correlation coefficients were calculated after accounting for confounding factors to determine the correlation of each network parameter to average cognition by calculating an average z score for each study participant. Using the backward stepwise selection procedure in the multivariable linear regression analysis, we would search for the most significant predictive factors for each of 5 neurocognitive domain test scores in MS. R^2 was estimated as the goodness-of-fit for each of the models. The higher the R^2 value, the better was the model fit. To evaluate significant influence from network predictors associated to neurocognitive domain scores, we performed the G^2 likelihood ratio test. The G^2 likelihood ratio statistic is the difference between $-2L$ (log

likelihood) of the fitted model (ie, the model includes both significant network predictors and demographic variables) and the reference null model (ie, the model includes only confounding factors of sex, education, global GM volume, and T1 and T2 lesion loads). The P value was obtained from the G^2 likelihood ratio χ^2 test, and $P < .05$ was considered statistically significant. Multicollinearity was tested using the variance inflation factor. All analyses were conducted by SAS, Version 9.4 for Windows (SAS Institute, Cary, North Carolina).

RESULTS

Group Demographics

Eighteen HC (mean age, 48.7 ± 7.2 years; 72% women) and 80 patients with MS (mean age, 51.8 ± 8.6 years; 68% women) with a mean education of 15 ± 2.4 years, disease duration of 15.8 ± 8.9 years, and mean Expanded Disability Status Scale score of 4.3 ± 2.3 were included. There was no difference in the frequency of disease-

modifying drug use between groups ($P = .80$).

CI was present in 25/80 (31%) of patients. Increased T1 and T2 lesion loads and reduced global GM volume and lower average and individual domain z scores were present in MS-CI versus MS-CP. A greater proportion of women composed the MS-CP cohort (75% versus 52%). Compared with HC, patients with MS demonstrated an average of 2 fewer years of education and reduced global GM volume and z scores for processing, learning, and average cognition (Table 1). Size and degree were higher in HC versus patients with MS (Table 2), but only degree remained significantly different after correcting for other confounders. Therefore, degree was added as an additional confounder when comparing the other network parameters between HCs and the MS cohort. Size, density, and degree were not significantly different between MS-CP and MS-CI.

Patients with MS demonstrated increased path length ($P = .03$) and reduced λ ($P = .02$) compared with HC. λ ($P = .006$) was reduced in MS-CI versus MS-CP (Table 2). Lower λ ($r = 0.36$, $P < .0004$) and greater path length ($r = -0.28$, $P < .0057$) demonstrated a correlation with average cognition when comparing HC with patients with MS. Similarly, MS-CI demonstrated a correlation between reduced λ ($r = 0.40$, $P < .001$) and lower average cognition.

Association between Network Parameters and Cognitive Domains

The On-line Table demonstrates the association in patients with MS between global GM network properties and the 5 cognitive domains. Network parameters positively associated with average cognition were density ($P = .002$), degree ($P = .02$), clustering

Table 2: Values of global gray matter network properties between HC and patients with MS and within the MS sample based on cognitive status^a

Network Properties (Mean) (SD)	MS			
	HC	Total Sample	MS-CP	MS-CI
No.	18	80	55	25
Size	6950.17 (700.80)	6677.81 (589.84)	6607.64 (575.60)	6832.20 (603.02)
Degree	1234.59 (129.73)	1064.42 (124.89) ^b	1080.08 (113.24)	1029.97 (143.86)
Density (%)	17.77 (0.77)	15.97 (1.59)	16.37 (1.31)	15.10 (1.82)
Clustering	0.439 (0.013)	0.396 (0.034)	0.405 (0.027)	0.377 (0.040)
Betweenness	5998.11 (609.99)	5816.27 (534.55)	5741.29 (513.53)	5981.22 (553.17)
Path length	1.863 (0.009)	1.871 (0.014) ^b	1.869 (0.012)	1.875 (0.016)
γ	1.086 (0.003)	1.081 (0.005)	1.081 (0.004)	1.079 (0.006)
λ	1.021 (0.003)	1.015 (0.004) ^b	1.016 (0.003)	1.012 (0.004) ^c
Small world	1.064 (0.003)	1.065 (0.004)	1.064 (0.004)	1.067 (0.005)

^a HC versus MS group was statistically compared taking into account sex, education, and global gray matter volume; and the MS-CP versus MS-CI groups were compared with 2 additional confounding factors of T1 and T2 lesion loads (log). Data are corrected for multiple comparisons.

^b Adjusted $P < .05$ (comparison of total sample of MS patients with healthy control).

^c Adjusted $P < .01$ (comparison within MS group based on cognitive impairment status).

Table 3: Predictors of neurocognitive domain scores in total groups of patients with MS^a

	Standardized Coefficients β		Comparing with the Reference Model ^b (G^2) (P Value)
	β (95% CI)	Significance	
Processing ($R^2 = 43.6\%$)			20.9 (<.0001)
NAWM volume	0.298 (0.047–0.616)	.0229	
λ	0.548 (0.236–0.895)	.0011	
Learning ($R^2 = 40.4\%$)			26.1 (<.0001)
Education	0.205 (0.022–0.388)	.0283	
T1 lesion loads (log)	–0.300 (–0.581 to –0.019)	.0369	
λ	0.622 (0.332–0.913)	<.0001	
Executive functioning ($R^2 = 41.0\%$)			4.4 (.1108)
Education	0.354 (0.170–0.539)	.0003	
NAWM volume	0.274 (0.020–0.527)	.0348	
Degree	0.313 (0.095–0.531)	.0055	
Visual ($R^2 = 27.5\%$)			9.2 (.0024)
Sex (M/F)	0.293 (0.056–0.530)	.0160	
T2 lesion loads (log)	0.367 (0.204–0.714)	.0383	
Density (%)	0.523 (0.236–0.809)	.0005	
Language ($R^2 = 35.8\%$)			7.9 (.0953)
EDSS (log)	–0.376 (–0.648 to –0.104)	.0074	
Disease duration (log)	0.224 (0.007–0.441)	.0433	
NAWM volume	0.318 (0.037–0.600)	.0274	
Degree	–0.254 (–0.486 to –0.021)	.0330	
Average score ($R^2 = 56.2\%$)			21.3 (<.0001)
Education	0.305 (0.139–0.471)	.0005	
T1 lesion loads (log)	–0.261 (–0.515 to –0.008)	.0434	
NAWM volume	0.343 (0.109–0.576)	.0046	
λ	0.404 (0.12–0.696)	.0073	

^a Backward stepwise elimination multivariable regression was conducted after accounting for sex, education, global gray matter volume, and T1 and T2 lesion loads (log). The Table shows the best regression model for each dependent variable (neurocognitive domain scores).

^b Reference model included only confounding factors of sex, education, global gray matter volume, and T1 and T2 lesion loads (log). The G^2 likelihood ratio test was used to compare the best regression model with the reference model. $P < .05$ was considered statistically significant.

($P = .001$), and λ ($P < .001$), while path length ($P = .04$) was inversely associated. Increased λ was associated with better performance for processing ($P < .001$), learning ($P < .001$), and executive domain function ($P = .0235$), while reduced path length was associated with better executive ($P = .0031$) and visual domains. Higher clustering was seen in association with executive ($P = .0004$) and visual ($P = .0007$) domains. Increased degree and

density were seen with better executive and visual ($P = .0269$ and $P = .0008$) domains, respectively, whereas size was increased with better executive functioning ($P = .0315$). Betweenness, γ , and small world parameters were not associated with any domains.

Predictors of Cognitive Impairment

Network parameters were significantly associated with models of cognitive impairment in each domain. The predictive models of cognitive performance that included the network parameters demonstrated a better model fit than the null model in the processing, learning, and visual domains and for average cognition. λ improved prediction for processing ($R^2 = 43.6\%$, $G^2 = 20.9$; $P < .0001$) and learning ($R^2 = 40.4\%$, $G^2 = 26.1$; $P < .0001$). Density improved prediction of impairment in the visual domain ($R^2 = 27.5\%$, $G^2 = 9.2$; $P = .0024$). While degree was significantly associated with executive and language domains, the parameter did not improve the predictive model significantly over the null model. A higher λ improved prediction of the average z score, ($G^2 = 21.3$; $P < .0001$) and, together with WM volume, explained 52% of average cognition model variance (Table 3).

DISCUSSION

We demonstrate a reduction in λ between HC and patients with MS-CP and MS-CI after correcting for confounding factors, including global GM, sex and education, and lesion load in the MS subgroup. Reduced λ was directly correlated with average cognition and associated with impaired performance in processing, learning, and executive domains. λ improved prediction for performance within the processing domain and accounted for 43.6% of the variance.

λ also accounted for 40% of the variance within the learning domain. Path length was increased in patients with MS compared with HC and correlated with reduced executive and visual domain functioning. No associations with cognition were found for betweenness, γ , or small world variables.

Graph theory or network neuroscience is used to represent the matrix of global brain organization and structural or

functional connectivity by providing a mathematic framework to model the pair-wise communications between elements of a network. This, in turn, gives insight into how cognitive function is linked to neuronal network structure. Loss of white matter structural integrity and network integration is posited as a significant determinant of cognitive impairment in the “disconnection hypothesis”; however, white matter lesions are characterized by varying degrees of axonal and myelin loss, despite similar macroscopic appearances on MR imaging.²² By controlling for multiple confounding factors, including both T1 and T2 white matter lesion load, our results indicate that network parameters explain variance in cognition beyond that of conventional structural parameters. Normalized path length or λ together with normal-appearing white matter volume added to a model of average z score explained 52% of variance. Rimkus et al¹³ demonstrated that a lower λ value was associated with worse average cognition, processing, and executive functioning, while Dicks et al²³ showed an association between λ reduction and executive functioning.

We extend these findings by showing that λ was also associated with the learning domain and improved predictive models, accounting for a high degree of variance for processing and learning. Reduction in λ is indicative of a more random network and mirrors prior findings in MS, mild cognitive impairment, and Alzheimer disease.^{13,23,24} Our results reinforce the link between reduced white matter integrity and impairment, particularly in executive functioning and processing speed.²⁵ fMRI studies suggest that executive functioning is dependent on a bilateral brain network that requires efficient pathways connecting the dorsolateral prefrontal, anterior cingulate, and parietal cortices. Similarly, macrostructural white matter abnormality is linked to impairment in processing speed in neurologically healthy elderly subjects from a population-based random sample.²⁶

A prior study showed that a short path length is a characteristic feature of the normal human cortex⁷ and corresponds to a high global efficiency. Progressive white matter disease burden in MS causes impairment in global efficiency, characterized by node disconnection and an increase in path length, similar to our findings.^{24,27} Reduced global efficiency is also consistent with prior fMRI studies demonstrating lower functional network integration in patients with MS.^{28,29} The relationship between white matter damage and global efficiency may support the axonal tension hypothesis, which purports that axonal tension between interrelated cortical areas induces gyration and influences the degree of compactness of neural circuits within the brain.⁹ The codependence of path length and white matter disease extent may also explain why path length did not appear in predictive modeling of cognitive domains. Our findings are disparate from those of Rimkus et al,¹³ who observed that a higher path length value could be a consequence of loss of density of connections and reported a shift with cognitive impairment from increased-to-reduced path length after correcting for density. We explored the association between degree and density and all network parameters including path length but revealed a confounding effect only for degree, not density. Degree depends on the number and quality of connections between nodes and thus provides more information than standard structural parameters. In contrast, GM atrophy decreases the volume available for creating nodes, directly

affecting graph size and explaining why only degree remained significant after correcting for GM volume.

Prior studies have reported both increased and reduced path lengths with cognitive impairment in MS, mild cognitive impairment, Alzheimer disease, and patients with diabetic retinopathy.^{6,12,13,23,27,30} Multiple potential explanations exist for this apparent disparity. There is a paucity of data characterizing changes in network parameters with disease duration or disease subtype, especially in MS. Study differences may therefore reflect cohort differences in disease subtype and duration between the 2 studies or indicate a nonlinear path length response with disease. Further clarification of the effect of MS disease subtype and longitudinal network changes is needed. Tewarie et al⁶ showed a heterogeneous pattern of spatial reconfiguration of interregional cortical thickness in RRMS. While the global structural covariance was unaffected compared with HC, the association between functional connectivity and covariation in cortical thickness showed both higher and lower functional connectivity, dependent on the magnetoencephalography frequency band. Differences were attributed to differential cortical layer responses to frequency and differences in local and global characteristics of the neuronal population. Similarly, functional and diffusion tensor MR imaging studies have demonstrated both increased and reduced cortical activations and connectivity, respectively, in patients with MS-CI compared with HC, thought to reflect network reorganization and cortical plasticity, a known hallmark of early disease.^{15,21}

Limitations of the study include the use of a 3×3 voxel size to represent individual nodes. It is uncertain what the optimum cube size is for adequate representation of cortical folding, convolution, and thickness. However, the cube size used in this study is consistent with prior publications. Reproducibility of node selection was not tested but is previously reported in HC.³¹ While we studied global network parameters and cognition, previous studies have shown correlations between regional (rather than global) parameters and cognitive outcomes for attention and executive functioning domains,¹⁵ average cognition, and information processing.⁶ A regional analysis would be useful to validate prior studies and better define the topographic relationship between graph parameters and cognitive domains. The cross-sectional design of this study cannot address temporal changes in network parameters or evaluate the impact of progressive cognitive or motor deterioration on these parameters. A better understanding of the impact of structural and clinical changes on network parameters is important but can only be addressed with longitudinal studies. Pathologic correlates of measured network parameters are unknown, and further study will be needed to ascertain the utility of these measures as biomarkers of disease assessment and prognostication. However, monitoring of graph parameters may potentially provide the clinician with insight into the structural or functional integrity of the connectome. Used in this way, the parameters could serve as surrogates for monitoring the efficacy of disease control and to detect early changes that may signify a decline in network efficiency that preempts cognitive impairment. The biologic processes underlying the graph theoretical approach are not yet fully understood.⁵ Further research is

needed to confirm that structural similarity is a suitable biomarker of physical connectedness.

CONCLUSIONS

Patients with MS with CI demonstrate more random network features and reduced global efficiency impacting multiple cognitive domains. A model of λ with normal-appearing white matter volume improved average cognitive z score prediction, explaining 52% of variance.

Disclosures: Liesly Lee—UNRELATED: Consultancy: Roche Canada Advisory Board, Genzyme Canada Advisory Board; Payment for Lectures Including Service on Speakers Bureaus: Genzyme Canada evening dinner lecture. Richard I. Aviv—RELATED: Grant: Physician Services Incorporated Foundation.* Sarah Morrow—UNRELATED: Board Membership: Consortium of Multiple Sclerosis Centers, Americas Committee for Treatment and Research in Multiple Sclerosis; Consultancy: Biogen, Celgene, EMD Serono, Genzyme, Novartis, Roche, Teva Neuroscience; Grants/Grants Pending: AbbVie, Biogen, EMD Serono, Genzyme, Novartis, Roche*; Payment for Lectures Including Service on Speakers Bureaus: Biogen, Celgene, EMD Serono, Genzyme, Novartis, Roche. *Money paid to the institution.

REFERENCES

1. Kipp M, van der Valk P, Amor S. **Pathology of multiple sclerosis.** *CNS Neurol Disord Drug Targets* 2012;11:506–17 CrossRef Medline
2. Sbardella E, Petsas N, Tona F, et al. **Assessing the correlation between grey and white matter damage with motor and cognitive impairment in multiple sclerosis patients.** *PLoS One* 2013;8:e63250 CrossRef Medline
3. Geurts JJ, Barkhof F. **Grey matter pathology in multiple sclerosis.** *Lancet Neurol* 2008;7:841–51 CrossRef Medline
4. Bo L, Geurts JJ, van der Valk P, et al. **Lack of correlation between cortical demyelination and white matter pathologic changes in multiple sclerosis.** *Arch Neurol* 2007;64:76–80 CrossRef Medline
5. Tijms BM, Series P, Willshaw DJ, et al. **Similarity-based extraction of individual networks from gray matter MRI scans.** *Cereb Cortex* 2012;22:1530–41 CrossRef Medline
6. Tewarie P, Steenwijk MD, Tijms BM, et al. **Disruption of structural and functional networks in long-standing multiple sclerosis.** *Hum Brain Mapp* 2014;35:5946–61 CrossRef Medline
7. He Y, Chen ZJ, Evans AC. **Small-world anatomical networks in the human brain revealed by cortical thickness from MRI.** *Cereb Cortex* 2007;17:2407–19 CrossRef Medline
8. Watts DJ, Strogatz SH. **Collective dynamics of ‘small-world’ networks.** *Nature* 1998;393:440–42 CrossRef Medline
9. Van Essen DC. **A tension-based theory of morphogenesis and compact wiring in the central nervous system.** *Nature* 1997;385:313–18 CrossRef Medline
10. He Y, Chen Z, Gong G, et al. **Neuronal networks in Alzheimer’s disease.** *Neuroscientist* 2009;15:333–50 CrossRef Medline
11. Tijms BM, Sprooten E, Job D, et al. **Grey matter networks in people at increased familial risk for schizophrenia.** *Schizophr Res* 2015; 168:1–8 CrossRef Medline
12. van Duinkerken E, Ijzerman RG, Klein M, et al. **Disrupted subject-specific gray matter network properties and cognitive dysfunction in type 1 diabetes patients with and without proliferative retinopathy.** *Hum Brain Mapp* 2016;37:1194–208 CrossRef Medline
13. Rimkus CM, Schoonheim MM, Steenwijk MD, et al. **Gray matter networks and cognitive impairment in multiple sclerosis.** *Mult Scler* 2018;25:382–91 CrossRef Medline
14. Pagani E, Rocca MA, Gallo A, et al. **Regional brain atrophy evolves differently in patients with multiple sclerosis according to clinical phenotype.** *AJNR Am J Neuroradiol* 2005;26:341–46 Medline
15. Fleischer V, Groger A, Koirala N, et al. **Increased structural white and grey matter network connectivity compensates for functional decline in early multiple sclerosis.** *Mult Scler* 2017;23:432–41 CrossRef Medline
16. Thompson AJ, Banwell BL, Barkhof F, et al. **Diagnosis of multiple sclerosis: 2017 revisions of the McDonald criteria.** *Lancet Neurol* 2018;17:162–73 CrossRef Medline
17. Walker LA, Marino D, Berard JA, et al. **Canadian Normative Data for Minimal Assessment of Cognitive Function in Multiple Sclerosis.** *Can J Neurol Sci* 2017;44:547–55 CrossRef Medline
18. Valverde S, Oliver A, Llado X. **A white matter lesion-filling approach to improve brain tissue volume measurements.** *Neuroimage Clin* 2014;6:86–92 CrossRef Medline
19. Rubinov M, Sporns O. **Complex network measures of brain connectivity: uses and interpretations.** *Neuroimage* 2010;52:1059–69 CrossRef Medline
20. Humphries MD, Gurney K. **Network ‘small-world-ness’: a quantitative method for determining canonical network equivalence.** *PLoS One* 2008;3:e0002051 CrossRef Medline
21. Staffen W, Mair A, Zauner H, et al. **Cognitive function and fMRI in patients with multiple sclerosis: evidence for compensatory cortical activation during an attention task.** *Brain* 2002;125:1275–82 CrossRef Medline
22. Hogan AM, Vargha-Khadem F, Saunders DE, et al. **Impact of frontal white matter lesions on performance monitoring: ERP evidence for cortical disconnection.** *Brain* 2006;129:2177–88 CrossRef Medline
23. Dicks E, Tijms BM, Ten Kate M, et al. **Gray matter network measures are associated with cognitive decline in mild cognitive impairment.** *Neurobiol Aging* 2018;61:198–206 CrossRef Medline
24. Tijms BM, Moller C, Vrenken H, et al. **Single-subject grey matter graphs in Alzheimer’s disease.** *PLoS One* 2013;8:e58921 CrossRef Medline
25. Prins ND, van Dijk EJ, den Heijer T, et al. **Cerebral small-vessel disease and decline in information processing speed, executive function and memory.** *Brain* 2005;128:2034–41 CrossRef Medline
26. Ylikoski R, Ylikoski A, Erkinjuntti T, et al. **White matter changes in healthy elderly persons correlate with attention and speed of mental processing.** *Arch Neurol* 1993;50:818–24 CrossRef Medline
27. He Y, Dagher A, Chen Z, et al. **Impaired small-world efficiency in structural cortical networks in multiple sclerosis associated with white matter lesion load.** *Brain* 2009;132:3366–79 CrossRef Medline
28. Gamba OL, Tagliazucchi E, von Wegner F, et al. **Working memory performance of early patients with MS correlates inversely with modularity increases in resting state functional connectivity networks.** *Neuroimage* 2014;94:385–95 CrossRef Medline
29. Louapre C, Perlberg V, Garcia-Lorenzo D, et al. **Brain networks disconnection in early multiple sclerosis cognitive deficits: an anatomofunctional study.** *Hum Brain Mapp* 2014;35:4706–17 CrossRef Medline
30. Lo CY, Wang PN, Chou KH, et al. **Diffusion tensor tractography reveals abnormal topological organization in structural cortical networks in Alzheimer’s disease.** *J Neurosci* 2010;30:16876–85 CrossRef Medline
31. Tijms BM, Wink AM, de Haan W, et al. **Alzheimer’s disease: connecting findings from graph theoretical studies of brain networks.** *Neurobiol Aging* 2013;34:2023–36 CrossRef Medline

SWAN-Venule: An Optimized MRI Technique to Detect the Central Vein Sign in MS Plaques

M.I. Gaitán, P. Yañez, M.E. Paday Formenti, I. Calandri, E. Figueiredo, P. Sati, and J. Correale



ABSTRACT

BACKGROUND AND PURPOSE: Multiple sclerosis lesions develop around small veins that are radiologically described as the so-called central vein sign. With 7T MR imaging and magnetic susceptibility–based sequences, the central vein sign has been observed in 80%–100% of MS lesions in patients' brains. However, a lower proportion ~50% has been reported at 3T using susceptibility-weighted angiography (SWAN). Our aim was to assess a modified version of SWAN optimized at 3T for sensitive detection of the central vein sign.

MATERIALS AND METHODS: Thirty subjects with MS were scanned on a 3T clinical MR imaging system. 3D T2-weighted FLAIR and optimized 3D SWAN called SWAN-venule, were acquired after injection of a gadolinium-based contrast agent. Patients showing >3 focal white matter lesions were included. The central vein sign was recorded by 2 trained raters on SWAN-venule images in the supratentorial brain.

RESULTS: Twenty patients showing >3 white matter lesions were included. A total of 380 white matter lesions (135 periventricular, 144 deep white matter, and 101 juxtacortical) seen on both FLAIR and SWAN-venule images were analyzed. Overall, the central vein sign was detected in 86% of the white matter lesions (periventricular, 89%; deep white matter, 95%; and juxtacortical, 78%).

CONCLUSIONS: The SWAN-venule technique is an optimized MR imaging sequence for highly sensitive detection of the central vein sign in MS brain lesions. This work will facilitate the validation and integration of the central vein sign to increase the diagnostic certainty of MS and further prevent misdiagnosis in clinical practice.

ABBREVIATIONS: CVS = central vein sign; RRMS = relapsing-remitting MS; SWAN = susceptibility-weighted angiography; WML = white matter lesion

Pathologic studies from last century¹ have shown that MS lesions develop around small veins and venules. With the recent advancement of magnetic susceptibility–based MR imaging, these veins located centrally within MS lesions can now be depicted *in vivo*.^{2–4} Due to the paramagnetic nature of deoxyhemoglobin, venous structures can be visualized as hypointense lines or dots on susceptibility-based MR imaging (eg, T2*–weighted, susceptibility-weighted imaging). Recently, the radiologic

definition of a vein located centrally within an MS lesion, the so-called central vein sign (CVS), has been proposed by the North American Imaging in Multiple Sclerosis Cooperative.⁵

By means of the higher image resolution and stronger susceptibility contrast provided by 7T MR imaging, the percentage of lesions with the CVS has been reported to vary between 80% and 100% of white matter lesions (WMLs) in the brains of patients with MS,³ with a decreased gradient from the periventricular areas to the neocortex,⁶ with similar percentages across the different MS phenotypes.⁷ Most interesting, a lower percentage of brain lesions with the CVS (0%–45%) was observed in other neurologic disorders such as aquaporin-4 immunoglobulin G4–positive neuromyelitis optica spectrum disorder,⁸ systemic autoimmune diseases,⁹ cerebral small vessel disease,¹⁰ Susac syndrome,¹¹ and white matter migraine lesions.¹ In a recent large multicenter study from the magnetic resonance imaging in multiple sclerosis (MAGNIMS) evaluating the diagnostic value of the CVS, a sensitivity of 68.1% and a specificity of 82.9% were reported for distinguishing MS using a 35% CVS proportion threshold.¹² Therefore, CVS is a promising imaging

Received October 1, 2019; accepted after revision January 8, 2020.

From the Department of Neurology (M.I.G., J.C.), Neuroimmunology Section, and Departments of Radiology (P.Y., M.E.P.F.) and Neurology (I.C.), FLENI, Buenos Aires, Argentina; GE healthcare (E.F.), Sao Paulo, Brazil; and Translational Neuroradiology Section (P.S.), National Institute of Neurological Disorders and Stroke, National Institutes of Health, Bethesda, Maryland.

Paper previously presented at: Annual Meeting of the European Committee for Treatment and Research in Multiple Sclerosis, September 11–13, 2019; Stockholm, Sweden.

Please address correspondence to María Inés Gaitán, MD, Montañeses 2325, C1428, AQC, Buenos Aires, Argentina; e-mail: minesgaitan@gmail.com or migaitan@fleni.org.ar

<http://dx.doi.org/10.3174/ajnr.A6437>

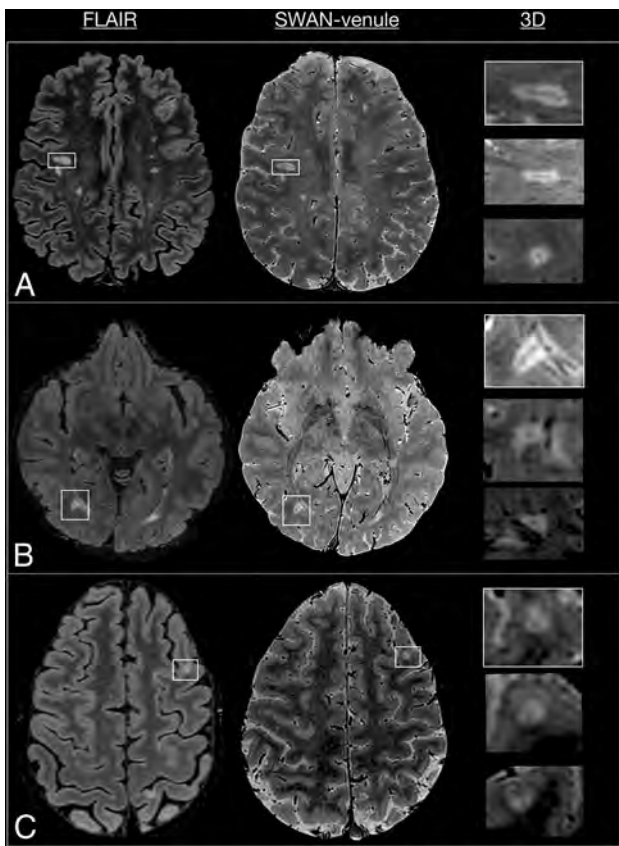


FIG 1. Comparison between FLAIR and SWAN-venule images from 3 patients with RRMS. Lesions seen in FLAIR are visible in SWAN-venule. *White boxes* mark lesions magnified in 3 planes. *A*, *White box* magnifies a deep white matter lesion. *B*, *White box* magnifies a periventricular lesion. *C*, *White box* magnifies a juxtacortical lesion.

biomarker that could help discriminate MS from its radiologic mimics and ultimately increase the accuracy of MS diagnosis⁵ and reduce misdiagnosis.¹³

A variety of susceptibility-based MR imaging sequences may be used to detect the CVS at clinical field strength (1.5T or 3T), such as susceptibility-weighted angiography (SWAN). However, SWAN has been shown to be less sensitive at 3T than optimized sequences, such as the T2*-weighted 3D echo-planar imaging sequence.¹⁴⁻¹⁶ The objective of the study was to assess the performance of a newly optimized SWAN sequence in detecting the CVS.

MATERIALS AND METHODS

Patients

Thirty patients from the FLENI MS Clinic were scanned consecutively. Brain MR imaging showing >3 typical hyperintense focal lesions was analyzed.

MR Image Acquisition

Subjects were scanned on a 3T MR imaging system (Discovery MR750; GE Healthcare, Milwaukee, Wisconsin) using a 32-channel head coil array. A comprehensive MS protocol was performed, including the following—3D T2-weighted FLAIR: FOV = 26 × 26 cm; number of slices = 146; voxel resolution = 0.47 × 0.47 × 1.2 mm; TE = 116 ms; TR = 6200 ms; TI = 1710

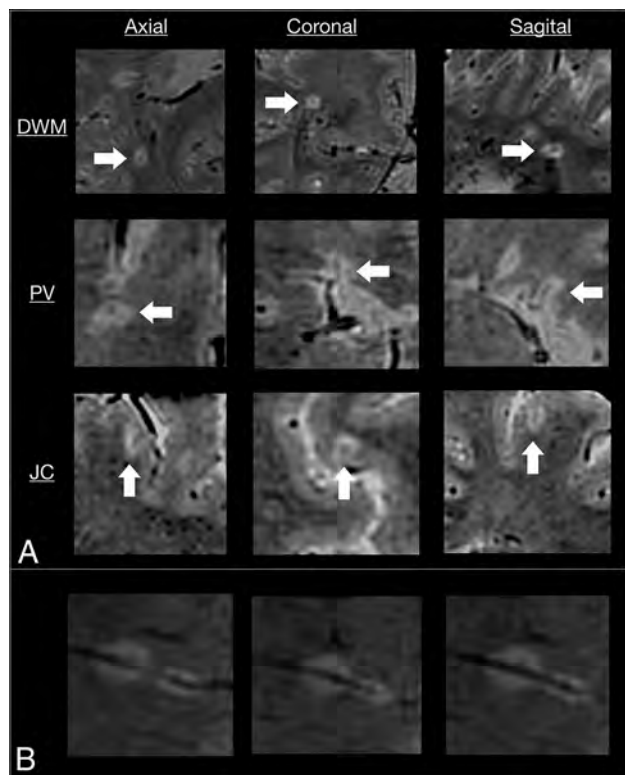


FIG 2. SWAN-venule acquired in 3 subjects with RRMS. *A*, Examples of lesions with central veins in 3 planes. In each row, *arrows* point the same lesion in three different planes. An example of a deep white matter (DWM) lesion, a periventricular lesion, and a juxtacortical lesion shows the central vein in 3 different planes. *B*, Example of 2 deep white matter lesions that developed along the same vein. PV indicates periventricular; JC, juxtacortical.

ms; echo-train length = 220; acquisition time = 4.18 minutes; and optimized 3D SWAN-venule: FOV = 22 × 16 cm; number of slices = 126; voxel resolution = 0.4 × 0.4 × 0.8 mm, with the possibility to reformat to 0.4 × 0.4 × 0.4 mm; TR = 47 ms; TE = 28 ms; flip angle = 8°; echo-train length = 9; acquisition time = 7.38 minutes. SWAN-venule was optimized by modifying the clinically available SWAN sequence in the following manner: reduction of the section thickness from 3 to 0.8 mm; reduction of the flip angle from 20° to 10° and finally to 8°, which minimized T1-weighted contrast and increased T2-weighted contrast; and reduction of the TR to the minimal value allowed by the gradient performance, reducing the acquisition time. Both FLAIR and SWAN-venule sequences were immediately acquired after the intravenous administration of 0.1 mmol/kg of gadolinium-based contrast agent (gadoterate meglumine, Dotarem; Guerbet, Aulnay-sous-Bois, France).

Image Analysis

A neuroradiologist (P.Y.) and a neurologist trained in MR imaging and MS (M.I.G.) were the 2 independent readers. Image interpretation was performed on a standard PACS workstation. The quality of SWAN-venule images for visualizing WMLs was compared with FLAIR images in 3 cases (Fig 1). SWAN-venule images were coregistered to FLAIR images using the synchronization tool of the workstation. All the supratentorial

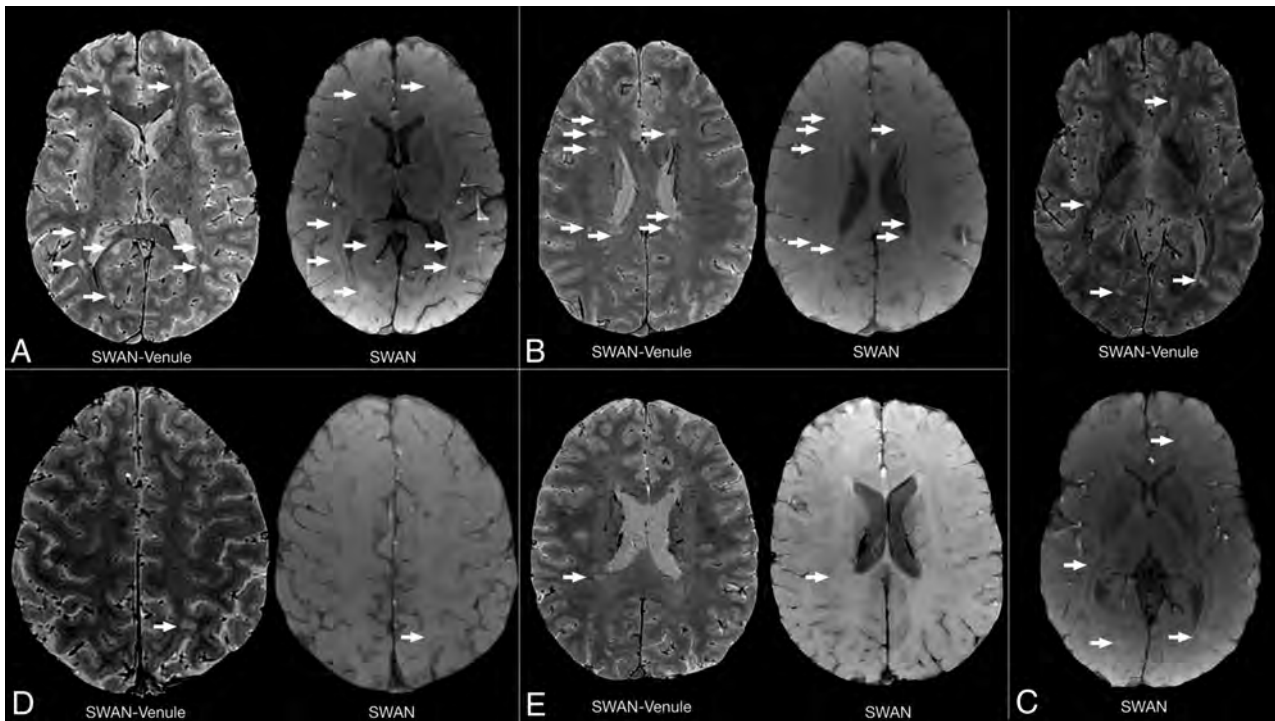


FIG 3. Quality comparison between standard SWAN and SWAN-venule. Comparison of SWAN and SWAN-venule acquired during the same year in 2 subjects with RRMS who were radiologically stable. Arrows point to lesions in SWAN-venule and the same area in SWAN, in which lesions are difficult to depict. A–C, A 28-year-old female patient with RRMS. D and E, A 31-year-old male patient with RRMS.

nonconfluent lesions, >3 mm and <15 mm in-plane, visible on both SWAN-venule and FLAIR images, were recorded. These lesions were then classified as periventricular (T2-hyperintense cerebral white matter lesions abutting the lateral ventricles without white matter in between, including lesions in the corpus callosum but excluding lesions in deep gray matter structures),^{17,18} deep white matter, or juxtacortical (T2-hyperintense cerebral white matter lesions abutting the cortex, not separated from it by white matter).^{17,18} Afterward, each lesion was evaluated for the CVS on SWAN-venule images according to the radiologic definition of the North American Imaging in Multiple Sclerosis Cooperative consensus statement:⁵ a thin hypointense line or small hypointense dot, visualized in at least 2 perpendicular MR imaging planes, centered on a lesion. Lesions with a vein located at the periphery or lesions with multiple veins were counted as negative for the CVS.

RESULTS

Participants

The complete brain MR imaging protocol was performed on 30 patients with MS. A total of 20 patients who presented with >3 supratentorial WMLs were included. Demographic and clinical information of the patients is the following: 19 with relapsing-remitting MS (RRMS); 1 with primary-progressive MS; 11 women and 9 men; mean age, 38.9 years; range, 34.8–42.9 years; mean disease duration, 5.8 years; range, 3.7–7.9 years; Expanded Disability Status Scale score range, 0–6.

White Matter Lesions

A total of 380 WMLs were analyzed, of which 135 were periventricular, 144 were deep white matter, and 101 were juxtacortical.

Central Vein Sign

Overall, 86% of the lesions (327/380) presented with the CVS. The agreement coefficient among the evaluators was 93%, with a substantial reliability of 0.71 (range, 0.61–0.81) (Cohen κ). When the lesions were classified according to their location, the central vein was detected in 89% of periventricular lesions, 95% of deep white matter lesions, and 78% of juxtacortical lesions (Fig 2).

DISCUSSION

The overinterpretation of focal nonspecific white matter lesions is an important factor contributing to MS misdiagnosis, mainly by erroneously fulfilling the radiologic criterion of dissemination in space.¹⁹ Therefore, there is an urgent need for the use of a novel radiologic biomarker specific to MS, such as the central vein sign.

In this work, an optimized SWAN sequence, called SWAN-venule, is proposed for imaging the central vein sign using 3T MR imaging. To our knowledge, there is only 1 publication that evaluated the performance of the standard SWAN sequence for detecting the CVS.¹⁵ Unlike this smaller prior study, we were able to detect 86% of CVSs when using SWAN-venule with contrast. As mentioned by the authors, it was difficult to visualize WMLs on SWAN images. We observed the same issue at our center when using the standard SWAN protocol. This problem was solved by our new SWAN-venule protocol, which uses a

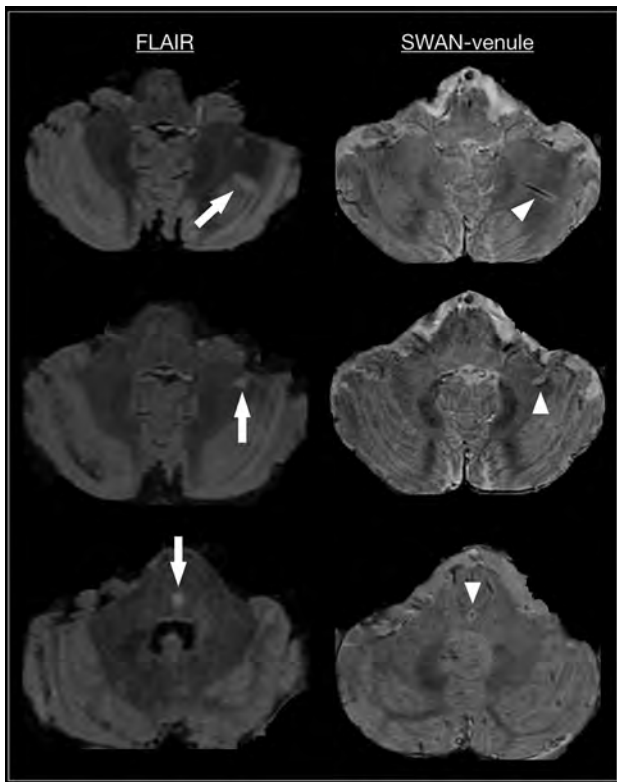


FIG 4. Axial FLAIR and SWAN-venule from 3 patients with RRMS. Arrow points to infratentorial lesions in FLAIR. Arrowhead points to the corresponding central vein in SWAN-venule.

lower flip angle, improving the tissue contrast (Fig 3). The increased sensitivity of our optimized MR imaging technique may also be due to the reduction in the voxel dimensions, allowing better capturing of small venules. Note that the use of high image resolution for SWAN-venule required a 32-channel head coil array for providing sufficient SNR. Another possible contribution is the injection of gadolinium-based contrast agent during the acquisition. As previously shown, gadolinium increases the phase effects around blood vessels, increasing the visibility of small veins.^{14,16} Because the recommended MR imaging brain protocols for MS^{20,21} require the intravenous injection of contrast followed by a 5-minute delay before the T1-weighted scan, acquiring SWAN-venule during the delay will not increase the overall scan time of the protocol. This higher percentage of WMLs centered by veins is in line with previous studies investigating the CVS in patients with MS at 7T^{3,4} or using optimized techniques at 3T, such as T2*-weighted 3D-EPI or FLAIR.^{9,13,16,22,23} Because of the use of small voxel dimensions and the 3D acquisition mode, SWAN-venule images could also be combined with 3D-FLAIR images to generate FLAIR* contrast,²⁴ thus facilitating the workflow of the CVS evaluation by requiring reading only 1 contrast image.

Although our image analysis focused on the supratentorial brain of patients with MS, we observed that most lesions visible in the brain stem and cerebellum also showed the CVS (Fig 4), similar to a previous study imaging infratentorial MS brains.² Moreover, we found a very high percentage (95%) of deep white matter lesions centered by veins. Therefore, the inclusion of

CVS-positive deep white matter lesions in future revisions of the McDonald criteria could help to achieve a more accurate and earlier MS diagnosis. Finally, recent data showed that cases of radiologically isolated syndrome can have a high proportion of CVS-positive lesions.²⁵ Therefore, CVS appears to be a radiologic biomarker present even in the presymptomatic phase of the disease.

One of the limitations of our study is that we did not perform a head-to-head comparison of the conventional SWAN sequence versus our newly optimized SWAN-venule sequence. Another limitation is the relatively long acquisition time (~7–8 minutes) of our SWAN-venule sequence, which most likely increases the risk of motion artifacts. Last, comprehensive MR imaging analysis, such as localized gray matter atrophy, which has a strong correlation with disease disability or progression, was not performed. Further work is needed to characterize the CVS as a potential biomarker for predicting disease severity and monitoring progression.

CONCLUSIONS

We introduce an optimized susceptibility-based MR imaging sequence, called SWAN-venule, a dedicated long-acquisition postcontrast imaging for sensitive detection of central veins inside brain lesions at 3T. MR imaging centers equipped with a clinical 3T system can easily integrate this optimized clinically available sequence, thus providing radiologists and neurologists with the opportunity to assess the clinical value of the CVS as an imaging biomarker for the differential diagnosis of MS.

ACKNOWLEDGMENT

Dr Sati is supported by the Intramural Research Program of NINDS.

Disclosures: Maria Ines Gaitán—RELATED: Support for Travel to Meetings for the Study or Other Purposes: Merck Serono Argentina, Comments: travel/accommodations/meeting expenses to European Committee for Treatment and Research in Multiple Sclerosis 2019, where I presented part of the data; UNRELATED: Payment for Development of Educational Presentations: Biogen Argentina, Merck Serono Argentina, Novartis Argentina; Travel/Accommodations/Meeting Expenses Unrelated to Activities Listed: Biogen Argentina, Merck Serono Argentina, Roche Argentina. Eduardo Figueiredo—UNRELATED: Employment: GE Healthcare. Jorge Correale—UNRELATED: Consultancy: Merck Serono Argentina, Biogen Argentina, Biogen Global, Genzyme Argentina, Genzyme Global, Novartis Argentina, Roche Argentina; Payment for Lectures Including Service on Speakers Bureaus: Merck Serono Argentina, Novartis Argentina, Genzyme Argentina, Roche Argentina, Biogen Argentina; Travel/Accommodations/Meeting Expenses Unrelated to Activities Listed: Merck Serono Argentina.

REFERENCES

- Adams CW. The onset and progression of the lesion in multiple sclerosis. *J Neurol Sci* 1975;25:165–82 CrossRef Medline
- Tan IL, van Schijndel RA, Pouwels PJ, et al. MR venography of multiple sclerosis. *AJNR Am J Neuroradiol* 2000;21:1039–42 Medline
- Tallantyre EC, Brookes MJ, Dixon JE, et al. Demonstrating the perivascular distribution of MS lesions in vivo with 7-Tesla MRI. *Neurology* 2008;70:2076–78 CrossRef Medline
- Tallantyre EC, Morgan PS, Dixon JE, et al. A comparison of 3T and 7T in the detection of small parenchymal veins within MS lesions. *Invest Radiol* 2009;44:491–94 CrossRef Medline

5. Sati P, Oh J, Constable RT, et al; NAIMS Cooperative. **The central vein sign and its clinical evaluation for the diagnosis of multiple sclerosis: a consensus statement from the North American Imaging in Multiple Sclerosis Cooperative.** *Nat Rev Neurol* 2016;12:714–22 CrossRef Medline
6. Kilsdonk ID, Lopez-Soriano A, Kuijter JP, et al. **Morphological features of MS lesions on FLAIR* at 7T and their relation to patient characteristics.** *J Neurol* 2014;261:1356–64 CrossRef Medline
7. Kuchling J, Ramien C, Bozin I, et al. **Identical lesion morphology in primary progressive and relapsing-remitting MS: an ultrahigh field MRI study.** *Mult Scler* 2014;20:1866–71 CrossRef Medline
8. Cortese R, Magnollay L, Tur C, et al. **Value of the central vein sign at 3T to differentiate MS from seropositive NMOSD.** *Neurology* 2018;90:e1183–90 CrossRef Medline
9. Maggi P, Absinta M, Grammatico M, et al. **Central vein sign differentiates multiple sclerosis from central nervous system inflammatory vasculopathies.** *Ann Neurol* 2018;83:283–94 CrossRef Medline
10. Kilsdonk ID, Wattjes MP, Lopez-Soriano A, et al. **Improved differentiation between MS and vascular brain lesions using FLAIR* at 7 Tesla.** *Eur Radiol* 2014;24:841–49 CrossRef Medline
11. Wuerfel J, Sinnecker T, Ringelstein EB, et al. **Lesion morphology at 7 Tesla MRI differentiates Susac syndrome from multiple sclerosis.** *Mult Scler* 2012;18:1592–99 CrossRef Medline
12. Sinnecker T, Clarke MA, Meier D, et al; MAGNIMS Study Group. **Evaluation of the central vein sign as a diagnostic imaging biomarker in multiple sclerosis.** *JAMA Neurol* 2019 Aug 19. [Epub ahead of print] CrossRef Medline
13. Solomon AJ, Schindler MK, Howard DB, et al. **“Central vessel sign” on 3T FLAIR* MRI for the differentiation of multiple sclerosis from migraine.** *Ann Clin Transl Neurol* 2016;3:82–87 CrossRef Medline
14. Sati P, Thomasson DM, Li N, et al. **Rapid, high-resolution, whole-brain, susceptibility-based MRI of multiple sclerosis.** *Mult Scler* 2014;20:1464–70 CrossRef Medline
15. Samaraweera AP, Clarke MA, Whitehead A, et al. **The central vein sign in multiple sclerosis lesions is present irrespective of the T2* sequence at 3 T.** *J Neuroimaging* 2017;27:114–21 CrossRef Medline
16. Dixon JE, Simpson A, Mistry N, et al. **Optimisation of T(2)*-weighted MRI for the detection of small veins in multiple sclerosis at 3 T and 7 T.** *Eur J Radiol* 2013;82:719–27 CrossRef Medline
17. Filippi M, Rocca MA, Ciccarelli O, et al; MAGNIMS Study Group. **MRI criteria for the diagnosis of multiple sclerosis: MAGNIMS consensus guidelines.** *Lancet Neurol* 2016;15:292–303 CrossRef Medline
18. Thompson AJ, Banwell BL, Barkhof F, et al. **Diagnosis of multiple sclerosis: 2017 revisions of the McDonald criteria.** *Lancet Neurol* 2018;17:162–73 CrossRef Medline
19. Solomon AJ, Bourdette DN, Cross AH, et al. **The contemporary spectrum of multiple sclerosis misdiagnosis: a multicenter study.** *Neurology* 2016;87:1393–99 CrossRef Medline
20. Maggi P, Absinta M, Sati P, et al. **The “central vein sign” in patients with diagnostic “red flags” for multiple sclerosis: a prospective multicenter 3T study.** *Mult Scler* 2019 Sep 19. [Epub ahead of print] CrossRef Medline
21. Champion T, Smith RJ, Altmann DR, et al. **FLAIR* to visualize veins in white matter lesions: a new tool for the diagnosis of multiple sclerosis?** *Eur Radiology* 2017;27:4257–63 CrossRef Medline
22. Wattjes MP, Rovira A, Miller D, et al; MAGNIMS study group. **Evidence-based guidelines: MAGNIMS consensus guidelines on the use of MRI in multiple sclerosis—establishing disease prognosis and monitoring patients.** *Nat Rev Neurol* 2015;11:597–606 CrossRef Medline
23. Rovira A, Wattjes MP, Tintore M, et al; MAGNIMS study group. **Evidence-based guidelines: MAGNIMS consensus guidelines on the use of MRI in multiple sclerosis—clinical implementation in the diagnostic process.** *Nat Rev Neurol* 2015;11:471–82 CrossRef Medline
24. Sati P, George IC, Shea CD, et al. **FLAIR*: a combined MR contrast technique for visualizing white matter lesions and parenchymal veins.** *Radiology* 2012;265:926–32 CrossRef Medline
25. Suthiphosuwana S, Sati P, Guenette M, et al. **The central vein sign in radiologically isolated syndrome.** *AJNR Am J Neuroradiol* 2019;40:776–83 CrossRef Medline

Ratio of T1-Weighted to T2-Weighted Signal Intensity as a Measure of Tissue Integrity: Comparison with Magnetization Transfer Ratio in Patients with Multiple Sclerosis

D. Pareto, A. Garcia-Vidal, M. Alberich, C. Auger, X. Montalban, M. Tintoré, J. Sastre-Garriga, and À. Rovira



ABSTRACT

SUMMARY: The study aim was to compare the ratio of T1WI to T2WI signal intensity (T1/T2) with magnetization transfer ratio, a marker of myelin integrity, in patients with multiple sclerosis. A moderate correlation ($r = 0.50$, $P = .034$) was found between the magnetization transfer ratio and T1/T2 in normal-appearing gray matter, and a strong correlation for normal-appearing white matter ($r = 0.63$, $P = .005$) and lesions ($r = 0.70$, $P = .001$). Results suggest that besides myelin integrity, other factors may be playing a role in T1/T2 measures.

ABBREVIATIONS: EDSS = Expanded Disability Status Scale; MTR = magnetization transfer ratio; NAGM = normal-appearing gray matter; NAWM = normal-appearing white matter; CSF = cerebrospinal fluid

The ratio of T1WI to T2WI signal intensity (T1/T2) on MR imaging has been recently proposed as a measure of myelin integrity in the brain.^{1,2} T1/T2 has been investigated in multiple sclerosis,³⁻⁵ though no conclusive validation of the T1/T2 pathologic substrate has been established. This method has the advantage of being easily obtained and available, a feature that enables analysis of retrospective cohorts with considerable clinical value. T1/T2 has been compared with the magnetization transfer ratio (MTR),⁴ considered a measure of tissue integrity related to myelin content,⁶ but only in specific portions of myelinated and demyelinated cortex in postmortem tissue samples of patients with MS. The aim of this study was to compare in vivo and regional T1/T2 with MTR in a cohort of patients with MS. The comparison involved 2 regions, normal-appearing gray (NAGM) and white matter (NAWM) and the lesion mask derived from T2WI. An

additional lesion-by-lesion comparison between the 2 measures was performed for each patient separately.

MATERIALS AND METHODS

Patients

Twenty-two patients with relapsing-remitting MS according to the 2017 McDonald criteria were included in this exploratory study. Clinical variables, the Expanded Disability Status Scale (EDSS) score, and disease duration were obtained for each patient. The study was approved by the Vall Hebron University Hospital local ethics committee, and patients signed informed consent.

MR Imaging Acquisition

Images were acquired on a 3T scanner (Tim Trio; Siemens, Erlangen, Germany) with a 12-channel phased array head coil and a whole-body transmit coil. The protocol included the following: 1) 3D T1WI MPRAGE (TR = 2300 ms; TE = 2.98 ms; FOV = 256 × 256 mm; 192 sections; voxel size = 1 × 1 × 1 mm); 2) 2D dual-echo T2WI (TR = 2500 ms; TE = 16/91 ms; FOV = 256 × 256; 46 sections; voxel size = 0.78 × 0.78 × 3.0 mm); and 3) 2D gradient-echo magnetization transfer performed without (TR = 1500 ms; TE = 10 ms; FOV = 250 × 250 mm; 50 sections; voxel size = 1 × 1 × 3 mm; flip angle = 20°) and with magnetization transfer saturation (equivalent flip angle = 500°; off-water resonance = 1.2 kHz; duration = 10 ms).

Image Analysis

Lesion masks were outlined semiautomatically with Jim software (<http://www.xinapse.com/home.php>) on the proton-density

Received November 5, 2019; accepted after revision January 5, 2020.

From the Neuroradiology Section (D.P., A.G.-V., M.A., C.A., A.R.), Department of Radiology and Department of Neuroimmunology-Cemcat (X.M., M.T., J.S.-G.), Vall d'Hebron University Hospital and Research Institute, Autonomous University, Barcelona, Spain; and Division of Neurology (X.M.), St. Michael's Hospital, University of Toronto, Toronto, Ontario, Canada.

This study was partly funded by the Spanish Multiple Sclerosis Network (Red Española de Esclerosis Múltiple) (RD07/0060, RD12/0032) and the project PI18/00823, which are sponsored by the Fondo de Investigación Sanitaria (Instituto de Salud Carlos III), by Financial Support for Research Groups in Catalonia (2009 SGR 0793), and by the Agency for Administration of University and Research Grants of the Generalitat de Catalunya in Spain.

Please address correspondence to Deborah Pareto, MD, Radiology Department, Vall Hebron University Hospital, Psg. Vall Hebron 119-129, Barcelona 08036, Spain; e-mail: deborah.pareto.idi@gencat.cat

Indicates open access to non-subscribers at www.ajnr.org

<http://dx.doi.org/10.3174/ajnr.A6481>

T2WI, by a technician with >10 years' experience (M.A.), supervised by an experienced neuroradiologist (A.R.). The T1/T2 was generated after coregistering and reslicing the T2WI to the T1WI and bias-correcting the T1WI and T2WI with Statistical Parametric Mapping (SPM12; <http://www.fil.ion.ucl.ac.uk/spm/software/spm12>). The NAGM, NAWM, and cerebrospinal fluid (CSF) compartment masks were obtained after segmenting the T1WI with SPM12 and thresholding ($P > .75$) and multiplying them by the inverse of the lesion mask to remove any contributions due to lesion misclassification. The MTR image was calculated as follows: $(MT_{off} - MT_{on}) / MT_{off}$, and it was coregistered to T1/T2 with SPM12. Finally, for each patient, mean values in NAGM, NAWM, the lesion mask, and each lesion separately (after splitting the lesion mask) were computed from the MTR and T1/T2 images.

Statistical Analysis

To assess the relationship between MTR and T1/T2, we ran partial correlations for NAGM, NAWM, CSF, and the lesion mask, with age and sex as covariates. In addition, a correlation for each patient was obtained after comparing their individual lesions in MTR and T1/T2. Partial correlations were also run to assess relationships between either MTR or T1/T2 and EDSS and disease duration. Significance for the comparisons was set at $P < .05$, and analyses were performed with the SPSS (IBM, Armonk, New York).

RESULTS

A total of 22 patients were analyzed (68% women; mean age, 41.13 ± 6.04 years; mean disease duration, 5.66 years; range, 0.08–20 years; mean EDSS score, 2.47; range, 0–6; and mean

lesion volume, 5.02 mL; range, 0.13–25.45 mL). For both methods, the differences within compartments were significant ($P < .05$) for all possible pairs (data not shown). Mean values and partial correlations between MTR and T1/T2 measures are reported in the Table. Lesion-by-lesion correlations were significant for cases with lesion volumes of >1 mL (17 cases of 22), with correlations ranging from 0.42 to 0.99. An individual example can be seen in the Figure. Both MTR ($r = -0.64, P = .004$) and T1/T2 ($r = -0.66, P = .003$) mean values in the lesion mask correlated with the EDSS, whereas only the T1/T2 lesion mask values correlated with disease duration ($r = -0.52, P = .021$).

DISCUSSION

This exploratory study compares the distribution in T1/T2 and MTR in a relatively small group of patients with relapsing-remitting MS. Healthy controls were not included in this study because the main goal was to investigate the correspondence between MTR and T1/T2 in damaged tissue. Comparisons were performed across subjects for NAGM, NAWM, and lesion masks and also across individual lesions in each subject. Several factors may have affected the lesion-by-lesion correlations, such as small coregistration errors between MTR and T1/T2, which may have displaced the lesion masks, as well as patient movement during acquisition.

The correlations ranged from moderate to strong, suggesting that most probably, the 2 methods are not sensitive to the same pathologic substrate. In addition, T1/T2 was associated with the EDSS and disease duration, while MTR was only associated with EDSS. The concept that T1/T2 is a proxy for myelin in gray matter has been derived from studies performed in healthy individuals,^{1,2} in whom neither myelin nor axonal loss nor inflammation is present. In MS, T1/T2 in gray matter has been related to dendrite density rather than myelin⁵ in a study performed ex vivo in tissue blocks from brain donors; and, again in an ex vivo study, T1/T2 has shown a moderate correlation with MTR in gray matter.⁴ However, it is expected that T1/T2 will also be affected by edema and iron content, because T1WI and T2WI separately are affected.³ MTR has been mainly related to both myelin and axonal damage and, to a lesser degree, to inflammation and gliosis in

Mean values of MTR and T1/T2 in the different compartments and partial correlations^a

	Mean MTR (SD)	Mean T1/T2 (SD)	r (P Value)
NAWM	0.510 (0.032)	1.022 (0.102)	0.631 (.005)
Lesions	0.477 (0.054)	0.604 (0.074)	0.699 (.001)
NAGM	0.435 (0.030)	0.537 (0.043)	0.502 (.034)
CSF	0.267 (0.028)	0.110 (0.043)	0.631 (.040)

^a Age and sex are covariates.

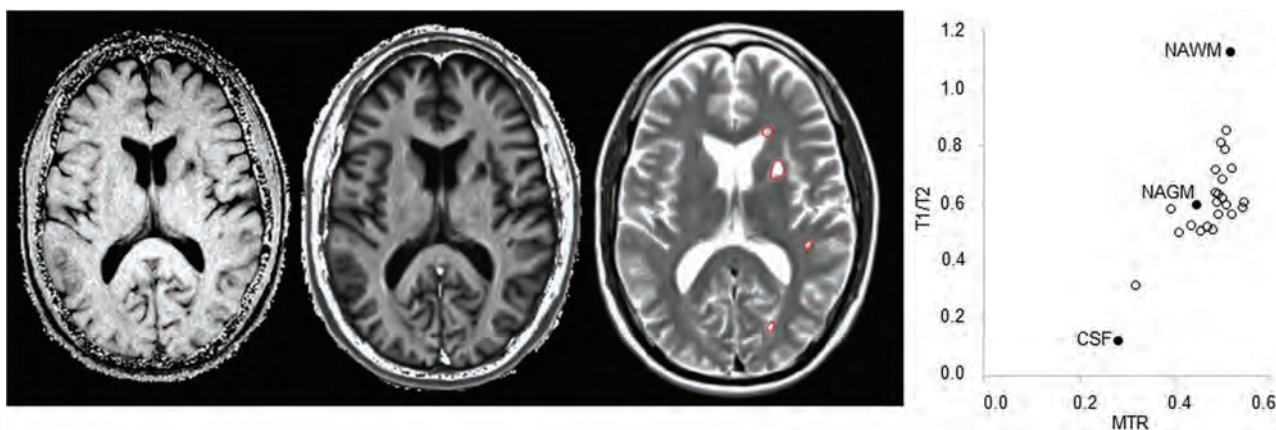


FIGURE. Representative MTR, T1/T2, and T2 with lesions outlined (left) and the corresponding scatterplot ($r = 0.630; P = .002$; 22 lesions; total volume = 3.39 mL). Empty symbols refer to the individual lesions; filled symbols refer to the mean value in CSF, NAGM, and NAWM.

MS.⁶ In this context, it is likely that compared with MTR, T1/T2 is more dependent on additional pathologic substrates and not just on myelin integrity, though new studies in vivo are needed to confirm the source of the signal in the T1/T2 approach. The main advantage of T1/T2 is that it provides a wider range of values than those given by MTR, as was seen in postmortem studies.⁴ Thus, an intermediate degree of tissue destruction would be more likely to be captured with T1/T2 than MTR. Nevertheless, these results could not be extrapolated to any T1WI, T2WI, or MTR sequence because T1/T2 and MTR contrast and, consequently, the correlation between them, depends on the acquisition parameters.⁷ Further longitudinal studies with larger sample sizes as well as further in-depth assessment of lesional tissue (including black holes and new lesions) are warranted to assess the validity of T1/T2 as a biomarker of tissue damage and lesion recovery in MS.

ACKNOWLEDGMENT

We thank C. Cavallo for English writing support.

Disclosures: Deborah Pareto—RELATED: Other: Novartis, Sanofi Genzyme, Comments: speaking honoraria, teaching activity, money paid to the individual. Xavier Montalban—UNRELATED: Consultancy: Actelion, Bayer AG, Biogen, Celgene, Genzyme, Merck, Novartis, Roche, Sanofi Genzyme, Teva Pharmaceutical Industries, EXCEMED, Multiple Sclerosis International Federation, and National Multiple Sclerosis Society. Jaume Sastre-Garriga—UNRELATED: Payment for Lectures Including Service on Speakers Bureaus: Genzyme, Biogen, Bayer AG, Merck, Almirall, Bial Pharmaceuticals, Novartis, Roche, Teva Pharmaceutical Industries, Celgene.* Alex Rovira—UNRELATED: Board Membership: Bayer AG, Biogen, Novartis, icometrix, Roche; Payment for Lectures Including Service on Speakers Bureaus: Bayer AG, Sanofi Genzyme, Bracco, Merck Serono, Teva Pharmaceutical Industries, Novartis, Roche, Biogen; Payment for Development of

Educational Presentations: Sanofi Genzyme, Merck Serono, Novartis, Roche, Biogen, Mar Tintoré—UNRELATED: Board Membership: Almirall, Bayer AG Schering Pharma, Biogen, Genzyme, Merck Serono, Novartis, Roche, Sanofi-Aventis, Teva Pharmaceutical Industries; Grants/Grants Pending: Biogen, Genzyme, Novartis*; Payment for Lectures Including Service on Speakers Bureaus: Almirall, Bayer AG, Biogen, Genzyme, Merck Serono, Novartis, Roche, Sanofi-Aventis, Viela Bio, Teva Pharmaceutical Industries; Payment for Development of Educational Presentations: Biogen. *Money paid to the institution.

REFERENCES

1. Glasser MF, Van Essen DC. **Mapping human cortical areas in vivo based on myelin content as revealed by T1- and T2-weighted MRI.** *J Neurosci* 2011;31:11597–616 CrossRef Medline
2. Ganzetti M, Wenderoth N, Mantini D. **Whole brain myelin mapping using T1- and T2-weighted MR imaging data.** *Front Hum Neurosci* 2014;8:671 CrossRef Medline
3. Beer A, Biberacher V, Schmidt P, et al. **Tissue damage within normal appearing white matter in early multiple sclerosis: assessment by the ratio of T1- and T2-weighted MR image intensity.** *J Neurol* 2016;263:1495–502 CrossRef Medline
4. Nakamura K, Chen JT, Ontaneda D, et al. **T1-/T2-weighted ratio differs in demyelinated cortex in multiple sclerosis.** *Ann Neurol* 2017; 82:635–39 CrossRef Medline
5. Righart R, Biberacher V, Jonkman LE, et al. **Cortical pathology in multiple sclerosis detected by the T1/T2-weighted ratio from routine magnetic resonance imaging.** *Ann Neurol* 2017;82:519–29 CrossRef Medline
6. Schmierer K, Scaravilli F, Altmann DR, et al. **Magnetization transfer ratio and myelin in postmortem multiple sclerosis brain.** *Ann Neurol* 2004;56:407–15 CrossRef Medline
7. Henkelman RM, Stanisz GJ, Graham SJ. **Magnetization transfer in MRI: a review.** *NMR Biomed* 2001;14:57–64 CrossRef Medline

Endovascular Thrombectomy of Calcified Emboli in Acute Ischemic Stroke: A Multicenter Study

C.J. Maurer, T. Dobrocky, F. Joachimski, U. Neuberger, T. Demerath, A. Brehm, A. Cianfoni, B. Gory, A. Berlis, J. Gralla, M.A. Möhlenbruch, K.A. Blackham, M.N. Psychogios, P. Zickler, and S. Fischer

ABSTRACT

BACKGROUND AND PURPOSE: Large intracranial vessel occlusion due to calcified emboli is a rare cause of major stroke. We assessed the prevalence, imaging appearance, the effectiveness of mechanical thrombectomy, and clinical outcome of patients with large-vessel occlusion due to calcified emboli.

MATERIALS AND METHODS: We performed a retrospective analysis of clinical and procedural data of consecutive patients who underwent mechanical thrombectomy due to calcified emboli in 7 European stroke centers.

RESULTS: We screened 2969 patients, and 40 patients matched the inclusion criteria, accounting for a prevalence of 1.3%. The mean maximal density of the thrombus was 327 HU (range, 150–1200 HU), and the mean thrombus length was 9.2 mm (range, 4–20 mm). Four patients had multiple calcified emboli, and 2 patients had an embolic event during an endovascular intervention. A modified TIC1 score of $\geq 2b$ was achieved in 57.5% (23/40), with minimal-to-no reperfusion (modified TIC1 0–1) in 32.5% (13/40) and incomplete reperfusion (modified TIC1 2a) in 10% (4/40). Excellent outcome (mRS 0–1) was achieved in only 20.6%, functional independence (mRS 0–2) in 26.5% and 90-day mortality was 55.9%.

CONCLUSIONS: Acute ischemic stroke with large-vessel occlusion due to calcified emboli is a rare entity in patients undergoing thrombectomy, with considerably worse angiographic outcome and a higher mortality compared with patients with noncalcified thrombi. Good functional recovery at 3 months can still be achieved in about a quarter of patients.

ABBREVIATIONS: CLASS = calcium load assessment; MT = mechanical thrombectomy; mTIC1 = modified TIC1

Calcified emboli are a rare, underreported cause of ischemic stroke.¹ Their prevalence has been estimated as between 2.7% and 5.9% of all patients presenting with acute ischemic stroke.^{1,2} Intravenous rtPA seems to be an ineffective treatment, probably due to the thrombus composition.³ Endovascular

therapy has been suggested as an alternative.⁴ There are several case reports and case series describing endovascular treatment of calcified cerebral emboli^{4–11} with low recanalization rates, but due to the small number of patients, no definite recommendation has been reported. In this study, we, therefore, aimed to assess the prevalence, angiographic outcome, and treatment effects of cerebral calcified emboli in large-vessel occlusion treated by an endovascular approach in a large multicenter cohort.

MATERIALS AND METHODS

Patient Demographics

This study was approved by the ethics review board of our institution and was conducted according to the principles of the Declaration of Helsinki. Due to the retrospective character of the data collection and analysis, written informed consent was waived. The data supporting the findings of this study are available from the corresponding author, upon reasonable request.

In this retrospective multicenter study, we analyzed data prospectively collected from patients with acute ischemic stroke who met the following inclusion criteria: Intracranial thrombectomy

Received October 5, 2019; accepted after revision December 23.

From the Departments of Diagnostic and Interventional Radiology and Neuroradiology (C.J.M., F.J., A.Berlis) and Neurology and Neurophysiology (P.Z.), Universitätsklinikum Augsburg, Augsburg, Germany; University Institute of Diagnostic and Interventional Neuroradiology (T.Dobrocky, J.G.), University of Bern, Inselspital, Bern, Switzerland; Department of Neuroradiology (U.N., M.A.M.), University of Heidelberg, Heidelberg, Germany; Department of Neuroradiology (T.Demerath, A.Brehm, K.A.B., M.N.P.), Clinic of Radiology and Nuclear Medicine, University Hospital Basel, Basel, Switzerland; Department of Neuroradiology (A.Brehm, M.N.P.), University Medical Center Göttingen, Göttingen, Germany; Department of Neuroradiology (A.C.), Neurocenter of Southern Switzerland, Lugano, Switzerland; Department of Diagnostic and Therapeutic Neuroradiology (B.G.), University Hospital of Nancy, Institut National de la Santé et de la Recherche Médicale U1254, Nancy, France; and Institut für Diagnostische und Interventionelle Radiologie, Neuroradiologie (S.F.), Nuklearmedizin, Knappschafts Krankenhaus Bochum-Langendreer, Universitätsklinik, Bochum, Germany.

Please address correspondence to Christoph J. Maurer, MD, Departments of Diagnostic and Interventional Radiology and Neuroradiology, Universitätsklinikum Augsburg, Stenglinstraße 2, 85221 Augsburg, Germany; e-mail: Christoph.Maurer@uk-augsburg.de; @Podaleirios5
<http://dx.doi.org/10.3174/ajnr.A6412>

was performed, and intracranial large-vessel occlusion due to a calcified embolus was diagnosed on unenhanced CT. A calcified embolus was defined as an oblong, not circular or semicircular, calcification with clearly intraluminal localization on CT angiography at the site of intracranial vessel occlusion. An ROI was drawn over the hyperdense thrombus, and the Hounsfield units were measured to identify emboli with a calcific component. Analogous to cardiology scoring systems, calcification was defined by a density of at least 130 HU on unenhanced CT.¹² Only definite cases of calcified emboli were included. Further patient work-up, including multitechnique diagnostic imaging and treatment, was performed according to international guidelines.¹³ All 7 participating comprehensive stroke centers are high-volume facilities and offer interventional stroke treatment 24/7 with long-time experience in endovascular thrombectomy.¹⁴

Outcome

We obtained demographic and clinical data, including the NIHSS score and mRS on admission, discharge, and after 90 days, if available, and the presence of cardiovascular risk factors. Time metrics were evaluated, including the time of symptom onset, hospital admission, first imaging, groin puncture, and recanalization. Imaging data included the ASPECTS on admission and after 24 hours, intracranial hemorrhage classified according to the European Cooperative Stroke Study (ECASS),¹⁵ thrombus localization, length and density together with the presumed source of the embolus, and the existence of multiple calcified emboli and concomitant extracranial stenosis. Additionally, procedural data were gathered, including materials, medication during the procedure, number of passes, complications, and angiographic outcome using the modified TICI (mTICI) classification.¹⁶

To estimate the extent of atherosclerosis-associated calcification as a potential source of calcified emboli, we developed a simple qualitative scoring system termed the calcium load assessment (CLASS) score, scoring the following regions, if available, on CT angiographic images: mitral valve, aortic valve, aortic arch, brachiocephalic artery, carotid bifurcation, and vertebral artery. For the carotid bifurcation and the vertebral artery, the more severely affected side was evaluated. The calcium load at each region was classified into 0 (none), 1 (mild), 2 (moderate), and 3 (extensive). The overall CLASS score was calculated by adding the scores for each available region and then dividing the sum by the number of available regions, with a potential score ranging from 0 to 3.

Statistical Analysis

Statistical analyses were performed with R, Version 3.5.3 (<http://www.r-project.org/>). Baseline characteristics are presented as frequencies, mean with SD, or median and interquartile range. Univariate analyses comparing demographic- and intervention-related variables that were potentially relevant for predicting the clinical outcome and recanalization were performed.

RESULTS

Patient Characteristics

In 7 European stroke centers in Germany, Switzerland, and France, a total of 2969 patients who underwent mechanical thrombectomy

Table 1: Baseline patient characteristics (n = 40)

Characteristics	
Demographic data and medical history	
Age (mean) (yr)	78 ± 9.6
Female sex	68% (27/40)
Current smoker	8% (3/38)
Hypertension	74% (28/38)
Diabetes mellitus	39% (15/38)
Hypercholesterolemia	41% (15/37)
Baseline NIHSS (mean)	15.4 ± 7.2
Pretreatment ASPECTS	
0–5	5.1% (2/39)
6–10	94.9% (37/39)
IV thrombolysis	47.5% (19/40)

(MT) were retrospectively screened. Forty patients matched the inclusion criteria, accounting for a prevalence of 1.3% in patients having undergone MT. The mean age was 77.9 ± 9.6 years (range, 56–100 years); 68% were women. The baseline patient characteristics are presented in Table 1.

The mean NIHSS on admission was 15.4 ± 7.2; the median, 14; and the interquartile range, 11–20. The median initial ASPECTS was 9 (interquartile range, 7–9); 47.5% of patients received IV rtPA before the intervention.

Occlusion Site and Clot Description

Clot location in most patients was in the middle cerebral artery, with 65% in the M1 segment and 12.5% in the M2 segment; 15% had a calcified clot in the carotid T, and 7.5%, in the basilar artery. A dual pathology with additional extracranial stenosis in the ipsilateral ICA requiring treatment was found in 2 patients (5%). In both cases, extensive calcification of the bifurcation was reported.

The mean maximal density of the thrombus was 327 HU (range, 150–1200 HU), and the mean thrombus length was 9.2 mm (range, 4–20 mm). The presumed source of embolization was unknown in 37.5% (15/40), cardiac in 17.5% (7/40), aortic arch in 15% (6/40), and ICA in 30% (12/40). Four patients had multiple calcified emboli, and 2 patients had an embolic event during an endovascular intervention (transcatheter aortic valve implantation and repair of an infrarenal aortic aneurysm). Extracranial calcification was most prominent at the carotid bifurcation and the aortic arch. The mean CLASS score was 1.1 (range, 0–2.5). Table 2 summarizes the occlusion site and clot properties. The Figure gives examples of intracranial calcified clots.

Procedural Characteristics and Clinical Outcome

The mean duration of the procedure was 93 minutes, ranging from 23 to 250 minutes. A balloon-guide catheter was used in 15% (6/40). Distal aspiration alone or stent retrieval alone was performed in 5%, respectively. The preferred recanalization method was a combination of stent retrieval and distal aspiration in 90% (36/40). The number of retrieving maneuvers ranged from 1 to 7, with a mean value of 2.7. Successful recanalization after 1 pass was achieved in 12 cases (30%), with a combination of distal aspiration and stent retrieval in 9 cases, distal aspiration alone in 2 cases, and stent retrieval alone in 1 case. Extracranial stent placement at the ICA bifurcation was performed in only 1 patient (2.5%); percutaneous transarterial angioplasty of the extracranial stenosis, in 2 patients (5%); and intracranial stent

placement after failed thrombectomy, in 2 patients (5%). An mTICI score of $\geq 2b$ was achieved in 57.5% (23/40), with mTICI 2b in 32.5% and mTICI 3 in 25%. Minimal-to-no reperfusion (mTICI 0–1) was reported in 32.5% (13/40); and incomplete reperfusion (mTICI 2a), in 10% (4/40). For 9 of the 13 patients with minimal-to-no reperfusion, 3-month follow-up was available with an mRS of 6 in 8/9 (89%) patients and mRS of 1 in 1/9 (11%) patients. The procedural data are summarized in Table 3; clinical outcome, in Table 4.

Procedural complications were reported in 4 patients. Two patients had a vessel perforation in a lenticulostriate branch and in M3, respectively. In 1 case, the pusher wire of the stent retriever broke and had to be left in the vessel without recanalization. One patient had nasopharyngeal bleeding, most probably due to IV thrombolysis. Symptomatic hemorrhage occurred in 5.3% (2/40); only 1 of these 2 patients had received IV rtPA. The ASPECTS 24 hours after treatment ranged from 0 to 10, with a median of 5. Ninety-day clinical outcome was available in 34 patients. Excellent outcome (mRS 0–1) was achieved in only 20.1% (7/34); functional independence (mRS 0–2), in 26.5% (9/34); and 90-day mortality was 55.9% (19/34).

Table 2: Clot location and characteristics (n = 40)

Characteristics	
Clot location (parent vessel)	
Right anterior circulation	55% (22/40)
Left anterior circulation	37.5% (15/40)
Posterior circulation	7.5% (3/40)
Clot location	
M1	65% (26/40)
M2	12.5% (5/40)
Carotid T	15% (6/40)
Basilar artery	7.5% (3/40)
Tandem pathology	10% (4/40)
Thrombus characteristics	
Maximal density (mean) (HU)	327 \pm 202
Length (mean) (mm)	9.2 \pm 4.3
Multiple emboli	10% (4/40)
CLASS score (mean)	1.1 \pm 0.7
Range of CLASS score	0–2.5
Spontaneous embolization	95% (38/40)
Embolization during endovascular treatment	5% (2/40)

In univariate analysis using a dichotomized mRS at discharge or at 3 months, no parameter correlated with good outcome. A multivariate analysis was not feasible due to the small sample size.

DISCUSSION

A high intracranial calcification burden has been proposed as a marker of worse clinical outcome in patients with occlusion of the middle cerebral artery.¹⁷ Thrombus density on unenhanced CT, on the other hand, has been discussed as a potential predictor of successful recanalization,¹⁸ though available data are equivocal.¹⁹ In most publications, no distinction is made between red blood cell-rich thrombi with a hyperdense appearance on CT and truly calcified emboli, probably due to the rare occurrence and reporting of the phenomenon. In our analysis, we clearly discriminated the 2 entities via imaging criteria and thus provided the most comprehensive analysis of this subtype of stroke and its endovascular therapy so far. In our patients, good angiographic outcome (mTICI $\geq 2b$) was achieved in 57.5%, which is comparable with the results of the MR CLEAN trial with a modified TICI score of 2b and 3 in 58.7%.²⁰ The pooled data of the Highly Effective Reperfusion Evaluated in Multiple Endovascular Stroke (HERMES) Trial collaborators, however, showed a good angiographic outcome in 71%.²¹ Other real-world data of mechanical thrombectomy with aspiration, stent retrieval, or combined approaches demonstrate angiographic results with mTICI scores of 2b or 3 in 65%–93%,^{22,23} depending on the thrombectomy technique. Compared with these data, the recanalization rate in our series with calcified emboli is clearly on the lower end of the range. A potential reason might be distinct friction properties of hard calcified clots, which could lead to less adhesion to the stent retriever during mechanical thrombectomy.²⁴

In our series, intracranial stent placement was performed in only 2 patients after 4 and 5 unsuccessful thrombectomy maneuvers, respectively. There are only limited data on intracranial stent placement after unsuccessful thrombectomy^{25,26} and on stent placement as a primary treatment of intracranial occlusion in acute stroke in the pre-stent-retriever era.^{27–29} Successful recanalization with primary intracranial stent placement (mTICI 2b–3 or Thrombolysis in Myocardial Infarction 2–3) is reported in 65%–100% of patients

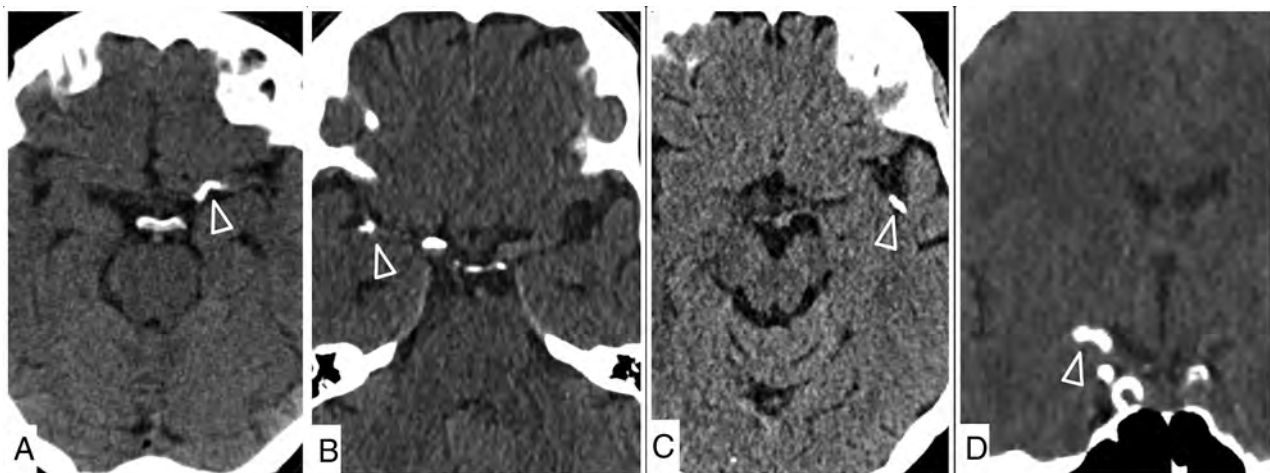


FIGURE. Examples of calcified emboli (arrowheads) in the left M1 (A), right middle cerebral artery bifurcation (B), left M2 (C), and carotid T (D).

Table 3: Procedural characteristics

Characteristics	
Unknown onset	32.5% (13/40)
Known onset to recanalization (n = 27/40) (mean) (min)	316 ± 216
Procedural time (mean) (min)	93 ± 57
No. of passes (mean)	2.7 ± 1.7
Range	1–7
Aspiration alone	5% (2/40)
Stent retrieval alone	5% (2/40)
Combination (stent retrieval and aspiration)	90% (36/40)
Additional intracranial stent placement	5% (2/40)
Angiographic results	
mTICI 0	25% (10/40)
mTICI 1	7.5% (3/40)
mTICI 2a	10% (4/40)
mTICI 2b	32.5% (13/40)
mTICI 3	25% (10/40)
Successful recanalization after 1 pass	30% (12/40)
IV heparin	35% (14/40)
IV ASA	10% (4/40)
IA rtPA	7.5% (3/40)

Note:—ASA indicates acetylsalicylic acid; IA, intra-arterial.

Table 4: Clinical outcome

Outcome	
Parenchymal hematoma type 1 and 2	7.5% (3/40)
Symptomatic hemorrhage	5.3% (2/38)
90-Day mRS available	85% (34/40)
0	2.9% (1/34)
1	17.1% (6/34)
2	5.9% (2/34)
3	5.9% (2/34)
4	0% (0/34)
5	11.8% (4/34)
6	55.9% (19/34)

and good clinical outcome after 30–90 days (mRS ≤2) in 40%–50% of patients. Thus, early intracranial stent placement after failed thrombectomy might be an option in patients with calcified thrombi. In our patients, however, stent placement as a last resort did not lead to good outcomes in either patient.

In our cohort, good clinical outcome after 90 days with an mRS of ≤2 was achieved in only 26.4%, compared with 46% in the HERMES data and 55.3% in the Trevo Registry.²³ A 55.9% mortality rate at 90 days in our cohort was dismal compared with 15.3% reported by the HERMES collaborators and 13.9% by the Trevo Registry. A potential reason for the worse clinical outcome in our cohort might be the older patient age, with a mean age of 78 years compared with 68 years in the HERMES data and Trevo Registry, though age does not seem to be associated with lower recanalization rates in patients with acute ischemic stroke undergoing endovascular therapy.^{30,31} In a recent meta-analysis that included HERMES data, only 27% of patients 80 years of age or older achieved a good functional outcome, while 34% of patients died.³² Successful recanalization was achieved in 78% in this analysis in contrast to 58% in our cohort. The combination of lower recanalization rates and patient age may explain the higher mortality in our group.

The extent of arteriosclerosis as measured with the CLASS score did not correlate with procedural time, number of passes, and angiographic or clinical outcome. Surprisingly, there was no significant correlation between procedural time or the number of

passes and outcome, though this was probably due to the small sample size.

In our patient population, the administration of IV rtPA did not lead to a better outcome or to a higher complication rate. The dissolution of calcification within an embolus by rtPA is unlikely.³³ The calcified material, however, could be associated with fibrin-rich thrombus and thus respond to rtPA.³⁴ Therefore, the complete rejection of rtPA for calcified emboli cannot be recommended on the basis of our data.

There are several limitations to our study. First, this was a retrospective analysis during 6 years with only a limited number of patients, yet it represents the largest cohort of patients undergoing thrombectomy due to calcified thrombi to date. Statistical analysis, however, is severely limited due to the small sample size, and we have no histopathologic data due to the retrospective nature of this study. Additionally, we included only definite cases of calcified emboli. Because there is an obvious overlap with intracranial atherosclerotic disease due to the calcific components, the number of unreported cases might be even higher. Furthermore, no information is available on patients with calcified emboli and large-artery occlusion not undergoing thrombectomy, so the outcome of all patients with calcified emboli—treated or not—might be even worse. Second, a control group is lacking, and the recanalization rates and clinical outcome can be compared with only similar published cohorts. Third, our study had a multicenter design with different logistic and procedural standards in each institution. Nevertheless, the thrombectomy strategy was similar in all institutions, with a combination of stent retrieval and large-bore distal aspiration catheter as a first-line approach.

CONCLUSIONS

Acute ischemic stroke with large-vessel occlusion due to calcified emboli is a rare entity in patients undergoing thrombectomy, with a higher age on average. These patients have a considerably worse angiographic outcome and a higher mortality rate compared with patients with noncalcified thrombi. Good functional outcome can be expected in approximately 1 in 4 patients.

Disclosures: Christoph J. Maurer—UNRELATED: Grants/Grants Pending: MicroVention, Stryker, Comments: educational grants. Ansgar Berlis—UNRELATED: Consultancy: proctoring MicroVention, Stryker, Medtronic; Payment for Lectures Including Service on Speakers Bureaus: Penumbra; Other: Clinical Ethics Committee phenox, Comments: Money paid to the individual. Jan Gralla—RELATED: Grant: Medtronic, Comments: Global Principal Investigator of the Swift Direct Study*; Fees for Participation in Review Activities Such as Data Monitoring Boards, Statistical Analysis, Endpoint Committees, and the Like: Penumbra, Comments: CEC of the Promise Study*; UNRELATED: Grants/Grants Pending: Schweizerischer Nationalfonds, Comments: MRI in stroke.* Markus A. Möhlenbruch—UNRELATED: Consultancy: Medtronic, MicroVention, Stryker; Grants/Grants Pending: Balt, MicroVention*; Payment for Lectures Including Service on Speakers Bureaus: Medtronic, MicroVention, Stryker. Kristine A. Blackham—UNRELATED: Consultancy: Medtronic.* Philipp Zickler—UNRELATED: Consultancy: Boehringer-Ingelheim; Payment for Lectures Including Service on Speakers Bureaus: Bristol-Myers-Squibb; Travel/Accommodations/Meeting Expenses Unrelated to Activities Listed: Bayer AG, Daiichi Sankyo. Sebastian Fischer—UNRELATED: Consultancy: MicroVention, phenox, Kaneka, Stryker.* *Money paid to the institution.

REFERENCES

- Walker BS, Shah LM, Osborn AG. Calcified cerebral emboli, a “do not miss” imaging diagnosis: 22 new cases and review of the literature. *AJNR Am J Neuroradiol* 2014;35:1515–19 CrossRef Medline

2. Bardon M, Hanson J, O'Brien B, et al. **Calcified cerebral emboli: incidence and implications.** *J Med Imaging Radiat Oncol* 2018 Apr 17. [Epub ahead of print] CrossRef Medline
3. Halloran JJ, Bekavac I. **Unsuccessful tissue plasminogen activator treatment of acute stroke caused by a calcific embolus.** *J Neuroimaging* 2004;14:385–87 CrossRef Medline
4. Raghib MF, Mutzenbach JS, Rösler C, et al. **Acute treatment of stroke due to spontaneous calcified cerebral emboli causing large vessel occlusion.** *J Clin Neurosci* 2018;47:56–61 CrossRef Medline
5. Schirmer CM, Thaler DE, Malek AM. **Stent-mediated wedging of a calcific embolus to recanalize an occluded middle cerebral artery: technical case report.** *Neurosurgery* 2008;63:E180–81; discussion E181 CrossRef Medline
6. Uneda A, Kanda T, Suzuki K, et al. **Acute cerebral artery occlusion by a calcified embolus with false patency sign on computed tomographic angiography.** *J Stroke Cerebrovasc Dis* 2017;26:e5–7 CrossRef Medline
7. Ramirez-Moreno JM, Trinidad-Ruiz M, Ceberino D, et al. **Trombectomía mecánica en un ictus isquémico debido a embolia cerebral cálcica.** *Neurologia* 2017;32:270–73 CrossRef Medline
8. Koh E, Kwak HS, Chung GH. **Manual aspiration thrombectomy in patients with acute stroke-related calcified cerebral emboli.** *J Stroke Cerebrovasc Dis* 2017;26:2050–54 CrossRef Medline
9. Kwak HS, Park JS. **Successful recanalization using the Embolus Retriever with Interlinked Cage for acute stroke due to calcified cerebral emboli.** *Interv Neuroradiol* 2018;24:674–77 CrossRef Medline
10. Dobrocky T, Piechowiak E, Cianfoni A, et al. **Thrombectomy of calcified emboli in stroke: does histology of thrombi influence the effectiveness of thrombectomy?** *J Neurointerv Surg* 2018;10:345–50 CrossRef Medline
11. Yogendrakumar V, Patro S, Dowlatshahi D, et al. **Calcified embolus mimics patent middle cerebral artery on CT angiogram.** *Pract Neurol* 2017;17:307–09 CrossRef Medline
12. Agatston AS, Janowitz WR, Hildner FJ, et al. **Quantification of coronary artery calcium using ultrafast computed tomography.** *J Am Coll Cardiol* 1990;15:827–32 CrossRef Medline
13. Ahmed N, Steiner T, Caso V, et al; ESO-KSU session participants. **Recommendations from the ESO-Karolinska Stroke Update Conference, Stockholm 13-15 November 2016.** *Eur Stroke J* 2017; 2:95–102 CrossRef Medline
14. Pierot L, Jayaraman MV, Szikora I, et al; Asian-Australian Federation of Interventional and Therapeutic Neuroradiology (AAFITN), Australian and New Zealand Society of Neuroradiology (ANZSNR), American Society of Neuroradiology (ASNR), Canadian Society of Neuroradiology (CSNR), European Society of Minimally Invasive Neurological Therapy (ESMINT), European Society of Neuroradiology (ESNR), European Stroke Organization (ESO), Japanese Society for NeuroEndovascular Therapy (JSNET), The French Society of Neuroradiology (SFNR), Ibero-Latin American Society of Diagnostic and Therapeutic Neuroradiology (SILAN), Society of Neuro-Interventional Surgery (SNIS), Society of Vascular and Interventional Neurology (SVIN), World Stroke Organization (WSO), World Federation of Interventional Neuroradiology (WFITN). **Standards of practice in acute ischemic stroke intervention: international recommendations.** *J Neurointerv Surg* 2018;10:1121–26 CrossRef Medline
15. Fiorelli M, Bastianello S, von KR, et al. **Hemorrhagic transformation within 36 hours of a cerebral infarct: relationships with early clinical deterioration and 3-month outcome in the European Cooperative Acute Stroke Study I (ECASS I) cohort.** *Stroke* 1999; 30:2280–84 CrossRef Medline
16. Suh SH, Cloft HJ, Fugate JE, et al. **Clarifying differences among thrombolysis in cerebral infarction scale variants: is the artery half open or half closed?** *Stroke* 2013;44:1166–68 CrossRef Medline
17. Lee SJ, Hong JM, Lee M, et al. **Cerebral arterial calcification is an imaging prognostic marker for revascularization treatment of acute middle cerebral arterial occlusion.** *J Stroke* 2015;17:67–75 CrossRef Medline
18. Mokin M, Morr S, Natarajan SK, et al. **Thrombus density predicts successful recanalization with Solitaire stent retriever thrombectomy in acute ischemic stroke.** *J Neurointerv Surg* 2015;7:104–07 CrossRef Medline
19. Brinjikji W, Duffy S, Burrows A, et al. **Correlation of imaging and histopathology of thrombi in acute ischemic stroke with etiology and outcome: a systematic review.** *J Neurointerv Surg* 2017;9:529–34 CrossRef Medline
20. Berkhemer OA, Fransen PSS, Beumer D, et al; MR CLEAN Investigators. **A randomized trial of intraarterial treatment for acute ischemic stroke.** *N Engl J Med* 2015;372:11–20 CrossRef Medline
21. Goyal M, Menon BK, van Zwam WH, et al; HERMES Collaborators. **Endovascular thrombectomy after large-vessel ischaemic stroke: a meta-analysis of individual patient data from five randomised trials.** *Lancet* 2016;387:1723–31 CrossRef Medline
22. Hesse AC, Behme D, Kemmling A, et al. **Comparing different thrombectomy techniques in five large-volume centers: a 'real world' observational study.** *J Neurointerv Surg* 2018;10:525–29 CrossRef Medline
23. Binning MJ, Bartolini B, Baxter B, et al. **Trevo 2000: results of a large real-world registry for stent retriever for acute ischemic stroke.** *J Am Heart Assoc* 2018;7:e010867 CrossRef Medline
24. Gunning GM, McArdle K, Mirza M, et al. **Clot friction variation with fibrin content: implications for resistance to thrombectomy.** *J Neurointerv Surg* 2018;10:34–38 CrossRef Medline
25. Chang Y, Kim BM, Bang OY, et al. **Rescue stenting for failed mechanical thrombectomy in acute ischemic stroke: a multicenter experience.** *Stroke* 2018;49:958–64 CrossRef Medline
26. Wareham J, Flood R, Phan K, et al. **A systematic review and meta-analysis of observational evidence for the use of bailout self-expandable stents following failed anterior circulation stroke thrombectomy.** *J Neurointerv Surg* 2019;11:675–82 CrossRef Medline
27. Sung SM, Lee TH, Cho HJ, et al. **Recanalization with Wingspan stent for acute middle cerebral artery occlusion in failure or contraindication to intravenous thrombolysis: a feasibility study.** *AJNR Am J Neuroradiol* 2012;33:1156–61 CrossRef Medline
28. Dumont TM, Natarajan SK, Eller JL, et al. **Primary stenting for acute ischemic stroke using the Enterprise vascular reconstruction device: early results.** *J Neurointerv Surg* 2014;6:363–72 CrossRef Medline
29. Mocco J, Hanel RA, Sharma J, et al. **Use of a vascular reconstruction device to salvage acute ischemic occlusions refractory to traditional endovascular recanalization methods.** *J Neurosurg* 2010;112: 557–62 CrossRef Medline
30. Broussalis E, Weymayr F, Hitzl W, et al. **Endovascular mechanical recanalization of acute ischaemic stroke in octogenarians.** *Eur Radiol* 2016;26:1742–50 CrossRef Medline
31. Slater LA, Coutinho JM, Gralla J, et al; STAR and SWIFT investigators. **TICI and age: what's the score?** *AJNR Am J Neuroradiol* 2016;37:838–43 CrossRef Medline
32. Hilditch CA, Nicholson P, Murad MH, et al. **Endovascular management of acute stroke in the elderly: a systematic review and meta-analysis.** *AJNR Am J Neuroradiol* 2018;39:887–91 CrossRef Medline
33. Kirchhof K, Sicking M, Welzel T, et al. **Does the result of thrombolysis with recombinant tissue-type plasminogen activator (rt-PA) in rabbits depend on the erythrocyte- and fibrin-content of a thrombus?** [in German] *Rofo* 2004;176:98–105 CrossRef Medline
34. Kissela BM, Kothari RU, Tomsick TA, et al. **Embolization of calcific thrombi after tissue plasminogen activator treatment.** *J Stroke Cerebrovasc Dis* 2001;10:135–38 CrossRef Medline

Comparison of Aspiration versus Stent Retriever Thrombectomy as the Preferred Strategy for Patients with Acute Terminal Internal Carotid Artery Occlusion: A Propensity Score Matching Analysis

P.F. Xing, P.F. Yang, Z.F. Li, L. Zhang, H.J. Shen, Y.X. Zhang, Y.W. Zhang, and J.M. Liu



ABSTRACT

BACKGROUND AND PURPOSE: There is no consensus on endovascular treatment for terminal ICA. The purpose of this study was to evaluate the comparative safety and efficacy of preferred aspiration thrombectomy and stent retriever thrombectomy for revascularization in patients with isolated terminal ICA occlusion.

MATERIALS AND METHODS: We conducted a retrospective analysis of patients with terminal ICA occlusion treated with aspiration thrombectomy or stent retriever thrombectomy in our center, from September 2013 to November 2018. To minimize the case bias, propensity score matching was performed. The primary outcomes were successful reperfusion defined by expanded TICI grades 2b–3 at the end of all endovascular procedures and puncture-to-reperfusion time.

RESULTS: A total of 109 consecutive patients with terminal ICA occlusion were divided into the aspiration thrombectomy group (40 patients) and the stent retriever thrombectomy group (69 patients), and 30 patients were included in each group after propensity score matching. The proportion of complete reperfusion was significantly higher in the aspiration thrombectomy group (OR 4.75 [95% CI, 1.10–1.38]; $P = .002$). The median puncture-to-reperfusion time in the aspiration thrombectomy group was shorter than that in the stent retriever thrombectomy group (38 versus 69 minutes; $P = .001$). Fewer intracerebral hemorrhage events were recorded in the aspiration thrombectomy group (OR 0.29 [95% CI, 0.09–0.90]; $P = .028$). No significant differences were observed for good outcomes (OR 1.92 [95% CI, 0.86–4.25]) and mortality (OR 0.84 [95% CI, 0.29–2.44]) at 90 days.

CONCLUSIONS: For the treatment of terminal ICA occlusion, aspiration thrombectomy was technically superior to stent retriever thrombectomy in the absence of a balloon guide catheter in achieving successful reperfusion with shorter puncture-to-reperfusion time and procedure-related adverse events.

ABBREVIATIONS: ASITN/SIRs = American Society of Interventional and Therapeutic Neuroradiology/Society of Interventional Radiology scale; ASPECTS = Alberta Stroke Program Early CT Score; AT = aspiration thrombectomy; BGC = balloon guide catheter; eTICI = expanded TICI; ICH = intracerebral hemorrhage; ID = internal diameter; PRT = puncture-to-reperfusion time; PSM = propensity score matching; SRT = stent retriever thrombectomy

Terminal ICA occlusion is a strong predictor of both lower revascularization success and subsequent clinical outcomes, which occur due to a large clot burden, insufficient collateral flow mediated via the contralateral ICA, and new territory emboli

being present during treatment.^{1–5} No consensus has been reached on the preferred endovascular treatment for isolated terminal ICA occlusion that leads to the use of either aspiration thrombectomy (AT) by using a large bore aspiration catheter or stent retriever thrombectomy (SRT). A previous study indicated that AT was useful for rapid clot burden reduction in endovascular therapy for ICA T/L occlusion (T or L indicate the shape of occlusive lesion), and it could facilitate thrombectomy of a large cerebral clot burden.⁴ In contrast to these findings, a retrospective study demonstrated that patients with a higher initial NIHSS score and ICA clot location should be considered for early crossover (manual AT crossed over to stent retriever-mediated AT) or even initial stent retriever-mediated AT for their clots.⁵ The randomized controlled trials, systematic reviews, and meta-analyses previously conducted did not yield consistent

Received October 29, 2019; accepted after revision December 23.

From the Department of Stroke Center, Changhai Hospital, Second Military Medical University, Shanghai, China.

P.F. Xing and P.F. Yang contributed equally to this work.

This study was funded by the Project of Research and Application of Effective Intervention Techniques for High-Risk Stroke Population of China in 2017 (GN-2017R0001).

Please address correspondence to Jian-Min Liu, MD, Department of Stroke Center, Changhai Hospital, Second Military Medical University, No. 168 Changhai Rd, Shanghai 200433, China; e-mail: Liu118@vip.163.com

Indicates open access to non-subscribers at www.ajnr.org

<http://dx.doi.org/10.3174/ajnr.A6414>

conclusions with regard to AT and SRT.⁶⁻⁹ Most of the patients in these studies had MCA occlusions and the proportion of the patients with a terminal ICA occlusion was lower. Moreover, subgroup analysis based on the occlusion location was not performed, which may have produced different results. The objective of the present retrospective study was to evaluate the comparative safety and efficacy of preferred AT and SRT for revascularization in patients with isolated terminal ICA occlusion by using propensity score matching (PSM) analysis.

MATERIALS AND METHODS

Patient Selection

A retrospective analysis was performed in patients with acute ischemic stroke who were admitted to our center between September 2013 and November 2018. The patients experienced isolated terminal ICA occlusion and were treated by using either AT or SRT within 16 hours of symptom onset. The patients were administered a standard dose (0.9 mg/kg) of rtPA if they experienced acute ischemic stroke symptoms within the 4.5-hour time window and in the absence of additional contraindications. The patients who presented with wake-up stroke or with acute ischemic stroke between 6 and 16 hours after symptom onset were included only if the initial infarct size was < 70 mL and if the mismatch ratio was ≥ 1.8 , as assessed by using RAPID software (iSchemaView, Menlo Park, California), which was based on CT perfusion imaging.^{10,11} The patients with tandem occlusions, severe stenosis (>70%), missing data, and/or mRS at the 90-day time period were excluded.

Mechanical Thrombectomy Procedure and Grouping

Balloon guide catheters (BGCs) were not available in our center before 2019. Therefore an 8F VISTA BRITE TIP guide catheter (internal diameter [ID] 0.088 inch, length 90 cm; Cordis, Miami Lakes, Florida) was placed at the ICA ostium for all procedures. The Traxcess 14 (diameter 0.014 inch, length 200 cm; MicroVention, Aliso Viejo, California) microwire, and the Rebar 27 microcatheter (ID 0.027 inch, length 150 cm; Medtronic, Minneapolis, Minnesota) were used in all cases. The 6F Navien (ID 0.072 inch, length 125 cm; Medtronic), ACE 64 (distal ID 0.064 inch, length 132 cm; Penumbra, Alameda, California), or 6F Sofia Plus (distal ID 0.070 in, length 125 cm; MicroVention) catheters were used as either intermediate or aspiration catheters in all cases. The Penumbra Pump MAX (Penumbra) and 60-mL syringes (Wego, Weihai, Shandong, China) were used to generate the aspiration force. The Solitaire FR (sizes 6 \times 30 mm or 4 \times 20 mm; Medtronic), Trevo ProVue (sizes 4 \times 20 mm; Stryker, Kalamazoo, Michigan), or the Revive SE (sizes 4.5 \times 22 mm; Codman, Raynham, Massachusetts) were the stent retrievers used in the present study. Visipaque contrast media (GE Healthcare, Piscataway, New Jersey) was used for all patients.

In AT, the intermediate catheter was deployed beyond the surface of the clot by continuous negative pressure aspiration. The microcatheter and microwire were withdrawn synchronously. The time of aspiration from the intermediate catheter with the Penumbra pump was at least 90 seconds in AT before its

removal. In SRT, the effective section of the stent retriever was deployed to cover the thrombus and to remain at this position for 3 minutes. However, the aspiration was applied only during stent retriever removal in SRT. Once obvious resistance was applied during stent retriever removal, the stent retriever was not completely withdrawn from the intermediate catheter. The withdrawal was conducted with the intermediate catheter under continuous aspiration. Aspiration was performed to the guide catheter (contacted with a 60-mL syringe) and to the intermediate catheter (contacted with a connecting tube of Penumbra pump) in the AT and SRT groups synchronously during thrombectomy. The illustrative cases of AT and SRT are shown in Figures 1 and 2, respectively.

The patients were divided into the AT and the SRT groups based on the initial treatment technique used. The initial treatment technique was based on the physician preference and on the availability of the aspiration catheters at the center. AT was initially selected for cervical ICA pseudo-occlusion. SRT was replaced by AT as rescue treatment when mechanical thrombectomy failed with 3 passes and vice versa. Other rescue strategies, including balloon dilation, stent placement, and glycoprotein IIb/IIIa receptor inhibitor treatment were used when mechanical thrombectomy failed to achieve adequate reperfusion. IV heparin (0.67 mg/kg) was used routinely from the femoral artery puncture until the end of the procedure for patients without rtPA.

Study Outcomes and Assessments

The collateral grade before endovascular therapy, including anterior cerebral artery occlusion, was assessed with the American Society of Interventional and Therapeutic Neuroradiology/Society of Interventional Radiology scale (ASITN/SIRs), which is a 5-point scale (0–4). The primary outcomes were the successful reperfusion (defined as expanded TICI [eTICI] grades 2, 2c, 3) and complete revascularization, defined as eTICI 3 at the end of the angiography. Complete revascularization was accomplished after the end of all endovascular treatments and the termination of the puncture-to-reperfusion time (PRT). The secondary outcomes included optimum functional outcomes, defined as a mRS score of 0–2 at 90 days, successful revascularization rates after the first pass with the first-line technique, a requirement for rescue treatment, 90-day mortality, and procedure-related adverse events. The main procedure-related adverse events were the following: intracerebral hemorrhage (ICH), malignant cerebral edema (brain tissue swelling with mass effect in the absence of hemorrhage), and downstream territory embolism. The latter was defined as new embolism in a downstream territory vessel that was not previously occluded, such as an embolus from the terminal ICA to the MCA M2 segment, or anterior cerebral artery A2 segment.

Statistical Analysis

The baseline patient demographic information was described with standard descriptive statistics. The outcome data were reported as frequency, mean \pm standard deviation, or median (interquartile range). When applicable, the χ^2 test, the rank sum test, and the *t* test were used to compare the differences between the groups. To reduce data bias and confounding variables, the

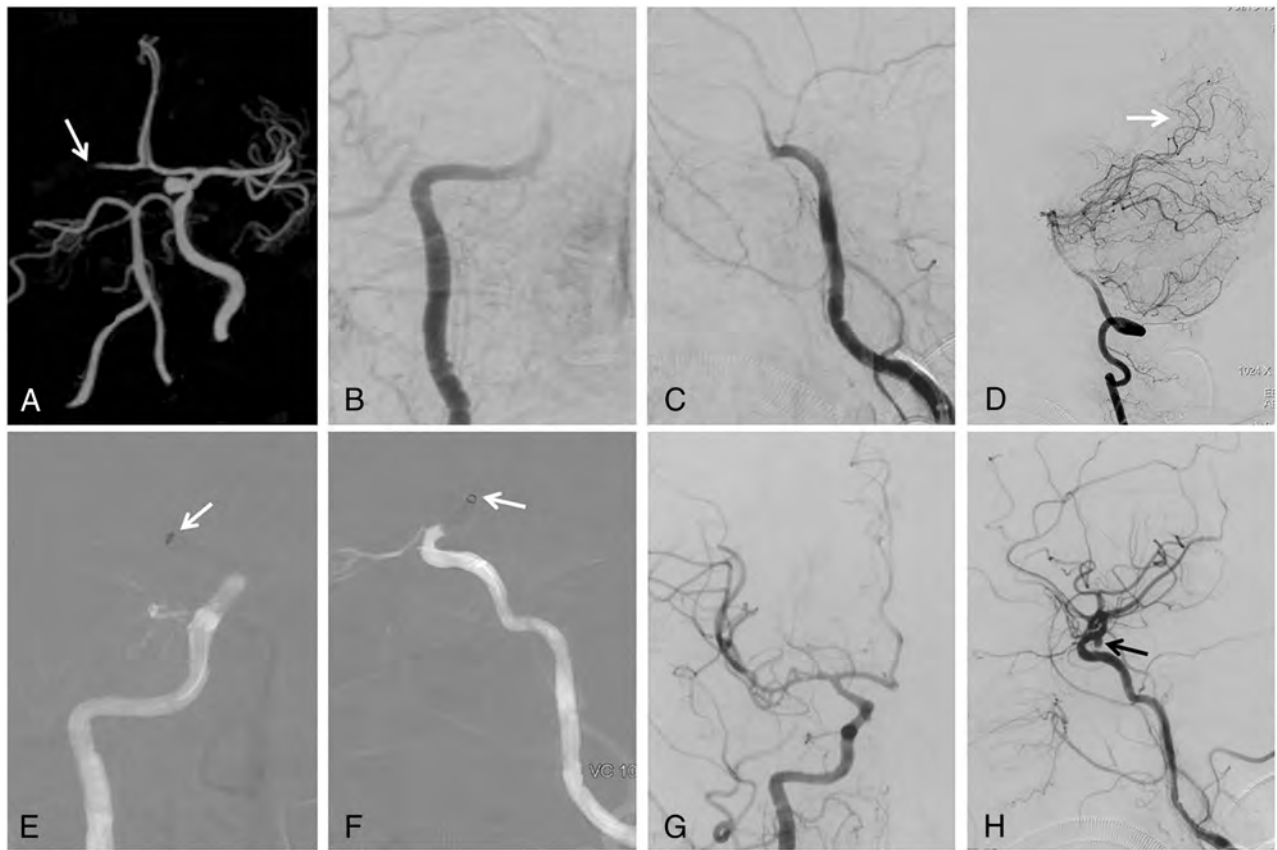


FIG 1. A, AT. Preprocedure CTA of the head indicated that the terminal end of the right ICA was occluded and that the blood flow from the left ICA was supplied to the right anterior cerebral artery and to the ostium of the A1 segment (white arrow) through the anterior communicating artery. B and C, DSA of the right ICA confirmed that the terminal ICA was occluded. D, A collateral blood supply was present from the posterior cerebral artery to the temporal lobe. E and F, A 6F Sofia Plus 125 cm (0.070 inch) catheter connected to a Penumbra pump was inserted into the terminal ICA via roadmap imaging and was placed beyond the face of the thrombus (white arrows). G and H, The ICA was recanalized, with eTICI 3 after 1-pass AT, and a supraclinoid segment aneurysm was present (H, black arrow).

PSM analysis was performed by matching patients in the 2 groups at a 1:1 ratio. The matched variables in the PSM of this study included sex, age, preprocedure NIHSS score, onset to puncture time, and ASITN/SIRs grade. After PSM, the 2 groups were again compared with the aforementioned statistical methods. A P value of $<.05$ was considered as a significant difference. All statistical analyses were conducted with the SPSS software (version 22.0; IBM, Armonk, New York).

RESULTS

Baseline Characteristics of the Groups

A total of 109 patients with acute ischemic stroke (mean \pm standard deviation age, 69.1 ± 11.2 years; 49 men [45.0%]) with isolated terminal ICA occlusions met the study inclusion criteria. A total of 40 of the 109 patients (36.7%) were treated with preferred AT, whereas the remaining 69 (63.3%) were treated with preferred SRT. After PSM, 30 cases were included in each group. The baseline characteristics were not significantly different between the groups in the overall sample or in the PSM sample (Table 1) (all $P > .05$). The median (interquartile range) preprocedure NIHSS score was 21 (15–23) in the AT group and 19 (16–22) in the SRT group ($P = .160$). The median collateral grades assessed by ASITN/SIRs, the median baseline Alberta Stroke

Program Early CT Score (ASPECTS), and the proportion of ASPECTS < 6 in the AT and SRT groups were similar for the overall and the PSM samples ($P > .05$) (Table 1).

Effectiveness of Endovascular Treatment of the Groups

In the overall sample, the successful revascularization rates in the AT group were significantly higher than those of the SRT group (eTICI 2b–3: OR 1.23 [95% CI, 1.10–1.38], $P = .002$; eTICI 2c–3: OR 4.62 [95% CI, 1.72–12.43], $P = .001$; and eTICI 3: OR 3.05 [95% CI, 1.32–7.06], $P = .008$) (Table 2, Figure 3). The median PRT in the AT group was significantly lower than that in the SRT group (46 minutes versus 83 minutes, $P = .001$). However, no significant differences were noted between the groups with regard to the first-pass revascularization rates (for eTICI 2b–3, 2c–3, or 3), the median number of thrombectomy passes, the median time from onset to reperfusion, the proportion of patients who required rescue treatment, the use of rtPA, the administration of glycoprotein IIb/IIIa receptor inhibitors, simple balloon angioplasty, stent placement, IV heparin treatment, and an mRS score of 0–2 at the 90-day period (all $P > .05$) (Table 2).

In the PSM sample, the findings were similar. The proportion of patients in the AT group with an eTICI 2c–3 (OR 6.50 [95% CI, 1.82–23.21]; $P = .006$) and eTICI 3 (OR 4.75 [95% CI,

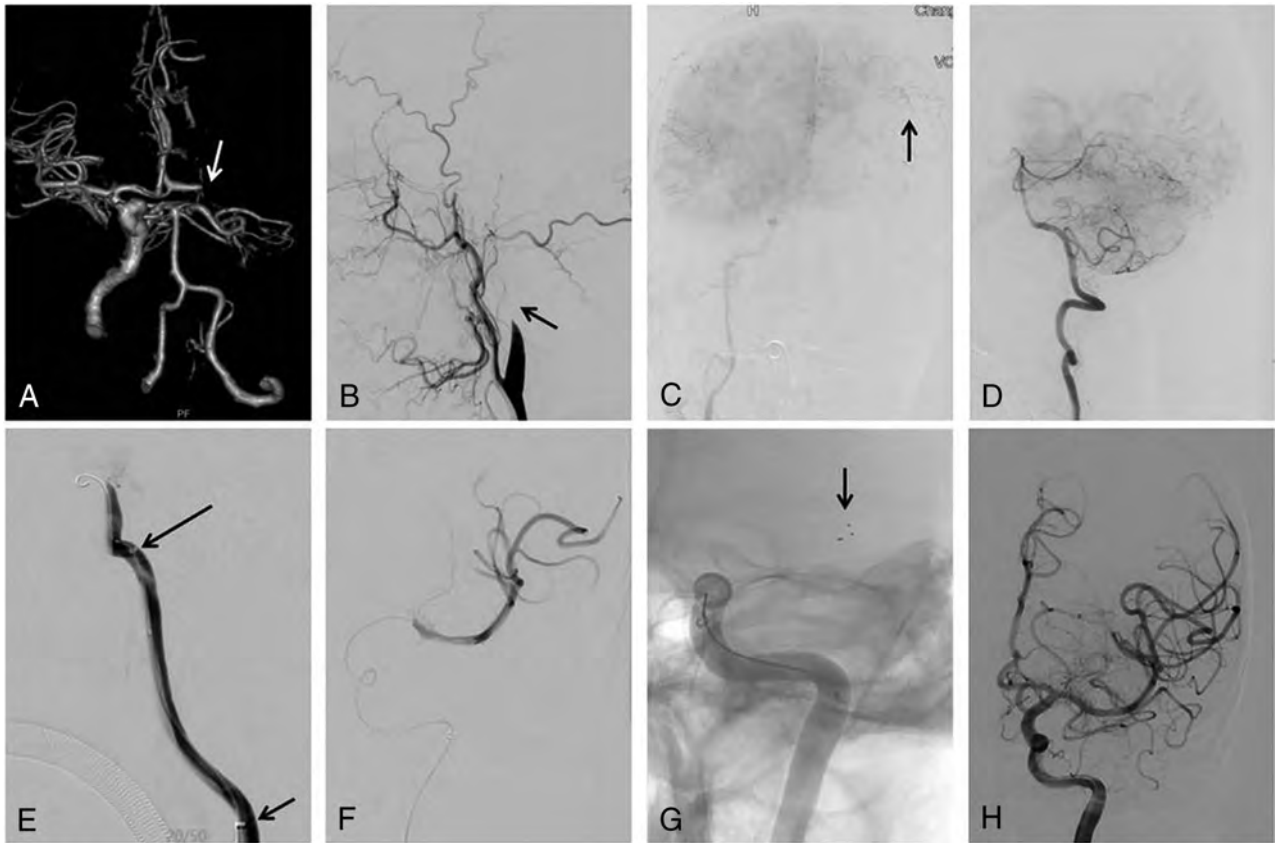


FIG 2. SRT. *A*, A preprocedural CTA of the head indicated that the terminal end of the left ICA was occluded and that the blood flow from the right ICA was supplied to the left anterior cerebral artery and to the ostium of the A1 segment (*white arrow*) through the anterior communicating artery. *B*, DSA of the left common carotid artery revealed that the left ICA was occluded (*black arrow*). *C*, DSA of the right ICA indicated similar results to (*A*) CTA, and no collateral blood supply was observed from the (*D*) posterior to the anterior circulation. *E*, DSA of the intermediate catheter (*long black arrow*) and guide catheter (*short black arrow*) demonstrated that the left carotid terminus was occluded, whereas the cervical ICA was not occluded (pseudo-occlusion) compared with that of image *B*. *F*, DSA was performed via the microcatheter crossing the occluded segment and the MCA was patent. *G*, A Solitaire FR 6 × 30 mm stent was used and inserted into the 6F Sofia Plus 125-cm catheter, which was advanced closer to the thrombus for local aspiration after the stent-retriever removal. *H*, The ICA was recanalized to eTICI 3 after a 1-pass SRT.

1.58–14.25]; $P = .004$) was significantly higher than that noted for the SRT group, though the groups did not significantly differ with regard to the parameter eTICI 2b–3 (OR 1.11 [95% CI, 0.99–1.25]; $P = .237$). The median PRT was significantly lower in the AT group compared with the SRT group (38 versus 69 minutes, $P = .001$), whereas the other outcomes were not significantly different between the different groups (all $P > .05$) (Table 2).

Procedure-Associated Adverse Events

The overall rate of the adverse events noted in the study was significantly lower in the AT group compared with that of the SRT group (52.5% versus 72.5%; OR 0.42 [95% CI, 0.19–0.95], $P = .035$), with the exception of malignant cerebral edema (10.0% versus 27.5%; OR 0.29 [95% CI, 0.09–0.93]; $P = .05$). The rates of any ICH, symptomatic ICH, or the downstream territory embolism were lower in the AT group compared with the SRT group. However, the differences were not significant. Similarly, the rate of all-cause mortality at the 90-day time period was 15% in the AT group and 17.4% in the SRT group (OR 0.84 [95% CI, 0.29–2.44]; $P = .746$). In the PSM sample, the rate of ICH in the

AT group was significantly lower than that in the SRT group (20.0% versus 46.7%; OR 0.29 [95% CI, 0.09–0.90], $P = .028$). However, with regard to the other adverse events, including the rate of mortality at the 90-day period, no significant differences were noted between the 2 groups (all $P > .05$) (Table 3).

DISCUSSION

The results of the present study indicated that the patients who presented within 16 hours of onset of terminal ICA occlusion and received treatment with direct AT as the preferred therapy exhibited a higher percentage of reperfusion, shorter PRT, and fewer ICH adverse events compared with the corresponding end points of the patients treated with preferred SRT. Although the eTICI 2b–3 rate was higher in the AT group, the results were not significantly different after PSM, which was similar to the results of the Contact Aspiration Versus Stent Retriever for Successful Revascularization (ASTER) and COMPASS Trial: a Direct Aspiration First Pass Technique (COMPASS) trials.^{6,7} However, in the present study, the rate of eTICI 2c–3 and eTICI 3 grade after the complete procedure was significantly higher in the AT

Table 1: Baseline characteristics of raw and PSM data of the 2 groups

	Overall Sample				PSM Sample			
	AT Group (n = 40)	SRT Group (n = 69)	OR (95% CI)	P	AT Group (n = 30)	SRT Group (n = 30)	OR (95% CI)	P
Sex, male, n (%)	21 (52.5)	28 (40.6)	1.62 (0.74–3.54)	.228	13 (43.3)	11 (36.7)	1.32 (0.47–3.72)	.598
Age, mean ± SD, y	68.3 ± 14.0	69.5 ± 9.2	NA	.631	69.2 ± 14.0	69.4 ± 7.9	NA	.946
Pre-NIHSS score, median (IQR)	21 (15–23)	19 (16–22)	NA	.160	21 (15–22)	18 (16–22)	NA	.342
Stroke etiology								
Cardioembolic, n (%)	37 (92.5)	57 (82.6)	2.60 (0.69–9.82)	.248	28 (93.3)	25 (83.3)	2.80 (0.50–15.73)	.421
Large vessel atherosclerosis, n (%)	1 (2.5)	10 (14.5)	0.15 (0.02–1.23)	.094	1 (3.3)	2 (6.7)	0.48 (0.04–5.63)	.999
Other etiology, n (%)	2 (5.0)	2 (2.9)	1.76 (0.24–13.02)	.973	1 (3.3)	3 (10.0)	0.31 (0.03–3.17)	.605
Onset to puncture time, median (IQR), min	288 (180–480)	240 (169–314)	NA	.061	250 (161–338)	243 (174–338)	NA	.859
ASITN/SIRs grade, median (IQR)	2 (1–2)	2 (1–2)	NA	.677	2 (1–2)	2 (1–2)	NA	.839
Baseline ASPECTS, median (IQR)	7 (5–8)	7 (6–8)	NA	.110	7 (5–8)	6 (5–7)	NA	.711
ASPECTS <6, n (%)	12 (30.0)	27 (39.1)	0.67 (0.29–1.53)	.338	9 (30.0)	11 (36.7)	0.74 (0.25–2.18)	.584

Note:—SD indicates standard deviation; IQR, interquartile range (25%–75%); NA, not applicable.

Table 2: Procedural details and clinical outcomes of the 2 groups

	Overall Sample				PSM Sample			
	AT Group (n = 40)	SRT Group (n = 69)	OR (95% CI)	P	AT Group (n = 30)	SRT Group (n = 30)	OR (95% CI)	P
eTICI 2b–3, n (%)	40 (100)	56 (81.2)	1.23 (1.10–1.38)	.002	30 (100)	27 (90.0)	1.11 (0.99–1.25)	.237
eTICI 2c–3, n (%)	34 (85.0)	38 (55.1)	4.62 (1.72–12.43)	.001	26 (86.7)	15 (50.0)	6.50 (1.82–23.21)	.006
eTICI 3, n (%)	29 (72.5)	32 (46.4)	3.05 (1.32–7.06)	.008	22 (73.3)	11 (36.7)	4.75 (1.58–14.25)	.004
First pass to eTICI 2b–3, n (%)	10 (25.0)	15 (21.7)	1.20 (0.48–3.00)	.696	9 (30.0)	9 (30.0)	1.00 (0.33–3.02)	.999
First pass to eTICI 2c–3, n (%)	10 (25.0)	12 (17.4)	1.58 (0.61–4.01)	.340	9 (30.0)	6 (20.0)	3.05 (1.00–9.93)	.044
First pass to eTICI 3, n (%)	8 (20.0)	11 (15.9)	1.32 (0.48–3.61)	.590	8 (26.7)	5 (16.7)	1.82 (0.52–6.38)	.347
No. passes of thrombectomy, median (IQR)	2 (2–3.7)	3 (2–4)	NA	.900	2 (1–3)	2.5 (1–3)	NA	.367
Rescue treatment, n (%)	6 (15.0)	8 (11.6)	1.35 (0.43–4.20)	.608	5 (16.7)	6 (20.0)	0.80 (0.22–2.97)	.739
PRT, median (IQR) (min)	46 (24–68)	83 (55–120)	NA	.001	38 (22–56)	69 (45–120)	NA	.001
Onset to reperfusion time, median (IQR) (min)	355 (222–550)	337 (264–420)	NA	.900	249 (205–391)	344 (248–450)	NA	.145
Use of rtPA, n (%)	12 (30.0)	33 (47.8)	0.47 (0.21–1.07)	.068	11 (36.7)	15 (50.0)	0.58 (0.19–1.59)	.297
Administration of GPI, n (%)	2 (5.0)	10 (14.5)	0.31 (0.06–1.50)	.227	1 (3.3)	3 (10.0)	0.31 (0.03–3.17)	.605
Balloon angioplasty, n (%)	1 (2.5)	2 (2.9)	0.86 (0.08–9.78)	.999	1 (3.3)	2 (6.7)	0.48 (0.04–5.63)	.999
Stent placement, n (%)	0 (0)	5 (7.2)	0.33 (0.04–2.91)	.156	0 (0)	2 (6.7)	1.07 (0.97–1.18)	.492
IV heparin, n (%)	28 (70.0)	36 (52.2)	2.14 (0.94–4.88)	.068	19 (63.3)	15 (50.0)	1.73 (0.62–4.85)	.297
mRS score 0–1 at 90 days, n (%)	13 (32.5)	15 (21.7)	1.73 (0.72–4.16)	.215	11 (36.7)	5 (16.7)	2.90 (0.86–9.75)	.080
mRS score 0–2 at 90 days, n (%)	17 (42.5)	22 (31.9)	1.92 (0.86–4.25)	.265	15 (50.0)	9 (30.0)	2.33 (0.81–6.73)	.114
mRS score 3–5 at 90 days, n (%)	17 (42.5)	35 (50.7)	0.72 (0.33–1.57)	.407	10 (33.3)	16 (53.3)	0.44 (0.15–1.24)	.118

Note:—NA indicates not applicable; GPI, glycoprotein IIb/IIIa receptor inhibitor.

group ($P = .008$), even after PSM ($P = .004$). This may be associated with the thrombectomy techniques. The aspiration catheter did not cross the occluded segment in the AT group, which would not disrupt the thrombus. Consequently, the thrombus would be totally removed. During SRT, the stent retriever may

disrupt the thrombus and cause embolization to the downstream territory.

Thrombectomy of these downstream territories was not attempted if an eTICI 2b or higher was achieved. Therefore, the proportion of the subjects who achieved eTICI 3 was significantly

expanded Thrombolysis In Cerebral Infarction (eTICI)

■ 3 ■ 2c ■ 2b ■ 2a ■ 1 ■ 0

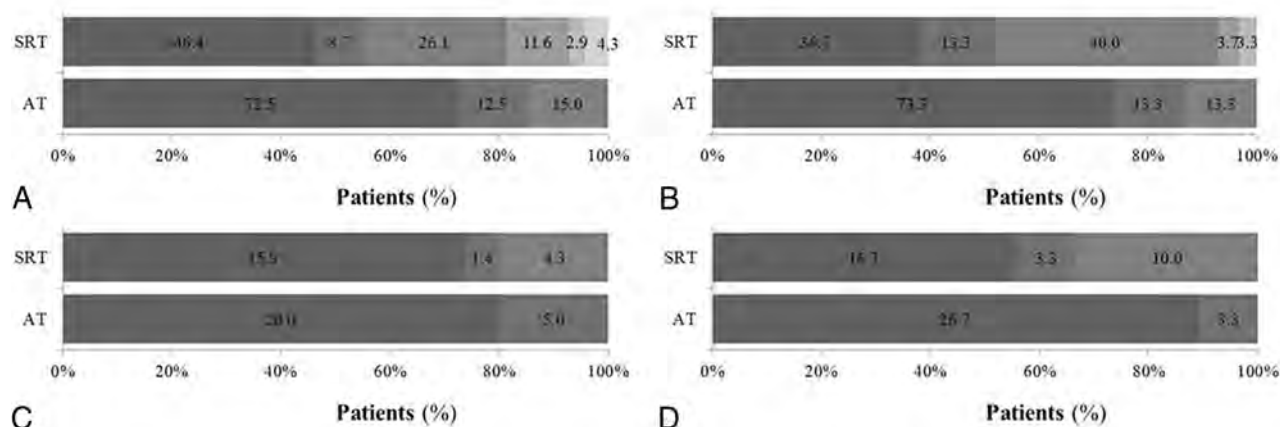


FIG 3. The eTICI grade distribution. The breakdown of the eTICI grade of the (A and C) AT and SRT groups in the overall sample and the (B and D) PSM sample. The grades included 0, 1, 2a, 2b, 2c, and 3, with 0 indicating no revascularization; 1 thrombus reduction without any revascularization of distal arteries; 2a, <50% revascularization; 2b, 50%–89% revascularization; 2c, 90%–99% revascularization; and 3 complete revascularization. A, The distribution of the final eTICI grade in the overall sample. Significant differences were noted between the AT and SRT groups in the overall sample in the successful revascularization rates (eTICI 2b–3: OR 1.23 [95% CI, 1.10–1.38]; eTICI 2c–3: OR 4.62 [95% CI, 1.72–12.43]; and eTICI 3: OR 3.05 [95% CI, 1.32–7.06]). B, The distribution of the final eTICI grade in the PSM sample. In the PSM sample, the groups did not significantly differ with regard to the eTICI 2b–3 (OR 1.11 [95% CI, 0.99–1.25]). C, The distribution of the first pass to eTICI 2b, 2c, and 3 in the overall sample. No significant differences were noted between the groups with regard to the first-pass revascularization rates (for eTICI 2b–3, 2c–3, or 3). D, The distribution of the first pass to eTICI 2b, 2c, and 3 in the PSM sample. In the PSM sample, the rate of eTICI 2c–3 in the AT group was higher than that in the SRT group (OR 3.05 [95% CI, 1.00–3.93]).

Table 3: Adverse events after mechanical thrombectomy in the 2 groups

	Overall Sample				PSM Sample			
	AT Group, n (%) (n = 40)	SRT Group, n (%) (n = 69)	OR (95% CI)	P	AT Group, n (%) (n = 30)	SRT Group, n (%) (n = 30)	OR (95% CI)	P
Overall adverse events	21 (52.5)	50 (72.5)	0.42 (0.19–0.95)	.035	14 (46.7)	20 (66.7)	0.44 (0.15–1.24)	.118
Any ICH	12 (30.0)	28 (40.6)	0.63 (0.27–1.44)	.269	6 (20.0)	14 (46.7)	0.29 (0.09–0.90)	.028
Symptomatic ICH	4 (10.0)	14 (20.3)	0.44 (0.13–1.43)	.260	3 (10.0)	8 (26.7)	0.31 (0.07–1.29)	.182
Downstream territory embolism	17 (42.5)	31 (44.9)	0.91 (0.41–1.99)	.806	11 (36.7)	11 (36.7)	1.00 (0.35–2.86)	.999
Malignant cerebral edema	4 (10.0)	19 (27.5)	0.29 (0.09–0.93)	.050	4 (13.3)	5 (16.7)	0.77 (0.19–3.20)	.999
All-cause mortality at 90 days	6 (15.0)	12 (17.4)	0.84 (0.29–2.44)	.746	6 (20.0)	6 (20.0)	1.00 (0.28–3.54)	.999

higher in the AT group, which was similar to the results noted in the COMPASS trial.⁷ Although the results were contrary to the ASTER trial,⁶ the rate of eTICI 3 in the present study was higher than that noted in the AT and SRT groups of the ASTER trial.⁶ However, this difference did not improve the favorable outcomes (mRS score, 0–2) noted at the 90-day period and no significant differences were noted in both the overall sample and in the PSM sample. The rates of mRS score of 0–2 in the AT and SRT groups were lower than those noted previously, which may be associated with the occluded location.^{6–9} Although no significant differences were noted between middle artery occlusions and ICA occlusions, the patients with ICA occlusions exhibited poor clinical outcomes.^{1,12,13} Moreover, the terminal ICA occlusion was considered to occur with lower complete recanalization in the presence of a

single thrombectomy device pass that renders it resistant to current techniques.¹⁴

The rates of the first pass to eTICI 2b–3, 2c–3, and 3 were similar in the overall samples (all $P > .05$), whereas the rate of the eTICI 2c–3 was higher after PSM ($P = .044$) in the AT group compared with that of the SRT group. These effects were lower than those noted in the ASTER and COMPASS trials,^{6,7} which included a higher proportion of MCA occlusions. Unlike SRT, AT enables the successful removal of the thrombus when the aspiration catheter is in contact with the core of thrombus. If the catheter does not contact the core of the thrombus, then the latter will not be removed. Therefore, a higher rate of rescue treatment was observed in the AT group, though the differences were not significant in the overall

sample ($P = .608$) and the PSM sample ($P = .739$). Nonterminal ICA occlusion was an independent predictor of achieving complete recanalization with a single thrombectomy device pass.¹⁴

An additional reason for observing a lower rate of the eTICI 2c–3 after the application of all the procedures and the first pass to eTICI 2c–3 in the SRT group may be attributed to the absence of the BGC. This device was considered an independent predictor of the first-pass effect success rate from a single thrombectomy device as well as a predictor of recanalization success and optimal clinical outcomes.^{15–19} Although it has been recommended as a routine adjuvant technique for stent retrieval by several studies,^{5,20} considerable controversy exists, notably when the distal access catheter is used in conjunction with the stent retriever, which may facilitate distal aspiration and minimize the impact of the absence of a BGC.⁶ BGCs were not available during the study in our center. Instead, 8F guide catheters were contacted with a 60 ml syringe both in the AT and SRT groups during thrombectomy, and intermediate catheters were used as a routine for distal aspiration in conjunction with stent retrievers in the SRT group. The absence of a BGC may have reduced the rate of the eTICI 2b–3 in the present study, notably in the SRT group. However, the final successful recanalization rates noted both in the AT and SRT groups were not inferior to the results obtained when using a BGC.^{15,16} Although results of one study indicated that the use of a BGC was significantly superior to the application of the distal access catheter, the higher baseline ASPECTS demonstrated less-frequent ICA occlusions in the BGC group that could lead to significant bias of the results.¹⁵

The median PRT in the AT group was significantly lower than that of the SRT group in the overall sample ($P = .001$) and the PSM sample ($P = .001$). This may be associated with reduced time caused by the lack of crossing over the occluded segment and opening the stent retriever in the AT group. In the presence of the direct AT, the catheter simply requires contact to the proximal surface of the thrombus and does not need to fully cross the occluded segment, as noted for SRT. This finding is in agreement with the results of the COMPASS trial and those reported from relevant meta-analysis studies.^{7–9} In the present study, AT was selected as the first-line thrombectomy approach for patients with a longer time of onset. Therefore, the AT group exhibited longer median onset to puncture time, though, when PSM was applied, the results were not significant ($P = .859$). The advantages of shorter PRT in the AT group were balanced by the longer onset to puncture time. Therefore, the median onset to reperfusion time was similar in the AT and SRT groups after PSM ($P = .145$). The similar values obtained in the onset to reperfusion time were associated with optimal outcomes.^{21,22} This could explain the similarity in these results noted at the 90-day period between the groups with comparable basic characteristics after PSM, including age, pre-NIHSS score, stroke etiology, and collateral circulation. In this study, AT was more efficient than SRT due to fewer passes and less operative time during the procedure. This advantage was not balanced by the application of rescue treatment; the latter proportion in the AT group was higher than in the SRT group in the overall sample but lower in the PSM sample.

The favorable outcome incidence at the 90-day period was 40.0% (24/60) after PSM, which was lower than the results obtained in the Highly Effective Reperfusion evaluated in Multiple Endovascular Stroke Trials (HERMES) collaboration (46.0%) and in the current meta-analysis (45.9%–49.0%).^{8,9,23} The all-cause mortality noted at the 90-day period after PSM was 20.0% (12/60), which was higher than that noted in most the published studies with the exception of the COMPASS trial.^{6–9,23} The poor outcomes noted and the higher mortality were possibly associated with the occluded location. The natural history terminal ICA occlusion was extremely poor without reperfusion therapy, even after endovascular treatment.^{2,24} Although no significant differences were noted between outcome and mortality between the different groups, the overall rate of adverse events was lower in the AT group. Moreover, the rate of any ICH incidence after PSM was lower in the AT group ($P = .001$).

Although PSM analysis was used to minimize the case selection bias and the impact of confounding variables, the present study still exhibited several limitations. First, the absence of a BGC was one of the major limitations, despite the presence of alternative strategies. Second, despite the use of the aspiration by an intermediate catheter (distal access catheter) in the SRT group, the aspiration was performed only during stent-retriever withdrawal. The adjustments in the timing of aspiration utilization with SRT (eg, in the CAPTIVE [Continuous Aspiration Prior to Intracranial Vascular Embolectomy] technique) may improve the reperfusion rate of the terminal ICA occlusions.²⁵ This could be a topic of future research. Third, it was a retrospective study that spanned nearly 5 years. The changes of surgical experience, materials, and imaging methods may reflect the outcomes. Moreover, the low sample size did not allow subgroup analysis due to the clot burden score, clot length, or different types of ICA occlusions, which may be associated with different outcomes. Fourth, the core infarct size was not evaluated in patients treated within 6 hours. Moreover, some patients with large-sized core infarctions (such as ASPECTS < 6) treated with mechanical thrombectomy may decrease the proportion of favorable outcomes. They are considered unsuitable for endovascular treatment due to poor outcomes and a high incidence of symptomatic ICH.^{26,27} Fifth, the absence of subgroup analysis due to the application of the device within the aspiration and the stent-retriever cohorts further limited the study design.

CONCLUSIONS

For acute ischemic stroke due to terminal ICA occlusion, the results demonstrated that the use of AT as the preferred treatment was technically superior to SRT without proximal flow arrest when using a BGC in achieving complete recanalization, shortening PRT, and reducing the rate of ICH events. Additional studies are required to validate our findings in the context of BGC-assisted SRT and to determine the optimal treatment strategy for terminal ICA occlusion.

REFERENCES

1. Liebeskind DS, Flint AC, Budzik RF, et al. **Carotid I's, L's and T's: collaterals shape the outcome of intracranial carotid occlusion in**

- acute ischemic stroke. *J Neurointerv Surg* 2015;7:402–07 CrossRef Medline
2. Kwak JH, Zhao L, Kim JK, et al. **The outcome and efficacy of recanalization in patients with acute internal carotid artery occlusion.** *AJNR Am J Neuroradiol* 2014;35:747–53 CrossRef Medline
 3. King S, Khatri P, Carrozella J, et al. **Anterior cerebral artery emboli in combined intravenous and intra-arterial tPA treatment of acute ischemic stroke in the IMS I and II trials.** *AJNR Am J Neuroradiol* 2007;28:1890–94 CrossRef Medline
 4. Eesa M, Almekhlafi MA, Mitha AP, et al. **Manual aspiration thrombectomy through balloon-tipped guide catheter for rapid clot burden reduction in endovascular therapy for ICA L/T occlusion.** *Neuroradiology* 2012;54:1261–65 CrossRef Medline
 5. Tonetti DA, Desai SM, Casillo S, et al. **Stentriever salvage after failed manual aspiration thrombectomy.** *J Neurointerv Surg* 2019;11:747–50
 6. Lapergue B, Blanc R, Gory B, et al. **Effect of endovascular contact aspiration vs stent retriever on revascularization in patients with acute ischemic stroke and large vessel occlusion: the ASTER randomized clinical trial.** *JAMA* 2017;318:443–52 CrossRef Medline
 7. Turk AS III, Siddiqui A, Fifi JT, et al. **Aspiration thrombectomy versus stent retriever thrombectomy as first-line approach for large vessel occlusion (COMPASS): a multicentre, randomised, open label, blinded outcome, non-inferiority trial.** *Lancet* 2019;393:998–1008 CrossRef Medline
 8. Phan K, Dmytriw AA, Teng I, et al. **A direct aspiration first pass technique vs standard endovascular therapy for acute stroke: a systematic review and meta-analysis.** *Neurosurgery* 2018;83:19–28 CrossRef
 9. Tsang COA, Cheung IHW, Lau KK, et al. **Outcomes of stent retriever versus aspiration-first thrombectomy in ischemic stroke: a systematic review and meta-analysis.** *AJNR Am J Neuroradiol* 2018;39:2070–76 CrossRef Medline
 10. Dargazanli C, Consoli A, Barral M, et al. **Impact of modified TIC1 3 vs modified TIC1 2b reperfusion score to predict good outcome following endovascular therapy.** *AJNR Am J Neuroradiol* 2017;38:90–96 CrossRef Medline
 11. Flottmann F, Leischner H, Broocks G, et al. **Recanalization rate per retrieval attempt in mechanical thrombectomy for acute ischemic stroke.** *Stroke* 2018;49:2523–25 CrossRef Medline
 12. Flint AC, Duckwiler GR, Budzik RF, et al. **Mechanical thrombectomy of intracranial internal carotid occlusion: pooled results of the MERCI and Multi MERCI part I trials.** *Stroke* 2007;38:1274–80 CrossRef Medline
 13. Protto S, Sillanpää N, Pienimäki JP, et al. **Stent retriever thrombectomy in different thrombus locations of anterior cerebral circulation.** *Cardiovasc Intervent Radiol* 2016;39:988–93 CrossRef Medline
 14. Zaidat OO, Castonguay AC, Linfante I, et al. **First pass effect: a new measure for stroke thrombectomy devices.** *Stroke* 2018;49:660–66 CrossRef Medline
 15. Zaidat OO, Mueller-Kronast NH, Hassan AE, et al. **Impact of balloon guide catheter use on clinical and angiographic outcomes in the STRATIS Stroke Thrombectomy Registry.** *Stroke* 2019;50:697–704 CrossRef Medline
 16. Baek JH, Kim BM, Kang DH, et al. **Balloon guide catheter is beneficial in endovascular treatment regardless of mechanical recanalization modality.** *Stroke* 2019;50:1490–96 CrossRef Medline
 17. Brinjikji W, Starke RM, Murad MH, et al. **Impact of balloon guide catheter on technical and clinical outcomes: a systematic review and meta-analysis.** *J Neurointerv Surg* 2018;10:335–39 CrossRef Medline
 18. Stampfl S, Pfaff J, Herweh C, et al. **Combined proximal balloon occlusion and distal aspiration: a new approach to prevent distal embolization during neurothrombectomy.** *J Neurointerv Surg* 2017;9:346–51 CrossRef Medline
 19. Nguyen TN, Malisch T, Castonguay AC, et al. **Balloon guide catheter improves revascularization and clinical outcomes with the Solitaire device: analysis of the North American Solitaire Acute Stroke Registry.** *Stroke* 2014;45:141–45 CrossRef Medline
 20. O'Neill D, Griffin E, Doyle KM, et al. **A standardized aspiration-first approach for thrombectomy to increase speed and improve recanalization rates.** *AJNR Am J Neuroradiol* 2019;40:1335–41 CrossRef Medline
 21. Hwang YH, Kang DH, Kim YW, et al. **Impact of time-to-reperfusion on outcome in patients with poor collaterals.** *AJNR Am J Neuroradiol* 2015;36:495–500 CrossRef Medline
 22. Kim BM, Baek JH, Heo JH, et al. **Collateral status affects the onset-to-reperfusion time window for good outcome.** *J Neurol Neurosurg Psychiatry* 2018;89:903–09 CrossRef Medline
 23. Goyal M, Menon BK, Zwam WH, et al. **Endovascular thrombectomy after large-vessel ischaemic stroke: a meta-analysis of individual patient data from five randomised trials.** *Lancet* 2016;387:1723–31 CrossRef Medline
 24. Hernández-Pérez M, Pérez de la Ossa N, Aleu A, et al. **Natural history of acute stroke due to occlusion of the middle cerebral artery and intracranial internal carotid artery.** *J Neuroimaging* 2014;24:354–58 CrossRef Medline
 25. McTaggart RA, Tung EL, Yaghi S, et al. **Continuous aspiration prior to intracranial vascular embolectomy (CAPTIVE): a technique which improves outcomes.** *J Neurointerv Surg* 2017;9:1154–59 CrossRef Medline
 26. Kimura K, Iguchi Y, Shibasaki K, et al. **Large ischemic lesions on diffusion-weighted imaging done before intravenous tissue plasminogen activator thrombolysis predicts a poor outcome in patients with acute stroke.** *Stroke* 2008;39:2388–91 CrossRef Medline
 27. Hao Y, Yang D, Wang H, et al. **Predictors for symptomatic intracranial hemorrhage after endovascular treatment of acute ischemic stroke.** *Stroke* 2017;48:1203–09 CrossRef Medline

Access-Site Complications in Mechanical Thrombectomy for Acute Ischemic Stroke: A Review of Prospective Trials

 S.Z. Shapiro,  K.A. Sabacinski,  K. Mantripragada,  S.S. Shah,  A.A. Stein,  N.B. Echeverry,  G.A. MacKinnon, and  B.M. Snelling

ABSTRACT

BACKGROUND: A shift has occurred in interventional cardiology from transfemoral to transradial access due to a 70%–80% decrease in complications. This shift has not yet taken place in other interventional specialties, perhaps owing to the lack of generalizability of findings in the cardiology data.

PURPOSE: Our aim was to assess data from the recent mechanical thrombectomy prospective trials to better understand the access-site complication rate.

DATA SOURCES: Articles were systematically sourced from the National Center for Biotechnology Information PubMed archive.

STUDY SELECTION: According to the Preferred Reporting Items for Systematic Reviews and Meta-Analysis guidelines, prospective, randomized controlled trials published after 2008 with mention of major and/or minor femoral access-site complications in neuroendovascular mechanical thrombectomies were included.

DATA ANALYSIS: Major and minor femoral access-site complications were extracted. A total complication rate was calculated with major access-site complications alone and combined with minor access-site complications.

DATA SYNTHESIS: Seven prospective studies of 339 total screened met the inclusion criteria. Eleven major access-site complications were identified in of 660 total interventions, revealing a major access-site complication rate of 1.67% for patients undergoing mechanical thrombectomy with transfemoral access. If minor access-site complications were included, 35 total incidents were detected in 763 interventions, resulting in a total complication rate of 4.59%.

LIMITATIONS: Multiple unspecified vessel and procedure-related complications were mentioned in the studies.

CONCLUSIONS: The overall rate of major access-site complications was 1.67% in this review, which is not low and poses a risk to patients. We suggest further investigation into the feasibility and complication rates of alternative access sites for neurointerventional procedures.

ABBREVIATION: PRISMA = Preferred Reporting Items for Systematic Reviews and Meta-Analysis

The field of interventional cardiology in the United States and internationally has shifted away from transfemoral access to transradial access, given the profound safety benefits, including a remarkable reduction in access-site complications such as major/minor bleeding, pseudoaneurysm, and hematoma

development.^{1–7} Transradial access also leads to earlier ambulation postoperatively, shorter hospital stays, reduced costs, and improved patient satisfaction.^{5,6} Furthermore, successful transradial access has been reported in cases of failed transfemoral access secondary to tortuosity, stenosis near the aortic arch, bilateral iliac occlusions, and aortic dissection.⁸ Despite numerous prospective, randomized trials in the interventional cardiology literature, a shift away from transfemoral access toward transradial access in neurointerventional surgery has not yet been realized, with only 0.3%–4.5% of patients undergoing thrombectomy having transradial access in cerebrovascular interventions.⁹

Multiple reasons behind this slower adoption include the learning curve associated with accessing the cerebrovasculature via transradial access¹⁰ and anatomic variants complicating radial

Received September 22, 2019; accepted after revision January 7, 2020.

From Florida Atlantic University Charles E. Schmidt College of Medicine (S.Z.S., K.A.S., K.M., N.B.E., G.A.M., B.M.S.), Boca Raton, Florida; University of Miami Miller School of Medicine (S.S.S.), Miami, Florida; Department of Neurological Surgery (A.A.S.), New York Medical College, Valhalla, New York; and Marcus Neuroscience Institute (B.M.S.), Boca Raton Regional Hospital, Boca Raton, Florida.

Please address correspondence to Brian M. Snelling, MD, Marcus Neuroscience Institute, Boca Raton Regional Hospital, 800 Meadows Rd, Boca Raton, FL 3348; e-mail: brian.m.snelling@gmail.com

<http://dx.doi.org/10.3174/ajnr.A6423>

access with failure to reach the anterior cerebral vasculature, reported to be due to proximal left common carotid and right subclavian tortuosity, while failure to catheterize the vertebral arteries has been reported due to acute angulation and proximal origin of the vertebral arteries.¹¹ Other reasons for the slower adoption include difficulty accessing the cerebrovasculature using current transfemoral devices and a perceived lack of transfemoral-access complications during neurointerventional procedures.

Furthermore, there is the question of whether the wealth of transfemoral access data from interventional cardiology is generalizable to our specialty, owing to differences in anticoagulation regimens, procedural type, and access and hemostasis regimens. For example, in cardiology, 6F is the largest diameter catheter that could be effectively used via the transradial access.¹² Prior studies in animal models have shown that the minimal inner-catheter diameter needed for successful thrombectomy of the middle cerebral or internal carotid arteries is >0.040 inches and >0.064 inches, respectively, thus presenting a limitation in the minimum catheter size with which thrombectomy can be effectively performed via transradial access.¹³

We sought to obtain an objective understanding of transfemoral access-site complications in our own field and performed a systematic review of the prospective trial data regarding mechanical thrombectomy.

MATERIALS AND METHODS

Search and Information Sources

This review was performed in accordance with the Preferred Reporting Items for Systematic Reviews and Meta-Analyses (PRISMA). The PRISMA statement consists of a 27-item checklist and a 4-phase flow diagram.¹⁴ The aim of the PRISMA statement is to help authors improve the reporting of systematic reviews and meta-analyses. In addition to the PRISMA statement, a supporting explanation and elaboration document has been produced following the style used for other reporting guidelines.¹⁵

Articles were sourced from the National Center for Biotechnology Information PubMed archive, the *New England Journal of Medicine*, *Stroke*, and *Lancet Neurology*. The search terminology entered into the PubMed archive included “mechanical thrombectomy + prospective OR mechanical thrombectomy + RCT,” to locate the specific articles analyzed in this review. Articles considered for the review were only those published from 2008 to 2018.

Eligibility Criteria and Study Selection

Articles included in this review had to meet the following criteria: prospective, randomized controlled trials. Studies that did not specifically identify groin or access-site complications were deemed ineligible, including several large transfemoral thrombectomy trials such as A Direct Aspiration, First Pass Technique (ADAPT), Multicenter Randomized Clinical Trial of Endovascular Treatment for Acute Ischemic Stroke in the Netherlands (MR CLEAN), and Solitaire With the Intention For Thrombectomy as Primary Endovascular Treatment (SWIFT PRIME), and were excluded from this review because these studies failed to identify access-site complications specifically, instead grouping

them under overall procedural complications. Accordingly, 3 full-text articles that met the initial screening criteria were subsequently excluded.¹⁶⁻¹⁸ Serious transfemoral access-site complications were assessed in mechanical thrombectomies during an acute ischemic stroke. In the context of the included articles, serious complications/adverse events are defined as complications that meet any of the following criteria: resulted in a >3-g hemoglobin or a 10% hematocrit drop, required surgical/interventional radiology intervention, required transfusion, prolonged the patient's stay in the hospital, or resulted in death. Examples include groin hematoma requiring transfusion, artery dissection, pseudoaneurysm, and occlusion requiring embolectomy. Studies that addressed only minor access-site complications (ie, access-site ecchymosis) were excluded. Any studies using nonfemoral access-sites, written in a language other than English, and written before 2008 were also excluded (Figure).

Data Collection Process

Articles were compiled into a single data base from which identical and irrelevant articles were removed. Of the remaining articles, 7 articles met the inclusion criteria.¹⁹⁻²⁵ The 7 publications included were critically evaluated by the authors, and access-site complication rates (major, minor, and total) were extracted and compiled into a single databank.

RESULTS

Individual Study Characteristics

The methodology for each clinical trial is summarized in Table 1. Of note, the studies differed in device use for mechanical thrombectomy, timing of intervention, location of vessel occlusion, and tPA administration.

Data Analysis

The access-site complication rates for each of the studies (Table 2) ranged from 0% to 11.65%. Access-site complication rates were calculated by dividing the total number of access-site complications by the total number of participants in the mechanical thrombectomy arm of each study. The access-site complication rate, including both major and minor adverse events, gleaned from pooled data was 35/763 (4.59%). Subgroup analysis revealed that 11 major access-site complications were identified of 660 total interventions, revealing a major access-site complication rate of 1.67% for patients undergoing mechanical thrombectomy with transfemoral access.

There is mention of vessel dissections and perforations in these studies; however, the vessel was unspecified in all cases.

DISCUSSION

The clinical efficacy of mechanical thrombectomy in the management of acute ischemic stroke has been investigated in numerous randomized controlled trials. While the benefits and indications of mechanical thrombectomy continue to unfold, there is a paucity of research into the access-site-associated complications from these procedures.

Prior retrospective series likely underreported the rate of transfemoral access-site complications²⁶ because these studies may not include major, non-life-threatening complications.

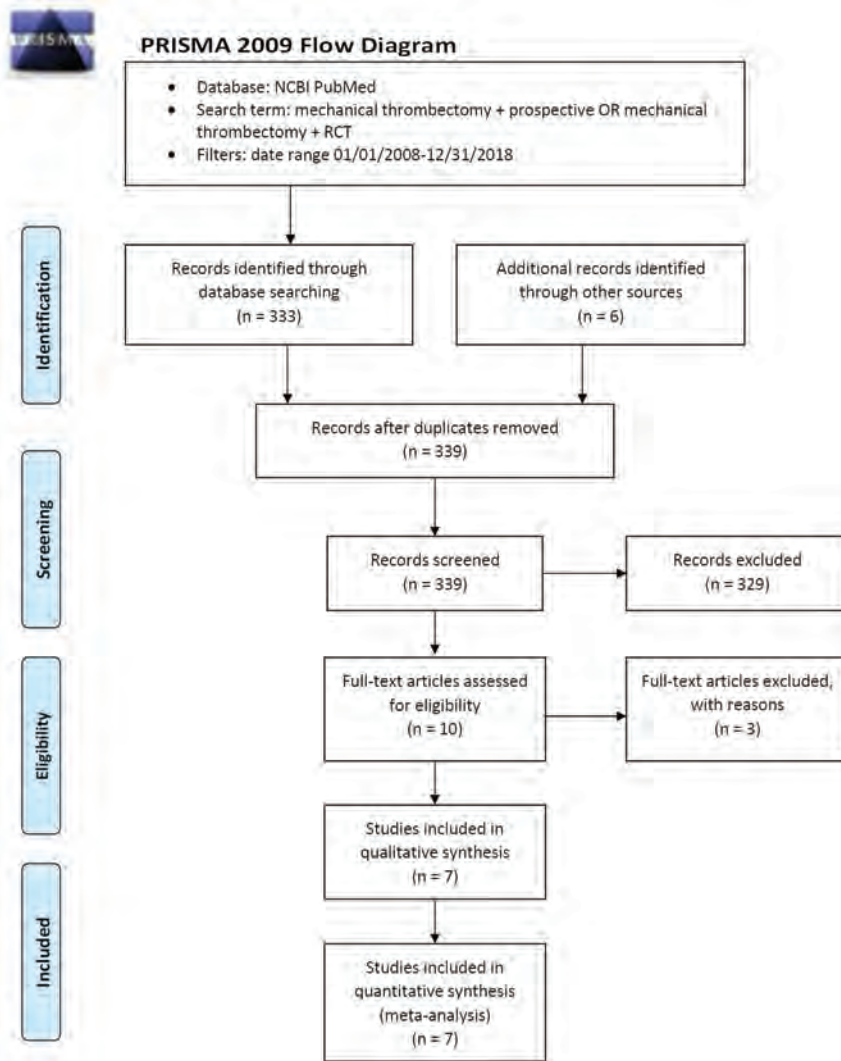


FIGURE. PRISMA flowchart.

Thus, our current understanding of access-site complications is limited, given the inherent limitations of retrospective review. This study sought to use high-level evidence to more accurately estimate the incidence of transfemoral access-site complications.

Our review found that the rate of serious access-site complications related to transfemoral access in mechanical thrombectomy was 1.67%, demonstrating that adverse events occurred in a notable percentage of transfemoral access stroke interventions. It is quite possible that the true rate of adverse events in our review was even greater than the reported figure because there were a number of adverse events that may have been access-site-related but could not be confirmed due to ambiguity in adverse event reporting in supplementary appendices.

Our findings are similar to meta-analyses on transfemoral access-site complications in interventional cardiology, which range from 2.2% to 4.8%.²⁷ Despite the technical differences between transfemoral access in interventional cardiology and stroke interventions, such as anticoagulation regimens, procedures, procedure lengths, and access/closure techniques and devices, access-site complication rates are similar. This

similarity suggests that the access-site itself, as the consistent factor between the 2 interventions, may play a larger role in the development of complications than expected and that these complications are, in essence, specialty agnostic.

In evaluating the limitations of our included trials, it is pertinent to differentiate major and minor access-site complications. Major access-site complications are defined as any complication that either requires further surgical intervention or prolongs the patient's hospital stay, consistent with definitions in most stroke trials. These major access-site complications include groin hematoma requiring transfusion and arterial dissection. Minor access-site complications are defined as complications that do not meet major criteria but were recorded in the trials. The minor access-site complications recorded in the studies were ecchymoses, local infection, and minor self-limiting femoral hematomas. Although our review sought to identify and report these major and minor access-site complications, all included studies except 1 (Endovascular Treatment for Small Core and Proximal Occlusion Ischemic Stroke [ESCAPE])²⁰ did not report minor complications. Lack of routine postprocedural sonography may have contributed to the underreporting of these complications.

When reporting vascular complications, many of the included studies did not specify a vessel. This vessel could be the femoral artery, and this would increase the access-site complication rate. Conversely, vessel complications in the cerebral vasculature would decrease the major-site-associated adverse event rate. Furthermore, there are complications listed in supplementary indices that are vague. Some of these include "arterial perforation," "vessel occlusion," and "vessel dissection." These complications may relate to the access-site; however, we could not be sure.

Last, the 4 studies that were excluded during eligibility assessment of access-site-associated adverse events may have altered the adverse event rate if details regarding these events were appropriately reported. Specifically, the Solitaire Flow Restoration Thrombectomy for Acute Revascularization (STAR) and Mechanical Embolus Removal in Cerebral Ischemia (MERCi) trials cited procedure-related adverse events and vessel dissections, and Endovascular Therapy Following Imaging Evaluation for Ischemic Stroke 3 (DEFUSE 3) reported vascular disorders and administration-site conditions. As mentioned in the above paragraph, failure to further subclassify vessel dissections further

Table 1: Summary of clinical trial methodology

Study	Device Used	Time since Stroke-Symptom Onset	Vessels	IV tPA	IA tPA
SWIFT ^{19a}	Solitaire FR (Covidien, Irvine, California); Merci Retriever (Concentric Medical, Mountain View, California)	<8 hr	Large-vessel occlusion	Contraindicated or failed	Excluded
ESCAPE ^{20b}	Any approved neurothrombectomy device	<12 hr	Large-vessel occlusion	Yes	Unspecified
REVASCAT ^{21c}	Solitaire FR	<8 hr	Anterior circulation occlusion	Yes	Allowed
EXTEND IA ^{22d}	Solitaire FR	<4.5 hr	Anterior circulation occlusion	Yes	Unspecified
DAWN ^{23e}	Trevo retriever (Stryker, Kalamazoo, Michigan)	6–24 hr	Anterior circulation occlusion	Contraindicated or failed	Excluded
MR RESCUE ^{24f}	Merci or Penumbra System (Penumbra, Alameda, California)	<8 hr	Large-vessel occlusion	Yes	Allowed
THRACE ^{25g}	Any approved neurothrombectomy device	<5 hr	Large-vessel occlusion	Yes	Allowed

Note:—IA indicates intra-arterial.

^a Solitaire With the Intention For Thrombectomy (SWIFT).

^b Endovascular Treatment for Small Core and Proximal Occlusion Ischemic Stroke (ESCAPE).

^c Endovascular Revascularization With Solitaire Device Versus Best Medical Therapy in Anterior Circulation Stroke Within 8 Hours (REVASCAT).

^d Extending the Time for Thrombolysis in Emergency Neurological Deficits—Intra-Arterial (EXTEND-IA).

^e Clinical Mismatch in the Triage of Wake Up and Late Presenting Strokes Undergoing Neurointervention With Trevo (DAWN).

^f Mechanical Retrieval and Recanalization of Stroke Clots Using Embolectomy (MR RESCUE).

^g Trial and Cost Effectiveness Evaluation of Intra-arterial Thrombectomy in Acute Ischemic Stroke (THRACE).

Table 2: Access-site complication rates

Trial	Non-Major AEs	Serious AEs	TAEs
SWIFT ^a	NA	4/144 (2.78%)	NA
ESCAPE ^b	12/165 (7.27%)	2/165 (1.21%)	14/165 (8.48%)
REVASCAT ^c	NA	NA	12/103 (11.65%)
EXTEND-IA ^d	NA	1/35 (2.86%)	NA
DAWN ^e	NA	1/107 (0.93%)	NA
MR RESCUE ^f	NA	0/64 (0%)	NA
THRACE ^g	NA	3/145 (2.07%)	NA

Note:—NA indicates not applicable; AE, adverse event; TAE, total adverse event.

^a No AE reported. Table 1 reports 4 groin complications; Table 5 reports 9 major adverse events at the access site.

^b Serious adverse events resulted in death, prolonged hospital stays, re-admission, or were severe or life-threatening. All minor events consisted of femoral hematomas.

^c TAEs are not stratified on the basis of whether they were AEs or major adverse events.

^d No AE reported. A major adverse event was a groin hematoma requiring transfusion.

^e No AE reported. A major adverse event was a vessel puncture-site hemorrhage requiring intervention.

^f No AE reported. A major adverse event consisted of 1 vessel dissection, though the vessel was not specified. There were no groin hematomas requiring intervention.

^g No AE reported. Dissections and arterial perforations do not indicate a vessel.

obfuscated the relation of the complication to the procedural access site.

CONCLUSIONS

The rate of major access-site complications following a transfemoral approach has not been investigated in the context of neurointerventional procedures in prior studies. Our analysis demonstrates rates of major access-site complications from transfemoral access, similar to those reported in the cardiology literature and that may, in fact, be higher. However, transradial access is not without its limitations. The radial artery has a small diameter, which presents clear challenges when introducing the 8F catheter required for cerebrovascular thrombectomies. We

suggest further investigation into the feasibility and complication rates of alternative access sites for neurointerventional procedures. Furthermore, given the benefits of a transradial approach, there is a clear need for radial artery-specific cerebrovascular catheters, which are both compatible with radial access while also permitting successful cerebrovascular interventions.

ACKNOWLEDGMENTS

The authors acknowledge Vivian R. Hagerty and Hunter R. Carlock for their assistance in writing this article.

Disclosures: Brian M. Snelling—UNRELATED: Stock/Stock Options: RIST Neurovascular. Comments: preclinical neurovascular medical device company, no conflict related to submitted article.

REFERENCES

- Windecker S, Kolh P, Alfonso F, et al; Authors/Task Force members. 2014 ESC/EACTS Guidelines on myocardial revascularization: the Task Force on Myocardial Revascularization of the European Society of Cardiology (ESC) and the European Association for Cardio-Thoracic Surgery (EACTS) developed with the special contribution of the European Association of Percutaneous Cardiovascular Interventions (EAPCI). *Eur Heart J* 2014;35:2541–49 CrossRef Medline
- Roffi M, Patrono C, Collet JP, et al; ESC Scientific Document Group. 2015 ESC Guidelines for the management of acute coronary syndromes in patients presenting without persistent ST-segment elevation: Task Force for the Management of Acute Coronary Syndromes in Patients Presenting without Persistent ST-Segment Elevation of the European Society of Cardiology (ESC). *Eur Heart J* 2016;37:267–315 CrossRef Medline
- Mehta SR, Jolly SS, Cairns J, et al; RIVAL Investigators. Effects of radial versus femoral artery access in patients with acute coronary syndromes with or without ST-segment elevation. *J Am Coll Cardiol* 2012;60:2490–99 CrossRef Medline
- Valgimigli M, Gagnor A, Calabro P, et al; MATRIX Investigators. Radial versus femoral access in patients with acute coronary

- syndromes undergoing invasive management: a randomised multicentre trial.** *Lancet* 2015;385:2465–76 CrossRef Medline
5. Snelling B, Sur S, Shah S, et al. **Transradial cerebral angiography: techniques and outcomes.** *J Neurointerv Surg* 2018;10:874–81 CrossRef Medline
 6. Patel P, Haussen DC, Nogueira RG, et al. **The neuro radialist.** *Interv Cardiol Clin* 2020;9:75–86 CrossRef Medline
 7. Jolly SS, Yusuf S, Cairns J, et al; RIVAL trial group. **Radial versus femoral access for coronary angiography and intervention in patients with acute coronary syndromes (RIVAL): a randomised, parallel group, multicentre trial.** *Lancet* 2011;377: 1409–20 CrossRef Medline
 8. Lee DG, Lee DH, Shim JH, et al. **Feasibility of the transradial or the transbrachial approach in various neurointerventional procedures.** *Neurointervention* 2015;10:74–81 CrossRef Medline
 9. Haussen DC, Nogueira RG, DeSousa KG, et al. **Transradial access in acute ischemic stroke intervention.** *J Neurointerv Surg* 2016;8:247–50 CrossRef Medline
 10. Snelling BM, Sur S, Shah SS, et al. **Transradial access: lessons learned from cardiology.** *J Neurointerv Surg* 2018;10:487–92 CrossRef Medline
 11. Snelling BM, Sur S, Shah SS, et al. **Transradial approach for complex anterior and posterior circulation interventions: technical nuances and feasibility of using current devices.** *Oper Neurosurg (Hagerstown)* 2019;17:293–302 CrossRef Medline
 12. Dahm JB, Vogelgesang D, Hummel A, et al. **A randomized trial of 5 vs. 6 French transradial percutaneous coronary interventions.** *Catheter Cardiovasc Interv* 2002;57:172–76 CrossRef Medline
 13. Nikoubashman O, Nikoubashman A, Büsen M, et al. **Necessary catheter diameters for mechanical thrombectomy with ADAPT.** *AJNR Am J Neuroradiol* 2017;38:2277–81 CrossRef Medline
 14. Moher D, Liberati A, Tetzlaff J, et al; PRISMA Group. **Preferred Reporting Items for Systematic Reviews and Meta-Analyses: the PRISMA Statement.** *Int J Surg* 2010;8:336–41 CrossRef Medline
 15. Liberati A, Altman DG, Tetzlaff J, et al. **The PRISMA statement for reporting systematic reviews and meta-analyses of studies that evaluate health care interventions: explanation and elaboration.** *PLoS Med* 2009;6:e1000100 CrossRef Medline
 16. Pereira VM, Gralla J, Davalos A, et al. **Prospective, multicenter, single-arm study of mechanical thrombectomy using Solitaire flow restoration in acute ischemic stroke.** *Stroke* 2013;44:2802–07 CrossRef Medline
 17. Smith WS, Sung G, Saver J, et al; Multi MERCI Investigators. **Mechanical thrombectomy for acute ischemic stroke.** *Stroke* 2008;39:1205–12 CrossRef Medline
 18. Albers GW, Marks MP, Kemp S, et al; DEFUSE 3 Investigators. **Thrombectomy for stroke at 6 to 16 hours with selection by perfusion imaging.** *N Engl J Med* 2018;378:708–18 CrossRef Medline
 19. Akins P, Amar A, Pakbaz R, et al; SWIFT Investigators. **Complications of endovascular treatment for acute stroke in the SWIFT trial with Solitaire and Merci devices.** *AJNR Am J Neuroradiol* 2014; 35:524–28 CrossRef Medline
 20. Goyal M, Demchuk AM, Menon BK, et al; ESCAPE Trial Investigators. **Randomized assessment of rapid endovascular treatment of ischemic stroke.** *N Engl J Med* 2015;372:1019–30 CrossRef Medline
 21. Jovin TG, Chamorro A, Cobo E, et al; REVASCAT Trial Investigators. **Thrombectomy within 8 hours after symptom onset in ischemic stroke.** *N Engl J Med* 2015;372:2296–2306 CrossRef Medline
 22. Campbell BC, Mitchell PJ, Kleinig TJ, et al; EXTEND-IA Investigators. **Endovascular therapy for ischemic stroke with perfusion-imaging selection.** *N Engl J Med* 2015;372:1009–18 CrossRef Medline
 23. Nogueira RG, Jadhav AP, Haussen DC, et al; DAWN Trial Investigators. **Thrombectomy 6 to 24 hours after stroke with a mismatch between deficit and infarct.** *N Engl J Med* 2018;378:11–21 CrossRef Medline
 24. Kidwell CS, Jahan R, Gornbein J, et al; MR RESCUE Investigators. **A trial of imaging selection and endovascular treatment for ischemic stroke.** *N Engl J Med* 2013;368:914–23 CrossRef Medline
 25. Bracard S, Ducrocq X, Mas JL, et al; THRACE investigators. **Mechanical thrombectomy after intravenous alteplase versus alteplase alone after stroke (THRACE): a randomised controlled trial.** *Lancet Neurol* 2016;15:1138–47 CrossRef Medline
 26. Mani R, Eisenberg RL, McDonald EJ Jr, et al. **Complications of catheter cerebral arteriography: analysis of 5,000 procedures. I: criteria and incidence.** *AJR Am J Roentgenol* 1978;131:861–65 CrossRef Medline
 27. Sobolev M, Slovut DP, Lee Chang A, et al. **Ultrasound-guided catheterization of the femoral artery: a systematic review and meta-analysis of randomized controlled trials.** *J Invasive Cardiol* 2015;27: 318–23 Medline

Implications of the Collar Sign in Incompletely Occluded Aneurysms after Pipeline Embolization Device Implantation: A Follow-Up Study

S. Gomez-Paz, Y. Akamatsu, J.M. Moore, C.S. Ogilvy, A.J. Thomas, and C.J. Griessenauer



ABSTRACT

BACKGROUND AND PURPOSE: The angiographic collar sign has been recently described in patients with incompletely occluded aneurysms after Pipeline Embolization Device implantation. The long-term implications of this sign are unknown. We report angiographic outcomes of patients with the collar sign with follow-up of up to 45 months and the implications of this angiographic finding.

MATERIALS AND METHODS: We performed a retrospective review of a prospectively maintained data base of patients who underwent Pipeline Embolization Device implantation for an intracranial aneurysm at our institution between January 2014 and December 2016. We included patients with a collar sign at the initial follow-up angiogram after Pipeline Embolization Device implantation.

RESULTS: A total of 198 patients with 285 aneurysms were screened for the collar sign on initial and subsequent follow-up angiograms. There were 226 aneurysms (79.3%) with complete occlusion at the first follow-up. Of 59 incompletely occluded aneurysms, 19 (32.2%) aneurysms in 17 patients were found to have a collar sign on the first angiographic follow-up (median, 6 months; range, 4.2–7.2). Ten (52.6%) aneurysms underwent retreatment with a second Pipeline Embolization Device, which resulted in aneurysm occlusion in 1 (10%) patient. There were only 3 (15.8%) aneurysms with complete occlusion at the last follow-up, 2 (10.5%) of which had a single Pipeline Embolization Device implantation and another single (5.3%) aneurysm with a second Pipeline Embolization Device implantation.

CONCLUSIONS: A collar sign on the initial angiogram after Pipeline Embolization Device placement is a predictor of poor aneurysm occlusion. Because the occlusion rates remain equally low regardless of retreatment in patients with a collar sign, radiologic follow-up may be more appropriate than retreatment.

ABBREVIATIONS: PED = Pipeline Embolization Device; ICAB = internal carotid artery bifurcation; PO = paraophthalmic; PCOMM = posterior communicating artery

We previously reported a series of incompletely occluded aneurysms after Pipeline Embolization Device (PED; Covidien, Irvine, California) implantation with an angiographic “collar sign,” an unopacified white line between the parent vessel and the aneurysm dome on follow-up angiography.¹ This finding was perceived to be indicative of near-yet-incomplete endothelialization of the PED. The long-term

implications of this finding are currently unknown. Here, we report the angiographic outcomes of patients with the collar sign with a follow-up of up to 45 months and the implications of this angiographic finding.

MATERIALS AND METHODS

After obtaining Institutional Review Board approval, we performed a retrospective review of a prospectively maintained data base of patients who underwent PED implantation for an intracranial aneurysm at Beth Israel Deaconess Medical Center between January 2014 and December 2016. We included patients with a collar sign at the initial follow-up angiogram after PED implantation. These radiographic images were obtained using the standard anteroposterior, lateral, and oblique digital subtraction angiography projections and were interpreted by 2 independent physicians with neuroendovascular training. Patients considered ineligible for this study were those without a collar sign on the

Received November 11, 2019; accepted after revision December 27.

From the Neurosurgical Service (S.G.-P., Y.A., J.M.M., C.S.O., A.J.T.), Beth Israel Deaconess Medical Center, Harvard Medical School, Boston, Massachusetts; Department of Neurosurgery (C.J.G.), Geisinger, Danville, Pennsylvania; and Research Institute of Neurointervention (C.J.G.), Paracelsus Medical University, Salzburg, Austria.

Please address correspondence to Christoph J. Griessenauer, MD, Department of Neurosurgery, Geisinger, 100 N Academy Ave, Danville, PA 17822; e-mail: christoph.griessenauer@gmail.com; @SantiagoGP92; @cgriessenauer



Indicates article with supplemental on-line table.

<http://dx.doi.org/10.3174/ajnr.A6415>

first follow-up angiogram or without long-term follow-up of at least 1 year.

RESULTS

A total of 198 patients with 285 aneurysms treated with a PED between 2014 and 2016 were screened for the collar sign on initial and subsequent follow-up angiograms. There were 226 aneurysms (79.3%) with complete occlusion at the first follow-up. Of 59 incompletely occluded aneurysms, 19 (32.2%) aneurysms in 17 patients were found to have a collar sign on the first angiographic follow-up (median, 6 months; range, 4.2–7.2). Two patients had 2 separate aneurysms with a collar sign. Fifteen (78.9%) aneurysms were paraophthalmic internal carotid artery aneurysms. Other locations included the middle cerebral artery (10.5%), internal carotid artery bifurcation (5.3%), and posterior communicating artery (5.3%). There were 14 (73.7%) aneurysms with branch vessels arising from the aneurysm dome. The median angiographic follow-up was 32.9 months (range, 11.9–45.2 months). Ten (52.6%) aneurysms underwent retreatment with a second PED device, which resulted in aneurysm occlusion in 1 (10%) aneurysm. The median time to retreatment was 15.8 months (range, 6.8–33.4 months). In terms of aneurysmal occlusion, there were 3 (15.8%) aneurysms with complete occlusion at last follow-up, 2 (10.5%) of which had a single PED implantation (time to occlusion, 11.9 and 42.2 months, respectively) and another single (5.3%) aneurysm with a second PED implantation (time to occlusion, 12.1 months from the second PED implantation).

Among the 16 (84.2%) aneurysms that did not occlude, a single (5.3%) aneurysm with intraluminal thrombus enlarged (aneurysm 15), two (10.5%) aneurysms did not change in size, and 13 (68.4%) decreased in size compared with the initial angiogram. Satisfactory wall apposition as demonstrated on fluoroscopy was achieved in all cases. There were no procedural complications or neurologic long-term sequelae. A full summary of patient characteristics and follow-up results, categorized in 4 groups based on occlusion status and retreatment, is shown in the On-line Table. A representative set of images from each of the 4 groups is shown in the Figure.

DISCUSSION

We report the angiographic outcomes of incompletely occluded intracranial aneurysms with a collar sign following PED implantation for up to 45 months. We observed a collar sign in 32.2% of incompletely occluded aneurysms at first follow-up. Of 19 aneurysms with a collar sign, complete occlusion was achieved in only 3 (15.8%) aneurysms, including 2 aneurysms that spontaneously occluded after initial treatment and 1 aneurysm that occluded after retreatment with a second PED. However, we observed an incomplete occlusion with a persistent collar sign in 16 (84.2%) aneurysms, even after a second or third PED implantation. Aneurysm enlargement was observed in a single large thrombosed aneurysm. More than two-thirds of incompletely occluded aneurysms decreased in size, and none ruptured during follow-up.

Endothelialization of the Pipeline Flow Diverter

As described in preclinical studies, endothelialization along the stent strut of the PED has been identified as the key underlying mechanism of aneurysmal exclusion from the intracranial circulation and subsequent aneurysm occlusion.^{2–6} Likewise, this mechanism of endothelialization along the PED strut has been confirmed in humans.^{1,7} Initially, the collar sign was thought to be indicative of future aneurysmal occlusion following PED implantation. Nonetheless, our results demonstrate that this sign is likely a sign of persistent aneurysmal flow even at long-term follow-up, regardless of any additional PED implantation.

Although the underlying mechanism is still unknown, we found branch arteries originating from the aneurysm dome in 14 of 19 cases (73.7%). On the basis of this finding, we hypothesized that an aspiration effect led by a pressure gradient between the parent arteries and branches is the likely cause of inhibition of complete endothelialization along the PED strut and subsequent persistence of flow into the branches through the aneurysm. Two of 3 aneurysms with complete occlusion did not have a branch arising from the aneurysm at the initial follow-up angiogram, which further supports this hypothesis. Furthermore, patient 1 had an ophthalmic artery that arose from the aneurysm dome, which had been opacified at the first follow-up angiogram. Subsequently, both the aneurysm and the ophthalmic artery were found to be occluded on the final follow-up angiogram without any visual sequelae, suggesting collateral compensation to the distal segment of the ophthalmic artery and depletion of aspiration effect. Therefore, the collar sign is likely an indication of partial endothelialization, seen more commonly in aneurysms with a branch arising from the dome, which demands persistent blood supply and subsequently inhibits complete endothelialization required to cover the aneurysm neck. A negative correlation between aneurysm occlusion and branch vessels arising from the aneurysm neck or dome following PED implantation in patients with paraophthalmic artery aneurysms has been reported.⁸

On the other hand, the collar sign was observed in a thrombosed aneurysm without an associated branch vessel (aneurysm 15). In the case of thrombosed aneurysms, reports have described a heterogeneous thrombosis status, in which both thrombotic and thrombolytic processes take place inside the aneurysm. These result from a cycle of repeat adventitial inflammation, capillary proliferation, and bleeding within the aneurysmal wall in such thrombosed aneurysms.^{9,10} Therefore, endothelialization along the aneurysm neck is less likely to occur following PED implantation.

Management Strategies for Incompletely Occluded Aneurysms with the Collar Sign

In the present study, complete occlusion was achieved in only 3 aneurysms (15.8%) with the collar sign. Aneurysm enlargement was observed in only 1 patient with a thrombosed aneurysm as mentioned previously. In contrast, most of the aneurysms with a collar sign were stable or even decreased in size (10.5% and 68.4%, respectively), suggesting a stabilizing effect of the PEDs on the aneurysm. Furthermore, because the rates of complete occlusion of the aneurysm were very low regardless of the number of

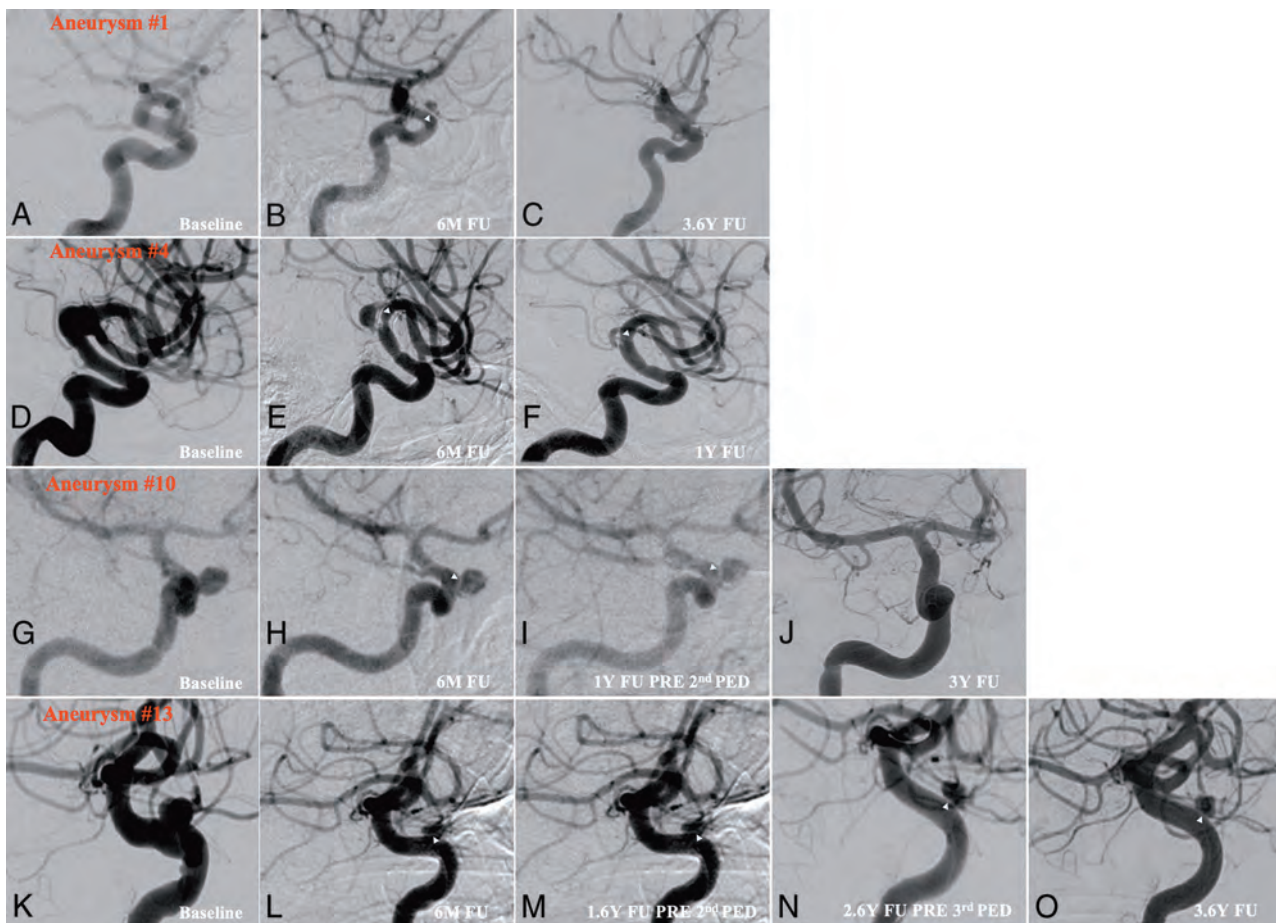


FIGURE. Digital subtraction angiograms showing the collar sign in incompletely occluded aneurysms after Pipeline embolization. Each row represents 1 aneurysm from each group corresponding to the On-line Table. The first column (far-left) shows the aneurysm before Pipeline embolization. The second column shows the residual aneurysm with the collar sign (*white arrowheads*) after Pipeline placement at initial follow-up. Further columns (3–5) are based on the patient group (eg, spontaneous occlusion during follow-up, residual filling and collar sign at last follow-up without intervention, occlusion during follow-up after a 2nd PED, and residual filling and collar sign at last follow-up after a 2nd PED). Aneurysm 1 for row 1: baseline, first follow-up, and last angiographic follow-up are shown. Aneurysm 4 for row 2: baseline, first follow-up, and last angiographic follow-up are shown. Aneurysm 10 for row 3: baseline, first follow-up, before the second PED, and last angiographic follow-up are shown. Aneurysm 13 for row 4: baseline, first follow-up, before the second PED, before the third PED, and last angiographic follow-up are shown. M indicates month; Y, year; FU, follow-up.

PED treatments, retreatment with adjunctive PED implantation is unlikely to be effective in aneurysms with a collar sign. Under these circumstances, radiologic follow-up may be more appropriate than retreatment. Thus, patients are not committed to the risk of an additional procedure in the absence of the expected benefit of aneurysm occlusion.

CONCLUSIONS

The collar sign is indicative of incomplete endothelialization and persistent aneurysmal flow even during medium-to-long-term follow-up periods. A collar sign on the initial angiogram after PED placement is therefore a predictor of poor aneurysm occlusion. Because the occlusion rates remain equally low regardless of retreatment in patients with a collar sign, radiologic follow-up may be more appropriate than retreatment. Thus, patients are not exposed to the risk of an additional procedure in the absence of the expected benefit of aneurysm occlusion. This study provides some

additional evidence that aneurysms with branches arising from the dome may not be suitable for flow diversion.

Disclosures: Ajith J. Thomas—UNRELATED: Consultancy: Stryker, Comments: Data Safety Monitoring Board*; Expert Testimony: CRICO, Comments: cerebrovascular disorders; Royalties: *Primer of Cerebrovascular Disorders*. *Money paid to the institution.

REFERENCES

- Griessenauer CJ, Gupta R, Shi S, et al. Collar sign in incompletely occluded aneurysms after Pipeline Embolization: evaluation with angiography and optical coherence tomography. *AJNR Am J Neuroradiol* 2017;38:323–26 CrossRef Medline
- Kadirvel R, Ding YH, Dai D, et al. Cellular mechanisms of aneurysm occlusion after treatment with a flow diverter. *Radiology* 2014; 270:394–99 CrossRef Medline
- Ding Y, Dai D, Kallmes DF, et al. Preclinical testing of a novel thin film nitinol flow-diversion stent in a rabbit elastase aneurysm model. *AJNR Am J Neuroradiol* 2016;37:497–501 CrossRef Medline

4. Marosfoi M, Langan ET, Strittmatter L, et al. **In situ tissue engineering: endothelial growth patterns as a function of flow diverter design.** *J Neurointerv Surg* 2017;9:994–98 CrossRef Medline
5. Matsuda Y, Chung J, Lopes DK. **Analysis of neointima development in flow diverters using optical coherence tomography imaging.** *J Neurointerv Surg* 2018;10:162–67 CrossRef Medline
6. Rouchaud A, Ramana C, Brinjikji W, et al. **Wall apposition is a key factor for aneurysm occlusion after flow diversion: a histologic evaluation in 41 rabbits.** *AJNR Am J Neuroradiol* 2016;37:2087–91 CrossRef Medline
7. Szikora I, Turanyi E, Marosfoi M. **Evolution of flow-diverter endothelialization and thrombus organization in giant fusiform aneurysms after flow diversion: a histopathologic study.** *AJNR Am J Neuroradiol* 2015;36:1716–20 CrossRef Medline
8. Griessenauer CJ, Ogilvy CS, Foreman PM, et al. **Pipeline Embolization Device for small paraophthalmic artery aneurysms with an emphasis on the anatomical relationship of ophthalmic artery origin and aneurysm.** *J Neurosurg* 2016;125:1352–59 CrossRef Medline
9. Yasui T, Sakamoto H, Kishi H, et al. **Rupture mechanism of a thrombosed slow-growing giant aneurysm of the vertebral artery—case report.** *Neurol Med Chir (Tokyo)* 1998;38:860–64 CrossRef Medline
10. Nagahiro S, Takada A, Goto S, et al. **Thrombosed growing giant aneurysms of the vertebral artery: growth mechanism and management.** *J Neurosurg* 1995;82:796–801 CrossRef Medline

The Collar Sign in Pipeline Embolization Device–Treated Aneurysms

The availability of the Pipeline Embolization Device (PED; Medtronic, Minneapolis, Minnesota) rapidly increased the number of aneurysms that were potentially treatable using endovascular therapy. The Pipeline Embolization Device for Uncoilable or Failed Aneurysms (PUFS) trial produced a superb occlusion rate (86% at 12 months) in a group of aneurysms that had previously been nearly impossible to treat with other available devices. Across time, the rate of occlusion in the PUFS trial continued to increase, reaching 95% at 5 years; there was also a low complication rate of 6%.¹ Following FDA approval in 2011, I enthusiastically began treatment of patients outside the trial. However, during the next several years, I noticed that the occlusion rates, while good, did not quite achieve the success reported in the PUFS trial. A few of these large, on-label-treated aneurysms as well as some smaller aneurysms were incompletely occluded; on follow-up DSA, some of these showed what was described by Griessenauer et al² as the “collar sign.”

As a first step in explaining differences between the PUFS trial results and my clinical experience, I first analyzed possible changes in the treatment technique. Because of the lengths of the aneurysm necks, parent artery size, and the maximum lengths of available devices (10–20 mm), many aneurysms in the PUFS trial were treated using multiple overlapping PEDs. The aneurysms in the PUFS trial averaged 3.1 PEDs per treatment. Also, in PUFS, to achieve excellent device apposition to the vessel wall and to other PEDs, after deployment, angioplasty often was performed to optimize wall apposition. Shortly after FDA approval in 2011, device lengths up to 35 mm became available. With this experience and some pressure from hospital administrators to reduce costs, the use of multiple devices decreased and the concept of “one and done” was developed. It was, also, in this same period that the results from the Stenting and Aggressive Medical Management for the Prevention of Recurrent Stroke in Intracranial Stenosis (SAMMPRIS) trial became available. This trial demonstrated that in the treatment of an atherosclerotic stenosis, angioplasty might have more risk than the best medical treatment.³ Because the segment of the parent artery from which an aneurysm arises often has atherosclerotic changes, many, including me, became somewhat hesitant to perform angioplasty when deploying a PED. Only if the PED failed to completely expand was angioplasty performed.

Other factors I considered related to the lower rate of complete occlusion were the amount of the vessel wall that was incorporated into the aneurysm neck, the degree of reduction of flow into an aneurysm after implantation, the apposition of the PED to the parent vessel wall, and the size of the deployed implant.⁴ I began to carefully calibrate the angiographic equipment because measurement of the vessel diameter was essential in choosing the appropriate size so that apposition and pore density were optimized.⁵

At that same time, a better understanding of the importance of platelets and their modification to prevent aggregation and activation with aspirin and thienopyridines became more widely known and accepted.^{6,7} The newer thienopyridines such as prasugrel and ticagrelor seem to have a much greater inhibitory effect than clopidogrel. In a review in the *American Journal of Roentgenology*, Palma⁸ demonstrated that metallic stents implanted in vessels are rapidly coated with a combination of platelets and white and red blood cells. This deposition was shown to have an important effect on the growth and healing of the intima.

Griessenauer et al^{2,9} from Beth Israel Deaconess Medical Center reported their experience with aneurysms treated with the Pipeline. Their initial report² included a group of patients whose aneurysms were incompletely occluded on follow-up angiograms. They observed a radiolucency parallel to the base of the nonoccluded aneurysms, which they described as the “collar sign.” Their first report retrospectively analyzed 135 aneurysms and found 10 incompletely occluded aneurysms that exhibited the sign. In the current issue,⁹ with an additional follow-up of 7 months, they now found 19 aneurysms exhibiting the collar sign.^{2,9} The occlusion rate in their entire cohort was approximately 80%, which is similar to data provided by PUFS. This current report of their 2014–2016 experience gives some insight into both the natural history of aneurysms and the patients whose aneurysms exhibited the collar sign. They separated the nonoccluded aneurysms into 2 groups, 10 had a second PED placed; only 1 of these was occluded on subsequent follow-up. The second group, consisting of 9 aneurysms were only observed; 2 of these were occluded on subsequent follow-up.⁹ Because of their busy clinical practice, these operators have overcome the learning curve associated with using the PED.¹⁰ In their 3-year study, 285 aneurysms in 198 patients were treated. In both publications, the

authors very nicely and thoroughly discussed the healing mechanisms of vessels and aneurysms in patients treated with the PED. They have detailed the current thoughts on healing, including the slowing of flow within the aneurysm by the flow diverter, the development of thrombus and its organization, and finally, the endothelialization of the PED and the restoration of the intima.^{2,11,12}

Possible explanations for the collar sign may be related to technical factors. At the time of deployment, the apposition of the PED was assessed fluoroscopically and subtle areas of nonapposition might have been only detectable using DSA. Although 15 of the 19 aneurysms were smaller than 10 mm, the amount of the vessel wall that was incorporated into the aneurysm should also be considered. Calibration of the angiography equipment might also have been inaccurate, resulting in the oversizing of the PED, which affects the pore density, the degree of flow restriction, and the appropriate framework for endothelial cell support.^{5,11,12}

I have observed seemingly excellent apposition of the device, but poor flow restriction within the aneurysm. Usually passing a microguidewire whose tip has been shaped in to the letter J through the device, perhaps in combination with the microcatheter and occasionally the intermediate catheter, increases flow restriction without any apparent change in the device. In the group treated with a second device, the size of that second device in comparison with the first device may also be important. There are some data that would suggest that pore density can be decreased by placing a larger device within the previous PED.

By means of optical coherence, uneven intimal growth on implanted devices has been observed.^{2,13} One must question whether the etiology of this irregular intimal growth may be due to the antiplatelet agents. This irregularity of the intima, which is on a microscopic level, may prevent complete apposition of the second device placed within the first PED. This possibility suggests that the first treatment should include placement of a second device if there is concern for adequate aneurysm neck coverage and aneurysmal flow restriction.

Griessenauer and Gornz-Paz^{2,9} reported that 74% of their patients with the collar sign had a branch vessel arising from the aneurysm. They discuss, at some length, the effect of the “sump” of this outflow vessel on the occlusion of the aneurysm. Complete occlusion of the aneurysm is usually the goal, but preservation of the outflow vessel may also be important.

Because only 3 of the 19 aneurysms were occluded on continued angiographic observation, the authors suggest that the low rate of further occlusion argues against additional routine follow-up angiography. Perhaps this suggestion may be judicious if one can accurately assess the aneurysm with CT or MR imaging. However, artifacts may make this difficult, especially when coils or aneurysm clips are present. If the aneurysm is small and has decreased in size with slower flow, this approach would seem to be reasonable, particularly if the aneurysm gives rise to a branch vessel. Finally, the authors report that only 1 aneurysm enlarged, 2 remained the same, and 13 of the 19 (68%) decreased in size. Most important, none of the aneurysms bled. While data suggesting a protective effect of the PED in aneurysms with the collar sign do not exist, I would suggest that with the absence of

hemorrhage, stability, and improvement in 18 of 19 aneurysms, a reasonable treatment outcome has been achieved.

Christopher J. Moran, is a consultant, procedure proctor, and technique instructor for Medtronic Neurovascular, the manufacturer of the Pipeline Embolization Device. Dr. Moran was an investigator in the PUFs PMA trial and the ASPIRE prospective registry. He also is a consultant for MicroVention and an investigator in the FRED trial.

REFERENCES

1. Becske T, Brinjikji W, Potts MB, et al. **Long-term clinical and angiographic outcomes following Pipeline embolization device treatment of complex internal carotid artery aneurysms: five-year results of the Pipeline for Uncoilable or Failed Aneurysms trial.** *Neurosurgery* 2017;80:40–48 CrossRef Medline
2. Griessenauer CJ, Gupta R, Shi S, et al. **Collar sign in incompletely occluded aneurysms after Pipeline embolization: evaluation with angiography and optical coherence tomography.** *AJNR Am J Neuroradiol* 2017;38:323–26 CrossRef Medline
3. Derdeyn CP, Fiorella D, Lynn MJ, et al; SAMMPRIS Investigators. **Nonprocedural symptomatic infarction and in-stent restenosis after intracranial angioplasty and stenting in the SAMMPRIS trial (Stenting and Aggressive Medical Management for the Prevention of Recurrent Stroke in Intracranial Stenosis).** *Stroke* 2017;48:1501–06 CrossRef Medline
4. Rouchaud A, Ramana C, Brinjikji W, et al. **Wall apposition is a key factor for aneurysm occlusion after flow diversion: a histological evaluation in 41 rabbits.** *AJNR Am J Neuroradiol* 2016;37:2087–91 CrossRef Medline
5. Shapiro M, Becske T, Nelson PK. **Learning from failure: persistence of aneurysms following pipeline embolization.** *J Neurosurg* 2017;126:578–85 CrossRef Medline
6. Akbari HS, Reynolds MR, Kadkhodayan Y, et al. **Hemorrhagic complications after prasugrel (Effient®) therapy for vascular neurointerventional procedures.** *J Neurointerv Surg* 2013;5:337–43 CrossRef Medline
7. Gandhi CD, Bulsara KR, Johanna F, et al; SNIS Standards and Guidelines Committee. **Platelet function inhibitors and platelet function testing in neurointerventional procedures.** *J Neurointerv Surg* 2014;6:567–77 CrossRef Medline
8. Plamaz JC. **Intravascular stents: tissue-stent interactions and design consideration.** *AJR Am J Roentgenol* 1993;160:613–18 CrossRef Medline
9. Gomez-Paz S, Akamatsu Y, Moore JM, et al. **Implications of the collar sign in incompletely occluded aneurysms after Pipeline Embolization Device: a follow-up study.** *AJNR Am J Neuroradiol*. In press
10. Jabbour P, Chalouhi N, Tjoumakaris S, et al. **The Pipeline Embolization Device: learning curve and predictors of complications and aneurysm obliteration.** *Neurosurgery* 2013;73:113–20 CrossRef Medline
11. Kadirvel R, Ding YH, Dai D, et al. **Cellular mechanisms of aneurysm occlusion after treatment with a flow diverter.** *Radiology* 2014;270:394–99 CrossRef Medline
12. Dai D, Ding YH, Kelly M, et al. **Histopathological findings following Pipeline embolization in a human cerebral aneurysm at the basilar tip.** *Interv Neuroradiol* 2016;22:153–57 CrossRef Medline
13. Matsuda Y, Chung J, Lopes DK. **Analysis of neointimal development in flow diverters using optical coherence tomography imaging.** *J Neurointerv Surg* 2018;10:162–67 CrossRef Medline

 **Christopher J. Moran**
Medtronic Neurovascular
Minneapolis, Minnesota
MicroVention
Tustin, California

<http://dx.doi.org/10.3174/ajnr.A6465>

Large Neck and Strong Ostium Inflow as the Potential Causes for Delayed Occlusion of Unruptured Sidewall Intracranial Aneurysms Treated by Flow Diverter

T. Su, P. Reymond, O. Brina, P. Bouillot, P. Machi, B.M.A. Delattre, L. Jin, K.O. Lövsblad, and M.I. Vargas



ABSTRACT

BACKGROUND AND PURPOSE: Flow diverter–induced hemodynamic change plays an important role in the mechanism of intracranial aneurysm occlusion. Our aim was to explore the relationship between aneurysm features and flow-diverter treatment of unruptured sidewall intracranial aneurysms.

MATERIALS AND METHODS: MR imaging, 4D phase-contrast, was prospectively performed before flow diverter implantation in each patient with unruptured intracranial aneurysm. Two postprocedure follow-ups were scheduled at 6 and 12 months. Responses were grouped according to whether the aneurysms were occluded or remnant. Preprocedural aneurysm geometries and ostium hemodynamics in 38 patients were compared between the 2 groups at 6 and 12 months. Receiver operating characteristic curve analyses were performed for significant geometric and hemodynamic continuous parameters.

RESULTS: After the 6-month assessment, 21 of 41 intracranial aneurysms were occluded, and 9 additional aneurysms were occluded at 12 months. Geometrically, the ostium maximum diameter was significantly larger in the remnant group at 6 and 12 months (both $P < .001$). Hemodynamically, the proximal inflow zone was more frequently observed in the remnant group at 6 months. Several preprocedural ostium hemodynamic parameters were significantly higher in the remnant group. As a prediction for occlusion, the areas under the curve of the ostium maximum diameter (for 6 and 12 months), systolic inflow rate ratio (for 6 months), and systolic inflow area (for 12 months) reached 0.843, 0.883, 0.855, and 0.860, respectively.

CONCLUSIONS: Intracranial aneurysms with a large ostium and strong ostium inflow may need a longer time for occlusion. Preprocedural 4D flow MR imaging can well illustrate ostium hemodynamics and characterize aneurysm treatment responses.

ABBREVIATIONS: FD = flow diverter; PC = phase-contrast; RA = rotational angiography

Intracranial aneurysm can cause hemorrhage associated with high mortality or residual neurologic deficits.¹ Compared with surgical clipping, interventions with lower complication rates and a shorter inpatient stay are preferred. With respect to intervention, the use of a flow diverter (FD) has recently been introduced for cerebral aneurysms. Previous studies showed that procedure-related complications, including ischemia or hemorrhage, did not differ between the FD and the coil groups, but flow diversion could provide higher occlusion rates and fewer necessary re-

treatments, especially for the sidewall type of aneurysm in the tortuous ICA.^{2,3}

On the one hand, the hemodynamic dampening effect by flow diversion is considered to play an important role in the mechanism of aneurysm occlusion. Results from different research groups showed the reduction of inflow velocity and intra-aneurysm flow velocity after FD deployment.⁴⁻⁶ Hemodynamically, they were related with specific metal coverage and porosity of the FD.⁷ On the other hand, the influence of aneurysm features on FD treatment responses remains unclear, and some treated aneurysms remain

Received October 13, 2019; accepted after revision December 23.

From the Department of Interventional Radiology (T.S., L.J.), Beijing Friendship Hospital, Capital Medical University, Beijing, People's Republic of China; Division of Neuroradiology and Neuro-Interventional Radiology (P.R., O.B., P.M., K.O.L., M.I.V.), and Division of Radiology (B.M.A.D.), University Hospitals of Geneva, Geneva, Switzerland; and Department of Quantum Matter Physics (P.B.), University of Geneva, Geneva, Switzerland.

This work originated at University Hospitals of Geneva, 4 Rue Gabrielle-Perret-Gentil, Geneva 1211, Switzerland.

Supported by Swiss National Funds (SNF 32003B_160222 and SNF 320030_156813) and Beijing Li Huanying Medical Foundation (2017).

Previously presented at: Radiological Society of North America 105th Scientific Assembly, Chicago, Illinois, December 1–6, 2019.

Please address correspondence to Maria Isabel Vargas, MD, Division of Neuroradiology, University Hospitals of Geneva, 4 Rue Gabrielle-Perret-Gentil, Geneva 1211, Switzerland; e-mail: Maria.I.Vargas@hcuge.ch

Indicates open access to non-subscribers at www.ajnr.org

Indicates article with supplemental on-line appendix and table.

Indicates article with supplemental on-line photo.

<http://dx.doi.org/10.3174/ajnr.A6413>

Table 1: Inclusion and exclusion criteria for patient selection

Inclusion Criteria	Exclusion Criteria
Image-based evidence of a sidewall intracranial aneurysm interventionally treated only by using a FD in our institution	Unavailable aneurysm-related 4D PC MRI data
No history of related subarachnoid hemorrhage or other rupture clues	Fusiform aneurysms without a well-defined ostium
No previous invasive treatment for target aneurysm	Undesirable deployment of FD
Preprocedural acquisition of 4D PC MRI and 3D RA, and at least CE MR imaging or DSA follow-up with conclusive results at 6 or 12 months	Missing all scheduled follow-ups

Note:—CE indicates contrast-enhanced.

patent in clinical practice,^{8,9} probably due to other hemodynamic reasons. Our experience with the utilization of 4D phase-contrast (PC) MR imaging for intracranial aneurysms helps us to investigate this reason before the deployment of an FD. By applying numerical simulation for a virtual flow diversion, computational fluid dynamic analyses have been used to evaluate the hemodynamic reduction inside the aneurysm.^{5,10,11} However, because of their specific assumptions, little predictive information on aneurysm outcome after flow diversion was provided.

In this study, we used 4D PC MRI, a powerful *in vivo* analytic tool that has already been used for the assessment of intra-aneurysmal flow modification after FD treatment⁶ to explore aneurysm hemodynamics and outcome. Other research groups have reported flow conditions at the aneurysm neck with an *in vivo* hemodynamic assessment by using a 1.5T MR scanner and with an emphasis on the measurability and influential factors of neck flow.¹²⁻¹⁴ Nevertheless, to our knowledge, few reports have investigated the relationship between the ostium and FD treatment response.^{15,16} We hypothesized that different FD treatment responses were related to aneurysm features, and our study focused on the aneurysm geometries and hemodynamics at the ostium. The aim of this study was to perform an *in vivo* investigation of the relationship between aneurysm features, particularly the geometric and hemodynamic parameters and their impact on FD treatment responses.

MATERIALS AND METHODS

Patients

We conducted a prospective study of 41 patients (4 men, 37 women; mean \pm standard deviation (SD) age, 53.8 \pm 13.1 years, [range, 26–81 years]) diagnosed with unruptured sidewall intracranial aneurysm and accepted for an FD procedure between November 2012 and November 2017. Two women were excluded because of preprocedural 4D PC MRI acquisition problems. One man was excluded because the follow-up examination showed a proximal displacement of the FD, which resulted in insufficient ostial coverage. Ethics approval was granted by the local ethics committee, and patient consent was obtained. Inclusion and exclusion criteria are shown in Table 1.

Image Acquisition and Postprocessing

MR imaging was performed within 72 hours before the endovascular procedure with a 3T PET/MR system (Ingenuity TF; Philips Healthcare, Best, the Netherlands) and an 8-channel head coil.

After 3D TOF imaging, 4D PC MRI acquisition slabs were positioned to cover the aneurysm bulge and its adjacent parent vessel. This sequence, triggered with the cardiac frequency, included velocity encoding in the 3 directions with the following parameters: field of view 190 \times 210 mm², typically 32 slices (adjusted according to the aneurysm), acquisition voxel size 1 \times 1 \times 1 mm³ reconstructed with 0.82 mm³, sensitivity encoding acceleration factor 2, TR/TE 4.6/2.9 ms,

and acquisition time 13 min. The number of cardiac phase acquisitions was based on the heart rate, and it typically ranged from 14 to 16 in this study.⁶ The 3D rotational angiography (RA) was acquired before FD stent implantation with a biplane angiographic unit (Allura FD20; Philips Healthcare).⁶ After raw data postprocessing (see Supplemental Materials and Methods) from the 4D PC MRI and 3D RA,^{17,18} velocity field information and the parent vessel flow rate were acquired for further analysis.

Geometric and Hemodynamic Parameters

Each aneurysm ostium plane was defined as the location from which the aneurysm sac bulged out of its parent vessel. Aneurysm sac size, perpendicular height, maximum height, ostium maximum diameter, and ostium area were measured on preprocedural 3D RA images.¹⁹ Aspect ratio (the ratio of aneurysm perpendicular height to the average ostium diameter) and size ratio (the ratio of the aneurysm maximum height to the parent vessel diameter) were computed on geometric parameters according to previously described formulas.²⁰ Image management and geometric measurements were performed with OsiriX MD (version 9.5; <http://www.osirix-viewer.com>).

According to velocity field information, hemodynamic parameters at the aneurysm neck were evaluated on the open-source software Paraview (version 5.6.0; Kitware, Clifton Park, New York). The hemodynamic inflow zone at the aneurysm neck level was qualitatively evaluated at the systolic peak, and its location was trichotomously classified as proximal, lateral side, and distal neck by 2 independent analysts, with a final consensus (Fig 1).¹³

The following hemodynamic quantitative parameters related to the ostium were based on the inflow velocity components that were normal to the ostial plane. Hemodynamic parameters of maximum inflow velocity and mean inflow velocity were computed at the systolic time. Only mean inflow velocity was spatially averaged over the inflow area. The maximum inflow rate was the product of the mean inflow velocity and systolic inflow area at the ostium. The systolic inflow rate ratio was the ratio of the maximum inflow rate at the ostium to the systolic flow rate in the parent vessel. The parent vessel flow rate was computed and averaged from different cross-sectional planes of the parent artery proximal to the aneurysm during the complete cardiac cycle.

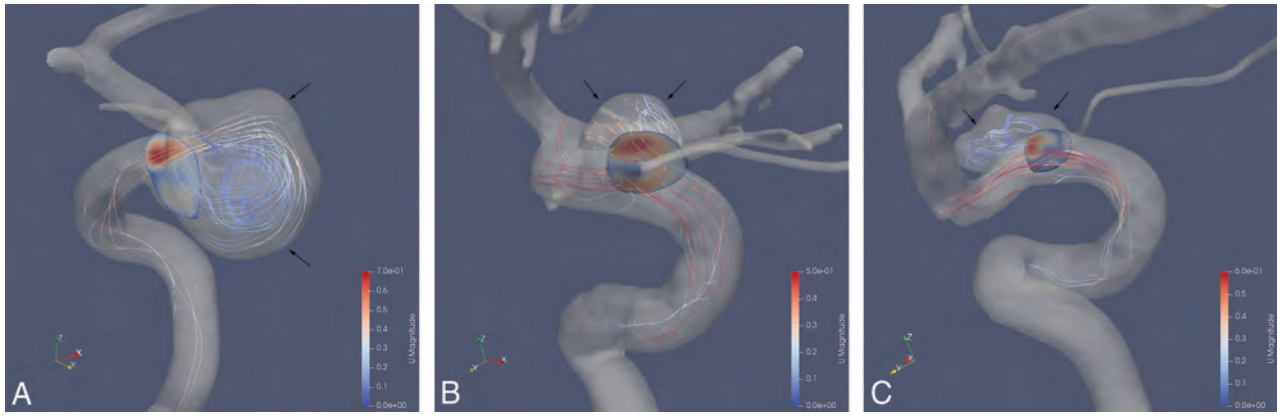


FIG 1. Different inflow zones at the aneurysm neck during systolic peak on (Paraview software). All blood flow directions are shown from the bottom to the top of the image. *A*, Proximal: aneurysm (black arrows) located at the medial C6 (ophthalmic/supraclinoid) segment of the right ICA and the inflow zone (red region in the aneurysm ostium) on the proximal part of the neck. *B*, Lateral side: aneurysm (black arrows) located at the dorsal C6 segment of the left ICA and inflow zone (red region in the aneurysmal ostium) on the lateral side of the neck. *C*, Distal: aneurysm (black arrows) located at the dorsal C6 segment of the right ICA and inflow zone (red region in the aneurysmal ostium) on the distal part of the neck.

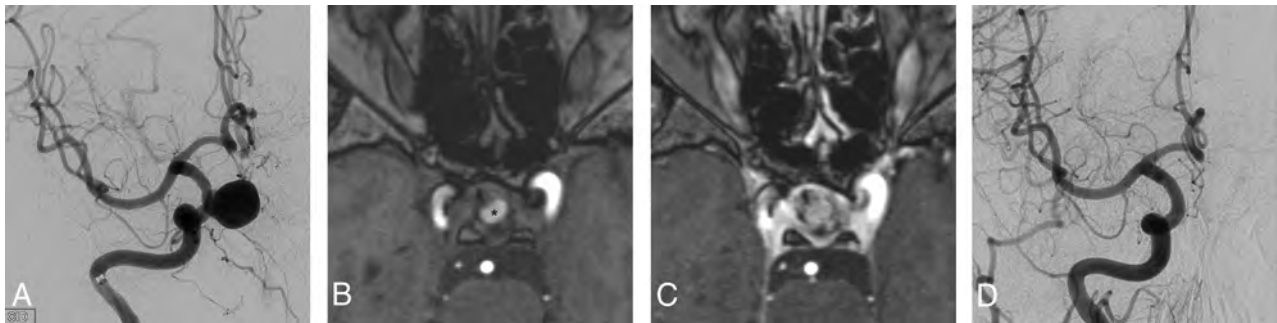


FIG 2. A 50-year-old man with an unruptured sidewall aneurysm at the medial C6 segment of the right ICA (the same case shown in Fig 1A). *A*, An initial anteroposterior angiogram of the intracranial segment of the ICA of the aneurysm. *B*, A follow-up at 6 months by using an axial 3D TOF sequence, showing partial thrombosis (*); the dark portion in the right ICA was the artifact that resulted from the FD. *C*, Axial 3D TOF sequence with gadolinium (acquired immediately after image B) showed enhancement inside the aneurysm compared with image B, and described a remnant. *D*, A follow-up anteroposterior angiogram of the intracranial segment of the ICA at 12 months did not show any residual, which represented a complete occlusion.

Interventional Procedures and Follow-Up

FD selection (see Supplemental Materials and Methods) was determined by navigability and implantation issues. No combination of coils was used. FDs were deployed by an experienced neurointerventionist, followed by a conebeam CT to confirm proper deployment. MR imaging follow-ups were completed on 3T scanners with routine and appropriate technical parameters in sequences of T1WI, T2WI, 3D TOF-MRA, contrast-enhanced MRA, and contrast-enhanced T1WI. Diagnostic angiographic follow-ups performed by the same neurointerventionist focused on the target aneurysms. For the diseased side of the ICA, 2D DSA and 3D RA were acquired by following standard protocols.²¹

According to 6- and 12-month contrast-enhanced MR imaging or DSA follow-ups by using a simplified 2-grade scale,^{22,23} FD-treated aneurysms were classified as either “occlusion” or “remnant” by 2 experienced neuroradiologists blinded to each other (Fig 2). In the case of a disagreement, a third expert was asked for a decision. Additional follow-up for extra time was not suggested because other treatment options were adopted for

remnant aneurysms after the 12-month follow-up. All the investigators were blinded to the acquisition parameters from the follow-up periods.

Statistical Analyses

Statistical analyses were performed by using PAWS Statistics (version 18.0; IBM, Armonk, New York). Interrater reliabilities were evaluated with the Cohen kappa coefficient (κ) for the preprocedure inflow zone classification and image follow-up assessment. Due to analytical consideration χ^2 analyses were performed to compare different inflow zones (proximal versus lateral side and distal neck) between the occlusion and remnant groups at the 2 follow-up time points. Preprocedural geometric and hemodynamic continuous parameters between the 2 groups were compared by using the Student *t* test. Receiver operating characteristic curve analyses and the Youden index were performed for the most significantly different geometric and hemodynamic continuous parameters.²⁴⁻²⁶ $P < .05$ was considered statistically significant.

Table 2: Preprocedural geometric and hemodynamic continuous parameters for different aneurysm treatment response groups at 6 months

Parameter	Remnant, Mean ± SD (n = 19)	Occlusion, Mean ± SD (n = 21)	t	P
Aneurysm sac size, mm	12.58 ± 4.91	7.36 ± 3.59	3.867	<.001
Perpendicular height, mm	9.29 ± 4.41	5.61 ± 2.88	3.089	.004
Maximum height, mm	10.36 ± 4.55	6.15 ± 2.99	3.418	.002
Ostium maximum diameter, mm	6.64 ± 2.76	3.46 ± 0.71	4.873	<.001
Ostium area, mm ²	41.43 ± 26.73	15.61 ± 9.05	4.007	.001
Size ratio	2.74 ± 1.30	1.77 ± 1.30	2.353	.02
Aspect ratio	1.49 ± 0.62	1.62 ± 0.80	-0.572	.57
Maximum inflow velocity, m/s	0.354 ± 0.176	0.245 ± 0.111	2.336	.03
Mean inflow velocity, m/s	0.132 ± 0.066	0.101 ± 0.049	1.670	.10
Maximum inflow rate, mL/s	2.451 ± 1.599	0.817 ± 0.579	4.211	<.001
Systolic inflow rate ratio	0.519 ± 0.307	0.167 ± 0.130	4.639	<.001
Systolic inflow area, mm ²	19.49 ± 11.79	7.47 ± 4.40	4.188	<.001
Parent vessel flow rate, mL/s	3.17 ± 0.75	3.50 ± 0.64	-1.509	.14

Note:—SD indicates standard deviation.

Table 3: Preprocedural geometric and hemodynamic continuous parameters for different aneurysm treatment response groups at 12 months

Parameter	Remnant, Mean ± SD (n = 10)	Occlusion, Mean ± SD (n = 30)	t	P
Aneurysm sac size, mm	15.00 ± 4.78	8.08 ± 3.74	4.722	<.001
Perpendicular height, mm	11.72 ± 4.50	5.86 ± 2.75	4.942	<.001
Maximum height, mm	12.52 ± 4.76	6.64 ± 3.07	4.545	<.001
Ostium maximum diameter, mm	7.69 ± 2.60	4.12 ± 1.70	4.954	<.001
Ostium area, mm ²	50.26 ± 26.69	20.82 ± 16.48	3.286	.007
Size ratio	3.36 ± 1.30	1.85 ± 1.19	3.392	.002
Aspect ratio	1.55 ± 0.60	1.44 ± 0.75	0.195	.85
Maximum inflow velocity, m/s	0.294 ± 0.133	0.302 ± 0.160	-0.143	.89
Mean inflow velocity, m/s	0.105 ± 0.034	0.121 ± 0.065	-0.722	.48
Maximum inflow rate, mL/s	2.382 ± 1.306	1.354 ± 1.373	2.074	.04
Systolic inflow rate ratio	0.552 ± 0.271	0.270 ± 0.258	2.955	.005
Systolic inflow area, mm ²	23.18 ± 11.37	10.00 ± 7.88	4.087	<.001
Parent vessel flow rate, mL/s	2.84 ± 0.73	3.50 ± 0.64	-2.746	.009

Note:—SD indicates standard deviation.

Table 4: Preprocedural hemodynamic qualitative inflow zone at the aneurysm neck

Response	6-Month Follow-Up		12-Month Follow-Up	
	Remnant (n=19)	Occlusion (n=21)	Remnant (n=10)	Occlusion (n=30)
Proximal neck	11	3	6	8
Lateral side + distal neck	7 + 1	12 + 6	4 + 0	15 + 7
χ ² analysis (P value)	Significant difference (.004)		No significant difference (.13)	

RESULTS

Patient Demographics

Thirty-eight patients (mean ± SD age, 53.7 ± 13.4 years [range, 26–81 years]) with 41 target aneurysms underwent subsequent FD procedures and were included in the study. In 3 patients, 2 target aneurysms were close to each other, and 1 FD was deployed for both to achieve the coverage of the 2 ostia at the same time. Three of the 38 patients (7.9%) were men (mean ± SD age, 48.3 ± 7.6 years [range, 40–55 years]), and 35 were women (mean ± SD age, 54.2 ± 13.7 years [range, 26–81 years]). There was no significant difference ($P > .05$) in age between sexes. Apart from 1 middle cerebral artery aneurysm (M1 segment), the aneurysms were situated in the C4 to C6 (cavernous, clinoid,

ophthalmic/supraclinoid) segments of the ICA (Bouthillier nomenclature).

Clinical Follow-Up

One patient without an aneurysm occlusion at 6 months missed the 12-month follow-up and only a 6-month comparison could be included. Another patient with an occlusion at 12 months missed the 6-month follow-up and only a 12-month comparison could be included (On-line Figure). Also, 40 aneurysms were screened for the comparison at 6 and 12 months. Two neuroradiologists had moderate interrater reliability ($\kappa = 0.738$, $P < .001$), with a third expert for the first two neuroradiologists' disagreements. After 6-month (173.7 ± 48.1 days) and 12-month (367.8 ± 83.4 days) follow-ups, 21 (21/40 [52.5%]) and 30 aneurysms (30/40 [75.0%]) were occluded, respectively.

Geometric Comparison

There were significant differences in the aneurysm sac size, perpendicular height, maximum height, ostium maximum diameter, ostium area, and size ratio for different treatment response groups at 6 and 12 months. Among these, the ostium maximum diameter showed the most pronounced difference (Tables 2 and 3). There was no significant difference in aspect ratio at either time point.

Hemodynamic Qualitative Comparison

Two independent analysts trichotomously determined hemodynamic inflow zone at the aneurysm neck level with good consensus ($\kappa = 0.754$, $P < .001$). Qualitative analyses at the

aneurysm neck revealed that subjects with an inflow zone on the proximal neck in the remnant group were statistically more frequent than subjects with other inflow zones at 6 months ($P = .004$) (Table 4) but not at 12 months ($P = .13$) (Table 4).

Hemodynamic Quantitative Comparison

For preprocedural hemodynamic quantitative parameters at the ostium, there were significant differences in maximum inflow velocity, maximum inflow rate, systolic inflow rate ratio, and the systolic inflow area between the different treatment response groups at 6 months (Table 2). Significant differences for preprocedural maximum inflow rate, systolic inflow rate ratio, systolic inflow area, and parent vessel flow rate were observed between the different groups at 12 months (Table 3). The most

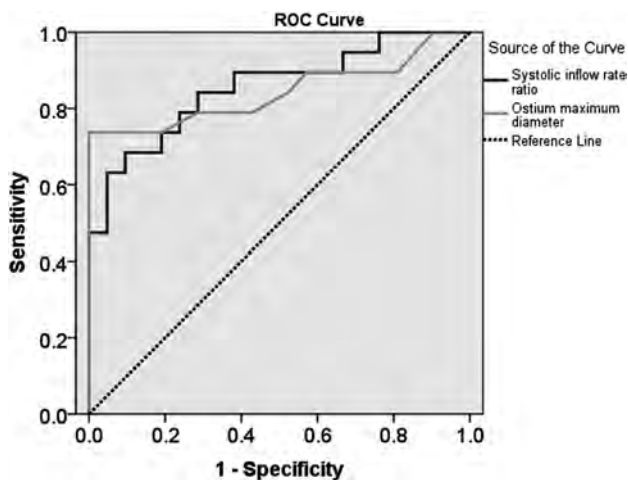


FIG 3. The receiver operating characteristic (ROC) curves of the systolic inflow rate ratio (*dark line*) and ostium maximum diameter (*light line*) against the occlusion at 6 months have areas under the curve (AUC) of 0.855 for the systolic inflow rate ratio and 0.843 for the ostium maximum diameter.

pronounced differences were observed for the systolic inflow rate ratio and systolic inflow area at 6 and at 12 months, respectively.

Receiver Operating Characteristic Prediction Parameters

As predicting parameters with receiver operating characteristic curves for the occlusion and remnant groups at 6 months, the areas under the curves of ostium maximum diameter and systolic inflow rate ratio reached 0.843 (95% CI, 0.707–0.980; $P < .001$) and 0.855 (95% CI, 0.735–0.974; $P < .001$), respectively (Fig 3). For the prediction of different responses at 12 months, areas under the curves of ostium maximum diameter and systolic inflow area were 0.883 (95% CI, 0.759–1.000; $P < .001$) and 0.860 (95% CI, 0.730–0.990; $P = .001$), respectively (Fig 4). Based on the Youden index for favorable sensitivity and specificity, the optimum predictive cutoff at 6 months was 4.9 mm for the ostium maximum diameter (sensitivity, 73.7%; specificity, 100%; Youden index, 0.737) and 0.343 for the systolic inflow rate ratio (sensitivity, 68.4%; specificity, 90.5%; Youden index, 0.589). The optimal predictive cutoff at 12 months was 4.9 mm for ostium maximum diameter (sensitivity, 90.0%; specificity, 83.3%; Youden index, 0.733) and 13.35 mm² for the systolic inflow area (sensitivity, 90.0%; specificity, 80.0%; Youden index, 0.700) (Fig 5).

DISCUSSION

This prospective study compared geometric and hemodynamic parameters in unruptured sidewall intracranial aneurysms for different FD treatment responses at 2 follow-up time points. Other studies have reported on the parameters for differentiation of the aneurysm response,^{15,16} but we highlighted the relationship between in vivo aneurysm hemodynamics and the treatment responses, and tried to give a hemodynamic explanation for the delayed occlusion. Our results showed geometric and hemodynamic differences between the occlusion and remnant groups at 6 and 12 months. In addition, 4D flow MR imaging before treatment with a FD gave important insights into the ostium hemodynamics that were helpful in predicting the treatment responses.

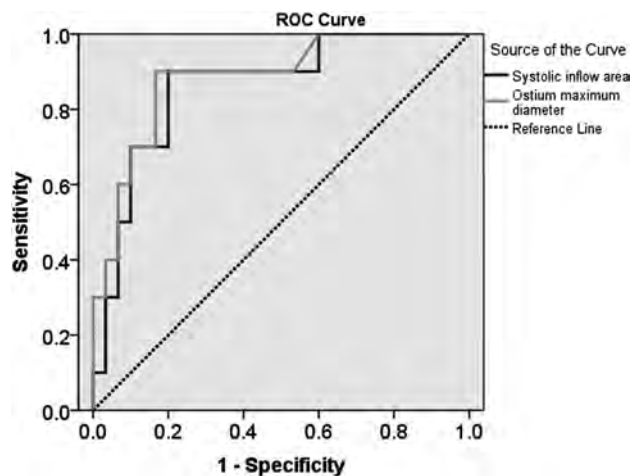


FIG 4. The receiver operating characteristic (ROC) curves of the systolic inflow area (*dark line*) and ostium maximum diameter (*light line*) against the occlusion at 12 months have areas under the curve (AUC) of 0.860 for the systolic inflow area and 0.883 for the ostium maximum diameter.

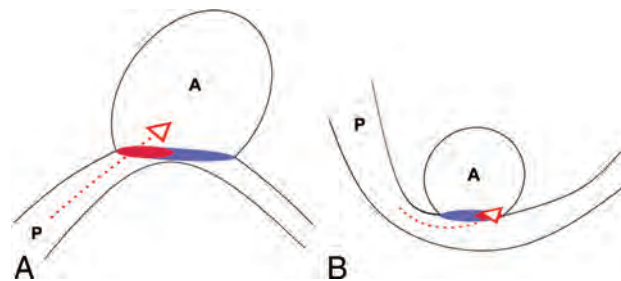


FIG 5. Illustrations of late and early occluded types of aneurysms reported in our results. A, A diagram of a late occluded aneurysm shows obvious sac size, height, ostium in geometries, and intense ostium hemodynamics with proximal neck inflow. B, Diagram of an early occluded aneurysm shows a smaller sac size, height, ostium in geometries, and mild ostium hemodynamics, with distal neck inflow. P and A represent parent vessels and aneurysms, respectively. Red dotted arrows symbolize inward blood flows. Oval red and purple regions at the ostium represent the inward and outward blood flow areas, respectively.

Among all the geometric parameters, a large ostium maximum diameter (>4.9 mm) was constantly and significantly associated with delayed occlusion, similar to a previous report.⁹

However, ostium hemodynamics provided new perspectives to investigate the influence of the FD. A proximal inflow area at the aneurysm neck represented a direct blood flow injecting into the aneurysm that might delay the occlusion. Because aneurysms in our study were mostly located in the tortuous ICA and the main flow often shifted to the lateral side of the artery by the inertial behavior after a sharp turn, the inflow zone on the lateral side was commonly observed.¹³

Furthermore, a strong inflow at the neck, especially a high systolic inflow rate ratio (>0.343) and large systolic inflow area (>13.35 mm²), indicated more blood flow impinging on the aneurysm ostium, which would hinder the dampening of blood flow and even result in long-term patency. Our results showed that these 2 parameters were of importance and could well

predict the FD treatment response. The advantage of this predictive tendency could be the possibility to plan a more individualized intervention to achieve a better patient outcome, such as a coiling aid or a combination of different patterns of FDs.

Although almost each geometric dimensional parameter shared the same trend between comparisons at 6 and 12 months, some variations could be observed in the hemodynamic parameters between the 2 time points. The preprocedural qualitative inflow zone and maximum inflow velocity were only significantly different between the different treatment response groups at 6 months and the parent flow rate between the different groups at 12 months. This suggests that some hemodynamic parameters may have different implications for short- and long-term responses, and provides a clue to further investigate the underlying reasons.

The FD may change local hemodynamics rather than simply covering the ostium and may need some time for a complete thrombosis inside the aneurysm and intimal endothelialization of the FD after the flow has been modified. According to the literature,²⁷⁻³⁰ the occlusion rate is variable. Our 6-month occlusion rate was slightly lower, but we found a similar rate at 12 months. Our results also showed that different hemodynamic initial conditions influenced the treatment response and thus provided more direct evidence to confirm the hemodynamic change effect on aneurysms. At present, due to metallic magnetic susceptibility and a low velocity from flow diversion, a direct in vivo hemodynamic MR imaging evaluation near the FD segment still has some limitations.

It is believed that the geometric and hemodynamic features are not the only influential factors. FD selection and deployment technique are also important to the treatment response.³¹ A fitted FD and its proper position in the target vessel are prerequisites, and thus we excluded 1 case with FD displacement at follow-up. Although 3 types of FDs were used, there was no obvious discrepancy in treatment responses (On-line Table). Antiplatelet therapy could also influence the thrombosis in the aneurysm.³² In our cohort, clopidogrel was stopped after the 6-month follow-up unless there was a definite in-stent stenosis, but aspirin was continued. At least 8 aneurysms from our cohort occluded during the second 6-month period, and this may have been due to an additional effect exerted by clopidogrel discontinuity.

This study had some limitations. First, we only admitted patients with sidewall aneurysms because this type is considered a frequent and appropriate indication for flow diversion.^{7,33,34} In addition, its ostium can be better defined than those of other types. Second, although this in vivo study applied optimal acquisition by using PC MRI on a 3T system, MR imaging itself still has inherent limitations. For example, the presetting of the velocity sensitivity encoding parameter, the moderate spatial and temporal resolution according to our scan protocol may reduce MRI accuracy.³⁵ Indeed, relatively low spatial resolution might imprecisely resolve a small region of interest for aneurysm ostium to some extent. Third, if the FD apparently changed the arterial angle because of its radial force, then the preprocedural hemodynamic analysis might not be fully consistent with the subsequent

situation. A multicenter study with a large number of cases would seem to be essential for further analysis.

CONCLUSIONS

Intracranial aneurysms with a large ostium, systolic inflow rate ratio, and systolic inflow area may need a longer time for occlusion. Apart from conventional aneurysm geometric differences between occlusion and remnant groups, 4D flow MR imaging as a functional technique has the potential to well evaluate ostium hemodynamics and to hemodynamically explain FD treatment response in sidewall intracranial aneurysms.

Disclosures: Tianhao Su—RELATED: Grant: Swiss National Funds, Beijing Li Huanying Medical Foundation, Comments: SNF 32003B_160222 and SNF 320030_156813, Beijing Li Huanying Medical Foundation 2017.* Long Jin—RELATED: Grant: Beijing Li Huanying Medical Foundation, Comments: Beijing Li Huanying Medical Foundation 2017.* *Money paid to institution.

REFERENCES

1. Villablanca JP, Duckwiler GR, Jahan R, et al. **Natural history of asymptomatic unruptured cerebral aneurysms evaluated at CT angiography: growth and rupture incidence and correlation with epidemiologic risk factors.** *Radiology* 2013;269:258–65 CrossRef Medline
2. Chalouhi N, Daou B, Barros G, et al. **Matched comparison of flow diversion and coiling in small, noncomplex intracranial aneurysms.** *Neurosurgery* 2017;81:92–97 CrossRef Medline
3. Chalouhi N, Tjoumakaris S, Starke RM, et al. **Comparison of flow diversion and coiling in large unruptured intracranial saccular aneurysms.** *Stroke* 2013;44:2150–54 CrossRef Medline
4. Karmonik C, Anderson JR, Elias S, et al. **Four-dimensional phase contrast magnetic resonance imaging protocol optimization using patient-specific 3-dimensional printed replicas for in vivo imaging before and after flow diverter placement.** *World Neurosurg* 2017; 105:775–82 CrossRef Medline
5. Ouared R, Larrabide I, Brina O, et al. **Computational fluid dynamics analysis of flow reduction induced by flow-diverting stents in intracranial aneurysms: a patient-unspecific hemodynamics change perspective.** *J Neurointerv Surg* 2016;8:1288–93 CrossRef Medline
6. Pereira VM, Brina O, Delattre BM, et al. **Assessment of intra-aneurysmal flow modification after flow diverter stent placement with four-dimensional flow MRI: a feasibility study.** *J Neurointerv Surg* 2015;7:913–19 CrossRef Medline
7. Alderazi YJ, Shastri D, Kass-Hout T, et al. **Flow diverters for intracranial aneurysms.** *Stroke Res Treat* 2014;2014:415653 CrossRef Medline
8. Madaelil TP, Grossberg JA, Howard BM, et al. **Aneurysm remnants after flow diversion: clinical and angiographic outcomes.** *AJNR Am J Neuroradiol* 2019;40:694–98 CrossRef Medline
9. Briganti F, Napoli M, Leone G, et al. **Treatment of intracranial aneurysms by flow diverter devices: long-term results from a single center.** *Eur J Radiol* 2014;83:1683–90 CrossRef Medline
10. Larrabide I, Geers AJ, Morales HG, et al. **Effect of aneurysm and ICA morphology on hemodynamics before and after flow diverter treatment.** *J Neurointerv Surg* 2015;7:272–80 CrossRef Medline
11. Karunanithi K, Lee CJ, Chong W, et al. **The influence of flow diverter's angle of curvature across the aneurysm neck on its haemodynamics.** *Proc Inst Mech Eng H* 2015;229:560–69 CrossRef Medline
12. Futami K, Kitabayashi T, Sano H, et al. **Inflow jet patterns of unruptured cerebral aneurysms based on the flow velocity in the parent artery: evaluation using 4D flow MRI.** *AJNR Am J Neuroradiol* 2016;37:1318–23 CrossRef Medline
13. Futami K, Sano H, Kitabayashi T, et al. **Parent artery curvature influences inflow zone location of unruptured sidewall internal**

- carotid artery aneurysms. *AJNR Am J Neuroradiol* 2015;36:342–48 CrossRef Medline
14. Futami K, Sano H, Misaki K, et al. **Identification of the inflow zone of unruptured cerebral aneurysms: comparison of 4D flow MRI and 3D TOF MRA data.** *AJNR Am J Neuroradiol* 2014;35:1363–70 CrossRef Medline
 15. Paliwal N, Tutino VM, Shallwani H, et al. **Ostium ratio and neck ratio could predict the outcome of sidewall intracranial aneurysms treated with flow diverters.** *AJNR Am J Neuroradiol* 2019;40:288–94 CrossRef Medline
 16. Paliwal N, Jaiswal P, Tutino VM, et al. **Outcome prediction of intracranial aneurysm treatment by flow diverters using machine learning.** *Neurosurg Focus* 2018;45:E7 CrossRef Medline
 17. Higgins WE, Ojard EJ. **Interactive morphological watershed analysis for 3D medical images.** *Comput Med Imaging Graph* 1993;17:387–95 CrossRef
 18. Fernand M. **Topographic distance and watershed lines.** *Signal Processing* 1994;38:113–25
 19. Wong SC, Nawawi O, Ramli N, et al. **Benefits of 3D rotational DSA compared with 2D DSA in the evaluation of intracranial aneurysm.** *Acad Radiol* 2012;19:701–07 CrossRef Medline
 20. Dhar S, Tremmel M, Mocco J, et al. **Morphology parameters for intracranial aneurysm rupture risk assessment.** *Neurosurgery* 2008;63:185–96; discussion 196–97 CrossRef Medline
 21. Ahn SH, Prince EA, Dubel GJ. **Basic neuroangiography: review of technique and perioperative patient care.** *Semin Intervent Radiol* 2013;30:225–33 CrossRef Medline
 22. Attali J, Benaissa A, Soize S, et al. **Follow-up of intracranial aneurysms treated by flow diverter: comparison of three-dimensional time-of-flight MR angiography (3D-TOF-MRA) and contrast-enhanced MR angiography (CE-MRA) sequences with digital subtraction angiography as the gold standard.** *J Neurointerv Surg* 2016;8:81–86 CrossRef Medline
 23. Cloft HJ, Kaufmann T, Kallmes DF. **Observer agreement in the assessment of endovascular aneurysm therapy and aneurysm recurrence.** *AJNR Am J Neuroradiol* 2007;28:497–500 Medline
 24. Raghavan ML, Ma B, Harbaugh RE. **Quantified aneurysm shape and rupture risk.** *J Neurosurg* 2005;102:355–62 CrossRef Medline
 25. Hanley JA, McNeil BJ. **The meaning and use of the area under a receiver operating characteristic (ROC) curve.** *Radiology* 1982;143:29–36 CrossRef Medline
 26. Bossuyt PM, Reitsma JB, Bruns DE, et al. **STARD 2015: an updated list of essential items for reporting diagnostic accuracy studies.** *Radiology* 2015;277:826–32 CrossRef Medline
 27. Foa Torres G, Roca F, Noguera A, et al. **Silk flow-diverter stent for the treatment of complex intracranial aneurysms: a one-year follow-up multicenter study.** *Interv Neuroradiol* 2018;24:357–62 CrossRef Medline
 28. Mohlenbruch MA, Herweh C, Jestaedt L, et al. **The FRED flow-diverter stent for intracranial aneurysms: clinical study to assess safety and efficacy.** *AJNR Am J Neuroradiol* 2015;36:1155–61 CrossRef Medline
 29. Murthy SB, Shah S, Shastri A, et al. **The SILK flow diverter in the treatment of intracranial aneurysms.** *J Clin Neurosci* 2014;21:203–06 CrossRef Medline
 30. Becske T, Kallmes DF, Saatci I, et al. **Pipeline for uncoilable or failed aneurysms: results from a multicenter clinical trial.** *Radiology* 2013;267:858–68 CrossRef Medline
 31. Ma D, Xiang J, Choi H, et al. **Enhanced aneurysmal flow diversion using a dynamic push-pull technique: an experimental and modeling study.** *AJNR Am J Neuroradiol* 2014;35:1779–85 CrossRef Medline
 32. Texakalidis P, Bekelis K, Atallah E, et al. **Flow diversion with the Pipeline embolization device for patients with intracranial aneurysms and antiplatelet therapy: a systematic literature review.** *Clin Neurol Neurosurg* 2017;161:78–87 CrossRef Medline
 33. Petr O, Brinjikji W, Cloft H, et al. **Current trends and results of endovascular treatment of unruptured intracranial aneurysms at a single institution in the flow-diverter era.** *AJNR Am J Neuroradiol* 2016;37:1106–13 CrossRef Medline
 34. Brown RD Jr, Broderick JP. **Unruptured intracranial aneurysms: epidemiology, natural history, management options, and familial screening.** *Lancet Neurol* 2014;13:393–404 CrossRef Medline
 35. Bouillot P, Delattre BMA, Brina O, et al. **3D phase contrast MRI: partial volume correction for robust blood flow quantification in small intracranial vessels.** *Magn Reson Med* 2018;79:129–40 CrossRef Medline

Contrast Enhancement of Intracranial Aneurysms on 3T 3D Black-Blood MRI and Its Relationship to Aneurysm Recurrence following Endovascular Treatment

S. Elsheikh, H. Urbach, and S. Meckel

ABSTRACT

BACKGROUND AND PURPOSE: Endovascular treatment of intracranial aneurysms aims at preventing aneurysm rupture. Contrast-enhanced black-blood MR imaging facilitates imaging of the vessel walls and the aneurysmal sac contents and is therefore suitable for studying the healing process. This study aims to describe imaging findings of aneurysmal contrast enhancement following endovascular treatment and its correlation to recurrence and elapsed time since coiling.

MATERIALS AND METHODS: Patients undergoing MR imaging follow-up after endovascular treatment of an intracranial aneurysm were included. Contrast-enhanced black-blood T1WI was acquired. Aneurysm wall and intra-aneurysmal enhancement were independently assessed by 2 neuroradiologists and were related to the time elapsed since coiling and the presence of recurrence.

RESULTS: Thirty aneurysms in 30 patients were included. The median time elapsed since treatment was 417 days (interquartile range, 189–1273 days). Aneurysmal contrast enhancement was seen in 24/30 (80%) aneurysms. Enhancement inside the sac in 55% ($n = 17$), the wall in 23% ($n = 7$), at the dome ($n = 1$), or at the base ($n = 6$) was observed. No statistically significant correlation between aneurysmal contrast enhancement and the elapsed time ($P = .83$) and presence of a recurrence ($P = .184$) was detected. In 28/30 patients, the images were of adequate diagnostic quality. Stent implants caused negligible image artifacts.

CONCLUSIONS: Intra-aneurysmal contrast enhancement following endovascular treatment of intracranial aneurysms is a common finding and likely reflects the healing process. A long-term study to examine changes occurring with time and their association with packing density, type of coils (bare platinum versus bioactive coils), and aneurysm recurrence is underway (German Clinical Trials Register, DRKS-ID: DRKS00014644).

The safety and efficacy of endovascular treatment of both ruptured and unruptured aneurysms have been shown in many large, multicenter trials.^{1–3} The main drawback of endovascular treatment is the recanalization of an initially occluded aneurysm. This occurs in about one-fourth to one-third of patients. In about 9% of patients, retreatment is required.⁴

Mechanisms leading to aneurysm recurrence include coil compaction secondary to poor packing or aneurysm growth⁵ and coil extrusion into the subarachnoid space or an intraluminal thrombus.^{6,7} Aneurysm recurrence is facilitated by poor thrombus organization due to the biologically inert platinum coil

material,⁸ instability of the fresh, unorganized thrombus and degradation by thrombolysis; continued transmission of pulsations from the parent vessel into the aneurysm;⁹ incomplete neointimal coverage of the aneurysm neck;¹⁰ and neovessel formation in the lumen of the aneurysm, exposing the aneurysmal cavity to continuous blood flow.¹¹

Following endovascular treatment of intracranial aneurysms, the aneurysms undergo a prolonged healing process. This process involves a cascade of events, including an inflammatory reaction occurring within the aneurysm and at its neck. This process may last >1 year. Ideally, aneurysm healing should end in a complete re-endothelialization of the aneurysm neck.¹¹

Contrast enhancement following aneurysm coiling is a known observation, which is only rarely reported in the current literature. The 2 largest series were published by the same research group reporting their patient cohort.^{12,13}

High-resolution T1-weighted contrast-enhanced MR black-blood imaging may depict not only enhancement of the vessel wall but also the sac contents.¹⁴ We hypothesized that contrast enhancement of the aneurysm wall and/or inside the intra-aneurysmal sac is associated with the healing process following

Received November 14, 2019; accepted after revision December 30.

From the Department of Neuroradiology, Faculty of Medicine, Medical Center—University of Freiburg, Freiburg, Germany.

Paper previously presented at: Annual Meeting of the German Society of Neuroradiology, October 3–6, 2018; Frankfurt, Germany.

This work was supported by the Research Committee, Albert-Ludwigs-Universität Freiburg.

Please address correspondence to Samer Elsheikh, MD, Klinik für Neuroradiologie, Breisacherstr 64, 79106 Freiburg, Germany; e-mail: samer.elsheikh@uniklinik-freiburg.de

<http://dx.doi.org/10.3174/ajnr.A6440>

Table 1: Black-blood MR imaging study sequence protocols

	2D T1WI TIRM Black-Blood	3D T1WI SPACE Black-Blood	3D T1WI CS-SPACE Black-Blood
Section orientation	Axial and coronal	Sagittal	Sagittal
TR, TE, TI (ms), FA, NEX, PAT	2000, 11, 1200, 150°, 2, GRAPPA 2	710, 11, N/A, N/A, 1, GRAPPA 2. echo train length 157 ms	800, 10, N/A, N/A, 1, GRAPPA 2. echo train length 269 ms
FOV	230 × 201 mm	230 × 230 mm	225 × 225 mm
Matrix	512 × 410	256 × 265	448 × 448
Section thickness	2 mm (10% gap)	0.9 mm	0.64 mm
Spatial resolution	0.45 × 0.45 × 2 mm	0.9 mm (isotropic)	0.5 × 0.5 × 0.64 mm
No. of slices	15	192	256
Scan time	4 min 6 sec	6 min 48 sec	6 min 54 sec

Note:—FA indicates flip angle; TRIM, turbo inversion recovery magnitude; CS-SPACE, sampling perfection with application-optimized contrasts by using different flip angle evolutions using compressed sensing; GRAPPA, generalized autocalibrating partially parallel acquisition; PAT, parallel acquisition technique.

aneurysm treatment, and as a corollary, contrast enhancement is associated with the stability of the result following aneurysm treatment. This study aims to describe the imaging findings of aneurysmal contrast enhancement on high-resolution 3D black-blood MR imaging following endovascular treatment and to assess the correlation between these findings and the presence of aneurysm recurrence and the elapsed time since coiling. Factors such as patient cooperation and image quality will also be addressed.

MATERIALS AND METHODS

Research Design

This was a nonrandomized, prospective, observational, diagnostic imaging study. The study was approved by the institutional review board. Informed written consent was obtained from all patients.

Patients

Consecutive patients, presenting for their regular follow-up MR imaging/MRA examination after endovascular treatment of a ruptured or unruptured intracranial aneurysm were included if they fulfilled the following criteria: 18 years of age or older and no known contraindication to gadolinium contrast agents (eg, previous moderate-to-severe allergic reaction or a glomerular filtration rate of <60 mL/min/1.73 m²). No restriction on the time elapsed since the last endovascular treatment was imposed.

MR Imaging Protocol

The study was conducted using vendor-supplied sequences approved for clinical application. All examinations were performed on a Magnetom Prisma 3T scanner (Siemens, Erlangen, Germany) using a 64-element head coil.

Study sequences (Table 1) included pre- and postcontrast axial 2D, turbo inversion recovery magnitude, black-blood, fat-suppressed T1WI and sagittal 3D sampling perfection with application-optimized contrasts by using different flip angle evolution (SPACE sequence; Siemens) T1WI with and without compressed sensing. During the administration of the contrast medium, a coronal flash 3D and a time-resolved MR angiography sequence were acquired. Gadolinium contrast agent (gadoteridol, ProHance; Bracco Imaging S.p.A, Milan, Italy) was administered in a weight-adapted dose of 0.1 mmol/kg body weight intravenously.

Study Sequences

The spatial resolution and other scan parameters are summarized in Table 1.

Assessment of Aneurysms and Black-Blood MR Imaging Sequences

We determined the following measures:

- Presence and location of aneurysmal contrast enhancement: at the base (interface to the parent vessel), at the dome, inside the aneurysm sac, and in the sidewalls.
- Subjective evaluation of the aneurysmal contrast-enhancement intensity performed and graded using a 4-point semi-quantitative scale: none/faint/moderate/strong.
- Analysis of the aneurysm size and location on the DSA and the interval between treatment and MRI examination.
- Image degradation due to artifacts after treatment using stents/flow diverters, subjectively determined.
- The rate of patient compliance for MRI—that is, the presence of motion artifacts and number of patients interrupting the examination.

Aneurysm Recurrence

The detection of aneurysm recurrence was based on the evaluation of images from nonenhanced TOF-MRA. It was defined as any visually detected signal inside an aneurysm of any size. Further DSA examinations were indicated only in the clinical context. The results of the DSA were not considered in this study.

Statistical Methods

Descriptive statistics were used for the demographic data of the patients. A 2-sided Fisher exact test was used to examine the correlation between aneurysm recurrence and the presence of contrast enhancement. An unpaired 2-sided *t* test was used to assess the correlation between elapsed time since endovascular treatment and contrast enhancement.

RESULTS

Between April 2017 and February 2018, we prospectively included all consecutive patients presenting for the MR imaging follow-up examination after endovascular treatment of an intracranial aneurysm. A total of 31 patients (20 women) were included. One patient discontinued the examination before

application of contrast medium. There were no observed adverse effects due to the administration of contrast medium.

Patient and Aneurysm Data

The demographic data of the patient cohort are summarized in Table 2. The different locations of the included aneurysms are summarized in Table 3.

Table 2: Patient demographic data

	Median	Range	Interquartile Range
Age (yr)	54	33–77	47–61
Days since treatment	417	87–5318	189–1273
Aneurysm diameter (cm)	7	3–20	5–10

Table 3: Location of intracranial aneurysms

Aneurysm Location	Frequency	Percentage
Basilar artery, tip	4	12.9%
Anterior cerebral artery, A1 segment	1	3.2%
Anterior communicating artery	12	38.7%
Internal carotid artery, paraophthalmic	2	6.5%
Internal carotid artery, terminus	1	3.2%
Anterior choroidal artery	2	6.5%
Vertebral artery	2	6.5%
Posterior communicating artery	7	22.6%

Table 4: Association between aneurysm recurrence and aneurysmal contrast enhancement

Aneurysm Recurrence	Contrast Enhancement		Total
	Yes	No	
Yes	16	2	18
No	8	4	12
Total	24	6	30

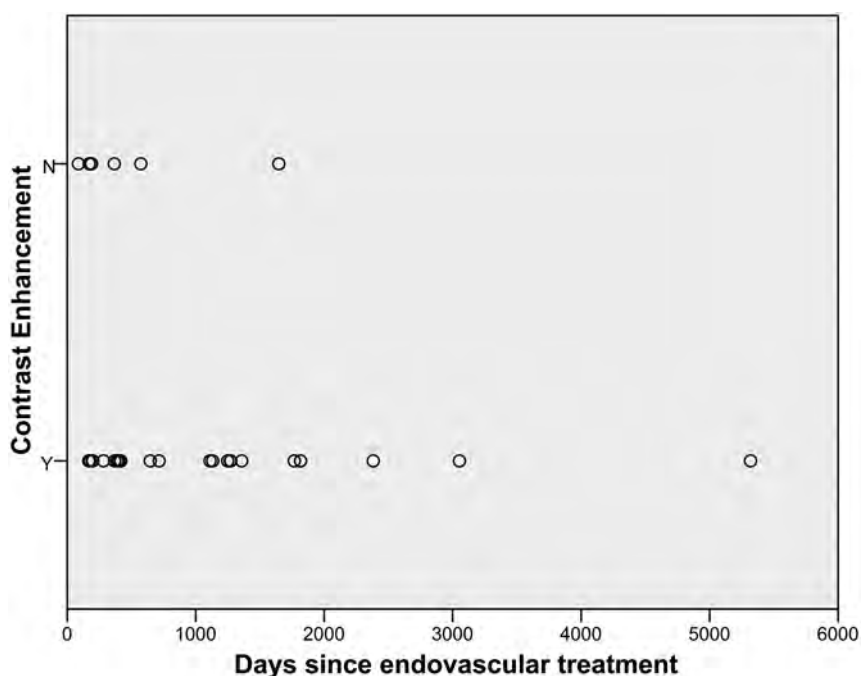


FIG 1. Temporal distribution of aneurysmal contrast enhancement analyzed in the days since endovascular treatment.

Association between Aneurysm Recurrence and Contrast Enhancement

The MR imaging–detected recurrence rate was 18/30 (60%). A 2-sided Fisher exact test (Table 4) showed no statistically significant association between aneurysm recurrence and aneurysmal enhancement ($P = .184$).

Elapsed Time since Coiling

The median elapsed time since endovascular treatment was 417 days (interquartile range, 189–1273 days) (Table 2 and Fig 1). All aneurysms except one that did not show any contrast enhancement were imaged within 2 years after treatment. One aneurysm without contrast enhancement was examined at an interval of 4.5 years following treatment (Fig 1). Aneurysms with any contrast enhancement were imaged up to an interval of 14.5 years. An unpaired 2-sided t test showed no statistically significant association between the elapsed time since endovascular treatment and contrast enhancement ($P = .83$).

Grading and Location of Aneurysmal Contrast Enhancement

In 24/30 patients, contrast enhancement of the embolized aneurysm was observed. Eighteen aneurysms showed contrast enhancement solely in 1 location; 5 aneurysms, in 2 locations of the same aneurysm; and 1 aneurysm, in 3 different locations of the same aneurysm. Thus, a total of 31 locations of contrast enhancement in 24 aneurysms were recorded (Figs 2–4). Contrast enhancement inside the aneurysm sac was the most common location (17/31, 55%), followed by contrast enhancement of the sidewalls (7/31, 23%), and at the aneurysm base (6/31, 19%). Last, contrast enhancement of the aneurysm dome was observed in only 1 patient (1/31, 3%). Faint enhance-

ment was observed 10/31 times, while moderate enhancement was observed 5/31 times. Strong enhancement was encountered 16/31 times. The results are listed in Table 5.

Image Degradation/Artifacts

Of 30 patients, 7 were treated using stents (flow diverter, $n = 2$; stent-assisted coiling, $n = 3$; and bifurcation aneurysm stent, $n = 2$). These metallic stent implants led to no or only minimal degradation of the image quality.

Patient Compliance

In 28/31 patients, the images acquired were of good diagnostic quality. One patient discontinued the examination before the administration of contrast medium, so postcontrast images were not available for evaluation. Slight motion artifacts were observed in 2/31 patients. These artifacts were deemed to not greatly affect the diagnostic quality of the images and were included in our

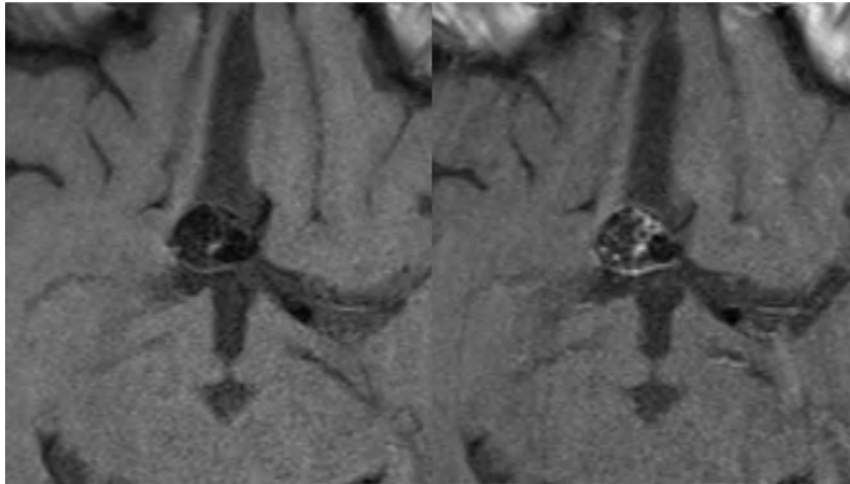


FIG 2. Anterior communicating artery aneurysm after endovascular treatment. Axial nonenhanced (*left*) and contrast-enhanced (*right*) black-blood MR images show enhancement of the sidewall and inside the aneurysm sac.

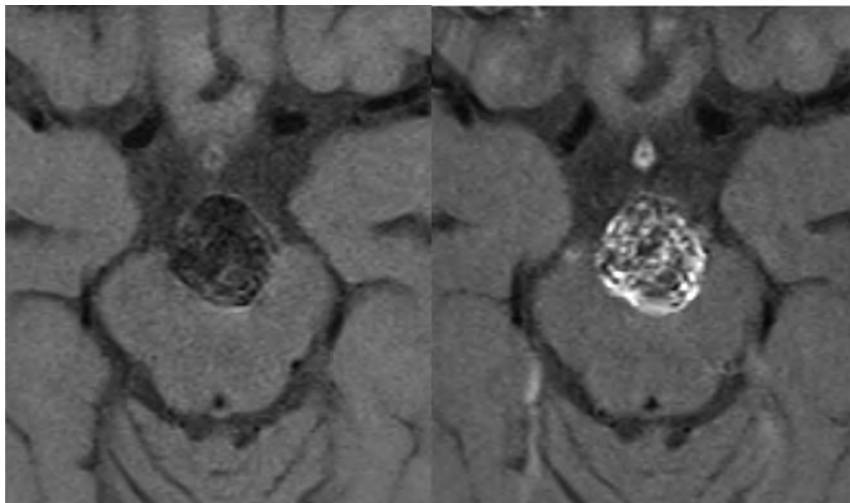


FIG 3. Tip of a basilar artery aneurysm after endovascular treatment. Axial nonenhanced (*left*) and contrast-enhanced (*right*) black-blood MR images show contrast enhancement of the sidewall and inside the aneurysm sac.

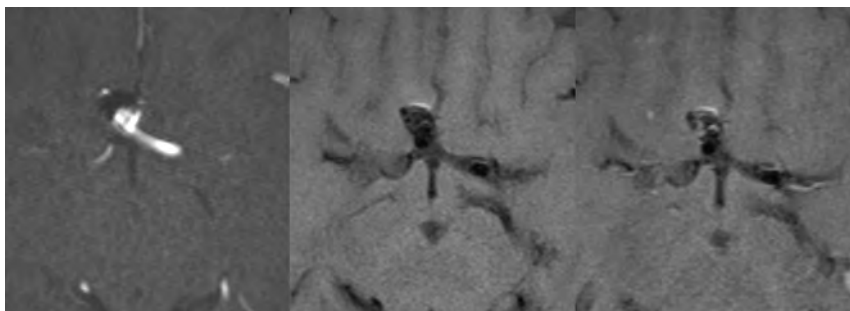


FIG 4. Anterior communicating artery aneurysm after endovascular treatment. Axial TOF-MRA (*left*) and axial nonenhanced (*middle*) and contrast-enhanced (*right*) black-blood MR images show recurrence at the base of the aneurysm. The same aneurysm shows contrast enhancement inside the aneurysm sac.

evaluation. These 2 patients neither had a recurrence following endovascular treatment nor showed aneurysmal contrast enhancement on the study sequences.

DISCUSSION

The standard of care for follow-up after endovascular treatment of intracranial aneurysms includes regular MR imaging/MRA examinations. Our institutional standard is to perform follow-up MR imaging/MRA of intracranial aneurysms after endovascular treatment using 3T MR imaging and 3D TOF-MRA after 6, 18, 36, and 60 months.¹⁵ The decision to perform re-angiography and consider retreatment is made on the basis of the detection of relevant flow signal at the aneurysm base or within the aneurysm, compaction or expansion of the coil mass, and/or aneurysm growth.

In this study, we used contrast-enhanced T1-weighted black-blood MR imaging sequences with a high spatial resolution at 3T. We used both axial and coronal 2D black-blood sequences with a high in-plane resolution (0.45×0.45 mm) at a section thickness of 2 mm and an isotropic 3D black-blood sequence (0.9 mm). The higher signal-to-noise ratio of the 2D sequences allows a better assessment of the vessel wall and the sac content, and because the position of the aneurysm is known, the limited coverage of the 2D sequences is not disadvantageous.¹⁶ A future direction to further improve the spatial resolution of 3D black-blood imaging with whole-brain coverage at adequate scan times may be the use of the recently introduced compressed sensing SPACE.¹⁷

The main result of our study was the detection of aneurysmal contrast enhancement in 80% (24/30) of the treated aneurysms. It occurred mostly within the aneurysm sac between the coils (55%), but also in about 20% of cases in the aneurysm walls and/or at the aneurysm base. The etiology of the contrast-enhancing tissue is not clear; however, it is most likely related to organized blood clot, granulation tissue, and the subsequent healing process of the treated aneurysm.

Table 5: Aneurysm enhancement location and grade in 24/31 aneurysms showing any enhancement

Case No.	Aneurysm Location	Location of Contrast Enhancement	Grading of Contrast Enhancement
1	AcomA	Inside the aneurysm	Moderate
2		Wall/sidewall	Strong
3	Vertebral artery	Inside the aneurysm	Strong
4		Wall/sidewall	Strong
5	Vertebral artery	Inside the aneurysm	Faint
6		Wall/sidewall	Faint
7	PcomA	Base	Faint
8	Basilar tip	Wall/sidewall	Strong
9	Carotid bifurcation	Inside the aneurysm	Faint
10	Paraophthalmic aneurysm	Inside the aneurysm	Faint
11	AcomA	Inside the aneurysm	Strong
12	AcomA	Base	Strong
13		Inside the aneurysm	Strong
14		Wall/sidewall	Strong
15	A1 segment	Base	Strong
16	AcomA	Base	Moderate
17	Anterior choroidal artery	Base	Strong
18	PcomA	Inside the aneurysm	Strong
19	PcomA	Inside the aneurysm	Faint
20	Paraophthalmic aneurysm	Inside the aneurysm	Moderate
21	PcomA	Inside the aneurysm	Faint
22	Basilar tip	Inside the aneurysm	Faint
23	Basilar tip	Base	Moderate
24	PcomA	Inside the aneurysm	Strong
25	AcomA	Inside the aneurysm	Strong
26		Wall/sidewall	Strong
27	PcomA	Inside the aneurysm	Strong
28		Wall/sidewall	Strong
29	AcomA	Inside the aneurysm	Faint
30	AcomA	Inside the aneurysm	Faint
31	AcomA	Dome	Moderate

Note:—AcomA indicates anterior communicating artery; PcomA, posterior communicating artery.

Most previously published studies using postgadolinium black-blood MR imaging sequences offered analysis of contrast enhancement in previously untreated, incidental intracranial aneurysms for potential use as an indicator of aneurysm instability or rupture risk^{18,19} or to define the site of an already ruptured aneurysm.^{20,21} Literature regarding contrast-enhanced MR imaging of intracranial aneurysms following endovascular treatment is limited to examining patients using standard T1WI.^{12,13} Thus, to our knowledge, there are no published data systematically addressing contrast enhancement of intracranial aneurysms following endovascular treatment using black-blood MR imaging sequences.

We found no statistically significant association between contrast enhancement and the time elapsed since treatment. We also found no significant association with the presence of an aneurysm recurrence on the same MR imaging examination. A correlation between the presence and/or temporal changes of the contrast enhancement and the durability of the treatment result after endovascular aneurysm occlusion across time may be more interesting to examine, but these relationships are outside the scope of our study due to the cross-sectional nature of our data and the small sample size.

Overall, the image quality of treated aneurysms was adequate in our study. Images of patients treated with intravascular stent implants (including flow-diverter stents) showed only minimal

artifacts without relevant image degradation. Guan et al²² reported similar findings regarding the utility of high-resolution 3D black-blood MR imaging in the follow-up of intracranial aneurysms treated with flow diverters.

Limitations of our study are the small sample size and the cross-sectional nature of the data in our study cohort. Our cohort included patients with a wide range of intervals following the treatment of the aneurysms (up to about 14.5 years). Moreover, because we examined only aneurysms following endovascular treatment, there is a lack of histopathologic correlation of the treated aneurysms, so the exact cause of the contrast enhancement following treatment cannot be verified.

On the basis of this study, we started a long-term follow-up study to evaluate temporal changes of contrast enhancement during the follow-up period and to test for an association of contrast enhancement with aneurysm recurrence. This study is registered in the German Clinical Trials Register (DRKS-ID: DRKS00014644).

CONCLUSIONS

Contrast enhancement of intracranial aneurysms following endovascular treatment is a common finding of unknown clinical significance. It is mostly observed within the aneurysmal sac and likely is a sign of a healing process. We are currently running a long-term study to examine changes in aneurysmal contrast enhancement occurring across time and their association with aneurysm recurrence.

Disclosures: Samer Elsheikh—*RELATED: Grant:* Research Committee, Faculty of Medicine, University of Freiburg, Freiburg, Germany*; *UNRELATED: Grants/Grants Pending:* Bracco SpA, *Comments:* research funding for another research article concerned with contrast enhancement of unruptured aneurysms, not yet published.* Horst Urbach—*UNRELATED: Board Membership:* Co-Editor of *Clinical Neuroradiology*, Editorial Board of *Neuroradiology*, *Comments:* 1000 €/year; *Payment for Lectures Including Service on Speakers Bureaus:* Bayer AG, Bracco SpA, Stryker, UCB Pharma, *Comments:* less than 10,000 € since 2016; *Other:* shareholder of VEObrain GmbH, *Comments:* no money paid. Stephan Meckel—*RELATED: Grant:* Bracco SpA*; *UNRELATED: Board Membership:* Acandis GmbH, *Comments:* modest consultant's fee as member of the Scientific Advisory Board; *Consultancy:* Novartis Pharma GmbH, *Comments:* modest consultant's fee; *Grants/Grants Pending:* Novartis Pharma GmbH, *Comments:* MR imaging study grant*; *Payment for Lectures Including Service on Speakers Bureaus:* Medtronic, *Comments:* modest lecture fee; *Payment for Development of Educational Presentations:* Medtronic, *Comments:* money from Medtronic was paid to an individual; *Travel/Accommodations/Meeting Expenses Unrelated to Activities Listed:* Balt/AB Medica, Microvention, Stryker.* *Money paid to the institution.

REFERENCES

1. Molyneux A, Kerr R; International Subarachnoid Aneurysm Trial Collaborative Group. **International Subarachnoid Aneurysm Trial**

- (ISAT) of neurosurgical clipping versus endovascular coiling in 2143 patients with ruptured intracranial aneurysms: a randomized trial. *J Stroke Cerebrovasc Dis* 2002;11:304–14 CrossRef
2. Pierot L, Cognard C, Ricolfi F, et al; CLARITY Investigators. Immediate anatomic results after the endovascular treatment of ruptured intracranial aneurysms: analysis in the CLARITY series. *AJNR Am J Neuroradiol*. 2010;31:907–11 CrossRef Medline
 3. Pierot L, Spelle L, Vitry F, et al. Immediate clinical outcome of patients harboring unruptured intracranial aneurysms treated by endovascular approach: results of the ATENA study. *Stroke* 2008; 39:2497–504 CrossRef Medline
 4. Naggara ON, White PM, Guilbert F, et al. Endovascular treatment of intracranial unruptured aneurysms: systematic review and meta-analysis of the literature on safety and efficacy. *Radiology* 2010;256:887–97 CrossRef Medline
 5. Hope JK, Byrne JV, Molyneux AJ. Factors influencing successful angiographic occlusion of aneurysms treated by coil embolization. *AJNR Am J Neuroradiol* 1999;20:391–99 Medline
 6. Ferns SP, van Rooij WJ, Sluzewski M, et al. Partially thrombosed intracranial aneurysms presenting with mass effect: long-term clinical and imaging follow-up after endovascular treatment. *AJNR Am J Neuroradiol* 2010;31:1197–205 CrossRef Medline
 7. Waldron JS, Halbach VV, Lawton MT. Microsurgical management of incompletely coiled and recurrent aneurysms: trends, techniques, and observations on coil extrusion. *Neurosurgery* 2009;64: 301–15; discussion 315–17 CrossRef Medline
 8. Yuki I, Lee D, Murayama Y, et al. Thrombus organization and healing in an experimental aneurysm model, Part II: the effect of various types of bioactive bioabsorbable polymeric coils. *J Neurosurg* 2007;107:109–20 CrossRef Medline
 9. Boecher-Schwarz HG, Ringel K, Kopacz L, et al. Ex vivo study of the physical effect of coils on pressure and flow dynamics in experimental aneurysms. *AJNR Am J Neuroradiol* 2000;21:1532–36 Medline
 10. Ozawa T, Tamatani S, Koike T, et al. Histological evaluation of endothelial reactions after endovascular coil embolization for intracranial aneurysm: clinical and experimental studies and review of the literature. *Interv Neuroradiol* 2003;9:69–82 CrossRef Medline
 11. Brinjikji W, Kallmes DF, Kadirvel R. Mechanisms of healing in coiled intracranial aneurysms: a review of the literature. *AJNR Am J Neuroradiol* 2015;36:1216–22 CrossRef Medline
 12. Fanning NF, Willinsky RA, ter Brugge KG. Wall enhancement, edema, and hydrocephalus after endovascular coil occlusion of intradural cerebral aneurysms. *J Neurosurg* 2008;108:1074–86 CrossRef Medline
 13. Su IC, Willinsky RA, Fanning NF, et al. Aneurysmal wall enhancement and perianeurysmal edema after endovascular treatment of unruptured cerebral aneurysms. *Neuroradiology* 2014;56:487–95 CrossRef Medline
 14. Tan HW, Chen X, Maingard J, et al. Intracranial vessel wall imaging with magnetic resonance imaging: current techniques and applications. *World Neurosurg* 2018;112:186–98 CrossRef Medline
 15. Urbach H, Dorenbeck U, von Falkenhausen M, et al. Three-dimensional time-of-flight MR angiography at 3 T compared to digital subtraction angiography in the follow-up of ruptured and coiled intracranial aneurysms: a prospective study. *Neuroradiology* 2008; 50:383–89 CrossRef Medline
 16. Eiden S, Beck C, Venhoff N, et al. High-resolution contrast-enhanced vessel wall imaging in patients with suspected cerebral vasculitis: prospective comparison of whole-brain 3D T1 SPACE versus 2D T1 black-blood MRI at 3 Tesla. *PLoS One* 2019;14: e0213514 CrossRef Medline
 17. Zhu C, Tian B, Chen L, et al. Accelerated whole brain intracranial vessel wall imaging using black blood fast spin echo with compressed sensing (CS-SPACE). *MAGMA* 2018;31:457–67 CrossRef Medline
 18. Etminan N, Rinkel GJ. Unruptured intracranial aneurysms: development, rupture and preventive management. *Nat Rev Neurol* 2016;12:699–713 CrossRef Medline
 19. Hackenberg KA, Hanggi D, Etminan N. Unruptured intracranial aneurysms. *Stroke* 2018;49:2268–75 CrossRef Medline
 20. Matouk CC, Mandell DM, Gunel M, et al. Vessel wall magnetic resonance imaging identifies the site of rupture in patients with multiple intracranial aneurysms: proof of principle. *Neurosurgery* 2013; 72:492–96; discussion 496 CrossRef Medline
 21. Nagahata S, Nagahata M, Obara M, et al. Wall enhancement of the intracranial aneurysms revealed by magnetic resonance vessel wall imaging using three-dimensional turbo spin-echo sequence with motion-sensitized driven-equilibrium: a sign of ruptured aneurysm? *Clin Neuroradiol* 2016;26:277–83 CrossRef Medline
 22. Guan J, Karsy M, McNally S, et al. High-resolution magnetic resonance imaging of intracranial aneurysms treated by flow diversion. *Interdiscip Neurosurg* 2017;10:69–74 CrossRef

Gadolinium Enhancement of the Aneurysm Wall in Extracranial Carotid Artery Aneurysms

C.J.H.C.M. van Laarhoven, M.L. Rots, V.E.C. Pourier, N.K.N. Jorritsma, T. Leiner, J. Hendrikse, M.D.I. Vergouwen, and G.J. de Borst



ABSTRACT

BACKGROUND AND PURPOSE: The natural history and optimal treatment of extracranial carotid artery aneurysms are unknown. Gadolinium enhancement of the aneurysm wall may reflect aneurysm wall inflammation and instability. In this study, we investigated the feasibility of extracranial carotid artery aneurysm wall imaging and explored a potential relationship of aneurysm wall enhancement with aneurysm growth and the presence of (silent) brain infarcts and white matter lesions.

MATERIALS AND METHODS: Fourteen conservatively treated patients with 15 asymptomatic extracranial carotid artery aneurysms underwent gadolinium-enhanced 3T MR imaging at 2 time points with a 12-month interval. Primary outcome was growth of the aneurysm sac (≥ 2.0 mm); secondary outcomes were the presence of (silent) brain infarcts and white matter lesions at baseline and follow-up. MR images were reviewed by 2 independent observers, and inter- and intraobserver reproducibility was assessed.

RESULTS: Seven (50%) patients were men; the median age was 55 years (range, 40–69 years). Eleven extracranial carotid artery aneurysms (73%) were saccular (median size, 11 mm; range, 5.0–38.5 mm), and 4 were fusiform (median size, 21.5 mm; range, 10.0–40.0 mm). Eleven of 15 aneurysms (73%) exhibited gadolinium enhancement at baseline. Four aneurysms (27%) showed growth at follow-up imaging, 2 gadolinium-positive (+) and 2 gadolinium-negative (–) ($P = .245$). Three patients (21%) had ipsilateral brain infarcts at baseline; 1 of them showed a new silent brain infarct at follow-up imaging (gadolinium+). Nine patients (64%) showed bilateral white matter lesions at baseline. In 3 patients, increased white matter lesion severity was observed at follow-up (2 gadolinium+). All observations showed excellent inter- and intraobserver reproducibility.

CONCLUSIONS: In this explorative study, we demonstrated that extracranial carotid artery aneurysm wall imaging was feasible. Future well-powered studies are needed to investigate whether extracranial carotid artery aneurysm gadolinium enhancement predicts aneurysm growth and thromboembolic complications.

ABBREVIATIONS: ECAA = extracranial carotid artery aneurysm; Gd = gadolinium; WML = white matter lesion; CAR = Carotid Aneurysm Registry

The optimal treatment and prognosis of extracranial carotid artery aneurysms (ECAAs) are still unclear. Most ECAAs are coincidental findings, and a conservative approach is presently considered justified in patients with asymptomatic ECAAs.¹ Several surgical and endovascular techniques have been

developed for ECAA exclusion, but these interventions are mostly reserved for patients with neurologic symptoms or proved growth.^{2,3}

Histopathologic research revealed dissection and degeneration as the 2 main causes of ECAAs, with the presence of inflammatory cells in the degenerative vessel wall.⁴ MR imaging and histopathologic studies of atherosclerotic carotid arteries have suggested that gadolinium (Gd) enhancement reflects the density of the vasa vasorum and inflammation in the arterial wall.^{5,6} Also, MR imaging has been proposed as a noninvasive tool for early detection of arterial wall changes and may be useful for routine monitoring and evaluation of disease activity.⁶ However, ECAA growth pattern and long-term risk of thromboembolization and subsequent stroke have yet to be elucidated.

Previous studies have shown that patients with carotid stenosis have (subclinical) microvascular cerebral damage due to

Received August 21, 2019; accepted after revision January 7, 2020.

From the Departments of Vascular Surgery (C.J.H.C.M.v.L., M.L.R., V.E.C.P., N.K.N.J., G.J.d.B.) and Radiology (T.L., J.H.), and UMC Utrecht Brain Center (M.D.I.V.), Department of Neurology and Neurosurgery, University Medical Center Utrecht, Utrecht University, Utrecht, the Netherlands.

C.J.H.C.M. van Laarhoven and M.L. Rots contributed equally to this work.

Please address correspondence to Gert J. de Borst, MD, PhD, University Medical Center Utrecht, Department of Vascular Surgery, G04.129 PO Box 85500, 3508 GA Utrecht, the Netherlands; e-mail: g.j.deborst-2@umcutrecht.nl

 Indicates article with supplemental on-line tables.

 Indicates article with supplemental on-line photos.

<http://dx.doi.org/10.3174/ajnr.A6442>

microembolic events.⁷ Silent brain infarction and white matter lesions (WMLs) have both been correlated with carotid plaque vulnerability and thus may be a reflection of microembolic events from a proximal source.^{8,9} Silent brain infarcts and WML presence were described to correlate with increased future risk of ischemic stroke and cognitive decline across time.¹⁰⁻¹² Assessment of both silent and symptomatic brain infarcts and WMLs may, therefore, be helpful surrogate markers for indicating cerebral outcome in patients with ECAs.

New imaging techniques are required to assess ECAA instability for predicting growth and cerebrovascular outcome. In this study of patients with conservatively treated asymptomatic ECAs, we aimed to investigate the feasibility of ECAA wall imaging and explored a potential relationship of aneurysm wall enhancement with aneurysm growth and the presence of (silent) brain infarcts and WMLs.

MATERIALS AND METHODS

Participants

Ethics approval for this study was provided by the Medical Research Ethics Committee of the University Medical Center Utrecht, Utrecht, the Netherlands, September 13, 2016 (protocol number 16-341), and all research was conducted according to the principles of the Declaration of Helsinki (59th Amendment, Seoul 2008) and in accordance with the Dutch Medical Research Involving Human Subjects Act. Included patients with an ECAA were selected from the Carotid Aneurysm Registry (CAR; <https://www.carotidaneurysmregistry.com/en/home>). The registry protocol has been published elsewhere.¹³ In short, any patient 18 years of age or older with an ECAA is included in this ongoing registry, independent of etiology or treatment strategy. Baseline characteristics and follow-up data are collected in a prospective manner. For the present study, we selected asymptomatic patients (no symptoms for at least 1 year before the start of the study) from the CAR with a conservatively treated ECAA. Exclusion criteria were impaired renal function (glomerular filtration rate of <30 mL/min/1.73m), Gd contrast allergy, or pregnancy. All selected patients provided informed consent and were recruited between February and September 2017.

MR Imaging

Included patients were asked to undergo MR imaging at the moment of inclusion and 1 year afterward. Two observers (C.J.H.C.M.v.L., M.L.R.), blinded to patient characteristics and previous imaging, independently scored each of the MR images according to a predefined protocol and case report form. Before scoring, both observers were trained with 2 test scans to familiarize them with the scoring protocol. Test results were compared to overcome interpretation differences. Aneurysm location, shape and size, vessel wall enhancement, and cerebral complications were reported for 2 series of MR images (baseline and follow-up), with a minimum of 2 weeks between the measurements. For a subset of MR images, a third series was re-evaluated after 2 weeks to determine intraobserver variability. For the final data analysis, disagreements were discussed until consensus was reached.

A 3T MR imaging scanner (Ingenia, Software release 5.3; Philips Healthcare, Best, the Netherlands) was used. Images were acquired with an 18-element neurovascular coil as a receiver coil. The MR imaging protocol consisted of a 3D time-of-flight sequence, a contrast-enhanced T1 3D sequence (spatial resolution, $0.5 \times 0.5 \times 0.5$ mm), and, for imaging of the vessel wall, a transverse T1 3D multishot spin-echo sequence of the ipsi- and contralateral extracranial carotid arteries with the following parameters: FOV, $200 \times 166 \times 45$ mm (by default but coverage could be adjusted in case of aneurysms of >45 mm); acquired resolution, $0.5 \times 0.5 \times 1.0$ mm; reconstructed resolution, $0.5 \times 0.5 \times 0.5$ mm; TR/TE, 1.5/0.04 s. An anti-driven equilibrium technique and a minimum flip angle of 25° in the variable flip angle refocusing pulse train were used for increased vessel wall contrast, fat suppression, and flow suppression of blood.^{14,15} This sequence was performed before and after contrast administration, with a duration of 8 m 3 s per sequence. FLAIR and T2 brain imaging series were performed for detection of infarcts and WMLs. Gadobutrol was used as a contrast agent (Gadovist; Bayer Schering Pharma, Berlin, Germany) (0.1 mL/kg [1 mmol] per kilogram of body weight); flow rate, 1.0 mL/s; time between contrast administration and vessel wall imaging, 11 minutes.

Aneurysm Size Assessment

Aneurysm size was determined on the contrast-enhanced T1-weighted images using double oblique multiplanar reconstructions, in which maximum diameters were measured. Diameters were rounded to 0.5 mm. A fusiform or spindle-shaped ECAA was defined as $\geq 150\%$ dilation of the arterial diameter, compared with the unaffected contralateral carotid artery diameter. In case of bilateral dilation, the diameter of the nonaffected part of the ipsilateral carotid artery was used for comparison. For saccular ECAs, all sizes were accepted.¹ In case of a saccular type, the length, width, and neck of the aneurysm were reported; in case of a fusiform type, the length and width were reported (Fig 1). It was decided to define growth as a minimum difference of at least 2.0 mm measured in at least 1 of the measured dimensions (length, width, and neck), to ensure reliable assessment of growth at the acquired resolution ($0.5 \times 0.5 \times 0.5$ mm). We considered differences of <1.0 mm in ECAA size to be clinically irrelevant.

Assessment of Gd ECAA Wall Enhancement

The appearance of the aneurysms was compared before and after administration of Gd to determine the presence of wall enhancement. Aneurysm wall enhancement was considered present if there was a hyperintensity of the vascular wall on MR imaging after Gd administration that was not present on the MR imaging before Gd administration (Fig 2). Ipsilateral aneurysm wall enhancement was reported as well as contralateral enhancement of the internal carotid artery at the level of the aneurysm as a reference.

Assessment of Brain Infarcts and WMLs

The presence of cortical, subcortical, and lacunar infarcts on the ipsi- or contralateral side was reported¹⁶ and expressed as

symptomatic or silent brain infarction. WMLs were semiquantitatively assessed at baseline and follow-up using the Fazekas scale.^{17,18} In short, WMLs were separated according to whether hyperintense lesions were contiguous with the lateral ventricular border (periventricular lesion) or distinct and subcortical (including those in the deep white matter). Subcortical extensions from cortical and lacunar infarcts were excluded.

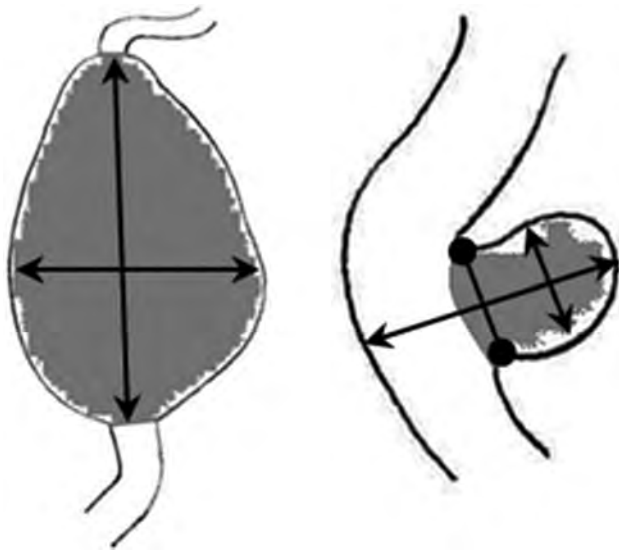


FIG 1. Schematic examples of diameter measurements of ECAAs, perpendicular to the nonaffected vessel. *Left:* fusiform ECAA length \times width. *Right:* saccular ECAA length \times width \times neck (round arrow).

Statistical Analysis

All observations were assessed in terms of reliability and agreement. Inter- and intraobserver reliability of each diameter was calculated by the intraclass correlation coefficient (model: 2-way mixed; type: absolute agreement) with 95% confidence intervals. Bland-Altman analysis was used to assess agreement for each diameter. For nominal and binary variables (aneurysm location, shape, Gd enhancement, and infarcts), κ values were calculated, and for ordinal variables (WMLs), the weighted κ was calculated.¹⁹ The 95% CIs for κ were obtained by use of the *psy* and *boot* packages (<http://cran.r-project.org>) in R Studio, Version 3.4.1, (www.rstudio.com). The proportion of agreement was calculated for both nominal and ordinal variables.²⁰ We studied the proportion of patients with aneurysm wall enhancement. Then, we investigated whether aneurysm wall enhancement was associated with signs of instability during follow-up. The primary outcome was the prevalence of aneurysm wall enhancement. Secondary outcomes were growth of the aneurysm sac during follow-up and the presence of WMLs and (silent) brain infarcts at baseline and follow-up. Patients were compared on the basis of Gd enhancement using the Fisher exact test and Mann-Whitney *U* test, and $P < .05$ was considered statistically significant. These statistical analyses were conducted using SPSS, Version 25.0 (Released 2017; IBM, Armonk, New York).

RESULTS

Fifteen patients with 16 ECAAs were included and underwent baseline MR imaging. Fourteen patients (with 15 aneurysms) underwent follow-up MR imaging after 1 year. Individual patient characteristics are listed in On-line Table 1. The patient who was

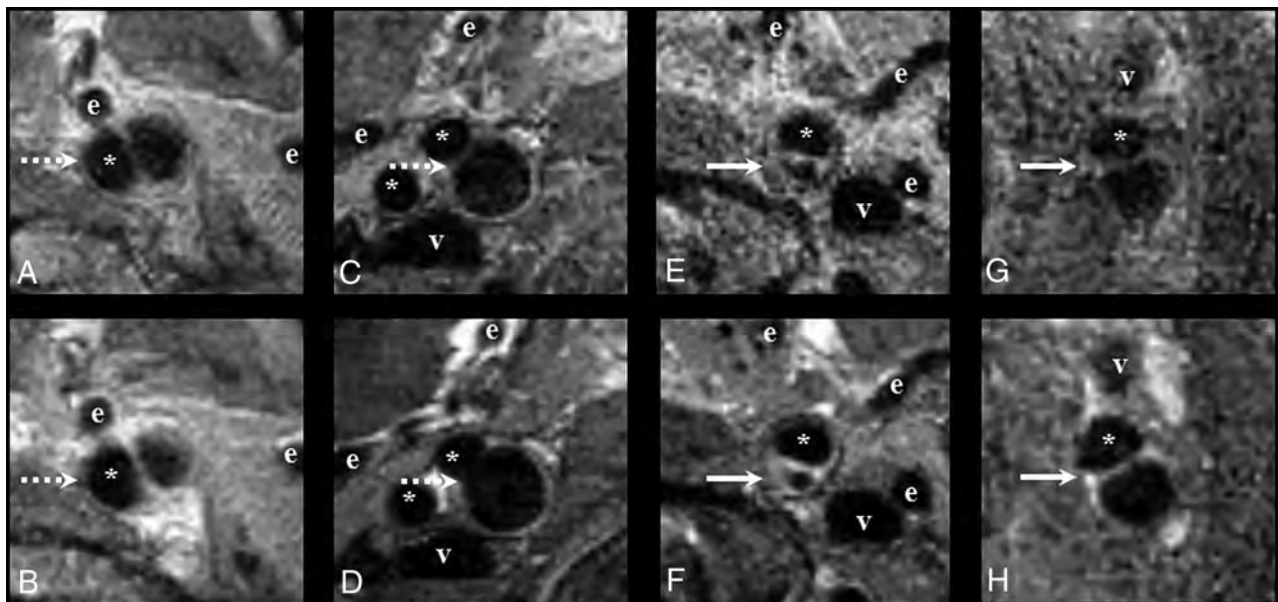


FIG 2. Examples of aneurysm wall enhancement (solid arrow) on 3T MR imaging with aneurysm wall imaging on the transaxial plane. *B, D, F, and H,* The sequence after administration of gadolinium. *A and B,* A 66-year-old woman with a 11.0-mm saccular left internal carotid artery aneurysm without enhancement (dashed arrow). *C and D,* A 54-year-old man with a 9.0-mm saccular right internal carotid artery aneurysm without enhancement (dashed arrow). *E and F,* A 51-year-old woman with a 7.5-mm saccular left internal carotid artery aneurysm with aneurysm enhancement (solid arrow). *G and H,* A 59-year-old woman with a 10.0-mm fusiform left internal carotid artery aneurysm with enhancement (solid arrow). The asterisk indicates the parent ICA; e, branches of the external carotid artery; v, internal jugular vein.

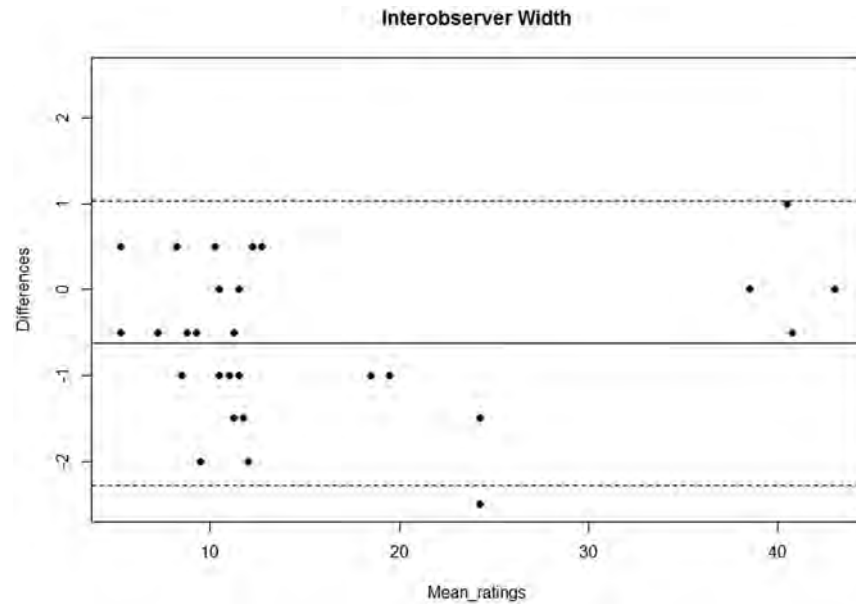


FIG 3. Bland-Altman plot of interobserver agreement. The *solid line* in the middle represents the mean difference of the diameter measurements between the 2 observers; the *dashed line* represents the upper and lower limits of agreement (mean difference $\pm 1.96 \times$ SD).

Aneurysm size for aneurysms with and without gadolinium enhancement

	No Gadolinium Enhancement (n = 4)	Gadolinium Enhancement (n = 12)	P
Length baseline median (range)	10.75 (6.5–46.0)	14.5 (7.00–66.5)	.316
Width baseline median (range)	10.5 (9.0–41.0)	11.5 (5.5 – 38.5)	.953
Neck baseline ^a median (range)	9.5 (8.0–11.0)	12.0 (3.5–22.0)	.482
Growth (length) median (range)	1.0 (–1.0–4.0)	0.5 (–0.5–4.5)	>.999
Growth (width) median (range)	1.0 (–1.0–4.0)	0.5 (–0.5–4.5)	>.999
Growth (neck) ^a median (range)	0.0 (–1.0–0.5)	2.0 (0.5–3.0)	.012 ^b
Growth (any direction ≥ 2 mm) (No.) (%)	2 (50)	2 (16.7)	.245

^a Only patients with saccular aneurysms.

^b $P < .05$.

lost to follow-up was unable to participate in study activities due to clinical deterioration as a result of a prior cerebral infarction. Eight of 15 patients (53%) were men. The median age was 55 years (range, 40–69 years). Detailed medical history is summarized in On-line Table 2.

All MR imaging observations showed excellent inter- and intraobserver reproducibility, with both intraclass correlation coefficients and weighted $\kappa > 0.9$ and acceptable differences for agreement (Fig 3, On-line Tables 3 and 4, and On-line Figs 1 and 2). In total, 666 observations per observer were made, about which 15% of disagreements were discussed.

Aneurysm Analysis

All 16 ECAAs were located in the extracranial internal carotid artery (8 on the right, 6 on the left, and 1 patient with bilateral ECAAs). Twelve aneurysms were saccular (75%); and 4, fusiform. The median length was 13.5 mm (range, 6.5–66.0 mm), and median width was 11.5 mm (range, 5.5–41.0 mm). The median neck width was 11 mm (range, 3.5–22.0 mm) in saccular ECAAs. Twelve of 16 (75%) aneurysms had Gd wall enhancement at baseline. Of the 15 aneurysms with follow-up imaging available, 4 (27%) had increased in size by ≥ 2.0 mm in at least 1 direction at

the follow-up MR imaging. Of these 4 aneurysms, 1 showed growth in length, width, and neck, 1 showed only increased width, and 2 showed only an increase in length in comparison with baseline. For further analysis, only patients with available follow-up MRA are included.

Aneurysm Wall Gd Enhancement

All 28 aneurysm wall scans showed good image quality, and no artifacts interfered with our assessment of wall enhancement. Of the 15 aneurysms with follow-up imaging, 11 exhibited ECAA wall enhancement at baseline. Length, width, and neck diameter of aneurysms with wall enhancement compared with those without were similar (Table). Of the 4 aneurysms that increased in size at follow-up, 2 (50%) showed aneurysm wall Gd enhancement on baseline MR imaging (Table). When absolute differences between baseline and follow-up MR imaging were compared, the median increase in neck size (only saccular aneurysms) was larger in the 8 Gd-positive (+) (median, 2.0 mm; range, 0.5–3.0 mm) compared with the 3 Gd-negative (–) ECAAs (median, 0.0 mm; range, –1.0–0.5 mm; $P = .012$). Other differences across time (length and width) were comparable in patients with and without aneurysm wall enhancement (Table). A total of 3 patients

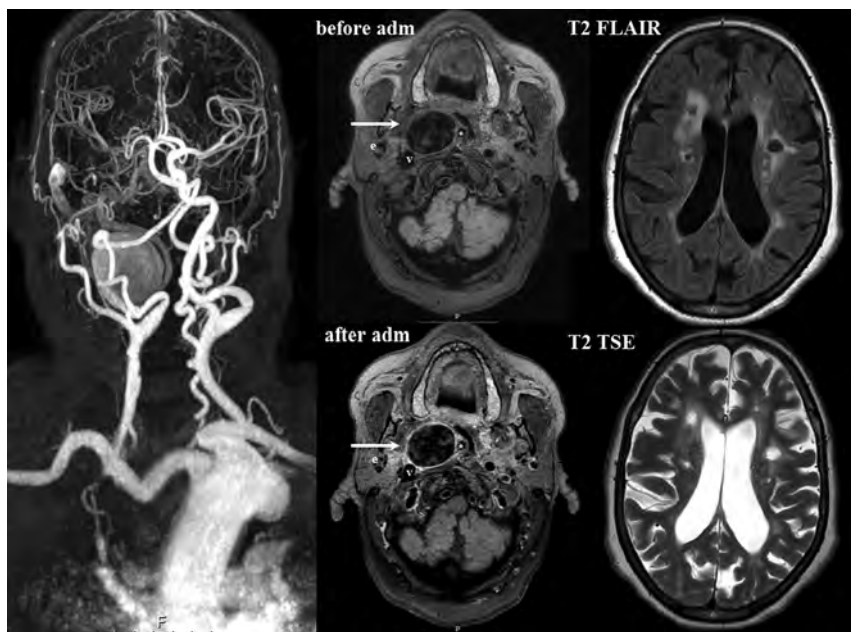


FIG 4. Overview baseline 3T Gd-enhanced MR imaging of 66-year-old woman with a saccular ECAA of the right internal carotid artery. At baseline, enhancement of the aneurysm wall was observed after contrast administration, indicated by the white arrows. T2 FLAIR and T2 TSE show both periventricular and deep white matter lesions and Fazekas 3 and multiple bilateral lacunar infarctions. adm indicates contrast administration.

showed wall enhancement of the contralateral carotid artery at the level of the aneurysm, all of whom also had ipsilateral enhancement of the ECAA wall. On follow-up, 9/15 aneurysms showed steady ipsilateral wall enhancement and 3/15 aneurysms consistently showed no enhancement. One Gd+ aneurysm at baseline no longer showed enhancement at follow-up, and 1 patient with Gd- at baseline showed novel enhancement at follow-up, whereas this was not present at baseline. For the remaining patient, follow-up enhancement could not be evaluated because the scan level was set intracranially.

Assessment of Brain Infarcts and WML

At baseline, 2 patients showed lacunar (silent) brain infarcts, 1 ipsilateral and 1 with multiple bilateral lacunar brain infarcts (Fig 4). Two other patients had cortical infarcts, 1 of them ipsilateral to the aneurysm and another with a cortical infarct contralateral to the aneurysm. In both of these patients, cortical infarcts were clinically symptomatic, though >1 year before the start of the study. No subcortical infarcts were observed, and none of the infarcts were located in posterior circulation. Follow-up MR imaging revealed that the patient who showed multiple bilateral lacunar infarcts at baseline had a bilateral increase in the number of lacunar silent brain infarcts on follow-up imaging. Another patient had 1 new contralateral lacunar silent brain infarct. All patients with infarcts at baseline or follow-up showed Gd enhancement at baseline.

The median Fazekas score at baseline was 1 (range, 0–3) for ipsilateral periventricular WMLs and 1 for contralateral periventricular WMLs (range, 0–3; $P = .705$). The median Fazekas score for deep WMLs was 1 (range, 0–3) at the site ipsilateral to the

aneurysm and 0 (range, 0–3) on the contralateral site ($P = .816$). Three of 14 patients with follow-up imaging showed an increase in the Fazekas score after 1 year, with 2 on the ipsilateral side (1 patient with an increase of deep WMLs and 1 patient with an increase of periventricular WMLs) and 1 patient with a bilateral increase of deep WMLs. Two of 3 patients who showed an increase of WMLs had Gd enhancement at baseline imaging.

DISCUSSION

In this explorative imaging study, we demonstrated that ECAA wall imaging was feasible, with good inter- and intraobserver reliability and agreement. Most aneurysms had Gd enhancement of the ECAA wall at baseline. Aneurysm growth occurred in 27% of all aneurysms.

No earlier studies investigated wall enhancement of extracranial carotid aneurysms. Only patients with Gd enhancement of atherosclerotic

plaques in the carotid arteries are described.^{21–23} It is believed that Gd enhancement reflects both the density of the vasa vasorum and endothelial permeability and can indicate local inflammation of the vessel wall.^{21–23} These previously performed studies used 1.5T^{21,23} or 3T²² MR imaging scanners, with double molality concentration of Gd and flow rate. The current scanning protocol was based on earlier studies investigating intracranial vessel wall imaging and reporting good image quality and few artifacts.¹⁴ Fine-tuning of the optimal imaging protocol for the carotid wall specifically, including the sequences used to suppress artifacts due to blood flow, contrast agent concentration, flow rate, and time between administration and vessel wall imaging, is warranted so that uniform reporting standards can be established and study results can be compared.

A follow-up study that included 65 intracranial aneurysms with a median follow-up of 27 months (range, 20–31 months) showed that 4 of 19 aneurysms with wall enhancement at baseline had instability during follow-up, compared with 0 of 46 aneurysms without wall enhancement.²⁴ Although our study in patients with ECAs was not powered to detect differences in aneurysm growth between patients with and without aneurysm wall enhancement, our follow-up results are of interest because we also found aneurysm growth in 2 of 4 patients without wall enhancement. Because healthy intracranial arteries lack an adventitial vasa vasorum,^{25,26} Gd enhancement of intracranial arteries may indicate stronger local pathologic neovascularization and thus inflammation than in extracranial carotid arteries.²⁶ Moreover, the discrimination between moderate or major enhancement in extracranial arteries, possibly indicating pathologic neovascularization of the aneurysm wall instead of

normal physiology of the vasa vasorum, is quite challenging and subject to the observer's interpretation.

Although acceptable reproducibility of Gd+ was observed in the present study, a Gd+ quantitative measure would accurately increase Gd grading. Density and thus enhancement of the vasa vasorum in normal extracranial arteries is poorly described in the current literature, and between-patient and within-patient variability and its influence on wall enhancement are, at this point, unknown. In contrast to other vascular wall enhancement studies, the present study partly anticipated this issue by also examining the contralateral artery as a reference. Of note, only a minority (3/11) of patients with ipsilateral enhancement also had contralateral enhancement (1 of whom had bilateral ECAAs), so although not predictive of aneurysm growth, Gd enhancement does seem to reflect disease activity of the vessel wall.

All 3 patients with ipsilateral brain infarcts showed ECAA wall enhancement, but most patients without infarcts also had aneurysm wall enhancement. Brain infarcts and especially (small) cortical infarcts are often caused by thromboemboli from a proximal source such as the carotid arteries.¹² Silent brain infarcts have been associated with a 3-fold increase in the risk of stroke.¹² In asymptomatic patients with atherosclerotic stenosis of the carotid artery, those with silent brain infarcts benefit more from revascularization procedures in terms of averting stroke risk compared with those without.¹¹ Patients with ECAAs at risk of thromboembolic complications may also be identified by assessment of ipsilateral (silent) brain infarcts, in addition to assessment of ECAA wall Gd enhancement or aneurysm growth. Structural imaging of the brain may contribute to clinical decision-making on whether to treat (eg, conservatively or surgically) these patients.

We found that two-thirds of patients had bilateral WMLs. Because there was no clear asymmetry and the presence of WMLs did not seem restricted to patients with ECAA wall enhancement, on the basis of our preliminary results, WMLs do not seem directly related to Gd enhancement of the aneurysm wall. Previous studies have shown that the cause of WMLs is multifactorial, and thrombo-embolism from a proximal source is only one of the potential causes of these radiographic findings.^{8,27} It is striking, however, that these relatively young patients included in our study (median age, 54 years) very often showed a high (bilateral) WML score compared with literature investigating WMLs in an otherwise healthy population.²⁸ WMLs have been used widely as a surrogate marker for small-vessel disease and have been closely associated with risk factors for atherosclerotic disease such as hypertension.²⁹ These findings suggest that not only a causal relationship exists between the presence of ECAAs and WMLs but also a shared etiology for the presence of both diseases. WMLs have been associated with an increased risk of future stroke³⁰ and cognitive decline.²⁹ Perhaps medical therapy in patients with ECAAs should be optimized to treat not only possible consequences of thromboemboli but also risk factors underlying generalized vascular disease.

Strengths and Limitations

The primary aim of our study was feasibility. Because of the small sample size, no conclusions can be drawn regarding the

predictive value of wall enhancement. Although good inter- and intraobserver reliabilities were found in our study, assessing the presence of WMLs by means of the Fazekas scale can be highly dependent on expertise and experience. Also, the Fazekas scale is insensitive to subtle lesions and subtle changes across time. Other quantitative or semiquantitative measures, such as the rating scale for age-related white matter changes or computerized assessment of lesion volume, may be more reliable and sensitive to small changes across time. Future studies should include quantitative methods for determining white matter lesion volume so that subtle changes can be detected in an objective manner. Nevertheless, our method is easily translated to clinical practice and can be straightforwardly applied on frequently used MR images (FLAIR and T2). Little is known yet regarding the reliability of using MR imaging for ECAA imaging compared with CT. Although high correlations between the 2 were found in studies on other types of aneurysms,³¹ comparison of these 2 imaging techniques should be a topic for future research.

The study sample is a reflection of clinical practice in ECAA disease; as a consequence, various shapes and sizes of aneurysms with different blood flow characteristics were included. Slow blood flow within the aneurysm sac could cause pseudoenhancement, which potentially affects the validity and clinical applicability of our results. Future computational hemodynamic and histologic studies of aneurysm wall tissue should further elucidate the relation of Gd enhancement and aneurysm wall instability. Last, one might argue that conventional diameter measurements fail to indicate ECAA growth. Because appropriate imaging tools to measure geometric differences are currently lacking, we might have missed cases that expanded in other directions than obliquely.

CONCLUSIONS

In this small exploratory study, we demonstrated that extracranial carotid artery aneurysm wall imaging was feasible and Gd wall enhancement was identified in most aneurysms. Aneurysm growth was relatively common in a follow-up period of 1 year. Larger prospective studies are warranted to investigate the relation between ECAA wall enhancement and aneurysm growth, (silent) brain infarcts, and white matter lesions.

Disclosures: Tim Leiner—UNRELATED: Grants/Grants Pending: Philips Healthcare, Pie Medical Imaging*; Payment for Lectures Including Service on Speakers Bureaus: Philips Healthcare, Bayer HealthCare Pharmaceuticals*; Patents (Planned, Pending or Issued): inventor, US Patent 10,176,575.* *Money paid to the institution.

REFERENCES

1. Pourier VE, Welleweerd JC, Kappelle LJ, et al. **Experience of a single center in the conservative approach of 20 consecutive cases of asymptomatic extracranial carotid artery aneurysms.** *Eur J Neurol* 2018;25:1285–89 CrossRef Medline
2. Welleweerd JC, Moll FL, De Borst GJ. **Technical options for the treatment of extracranial carotid aneurysms.** *Expert Rev Cardiovasc Ther* 2012;10:925–31 CrossRef Medline
3. Welleweerd JC, Den Ruijter HM, Nelissen BG, et al. **Management of extracranial carotid artery aneurysm.** *Eur J Vasc Endovasc Surg* 2015;50:141–47 CrossRef Medline

4. Welleweerd JC, Nelissen BG, Koole D, et al. **Histological analysis of extracranial carotid artery aneurysms.** *PLoS One* 2015;10:e0117915–19 CrossRef
5. Backes D, Hendrikse J, van der Schaaf I, et al. **Determinants of gadolinium-enhancement of the aneurysm wall in unruptured intracranial aneurysms.** *Neurosurgery* 2018;83:719–25 CrossRef Medline
6. Oppenheim C, Naggara O, Touzé E, et al. **High-resolution MR imaging of the cervical arterial wall: what the radiologist needs to know.** *Radiographics* 2009;29:1413–31 CrossRef Medline
7. Jayasooriya G, Thapar A, Shalhoub J, et al. **Silent cerebral events in asymptomatic carotid stenosis.** *J Vasc Surg* 2011;54:227–36 CrossRef Medline
8. van den Bouwhuijsen QJ, Vernooij MW, Verhaaren BFJ, et al. **Carotid plaque morphology and ischemic vascular brain disease on MRI.** *AJNR Am J Neuroradiol* 2017;38:1776–82 CrossRef Medline
9. Altaf N, Morgan PS, Moody A, et al. **Hyperintensities are associated with carotid intraplaque hemorrhage.** *Radiology* 2008;248:202–09 CrossRef
10. Gensicke H, Van Der Worp HB, Nederkoorn PJ, et al; ICSS-MRI Substudy Investigators. **Ischemic brain lesions after carotid artery stenting increase future cerebrovascular risk.** *J Am Coll Cardiol* 2015;65:521–29 CrossRef Medline
11. Streifler JY, den Hartog AG, Pan S, et al; ACST-1 trial Collaborators. **Ten-year risk of stroke in patients with previous cerebral infarction and the impact of carotid surgery in the Asymptomatic Carotid Surgery Trial.** *Int J Stroke* 2016;11:1020–27 CrossRef Medline
12. Vermeer SE, Prins ND, den Heijer T, et al. **Silent brain infarcts and the risk of dementia and cognitive decline.** *N Engl J Med* 2003;348:1215–22 CrossRef Medline
13. Welleweerd JC, Bots ML, Kappelle LJ, et al. **Rationale and design of the extracranial Carotid artery Aneurysm Registry (CAR).** *J Cardiovasc Surg (Torino)* 2018;59:692–98 CrossRef Medline
14. Dieleman N, Yang W, Van Der Kolk AG, et al. **Qualitative evaluation of a high-resolution 3D multi-sequence intracranial vessel wall protocol at 3 Tesla MRI.** *PLoS One* 2016;11:e0160781–11 CrossRef
15. Yang H, Zhang X, Qin Q, et al. **Improved cerebrospinal fluid suppression for intracranial vessel wall MRI.** *J Magn Reson Imaging* 2016;44:665–72 CrossRef Medline
16. de Leeuw F, de Groot J, Bots M, et al. **Carotid atherosclerosis and cerebral white matter lesions in a population based magnetic resonance imaging study.** *J Neurol* 2000;247:291–96 CrossRef Medline
17. Fazekas F, Chawluk JB, Alavi A, et al. **MR signal abnormalities at 1.5-T in Alzheimer dementia and normal aging.** *AJR Am J Roentgenol* 1987;149:351–56 CrossRef Medline
18. Kim KW, MacFall JR, Payne ME. **Classification of white matter lesions on magnetic resonance imaging in the elderly.** *Biol Psychiatry* 2008;64:273–80 CrossRef Medline
19. Kottner J, Audige L, Brorson S, et al. **Guidelines for Reporting Reliability and Agreement Studies (GRRAS) were proposed.** *Int J Nurs Stud* 2011;48:661–71 CrossRef Medline
20. de Vet HC, Terwee CB, Knol DL, et al. **When to use agreement versus reliability measures.** *J Clin Epidemiol* 2006;59:1033–39 CrossRef Medline
21. Aoki S, Aoki K, Ohsawa S, et al. **Dynamic MR imaging of the carotid wall.** *J Magn Reson Imaging* 1999;9:420–27 CrossRef Medline
22. Qiao Y, Etesami M, Astor BC, et al. **Carotid plaque neovascularization and hemorrhage detected by MR imaging are associated with recent cerebrovascular ischemic events.** *AJNR Am J Neuroradiol* 2012;33:755–60 CrossRef Medline
23. Kerwin WS, Brien KD, Ferguson MS, et al. **Inflammation in carotid atherosclerotic plaque: a dynamic contrast-enhanced MR imaging study.** *Radiology* 2006;241:459–68 CrossRef Medline
24. Vergouwen MD, Backes D, van der Schaaf IC, et al. **Gadolinium enhancement of the aneurysm wall in unruptured intracranial aneurysms is associated with an increased risk of aneurysm instability: a follow-up study.** *AJNR Am J Neuroradiol* 2019;40:111–16 CrossRef Medline
25. Krings T, Mandell DM, Kiehl TR, et al. **Intracranial aneurysms: from vessel wall pathology to therapeutic approach.** *Nat Rev Neurol* 2011;7:547–59 CrossRef Medline
26. Portanova A, Hakakian N, Mikulis DJ, et al. **Vasa vasorum 2013 insights and implications for imaging.** *Radiology* 2013;267:667–79 CrossRef Medline
27. Potter GM, Doubal FN, Jackson CA, et al. **Lack of association of white matter lesions with ipsilateral carotid artery stenosis.** *Cerebrovasc Dis* 2012;33:378–84 CrossRef Medline
28. Leeuw FE, De Groot JC, De Achten E, et al. **Prevalence of cerebral white matter lesions in elderly people: a population based magnetic resonance imaging study—the Rotterdam Scan Study.** *J Neurol Neurosurg Psychiatry* 2001;70:9–14 Medline
29. Van Dijk EJ, Prins ND, Vrooman HA, et al. **Progression of cerebral small vessel disease in relation to risk factors and cognitive consequences: Rotterdam Scan Study.** *Stroke* 2008;39:2712–19 CrossRef Medline
30. Streifler JY, Eliasziw M, Benavente OR, et al; North American Symptomatic Carotid Endarterectomy Trial Group. **Prognostic importance of leukoaraiosis in patients with symptomatic internal carotid artery stenosis.** *Stroke* 2002;33:1651–55 CrossRef Medline
31. Acar T, Karakas AB, Ozer MA, et al. **Building three-dimensional intracranial aneurysm models from 3D-TOF MRA: a validation study.** *J Digit Imaging* 2019;32:963–70 CrossRef Medline

Functional and Structural Connectivity Patterns Associated with Clinical Outcomes in Deep Brain Stimulation of the Globus Pallidus Internus for Generalized Dystonia

L. Okromelidze, T. Tsuboi, R.S. Eisinger, M.R. Burns, M. Charbel, M. Rana, S.S. Grewal, C.-Q. Lu, L. Almeida, K.D. Foote, M.S. Okun, and E.H. Middlebrooks



ABSTRACT

BACKGROUND AND PURPOSE: Deep brain stimulation is a well-established treatment for generalized dystonia, but outcomes remain variable. Establishment of an imaging marker to guide device targeting and programming could possibly impact the efficacy of deep brain stimulation in dystonia, particularly in the absence of acute clinical markers to indicate benefit. We hypothesize that the stimulation-based functional and structural connectivity using resting-state fMRI and DTI can predict therapeutic outcomes in patients with generalized dystonia and deep brain stimulation.

MATERIALS AND METHODS: We performed a retrospective analysis of 39 patients with inherited or idiopathic-isolated generalized dystonia who underwent bilateral globus pallidus internus deep brain stimulation. After electrode localization, the volumes of tissue activated were modeled and used as seed regions for functional and structural connectivity measures using a normative data base. Resulting connectivity maps were correlated with postoperative improvement in the Unified Dystonia Rating Scale score.

RESULTS: Structural connectivity between the volumes of tissue activated and the primary sensorimotor cortex was correlated with Unified Dystonia Rating Scale improvement, while more anterior prefrontal connectivity was inversely correlated with Unified Dystonia Rating Scale improvement. Functional connectivity between the volumes of tissue activated and primary sensorimotor regions, motor thalamus, and cerebellum was most correlated with Unified Dystonia Rating Scale improvement; however, an inverse correlation with Unified Dystonia Rating Scale improvement was seen in the supplemental motor area and premotor cortex.

CONCLUSIONS: Functional and structural connectivity with multiple nodes of the motor network is associated with motor improvement in patients with generalized dystonia undergoing deep brain stimulation. Results from this study may serve as a basis for future development of clinical markers to guide deep brain stimulation targeting and programming in dystonia.

ABBREVIATIONS: ACPC = anterior/posterior commissure; DBS = deep brain stimulation; GPi = globus pallidus internus; MNI = Montreal Neurological Institute; UDRS = Unified Dystonia Rating Scale; VTA = volume of tissue activated

Dystonia is a debilitating movement disorder with the primary features being intermittent or sustained muscle co-contractions with abnormal postures and/or repetitive movements.¹ Of the different recognized forms of dystonia, generalized dystonia affecting the trunk and a minimum of 2 other body regions can be particularly debilitating.² Oral medications such as anticholinergics, benzodiazepines, or muscle relaxants can be attempted but are often poorly tolerated due to adverse effects such as

sedation and cognitive dysfunction. Deep brain stimulation (DBS) is a well-established treatment for generalized forms of dystonia.^{3,4} Although the mechanism of action is not well-understood, globus pallidus internus (GPi) DBS has been one of the most widely adopted targets for the treatment of generalized and cervical dystonia.⁵ Despite the increasing use of DBS, patient outcomes have been highly variable, with multiple factors potentially playing a role, including phenomenology and body parts affected as well as a delayed response to the settings implemented.^{3,4,6,7}

Received October 22, 2019; accepted after revision January 7, 2020.

From the Departments of Radiology (L.O., C.-Q.L., E.H.M.) and Neurosurgery (S.S.G., E.H.M.), Mayo Clinic, Jacksonville, Florida; Department of Neurology (T.T., R.S.E., M.R.B., L.A., K.D.F., M.S.O.), Norman Fixel Institute for Neurological Diseases, Department of Neurosurgery (K.D.F.), and J. Crayton Pruitt Family Department of Biomedical Engineering (M.C.), University of Florida, Gainesville, Florida; and Institute of Medical Psychology and Behavioural Neurobiology (M.R.), University of Tübingen, Tübingen, Germany.

L. Okromelidze and T. Tsuboi contributed equally to this work.

Paper previously presented in abstract form at: Annual Meeting of the Radiological Society of North America, December 1–6, 2019; Chicago, Illinois.

Please address correspondence to Erik H. Middlebrooks, MD, Departments of Radiology and Neurosurgery, Mayo Clinic, 4500 San Pablo Rd, Jacksonville, FL 32224; e-mail: middlebrooks.erik@mayo.edu; @EMiddlebrooksMD

Indicates article with supplemental on-line appendix.

Indicates article with supplemental on-line photo.

<http://dx.doi.org/10.3174/ajnr.A6429>

A fundamental factor in patient outcomes from DBS is related to appropriate targeting and device programming; however, intraoperative macrostimulation and subsequent programming are problematic in dystonia due to the typical delay in symptom improvement (days-weeks) compared with the near-immediate effect in some other movement disorders (eg, Parkinson disease and essential tremor).⁸ Thus, establishment of accurate markers for targeting and programming is an imperative step to maximize outcomes of patients with dystonia undergoing DBS.

The role of MR imaging–derived connectivity measures from fMRI and DTI has been increasingly explored in DBS for movement disorders, particularly for essential tremor and Parkinson disease.^{9–13} While functional neurosurgical targeting has historically relied heavily on coordinate-based stereotaxy using easily identified landmarks (eg, anterior/posterior commissure [ACPC] line), such fixed anatomic coordinate systems have been shown to not account for patient-specific anatomic and network differences, yielding significant variability with respect to the underlying brain being impacted by neuromodulation.¹⁴ Thus, ACPC coordinates of active DBS contacts have previously failed to correlate with outcomes in dystonia.¹⁵

On the basis of the predictability of outcomes from fMRI and DTI measures shown in previous studies of DBS in other movement disorders, we hypothesized that connectivity data could be used as an independent biomarker of GPi DBS success in inherited or idiopathic-isolated dystonia (formerly, primary dystonia).^{9,10,13} In this study, we evaluated the functional and structural connectivity patterns that correlate with successful outcomes in GPi DBS for inherited or idiopathic-isolated generalized dystonia.

MATERIALS AND METHODS

A retrospective analysis of the INFORM Patient Research Database (Norman Fixel Institute for Neurological Diseases, University of Florida, Gainesville, Florida) was approved by the University of Florida institutional review board. Patients meeting the following criteria were placed with the corresponding Unified Dystonia Rating Scale (UDRS) score: 1) diagnosis of inherited or idiopathic-isolated generalized dystonia according to consensus criteria,¹ diagnosed by a movement disorder neurologist with a preoperative UDRS score; 2) simultaneous or staged DBS of the bilateral GPi; 3) absence of other brain operations or prior DBS; 4) preoperative MR imaging and postoperative CT; and 5) ≥ 6 -month postoperative follow-up after both electrodes were placed. The primary end point was defined as percentage improvement in the UDRS from the preoperative-to-postoperative follow-up UDRS. The patients' charts and programming data were retrospectively reviewed, and we chose the time point when the DBS settings were considered optimum (range, 6–24 months).

Patient Selection and Surgical Procedure

The DBS candidacy was decided after a consensus review at a multidisciplinary conference, including neurology, neurosurgery, psychiatry, neuropsychology, and rehabilitation medicine. Patients were evaluated monthly for the first 6 postoperative

months to optimize stimulation settings, followed by biannual visits. Nonresponders were defined as having achieved $\leq 25\%$ improvement in the UDRS postoperatively, consistent with a previously published classification.^{4,15,16}

Image Processing

Electrode localization and stimulation of volumes of tissue activated (VTAs) were performed in the LEAD-DBS software package (<http://www.lead-dbs.org>).¹⁷ Full details of imaging preprocessing and electrode localization can be found in the On-line Appendix.

Functional Connectivity

VTAs were generated from each patient's most effective programming settings, as described in Horn et al.⁹ All right-hemisphere VTAs underwent a nonlinear mirroring to the left side. Each left hemisphere and mirrored right-hemisphere VTA then served as a seed point for functional connectivity measures. Functional connectivity data were estimated from 1000 healthy subjects in the Brain Genomics Superstruct Project (<https://dataverse.harvard.edu/dataverse/GSP>)¹⁸ using previously described methods.⁹ Details of the fMRI acquisition and preprocessing are presented in the On-line Appendix. After correlation between the VTA seed and all brain voxels, the resultant *r*-maps underwent Fisher *z*-transformation. The individual connectivity maps were then correlated with improvement in the UDRS and controlled for age and stimulation frequency using a general linear model, as implemented in Statistical Parametric Mapping (SPM; Version 12; <https://www.fil.ion.ucl.ac.uk/spm/>). Maps for positive and negative correlation with UDRS were generated and thresholded at a *t*-score corresponding to $P < .05$.

Structural Connectivity

The left-hemisphere and mirrored right-hemisphere VTAs were used as seed volumes for structural connectivity as implemented in LEAD-DBS. The structural connectivity was estimated on the basis of a normative dataset of 32 healthy subjects in the Human Connectome Project imaged at Massachusetts General Hospital (<https://ida.loni.usc.edu/login.jsp>). Resultant structural connectivity maps underwent a voxelwise correlation analysis using SPM, Version 12. A general linear model was used to assess positive and negative correlations with the percentage of UDRS improvement, controlled for age and stimulation frequency. The resulting *t*-maps were thresholded to $P < .05$.

VTA Analysis

Group-level analysis of the normalized VTAs was then performed. Each VTA was associated with the corresponding improvement in the UDRS score, and a 2-sample *t* test was used to assign a *t*-score to each voxel, which rendered a "heat map" of the treatment response. Both positive and negative correlations were assessed to compare with previously published results of spatial correlation with outcomes.¹⁵ Clusters were assessed for peak *t*-score and center of gravity to determine the spatial localization of peak improvement in the UDRS percentage change using the "cluster" function of FSL (Version 6; <https://fsl.fmrib.ox.ac.uk/fsl/fslwiki/>). VTAs for responders and nonresponders

Table 1: Demographic, clinical, and deep brain stimulation information for the patient group

Characteristic	DBS Programming Information				
	Left		Right		
Age at surgery (yr)	42.9 (7–83)	Frequency (Hz)	105.8 (±45.1)	Frequency (Hz)	108.1 (±45.5)
Sex (M/F)	21:18	Pulse width (μs)	216.9 (±99.4)	Pulse width (μs)	219.8 (±110.9)
Age of onset (yr)	31.1 (2–65)	Voltage (V)	2.9 (±0.7)	Voltage (V)	2.8 (±0.6)
Disease duration before DBS (yr)	14.3 (±14.0)	Impedance (Ω; n = 35)	1066.6 (±355.0)	Impedance (Ω; n = 35)	1129.5 (±532.6)
Follow-up period after DBS (mo)	13.4 (±6.6)	No. (%) leads in bipolar mode ^a	17 (43.6%)	No. (%) leads in bipolar mode ^a	19 (48.7%)
Positive for <i>DYT1</i> mutation	9				
Baseline UDRS	33 (±23.3)				
Postoperative UDRS	14.6 (±15)				
UDRS improvement (%)	53.2% (±34.5%)				
Nonresponders (No.) (%) ≤25% improvement	7 (17.9%)				

^aPatients programmed with bilateral bipolar configuration (n = 13).

were averaged separately, and the center of gravity for the resulting VTA clusters was calculated.

Coordinates from the current study and previous studies^{15,19–21} were transformed between ACPC space and Montreal Neurological Institute (MNI) template space using a probabilistic transformation²² based on nonlinear deformation fields of 14 patients with dystonia (age range, 7–65 years), as implemented in LEAD-DBS software, to compare with previously reported spatial coordinates of maximal GPi DBS efficacy in dystonia.

VTAs were also assessed for the volume of overlap with the GPi, as defined in the DBS Intrinsic Template Atlas²³ and correlated with the percentage change in the UDRS. A 2-tailed *t* test was also performed to compare the normalized volume of overlap between the GPi and VTA in responders versus nonresponders.

Statistical Analysis

Demographic and DBS programming data were expressed as mean and SD. The Mann-Whitney test was used to compare differences in demographics and DBS programming data between responders and nonresponders using GraphPad Prism, Version 8.1.1 (GraphPad Software, San Diego, California). A *P* value < .05 was considered statistically significant.

RESULTS

A total of 43 patients meeting the inclusion criteria were identified. Four were excluded due to inadequate imaging quality and resultant suboptimal electrode localization, leaving a total of 39 subjects. Demographic data, clinical outcomes, and DBS programming parameters are summarized in Table 1. Active contact positions relative to the GPi are illustrated in Fig 1A–C. Of 78 total leads, 71.8% (n = 56) had at least 1 of the 2 dorsal contacts (k2/k3) activated. There was no correlation between VTA overlap with the GPi and UDRS improvement ($r^2 = 0.05$; *P* = .4) (Fig 1D).

Seven patients (17.9%) were classified as nonresponders (≤25% UDRS improvement). There was no significant difference in age of onset, age at the operation, duration of follow-up, or disease duration between responders and nonresponders (all, *P* > .13). There was no significant difference in voltage, frequency, pulse width, impedance, or number of bipolar configurations used (all *P* > .1). There was no significant difference in the volume of overlap between the GPi and VTA in responders versus nonresponders (*P* = .32). Additionally, the center of gravity

for the averaged VTA clusters was identical between the responders and nonresponders (MNI = –24/–9/–3).

Assessment of VTA regions correlating with UDRS improvement (Fig 2) showed the highest correlation in the ventrolateral GPi along its border with the globus pallidus externus (cluster center-of-gravity MNI: right = 23.5/–7/–3 and left = –24.5/–8/–3.5). Peak *t*-scores for the positive clusters were 2.86 on the right and 3.14 on the left. Two significant clusters were identified on each side, corresponding to a negative correlation with UDRS improvement. On the left, there was 1 cluster center of gravity at MNI = –25/–9.5/2 with a peak *t*-score of –3.07 and a second at MNI = –22/–4.5/–4.5 with a peak *t*-score of –2.87. On the right, there was 1 cluster center of gravity at MNI = 23/–5.5/2, with a peak *t*-score of –2.46 and a second at MNI = 22.5/–12/–4.5 with a peak *t*-score of –2.58. The cluster most correlated with UDRS improvement corresponded to an estimated spheric VTA with a 3-mm radius centered at MNI = –24/–10.2/–3.7, which showed a similar connectivity pattern to the regions correlated with greater UDRS score improvement (On-line Figure).

Structural connectivity correlating with the UDRS score (Fig 3A) showed multiple areas predictive of UDRS improvement, such as along the dorsal primary motor cortex corresponding to areas responsible for motor function of the trunk, arm, and hand. Additional areas of connectivity correlating with UDRS improvement were present in the lateral frontal, inferior parietal, and lateral temporo-occipital lobes. Structural connectivity correlated with worse UDRS improvement was greatest in the medial prefrontal region.

Functional connectivity (Fig 3B) was strongly correlated with improved UDRS scores in many nodes of the motor network, including the primary sensorimotor regions, motor thalamus (Fig 3C), and cerebellum (Fig 3D). There was also a positive correlation with the superior temporal gyrus and lateral occipital lobe. A negative correlation with UDRS improvement was present in multiple areas, including the supplemental motor area, lateral occipital, inferior temporal, and superior, middle, and inferior frontal gyri.

DISCUSSION

In this study, we have demonstrated the functional and structural connectivity patterns associated with clinical improvement in generalized dystonia after DBS. Although the pathophysiology of

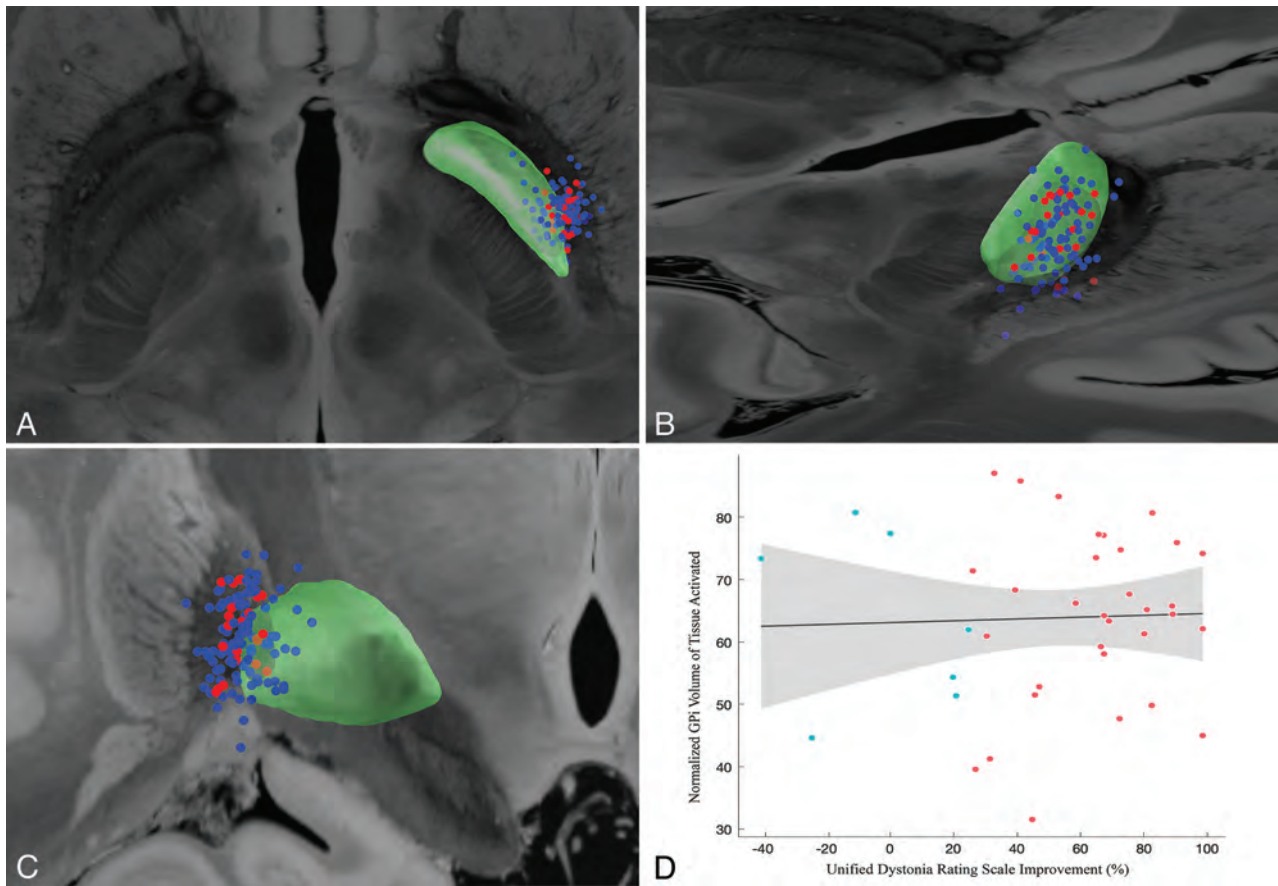


FIG 1. Axial (A), posterior oblique (B), and coronal (C) views of the position of the active contacts for all subjects relative to the globus pallidus internus (green). Contacts for nonresponders ($\leq 25\%$ improvement) are shown as red and responders as blue. All active contacts are nonlinearly mirrored to the same side. D, Normalized volume of tissue activated overlapping the globus pallidus internus and the Unified Dystonia Rating Scale improvement shows no significant correlation ($r^2 = 0.05$; $P = .4$).

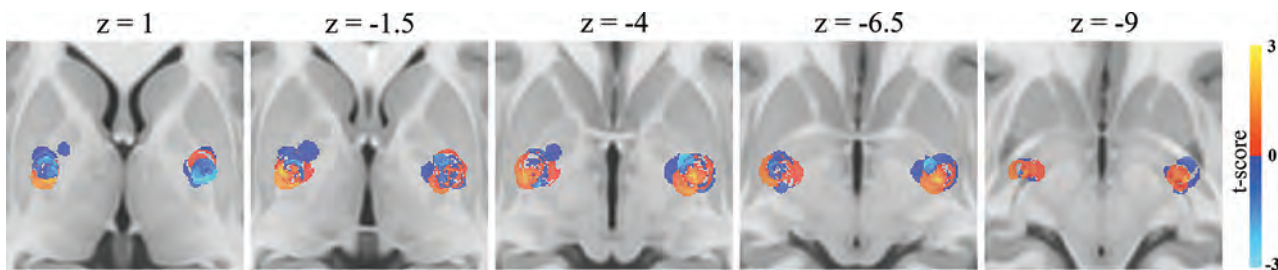


FIG 2. Heat maps showing spatial correlation of volumes of tissue activated positively (red) and negatively (blue) correlated with improvement in the Unified Dystonia Rating Scale score.

inherited or idiopathic-isolated dystonia is poorly understood, existing studies have revealed disturbances within multiple nodes of the motor network.²⁴⁻²⁶ The results of our study are concordant with earlier findings showing a positive correlation between motor improvement and connectivity to the primary sensorimotor cortex, motor thalamus, and cerebellum.^{24,27}

DBS has been shown to be an effective treatment for dystonia; however, nonresponder rates of up to 25% have been reported.²⁸ This variability may be due to multiple factors, such as the age at disease onset, dystonia severity, genetic status, skeletal deformities, and lead location.^{15,28-30} Genetic factors may also play a role. For example, patients having the *TOR1A* (*DYT1*)

mutation—often leading to appendicular phenomenology at presentation—have been described as benefitting more from DBS treatment in comparison with patients with *THAP1* (*DYT6*), which often presents with cranio-cervico-laryngeal symptoms.²⁸ Furthermore, no consensus has been reached regarding screening procedures, training requirements for treatment providers, and patient management guidelines for complications.³¹ In contrast to other common movement disorders treated with DBS, 1 problematic feature of dystonia DBS treatment is the delay in therapeutic response, which is typically observed after days–months following the adjustment of stimulation.³² The lack of near-instantaneous feedback of the treatment response to a particular

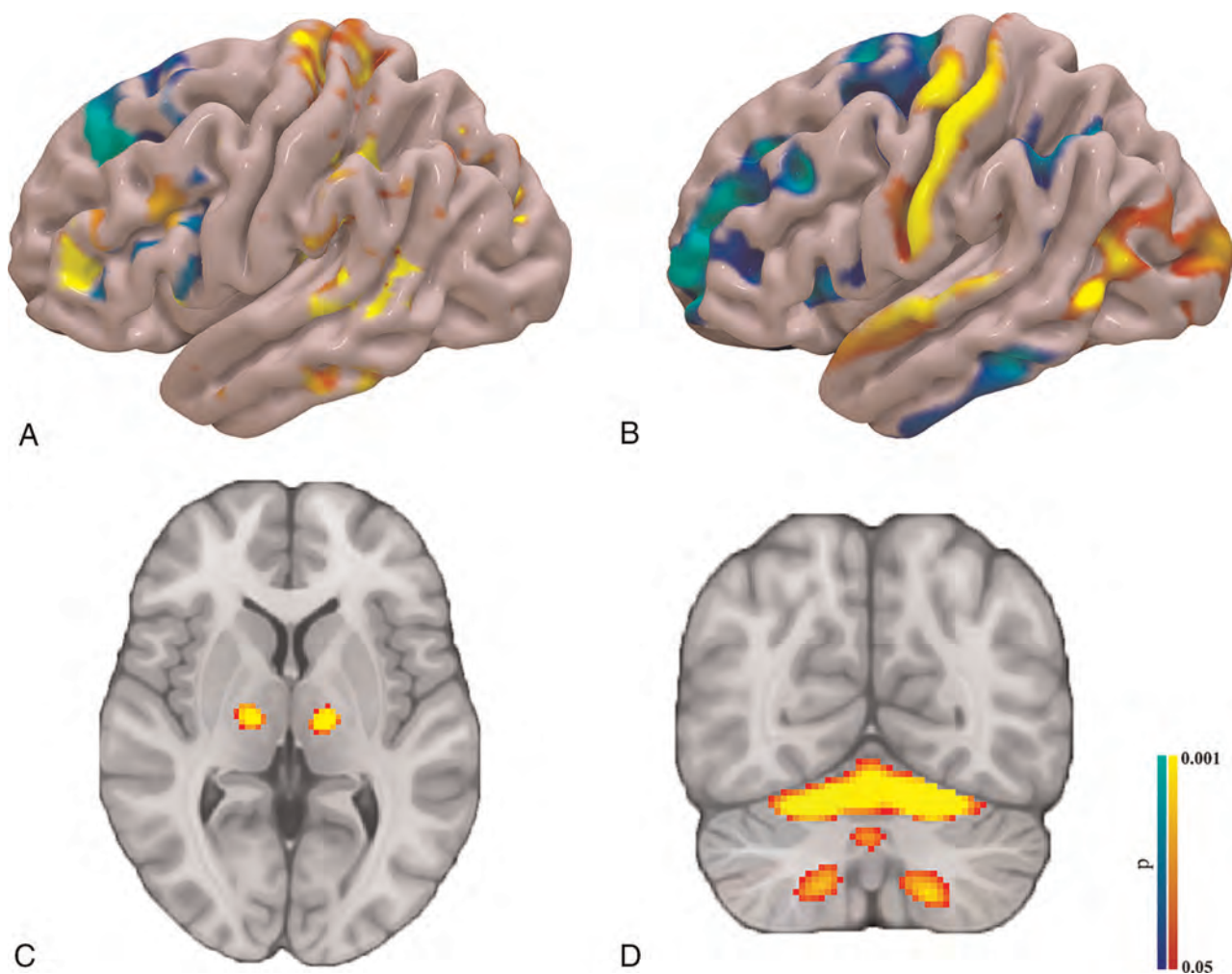


FIG 3. (A) Group-level structural connectivity (DTI) results showing cortical connections positively (red) and negatively (blue) correlated with improvement in the UDRS score. Resting-state functional connectivity results show cortical (B), subcortical (C), and cerebellar (D) connectivity profiles correlated with improvement in the UDRS score.

stimulation setting limits accurate device programming.³² The summation of these findings highlights the complexity of achieving maximal therapeutic benefit for dystonia with DBS and the necessity for new biomarkers.

DBS targeting accuracy has historically been assessed primarily as a function of the electrode contact position relative to the target nucleus; however, Reich et al¹⁵ have shown the poor predictability of such rudimentary measures on outcomes for movement disorders. In our study, we observed no distinct correlation between the relationship of the electrode position relative to the GPi. While assessment of VTA may be a more predictive feature of DBS outcome, overall VTA overlap with the GPi was not predictive of UDRS improvement. Heat maps of VTA overlap and UDRS improvement, however, did reveal a “sweet spot” of stimulation lying along the ventrolateral GPi along its border with the globus pallidus externus. Our findings were concordant with those reported by other groups, as summarized in Table 2.^{15,19-21} Minor variations in ideal coordinates for the anti-dystonic effect are potentially related to differences in the phenomenology of the sample, the surgical targeting technique, and the actual stimulation settings.

Recent DTI studies of the human pallidum have suggested a more complex structural connectivity pattern than considered initially.^{13,27,33-35} In particular, a bipartite pattern of connectivity within the posterior “sensorimotor” pallidum from dorsal to ventral has been shown and may be a predictor of DBS outcome in various movement disorders.¹³ Rozanski et al²⁷ had shown, in a small cohort with focal dystonia, that greater structural connectivity to more posterior cortical regions, including the primary motor and sensory cortices, correlated with a greater anti-dystonic effect, while more anterior motor and premotor regions were associated with less clinical improvement. Our results show similar findings within a larger generalized dystonia population undergoing DBS. Specifically, greater connectivity with the ipsilateral medial peri-Rolandic region correlated with greater motor improvement, while more anterior prefrontal connectivity was inversely correlated with motor improvement.

In a recent study of network connectivity associated with acquired cervical dystonia from brain lesions, Corp et al²⁴ found that lesions with connectivity to lobule IX of the cerebellum and the somatosensory cortex had the greatest sensitivity and specificity for development of cervical dystonia. When examining the

Table 2: Comparison of stereotactic coordinates from prior studies reporting maximum anti-dystonic effect

	MNI Coordinate (mm)			ACPC Coordinate (mm)		
	x	y	z	x	y	z
Current Study	-24	-7.5	-3.25	-21.9	3.6	-0.2
Cheung et al ¹⁹	-22.1	-8	-2.5	-20.2	3	0.7
Reich et al ¹⁵	-19.4	-10.1	-5.9	-19.4	3.2	-1.9
Starr et al ^{20a}	-21.6	-5.5	-4.3	-19.8	5.6	-0.6
Pauls et al ²¹	-22.9	-7.2	-5.9	-20.9	4.1	-2.1

^a Patients with >70% Burke-Fahn-Marsden Dystonia Rating Scale improvement.

connectivity pattern within these 2 brain regions from a cohort of good and poor DBS responders with dystonia, good responders exhibited a greater positive correlation with the cerebellum and greater negative correlation with the somatosensory cortex.²⁴ In our generalized dystonia cohort, we found a similar pattern of DBS connectivity correlating with clinical improvement, including the cerebellum and somatosensory cortex; however, we also found positive and negative correlations in multiple areas outside those interrogated by Corp et al.²⁴

Our results revealed connectivity correlations with multiple areas outside the primary somatosensory and cerebellar regions, including the supplementary motor area, prefrontal cortex, inferior parietal lobule, lateral temporal, and lateral occipital regions. Most interesting, many of these areas were noted to exhibit cortical thickness differences between patients with poor response versus good response to GPi DBS for segmental and generalized dystonia in a recent study by Gonzalez-Escamilla et al.³⁶ Using graph theory, their study posited that changes in centrality and the clustering coefficient in these prefrontal, parietal, temporal, and lateral occipital regions suggest that they may be a cause of network failure and decreased DBS effectiveness.³⁶ Our findings of negative functional connectivity correlation with UDRS improvement in many of these regions support the idea that they may play a role in limiting the neuromodulatory effect of GPi DBS for dystonia.

Several limitations of our study are noteworthy. The use of normative connectomes is a common practice in DBS research due to the inherent difficulty of obtaining such information in a large cohort of patients with movement disorders. Nevertheless, it is currently unknown whether such normative data are directly applicable to individual patients. Additionally, the variation in stimulation parameters, such as frequency and pulse width, can further complicate the understanding of the mechanism of action for DBS. While we have attempted to account for these variations in our study design, it is uncertain whether these findings are directly applicable to patients undergoing different stimulation parameters. Finally, interrater agreement of UDRS assessments was fair to good in some body regions, as is the case with the Burke-Fahn-Marsden Dystonia Rating Scale.³⁷ Additionally, the UDRS and Burke-Fahn-Marsden Dystonia Rating Scale allow clinicians to assess overall dystonia severity but may be less sensitive for cervical dystonia assessments compared with the Toronto Western Spasmodic Torticollis Rating Scale.³⁸ Better clinometric scales are warranted in future studies.

CONCLUSIONS

DBS is a promising therapy for patients with generalized dystonia; however, its applicability is currently limited by delays in

achieving a reproducible and optimal therapeutic outcome and the lack of an acute bedside marker of the success of DBS programming. The major challenge in dystonia DBS is the determination of an ideal stimulation parameter setting due to the delay in appearance of improvement in motor symptoms compared with DBS in other common movement disorders. The development of an accurate marker may help maximize treatment outcomes. We have shown a pattern of structural and functional connectivity associated with clinical improvement in generalized dystonia that may serve as a basis for an imaging marker for DBS programming. Additional studies will be required to determine the clinical applicability of our model.

ACKNOWLEDGMENTS

The authors acknowledge the assistance of Lucy Bahn, PhD, in preparation of this article.

Disclosures: Robert S. Eisinger—UNRELATED: Grants/Grants Pending: National Institute of Neurological Disorders and Stroke F30 Award. Leonardo Almeida—UNRELATED: Consultancy: Medtronic, Boston Scientific, Comments: I have worked for and received honoraria from Medtronic and Boston Scientific as a consultant for the Scientific and Product Advisory Board. Kelly Foote—UNRELATED: Consultancy: Medtronic, Boston Scientific, Comments: occasional paid consultant for deep brain stimulation-related issues; Grants/Grants Pending: Medtronic, Boston Scientific, Functional Neuromodulation, Comments: Medtronic, research support (investigational devices and engineering support) provided for multiple investigator-initiated closed-loop deep brain stimulation research projects; Medtronic, grant for partial support of a functional neurosurgery fellowship at the University of Florida; Boston Scientific and Functional Neuromodulation, grant support to our institution for participation in industry-sponsored deep brain stimulation research (Parkinson and Alzheimer diseases)*; Payment for Development of Educational Presentations: Medtronic, Comments: support paid to the University of Florida in exchange for education provided to visiting deep brain stimulation practitioners.* Michael S. Okun—RELATED: Grant: National Institutes of Health and Parkinson's Foundation, Comments: I have grants from the National Institutes of Health and Parkinson's Foundation but not directly attached to this work*; UNRELATED: Consultancy: Parkinson's Foundation, Comments: Medical Director. *Money paid to the institution.

REFERENCES

- Albanese A, Bhatia K, Bressman SB, et al. **Phenomenology and classification of dystonia: a consensus update.** *Mov Disord* 2013;28:863–73 CrossRef Medline
- Jahanshahi M, Czernecki V, Zurovski AM. **Neuropsychological, neuropsychiatric, and quality of life issues in DBS for dystonia.** *Mov Disord* 2011;26(Suppl 1):S63–S78 CrossRef Medline
- Vidailhet M, Vercueil L, Houeto JL, et al; French SPIDY Study Group. **Bilateral, pallidal, deep-brain stimulation in primary generalised dystonia: a prospective 3 year follow-up study.** *Lancet Neurol* 2007;6:223–29 CrossRef Medline
- Volkman J, Wolters A, Kupsch A, et al. **Pallidal deep brain stimulation in patients with primary generalised or segmental dystonia: 5-year follow-up of a randomised trial.** *Lancet Neurol* 2012;11:1029–38 CrossRef Medline

5. Moro E, LeReun C, Krauss JK, et al. **Efficacy of pallidal stimulation in isolated dystonia: a systematic review and meta-analysis.** *Eur J Neurol* 2017;24:552–60 CrossRef Medline
6. Vidailhet M, Vercueil L, Houeto JL, et al; French Stimulation du Pallidum Interne dans la Dystonie (SPIDY) Study Group. **Bilateral deep-brain stimulation of the globus pallidus in primary generalised dystonia.** *N Engl J Med* 2005;352:459–67 CrossRef Medline
7. Volkman J, Mueller J, Deuschl G, et al; DBS Study Group for Dystonia. **Pallidal neurostimulation in patients with medication-refractory cervical dystonia: a randomised, sham-controlled trial.** *Lancet Neurol* 2014;13:875–84 CrossRef Medline
8. Hu W, Stead M. **Deep brain stimulation for dystonia.** *Transl Neurodegener* 2014;3:2 CrossRef Medline
9. Horn A, Reich M, Vorwerk J, et al. **Connectivity predicts deep brain stimulation outcome in Parkinson disease.** *Ann Neurol* 2017;82:67–78 CrossRef Medline
10. Akram H, Dayal V, Mahlknecht P, et al. **Connectivity derived thalamic segmentation in deep brain stimulation for tremor.** *Neuroimage Clin* 2018;18:130–42 CrossRef Medline
11. Middlebrooks EH, Grewal SS, Stead M, et al. **Differences in functional connectivity profiles as a predictor of response to anterior thalamic nucleus deep brain stimulation for epilepsy: a hypothesis for the mechanism of action and a potential biomarker for outcomes.** *Neurosurg Focus* 2018;45:E7 CrossRef Medline
12. Middlebrooks EH, Holanda VM, Tuna IS, et al. **A method for pre-operative single-subject thalamic segmentation based on probabilistic tractography for essential tremor deep brain stimulation.** *Neuroradiology* 2018;60:303–09 CrossRef Medline
13. Middlebrooks EH, Tuna IS, Grewal SS, et al. **Segmentation of the globus pallidus internus using probabilistic diffusion tractography for deep brain stimulation targeting in Parkinson disease.** *AJNR Am J Neuroradiol* 2018;39:1127–34 CrossRef Medline
14. Middlebrooks EH, Tuna IS, Almeida L, et al. **Structural connectivity-based segmentation of the thalamus and prediction of tremor improvement following thalamic deep brain stimulation of the ventral intermediate nucleus.** *Neuroimage Clin* 2018;20:1266–73 CrossRef Medline
15. Reich MM, Horn A, Lange F, et al. **Probabilistic mapping of the antidystonic effect of pallidal neurostimulation: a multicentre imaging study.** *Brain* 2019;142:1386–98 CrossRef Medline
16. Tsuboi T, Jabarkheel Z, Foote KD, et al. **Importance of the initial response to GPi deep brain stimulation in dystonia: a nine year quality of life study.** *Parkinsonism Relat Disord* 2019;64:249–55 CrossRef Medline
17. Horn A, Li N, Dembek TA, et al. **Lead-DBS v2: towards a comprehensive pipeline for deep brain stimulation imaging.** *Neuroimage* 2019;184:293–316 CrossRef Medline
18. Buckner RL, Roffman JL, Smoller JW. **Brain Genomics Superstruct Project (GSP) Dataverse.** 2014. Harvard Dataverse, V10 CrossRef
19. Cheung T, Noecker AM, Alterman RL, et al. **Defining a therapeutic target for pallidal deep brain stimulation for dystonia.** *Ann Neurol* 2014;76:22–30 CrossRef Medline
20. Starr PA, Turner RS, Rau G, et al. **Microelectrode-guided implantation of deep brain stimulators into the globus pallidus internus for dystonia: techniques, electrode locations, and outcomes.** *J Neurosurg* 2006;104:488–501 CrossRef Medline
21. Pauls KA, Brockelmann PJ, Hammesfahr S, et al. **Dysarthria in pallidal deep brain stimulation in dystonia depends on the posterior location of active electrode contacts: a pilot study.** *Parkinsonism Relat Disord* 2018;47:71–75 CrossRef Medline
22. Horn A, Kuhn AA, Merkl A, et al. **Probabilistic conversion of neurosurgical DBS electrode coordinates into MNI space.** *Neuroimage* 2017;150:395–404 CrossRef Medline
23. Ewert S, Plettig P, Li N, et al. **Toward defining deep brain stimulation targets in MNI space: a subcortical atlas based on multimodal MRI, histology and structural connectivity.** *Neuroimage* 2018;170:271–82 CrossRef Medline
24. Corp DT, Joutsa J, Darby RR, et al. **Network localization of cervical dystonia based on causal brain lesions.** *Brain* 2019;142:1660–74 CrossRef Medline
25. Balint B, Mencacci NE, Valente EM, et al. **Dystonia.** *Nat Rev Dis Primers* 2018;4:25 CrossRef Medline
26. Jinnah HA, Neychev V, Hess EJ. **The anatomical basis for dystonia: the motor network model.** *Tremor Other Hyperkinet Mov (N Y)* 2017;7:506 CrossRef Medline
27. Rozanski VE, Vollmar C, Cunha JP, et al. **Connectivity patterns of pallidal DBS electrodes in focal dystonia: a diffusion tensor tractography study.** *Neuroimage* 2014;84:435–42 CrossRef Medline
28. Lozano AM, Lipsman N, Bergman H, et al. **Deep brain stimulation: current challenges and future directions.** *Nat Rev Neurol* 2019;15:148–60 CrossRef Medline
29. Isaias IU, Alterman RL, Tagliati M. **Outcome predictors of pallidal stimulation in patients with primary dystonia: the role of disease duration.** *Brain* 2008;131:1895–902 CrossRef Medline
30. Pauls KA, Krauss JK, Kampfer CE, et al. **Causes of failure of pallidal deep brain stimulation in cases with pre-operative diagnosis of isolated dystonia.** *Parkinsonism Relat Disord* 2017;43:38–48 CrossRef Medline
31. Okun MS, Tagliati M, Pourfar M, et al. **Management of referred deep brain stimulation failures: a retrospective analysis from 2 movement disorders centers.** *Arch Neurol* 2005;62:1250–55 CrossRef Medline
32. Reese R, Volkman J. **Deep brain stimulation for the dystonias: evidence, knowledge gaps, and practical considerations.** *Mov Disord Clin Pract* 2017;4:486–94 CrossRef Medline
33. Grewal SS, Holanda VM, Middlebrooks EH. **Corticopallidal connectome of the globus pallidus externus in humans: an exploratory study of structural connectivity using probabilistic diffusion tractography.** *AJNR Am J Neuroradiol* 2018;39:2120–25 CrossRef Medline
34. Cacciola A, Calamuneri A, Milardi D, et al. **A connectomic analysis of the human basal ganglia network.** *Front Neuroanat* 2017;11:85 CrossRef Medline
35. Cacciola A, Milardi D, Quartarone A. **Role of cortico-pallidal connectivity in the pathophysiology of dystonia.** *Brain* 2016;139:e48 CrossRef Medline
36. Gonzalez-Escamilla G, Muthuraman M, Reich MM, et al. **Cortical network fingerprints predict deep brain stimulation outcome in dystonia.** *Mov Disord* 2019;34:1536–45 CrossRef Medline
37. Comella CL, Leurgans S, Wu J, et al; Dystonia Study Group. **Rating scales for dystonia: a multicenter assessment.** *Mov Disord* 2003;18:303–12 CrossRef Medline
38. Albanese A, Sorbo FD, Comella C, et al. **Dystonia rating scales: critique and recommendations.** *Mov Disord* 2013;28:874–83 CrossRef Medline

Early Detection of Cancer: Evaluation of MR Imaging Grading Systems in Patients with Suspected Nasopharyngeal Carcinoma

A.D. King, J.K.S. Woo, Q.-Y. Ai, F.K.F. Mo, T.Y. So, W.K.J. Lam, I.O.L. Tse, A.C. Vlantis, K.W.N. Yip, E.P. Hui, B.B.Y. Ma, R.W.K. Chiu, A.T.C. Chan, Y.M.D. Lo, and K.C.A. Chan



ABSTRACT

BACKGROUND AND PURPOSE: We evaluated modifications to our contrast-enhanced MR imaging grading system for symptomatic patients with suspected nasopharyngeal carcinoma, aimed at improving discrimination of early-stage cancer and benign hyperplasia. We evaluated a second non-contrast-enhanced MR imaging grading system for asymptomatic patients from nasopharyngeal carcinoma plasma screening programs.

MATERIALS AND METHODS: Dedicated nasopharyngeal MR imaging before (plain scan system) and after intravenous contrast administration (current and modified systems) was reviewed in patients from a nasopharyngeal carcinoma–endemic region, comprising 383 patients with suspected disease without nasopharyngeal carcinoma and 383 patients with nasopharyngeal carcinoma. The modified and plain scan systems refined primary tumor criteria, added a nodal assessment, and expanded the system from 4 to 5 grades. The overall combined sensitivity and specificity of the 3 systems were compared using the extended McNemar test (a χ^2 value $\chi^2_{(2)} > 5.99$ indicates significance).

RESULTS: The current, modified, and plain scan MR imaging systems yielded sensitivities of 99.74%, 97.91%, and 97.65%, respectively, and specificities of 63.45%, 89.56% and 86.42%, respectively. The modified system yielded significantly better performance than the current ($\chi^2_{(2)} = 122$) and plain scan ($\chi^2_{(2)} = 6.1$) systems. The percentages of patients with nasopharyngeal carcinoma in grades 1–2, grade 3, and grades 4–5 for the modified and plain scan MR imaging systems were 0.42% and 0.44%; 6.31% and 6.96%; and 90.36% and 87.79%, respectively. No additional cancers were detected after contrast administration in cases of a plain scan graded 1–2.

CONCLUSIONS: We propose a modified MR imaging grading system that improves diagnostic performance for nasopharyngeal carcinoma detection. Contrast was not valuable for low MR imaging grades, and the plain scan shows potential for use in screening programs.

ABBREVIATION: NPC = nasopharyngeal carcinoma

The early diagnosis of nasopharyngeal carcinoma (NPC) is essential to future improvements in patient survival and reduction of the long-term adverse effects of aggressive treatment regimens.¹ Recently, we found that a high percentage of patients with early-stage NPC could be identified by population screening in Hong Kong using persistently elevated plasma Epstein-Barr virus DNA (71% versus 20% compared with historical data).²

However, subsequent investigations must be able to detect these early cancers.

Cancers of the nasopharynx are notorious for being submucosal, located deep in the pharyngeal recess, or masked by adenoidal hyperplasia in the nasopharyngeal roof. Accordingly, endoscopic tumor detection is challenging at this site, not only for asymptomatic patients in the screening setting but also for symptomatic patients in the clinical setting. Several studies investigating patients with suspected NPC from endemic

Received September 23, 2019; accepted after revision December 14.

From the Departments of Imaging and Interventional Radiology (A.D.K., Q.Y.A., T.Y.S., K.W.N.Y.), Otorhinolaryngology, Head and Neck Surgery (J.K.S.W., A.C.V.), Clinical Oncology (F.K.F.M., E.P.H., B.B.Y.M., A.T.C.C.), and Chemical Pathology (W.K.J.L., I.O.L.T., R.W.K.C., Y.M.D.L., K.C.A.C.), and Li Ka Shing Institute of Health Sciences (F.K.F.M., W.K.J.L., I.O.L.T., E.P.H., B.B.Y.M., R.W.K.C., A.T.C.C., Y.M.D.L., K.C.A.C.), The Chinese University of Hong Kong, Prince of Wales Hospital, Hong Kong SAR, China; and State Key Laboratory of Translational Oncology (F.K.F.M., W.K.J.L., I.O.L.T., E.P.H., B.B.Y.M., R.W.K.C., A.T.C.C., Y.M.D.L., K.C.A.C.), The Chinese University of Hong Kong, Hong Kong SAR, China.

This work was supported partially by Kadoorie Charitable Foundation and the Research Grants Council of the Hong Kong Special Administrative Region, China (Project No. SEG_CUHK02, 14107216 and T12-404/11).

Please address correspondence to Ann D. King, MD, Department of Imaging and Interventional Radiology, Chinese University of Hong Kong, Prince of Wales Hospital, 30-32 Ngan Shing St, Shatin, Hong Kong SAR, China; e-mail: king2015@cuhk.edu.hk

Indicates open access to non-subscribers at www.ajnr.org

Indicates article with supplemental on-line table.

Indicates article with supplemental on-line photos.

<http://dx.doi.org/10.3174/ajnr.A6444>

Table 1: CUHK MR imaging grading systems for detection of NPC using a modified system with a contrast-enhanced scan^a and a plain scan system with a noncontrast-enhanced scan^b

MR Imaging Grade ^c	Walls	Adenoid
Grade 1: normal	Contrast-enhanced/plain scan: thin wall, 1–3 mm	Contrast-enhanced/plain scan: absent/vestigial tags/nubbin
Grade 2: probably benign hyperplasia	Contrast-enhanced/plain scan: diffuse thickening (>3 mm), symmetric ^d size, signal intensity, and contour	Contrast-enhanced scan: composed of Thornwaldt cyst/multiple cysts, OR symmetric ^d size, signal intensity, and contour with preserved symmetric contrast-enhancing septa perpendicular to the roof, separated by less enhancing columns (ie, stripped appearance) Plain scan: composed of Thornwaldt cyst/multiple cysts
Grade 3: indeterminate	Contrast-enhanced/plain scan: diffuse thickening (>3 mm); asymmetric size or signal intensity or contour, which is nonexpansile	Contrast-enhanced scan: asymmetric size, signal intensity, OR contour with preserved or partial disruption/internal distortion of contrast-enhancing septa Plain scan: symmetric ^d size, signal intensity, and contour
Grade 4: suspicious for NPC	Contrast-enhanced/plain scan: diffuse thickening (>3 mm); asymmetric size or signal intensity or contour, which is expansile (superficial or deep margins)	Contrast-enhanced scan: absent contrast-enhancing septa in a focal adenoid, OR external distortion of contrast-enhancing septa by an adjacent roof mass Plain scan: asymmetric size, signal intensity, or contour
Grade 5: probably NPC		
5a	Contrast-enhanced/plain scan: focal mass	Contrast-enhanced scan: absent contrast-enhancing septa in an adenoid filling the whole roof on at least 1 section Plain scan: no grade
5b	Contrast-enhanced/plain scan: spread outside the nasopharynx (superficial or deep)	
5c	Contrast-enhanced/plain scan: metastatic retropharyngeal or upper cervical nodes ^e	

Note: —CUHK indicates Chinese University of Hong Kong; NPC, nasopharyngeal carcinoma.

^a Modified MR imaging protocol: T2- and T1-weighted images without and with intravenous contrast enhancement.

^b Plain scan MR imaging protocol: T2- and T1-weighted images without intravenous contrast enhancement.

^c For the modified grading system, the grade for contrast-enhanced images outranks the grade for non-contrast-enhanced images.

^d Symmetry refers to a comparison of the right and left halves of the nasopharynx for size, signal intensity, and contour; cysts do not contribute to wall or adenoid asymmetry or to distortion of adenoidal septa.

^e Diagnosis of a metastatic node is based on size (minimum axial nodal diameter: retropharyngeal, ≥ 6 mm; jugulodigastric, ≥ 11 mm; all other nodes, ≥ 10 mm or groups of ≥ 3 nodes with a minimal axial diameter of ≥ 8 mm) or any node with necrosis or extracapsular spread.

regions,^{3,4} as well as nonendemic regions,⁵ have shown that MR imaging can detect NPCs hidden from endoscopic view. In an MR imaging study of predominantly symptomatic patients referred to the outpatient clinic with suspected NPC, we found that MR imaging detects the 10% of tumors that are hidden from endoscopic view.³ This figure rises to 17% in asymptomatic patients screened for NPC using persistently elevated plasma Epstein-Barr virus DNA.⁴ In both studies, MR imaging detected tumors up to 3 years before they became visible endoscopically.^{4,6} MR imaging, therefore, has a complementary role in early NPC detection.

We have shown that the standardized MR imaging grading system used at our institution has a high sensitivity for NPC detection,^{3,4,7} which includes early-stage tumors hidden on the endoscopic examination that tend to form a focal mass in the roof or pharyngeal recess.^{3,4} However, some early-stage cancers confined within the nasopharynx are diffuse rather than focal. In these diffuse early-stage NPCs, the wall thickening is usually greater on one side of the nasopharynx, so discrimination of NPC from benign hyperplasia of the walls and adenoid relies heavily on finding asymmetry on bilateral nasopharyngeal MR imaging evaluations.^{3,4,8,9} Unfortunately, on scrutiny of the images for small early-stage tumors, benign hyperplasia is often slightly asymmetric. This characteristic is challenging in screened subjects with benign lesions and

could produce false-positive findings leading to unnecessary alarm and resource usage.⁴ Moreover, in a study of a large group of stage T1 NPCs confined to the nasopharynx, we observed that a small number of these early-stage tumors were symmetrically diffuse and overlapped in appearance with benign hyperplasia.⁸ These early-stage tumors could potentially reduce the high sensitivity of MR imaging.

In the first part of the study, we modified the current contrast-enhanced MR imaging grading system, which can be used worldwide as a complementary investigation in symptomatic patients with suspected NPC when endoscopic examination findings are negative or indeterminate. The aim was to improve the specificity of MR imaging and maintain a high sensitivity, by adding focal expansion in asymmetric diffuse thickening, absent or external distortion of contrast-enhancing adenoidal septa, and the presence of metastatic nodes to indicate NPC. In the second part of the study, we evaluated a new plain scan MR imaging grading system involving a short protocol without intravenous contrast for use in screening programs in endemic regions such as east and southeast parts of Asia, where the incidence in middle-aged men is up to 35 per 100,000.¹⁰ Most patients with persistently elevated plasma or serology markers for NPC referred for investigation do not have NPC. In these patients, it would be advantageous to limit the use of gadolinium MR imaging contrast

Table 2: Patients with and without NPC in each MR imaging grade as determined using the current, modified, and plain scan MR imaging grading systems

Grading Systems	No. of Patients without NPC		No. of Patients with NPC	
	Nodes Not Assessed	Nodes Assessed	Nodes Not Assessed	Nodes Assessed
Grade 1				
Current	69	—	0	—
Modified	69	69	0	0
Plain scan	79	78	0	0
Grade 2				
Current	174	—	1	—
Modified	174	170	1	1
Plain scan	147	146	2	1
Grade 3				
Current	132	—	47	—
Modified	109	104	13	7
Plain scan	112	107	15	8
Grade 4				
Current	8	—	335	—
Modified	28	26	91	26
Plain scan	42	38	123	32
Grade 5				
Current	—	—	—	—
Modified	3	14	278	349
Plain scan	3	14	243	342

Note:— indicates not applicable; NPC, nasopharyngeal carcinoma.

agents. Furthermore, a short plain scan has greater potential for use in screening programs in NPC endemic regions to prioritize or even select patients for endoscopic examination. Finally, observers with different levels of experience in head and neck MR imaging tested the modified and plain scan MR imaging systems.

MATERIALS AND METHODS

Patients

This retrospective evaluation of MR imaging grading systems in patients who underwent MR imaging for the staging of known NPC or investigation of suspected NPC was approved by the institutional review board (the Chinese University of Hong Kong), which waived the requirement for written informed consent. Nasopharyngeal MR imaging data obtained from 766 patients before and after intravenous contrast were reviewed. Patients did not have a history of head and neck cancer before they underwent the MR imaging for suspected or biopsy-proved NPC. The first group comprised 383 patients without NPC (304 men and 79 women; mean age, 52 years; age range, 18–83 years) who had undergone an endoscopic examination and MR imaging for suspected NPC (based on clinical symptoms, clinical signs, or elevated blood markers for NPC) between 2005 and 2016, but had not been diagnosed with head and neck cancer (minimum follow-up of 2 years). Details are shown in On-line Fig 1. These included 358 patients recruited for 2 previous prospective NPC-detection studies.^{3,4} The second group comprised a similar sample size of 383 patients referred for suspected NPC (based on clinical symptoms, clinical signs, or elevated blood markers for NPC) who had biopsy-proved undifferentiated NPC (282 men and 101 women; mean age, 53 years; age range, 19–92 years). These patients were randomly selected from consecutive patients with NPC scanned between 2005 and 2016 according to the expected T-stage¹¹

distribution in a screened population: stage T1 (nasopharynx), 246 patients (64.2%); T1 (nasal cavity/oropharynx), 13 (3.4%); T2, 33 (8.6%); T3, 80 (20.9%); and T4, 11 (2.9%). These include 134 patients with T1 cancer reported previously.⁸

MR Imaging Acquisition

Targeted nasopharyngeal MR imaging was performed using a 1.5T or 3T whole-body MR imaging system (Philips Healthcare, Best, the Netherlands). During a scan duration of approximately 15–20 minutes, axial fat-suppressed T2-weighted, coronal T2-weighted, and axial T1-weighted images, and axial and coronal T1-weighted images were obtained after a bolus injection of 0.1 mmol per kilogram of body weight of gadoterate meglumine (Dotarem; Guerbet, Aulnay-sous-Bois, France).

MR Imaging Grading

The current MR imaging grading system³ is shown in the On-line Table. The modified and plain scan MR imaging grading systems are shown in Table 1 (which differ only in grading the adenoid because contrast-enhancing septa cannot be assessed on the plain scan) and are illustrated in On-line Figs 2 and 3, respectively. The diagnosis of a metastatic node was based on recognized imaging criteria shown in Table 1.^{12,13} The MR imaging data were graded by readers blinded to the diagnosis of NPC or no NPC. Initially, non-contrast-enhanced images (T2- and T1-weighted images) were graded according to the proposed plain scan MR imaging grading system. Subsequently, the full scan, including contrast-enhanced images (T2- and T1-weighted images pre- and post-contrast enhancement) was graded according to our current and proposed modified MR imaging grading systems.

Results were from the MR imaging data assessed by a radiologist with >20 years of experience in MR imaging of NPC (observer 1). The grading systems were tested by 2 further observers, a researcher with 5 years of experience in MR imaging of NPC

Table 3: Diagnostic performance of MR imaging after grouping of grades into benign or malignant according to grades in the current, modified, and plain scan grading systems

MR Imaging Grade Grouping to Indicate NPC	FP	FN	TP	TN	Sen %	Spec %	PPV %	NPV %	Accuracy %
Grades in the current system									
Primary tumor 3, 4 ^a	140	1	382	243	99.74	63.45	73.18	99.59	81.59
Primary tumor only 4	8	48	335	375	87.47	97.91	97.67	88.65	92.69
Grades in the modified system									
Primary tumor 3, 4, 5	140	1	382	243	99.74	63.45	73.18	99.59	81.59
Primary tumor 4, 5	31	14	369	352	96.34	91.91	92.25	96.17	94.13
Primary tumor 4, 5 + node 5 ^a	40	8	375	343	97.91	89.56	90.36	97.72	93.73
Grades in the plain scan system									
Primary tumor 4, 5	45	17	366	338	95.56	88.25	89.05	95.21	91.91
Primary tumor 4, 5 + node 5 ^a	52	9	374	331	97.65	86.42	87.79	97.35	92.04

Note:—FP indicates false-positive; FN, false-negative; TP, true-positive; TN, true-negative; Sen, sensitivity; Spec, specificity; PPV, positive predictive value; NPV, negative predictive value.

^aCombination of grades in the respective current, modified, and plain scan systems in Table 2.

(observer 2) and a general radiologist with a 1-year postqualification in radiology (after training on 50 patients not included the study analysis comprising 25 without and 25 with NPC with a distribution of T-stages similar to that in the study) (observer 3).

Statistical Analysis

The performance of MR imaging for NPC detection and classification of lesions as benign and malignant was assessed by calculating the sensitivity, specificity, positive predictive value, negative predictive value, and accuracy based on groupings of grades. The concordance rates between MR imaging grading systems were analyzed according to Hawass.¹⁴ The McNemar test was used to test the sensitivity or specificity individually. A calculated χ^2 value exceeding the critical value of $\chi^2_{(2)} = 3.84$ indicated a significant difference. Moreover, the extended McNemar test was used to test the overall significance of the sensitivity and specificity with a fixed error rate; a calculated χ^2 value exceeding the critical value of $\chi^2_{(2)} = 5.99$ indicated a significant difference. The Youden index was applied if one system exhibited significant differences in sensitivity while the other exhibited significant differences in specificity. The highest Youden index denoted the system with the best performance.

The κ and weighted κ analyses were calculated to determine the interobserver agreement among 3 observers using 2 scales (grades 1–3 versus grades 4–5) and 3 scales (grades 1–2 versus grade 3 versus grades 4–5), respectively. κ values of ≤ 0.20 , 0.21–0.40, 0.41–0.60, 0.61–0.80, and 0.81–1.00 indicated slight, fair, moderate, substantial, and almost perfect agreement, respectively.¹⁵ All statistical analyses were 2-sided, and a P value $< .05$ was a statistically significant difference. The analyses were performed using SPSS software (Version 25.0; IBM, Armonk, New York) and SAS software (Version 9.4; SAS Institute, Cary North Carolina).

RESULTS

The results for each grade using the current, modified, and plain scan MR imaging systems are shown in Table 2. Metastatic nodes were present in 62.6% (154/246) of patients with stage T1 primary tumors confined to the nasopharynx. All 6 cases with stage T1 NPC detected by nodal assessment alone had abnormal nodes in the upper internal jugular chain, whereas 7/9 patients with benign hyperplasia had abnormal nodes in the retropharyngeal group only. The percentage of patients with NPC in grades 1–2,

3, and 4–5 were 0.42% (1/240), 6.31% (7/111), and 90.36% (375/415), respectively, for the modified grading system, and 0.44% (1/225), 6.96% (8/115), 87.79% (374/426), respectively, for the plain scan MR imaging grading system.

The diagnostic performance using the current, modified, and plain scan MR imaging grading systems for grouped grades are presented in Table 3, and the statistical comparisons of the systems are shown in Table 4. The modified grading system yielded statistically significant better overall performance than the current and the plain scan grading systems. The modified grading system yielded statistically significant better overall performance using the indeterminate grade 3 to indicate benign versus malignant and without nodal assessment versus with nodal assessment.

Observer Results

The sensitivity, specificity, and accuracy using grades 4 and 5 to indicate malignancy (Table 1) for the plain scan grading system were 96.61%, 91.91%, and 94.26%, respectively, for observer 2, and 95.04%, 96.87%, and 95.95%, respectively, for observer 3; and for the modified grading system, they were 97.65%, 92.69%, and 95.17%, respectively, for observer 2 and 97.13%, 97.13%, and 97.13%, respectively, for observer 3. The respective interclass correlation coefficients (κ and weighted κ) for the modified systems, which were determined using 2 (grades 1–3 versus grades 4–5) and 3 scales (grades 1–2 versus grade 3 versus grades 4–5), were 0.87 and 0.81 between observers 1 and 2 and 0.88 and 0.76 between observers 1 and 3. The respective interclass correlation coefficients for the plain scan systems using 2 and 3 scales were 0.87 and 0.83 between observers 1 and 2 and 0.84 and 0.81 between observers 1 and 3.

DISCUSSION

We modified our MR imaging grading system for NPC detection to meet the challenge of using MR imaging to investigate patients with suspected NPC from both the clinical setting (symptomatic) and the screening setting (asymptomatic). We analyzed tumors with a T-stage distribution similar to that expected in a screening population—that is, a high percentage of early-stage primary tumors. Tumors with spread outside the nasopharynx were retained in the analysis to ensure that the grading system reflected the full range of T-stage tumors that may be encountered in both of these settings and to allow us to evaluate the new plain scan

Table 4: Differences in the diagnostic performances of the current, modified, and plain scan grading systems

Grading Systems to Indicate NPC	Sens $\chi^2_{(2)}$ (Significance, >3.84)	Spec	Combined Sens and Spec $\chi^2_{(2)}$ (Significance, >5.99)	Youden Index
Current system, primary tumor (3, 4) ^a vs Modified system using only primary tumor (4, 5) ^b	13 ^a	109 ^b	122 ^b	a = 72.8%; b = 88.4%
Current system, primary tumor (3, 4) ^a vs modified system, primary tumor (4, 5) + node (5) ^c	7 ^a	21.3 ^c	28.3 ^c	a = 72.8%; c = 88.1%
Modified system using only primary tumor (4, 5) ^d vs modified system, primary tumor (4, 5) + node (5) ^c	6 ^c	9 ^d	15 ^d	c = 88.4%; d = 88.1%
Modified system, primary tumor (4, 5) + node (5) ^c vs plain scan system, primary tumor (4, 5) + node (5) ^e	1	5.14 ^c	6.14 ^c	c = 88.1%; e = 85.2%

Note:—Superscript refers to the grading system with the best performance; NPC indicates nasopharyngeal carcinoma; sens, sensitivity; spec, specificity.

^a Current system, primary tumor (3, 4).

^b Modified system using only primary tumor (4, 5).

^c Modified system, primary tumor (4, 5) + node (5).

^d Modified system using only primary tumor (4, 5).

^e Plain-scan system, primary tumor (4, 5) + node (5).

MR imaging grading system that would be advantageous in screening programs.

Current versus Modified Grading Systems for Detection of the Primary Tumor

The grading system was modified primarily to improve the specificity for primary tumor detection. The current grading system had a low specificity for NPC detection (63.5%) because of false-positive results from cases of benign hyperplasia with asymmetry (grade 3). Using grade 4 only in the current grading system (focal mass or extension beyond the nasopharynx) to indicate NPC greatly improved the specificity to 97.9%, but this was at the expense of sensitivity, which decreased from 99.7% to 87.5%.

The modified grading system yielded a statistically significant better overall performance and better balance between specificity and sensitivity (91.9% and 96.3%, respectively), producing high positive and negative predictive values (90.4% and 97.7%, respectively). This result was achieved mainly by the subdivision of asymmetric diffuse wall thickening into asymmetry without focal expansion, which is less indicative of NPC (new indeterminate grade 3), and into asymmetry with focal expansion, which indicates a higher risk of NPC (new grade 4). Moreover, a focal mass or extension beyond the nasopharynx was elevated to grade 5, thus expanding the 4-grade system to 5 grades. The refined criteria also incorporated absent contrast-enhancing septa⁸ and external distortion of contrast-enhancing septa in the adenoid into the new grades 4–5 to indicate suspicious or probable NPC.

Modified Grading System for NPC Detection with and without Metastatic Node Assessment

The incidence of regional spread to retropharyngeal and upper internal jugular chain nodes covered on the short MR imaging protocol was high for stage T1 tumors confined to the nasopharynx (62.6%) and is consistent with the reported incidence for early-stage NPC (71.1%).¹⁶ The inclusion of nodal assessment increased the sensitivity of the modified grading system by detecting 6 additional cases of NPC that would have been missed using

the primary tumor criteria alone. However, nodal assessment also reduced the specificity because of an overlap in the size of enlarged reactive nodes and metastatic nodes. Most interesting, false-positive results for malignancy occurred in the retropharyngeal group despite using the 6-mm¹³ rather than 5-mm¹⁷ threshold for metastatic node diagnosis. The decrease in specificity outweighed the increase in sensitivity, but the difference in overall performance was small, so we believe that nodal assessment still has a role because it detects primary cancers that would otherwise be missed by MR imaging.

Modified versus Plain Scan Grading Systems for NPC Detection

As expected, the modified full-protocol grading system, which includes T2- and T1-weighted images before and after contrast enhancement, yielded better overall NPC diagnostic performance than the plain scan grading system. The plain scan grading system, nevertheless, performed well, with high sensitivity and specificity (97.7% and 86.4%, respectively) and high negative and positive predictive values (97.3% and 87.8%, respectively). Contrast-enhanced images detected only 1 additional primary cancer and, surprisingly, no additional spread beyond the nasopharynx; this finding is encouraging because it is an important MR imaging indicator of malignancy. Contrast-enhanced images did not detect any additional metastatic nodes. In a screening setting, avoidance of intravenous contrast would enable more rapid, less expensive scans and eliminate the need for intravenous MR imaging contrast agents in healthy patients with false-positive blood tests.

We suggest that for plain scan MR imaging graded 1 or 2, the risk of NPC is low (0.44%) and the patient can be reassured. Intravenous contrast is of limited benefit and can be withheld, especially in the absence of abnormal findings on endoscopy. On the other hand, for plain scan MR imaging graded 4 or 5, the risk of NPC is high (87.80%) and intravenous contrast is suggested irrespective of the endoscopy findings. For plain scan MR imaging graded 3, the risk of NPC is intermediate (6.96%) and the role

of intravenous contrast is unclear, though results suggest that contrast is more beneficial when the MR imaging is graded by a less experienced assessor or to increase the confidence that a symmetric enlarged adenoid is due to benign hyperplasia (striped appearance with alternating septal and lymphoid columns).

Observer Results

This study aimed to produce a simple MR imaging grading system based on conventional sequences for a quick assessment by radiologists with differing levels of experience. Therefore, we did not include subtle abnormalities of malignancy such as loss of the white line sign⁸ or functional sequences such as diffusion-weighted imaging,¹⁸ which require quantification and use of thresholds that are not easily implemented across centers. Using our proposed modified and plain scan grading systems yielded substantial agreement between the most and the least experienced observers when assessing grades 1–2 versus grade 3 versus grades 4–5 on contrast MR imaging. All other agreement among the 3 observers was almost perfect. Therefore, we believe that these new MR imaging grading systems can be used by specialists and generalists. Most interesting, the number of false-positive cases increased with experience, which lowered the overall accuracy.

Limitations

The use of MR imaging in NPC detection is still in its infancy, so our results are from a single-center setting and include cases reported previously. Therefore, to ensure generalizability, the data should be validated at outside institutions, and we hope our proposed systems will be tested and developed by researchers in this field. Moreover, future studies should explore the potential use of only a non-contrast-enhanced MR imaging protocol and the plain scan grading system in screening settings. We envisage future refinements of the MR imaging grading systems, and our proposal regarding the use of intravenous contrast may evolve as advances in the circulating Epstein-Barr virus DNA evaluations reduce the number of healthy subjects referred for further investigation after a false-positive blood test.¹⁹ Finally, the grading systems are proposed for use only in patients with suspected NPC who have a dedicated nasopharyngeal MR imaging and not for use in a general population.

CONCLUSIONS

We refined our current MR imaging grading system for NPC detection, with the intent to meet the challenge of applying MR imaging not only in the clinical setting but also in a screening setting involving greater numbers of patients with early-stage primary cancers that must be discriminated from benign hyperplasia. We added focal expansion in diffuse asymmetric wall thickening, absent or external distortion of contrast-enhancing adenoidal septa, and the presence of metastatic nodes as indicators of malignancy. The modified MR imaging grading system improved the overall diagnostic performance of MR imaging when compared with the current MR imaging grading system and produced sensitivity and specificity rates of 96.3% and 91.9%, respectively. The modified MR imaging grading system was used by specialists and generalists to classify patients into low (grades 1, 2), indeterminate (grade 3), and high-risk (grades 4, 5) categories

for NPC. Patients with a low-risk MR imaging grade can be spared an injection of intravenous contrast. We hope the grading system will help disseminate knowledge to other centers and act as the foundation for building a consensus on future guidelines for a Nasopharynx Imaging Reporting and Data System. Finally, the plain scan alone exhibited potential usefulness in future screening programs.

Disclosures: Rossa W.K. Chiu—RELATED: Grant: Research Grants Council of Hong Kong Special Administrative Region Government Theme-Based Research Grant (T12-401/16-W)*; UNRELATED: Consultancy: GRAIL; Grants/Grants Pending: contract research agreement from GRAIL*; Patents (Planned, Pending or Issued): both pending and issued patents on cancer diagnostics*; Royalties: from patents on cancer diagnostics*; Stock/Stock Options: GRAIL, Take2 Healthcare; Other: founder of Take2 Healthcare. K.C. Allen Chan—RELATED: Grant: GRAIL, Cirina, Comments: This work is partially supported by GRAIL/Cirina*; Consulting Fee or Honorarium: GRAIL, Comments: I am a consultant to GRAIL; UNRELATED: Board Membership: Take2 Healthcare, DRA, Comments: I am a director of Take2 Healthcare and DRA; Consultancy: GRAIL, Comments: I am a consultant of GRAIL; Grants/Grants Pending: GRAIL/Cirina, Comments: My institution received funding support from GRAIL/Cirina*; Patents (Planned, Pending or Issued): patents on molecular diagnostics; Royalties: GRAIL, Sequenom, Illumina, Take2, Xcelom; Stock/Stock Options: GRAIL, DRA, Take2 Healthcare, Comments: I hold equities. Wai Kei Jacky Lam—UNRELATED: Patents (Planned, Pending or Issued): enhancement of cancer screening using cell-free viral nucleic acids (pending); Stock/Stock Options: GRAIL. Edwin P. Hui—UNRELATED: Consultancy: Merck Sharp & Dohme; Payment for Lectures Including Service on Speakers Bureaus: Merck Serono, Merck Sharp & Dohme. Brigitte Ma—UNRELATED: Grants/Grants Pending: Novartis, Boehringer Ingelheim, Comments: research grant; Payment for Lectures Including Service on Speakers Bureaus: Merck Sharp & Dohme, Bristol-Myers Squibb.* Anthony Chan—UNRELATED: Consultancy: Merck Serono, Merck Sharp & Dohme, Cullinan Management Inc; Employment: The Chinese University of Hong Kong; Grants/grants pending: Boehringer Ingelheim, Bristol Myers Squibb, Amgen, Pfizer, Eli Lilly, Merck Serono, Merck Sharp & Dohme*. Yuk Ming Dennis Lo—RELATED: Grant: Kadoorie Charitable Foundation, GRAIL Inc, Li Ka Shing Foundation, Hong Kong Research Grants Council, Comments: Hong Kong Research Grants Council Theme-Based Research Grant (T12-401/16-W)*; Consulting fees or honorarium: GRAIL Inc, Decheng Capital*; Other: Take2 Holdings Limited, GRAIL Inc, Comments: Take2 Holdings Limited - Co-founder, Shareholder, Chairman of the Board, GRAIL Inc - Scientific Co-founder, shareholder, member of Scientific Advisory Board; UNRELATED: Board membership: DRA Limited, Comments: Chairman of the Board; Patents (Planned, Pending or Issued): Illumina, Sequenom, Xcelom Limited, DRA Limited, Comments: Licensed patents or patent applications in the area of non-invasive prenatal testing; Royalties: Illumina, Sequenom, Xcelom Limited, DRA Limited, Comments: Royalties for licensed patents or patent applications in the area of non-invasive prenatal testing; Stock/stock options: DRA Limited; Other: KingMed Future, Comments: Service agreement in the area of non-invasive prenatal testing. *Money paid to the institution.

REFERENCES

1. Lee AW, Ng WT, Chan LL, et al. Evolution of treatment for nasopharyngeal cancer: success and setback in the intensity-modulated radiotherapy era. *Radiother Oncol* 2014;110:377–84 CrossRef Medline
2. Chan KC, Woo JK, King A, et al. Analysis of plasma Epstein-Barr virus DNA to screen for nasopharyngeal cancer. *N Engl J Med* 2017;377:513–22 CrossRef Medline
3. King AD, Vlantis AC, Bhatia KS, et al. Primary nasopharyngeal carcinoma: diagnostic accuracy of MR imaging versus that of endoscopy and endoscopic biopsy. *Radiology* 2011;258:531–37 CrossRef Medline
4. King AD, Woo JK, Ai QY, et al. Complementary roles of MRI and endoscopic examination in the early detection of nasopharyngeal carcinoma. *Ann Oncol* 2019;30:977–82 CrossRef Medline
5. Shayah A, Wickstone L, Kershaw E, et al. The role of cross-sectional imaging in suspected nasopharyngeal carcinoma. *Ann R Coll Surg Engl* 2019;101:325–27 CrossRef Medline
6. King AD, Vlantis AC, Yuen TW, et al. Detection of nasopharyngeal carcinoma by MR imaging: diagnostic accuracy of MRI compared with endoscopy and endoscopic biopsy based on

- long-term follow-up.** *AJNR Am J Neuroradiol* 2015;36:2380–85 CrossRef Medline
7. King AD, Vlantis AC, Tsang RK, et al. **Magnetic resonance imaging for the detection of nasopharyngeal carcinoma.** *AJNR Am J Neuroradiol* 2006;27:1288–91 CrossRef Medline
 8. King AD, Wong LY, Law BK, et al. **MR imaging criteria for the detection of nasopharyngeal carcinoma: discrimination of early-stage primary tumors from benign hyperplasia.** *AJNR Am J Neuroradiol* 2018;39:515–23 CrossRef Medline
 9. Wang ML, Wei XE, Yu MM, et al. **Value of contrast-enhanced MRI in the differentiation between nasopharyngeal lymphoid hyperplasia and T1 stage nasopharyngeal carcinoma.** *Radiol Med* 2017;122:743–51 CrossRef Medline
 10. Li K, Lin GZ, Shen JC, et al. **Time trends of nasopharyngeal carcinoma in urban Guangzhou over a 12-year period (2000–2011): declines in both incidence and mortality.** *Asian Pac J Cancer Prev* 2014;15:9899–903 CrossRef Medline
 11. Amin MB, Edge SB, Greene FL, et al, eds. *AJCC Cancer Staging Manual*. 8th ed. New York: Springer-Verlag; 2017
 12. van den Brekel MW, Stel HV, Castelijns JA, et al. **Cervical lymph node metastasis: assessment of radiologic criteria.** *Radiology* 1990; 177:379–84 CrossRef Medline
 13. Zhang G, Liu L, Wei W, et al. **Radiologic criteria of retropharyngeal lymph node metastasis in nasopharyngeal carcinoma treated with radiation therapy.** *Radiology* 2010;255:605–12 CrossRef Medline
 14. Hawass N. **Comparing the sensitivities and specificities of two diagnostic procedures performed on the same group of patients.** *Br J Radiol* 1997;70:360–66 CrossRef Medline
 15. Kundel HL, Polansky M. **Measurement of observer agreement.** *Radiology* 2003;228:303–08 CrossRef Medline
 16. Guo R, Tang LL, Mao YP, et al. **Proposed modifications and incorporation of plasma Epstein-Barr virus DNA improve the TNM staging system for Epstein-Barr virus-related nasopharyngeal carcinoma.** *Cancer* 2019;125:79–89 CrossRef Medline
 17. King AD, Ahuja AT, Leung SF, et al. **Neck node metastases from nasopharyngeal carcinoma: MR imaging of patterns of disease.** *Head Neck* 2000;22:275–81 CrossRef Medline
 18. Ai QY, King AD, Chan JS, et al. **Distinguishing early-stage nasopharyngeal carcinoma from benign hyperplasia using intravoxel incoherent motion diffusion-weighted MRI.** *Eur Radiol* 2019;29:5627–34 CrossRef Medline
 19. Lam WK, Jiang P, Chan KCA, et al. **Sequencing-based counting and size profiling of plasma Epstein-Barr virus DNA enhance population screening of nasopharyngeal carcinoma.** *Proc Natl Acad Sci U S A* 2018;115:E5115–24 CrossRef Medline

4D–Dynamic Contrast-Enhanced MRI for Preoperative Localization in Patients with Primary Hyperparathyroidism

J.L. Becker, V. Patel, K.J. Johnson, M. Guerrero, R.R. Klein, G.F. Ranvier, R.P. Owen, P. Pawha, and K. Nael



ABSTRACT

BACKGROUND AND PURPOSE: Our aim was to test the hypothesis that our recently introduced 4D–dynamic contrast-enhanced MR imaging with high spatial and temporal resolution has equivalent accuracy to 4D-CT for preoperative gland localization in primary hyperparathyroidism without requiring exposure to ionizing radiation.

MATERIALS AND METHODS: Inclusion criteria were the following: 1) confirmed biochemical diagnosis of primary hyperparathyroidism, 2) preoperative 4D–dynamic contrast-enhanced MR imaging, and 3) surgical cure with >50% decrease in serum parathyroid hormone intraoperatively. 4D–dynamic contrast-enhanced studies were reviewed independently by 2 neuroradiologists to identify the side, quadrant, and number of abnormal glands, and compared with surgical and pathologic results.

RESULTS: Fifty-four patients met the inclusion criteria: 37 had single-gland disease, and 17, multigland disease (9 with double-gland hyperplasia; 3 with 3-gland hyperplasia; and 5 with 4-gland hyperplasia). Interobserver agreement (κ) for the side (right versus left) was 0.92 for single-gland disease and 0.70 for multigland disease. Interobserver agreement for the quadrant (superior versus inferior) was 0.70 for single-gland disease and 0.69 for multigland disease. For single-gland disease, the gland was correctly located in 34/37 (92%) patients, with correct identification of the side in 37/37 (100%) and the quadrant in 34/37 (92%) patients. For multigland disease, the glands were correctly located in 35/47 (74%) patients, with correct identification of the side in 35/47 (74%) and the quadrant in 36/47 (77%).

CONCLUSIONS: The proposed high spatial and temporal resolution 4D–dynamic contrast-enhanced MR imaging provides excellent diagnostic performance for preoperative localization in primary hyperparathyroidism, with correct gland localization of 92% for single-gland disease and 74% in multigland disease, superior to 4D-CT studies.

ABBREVIATIONS: CAIPIRINHA = controlled aliasing in parallel imaging results in higher acceleration; DCE = dynamic contrast-enhanced; MGD = multigland disease; PHPT = primary hyperparathyroidism; PTA = single parathyroid adenoma; PTH = parathyroid hormone; SGD = single-gland disease; TRICKS = time-resolved imaging of contrast kinetics; TWIST = time-resolved imaging with stochastic trajectories

Primary hyperthyroidism (PHPT) causes overproduction of the parathyroid hormone (PTH) leading to hypercalcemia and is the most common parathyroid disease. It is caused by single parathyroid adenoma (PTA) in 80%–90%,¹ multigland disease (MGD) in 5%–15%, and carcinoma in <1%.² MGD glands are usually smaller than in adenoma and hyperplasia and can

asymmetrically involve any number or all of the 4 parathyroid glands.³ Accurate preoperative localization of abnormal parathyroid tissue is essential for guiding curative, focused unilateral neck exploration for SGD and is particularly crucial for re-operative parathyroidectomy surgery, which currently has a failure rate 4× that of primary surgery.⁴ Other advantages include smaller scars, shorter operations, reduced complication rates, and lower surgical cost.^{5–9}

4D-CT has gained wide acceptance for presurgical PHPT planning, with multiphase imaging having superior diagnostic performance compared with both sonography and technetium (Tc99m) sestamibi scintigraphy.^{10–12} 4D-CT is, however, associated with high radiation doses of 5.56–10.4 mSv, depending on the number of phases scanned.^{13–15} It can have radiation doses to the thyroid gland of up to 57× that of Tc99m scintigraphy (92.0 versus 1.6 mGy).¹⁵ Radiation exposure is the main risk for

Received November 2, 2018; accepted after revision January 1, 2020.

From the Departments of Medical Imaging (J.L.B., V.P., K.J.J.), Surgery (M.G.), and Pathology (R.R.K.), University of Arizona, Tucson, Arizona; Departments of Surgery (G.F.R., R.P.O.), and Radiology (P.P., K.N.), Icahn School of Medicine at Mount Sinai, New York, New York; and Department of Radiological Sciences (K.N.), David Geffen School of Medicine at University of California, Los Angeles, Los Angeles, California.

Please address correspondence to Jennifer Becker, BMBS, FRCS, Department of Medical Imaging, University of Arizona, 1501 North Campbell Ave, Tucson, AZ, 85724; e-mail: jbecker@radiology.arizona.edu

<http://dx.doi.org/10.3174/ajnr.A6482>

development of thyroid cancer, with increased risk to younger patients and with thyroid doses of 50–100 mGy.¹⁶ Thus, judicious use of 4D-CT has recently been recommended.¹³ Dual-phase CT has been suggested as an alternative to 3- or 4-phase imaging and is associated with lower radiation doses, but at a cost of reduced accuracy for localizing PTAs to the correct side (79%–81%) and quadrant (55%–76%).^{17–20}

4D–dynamic contrast-enhanced (DCE) MR imaging is, therefore, a very attractive alternative to 4D-CT. Like 4D-CT, it exploits the hypervascular nature of abnormal parathyroid lesions, but without the risk to the patient arising from radiation exposure.²¹ Until recently, the competing requirements for high spatial and high temporal resolution imaging over a large FOV prohibited a true 4D application for MR imaging.^{21,22}

This study tests the hypothesis that our recently introduced 4D-DCE MR imaging has diagnostic accuracy equivalent to that of 4D-CT for preoperative localization of abnormal parathyroid glands in patients with PHPT, without the need for ionizing radiation.

MATERIALS AND METHODS

Patients

This Health Insurance Portability and Accountability Act–compliant prospective study was performed under the approval of the institutional review board at the University of Arizona and Icahn School of Medicine. Consecutive new patients with PHPT presenting to 2 surgeons from December 2013 to December 2015 were eligible for the study. Inclusion criteria were the following: 1) no previous neck surgery, 2) PHPT confirmed with biochemical confirmation of elevated serum PTH and calcium levels, 3) MR imaging consent with no MR imaging contraindication, 4) preoperative 4D-DCE MR imaging of the neck, and 5) surgical cure guided by MR imaging and confirmed by >50% reduction of serum PTH.

Image Acquisition

MR imaging was performed using a 3T Magnetom Skyra MR imaging system (Siemens, Erlangen, Germany) with the patient breathing freely. A combination 20-element head and neck coil was used for radiofrequency signal reception. 4D-DCE MR imaging was performed using a 3D volumetric interpolated examination sequence using the following parameters: TR = 4.06 ms, dual-echo for Dixon fat suppression (first TE = 1.31 ms, second TE = 2.54 ms), flip angle = 9°, matrix = 160 mm, FOV = 200 mm, 60 sections × 2 mm thick.

Time-resolved imaging with stochastic trajectories (TWIST)²³ with a sampling density of 33% and controlled aliasing in parallel imaging results in higher acceleration (CAIPIRINHA)²⁴ with an acceleration factor of 4 were incorporated, resulting in a net acceleration of 8, which was used to acquire a 3D dataset with a voxel size of $1.3 \times 1.3 \times 2.3 \text{ mm}^3$ and a temporal resolution of 6 seconds over a craniocaudal coverage of 120 mm, spanning the inferior mandibular rim to the carina. Twenty-four temporal frames were obtained during 144 seconds of acquisition time after intravenous injection of 0.1 mmol/kg of MultiHance (gadobenate dimeglumine, 529 mg/mL; Bracco Diagnostics, Princeton, New Jersey) at 4 mL/s followed by 20 mL of saline at 4 mL/s.

Image Analysis

The 4D-DCE MR imaging datasets were independently analyzed by 2 neuroradiologists blinded to the patient's previous imaging and clinical, surgical, and pathologic data. The 4D-MR imaging studies were analyzed systematically on our PACS. Abnormal parathyroid glands were identified as arterial enhancing nodules that demonstrated early increased signal intensity at the same time as or within 1–2 frames (up to 12 seconds) of the onset of carotid enhancement, with maximal signal intensity and enhancement during the early venous phase and decreased signal intensity due to contrast washout in the later venous phase.¹⁰

Readers searched the most common locations of the parathyroid glands (native) as well as all possible ectopic locations.¹⁵ Discrepancies between readers were resolved by consensus and used for assessment of diagnostic accuracy in comparison with surgical and pathologic findings. For each gland, the side was recorded in relation to the midline, and the quadrant was recorded as superior or inferior, depending on the relation to the midpole of the thyroid gland.

Parathyroid volumes were calculated using the ellipsoid formula $[(4/3)abxc]$, where *a* represent the maximum short axis diameter, *b* the maximum long axis diameter and *c* the maximum diameter of the gland in the coronal plane.

Surgical Confirmation

All patients underwent surgical resection with the side, quadrant, and size of the resected parathyroid glands recorded. The position of the gland was recorded in relation to the recurrent laryngeal nerve. The origin of the arterial supply to the abnormal gland overrode anatomic location if discrepant in determining the gland location as superior or inferior. All patients included in the study had surgical cure. This was confirmed by a decrease in the intraoperative serum parathyroid hormone level of at >50% 10 minutes following resection compared with the intraoperative pre-excision level. The pathologist measured the weight and dimensions of the excised glands, and their volume was calculated with the same ellipsoid formula used for the imaging volume.

Statistical Analysis

Statistical analysis was performed using MedCalc for Windows (Version 12.2.1; MedCalc Software, Mariakerke, Belgium). Clinical and lesion characteristics were compared between subjects with SGD and MGD using univariate analysis, with the Fisher exact test for categorical variables and the unpaired 2-tailed *t* test for continuous variables.

Interobserver agreement was tested using a linear weighted κ test. By means of consensus reads, the ratios of correctly identified lesion sides and quadrants were calculated against the final lesion assignment, and the percentages (sensitivities) were calculated for SGD and MGD. The significance level was defined as $P < .05$.

RESULTS

A total of 54 patients met our inclusion criteria. All patients had parathyroid glands identified. Thirty-seven patients had a single adenoma (Fig 1), and 17 patients had MGD with a total of 47

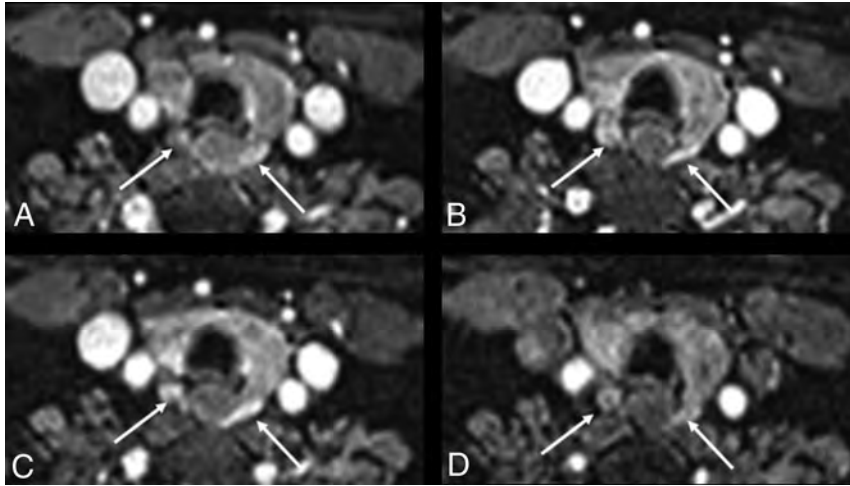


FIG 1. A 39-year-old woman with PHPT and MGD with bilateral glands imaged in the lower quadrants. *A*, Axial early arterial phase. *B*, Early venous phase. *C*, Midvenous phase. *D*, Later venous phase. The contour of the glands is different in *A* and *B* due to interval patient motion without image degradation. Images show bilateral MGD glands (*white arrows*) with early arterial enhancement and increased signal intensity compared with the adjacent thyroid gland (*A*). Signal intensity increases into the early venous phase, with MGD glands having signal intensity similar to that of the carotid artery on the early venous phase and increased signal compared with the thyroid gland (*B*). At the mid-venous phase, the MGD glands have decreased signal intensity compared with the carotid artery due to early washout but still have increased signal compared with the thyroid gland (*C*). The MGD gland signal decreases further in the later venous phase, becoming isointense with the thyroid gland (*D*).

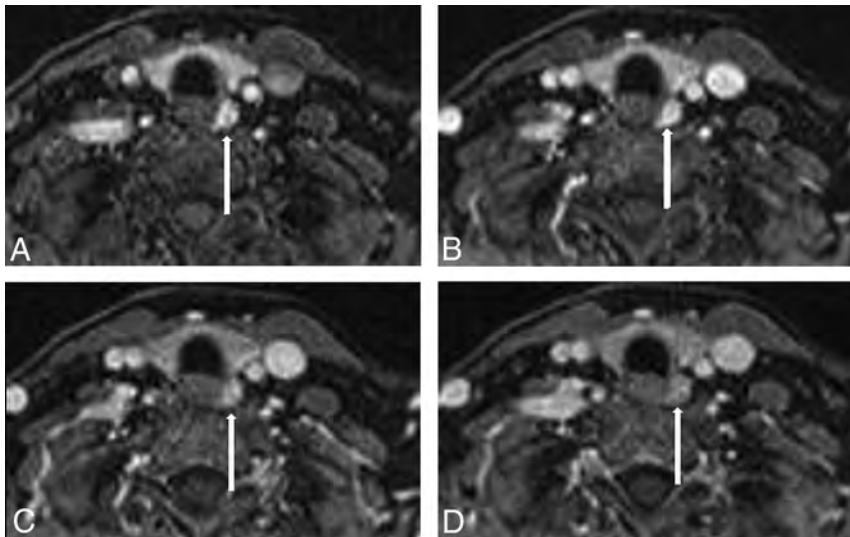


FIG 2. A 54-year-old woman with PHPT and SGD in the left lower quadrant. *A*, Axial early arterial phase. *B*, Early venous phase. *C*, Midvenous phase. *D*, Later venous phase. Images show a left lower quadrant parathyroid adenoma (*white arrow*) with early arterial enhancement (*A*), increasing with signal intensity similar to that of the internal carotid artery (*B*), with mildly decreased signal intensity compared with the carotid artery due to early venous washout (*C*), and decreased signal intensity compared with the adjacent internal carotid artery and jugular vein in the later venous phase (*D*).

hyperplastic glands (Fig 2): 9 with double-gland hyperplasia, 3 with asymmetric 3-gland hyperplasia, and 5 with 4-gland hyperplasia. Demographic data and basic clinical information for the entire cohort, subdivided between patients with SGD versus

MGD, are provided in Table 1. There were 3 ectopic glands: 1 within the thyroid gland and 2 in the superior mediastinum, all correctly identified as inferior glands. All other glands were posterior to the thyroid gland or related to the tracheal esophageal groove. There was no statistically difference in age, sex, preoperative serum PTH levels, and calcium levels between SGD and MGD (Table 1). The size and volume of the resected abnormal parathyroid glands were significantly smaller in patients with MGD (Table 1).

Surgical Findings

Intraoperative findings and operative reports were reviewed in conjunction with 4D-DCE MR imaging in a joint meeting between a neuroradiologist and surgeon. The surgical location of parathyroid lesions for each gland was determined as superior versus inferior and right versus left and was used as the reference standard to determine the accuracy of MR imaging reads. For the SGD, the location and side of 37 resected glands were recorded as left ($n = 20$, 54%), right ($n = 17$, 46%), superior ($n = 26$, 70%), and inferior ($n = 11$, 30%). For the 47 MGD glands, the side and location of each gland were recorded as left ($n = 27$, 57%), right ($n = 20$, 43%), superior ($n = 27$, 57%), and inferior ($n = 20$, 42%). All ectopic glands were inferior. Resection was recorded as 2, 3, or 3.5 glands and was recorded as 3.5 glands if any of the fourth gland was resected.

4D-DCE MR Imaging in SGD

A total of 36/37 (97%) glands were correctly localized to the right or left by both readers, resulting in an interobserver agreement of $\kappa = 0.92$ (95% CI, 0.80–1.0). One observer incorrectly identified 1/20 (5%) glands as right-sided, resolved by consensus, resulting in 100% sensitivity for correct side identification.

For determination of quadrant (superior versus inferior), readers 1 and 2 correctly identified 34/37 (92%) and 30/37 (81%) glands, respectively, resulting in an interobserver agreement of $\kappa = 0.70$ (95% CI, 0.45–0.920). Three glands were identified as superior by reader 1 and inferior by reader 2; 2 glands, as inferior by reader 1 and superior by

Table 1: Baseline and clinical data in patients with single adenoma and multiglandular disease (univariate analysis)

Variable	Total (54)	SGD (n = 37)	MGD (n = 17)	P Value
Age (mean) (SD) (yr)	58.6 (13.2)	59.1 (12.0)	57.4 (15.5)	.66
Sex (M/F)	(14/40)	(10/27)	(4/13)	.70
Preoperative PTH (mean) (SD)	131.6 (62.6)	134.2 (63.2)	148.8 (109.2)	.56
Preoperative calcium (mean) (SD)	10.8 (0.6)	10.8 (0.7)	10.7 (0.47)	.47
Volume (cm ³) (mean) (SD)	4.25 (6.51)	4.38 (1.09)	1.01 (2.24)	.02
Weight (mean) (SD) (g)	0.60 (0.51)	0.95 (0.60)	0.34 (0.26)	.001

Table 2: MGD—results for identification of side and quadrant of glands

	No. of Glands (Total, 47)		
	Reader 1	Reader 2	Consensus
Side (right or left)			
Total correctly localized	35 (74%)	33 (70%)	35 (74%)
Total incorrectly localized	2 (4%)	1 (2%)	2 (4%)
Total not identified at all	10 (21%)	13 (28%)	10 (21%)
Quadrant (superior or inferior)			
Total correctly localized	33 (70%)	32 (68%)	36 (77%)
Total incorrectly localized	3 (6%)	2 (4%)	2 (4%)
Total not identified at all	11 (23%)	13 (28%)	9 (19%)

reader 2. Following consensus reads, glands were correctly localized in 34/37 (92%) patients and incorrectly identified in 3/37 (8%) patients. No patient with SGD was mistakenly identified as having MGD.

4D-DCE MR Imaging in MGD

A total of 35/47 (74%) and 33/47 (70%) removed MGD glands were correctly localized for side by readers 1 and 2, respectively, resulting in interobserver agreement of $\kappa = 0.70$ (95% CI, 0.51–0.86). More glands were not identified at all by both readers than were incorrectly localized. Ten of 47 (21%) and 13/47 (28%) glands were not identified by readers 1 and 2, respectively, with 2/47 (4%) and 1/47 (2%) glands incorrectly localized for side. Seven of the 10 glands (70%) not identified by reader 1 and 9 of the 13 glands (69%) not identified by reader 2 were in patients who had 3.5 glands removed. Consensus reads showed an overall sensitivity for side of 74% (35/47), with the side of disease correctly identified in 14/17 (82%) patients. Only 2/17 patients (12%) required bilateral neck dissection for unidentified single glands, contralateral to correctly identified single (1/17, 6%) and double (1/17, 6%) glands. In addition, 1 patient with 2 removed ipsilateral glands (6%) was incorrectly identified with SGD.

For determination of the quadrant (superior versus inferior), readers 1 and 2 correctly identified 33/47 (70%) and 32/47 (68%) glands, respectively, resulting an interobserver agreement of $\kappa = 0.69$ (95% CI, 0.52–0.87). The quadrants were not identified at all for 11/47 (23%) and 13/47 (28%) glands by readers 1 and 2, respectively. Two of 47 (4%) glands were incorrectly localized by both readers. Consensus reads showed an overall sensitivity of 77% (36/47) for identification of the gland quadrant in MGD and incorrect localization of 2 (4%) glands with 9 (19%) glands not identified at all. Consensus reads showed the quadrant of disease correctly identified in 9/17 (53%) patients. Seven of 9 (78%) patients with 2 glands removed had both glands correctly localized, with 1 gland not

identified in 2/9 (22%). Of the 3 patients with 3 glands removed, 1/3 (33%) had all glands correctly localized, with 1 gland not identified in 1/3 (33%) and incorrectly localized in 1/3 (33%). Of the 5 patients with 3.5 glands removed, only 1/5 (20%) had all glands correctly localized, 1 of 5 (20%) had 1 gland not identified, 1/5 (20%) had 1 gland not identified and 1 incorrectly localized, and 2/5 (40%) had 1 gland not recognized (Tables 2 and 3).

DISCUSSION

This study proves that the described 4D-DCE MR imaging is highly accurate for preoperative localization of abnormal parathyroid glands in patients with PHPT. The image interpretation is straightforward without the need for off-line postprocessing and takes >10 minutes with high interobserver agreement for correct identification of the side and quadrant.

For SGD, our 4D-DCE MR imaging has a sensitivity of 100% for side and 92% for quadrant. This compares very favorably with 4D-CT, with its sensitivity of 73%–97% for side and 55%–88% for quadrant.^{4,10,11,19,20,25,26} No patient with SGD required bilateral neck surgery. Accurate identification of the side of the gland within the neck can be as important to the surgeon as identification of the quadrant. Identification of the quadrant may simply give a starting point for the operation with ipsilateral extension of a search being less invasive than a bilateral dissection. For MGD, we showed an overall sensitivity of 74% for the side and 77% for the quadrant, superior to 4D-CT studies with a reported sensitivity of 29%–42.9%.^{27,28} Only 12% of our patients with MGD required bilateral neck dissection for unidentified contralateral disease.

Our results compare favorably with those of nondynamic conventional MR imaging with a sensitivity for detection of SGD and MGD of 57%–91%,^{29–35} often using small study populations and selected patients, with many having MGD glands larger than those in our study. Like MR imaging and 4D-CT, our 4D-DCE MR imaging was more successful in detecting the larger SGD glands, with mean volume of 4.38 cm³, than the smaller MGD glands, with mean volume of 1.01 cm³.^{3,29} For MGD, more glands went unrecognized and unrecorded than were incorrectly localized. Satisfaction of search when looking for multiple small glands most likely accounts for this finding, with the number of unrecorded glands increasing with increasing numbers of glands removed, with the highest with 4 removed glands.

A number of investigators have used DCE MR imaging for preoperative localization of parathyroid adenomas with mixed results. Merchavy et al²² used a 4D-DCE T1 volumetric interpolated brain examination sequence at 1.5T with precontrast images and postcontrast images at 13-second intervals for 10 timeframes to identify 7/7 (100%) selected PTAs. The size of these glands was not reported, but PTA detection using ultrasound and sestamibi (MIBI) in this study was 90%; higher than reported in other studies.²²

Table 3: SGD and MGD—patient results for identification of side and quadrant of glands

	No. of Patients (Total, 17)	
Side (right or left)		
Total with all glands correctly localized	14 (82%)	
Total with 1 gland incorrectly localized	2 (12%)	2/9 with 2-gland disease
Total with 1 gland not identified at all	1 (6%)	1/9 with 2-gland disease
Quadrant (superior or inferior)		
Total with all glands correctly localized	9 (53%)	7/9 with 2-gland disease 1/3 with 3-gland disease 1/5 with 3.5-gland disease
Total with 1 gland incorrectly localized	2 ^a	1/3 with 3-gland disease 1 with 3.5-gland disease also had 1 gland not identified and counted twice ^a
Total with 1 gland not identified	6 ^a	2/9 with 2-gland disease 1/3 with 3-gland disease 3/5 with 3.5-gland disease
Total with 2 glands not identified	1	1/5 with 3.5-gland disease

^a One also had 1 gland incorrectly localized and counted twice.

Ozturk et al³⁶ used 4D-DCE at 3T with precontrast and postcontrast images at 15-second intervals for 8 timeframes with 83%–86% sensitivity for abnormal glands. Their postprocessing was more labor-intensive than ours with precontrast images subtracted from postcontrast images on a pixel-by-pixel basis, with glands defined by the following: 1) vivid enhancement compared with the thyroid on the first or second postcontrast images, and 2) washout on delayed images. Signal intensity was measured using ROIs drawn on consecutive images for doubtful cases.³⁶ Another study using a limited (4-phase) dynamic postcontrast MR imaging showed a sensitivity of 80% for detection of PTAs.³⁷

Turski et al³⁸ used dynamic 4D-MR imaging with incorporation of time-resolved imaging of contrast kinetics (TRICKS) angiography with a temporal resolution of 5.4 seconds, demonstrating a 64% sensitivity for detection of PTAs.³⁰ To date, dynamic MR imaging has had better success at identifying parathyroid glands in the re-operative neck with studies at 1.5T showing 90%³⁷ and 93%³⁹ of PTAs detected. The temporal resolution of this latter study, identical to ours at 6 seconds, may account for superior lesion detection, with the glands between 6 and 28 mm in diameter detected.

Our study showed that our described 4D-DCE MRI technique can be successfully used for accurate preoperative localization in patients with PHPT. We would like to highlight the following primary findings from our study.

Using the fast imaging tools TWIST²³ and CAIPIRINHA^{14,24} has enabled very high spatial resolution (voxel size = $1.3 \times 1.3 \times 2.3 \text{ mm}^3$) without sacrificing coverage or resulting in an increase in acquisition time. A large FOV (20 cm) from the angle of the mandible to the manubrium was scanned every 6 seconds, providing high temporal resolution and a truly dynamic interrogation exploiting the hypervascular characteristics of parathyroid glands, a characteristic that has also been targeted by 4D-CT.

The short scan time required for our technique is an advantage over conventional MR imaging, with the patient not required to hold his or her breath. The DCE images acquired at each 6-second timeframe appear as separate sequences on the PACS for analysis, allowing independent evaluation. None of our 6-second images were degraded by motion, even when the patient moved

slightly between images (Fig 1). In addition to the short overall scan time of 144 seconds for our 4D-DCE MRI, our technique also has the advantage of a relatively short postprocessing time, performed without postprocessing software.

High-temporal-resolution DCE MR imaging allows differentiation of the parathyroid glands from lymph nodes and thyroid tissue due to their faster arterial enhancement and earlier contrast washout, with a mean parathyroid maximal enhancement of 13 seconds earlier than thyroid tissue and 29 seconds earlier than lymph nodes using this technique.²¹ At 6 seconds, our DCE temporal resolution

is higher than that used by some other MR imaging authors and may account for our superior results compared with some of these other DCE MR imaging techniques.²² We have previously shown parathyroid glands to have arterial enhancement at the same time or within 1–2 timeframes (6–12 seconds) of the carotid artery and at least 2–3 timeframes (12–18 seconds) before the thyroid gland.²¹ This feature aids depiction of glands lying adjacent to the thyroid, those most frequently missed with 4D-CT.⁴⁰

The gadolinium contrast agent for this study was MultiHance, used at the time of the study for head and neck imaging at both the University of Arizona and Icahn School of Medicine. Its relaxivity is approximately twice that of some other agents, giving excellent contrast enhancement⁴¹ and superior results for first-pass angiography compared with a macrocyclic agent.⁴² Because we lack experience using other agents, recommendations for alternative agents using our technique cannot be made.

Additionally, incorporation of the Dixon technique into our sequence resulted in excellent and uniform fat suppression,⁴³ with good contrast-to-noise aiding identification of small lesions. Our high spatial resolution, combined with excellent fat saturation, enabled detection of very small parathyroid glands, with 11 MGD glands of $<0.5 \text{ cm}^3$, an improvement over conventional T1 and T2 sequences, having poor detection of glands of $<0.31 \text{ cm}^3$ and a mean size of nondetected glands of 1.4 cm^3 .^{3,31} Uniform fat suppression is necessary to distinguish small enhancing glands from fat but can be difficult to achieve using other techniques due to the presence of air within the lungs and upper airways and digestive tract and complex anatomy. Unlike other described dynamic techniques, TRICKS, the described protocol, does not use a subtraction methodology, avoiding degradation of images by subtraction and ghost artifacts.

Three- or 4-phase 4D-CT exposes the thyroid gland to significant radiation doses. The major advantage of 4D-DCE MRI over 4D-CT is the lack of exposure of the neck to the hazards of ionizing radiation, particularly for young patients whose thyroid glands are more sensitive to the carcinogenic effect of ionizing radiation,⁴⁴ with the risk of differentiated thyroid cancer lasting several decades.⁴⁵ This risk increases with the increased radiation

dose.¹⁶ 4D-DCE MR imaging should, therefore, be considered as an alternative to 4D-CT for first-line investigation of PHPT in young patients requiring imaging.

Debate in the 4D-CT literature continues regarding the relative merits of CT acquisition at 2, 2.5, or 3 or 4 time points for 30–90 seconds for optimal lesion detection, much lower than our temporal resolution, with limitations imposed by the level of radiation exposure.^{25,27,46–49} Although it may be tempting to lower the temporal resolution of 4D-DCE, our experience during protocol development has shown that this results in inferior gland detection and is therefore not recommended.

Our study has several limitations. First, our sample size was relatively small, which may affect the power of our analysis. Because this was a dual-institutional study without patient selection, we would expect our results to be generalizable to larger patient cohorts referred to surgeons in other institutions. Second, comparison with surgical pathology findings is not ideal, particularly for MGD, in which normal small glands may be removed or biopsied. This feature may account for the higher rate of non-identified glands in those with higher numbers of removed glands. Additionally, some of the discrepancies in quadrant identification may be related to minor reporting differences between neuroradiologists and surgeons with regard to the anatomic location of the gland in relation to the midpole of the thyroid gland.

CONCLUSIONS

Our 4D-DCE MR imaging using the modified 4D-DCE TWIST or CAIPIRINHA technique with high spatial and temporal resolution exploits the hypervascular nature of parathyroid glands, resulting in sensitivities for gland detection of 92% and 74% for SGD and MGD, respectively, for patients undergoing primary surgery. 4D-DCE MRI has superior diagnostic accuracy compared with 4D-CT for both SGD and MGD and superior accuracy compared with unselected patients undergoing primary surgery using other dynamic MR imaging techniques. 4D-DCE MRI does not expose the neck to ionizing radiation, and it should be considered as an alternative to 4D-CT for first-line investigation in patients with HPT, particularly young patients for whom the risk of cancer from radiation to the thyroid gland is the highest.

Disclosures: Jennifer L. Becker—UNRELATED: Consultancy: Siemens, Comments: Syngo Via consultancy.* Randall P. Owen—UNRELATED: Grants/Grants Pending: Neurovision Medical Products, Comments: grant for intraoperative video laryngoscopy.* Kambiz Nael—UNRELATED: Board Membership: Olea Medical, Comments: Medical Advisory Board. *Money paid to the institution.

REFERENCES

1. Ruda JM, Hollenbeak CS, Stack BC Jr. **A systematic review of the diagnosis and treatment of primary hyperparathyroidism from 1995 to 2003.** *Otolaryngol Head Neck Surg* 2005;132:359–72 CrossRef Medline
2. Heath H 3rd, Hodgson SF, Kennedy MA. **Primary hyperparathyroidism: incidence, morbidity, and potential economic impact in a community.** *N Engl J Med* 1980;302:189–93 CrossRef Medline
3. Ghandur-Mnaymneh L, Kimura N. **The parathyroid adenoma: a histopathologic definition with a study of 172 cases of primary hyperparathyroidism.** *Am J Pathol* 1984;115:70–83 Medline
4. Kazzaure HS, Thomas S, Scheri RP, et al. **The devil is in the details: assessing treatment and outcomes of 6,795 patients undergoing**

- remedial parathyroidectomy in the Collaborative Endocrine Surgery Quality Improvement Program.** *Surgery* 2019;165:242–49 CrossRef Medline
5. Kunstman JW, Udelsman R. **Superiority of minimally invasive parathyroidectomy.** *Adv Surg* 2012;46:171–89 CrossRef Medline
6. Beland MD, Mayo-Smith WW, Grand DJ, et al. **MDCT for localization of occult parathyroid adenomas in 26 patients with primary hyperparathyroidism.** *AJR Am J Roentgenol* 2011;196:61–65 CrossRef Medline
7. Udelsman R, Lin Z, Donovan P. **The superiority of minimally invasive parathyroidectomy based on 1650 consecutive patients with primary hyperparathyroidism.** *Ann Surg* 2011;253:585–91 CrossRef Medline
8. Harari A, Zarnegar R, Lee J, et al. **Computed tomography can guide focused exploration in select patients with primary hyperparathyroidism and negative sestamibi scanning.** *Surgery* 2008;144:970–76; discussion 976–79 CrossRef Medline
9. Smith N, Magnuson JS, Vidrine DM, et al. **Minimally invasive parathyroidectomy: use of intraoperative parathyroid hormone assays after 2 preoperative localization studies.** *Arch Otolaryngol Head Neck Surg* 2009;135:1108–11 CrossRef Medline
10. Rodgers SE, Hunter GJ, Hamberg LM, et al. **Improved preoperative planning for directed parathyroidectomy with 4-dimensional computed tomography.** *Surgery* 2006;140:932–40; discussion 940–41 CrossRef Medline
11. Hoang JK, Sung WK, Bahl M, et al. **How to perform parathyroid 4D-CT: tips and traps for technique and interpretation.** *Radiology* 2014;270:15–24 CrossRef Medline
12. Day KM, Elsayed M, Beland MD, et al. **The utility of 4-dimensional computed tomography for preoperative localization of primary hyperparathyroidism in patients not localized by sestamibi or ultrasonography.** *Surgery* 2015;157:534–39 CrossRef Medline
13. Mahajan A, Starker LF, Ghita M, et al. **Parathyroid four-dimensional computed tomography: evaluation of radiation dose exposure during preoperative localization of parathyroid tumors in primary hyperparathyroidism.** *World J Surg* 2012;36:1335–39 CrossRef Medline
14. Kelly HR, Hamberg LM, Hunter GJ. **4D-CT for preoperative localization of abnormal parathyroid glands in patients with hyperparathyroidism: accuracy and ability to stratify patients by unilateral versus bilateral disease in surgery-naïve and re-exploration patients.** *AJNR Am J Neuroradiol* 2014;35:176–81 CrossRef Medline
15. Madorin CA, Owen R, Coakley B, et al. **Comparison of radiation exposure and cost between dynamic computed tomography and sestamibi scintigraphy for preoperative localization of parathyroid lesions.** *JAMA Surg* 2013;148:500–03 CrossRef Medline
16. Ron E, Lubin JH, Shore RE, et al. **Thyroid cancer after exposure to external radiation: a pooled analysis of seven studies—1995.** *Radiat Res* 2012;178:AV43–60 CrossRef Medline
17. Kluijfhout WP, Pasternak JD, Beninato T, et al. **Diagnostic performance of computed tomography for parathyroid adenoma localization; a systematic review and meta-analysis.** *Eur J Radiology* 2017;88:117–28 CrossRef Medline
18. Griffith B, Chaudhary H, Mahmood G, et al. **Accuracy of 2-phase parathyroid CT for the preoperative localization of parathyroid adenomas in primary hyperparathyroidism.** *AJNR Am J Neuroradiol* 2015;36:2373–79 CrossRef Medline
19. Hunter GJ, Ginat DT, Kelly HR, et al. **Discriminating parathyroid adenoma from local mimics by using inherent tissue attenuation and vascular information obtained with four-dimensional CT: formulation of a multinomial logistic regression model.** *Radiology* 2014;270:168–75 CrossRef Medline
20. Ramirez AG, Shada AL, Martin AN, et al. **Clinical efficacy of 2-phase versus 4-phase computed tomography for localization in primary hyperparathyroidism.** *Surgery* 2016;160:731–37 CrossRef Medline

21. Nael K, Hur J, Bauer A, et al. **Dynamic 4D MRI for characterization of parathyroid adenomas: multiparametric analysis.** *AJNR Am J Neuroradiol* 2015;36:2147–52 CrossRef Medline
22. Merchavy S, Luckman J, Guindy M, et al. **4D MRI for the localization of parathyroid adenoma: a novel method in evolution.** *Otolaryngol Head Neck Surg* 2016;154:446–48 CrossRef Medline
23. Le Y, Kroeker R, Kipfer HD, et al. **Development and evaluation of TWIST Dixon for dynamic contrast-enhanced (DCE) MRI with improved acquisition efficiency and fat suppression.** *J Magn Reson Imaging* 2012;36:483–91 CrossRef Medline
24. Breuer FA, Blaimer M, Heidemann RM, et al. **Controlled aliasing in parallel imaging results in higher acceleration (CAIPIRINHA) for multi-slice imaging.** *Magn Reson Med* 2005;53:684–91 CrossRef Medline
25. Starker LF, Mahajan A, Bjorklund P, et al. **4D parathyroid CT as the initial localization study for patients with de novo primary hyperparathyroidism.** *Ann Surg Oncol* 2011;18:1723–28 CrossRef Medline
26. Lundstroem AK, Trolle W, Soerensen CH, et al. **Preoperative localization of hyperfunctioning parathyroid glands with 4D-CT.** *Eur Arch Otorhinolaryngol* 2016;273:1253–59 CrossRef Medline
27. Chazen JL, Gupta A, Dunning A, et al. **Diagnostic accuracy of 4D-CT for parathyroid adenomas and hyperplasia.** *AJNR Am J Neuroradiol* 2012;33:429–33 CrossRef Medline
28. Bahl M, Sepahdari AR, Sosa JA, et al. **Parathyroid adenomas and hyperplasia on four-dimensional CT scans: three patterns of enhancement relative to the thyroid gland justify a three-phase protocol.** *Radiology* 2015;277:454–62 CrossRef Medline
29. Stevens SK, Chang JM, Clark OH, et al. **Detection of abnormal parathyroid glands in postoperative patients with recurrent hyperparathyroidism: sensitivity of MR imaging.** *AJR Am J Roentgenol* 1993;160:607–12 CrossRef Medline
30. Grayev AM, Gentry LR, Hartman MJ, et al. **Presurgical localization of parathyroid adenomas with magnetic resonance imaging at 3.0 T: an adjunct method to supplement traditional imaging.** *Ann Surg Oncol* 2012;19:981–89 CrossRef Medline
31. McDermott VG, Fernandez RJ, Meakem TJ, et al. **Preoperative MR imaging in hyperparathyroidism: results and factors affecting parathyroid detection.** *AJR Am J Roentgenol* 1996;166:705–10 CrossRef Medline
32. Lopez Hanninen E, Vogl TJ, Steinmuller T, et al. **Preoperative contrast-enhanced MRI of the parathyroid glands in hyperparathyroidism.** *Invest Radiol* 2000;35:426–30 CrossRef Medline
33. Ruf J, Lopez Hanninen E, Steinmuller T, et al. **Preoperative localization of parathyroid glands: use of MRI, scintigraphy, and image fusion.** *Nuklearmedizin* 2004;43:85–90 CrossRef Medline
34. Krubsack AJ, Wilson SD, Lawson TL, et al. **Prospective comparison of radionuclide, computed tomographic, sonographic, and magnetic resonance localization of parathyroid tumors.** *Surgery* 1989;106:639–44; discussion 644–46 Medline
35. Seelos KC, DeMarco R, Clark OH, et al. **Persistent and recurrent hyperparathyroidism: assessment with gadopentetate dimeglumine-enhanced MR imaging.** *Radiology* 1990;177:373–78 CrossRef Medline
36. Ozturk M, Polat AV, Celenk C, et al. **The diagnostic value of 4D MRI at 3T for the localization of parathyroid adenomas.** *Eur J Radiol* 2019;112:207–13 CrossRef Medline
37. Kluijfhout WP, Venkatesh S, Beninato T, et al. **Performance of magnetic resonance imaging in the evaluation of first-time and reoperative primary hyperparathyroidism.** *Surgery* 2016;160:747–54 CrossRef Medline
38. Turski PA, Korosec FR, Carroll TJ, et al. **Contrast-enhanced magnetic resonance angiography of the carotid bifurcation using the time-resolved imaging of contrast kinetics (TRICKS) technique.** *Top Magn Reson Imaging* 2001;12:175–81 CrossRef Medline
39. Aschenbach R, Tuda S, Lamster E, et al. **Dynamic magnetic resonance angiography for localization of hyperfunctioning parathyroid glands in the reoperative neck.** *Eur J Radiol* 2012;81:3371–77 CrossRef Medline
40. Sho S, Yuen AD, Yeh MW, et al. **Factors associated with discordance between preoperative parathyroid 4-dimensional computed tomographic scans and intraoperative findings during parathyroidectomy.** *JAMA Surg* 2017;152:1141–47 CrossRef Medline
41. Shen Y, Goerner FL, Snyder C, et al. **T1 relaxivities of gadolinium-based magnetic resonance contrast agents in human whole blood at 1.5, 3, and 7 T.** *Invest Radiol* 2015;50:330–38 CrossRef Medline
42. Schneider G, Pasowicz M, Vymazal J, et al. **Gadobenate dimeglumine and gadofosveset trisodium for MR angiography of the renal arteries: multicenter intraindividual crossover comparison.** *AJR Am J Roentgenol* 2010;195:476–85 CrossRef Medline
43. Gaddikeri S, Mossa-Basha M, Andre JB, et al. **Optimal fat suppression in head and neck MRI: comparison of multipoint Dixon with 2 different fat-suppression techniques, spectral presaturation and inversion recovery, and STIR.** *AJNR Am J Neuroradiol* 2018;39:362–68 CrossRef Medline
44. Iglesias ML, Schmidt A, Ghuzlan AA, et al. **Radiation exposure and thyroid cancer: a review.** *Arch Endocrinol Metab* 2017;61:180–87 CrossRef Medline
45. Sinnott B, Ron E, Schneider AB. **Exposing the thyroid to radiation: a review of its current extent, risks, and implications.** *Endocr Rev* 2010;31:756–73 CrossRef Medline
46. Mortenson MM, Evans DB, Lee JE, et al. **Parathyroid exploration in the reoperative neck: improved preoperative localization with 4D-computed tomography.** *J Am Coll Surg* 2008;206:888–95; discussion 895–96 CrossRef Medline
47. Linda DD, Ng B, Rebello R, et al. **The utility of multidetector computed tomography for detection of parathyroid disease in the setting of primary hyperparathyroidism.** *Can Assoc Radiol J* 2012;63:100–08 CrossRef Medline
48. Gafton AR, Glastonbury CM, Eastwood JD, et al. **Parathyroid lesions: characterization with dual-phase arterial and venous enhanced CT of the neck.** *AJNR Am J Neuroradiol* 2012;33:949–52 CrossRef Medline
49. Noureldine SI, Aygun N, Walden MJ, et al. **Multiphase computed tomography for localization of parathyroid disease in patients with primary hyperparathyroidism: how many phases do we really need?** *Surgery* 2014;156:1300–06; discussion 13006–07 CrossRef Medline

Value of Endolymphatic Hydrops and Perilymph Signal Intensity in Suspected Ménière Disease

J.M. van Steekelenburg, A. van Weijnen, L.M.H. de Pont, O.D. Vijlbrief, C.C. Bommeljé, J.P. Koopman, B.M. Verbist, H.M. Blom, and S. Hammer



ABSTRACT

BACKGROUND AND PURPOSE: Ménière disease is characterized by endolymphatic hydrops, whereas perilymphatic enhancement on MR imaging has been suggested to be of additional value in diagnosing Ménière disease. This study evaluates the presence of endolymphatic hydrops and perilymphatic enhancement in patients with Ménière disease and with other vertigo-associated inner ear pathology.

MATERIALS AND METHODS: A 3D-FLAIR sequence 4 hours after intravenous gadolinium injection was performed to visualize the endolymph and perilymph in 220 patients suspected of having Ménière disease. Patients' ears were retrospectively categorized as having Ménière disease (probable or definite) or other vertigo-associated inner ear pathology not attributable to Ménière disease. Endolymphatic hydrops was evaluated using a visual classification system, and perilymphatic enhancement was scored both visually and quantitatively.

RESULTS: Endolymphatic hydrops was present in 137 (91.9%) of the definite Ménière disease ears and in 9 (7.0%) of the ears with other vertigo-associated inner ear pathology ($P < .001$). The combination of endolymphatic hydrops and visually increased perilymphatic enhancement was present in 122 (81.9%) definite Ménière disease ears compared with 4 (3.1%) ears with other vertigo-associated inner ear pathology ($P < .001$). This combination increases the positive predictive value from 0.94 for endolymphatic hydrops and 0.91 for perilymphatic enhancement to 0.97. The addition of measured perilymphatic enhancement leads to a moderate decrease in sensitivity from 0.92 for endolymphatic hydrops to 0.86.

CONCLUSIONS: The combination of perilymphatic enhancement and endolymphatic hydrops in patients suspected of having Ménière disease increases the positive predictive value in the diagnosis of definite Ménière disease.

ABBREVIATIONS: EH = endolymphatic hydrops; MD = Ménière disease; PE = perilymphatic enhancement; SIR = signal intensity ratio; VAIEP = vertigo-associated inner ear pathology

Ménière disease (MD) is characterized by attacks of vertigo, low-frequency hearing loss, and tinnitus. In the absence of a diagnostic standard, clinical diagnostic criteria were defined by the American Academy of Otolaryngology–Head and Neck Surgery and updated into a consensus of diagnostic guidelines by

the Bárány Society in 2015. This includes 2 distinct diagnostic entities: definite and probable MD, based on differences in vertigo episode duration and documented low-frequency hearing loss.¹ Because key clinical symptoms overlap other clinical entities such as vestibular migraine, it remains difficult to distinguish MD from other vertigo-associated inner ear pathologies.^{2–4}

Although the etiology of MD remains unclear, endolymphatic hydrops (EH) is generally accepted as the pathologic hallmark of the disease.⁵ 3T MR imaging after delayed intravenous gadolinium allows visualization of the endolymphatic space, with EH findings similar to histopathologic findings.^{6,7} However, EH is

Received September 7, 2019; accepted after revision January 1, 2020.

From the Departments of Radiology (J.M.v.S., L.M.H.d.P., S.H.) and Otorhinolaryngology (A.v.W., C.C.B., J.P.K., H.M.B.), Haga Teaching Hospital, The Hague, the Netherlands; Department of Radiology (O.D.V.), Ziekenhuis Groep Twente, Almelo, the Netherlands; and Department of Radiology (B.M.V.), Leiden University Medical Centre, Leiden, the Netherlands

J.M. van Steekelenburg and A. van Weijnen are shared first author; H.M. Blom and S. Hammer are shared senior authors.

This work was supported by the Radiology Research Fund of the Radiological Society of the Netherlands.

Paper previously presented at: Annual Meeting of the European Society of Neuroradiology, September 19–23, 2018, Rotterdam, the Netherlands; Annual Meeting of the European Society of Head and Neck Radiology, September 27–29, 2018, Kensington, UK; and Annual Meeting of the European Congress of Radiology, February 27–March 3, 2019, Vienna, Austria.

Please address correspondence to Josephine M. van Steekelenburg, MD, Haga Teaching Hospital, Department of Radiology, Els Borst-Eilersplein 275, 2545 AA, The Hague, the Netherlands; e-mail: j.vansteekelenburg@hagaziekenhuis.nl

Indicates open access to non-subscribers at www.ajnr.org

<http://dx.doi.org/10.3174/ajnr.A6410>

currently not part of the diagnostic criteria for definite MD. Most interesting, EH is not exclusively seen in MD but is also reported in healthy ears, monosymptomatic disease (vertigo, tinnitus, or hearing loss), and vestibular migraine.⁸⁻¹⁰ Based on the potential relevance of EH in patients suspected of having MD, new diagnostic criteria have been proposed, differentiating primary hydroptic ear disease (old terminology “definite MD” and “probable MD”) from hydrops due to secondary causes such as labyrinthitis or congenital hearing loss.¹¹

Vestibular hydrops, in particular in the saccule, seems strongly correlated with MD, as demonstrated by recent MR imaging studies.¹²⁻¹⁴ To improve the diagnostic accuracy in patients with suspected MD based on imaging, a few recent studies introduced perilymphatic enhancement (PE) as an additional MD-discriminating parameter.^{14,15} However, its presence and value in other vertigo-associated inner ear pathology (VAIEP) remains unclear.

Therefore, the purpose of this study was to evaluate the presence of EH and the additional value of PE in the diagnosis of patients with MD and in patients with other VAIEP not attributable to MD.

MATERIALS AND METHODS

Patients

From November 2017 to July 2018, two hundred twenty-seven consecutive patients who visited the Department of Otorhinolaryngology of our vertigo referral center (Haga Teaching Hospital, The Hague) with inner ear pathology and were suspected of having MD were retrospectively analyzed. Inclusion criteria were 18 years of age or older and a clinical diagnosis of definite MD or probable MD according to the 2015 updated Bárány criteria.¹ Patients not fulfilling the criteria for definite or probable MD were included if they had attacks of vertigo with or without hearing loss and with or without tinnitus (other VAIEP). Exclusion criteria were prior operations of the inner ear, an insufficient medical record, or a technically inadequate MR imaging (motion artifacts, insufficient CSF suppression on 3D-FLAIR).

Patient anamnestic characteristics and hearing tests were evaluated twice by 3 otorhinolaryngologists, independently and blinded to the MR imaging results. Diagnoses were assigned for each ear separately, according to the latest Bárány criteria.¹ Patients’ ears were confined to 1 of the 4 groups: definite MD, probable MD, other VAIEP, or asymptomatic (contralateral MD and other VAIEP ears). Consensus judgment was reached if evaluations were not congruent. This institutional review board–approved study was performed with a waiver of informed consent.

Imaging Protocol

All patients underwent delayed 3T MR imaging (Magnetom Skyra; Siemens, Erlangen, Germany) using a 20-channel array head coil, 4 hours after intravenous gadolinium (30 mL of gadoterate meglumine, Dotarem; Guerbet, Aulnay-sous-Bois, France). Patients were evaluated in the supine position with additional fixation between the patient’s head and the receiver coil.

High-resolution T2 sampling perfection with application-optimized contrasts by using different flip angle evolution (SPACE sequence; Siemens) images of the inner ear were

obtained for anatomic reference using the following parameters: FOV = 160 mm, section thickness = 0.5 mm, TR = 1400 ms, TE = 155 ms, number of excitations = 1, flip angle = 120°, matrix = 320 × 320, bandwidth = 289 Hz/pixel, turbo factor = 96, voxel size = 0.5 × 0.5 × 0.5 mm, and acquisition time = 5 minutes. A 3D-FLAIR sequence was performed on the basis of previously reported parameters.¹⁴ In short, we used the following parameters: FOV = 190 mm, section thickness = 0.8 mm, TR = 6000 ms, TE = 177 ms, number of excitations = 1, TI = 2000 ms, flip angle = 180°, matrix = 384 × 384, bandwidth = 213 Hz/pixel, turbo factor = 28, voxel size = 0.5 × 0.5 × 0.8 mm, and acquisition time = 14 minutes.

MR Imaging Analysis

Images were analyzed using IntelliSpace PACS, Version 4.4 (Philips Healthcare, Best, the Netherlands). Images were scored for hydrops and visual signal intensity of the basal cochlear turn by 2 neuroradiologists (S.H. and O.D.V. with, respectively, 5 and 6 years of experience in MR imaging interpretation), independently and blinded to the clinical evaluation. EH was scored for the cochlea and vestibule separately using the 3 categories described by Barath,⁶ none, grade I (moderate), or grade II (severe). In addition to this grading system, a dilated saccule not confluent with the utricle was considered a mild isolated vestibular hydrops, according to a recently published modified scoring system.^{12,14} EH was considered present when either or both the cochlea and vestibule were affected (Fig 1).

The postcontrast signal intensity of the basal cochlear turn on 3D-FLAIR images was scored both visually and quantitatively. Visually increased enhancement was defined as higher signal intensity compared with the contralateral ear or as matching the visual intensity level of patients with acute blood-labyrinth barrier breakdown/acute inflammation as shown in Fig 2. Quantitative signal intensity was scored by 1 of the authors (L.M.H.d.P.) and was calculated as the signal intensity ratio (SIR) with an oval symmetric ROI measurement in the basal cochlear turns divided by a reference measurement of 0.5 cm² in the left middle cerebellar peduncle using the multiplanar reformation (Fig 3). Shi et al¹⁵ and Tagaya et al¹⁶ used the cerebellar hemispheres as a reference measurement, whereas Yamazaki et al¹⁷ used the medulla oblongata. In the present study, we evaluated the homogeneity of the left middle cerebellar peduncle, cerebellar hemisphere, pons, and temporal muscle (data not shown). The former proved to be the most consistent and was accordingly used as a reference to calculate the SIR.

Statistical Analysis

Interobserver agreement between clinicians and neuroradiologists was calculated using the Cohen κ test. The Fisher exact test was used to compare the difference in the presence of EH and visual PE between the groups. For quantitative PE analysis, a generalized estimating equation was performed. Sensitivity, specificity, positive predictive value, and negative predictive value were calculated. Among patients, a wide variability in measured PE led to the inability to quantify an absolute PE cutoff. Therefore, the added value of measured PE on EH and visual PE was calculated by adding the presence of measured PE asymmetry to the

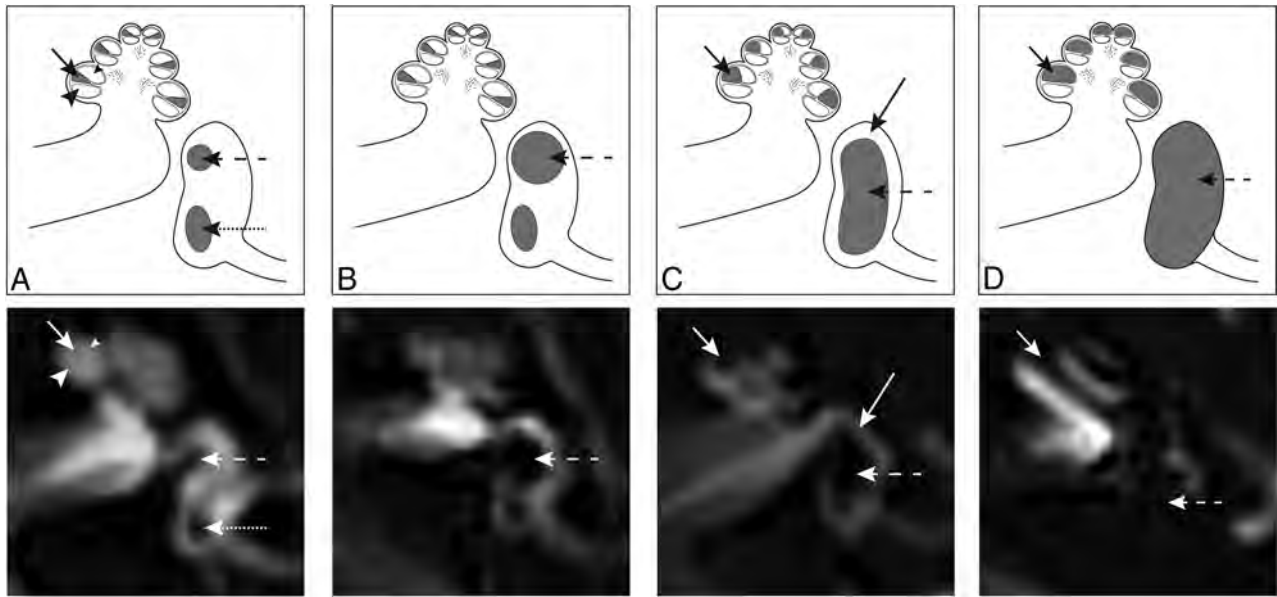


FIG 1. Axial delayed gadolinium-enhanced 3D-FLAIR MR imaging centered at the pars inferior of the vestibule, with graphic correlations. *A*, Normal labyrinth: saccule (*dashed arrow*), utricle (*dotted arrow*), scala media (*short arrow*), scala vestibuli (*small arrowhead*), and scala tympani (*large arrowhead*). *B*, Mild vestibular EH: the saccule (*dashed arrow*) is equal in size or larger than the utricle, but not confluent. *C*, Moderate vestibular EH with confluence of the saccule and utricle that encompasses >50% of the vestibule (*dashed arrow*). A rim of surrounding perilymph remains visible (*long arrow*). Moderate cochlear EH with dilation of the scala media (*short arrow*), resulting in partial obliteration of the scala vestibuli. *D*, Severe vestibular EH with total effacement of the perilymphatic space in the vestibule (*dashed arrow*). Severe cochlear EH with complete obliteration of the scala vestibuli (*short arrow*).

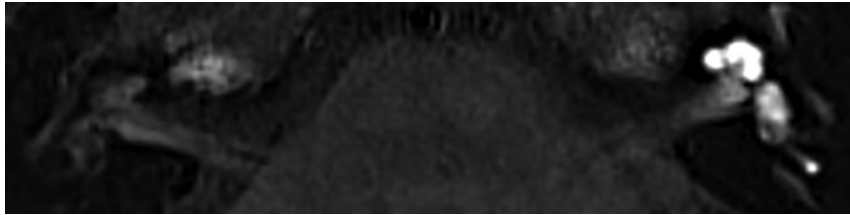


FIG 2. Axial 3D-FLAIR image 4 hours after intravenous gadolinium at the midcochlear level in a patient with unilateral left-sided sudden deafness, showing diffuse perilymphatic enhancement in the cochlea and vestibule.

equation in patients with unilateral definite MD. The other VAIEP group is considered a control group unless specifically stated otherwise. A P value < .05 was considered significant.

RESULTS

Two hundred twenty consecutive patients from the outpatient clinic were included (127 women and 93 men; median age, 55.8 years; range, 21.5–83.2 years; median duration of sickness, 3.0 years; range, 0.005–43.0 years). Seven patients were excluded from analysis due to a prior surgical history ($n = 2$), an insufficient medical record ($n = 3$), and technically inadequate MR imaging ($n = 2$).

In this cohort, 19 patients were diagnosed with bilateral definite MD; 111, with unilateral definite MD (of which 5 with a contralateral other VAIEP ear); 2, with bilateral probable MD; 10, with unilateral probable MD (of which 2 with a contralateral other VAIEP ear); 43, with bilateral ears with other VAIEP; and 35, with unilateral ears with other VAIEP. Definite diagnoses of other VAIEP ears not attributable to MD are listed in Table 1.

The interobserver agreement among the clinicians to assess the diagnosis and among the neuroradiologists to assess PE and EH is shown in Table 2.

The presence of EH in the 4 patient categories is shown in Table 3. This results in a sensitivity of 0.92 and specificity of 0.93 for definite MD ears compared with other VAIEP ears (Table 4). The MD ears (probable and definite combined) showed a sensitivity of 0.90 and specificity of 0.93, whereas the probable MD ears alone demonstrated a sensitivity and specificity of, respectively, 0.64 and 0.93. No significant differences in EH were found between the asymptomatic ears and the other VAIEP ears (respectively, 4.7% and 7.0%; Fisher exact test, $P = .45$).

The results of visually scored PE in different groups are listed in Table 3. Increased PE was more prevalent in definite and probable MD ears compared with other VAIEP ears (respectively, $P < .001$ and $P = .003$) and asymptomatic ears (both, $P < .001$).

In addition, a significant difference was found in the presence of PE in other VAIEP ears compared with asymptomatic ears ($P < .05$) as illustrated in Fig 2.

The results of the quantitative measurements of PE are shown in Table 5. The SIR of the clinically affected definite MD ears showed an increased PE of the basal cochlear turn compared with other VAIEP ears ($P < .001$). The probable MD ears showed no differences in the SIR compared with other VAIEP ears ($P = .17$) and definite MD ears ($P = .06$).

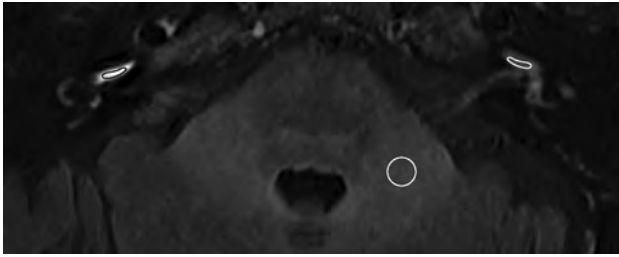


FIG 3. Axial 3D-FLAIR image 4 hours after intravenous gadolinium at the level of the basal cochlear turn of a patient with unilateral right-sided definite MD and a visually increased perilymphatic enhancement. The basal cochlear turn (oval) and the left middle cerebellar peduncle (circle) indicate the region of interest to calculate the SIR.

Table 1: Clinical diagnosis of ears with other VAIEP

Clinical Diagnosis	Ears (n = 128) (%)
Autoimmune inner ear disease	2 (1.6)
Benign paroxysmal positional vertigo	6 (4.7)
Cochlear migraine	1 (0.8)
Fluctuating low-to-medium frequency sensorineural hearing loss eci	3 (2.3)
Focal monostotic fibrous dysplasia	1 (0.8)
Hyperventilation	14 (10.9)
Labyrinthitis	1 (0.8)
Migraine	3 (2.3)
Presbycusis	10 (7.8)
Schwannoma	1 (0.8)
Sudden deafness	10 (7.8)
Tinnitus eci	1 (0.8)
Vertigo eci	43 (33.6)
Vestibular migraine	24 (18.8)
Vestibular neuritis	8 (6.3)

Note:—eci indicates e causa ignota (Latin for no cause found).

Table 2: Interobserver agreement

	κ (95% CI)
Clinicians	0.81 (0.73–0.88)
Neuroradiologists	
EH (cochlear and/or vestibular)	0.92 (0.88–0.97)
Cochlear hydrops	0.93 (0.89–0.98)
Vestibular hydrops	0.92 (0.87–0.97)
PE visual	0.90 (0.85–0.96)

Four patients with unilateral definite MD showed no evidence of EH. In addition, the quantified PE was not increased in the clinically affected ear compared with the contralateral asymptomatic ear. Six of the 10 patients with unilateral definite MD with EH but without visually increased PE showed an increased measured PE in their symptomatic ear compared with their asymptomatic ear.

The combination of EH and visually increased PE was present in 81.9% of the definite MD ears, whereas it was seen in only 3.1% of the ears with other VAIEP ($P < .001$). Consequently, this combination increased the specificity in definite MD from 0.93 to 0.97 compared with EH alone (positive predictive value from 0.94 to 0.97 and decreased the negative predictive value from 0.91 to 0.82 and sensitivity from 0.92 to 0.82). The sensitivity increased to 0.86 when measured PE was added as shown in Table 4. The combination of EH and visually increased PE was seen in 42.9% of the

probable MD ears, resulting in a sensitivity of 0.43 and specificity of 0.97.

The 4 ears with other VAIEP that demonstrated the combination of EH and PE were diagnosed with vestibular migraine ($n = 3$) and autoimmune inner ear disease ($n = 1$).

DISCUSSION

The present study shows that EH and increased PE are frequently present in patients with MD, whereas this combination is uncommon in patients with other VAIEP. Furthermore, the study emphasizes the relevance of EH as a hallmark of definite MD because vestibular or cochlear EH or both were present in 91.9% of the definite MD ears. This finding is in concordance with previously published studies with an EH prevalence ranging from 95% to 96%.^{6,15} In our dataset, EH is seen in only 4.7% of the asymptomatic ears, whereas percentages of 6% and 22% have been documented in contralateral MD ears in other studies.^{6,8} Even in patients with other VAIEP, a clinically relevant group, EH was demonstrated in only 7% of symptomatic ears. This finding is in line with previously published prevalence data in healthy control ears by Ito et al,⁸ in which EH (vestibular or cochlear) was present in 10% of the ears.

Recent studies suggest that vestibular hydrops is more specific for MD than cochlear hydrops.^{18,19} In our study, isolated EH (vestibular or cochlear) is a relatively scarce finding, though isolated vestibular hydrops is more pronounced in the definite MD group. Attyé et al¹² demonstrated that half of patients with MD presented with inversion of the saccule-to-utricle ratio, whereas this was not present in the healthy subjects. This finding is in concordance with a recent published study by Shi et al.¹³ They showed that vestibular hydrops is more common in patients with definite MD compared with cochlear hydrops,¹³ though saccular hydrops may be a reflection of sensorineural hearing loss rather than MD.^{20,21} MR imaging evaluation of EH is robust, reflected in a high interobserver agreement ranging from 0.92 for the vestibule to 0.93 for cochlear findings (normal and abnormal). This level of agreement is higher than the clinical interobserver agreement to assess the diagnosis, which is in line with a previously published study.¹⁴

The definite MD ears showed increased PE both visually and in quantitative measurements compared with asymptomatic ears. This is in concordance with previously published studies, though references for the signal intensity ratio are different. Shi et al¹⁵ and Tagaya et al¹⁶ used the cerebellar hemispheres and found a difference in the SIR in the affected ear compared with the contralateral ear in patients with MD, whereas Yamazaki et al¹⁷ used the medulla oblongata. In our study, the left middle cerebellar peduncle was used as a reference to calculate the SIR.

The ears with other VAIEP showed an increased PE compared with asymptomatic ears. According to Kim et al,²² increased PE was also seen on the affected side with sudden sensorineural hearing loss and vestibular neuritis compared with the unaffected side. This finding shows that increased PE is a marker of disease activity in the inner ear, rather than exclusively seen in definite MD. Therefore, PE alone cannot be used to distinguish a definite MD ear from an ear with other VAIEP.

Table 3: Presence of EH and PE^a

	Definite MD (n = 149) (%)	Probable MD (n = 14) (%)	Asymptomatic (n = 149) (%)	Other VAIEP (n = 128) (%)
EH	137 (91.9) ^b	9 (64.3) ^b	7 (4.7) P = .45	9 (7.0)
Vestibular EH	133 (89.3) ^b	9 (64.3) ^b	7 (4.7) NS	8 (6.3)
Cochlear EH	126 (84.6) ^b	8 (57.1) ^b	3 (2.0) NS	4 (3.1)
Isolated vestibular EH	11 (7.4) NS	1 (7.1) (P = .47)	4 (2.7) NS	5 (3.9)
Isolated cochlear EH	4 (2.7) NS	0 (0.0) NS	0 (0.0) NS	1 (0.8)
PE	123 (82.6) ^b	6 (42.9) (P = .003)	5 (3.4) P = .045	12 (9.4)
PE and hydrops	122 (81.9) ^b	6 (42.9) ^b	2 (1.3) P = .42	4 (3.1)
PE and vestibular EH	119 (79.9) ^b	6 (42.9) ^b	2 (1.3) P = .42	4 (3.1)
PE and cochlear EH	118 (79.2) ^b	6 (42.9) ^b	2 (1.3) NS	3 (2.3)

Note:—NS indicates not significant.

^a PE is scored visually.

^b P < .001 (Fisher Exact) compared with other VAIEP ears.

Table 4: Sensitivity, specificity, PPV, and NPV in definite MD ears

	Sensitivity	Specificity	PPV	NPV
EH	0.92	0.93	0.94	0.91
PE	0.83	0.91	0.91	0.82
EH + PE visual	0.82	0.97	0.97	0.82
EH + PE visual or measured	0.86	0.97	0.97	0.86

Note:—PPV indicates positive predictive value; NPV, negative predictive value.

Table 5: Generalized estimating equation for the mean SIR of PE with other VAIEP as a reference category

	B	SE	P Value
Intercept	1.094	0.0282	P < .001
Definite MD	0.550	0.0590	P < .001
Probable MD	0.221	0.1603	P = .167
Asymptomatic	0.218	0.0844	P = .010

Note:—SE indicates standard error; B, beta coefficient.

In patients with other VAIEP, the combination of EH and PE is seen in only 3.1% of the ears. This shows that this combination could play an essential role in diagnosing MD in this clinically relevant group. For example, an increased PE is seen in ears with idiopathic sensorineural hearing loss,²³ whereas the detection of EH is higher in MD compared with sudden deafness²⁴ or not even demonstrated at all.²⁵

Our results demonstrate that PE measurements have an additional value compared with a visual score because the sensitivity increases from 0.82 to 0.86 when measured PE is added to EH, combined with visually scored PE.

The 4 patients with unilateral definite MD without EH showed no increased measured PE. However, 1 patient demonstrated an asymmetric visual PE in the vestibule with nonvisualization of the saccule, which is presumed to be the result of an intralabyrinthine fistula.²⁶

Most interesting, 3 of the 4 ears with other VAIEP that showed both EH and PE were diagnosed with vestibular migraine, though this diagnosis as a separate clinical entity is under debate.²⁷ However, with the current clinical criteria, it remains difficult to distinguish MD from vestibular migraine. This difficulty is in concordance with previously published studies suggesting that they share similar pathophysiological mechanisms³ or that describe a group of patients who fulfill both diagnostic criteria.²⁸

Bernaerts et al¹⁴ demonstrated that the 2 most distinctive characteristics to distinguish MD ears from asymptomatic ears are cochlear PE and vestibular EH. Our study confirms that the combination of EH (vestibular or cochlear) and PE is distinctive for definite MD and shows, in addition, that this combination is rarely present in the ears with other VAIEP. Furthermore, PE alone cannot be used to distinguish a definite MD ear from an ear with other VAIEP.

The retrospective design of the conducted study hampers the potential to correlate the imaging findings with clinical parameters (attack frequency and time interval of last attack relative to imaging) and assess their relation with the severity of EH in the current grading systems. Furthermore, the group with other VAIEP, though clinically relevant, shows heterogeneous patient characteristics. This feature hampers the possibility to draw conclusions within this group. Another limitation is the presumption that a contralateral ear of a patient with definite MD, probable MD, and other VAIEP is considered healthy and is added to the group with asymptomatic ears.

Practical Use of MR Imaging in (Suspected) Ménière Disease

Previous studies have mainly focused on identifying inner ear abnormalities on 3D-FLAIR MR imaging by comparing symptomatic and asymptomatic ears in patients with MD.^{6,14,16-18} These studies showed MR imaging to be highly sensitive and specific in discriminating the affected ear in patients with MD. However, considering the variable spectrum of clinical presentations in MD, a comparison with patients with other VAIEP seems relevant.^{9,29} The present study demonstrates the value of delayed gadolinium-enhanced 3D-FLAIR MR imaging in diagnosing MD in a cohort with a wide range of vertigo-associated inner ear diseases and shows that the combination of EH and increased PE is uncommon in patients with other VAIEP; this finding could be of particular relevance in patients in whom an atypical clinical presentation hampers a definite diagnosis, as is the case with probable MD. Although the number of patients with probable MD in our cohort is limited, 43% of these patients demonstrated the combination of EH and increased PE. On the basis of our study results, this finding suggests a (definite) MD diagnosis, which may alter treatment strategies. However, longitudinal research is necessary to evaluate clinical progression to definite MD.

In 20% of patients with MD, the vestibular and cochlear symptoms coincide after >5 years, resulting in diagnostic delay.⁹ Moreover, the lower interobserver agreement in the diagnoses of the clinicians compared with the hydrops scoring of neuroradiologists reflects the additional value of imaging.

Even in patients with evident, clinically definite MD, imaging is helpful in the evaluation of hydrops when conservative treatment fails, or in assessing possible bilateral hydropic disease (with unilateral symptoms) before considering, for example,

sacrificing 1 ear with a destructive inner ear operation in selected cases.^{30,31}

CONCLUSIONS

The combined presence of EH and increased PE is associated with the clinical diagnosis of definite MD and not with other VAIEP. These findings may help to differentiate patients with vertigo attributable to MD.

ACKNOWLEDGMENTS

The authors thank Vera de Pont and Anne de Bokx for their assistance in preparing the graphics.

Disclosures: Berit M. Verbit—UNRELATED: Payment for Lectures Including Service on Speakers Bureaus: Bayer Pharmaceuticals. Sebastiaan Hammer—RELATED: Grant: Dutch Society of Radiology. Comments: A grant was awarded to assess the technical feasibility of MRI-evaluated endolymphatic hydrops and allow development of optimizing imaging techniques.

REFERENCES

1. Lopez-Escamez JA, Carey J, Chung WH, et al; Korean Balance Society. **Diagnostic criteria for Ménière's disease.** *J Vestib Res Equilib Res* 2015;25:1–7 CrossRef Medline
2. Nakashima T, Pyykkö I, Arroll MA, et al. **Ménière's disease.** *Nat Rev Dis Primer* 2016;2:16028 CrossRef Medline
3. Pyykkö I, Manchaiah V, Färkkilä M, et al. **Association between Ménière's disease and vestibular migraine.** *Auris Nasus Larynx* 2019;46:724–33 CrossRef Medline
4. Neff BA, Staab JP, Eggers SD, et al. **Auditory and vestibular symptoms and chronic subjective dizziness in patients with Ménière's disease, vestibular migraine, and Ménière's disease with concomitant vestibular migraine.** *Otol Neurotol* 2012;33:1235–44 CrossRef Medline
5. Cairns H, Hallpike F. **Observations on the pathology of Meniere's syndrome.** *Proc R Soc Med* 1938;31:1317–36 Medline
6. Barath K. **Detection and grading of endolymphatic hydrops in Meniere disease using MR imaging.** *AJNR Am J Neuroradiol* 2014; 35:1387–92 CrossRef Medline
7. Naganawa S, Nakashima T. **Visualization of endolymphatic hydrops with MR imaging in patients with Ménière's disease and related pathologies: current status of its methods and clinical significance.** *Jpn J Radiol* 2014;32:191–204 CrossRef Medline
8. Ito T, Kitahara T, Inui H, et al. **Endolymphatic space size in patients with Meniere's disease and healthy controls.** *Acta Otolaryngol* 2016;136:879–82 CrossRef Medline
9. Pyykkö I, Nakashima T, Yoshida T, et al. **Ménière's disease: a reappraisal supported by a variable latency of symptoms and the MRI visualisation of endolymphatic hydrops.** *BMJ Open* 2013;3:e001555–10 CrossRef Medline
10. Nakada T, Yoshida T, Suga K, et al. **Endolymphatic space size in patients with vestibular migraine and Ménière's disease.** *J Neurol* 2014;261:2079–84 CrossRef Medline
11. Gürkov R, Hornibrook J. **On the classification of hydropic ear disease (Ménière's disease).** *HNO* 2018;66:455–63 CrossRef Medline
12. Attyé A, Eliezer M, Boudiaf N, et al. **MRI of endolymphatic hydrops in patients with Meniere's disease: a case-controlled study with a simplified classification based on saccular morphology.** *Eur Radiol* 2017;27:3138–46 CrossRef Medline
13. Shi S, Zhou F, Wang W. **3D-real IR MRI of Meniere's disease with partial endolymphatic hydrops.** *Am J Otolaryngol* 2019;40:589–93 CrossRef Medline
14. Bernaerts A, Vanspauwen R, Blaivie C, et al. **The value of four stage vestibular hydrops grading and asymmetric perilymphatic enhancement in the diagnosis of Ménière's disease on MRI.** *Neuroradiology* 2019;61:421–29 CrossRef Medline
15. Shi S, Guo P, Wang W. **Magnetic resonance imaging of Ménière's disease after intravenous administration of gadolinium.** *Ann Otol Rhinol Laryngol* 2018;127:777–82 CrossRef Medline
16. Tagaya M, Yamazaki M, Teranishi M, et al. **Endolymphatic hydrops and blood-labyrinth barrier in Ménière's disease.** *Acta Otolaryngol* 2011;131:474–79 CrossRef Medline
17. Yamazaki M, Naganawa S, Tagaya M, et al. **Comparison of contrast effect on the cochlear perilymph after intratympanic and intravenous gadolinium injection.** *AJNR Am J Neuroradiol* 2012;33:773–78 CrossRef Medline
18. Li X, Wu Q, Sha Y, et al. **Gadolinium-enhanced MRI reveals dynamic development of endolymphatic hydrops in Ménière's disease.** *Braz J Otorhinolaryngol* 2018 Dec 20. [Epub ahead of print] CrossRef Medline
19. Yoshida T, Sugimoto S, Teranishi M, et al. **Imaging of the endolymphatic space in patients with Ménière's disease.** *Auris Nasus Larynx* 2018;45:33–38 CrossRef Medline
20. Attyé A, Eliezer M, Medici M, et al. **In vivo imaging of saccular hydrops in humans reflects sensorineural hearing loss rather than Meniere's disease symptoms.** *Eur Radiol* 2018;28:2916–22 CrossRef Medline
21. Sepahdari AR, Ishiyama G, Vorasubin N, et al. **Delayed intravenous contrast-enhanced 3D FLAIR MRI in Meniere's disease: correlation of quantitative measures of endolymphatic hydrops with hearing.** *Clin Imaging* 2015;39:26–31 CrossRef Medline
22. Kim TY, Park DW, Lee YJ, et al. **Comparison of inner ear contrast enhancement among patients with unilateral inner ear symptoms in MR images obtained 10 minutes and 4 hours after gadolinium injection.** *AJNR Am J Neuroradiol* 2015;36:2367–72 CrossRef Medline
23. Pakdaman MN, Ishiyama G, Ishiyama A, et al. **Blood-labyrinth barrier permeability in Meniere disease and idiopathic sudden sensorineural hearing loss: findings on delayed postcontrast 3D-FLAIR MRI.** *AJNR Am J Neuroradiol* 2016;37:1903–08 CrossRef Medline
24. Horii A, Osaki Y, Kitahara T, et al. **Endolymphatic hydrops in Meniere's disease detected by MRI after intratympanic administration of gadolinium: comparison with sudden deafness.** *Acta Otolaryngol* 2011;131:602–09 CrossRef Medline
25. Tagaya M, Teranishi M, Naganawa S, et al. **3 Tesla magnetic resonance imaging obtained 4 hours after intravenous gadolinium injection in patients with sudden deafness.** *Acta Otolaryngol* 2010;130:665–69 CrossRef Medline
26. Attyé A, Eliezer M, Galloux A, et al. **Endolymphatic hydrops imaging: differential diagnosis in patients with Meniere disease symptoms.** *Diagn Interv Imaging* 2017;98:699–706 CrossRef Medline
27. Phillips J, Longridge N, Mallinson A, et al. **Migraine and vertigo: a marriage of convenience?** *Headache* 2010;50:1362–65 CrossRef Medline
28. Tabet P, Saliba I. **Ménière's disease and vestibular migraine: updates and review of the literature.** *J Clin Med Res* 2017;9:733–44 CrossRef Medline
29. Rauch SD. **Clinical hints and precipitating factors in patients suffering from Meniere's disease.** *Otolaryngol Clin North Am* 2010;43: 1011–17 CrossRef Medline
30. Gluth MB. **On the relationship between Ménière's disease and endolymphatic hydrops.** *Otol Neurotol* 2020;41:242–49 CrossRef Medline
31. Da Costa SS, De Sousa LCA, De Toledo Piza MR. **Ménière's disease: overview, epidemiology, and natural history.** *Otolaryngol Clin North Am* 2002;35:455–95 CrossRef Medline

Fractional Flow on TOF-MRA as a Measure of Stroke Risk in Children with Intracranial Arterial Stenosis

A.Y. Ibrahim, A. Amirabadi, M.M. Shroff, N. Dlamini, P. Dirks, and P. Muthusami

ABSTRACT

BACKGROUND AND PURPOSE: Conventional angiography is the criterion standard for measuring intracranial arterial stenosis. We evaluated signal intensity ratios from TOF-MRA as a measure of intracranial stenosis and infarct risk in pediatric stroke.

MATERIALS AND METHODS: A retrospective study was undertaken in children with intracranial arterial stenosis, who had TOF-MRA and conventional angiography performed within 6 months. Arterial diameters were measured for percentage stenosis. ROI analysis on TOF-MRA measured signal intensity in pre- and poststenotic segments, with post-/pre-signal intensity ratios calculated. The Pearson correlation was used to compare percentage stenosis on MRA with conventional angiography and signal intensity ratios with percentage stenosis; the point-biserial correlation was used for infarcts compared with percentage stenosis and signal intensity ratios. Sensitivity, specificity, and positive and negative predictive values were calculated for determining severe ($\geq 70\%$) stenosis from MRA and signal intensity ratios against the criterion standard conventional angiography. $P < .05$ was considered statistically significant.

RESULTS: Seventy stenotic segments were found in 48 studies in 41 children (median age, 11.0 years; range, 5 months to 17.0 years; male/female ratio, 22:19): 20/41 (48.8%) bilateral, 11/41 (26.8%) right, and 10/41 (24.4%) left, with the most common site being the proximal middle cerebral artery (22/70, 31%). Moyamoya disease accounted for 27/41 (65.9%). Signal intensity ratios and conventional angiography stenosis showed a moderate negative correlation ($R = -0.54$, $P < .001$). Receiver operating characteristic statistics showed an area under the curve of 0.86 for using post-/pre-signal intensity ratios to determine severe ($\geq 70\%$) carotid stenosis, yielding a threshold of 1.00. Sensitivity, specificity, and positive and negative predictive values for severe stenosis were the following—MRA: 42.8%, 58.8%, 30.0%, and 71.4%; signal intensity ratio > 1.00 : 97.1%, 77.8%, 71.7%, and 97.4%; combination: 75.5%, 100%, 100%, and 76.8%, respectively. Signal intensity ratios decreased with increasing grade of stenosis (none/mild-moderate/severe/complete, $P < .001$) and were less when associated with infarcts (0.81 ± 0.52 for arteries associated with downstream infarcts versus 1.31 ± 0.55 for arteries without associated infarcts, $P < .001$).

CONCLUSIONS: Signal intensity ratios from TOF-MRA can serve as a noninvasive measure of intracranial arterial stenosis and allow identification of high-risk lesions in pediatric stroke.

ABBREVIATIONS: CA = conventional angiography; SI = signal intensity

Stroke in children is 1 of the top 10 causes of death in childhood.^{1,2} The incidence of all strokes in children is reported to be 2–13 per 100,000 person-years in developed countries.^{3–6}

Received August 16, 2019; accepted after revision January 4, 2020.

From the Department of Diagnostic Imaging (A.Y.I., A.A., M.M.S., P.M.), Division of Neurology (N.D.) and Division of Neurosurgery (P.D.), Department of Surgery, The Hospital for Sick Children, University of Toronto, Toronto, Ontario, Canada; and Department of Clinical Sciences (A.Y.I.), Faculty of Medicine, Yarmouk University, Irbid, Jordan.

The study was approved by the Institutional Research Ethics Board with REB 1000062860. Written informed consent was obtained from all patients/parents prior to the procedures.

Please address correspondence to Ala' Y. Ibrahim, MD, Department of Clinical Sciences, Faculty of Medicine, Yarmouk University, P.O. Box 566, 21163 Irbid, Jordan; e-mail: dr.alaa_yonis@yahoo.com; @Ala_Y_Ibrahim

<http://dx.doi.org/10.3174/ajnr.A6441>

Childhood arteriopathies are the most common identifiable cause of arterial ischemic stroke, accounting for up to two-thirds of cases in a previously healthy child.^{7–11} The most common causes of intracranial arterial steno-occlusive disease in children are Moyamoya disease, focal dissection, transient cerebral arteriopathy, and post-varicella arteriopathy,^{12–14} though a number of other syndromic and nonsyndromic associations exist.¹⁵

Stroke in children is commonly assessed and followed by MR imaging, which is noninvasive and free of ionizing radiation.¹² Vascular assessment is commonly performed using TOF-MRA, which gives a global assessment of vascular disease. However, TOF-MRA is amenable to several artifacts resulting from the inherent technique and is known to overestimate stenotic lesions while undervaluing arteries that are severely affected.^{16–18}

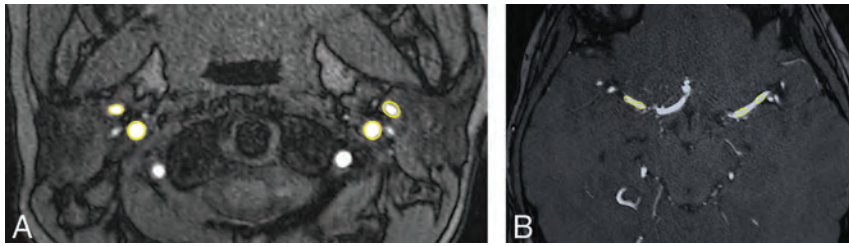


FIG 1. Measurement of arterial signal intensity from TOF-MRA using ROI analysis. A, Prestenotic ROI. B, Poststenotic ROI.

Often, for further clarification of equivocal findings, contrast-enhanced MR imaging or CT angiography is performed, though these too have certain drawbacks. Conventional angiography (CA) remains the criterion standard test to diagnose intracranial arterial stenosis and accurately quantify severity.¹⁹⁻²¹ This is, however, an invasive test, using ionizing radiation and requires general anesthesia in most children and a dedicated pediatric neuroangiographic service to maximize safety.

The signal intensity (SI) within arteries on TOF-MRA is dependent on the number of moving spins and the velocity of blood flow and thus has the potential to noninvasively assess the downstream effect of arterial stenosis. Ratios derived from SI on TOF-MRA have been shown to correlate with cerebral perfusion as measured by CT perfusion and SPECT in adults with intracranial carotid stenosis.^{22,23} It is not known whether arterial SI ratios measured from TOF-MRA can accurately estimate the degree of intracranial carotid stenosis as measured on conventional angiography in children presenting with stroke and whether these ratios can help identify high-risk lesions. We hypothesized the following: 1) SI ratios calculated from TOF-MRA are significantly correlated with percentage stenosis measured from conventional angiography, 2) SI ratios calculated from TOF-MRA are significantly correlated with infarct burden, and 3) SI ratios serve as stronger predictors of severe (>70%) intracranial arterial stenosis than stenosis measured from TOF-MRA.

MATERIALS AND METHODS

Subjects and Imaging

An institutional review board–approved retrospective study was undertaken on children 18 years of age or younger with an imaging diagnosis of intracranial carotid artery stenosis at our tertiary pediatric institution (The Hospital for Sick Children) between January 1, 2000, and November 10, 2018. The need for individual consent for this retrospective review was waived by the Institutional Research Ethics Board. A keyword search was performed on the radiology departmental data base to identify all studies reported with intracranial arterial stenosis. Studies were included that had both TOF-MRA and conventional angiography performed within 6 months of each other. Patients with tandem lesions (ie, 2 noncontiguous stenotic lesions), those with MRA and conventional angiography performed more than 6 months apart, and patients with suboptimal imaging quality resulting in unreliable SI or stenosis measurement were excluded.

MR imaging was performed on a 1.5T magnet (Achieva; Philips Healthcare, Best, the Netherlands) or a 3T magnet (Magnetom Skyra; Siemens, Erlangen, Germany, or Achieva) with a 32-channel transmit-receive head coil. The examination included standard T1-, T2-, and FLAIR-weighted sequences, followed by TOF-MRA with the following parameters—1.5T MRA: TR/TE = 25/6.91 ms, flip angle = 20°, bandwidth = 109 Hz, FOV = 18 cm, spatial resolution = 0.70 × 0.90 × 1.0 mm (interpolated to 0.5 × 0.5 × 0.5 mm), 1-mm section thickness with 0.5-mm overlap; 3T MRA: TR/TE = 25/3.81 ms, flip angle = 18°, bandwidth = 186 Hz, FOV = 18 cm, spatial resolution = 0.40 × 0.70 × 1.0 mm (interpolated to 0.5 × 0.5 × 0.5 mm), 1.0-mm section thickness with 0.5-mm overlap. Conventional angiography was performed by 1 of 2 interventional neuroradiologists (P.M. or M.M.S.) in a biplane neuroangiography suite (Artis Q; Siemens). All procedures were performed with the patient under general anesthesia through femoral artery access and systemic heparinization using a 4F diagnostic catheter with standard projections and an iodinated contrast agent (iohexol, Omnipaque 300 mg I/mL; GE Healthcare, Piscataway, New Jersey) injected through a power injector at 3–5 mL/s, depending on the age and arterial size.

Data Analysis and Image Processing

Images and reports were analyzed by a fellowship-trained pediatric neuroradiologist (A.Y.I.), with discrepancies resolved by the senior author (P.M.). Electronic chart review and image analysis on the PACS system were performed for included patients to collect the following data: demographics (age at diagnosis, sex), time interval between MRA and conventional angiography, laterality of stenosis (right/left/bilateral), specific location/segment of artery involved (petrous ICA, cavernous ICA, paraclinoid ICA, pre-communicating ICA, terminal ICA, postbifurcation), any ischemic events regardless of the association with the territory of the stenotic lesion, and any ischemic or hemorrhagic events not associated with the stenotic lesion. Stenosis was regarded as symptomatic if ischemic lesions on MR imaging were territorially consistent with the stenotic lesion. Downstream infarcts were defined as any abnormal bright T2/FLAIR lesions in the vascular distribution of the stenotic segment without mass effect.

Arterial diameters were measured to assess the percentage of ICA stenosis on MRA and CA. The percentage stenosis on MRA and catheter cerebral angiography was measured as described previously.²⁴ In summary, percentage stenosis of an intracranial artery is $[(1 - (D_{\text{stenosis}} / D_{\text{normal}}))] \times 100$, where D_{stenosis} is the diameter of the ICA at the maximally stenotic segment and D_{normal} is the diameter of the most adjacent proximal normal artery (usually the petrous ICA). If the proximal segment was diseased, contingency sites were chosen to measure D_{normal} : the most adjacent nondiseased distal artery (second choice, usually the terminal ICA); if the entire intracranial artery was diseased, the most distal, parallel, nontortuous normal segment was measured (third choice). ROI analysis was performed to measure intravascular SI

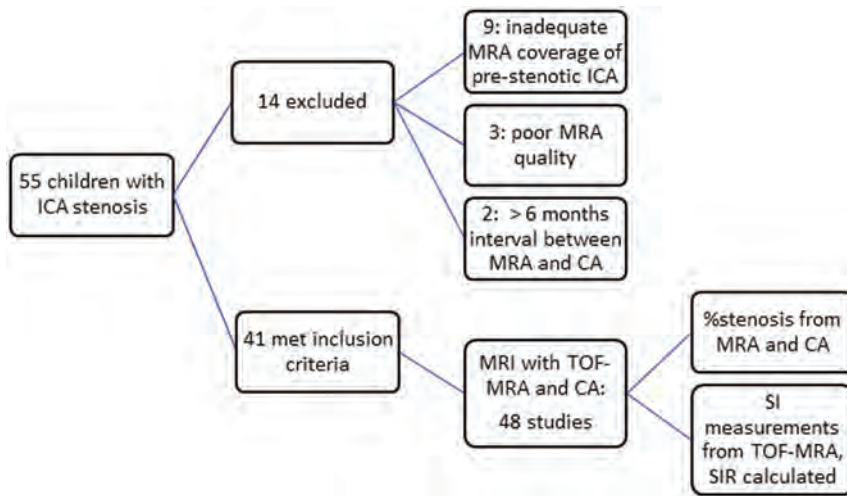


FIG 2. Flow chart showing patient selection for our study. SIR indicates signal intensity ratios.

Table 1: Sites of intracranial arterial stenosis in our cohort (n = 70 stenotic segments)

Sites	
Right	14
Left	12
Bilateral	22
Associated with infarct	36/70 (51.4%)
Specific location	
Cervical and petrous	4 (6%)
Cavernous	3 (4%)
Postclinoid	20 (29%)
Postcommunicating and terminal	21 (30%)
Postterminal (A1 ACA or M1 MCA)	22 (31%)

Note:—ACA indicates anterior cerebral artery.

Table 2: Underlying diagnosis in our cohort of children with stroke and intracranial arterial stenosis (n = 41)

Clinical Diagnosis	No.
Moyamoya disease	15
Neurofibromatosis type 1 with Moyamoya	6
Trisomy-21 with Moyamoya	3
Dissection	2
Primary CNS vasculitis	3
Varicella vasculitis	2
TCA	3
Sickle cell disease with Moyamoya	3
Other	
Systemic large vessel vasculitis	1
Hemolytic uremic syndrome	1
Thalassemia with Moyamoya	1
Hurler syndrome	1

Note:—TCA indicates transient cerebral arteriopathy.

from TOF-MRA. ROIs were manually drawn on TOF-MRA axial source images (Fig 1). The upper cervical ICA SI was measured at approximately the C2 vertebral level for the prestenotic segment (henceforth, SI-ICA-pre) and from the MCA for the poststenotic segment (henceforth, SI-ICA-post). Each SI-ICA value was measured as the mean of 2 ROIs drawn on adjacent axial sections or adjacent arterial segments with no overlap of ROIs. Ratios of SI were calculated, as SI-post/SI-pre-stenosis.

Statistical Analysis

Categorical variables were expressed as number and percentage; continuous variables were expressed as median and range. For statistical purposes, stenosis was graded as follows: none (0%), mild (<50%), moderate (50%–69%), severe (70%–99%), and complete (100%), as previously described.²⁴ Correlations of percentage stenosis on MRA with percentage stenosis on conventional angiography and with SI ratios were performed using the Pearson correlation; the presence of infarcts and the development of new infarcts were compared with percentage stenosis and SI ratios using a point-biserial correlation. Receiver operating characteristic curve analysis was performed on SI ratios as a determinant

of percentage stenosis (from CA), from which the area under the curve and threshold value were obtained. Sensitivity, specificity, positive predictive value, and negative predictive value for determining severe ($\geq 70\%$) stenosis by MRA and SI ratios were calculated, with conventional angiography percentage stenosis as the criterion standard. A *P* value < .05 was considered statistically significant. All analyses were performed with SPSS (Version 25.0; IBM, Armonk, New York).

RESULTS

Of 55 children with intracranial ICA stenosis, 41 met the inclusion criteria, which resulted in 48 studies with 70 stenotic arteries and 36 associated downstream arterial infarcts. Figure 2 shows the flow chart for patient selection. The median age of our cohort was 11 years (range, 5 months to 17 years). Of these, 19/41 patients (46.3%) were girls. MR imaging was performed at 1.5T in 25/48 and 3T in 23/48 studies. Bilateral stenosis was seen in 20/41 patients (48.8%); 11/41 patients (26.8%) had stenosis on the right side only and 10/41 patients (24.4%) had stenosis on the left side only. The most common site for stenosis (Table 1) was distal to the ICA bifurcation (22/70, 31%), (ie, the MCA), followed by the terminal ICA (21/70, 30%). The most common underlying diagnosis was Moyamoya disease (alone or in association with neurofibromatosis 1, Trisomy-21, sickle cell disease, or thalassemia) accounting for nearly two-thirds of patients (27/41, 65.9%). Other diagnoses are shown in Table 2. Associated downstream infarcts were seen in 36/48 studies (75%), 24/48 (50%) had nonspecific white matter lesions, and 4/48 (8.3%) had hemorrhage.

The mean interval between MR imaging and CA was 22.7 ± 32.7 days (range, 0–123 days). Severe stenosis ($\geq 70\%$) was detected by MRA in 50/70 segments (71.4%) and by conventional angiography in 46/70 segments (65.7%) (Table 3). Although there was excellent correlation between MRA and conventional angiographic stenosis (Pearson $R = 0.93$, $P < .001$), MRA had a sensitivity, specificity, positive predictive value, and negative predictive value of 42.8%, 58.8%, 30.0%, and 71.4%, respectively,

for severe (>70%) stenosis. The severity of stenosis on MRA correlated with the infarct burden ($r_{pb} = 0.44, P < .001$). Figure 3 shows 2 relevant sample cases.

Mean ratios of SI (post/pre) were as follows: 1.58 ± 0.51 (no stenosis), 1.40 ± 0.50 (mild-moderate stenosis, <70%), 0.90 ± 0.48 (severe stenosis, 70%–99%), and 0.60 ± 0.33 (complete, 100%), with a significant difference of means by 1-way ANOVA ($P < .001$). A significant moderate negative correlation was seen between post-/prestenosis SI ratios and percentage stenosis on conventional angiography ($R = -0.54, P < .001$). Receiver operating characteristic statistics (Fig 4) showed an area under the curve of 0.86 (95% CI, 0.78–0.94) for using post-/pre-ICA SI ratios to determine severe ($\geq 70\%$) stenosis. An SI ratio of 1.00 was determined to be the threshold for obtaining maximum sensitivity and specificity for severe stenosis. By means of this SI ratio cutoff value alone and in combination with MRA percentage stenosis, the sensitivity, specificity, positive predictive value, and negative predictive value for determining severe (>70%) stenosis were 97.1%, 77.8%, 71.7%, 97.4%, and 75.5%, 100%, 100%, and 76.8%, respectively.

Table 3: ICA stenosis severity, comparison of MRA with catheter angiography evaluations (n = 96 arteries: 70 stenotic and 26 nonstenotic)

% Stenosis	Arteries on MRA (No.)	Arteries on CA (No.)
≤50	31	29
51–69	16	21
70–99	4	32
100	46	14

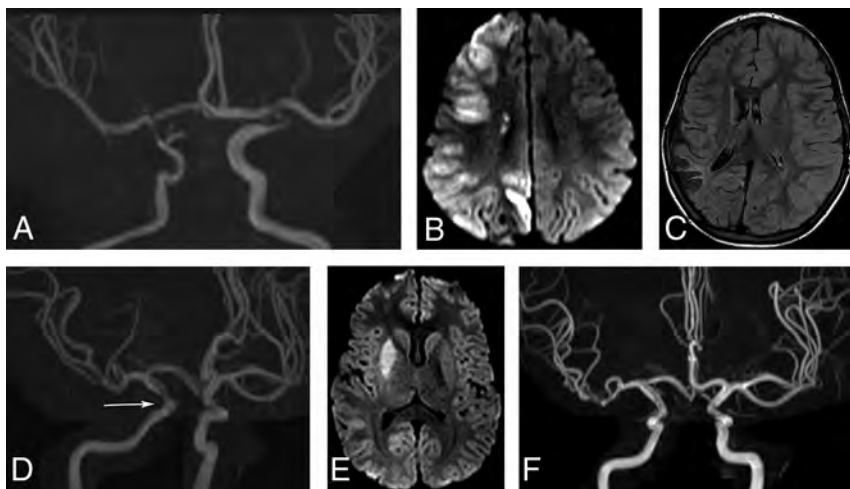


FIG 3. A–C, A 15-month-old boy with intracranial vasculopathy and bilateral intracranial arterial stenosis. A, Maximum-intensity-projection reformat from TOF-MRA shows bilateral terminal ICA stenosis, measured on MRA as right: 100%; left: 86%. SI ratios were measured as right: 1.0; left: 1.3. B, The child presented with extensive MCA territory infarct. C, MR imaging performed 5 years later. Axial FLAIR image shows no new infarcts in the left cerebral hemisphere. D–F, A 15-year-old boy with right-sided intracranial arteriopathy. D, Maximum-intensity-projection reformat from TOF-MRA shows 60% stenosis of the supraclinoid right ICA, with additional mild narrowing of the proximal A1 anterior cerebral artery and a normal appearance of the left ICA. The SI ratios were measured as right: 0.60; left: 1.3. E, The patient presented with acute infarction of the right basal ganglia. F, MRA performed 22 months later shows near-complete resolution of the supraclinoid ICA stenosis, consistent with transient cerebral arteriopathy.

There was a moderate negative correlation between the presence of infarcts and SI ratios ($r_{pb} = -0.4, P < .001$). The mean post-/pre-SI-ratio for arteries associated with downstream infarcts was 0.81 ± 0.52 , whereas for arteries without associated infarcts, it was 1.31 ± 0.55 , the difference being significant by an unpaired *t* test ($P < .001$).

DISCUSSION

There is a strong relationship between impaired hemodynamics related to intracranial arterial stenosis and increased stroke risk.¹⁹ The severity of intracranial arterial stenosis and its progression with time dictate treatment protocols and clinical decision-making, including the decision to surgically revascularize. Conventional angiography is the criterion standard for the diagnosis of the presence and severity of intracranial arterial stenosis.¹⁹ Noninvasive MR angiography and CTA have partially replaced conventional angiography, which has up to a 1% risk of stroke, a 4% risk of TIA, and nearly a 1% mortality rate.^{25–27} Additionally, in children, there are the added concerns with ionizing radiation and general anesthesia. Most institutions worldwide have now accepted MRA as the optimal technique for following pediatric patients with stroke over the course of their disease. However, measuring the severity of mild-moderate stenosis and detecting severe stenosis (>70%) by TOF-MRA in children is fraught with challenges resulting from artifacts inherent to the TOF technique. These factors, as well as technical differences among scans make interpretation of the progression of arterial stenosis across time an imprecise science. Basing disease severity on SI alone would also imply that the physiologic state at the time of scanning would be an important consideration. More

recent versions of TOF-MRA have focused on improving the spatial resolution and signal-to-noise ratios using overlapping slices (multiple overlapping thin-slab acquisition) or variable flip angles to maintain the relative spin saturations. How these affect SI in a diseased vessel is not fully known and can result in over- or underestimation of stenosis. To minimize the influence of acquisition parameters, we used the SI ratios instead. Signal intensity ratios on TOF-MRA have the potential to assess the fractional flow reserve of the assessed artery, thus serving as a noninvasive surrogate to identify high-risk intracranial stenosis, its severity, and functional significance.¹⁹

A recent evaluation of adult patients in the Stroke Outcomes and Neuroimaging of Intracranial Atherosclerosis (SONIA) and Warfarin-Aspirin Symptomatic Intracranial Disease (WASID) trials showed that decreased SI ratios across intracranial arterial stenoses correlated with misery perfusion to the downstream brain territories, thereby

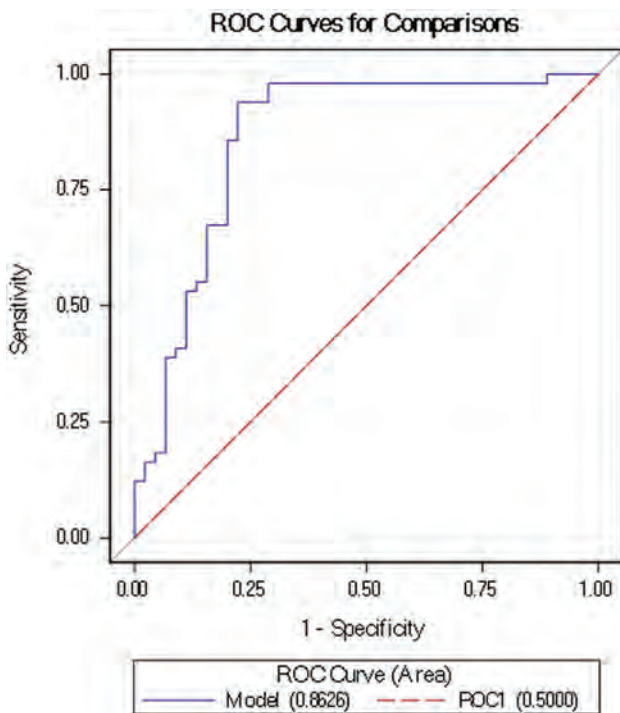


FIG 4. Receiver operator characteristic curve for post-/prestenotic SI ratios to diagnose severe (>70%) intracranial arterial stenosis. The area under the curve was 0.86, with a determined cutoff of 1.00 (see text).

providing a simple and noninvasive predictor of high-risk intracranial stenosis.^{23,28} Signal intensities from TOF-MRA have also been shown to significantly correlate with end-diastolic flow velocities on duplex sonography performed 1 year following pial synangiosis in patients with symptomatic intracranial stenosis.²⁹ The reproducibility of SI ratios was shown in a recent study on atherosclerotic intracranial stenosis, with interobserver agreements of >80%.³⁰ In the present study, we add to this growing body of literature by showing that SI ratios derived from TOF-MRA in pediatric patients with stroke correlate with catheter angiographic severity of stenosis, serve as a strong discriminant for diagnosing severe (>70%) intracranial stenosis in these children, and are stronger predictors of infarct burden and risk than percentage stenosis.

Although there are studies comparing MRA and conventional angiography in various adult cohorts,^{31,32} this is, to the best of our knowledge, the first time this correlation is being reported in the pediatric stroke literature. The estimation of percentage stenosis for intracranial arteries from TOF-MRA is challenging, with the proximal arterial segments diminishing in size due to reduced flow, poststenotic dilation often being present, TOF-MRA artifacts in the stenotic and poststenotic segments, and a normal reduction in size after bifurcation. Selection of the segments used for this analysis is critical. As described above, we used a predefined method, choosing contingency sites if this was not possible. In our cohort of 41 children with 70 stenotic arterial segments, though we found a strong correlation ($R = 0.93$) between MRA and angiographic stenosis, we also showed that MRA was a poor discriminant of severe and mild-moderate intracranial stenosis. Serving as an estimate of the fractional flow

across the stenosis, SI ratios had higher sensitivity and specificity than percentage stenosis from MRA (97% and 78% versus 43% and 59%, respectively) and higher positive and negative predictive values (72% and 97% versus 30% and 71%, respectively). This finding is not dissimilar to the large body of literature regarding fractional flow reserve assessments in coronary artery disease, which illustrates that percentage stenosis is not an optimal marker for identifying disease of physiologic significance. Due to the invasiveness of intra-arterial wire measurements, noninvasive methods to measure fractional flow reserve have also been developed using coronary CT angiography.^{33,34}

While a similar severity of arterial stenosis may have different hemodynamic and functional significance in the cerebral circulation than it does in the coronary tree, it is conceivable that there are better predictors of stroke risk than the severity of stenosis as measured by percentage stenosis. Cerebrovascular reserve studies have shown that the measurement of cerebral blood flow is a strong predictor of stroke risk, independent of the severity of stenosis.³⁵ Several different methods have been used for this, including SPECT, PET, CT perfusion, MR imaging perfusion, and blood oxygen level-dependent MR imaging. A retrospective analysis of the WASID trial suggested that impaired collaterals on angiography may be a better predictor of stroke in the territory than percentage stenosis, suggesting a key role for impaired hemodynamics.^{22-24,28,36-38} This finding is not wholly unexpected, given that the intracranial circulation can effectively compensate for a stenotic lesion in a carotid artery by flow across the circle of Willis from the contralateral carotid artery and/or from the posterior circulation. Our finding of a stronger correlation of TOF-MRA-derived SI ratios than percentage stenosis with infarct burden implies that SI ratios could serve as a surrogate biomarker for impaired cerebrovascular reserve, independent of the severity of the stenosis. Liebeskind et al,²⁸ in a recent study, had similarly shown that SI ratios derived from TOF-MRA were a strong predictor of increased stroke risk in an adult cohort with intracranial atherosclerotic stenosis.

Our study had some limitations. The retrospective design of the study implied that all data were extracted from medical and imaging records. However, all images were analyzed and postprocessed by study authors using a standard method. Although our cohort included heterogeneous vascular pathologies, these are indicative of the diverse etiologies of pediatric stroke and retain their clinical relevance for neurologists and pediatricians involved in the care of children with stroke. Second, the use of MR imaging scanners of different strengths (1.5 and 3T) could result in some variability in TOF-MRA appearances and the measurement of stenosis. Again, however, the comparison with angiographic stenosis is useful information for clinical settings that commonly toggle between these scanners. Additionally, our use of SI ratios rather than SI itself is expected to negate scanner-related differences. Further research is required to analyze and compare SI ratio differences among scanners. Also, TOF-MRA has several artifacts that are known to affect stenosis measurements and could potentially affect SI values. We attempted to minimize this issue by measuring every value as the mean of 2 ROIs; Liebeskind et al,²⁸ using this method, had shown excellent inter-reader agreement.

Third, selecting an appropriate segment for placing an ROI for SI was challenging in several cases. Manual placement of the ROI, the level, and location chosen for measurement is subjective. We attempted to maintain consistency by acquiring measurements of arterial SI in the ICA at approximately the C2 vertebral level for the prestenotic segment and from at least 2 arterial segments downstream of the poststenotic segment. Last, intracranial flow measurements are subject to the immediate poststenotic flow effects being altered by the circle Of Willis, as well as by pial/dural collaterals.³⁹ The selection of the MCA as the site for measurement of poststenotic SI was based on this factor: This location would account for compensatory flow from the anterior and/or posterior communicating arteries into the poststenotic artery, for which direct measurements of percentage stenosis would not account.

CONCLUSIONS

SI ratios measured from TOF-MRA serve as a reliable estimate of the severity of intracranial ICA stenosis in pediatric stroke and can be used as a surrogate for noninvasively following the severity of stenosis across time. These ratios serve as fractional flow measurements, assessing the hemodynamic significance of stenosis and allowing identification of high-risk stenotic lesions. Future prospective studies in pediatric stroke, comparing these with more established cerebrovascular reserve methods, are required to further corroborate our findings.

ACKNOWLEDGMENTS

We would like to acknowledge the neuroradiologists and neurosurgeons at our institution and the Ontasian Imaging Lab office for their support through this project. We would also like to acknowledge the MR imaging, CT, and interventional radiology technologists who played a key role in the acquisition of images used in this study.

Disclosures: Manohar Shroff—UNRELATED: Expert testimony: Occasional medical expert on birth injury cases; Payment for lectures including service on speakers bureaus: Speakers bureau – one time for BioMarin, stipend for speaking at conference organized by Siemens Brazil – one time.

REFERENCES

1. Heideman RL, Packer RJ, Albright LA, et al. Tumors of the central nervous system. In: Pizzo PA, ed. *Principles and Practice of Pediatric Oncology*. 3rd ed. Philadelphia: Lippincott; 1997:633–97
2. National Center for Health Statistics. **Deaths, percentage of total deaths, and death rates for the 10 leading causes of death in selected age groups, by race and sex in the United States.** 2002. https://www.cdc.gov/nchs/data/nvsr/nvsr53/nvsr53_17.pdf. Accessed June 16, 2019
3. Giroud M, Lemesle M, Madinier G, et al. **Stroke in children under 16 years of age: clinical and etiological difference with adults.** *Acta Neurol Scand* 1997;96:401–06 CrossRef Medline
4. Lynch JK, Hirtz DG, DeVeber G, et al. **Report of the National Institute of Neurological Disorders and Stroke Workshop on Perinatal and Childhood Stroke.** *Pediatrics* 2002;109:116–23 CrossRef Medline
5. Chung B, Wong V. **Pediatric stroke among Hong Kong Chinese subjects.** *Pediatrics* 2004;114:e206–12 CrossRef Medline

6. Fullerton HJ, Wu YW, Zhao S, et al. **Risk of stroke in children: ethnic and gender disparities.** *Neurology* 2003;61:189–94 CrossRef Medline
7. Fullerton HJ, Wu YW, Sidney S, et al. **Risk of recurrent childhood arterial ischemic stroke in a population-based cohort: the importance of cerebrovascular imaging.** *Pediatrics* 2007;119:495–501 CrossRef Medline
8. Ganesan V, Prengler M, McShane MA, et al. **Investigation of risk factors in children with arterial ischemic stroke.** *Ann Neurol* 2003;53:167–73 CrossRef Medline
9. Sträter R, Becker S, von Eckardstein A, et al. **Prospective assessment of risk factors for recurrent stroke during childhood: a 5-year follow-up study.** *Lancet* 2002;360:1540–05 CrossRef Medline
10. Chabrier S, Husson B, Lasjaunias P, et al. **Stroke in childhood: outcome and recurrence risk by mechanism in 59 patients.** *J Child Neurol* 2000;15:290–94 CrossRef Medline
11. Zimmer JA, Garg BP, Williams LS, et al. **Age-related variation in presenting signs of childhood arterial ischemic stroke.** *Pediatr Neurol* 2007;37:171–75 CrossRef Medline
12. Wintermark M, Hills NK, DeVeber GA, et al; VIPS Investigators. **Clinical and imaging characteristics of arteriopathy subtypes in children with arterial ischemic stroke: results of the VIPS study.** *AJNR Am J Neuroradiol* 2017;38:2172–79 CrossRef Medline
13. Sèbire G, Fullerton H, Riou E, et al. **Toward the definition of cerebral arteriopathies of childhood.** *Curr Opin Pediatr* 2004;16:617–22 CrossRef Medline
14. Sèbire G, Meyer L, Chabrier S. **Varicella as a risk factor for cerebral infarction in childhood: a case-control study.** *Ann Neurol* 1999;45:679–80 CrossRef Medline
15. Earley CJ, Kittner SJ, Feeser BR, et al. **Stroke in children and sickle-cell disease: Baltimore-Washington Cooperative Young Stroke Study.** *Neurology* 1998;51:169–76 CrossRef Medline
16. Pandey S, Hakky M, Kwak E, et al. **Application of basic principles of physics to head and neck MR angiography: troubleshooting for artifacts.** *Radiographics* 2013;33:e113–23 CrossRef Medline
17. Corfield L, Speirs A, McCormack DJ, et al. **Time of flight magnetic resonance angiography: a trap for the unwary.** *EJVES Extra* 2010;19:e35–37 CrossRef
18. Takhtani D, Dundamadappa S, Puri AS, et al. **Flow artifact in the anterior communicating artery resembling aneurysm on the time of flight MR angiogram.** *Acta Radiol* 2014;55:1253–57 CrossRef Medline
19. Silvennoinen HM, Ikonen S, Soinnie L, et al. **CT angiographic analysis of carotid artery stenosis: comparison of manual assessment, semiautomatic vessel analysis, and digital subtraction angiography.** *AJNR Am J Neuroradiol* 2007;28:97–103 Medline
20. van den Wijngaard IR, Holswilder G, van Walderveen MA, et al. **Treatment and imaging of intracranial atherosclerotic stenosis: current perspectives and future directions.** *Brain Behav* 2016;6:e00536 CrossRef Medline
21. Qureshi AI, Caplan LR. **Intracranial atherosclerosis.** *Lancet* 2014;383:984–98 CrossRef Medline
22. Lan L, Leng X, Abrigo J, et al. **Diminished signal intensities distal to intracranial arterial stenosis on time-of-flight MR angiography might indicate delayed cerebral perfusion.** *Cerebrovasc Dis* 2016;42:232–39 CrossRef Medline
23. Miura M, Nakajima M, Fujimoto A, et al. **Decreased signal intensity ratio on MRA reflects misery perfusion on SPECT in patients with intracranial stenosis.** *J Neuroimaging* 2018;28:206–11 CrossRef Medline
24. Samuels OB, Joseph GJ, Lynn MJ, et al. **A standardized method for measuring intracranial arterial stenosis.** *AJNR Am J Neuroradiol* 2000;21:643–46 Medline
25. Hankey GJ, Warlow CP, Molyneux AJ. **Complications of cerebral angiography for patients with mild carotid territory ischaemia being considered for carotid endarterectomy.** *J Neurol Neurosurg Psychiatry* 1990;53:542–48 CrossRef Medline

26. Davies KN, Humphrey PR. **Complications of cerebral angiography in patients with symptomatic carotid territory ischaemia screened by carotid ultrasound.** *J Neurol Neurosurg Psychiatry* 1993;56:967–72 CrossRef Medline
27. Johnston DC, Chapman KM, Goldstein LB. **Low rate of complications of cerebral angiography in routine clinical practice.** *Neurology* 2001;57:2012–14 CrossRef Medline
28. Liebeskind DS, Kosinski AS, Lynn MJ, et al. **Noninvasive fractional flow on MRA predicts stroke risk of intracranial stenosis.** *J Neuroimaging* 2015;25:87–91 CrossRef Medline
29. Matsuo S, Nakamizo A, Fujioka Y, et al. **Time-of-flight MRA signal intensity predicts the cerebral hemodynamic status after superficial temporal artery to middle cerebral artery anastomosis.** *J Clin Neurosci* 2019;59:124–29 CrossRef Medline
30. Leng X, Ip HL, Soo Y, et al. **Interobserver reproducibility of signal intensity ratio on magnetic resonance angiography for hemodynamic impact of intracranial atherosclerosis.** *J Stroke Cerebrovasc Dis* 2013;22:e615–19 CrossRef Medline
31. Verlhac S, Bernaudin F, Tortrat D, et al. **Detection of cerebrovascular disease in patients with sickle cell disease using transcranial Doppler sonography: correlation with MRI, MRA and catheter angiography.** *Pediatr Radiol* 1995;25:S14–19
32. Kandeel AY, Zimmerman RA, Ohene-Frempong K, et al. **Comparison of magnetic resonance angiography and catheter angiography in sickle cell disease: clinical significance and reliability.** *Neuroradiology* 1996;38:409–16 CrossRef Medline
33. Koo BK, Erglis A, Doh JH, et al. **Diagnosis of ischemia-causing coronary stenoses by noninvasive fractional flow reserve computed from coronary computed tomographic angiograms: results from the prospective multicenter DISCOVER-FLOW (Diagnosis of Ischemia-Causing Stenoses Obtained Via Noninvasive Fractional Flow Reserve) study.** *J Am Coll Cardiol* 2011;58:1989–97 CrossRef Medline
34. Min JK, Koo BK, Erglis A, et al. **Usefulness of noninvasive fractional flow reserve computed from coronary computed tomographic angiograms for intermediate stenoses confirmed by quantitative coronary angiography.** *Am J Cardiol* 2012;110:971–76 CrossRef Medline
35. Gupta A, Chazen JL, Hartman M, et al. **Cerebrovascular reserve and stroke risk in patients with carotid stenosis or occlusion: a systematic review and meta-analysis.** *Stroke* 2012;43:2884–91 CrossRef Medline
36. Baradaran H, Patel P, Gialdini G, et al. **Quantifying intracranial internal carotid artery stenosis on MR angiography.** *AJNR Am J Neuroradiol* 2017;38:986–90 CrossRef Medline
37. Chimowitz MI, Lynn MJ, Howlett-Smith H, et al; Warfarin-Aspirin Symptomatic Intracranial Disease Trial Investigators. **Comparison of warfarin and aspirin for symptomatic intracranial arterial stenosis.** *N Engl J Med* 2005;352:1305–16 CrossRef Medline
38. Hirooka R, Ogasawara K, Inoue T, et al. **Simple assessment of cerebral hemodynamics using single-slab 3D time-of-flight MR angiography in patients with cervical internal carotid artery stenocclusive diseases: comparison with quantitative perfusion single-photon emission CT.** *AJNR Am J Neuroradiol* 2009;30:559–63 CrossRef Medline
39. Miralles M, Dolz JL, Cotillas J, et al. **The role of the circle of Willis in carotid occlusion: assessment with phase contrast MR angiography and transcranial duplex.** *Eur J Vasc Endovasc Surg* 1995;10:424–30 CrossRef Medline

Is Low-Grade Intraventricular Hemorrhage in Very Preterm Infants an Innocent Condition? Structural and Functional Evaluation of the Brain Reveals Regional Neurodevelopmental Abnormalities

M.I. Argyropoulou, L.G. Astrakas, V.G. Xydis, A. Drougia, V. Mouka, I. Goel, V. Giapros, and S. Andronikou



ABSTRACT

BACKGROUND AND PURPOSE: There is increasing evidence of abnormal neurodevelopmental outcomes in very preterm infants with low-grade intraventricular hemorrhage grades I and II. Our purpose was to evaluate the effects of low-grade intraventricular hemorrhage on gray and white matter integrity.

MATERIALS AND METHODS: MR imaging at around term-equivalent age was performed in 16 very preterm infants (mean gestational age, 28.8 ± 5.3 weeks) with mild intraventricular hemorrhage on brain sonography and 13 control subjects (mean gestational age, 29.6 ± 4.1 weeks) without intraventricular hemorrhage. Structural and functional evaluation of the cortex was performed using regional measurements of surface area, thickness and volume, and resting-state fMRI, respectively, and of WM microstructural integrity, applying Tract-Based Spatial Statistics to diffusion tensor imaging data.

RESULTS: Compared with the control infants, the infants with low-grade intraventricular hemorrhage had decreases in the following: 1) GM surface area in Brodmann areas 19 left and 9 and 45 right, and GM volume in Brodmann areas 9 and 10 right; 2) fractional anisotropy bilaterally in major WM tracts; and 3) brain activity in the left lower lateral and in the right higher medial somatosensory cortex.

CONCLUSIONS: Very premature infants with low-grade intraventricular hemorrhage at around term-equivalent age may present with regional abnormalities, appearing on imaging studies as cortical underdevelopment, functional impairment, and microstructural immaturity of major WM tracts.

ABBREVIATIONS: BA = Brodmann area; BOLD = blood oxygen level–dependent; FA = fractional anisotropy; fALFF = fractional amplitude of low-frequency fluctuations; GA = gestational age; GABA = gamma-aminobutyric acid; GMH = germinal matrix hemorrhage; IVH = intraventricular hemorrhage; PALSBI2 = Population-Average, Landmark- and Surface-Based atlas; SSC = somatosensory cortex

Germinal matrix hemorrhage (GMH) is hemorrhage in the ganglionic eminence, which is the longest lasting germinal ventricular/subventricular zone, producing precursors of neurons, of oligodendrocytes, and of astrocytes.¹ GMH may rupture through the ventricular ependyma and evolve into intraventricular hemorrhage (IVH). The severity of GMH-IVH has been graded according to the Papile classification system, in which grade I is GMH alone, grade II is IVH occupying <50% of the

lateral ventricle, grade III is IVH occupying >50% of the lateral ventricle, and grade IV is grade III associated with periventricular venous infarction.² GMH-IVH is one of the most common neuropathologic conditions of prematurity, presenting increasing incidence with decreasing gestational age (GA) and birth weight.^{3–5} In very preterm infants (GA, <32 gestational weeks; birth weight, <1500 g), the incidence of GMH-IVH is 25%–30%, and this number remains stable despite advances in neonatal intensive care.^{3,5} Severe IVH (grades III and IV) is associated with adverse neurodevelopmental outcomes, including motor dysfunction and cerebral palsy, impairment of high-level cognitive functions, and visual and hearing disturbances.^{3,6} Destruction of the periventricular WM due to hydrocephalus and periventricular venous infarction has been suggested as the main cause of these morbidities.^{3,6}

Low-grade IVH (grades I and II) had long been considered free of risk of adverse neurodevelopmental outcomes, but new

Received October 20, 2019; accepted after revision January 4, 2020.

From the Departments of Radiology (M.I.A., V.G.X., V.M., I.G.), and Medical Physics (L.G.A.), and Neonatology Unit (A.D., V.G., S.A.), Faculty of Medicine, University of Ioannina, Ioannina, Greece.

Please address correspondence to Maria I. Argyropoulou, MD, Department of Radiology, Faculty of Medicine, School of Health Sciences, University of Ioannina, PO Box 1186, 45110 Ioannina, Greece; e-mail: margyrop@uoi.gr

Indicates article with supplemental on-line tables.

<http://dx.doi.org/10.3174/ajnr.A6438>

evidence is challenging this belief.^{3,6} Abnormal neurodevelopmental outcomes have also been recently reported in infants with low-grade IVH, though to a lesser extent and severity than in those with severe IVH.³ During the peak period of vulnerability for GMH-IVH (gestational weeks 25–32), major developmental events are taking place, including generation of late-migrating gamma-aminobutyric acid (GABA)ergic interneurons, critical for the development of the cortex and thalamus, and of oligodendroglial precursor cells, which give rise to premyelinating oligodendrocytes, along with rapid axonal growth and elongation.^{1,5,7} An increasing body of evidence shows that GMH-IVH may intervene in these events, arresting germ cell proliferation and impairing cell differentiation and migration and axonal growth.^{5,6,8–10}

The period between 28 and 40 gestational weeks is crucial for structural and functional development of the brain, and MR imaging evaluation at around term-equivalent age could be a useful means of assessing the effects of GMH-IVH. MR imaging offers powerful tools for evaluating maturational structural and functional integrity of the brain. Gyration has been associated with structural connectivity and can be evaluated at the regional level by voxel wise measurements of the cortical surface area, thickness, and volume.¹¹ Functional connectivity of the brain can be assessed by resting-state fMRI, which detects low-frequency (0.01–0.10 Hz) fluctuations of the blood oxygen level-dependent (BOLD) signal in specific anatomic areas. Anatomic areas presenting with temporal correlations in these fluctuations are considered functionally connected and form a network.¹² WM integrity can be evaluated with DTI, and one of the most frequently used methods for voxel wise assessment is Tract-Based Spatial Statistics (TBSS; <http://fsl.fmrib.ox.ac.uk/fsl/fslwiki/TBSS>).¹² The few MR imaging studies on the effect of low-grade IVH on brain structure have reported decreased total GM volume and microstructural abnormalities of major WM tracts.^{13,14} To our knowledge, no study evaluating the effect of GMH-IVH on functional connectivity of the brain has been published.

Because structural and functional maturation of the brain are interrelated, we considered it useful to evaluate both in a series of very premature infants with low-grade IVH, in comparison with premature control subjects without IVH. We hypothesized that low-grade IVH may intervene in the development of GM and WM, affecting the microstructure and function of the brain. We assessed changes in structural and functional maturation of the cortex using voxel wise regional measurements of surface area, thickness, and volume and resting-state fMRI, respectively, and WM microstructural integrity by applying TBSS to DTI data.

MATERIALS AND METHODS

Study Population

Very preterm neonates, born between January 2014 and May 2017 and admitted to the neonatal intensive care unit of the University Hospital of Ioannina, were evaluated with MR imaging at around term-equivalent age. After we applied the exclusion criteria (congenital malformations; syndromes; congenital TORCH [toxoplasmosis, other agents, ie, syphilis, varicella-zoster, parvovirus B19, rubella, cytomegalovirus, and herpes simplex infections] infection; punctuate WM hyperintensities; periventricular leuko-

malacia; high-grade IVH; infarction; stroke; and inappropriate quality of the MR imaging examination), the study population consisted of 16 premature infants with low-grade IVH on brain ultrasound and MR imaging and 13 control subjects with normal brain ultrasound and MR imaging findings. All infants included in the final study population had been discharged at 36 weeks' postmenstrual age or with 1800-g body weight and were free of problems. The study was performed with the approval of the institutional review board, and the parents of all the infants eligible to participate in the study provided their informed written consent for inclusion of their infants in the study.

MR Imaging Protocol

MR imaging was performed using an Intera 1.5T MR imaging scanner (Philips Healthcare, Best, the Netherlands). All examinations were performed with the infant under sedation with oral chloral hydrate (20–30 mg/Kg). The imaging protocol comprised anatomic MR imaging, resting-state fMRI, and DTI. Anatomic MR imaging was performed with a T1-weighted high-resolution 3D spoiled gradient-echo sequence (TR/TE/flip angle, 25 ms/4.6 ms/6°; voxel size, $0.86 \times 0.86 \times 1 \text{ mm}^3$) and T2-weighted sequences (TR/TE, 3500/90 ms; section thickness, 2.5 mm; section gap, 0 mm). A single-shot echo-planar sequence was used in all resting-state fMRI imaging scans, with the following parameters: TR/TE/flip angle, 2000 ms/40 ms/90°; number of signal averages, 1; dynamic scans, 200 real + 2 dummy scans; voxel size, $3.4 \times 3.4 \times 4 \text{ mm}^3$. DTI was performed with a single-shot spin-echo echo-planar sequence with the following parameters: TR/TE, 9807/131 ms; voxel size, $1.8 \times 1.8 \times 3 \text{ mm}^3$; maximum b-value, 700 s/mm^2 ; 16 noncolinear diffusion directions; number of signal intensity averages, 2.

Image Analyses

Brain Surface Analysis. Cortical surface analysis of the T1-weighted images was performed using a FreeSurfer (<http://surfer.nmr.mgh.harvard.edu>) image-processing pipeline developed especially for infant clinical MR images.¹⁵ The pipeline consists of 3 steps: skull-stripping, brain segmentation, and surface extraction. Surface analysis was provided for each subject and for each hemisphere map of cortical thickness and cortical area. Group comparison of each map was performed at the ROI level after parcellating each brain using the Brodmann Population-Average, Landmark- and Surface-Based (PALSBI2) atlas.¹⁶ Area, thickness, volume, and curvature in the Brodmann areas (BAs) of the surface maps were compared between neonates with and without IVH using the Mann-Whitney *U* test combined with a Bonferroni correction for multiple comparison differences (SPSS, Version 21; IBM, Armonk, New York).

White Matter Microstructural Analysis. Images were processed using the FMRIB Software Library (FSL; <http://www.fmrib.ox.ac.uk/fsl>). Using the FMRIB Diffusion Toolbox (<http://fsl.fmrib.ox.ac.uk/fsl/fslwiki/FDT>) for each subject, we performed the following steps: 1) All images were corrected for distortion and subject motion effects; 2) the skull was extracted using the Brain Extraction Tool (<http://fsl.fmrib.ox.ac.uk/fsl/fslwiki/BET>); 3) a diffusion tensor model was fitted to the data and produced maps

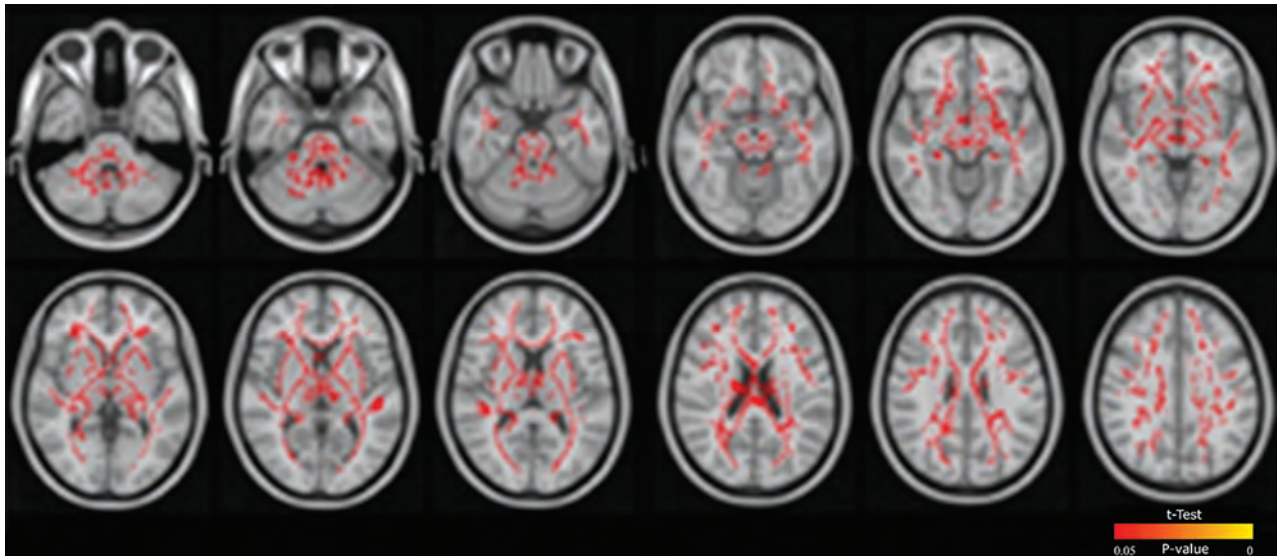


FIG 1. Low-grade IVH in very premature infants: white matter areas (in red) with reduced FA overlaid on a template T1-weighted image.

of fractional anisotropy (FA), measuring the degree of directionality of WM tracts, mean diffusivity, radial diffusivity measuring diffusion perpendicular to the WM tracts, and axial diffusivity measuring diffusion parallel to the WM tracts; 4) FA images were aligned to a target in a common space using an optimized TBSS protocol for neonates;¹⁷ 5) a mean FA map was created and thinned (FA > 0.15) to create a mean FA skeleton; and 6) aligned FA, axial diffusivity, and radial diffusivity data were projected onto the mean FA skeleton. Differences in FA, mean diffusivity, radial diffusivity, and axial diffusivity between neonates with and without IVH were assessed using voxel wise statistics, based on a permutation-based inference with 5000 permutations. The results were corrected for multiple comparisons by controlling the family-wise error rate following threshold-free cluster enhancement, with a threshold of $P < .05$. The labeling of the significant clusters was based on the Johns Hopkins University white matter tractography atlas.

fMRI Analysis. Functional connectivity was assessed using the CONN toolbox (<https://web.conn-toolbox.org/>). Preprocessing steps were applied to correct for head movement and differences in section timing. Functional images were registered to high-resolution anatomic images and normalized and smoothed with a Gaussian kernel of 6-mm full width at half maximum. The Template-O-Matic toolbox (<https://irc.cchmc.org/software/tom.php>) was used for the normalization step. Physiologic and movement components in the BOLD signal were removed using the Component Based Noise Correction Method (CompCor; <https://www.ncbi.nlm.nih.gov/pmc/articles/PMC2214855>).

Slow fluctuations in activity are a fundamental feature of the resting brain and can be used to determine correlated activity between brain regions and to define resting-state networks. The relative magnitude of these fluctuations can differ between brain regions and between subjects and thus may act as a marker of individual differences or dysfunction. The fractional amplitude of low-frequency fluctuations (fALFF) is a measure that quantifies these low-frequency oscillations. The fALFF was calculated at

each individual voxel as the relative amplitude (root mean square ratio) of the BOLD signal fluctuations at the frequency band of 0.008–0.09 Hz, compared with the entire frequency band.¹⁸ Group analysis of fALFF maps was performed using a t test at the voxel level. The t maps were thresholded using a combination of height threshold ($P = .001$ uncorrected) and cluster extent threshold ($P = .05$, family-wise error corrected).

RESULTS

None of the studied infants presented with necrotic enterocolitis or retinopathy of prematurity. There was no significant difference between infants with low-grade IVH and the control subjects in GA, birth weight, postmenstrual age at MR imaging, body weight at MR imaging, antenatal steroid administration, duration of mechanical ventilation, infection, patent ductus arteriosus, or chronic lung disease (On-Table 1).

Brain Surface Analysis

ROI surface analysis, based on the FreeSurfer PALS12 atlas, showed that low-grade IVH affects BAs 19, 9, 45, and 10 (On-line Tables 2–9). Specifically, it reduced the volume of BAs 9 and 10 in the right hemisphere (On-line Table 9), the area of BAs 9 and 45 in the right hemisphere (On-line Table 3), and the area of Brodmann area 19 in the left hemisphere (On-line Table 2).

White Matter Microstructural Analysis

TBSS analysis revealed that low-grade IVH produces an extensive decrease in FA in multiple WM tracts, including the anterior thalamic radiation, corticospinal tract, cingulum, forceps minor and major, inferior fronto-occipital fasciculus, inferior and superior longitudinal fasciculus, and uncinate fasciculus (On-line Table 10 and Fig 1). The other diffusion metrics remained unaffected.

fMRI Analysis

fALFF analysis showed decreased brain activity in the resting state of the infants with low-grade IVH in the left lower lateral

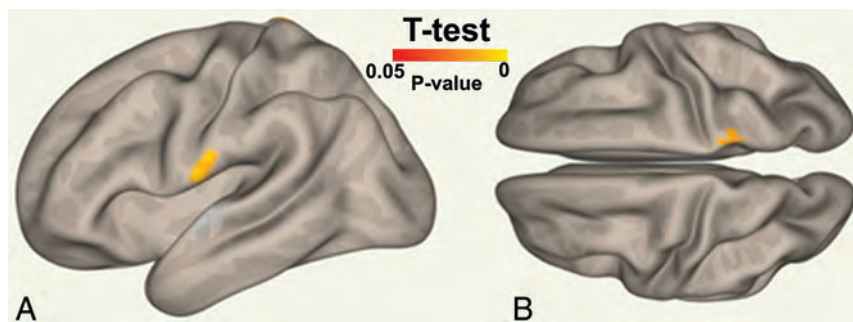


FIG 2. Brain area with decreased fALFF (yellow) in the left lower lateral (A) and right higher medial (B) somatosensory cortex, overlaid on a Montreal Neurological Institute template, of very premature infants with low-grade IVH.

and the right higher medial somatosensory cortex (Fig 2 and Online Table 11).

DISCUSSION

The primary goal of this study was to evaluate, in very preterm infants, the effects of low-grade IVH on brain structure and function. Analysis of DTI data for WM microstructural changes was performed with TBSS, which offers advanced registration capabilities and robust nonparametric assessment of local differences between groups.¹⁹ The cortical structure was studied with FreeSurfer, a state-of-the-art software capable of quantifying thickness, area, and curvature, not available with standard volumetric analysis. fMRI analysis was performed with fALFF, which is insensitive to physiologic noise.

The main findings of the present study were the following: 1) reduced activation in the left lower lateral and the right higher medial somatosensory cortex; 2) decreased cortical surface area in the right BAs 9 and 45 and the left BA 19 and decreased cortical volume in BAs 9 and 10; and 3) reduced FA in major WM tracts.

Histologic studies have demonstrated that 12–24 hours after the occurrence of GMH, the proliferation of germ cells in the ganglionic eminence is arrested for up to 4 weeks.⁹ Thrombin and plasmin and toxic neurotransmitters (glutamate and γ -aminobutyric acid) have been implicated in the pathogenesis of this damage.⁹ Further changes related to GMH-IVH are the presence of extracellular hemoglobin in the periventricular WM and microglia activation.^{5–7,10} Extracellular hemoglobin is rapidly oxidized from the ferrous state to the highly reactive ferric state, which, by activating cytotoxic, oxidative, and inflammatory pathways, may lead to tissue damage.^{5,7,9,10} Damage to the cerebellum has been previously reported after low-grade IVH and has been considered due to the effects of blood products on the superficial granular layer, which represents a germinal matrix.²⁰ During the third trimester of gestation, brain microglia are at their highest levels, and after activation, they generate free radicals, secrete cytokines, and promote excitotoxicity.^{5,7} The end result might be injury of the premyelinating oligodendrocytes, axons, subplate neurons, and late-migrating GABAergic neurons present in the WM of very preterm infants.^{5,7} The damage detected depends on the regional developmental stage of the GM and WM at the peak period of GMH-IVH and at the time of MR imaging.

The present study demonstrated decreased fALFF in the right and left somatosensory cortex (SSC). The functional development of the SSC is strongly associated with thalamic input through thalamocortical fibers and depends on thalamic, axonal, and cortical maturational integrity. GMH deprives the thalamus of the late-migrating GABAergic interneurons, while oxidative stress may affect thalamocortical fibers destined for the SSC at a period of maximum developmental vulnerability, which is 1–2 weeks earlier than that of fibers directed to the frontal and occipital association cortex.²¹ The lower fALFF in the left lower lateral and right higher medial SSC is probably related to the right-left thalamic and SSC and rostral-caudal SSC developmental hierarchy.^{22,23} The right thalamus and the right SSC develop before the left, and the lower lateral, before the higher medial SSC.^{22,23} Abnormal fALFF in areas assigned to the face on the left and to the feet on the right SSC, is probably related to the coincidence of the adverse effects with the higher developmental activity and thus the increased vulnerability of these areas.^{24,25} Sensory processing disorder has been reported in 39%–52% of children born preterm, with a higher incidence in those born earlier than 32 weeks' GA. Sensory processing disorder comprises difficulties in interpreting and using sensory information from the environment, resulting in hypo- or hyper-reaction to sensory stimuli.²⁶ The results of the present study suggest that decreased resting-state activity in the SSC of very premature infants with low-grade GMH-IVH might herald the future development of sensory processing impairment. Follow-up of these children would be useful to evaluate this hypothesis.

A decrease in total cortical GM volume has been reported in very premature infants with low-grade IVH.¹³ In the present study, local decreases in surface area and volume were detected. During the third trimester, cortical surface area increase is a prominent process, and it has been associated with the gyration process. A disproportionate increase in the superficial cortical layers (II and III) results in cortical folding.^{1,7} BAs 9, 10, and 45 belong to the dorsolateral, medial, and anterolateral prefrontal cortex, which present a protracted developmental window. GMH, by arresting proliferation of the progenitors and by intervening with axonal development, deprives the prefrontal cortex of the late GABAergic neurons and axons and thus impairs cortical maturation.

The right prefrontal cortex is more mature than the left at around term; its developmental vulnerability depends on the GA, and the effects of GMH-IVH probably coincide with the highest developmental activity of these areas; this feature explains the findings of this study.¹² The prefrontal cortex is associated with higher level cognitive functions, including organization of input from sensory modalities, maintenance of attention, monitoring of information in the working memory, coordination of goal-directed behaviors, emotional processing, sociality, linguistic

sequencing, planning, syntax, and phonological processing.²⁷ An increased incidence of cognitive problems, autism, schizophrenia, and difficulties with complex language functions have been reported in subjects born prematurely, especially those born very preterm.^{26,27}

BA 19 belongs to the prestriate cortex, which is a visual-association cortex, and in contrast to the primary visual cortex, it receives afferents predominantly from the pulvinar of the thalamus.²⁸ The left prestriate cortex develops before the right, and GMH may result in decreased numbers of late-migrating GABAergic neurons, which could explain the decreased cortical surface area demonstrated here. Cognitive visual dysfunction is a spectrum of abnormalities, ranging from neurosensory impairment to higher order deficits in visual perception, visual attention, and visuospatial working memory, and it is one of the common abnormalities in children born prematurely.²⁹ Overall, the cortical developmental abnormalities reported in this study suggest that low-grade IVH may be associated with these morbidities.

The present study demonstrated decreased FA in major projection, commissural, and association WM tracts. During the third trimester, WM, though unmyelinated, presents with anisotropy related to ensheathment of axons by premyelinating oligodendrocytes, decreases in the extra-axonal space due to water reduction, and increases in fiber diameter and axoplasmic flow.^{7,30} IVH, by arresting the development of oligodendroglia precursor cells and by injuring premyelinating oligodendrocytes and axons, may lead to a decrease in FA. FA derives from the SD of the 3 eigenvalues (λ_1 , λ_2 , λ_3) and thus depends on axial diffusivity and radial diffusivity.³¹ Disproportionate changes in axial diffusivity and radial diffusivity, even to a degree not reaching statistical significance, may affect FA and lead to significant changes. One previous study in premature infants with low-grade IVH¹⁴ demonstrated an isolated decrease of FA in major WM tracts in infants with a GA > 29 weeks, in agreement with the present study. Some differences in the affected WM tracts are probably related to the different GAs of the infants included in the 2 studies.¹⁴

Low-grade IVH has been associated with a 2-fold increase in the risk of lower cognitive performance and a 2.6-fold increase in the risk of neuromotor abnormalities.^{4,32} Most of the WM tracts implicated in the present study have been associated with these functions. Specifically, the superior longitudinal fasciculus is involved in the processes of attention, memory, and emotion; the inferior longitudinal fasciculus and the inferior fronto-occipital fasciculus are associated with the thought process, visual emotion, and cognition; the uncinate fasciculus is critical in emotion and memory; the anterior thalamic radiation is associated with mood regulation; and the cingulum, with emotion, reward, and memory.^{18,22} Previous studies have reported that preterm infants with severe IVH are at risk of developing spastic diplegia, and damage to the corticospinal tracts traveling in the periventricular matter is considered the underlying cause.³³ Our findings are in agreement with a previous study in very premature infants with low-grade IVH, which demonstrated low FA of the corticospinal tracts,³⁴ suggesting that the corticospinal tracts may also be affected by low-grade IVH.

This study has some limitations, primarily the small sample size, which does not allow correlation with neurodevelopmental data, weakens the statistical power, and possibly masks differences among important clinical confounders. Additionally, the low-angular-resolution DTI cannot handle adequately the “crossing-fiber” problem or the non-Gaussian nature of diffusion. Larger cohorts and more advanced diffusion protocols are required to extend and validate this study.

CONCLUSIONS

The present study shows that at around term-equivalent age, very premature infants with low-grade IVH may present imaging findings of regional abnormalities of the brain, appearing as cortical underdevelopment, functional impairment, and microstructural immaturity of major WM tracts.

REFERENCES

1. Raybaud C, Ahmad T, Rastegar N, et al. **The premature brain: developmental and lesional anatomy.** *Neuroradiology* 2013;55(Suppl 2): 23–40 CrossRef Medline
2. Papile LA, Burstein J, Burstein R, et al. **Incidence and evolution of subependymal and intraventricular hemorrhage: a study of infants with birth weights less than 1,500 gm.** *J Pediatr* 1978;92:529–34 CrossRef Medline
3. Mukerji A, Shah V, Shah PS. **Periventricular/intraventricular hemorrhage and neurodevelopmental outcomes: a meta-analysis.** *Pediatrics* 2015;136:1132–43 CrossRef Medline
4. Inder TE. **Neurodevelopmental impact of low-grade intraventricular hemorrhage in very preterm infants.** *J Pediatr* 2006;149:152–54 CrossRef Medline
5. Volpe JJ. **Impaired neurodevelopmental outcome after mild germinal matrix-intraventricular hemorrhage.** *Pediatrics* 2015;136:1185–87 CrossRef Medline
6. Volpe JJ. **Brain injury in premature infants: a complex amalgam of destructive and developmental disturbances.** *Lancet Neurol* 2009;8: 110–24 CrossRef Medline
7. Volpe JJ. **The encephalopathy of prematurity–brain injury and impaired brain development inextricably intertwined.** *Semin Pediatr Neurol* 2009;16:167–78 CrossRef Medline
8. McAllister JP, Guerra MM, Ruiz LC, et al. **Ventricular zone disruption in human neonates with intraventricular hemorrhage.** *J Neuropathol Exp Neurol* 2017;76:358–75 CrossRef Medline
9. Del Bigio MR. **Cell proliferation in human ganglionic eminence and suppression after prematurity-associated haemorrhage.** *Brain* 2011;134:1344–61 CrossRef Medline
10. Ley D, Romantsik O, Vallius S, et al. **High presence of extracellular hemoglobin in the periventricular white matter following preterm intraventricular hemorrhage.** *Front Physiol* 2016;7:330 CrossRef Medline
11. Tamnes CK, Herting MM, Goddings AL, et al. **Development of the cerebral cortex across adolescence: a multisample study of inter-related longitudinal changes in cortical volume, surface area, and thickness.** *J Neurosci* 2017;37:3402–12 CrossRef Medline
12. Mouka V, Drougia A, Xydis VG, et al. **Functional and structural connectivity of the brain in very preterm infants: relationship with gestational age and body and brain growth.** *Pediatr Radiol* 2019; 49:1078–84 CrossRef Medline
13. Vasileiadis GT, Gelman N, Han VK, et al. **Uncomplicated intraventricular hemorrhage is followed by reduced cortical volume at near-term age.** *Pediatrics* 2004;114:e367–72 CrossRef Medline
14. Tortora D, Martinetti C, Severino M, et al. **The effects of mild germinal matrix-intraventricular haemorrhage on the developmental**

- white matter microstructure of preterm neonates: a DTI study. *Eur Radiol* 2018;28:1157–66 CrossRef Medline
15. Zollei L, Martinos A. **FreeSurfer image processing pipeline for infant clinical MRI images.** In: *Proceedings of the 23rd Annual Meeting of the Organization for Human Brain Mapping*, Vancouver, British Columbia, Canada; June 25–29, 2017
 16. Van Essen DC. **A Population-Average, Landmark- and Surface-Based (PALS) atlas of human cerebral cortex.** *Neuroimage* 2005;28:635–62 CrossRef Medline
 17. Ball G, Counsell SJ, Anjari M, et al. **An optimised tract-based spatial statistics protocol for neonates: applications to prematurity and chronic lung disease.** *Neuroimage* 2010;53:94–102 CrossRef Medline
 18. Zou QH, Zhu CZ, Yang Y, et al. **An improved approach to detection of amplitude of low-frequency fluctuation (ALFF) for resting-state fMRI: fractional ALFF.** *J Neurosci Methods* 2008;172:137–41 CrossRef Medline
 19. Papageorgiou I, Astrakas LG, Xydis V, et al. **Abnormalities of brain neural circuits related to obesity: a diffusion tensor imaging study.** *Magn Reson Imaging* 2017;37:116–21 CrossRef Medline
 20. Tam EW, Miller SP, Studholme C, et al. **Differential effects of intraventricular hemorrhage and white matter injury on preterm cerebellar growth.** *J Pediatr* 2011;158:366–71 CrossRef Medline
 21. Krsnik Z, Majic V, Vasung L, et al. **Growth of thalamocortical fibers to the somatosensory cortex in the human fetal brain.** *Front Neurosci* 2017;11:233 CrossRef Medline
 22. Whitehead K, Papadelis C, Laudiano-Dray MP, et al. **The emergence of hierarchical somatosensory processing in late prematurity.** *Cereb Cortex* 2019;29:2245–60 CrossRef Medline
 23. Tzarouchi LC, Astrakas LG, Xydis V, et al. **Age-related grey matter changes in preterm infants: an MRI study.** *Neuroimage* 2009;47:1148–53 CrossRef Medline
 24. Kostovic I, Judas M. **The development of the subplate and thalamocortical connections in the human foetal brain.** *Acta Paediatr* 2010;99:1119–27 CrossRef Medline
 25. Dall’Orso S, Steinweg J, Allievi AG, et al. **Somatotopic mapping of the developing sensorimotor cortex in the preterm human brain.** *Cereb Cortex* 2018;28:2507–15 CrossRef Medline
 26. Ryckman J, Hilton C, Rogers C, et al. **Sensory processing disorder in preterm infants during early childhood and relationships to early neurobehavior.** *Early Hum Dev* 2017;113:18–22 CrossRef Medline
 27. Teffer K, Semendeferi K. **Human prefrontal cortex: evolution, development, and pathology.** *Prog Brain Res* 2012;195:191–218 CrossRef Medline
 28. Kostovic I, Rakic P. **Development of prestriate visual projections in the monkey and human fetal cerebrum revealed by transient cholinesterase staining.** *J Neurosci* 1984;4:25–42 CrossRef Medline
 29. Ceschin R, Wisnowski JL, Paquette LB, et al. **Developmental synergy between thalamic structure and interhemispheric connectivity in the visual system of preterm infants.** *Neuroimage Clin* 2015;8:462–72 CrossRef Medline
 30. Suzuki Y, Matsuzawa H, Kwee IL, et al. **Absolute eigenvalue diffusion tensor analysis for human brain maturation.** *NMR Biomed* 2003;16:257–60 CrossRef Medline
 31. Jellison BJ, Field AS, Medow J, et al. **Diffusion tensor imaging of cerebral white matter: a pictorial review of physics, fiber tract anatomy, and tumor imaging patterns.** *AJNR Am J Neuroradiol* 2004;25:356–69 Medline
 32. Patra K, Wilson-Costello D, Taylor HG, et al. **Grades I-II intraventricular hemorrhage in extremely low birth weight infants: effects on neurodevelopment.** *J Pediatr* 2006;149:169–73 CrossRef Medline
 33. Linsell L, Malouf R, Morris J, et al. **Prognostic factors for cerebral palsy and motor impairment in children born very preterm or very low birthweight: a systematic review.** *Dev Med Child Neurol* 2016;58:554–69 CrossRef Medline
 34. Morita T, Morimoto M, Yamada K, et al. **Low-grade intraventricular hemorrhage disrupts cerebellar white matter in preterm infants: evidence from diffusion tensor imaging.** *Neuroradiology* 2015;57:507–14 CrossRef Medline

Lumbar Puncture: Creation and Resident Acceptance of a Low-Cost, Durable, Reusable Fluoroscopic Phantom with a Fluid-Filled Spinal Canal for Training at an Academic Program

 D.J. Lerner,  S.E. Gifford,  N. Olafsen,  A. Mileto, and  E. Soloff



ABSTRACT

SUMMARY: Simulation-based medical training provides learners a method to develop technical skills without exposing patients to harm. Although fluoroscopic phantoms are already adopted in some areas of radiology, this has historically not been for lumbar puncture. Commercially available phantoms are expensive. We report a cost-effective, accessible solution by creation of an inexpensive phantom for resident training to perform fluoroscopically guided lumbar puncture, as well as instructions on how to make a phantom for residency education. An anthropomorphic ballistics-gel phantom that contains a plastic lumbar vertebral column and simulated CSF space was created. Radiology residents with minimum or no experience with fluoroscopically guided lumbar punctures were given a brief education and practiced fluoroscopically guided lumbar punctures on the phantom. A survey from the residents was then done. The phantom was qualitatively quite durable and deemed adequate for educational purposes. All the residents surveyed expressed the desire to have this phantom available and it increased comfort, knowledge, and perceived likelihood of success. Few articles have been published that focused on low-cost phantom creation for fluoroscopic-procedure training. This study supports the benefits of using phantoms for fluoroscopic training as well as step-by-step instructions for creation of this phantom. The residents responded positively and felt more confident in their fluoroscopically guided techniques. The ability to make a long-term training device for resident education would be inexpensive and relatively easy to implement in academic programs.

ABBREVIATION: LP = lumbar puncture

Simulation-based training provides learners in the medical field a method to develop technical skills without exposing patients to harm.¹ From temporal bone labs to practice drilling on cadaveric temporal bones for otolaryngology to mannequins for intubation, training devices are used across nearly all medical fields. In radiology, anthropomorphic phantoms are used for optimization of imaging hardware and procedural training purposes.² For training, they are often used in sonography-guided procedures. Although fluoroscopic phantoms are adopted in some areas of radiology, such as breast imaging to practice interventions, this has historically not been for other fluoroscopically

guided procedures, including lumbar puncture (LP), which is commonly performed in practice.

Although anthropomorphic training devices for this purpose are commercially available, they are prohibitively expensive (\$3,999.00, Blue-Phantom; CAE-Healthcare, Sarasota, Florida), which limits accessibility to most residents. Few examples in the literature, even across specialties, discuss solutions to solve this challenge for fluoroscopic procedures.^{1,2} Here, we report a cost-effective, accessible solution: creation of an inexpensive phantom for resident training to perform fluoroscopically guided LP. The phantoms are built with only a few readily available components and use fluid-filled spaces that allow trainees to experience simulated CSF return, which gives a realistic opportunity for accurate simulation. We demonstrate how residents with minimum exposure were able to improve their comfort level after receiving hands-on phantom-based training.

MATERIALS AND METHODS

Phantom Development

An anthropomorphic ballistics-gel phantom that contains a plastic lumbar vertebral column and simulated CSF space was created. It was built by using a lumbar vertebral column (4-Part Human

Received November 1, 2019; accepted after revision December 23.

From the Department of Radiology (D.J.L., A.M., E.S.), University of Washington School of Medicine, Seattle, Washington; and Department of Physical Medicine and Rehabilitation (S.E.G., N.O.), Washington University School of Medicine, St. Louis, Missouri.

Please address correspondence to David J. Lerner, MD, University of Washington, Department of Radiology, Section of Abdominal Imaging, 1959 NE Pacific Street, Box 357115, Seattle, WA 98195; e-mail: djlerner@uw.edu.

 Indicates article with supplemental on-line appendix and table.

 Indicates article with supplemental on-line photos.

 Indicates article with supplemental on-line video.

<http://dx.doi.org/10.3174/ajnr.A6439>

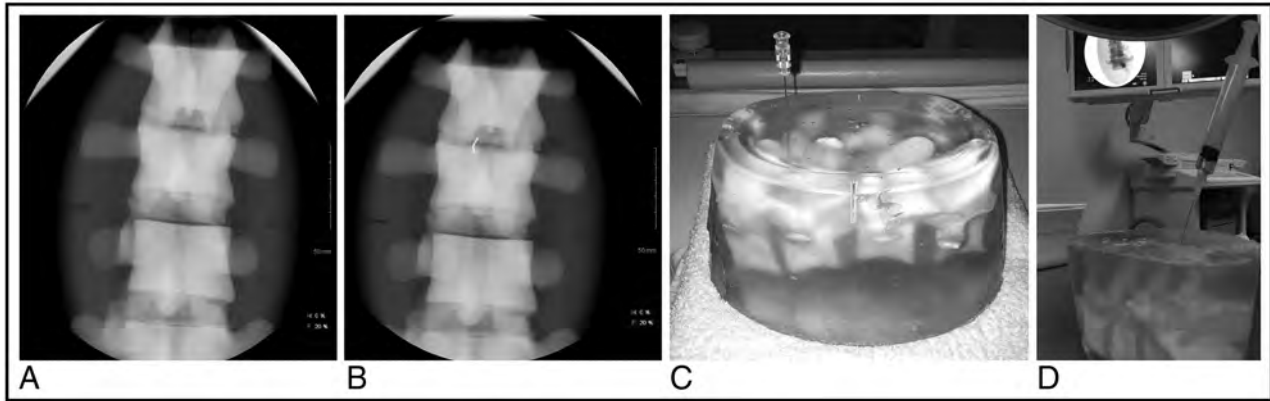


FIG 1. A and B, Fluoroscopic appearance of phantom without and with access needle. C, Phantom, with access needle in place. D, Separate phantom, with access needle in place with syringe aspiration displaying simulated spinal fluid.

Lumbar Vertebrae Spine Set; Anatomical, Inc, Lexington, South Carolina) purchased on-line. One 10% Ballistic-Gelatin Air Block (9 × 4 × 4 in) was also purchased on-line (ClearBallistics; Lexington, South Carolina). A plastic storage tub was used as a container for creation of the phantom. Latex membranes simulated the thecal sac (latex probe covers; extra-large condoms when probe covers were not available). Certain spinal columns include a rubber-insert re-creation of the spinal cord and nerve roots, which, if present, was removed. The vertebral model was held together by an internal malleable rod.

Malleable properties of the rod were used to create different challenge levels within the lumbar spaces. For example, one level was positioned kyphotically to open up the interspinous space, another was held in neutral position, whereas a different level was placed in the lordotic position, which simulated more difficult patient positioning. The ballistics gel was heated in a soup pot on medium high until fully melted. While the ballistics gel was heating, the latex membrane was placed through the canal of the spine and filled with water until completely filling the canal. The latex membrane was tied off, and the lumbar spine that contained the fluid-filled latex membrane was positioned within the container. Once the ballistics gel was completely melted, it was carefully poured into the container. This was cooled until solid, (approximately 6 hours). (On-line Video and On-line Fig 1.)

After cooling, the phantom was removed from the plastic mold. A small cut was made adjacent to the metal rod insertion in the lumbar spine and removed because this would cause opacification on fluoroscopy and limit device effectiveness. The result is an anthropomorphic ballistics-gel phantom that can be used under fluoroscopy with fluid-containing space-simulating CSF. The total cost of creating the phantom was approximately \$54. The total time spent was approximately 30 minutes to 1 hour (not including the time for the gel to cool). The phantom was qualitatively viewed under fluoroscopy by board-certified radiologists to ensure acceptable accuracy for the purposes of resident training.

RADIOLOGY RESIDENT TRAINING WITH THE PHANTOM

Radiology residents with minimum or no experience with fluoroscopically guided LPs were given a brief lecture, of approximately

15 minutes, on techniques, including needle localization, starting location, advancement technique, and fluoroscopic pedal control. Residents then had an opportunity to practice the techniques while supervised by a faculty member experienced in fluoroscopically guided LPs. This was performed with single-plane fluoroscopy and a median-paramedian interspinous approach, with the phantom in a simulated prone position. Technical success was demonstrated by return of simulated CSF through the needle and visualization of the needle within the spinal canal on fluoroscopy (Fig 1). Surveys from the residents were performed at the end of the workshop to determine the levels of comfort and confidence for performing LP before and after hands-on instruction with the phantom, and whether residents would like to permanently have such a training phantom available for practicing throughout the year (On-line Table and On-line Appendix).

RESULTS

Attenuation of the 10% gel block was 0.91 g/mL, whereas human adipose attenuation is approximately 0.91 g/mL and muscle 1.06 g/mL. The phantom was qualitatively quite durable. At least 100 attempts were performed during evaluation by faculty and training by residents without functional wear or loss of function. Qualitatively, the phantom displayed adequate differentiation between soft tissue and simulated spine and/or osseous structures, which allows for use as a practice mechanism for resident training. Needle visualization throughout the procedure with all calibers (20–22 gauge) used was qualitatively found to be easily identifiable by a staff radiologist who performs LPs. Some residents stated during practice that they were able to feel a “pop” through the needle as they entered the simulated CSF space.

All the residents surveyed expressed a desire to have this phantom available to the residency program for future practice. All the residents gave the highest rank (5/5) for the helpfulness of the phantom. The average comfort level for performing a LP improved from 1.8 to 3.9. The knowledge base for performing a LP increased from 2.7 to 4.4. Expectation for successfully performing a LP increased from 2.8 to 4.3 (On-line Fig 2).

DISCUSSION

Across medical specialties, simulation-based training devices are used for clinicians to gain technical skill sets and improve quality and efficiency for real patient interactions.^{3,4} Some of the most well known are mannequins used for Basic Life Support and Advanced Cardiovascular Life Support training. The use of training devices expands into other fields, in which the potential for poor outcomes is possible. For example, the aerospace industry commonly uses flight simulators for pilots to practice certain situations to achieve confidence as well as decrease costs of training.^{5,6}

Fluoroscopically guided LP is a commonly performed procedure in most radiologic practices. Historically, trainees have been required to learn these techniques on real patients, which creates risk associated with the inexperience of trainees. Although realistic training devices are available, in many situations, their frequent use is cost prohibitive to many training programs. Having an inexpensive way to allow residents to repeatedly train on a device to build technical competence for fluoroscopically guided LPs before direct patient interaction might be beneficial for improved outcomes.⁷ The anthropomorphic phantom herein developed fits such a description.

The ClearBallistics gel was chosen for certain beneficial properties. This gel was developed to simulate the average soft-tissue attenuation of a human, which allows an overall accurate but not necessarily exact duplication of a patient's soft tissue. As a result of their properties, some homemade ballistic gels must be refrigerated to avoid mold formation and/or rotting and may only have a 3-week shelf life, despite refrigeration. However, the ClearBallistics gel does not require refrigeration and will not rot. The long-term shelf life of this product is significant. For example, one model that we developed was still in use for >3 years and showed no significant loss of function or decomposition. In addition, if, after frequent use, the phantom is no longer accurate, the gel can be remelted and cooled for reuse. For repair of superficial components of the phantom, (ie, too many amassed puncture sites), a butane torch can be applied to those areas until just melted and then the phantom is set aside to re-cool. A more complete reconstruction is performed by manually removing the ballistic gel from the other components at room temperature and rebuilding the phantom as described above and in the On-line Video.

Very few articles have been published that focus on low-cost phantom creation for fluoroscopic procedure training.^{1,2} This article adds to the literature to further support the benefits of using phantoms for fluoroscopic training by increasing resident confidence and comfort as well as improving patient safety. In addition, compared with previous reported literature of creating an inexpensive phantom, our unit is approximately \$90 less expensive² to create than previously described low-cost phantoms, and up to \$3,945 less than commercially available phantoms while supplying acceptable re-creation for resident training purposes. Our phantom is also unique in that it has a fluid-filled pocket to better simulate the spinal canal for the purposes of fluoro-

scopically guided LP. This potentially improves the experience because it can replicate the "pop" sensation that can be felt when entering the thecal sac and allows return of fluid through the spinal access needle. A review of the literature for low-cost fluoroscopic LP phantoms did not reveal this type of fluid-filled canal technique.

The residents responded positively to this training mechanism and felt more confident in their fluoroscopically guided procedural techniques. Having the novel opportunity to practice with different anatomic "difficulty" levels in the lumbar spine phantom allowed the residents to progress in an organized manner and to fine tune their technique over the course of multiple attempts, which is also unique to previously described LP phantoms. If more realistic simulation is desired, 3D printed spines with varying degrees of spondylosis and/or scoliosis could be used. A previous article has shown that such training can decrease patient radiation exposure.¹ The ability to make a long-term training device for resident education would be inexpensive and relatively easy to implement in academic programs.

ACKNOWLEDGMENTS

We thank Kirang Patel, MD, from the University of Missouri Kansas City School of Medicine, for contributions.

Nathan Olafsen—UNRELATED: Employment: Washington University School of Medicine. Achille Mileto—UNRELATED: Employment: University of Washington School of Medicine; Grants/Grants Pending: GE Healthcare.* Erik Soloff—UNRELATED: Payment for Lectures Including Service on Speakers Bureaus: JADPRO, Comments: I received an honorarium to speak at the JADPRO live meeting which is for advanced practitioners in oncology. The talk was unrelated to the contents of this manuscript. *Money paid to institution.

REFERENCES

1. Faulkner AR, Bourgeois AC, Bradley YC, et al. **Simulation-based educational curriculum for fluoroscopically guided lumbar puncture improves operator confidence and reduces patient dose.** *Acad Radiol* 2015;22:668–73 CrossRef Medline
2. Faulkner AR, Bourgeois AC, Bradley YC, et al. **A robust and inexpensive phantom for fluoroscopically guided lumbar puncture training.** *Simul Healthc* 2015;10:54–58 CrossRef Medline
3. McGaghie WC, Issenberg SB, Petrusa ER, et al. **A critical review of simulation-based medical education research: 2003–2009.** *Med Educ* 2010;44:50–63 CrossRef Medline
4. Aldosary FF. **The use of high-fidelity mannequin training to improve the quality of healthcare providers? Performance of CP.** *J Transl Sci* 2018;4 CrossRef
5. Shy KS, et al. *The role of aircraft simulation in improving flight safety through control training.* American Institute of Aeronautics and Astronautics 2002 NASA TM-2002-210731 https://www.nasa.gov/centers/dryden/pdf/88743main_H-2501.pdf. Accessed September 12, 2019
6. Landman A, van Oorschot P, van Paassen MMR, et al. **Training pilots for unexpected events: a simulator study on the advantage of unpredictable and variable scenarios.** *Hum Factors* 2018;60:793–805 CrossRef
7. See KW, Chui KH, Chan WH, et al. **Evidence for endovascular simulation training: a systematic review.** *Eur J Vasc Endovasc Surg* 2016; 51:441–51 CrossRef Medline

Neuronavigation in the Identification and Presurgical Planning of Cortical Focal Dysplasia

I have read with great interest the article by Bartolini et al¹ that appears in the previous issue of this journal.

The authors highlight the high sensitivity of 7T T2*-weighted MR imaging in the identification and anatomic delimitation of cortical focal dysplasia (CFD) type IIb, specifying that this study will help more precise surgical planning, as well as explain the cases of failure in epilepsy operations. While it is true that 7T MR imaging has these advantages, it is also true that not all centers where epilepsy surgery is performed have the possibility of having such a team.

Probably more affordable is the availability of a neuronavigation team that could achieve quite similar results.²

I present the case of a 3-year-old boy with a history of intellectual disability and 12–16 simple partial motor daily seizures secondarily generalized from 3 months of age despite different schemes of antiepileptic polytherapy, in which an extensive and diffuse right parieto-occipital cortico-subcortical lesion was diagnosed, congruent with the site of the onset of epileptogenic discharges.

With neuronavigator and neurophysiologic monitoring with a subdural grid electrode of 32 contacts placed over the lesion and 2 interhemispheric strip electrodes of 4 contacts, the anatomic-functional margins of the lesion could be identified with

high precision, and by means of a right parietal quadrantectomy with disconnection of the splenium, the entire lesion was resected (Figure).

Pathology confirmed CFD type IIb. At 18 months after the operation, the patient remained free of seizures (Engel I), with a sequential homonymous left hemianopia.

Neuronavigation proved to be an instrument of remarkable utility in the identification, delimitation, and complete resection of this voluminous cortical dysplasia. The advantage of the neuronavigation is that it allows a volumetric location of the lesion, which increases the accuracy of the resection of the lesion.

REFERENCES

1. Bartolini E, Cosottini M, Costagli M, et al. **Ultra-high-field targeted imaging of focal cortical dysplasia: the intracortical black line sign in type IIb.** *AJNR Am J Neuroradiol* 2019;40:2137–42 CrossRef Medline
2. Minkin K, Gabrovski K, Sirakov S, et al. **Three-dimensional neuronavigation in SEEG-guided epilepsy surgery.** *Acta Neurochir (Wien)* 2019;161:917–23 CrossRef Medline

© C.J. Valencia-Calderón

Department of Neurosurgery
Hospital Universitario Central de Asturias
Oviedo, Spain

<http://dx.doi.org/10.3174/ajnr.A6417>

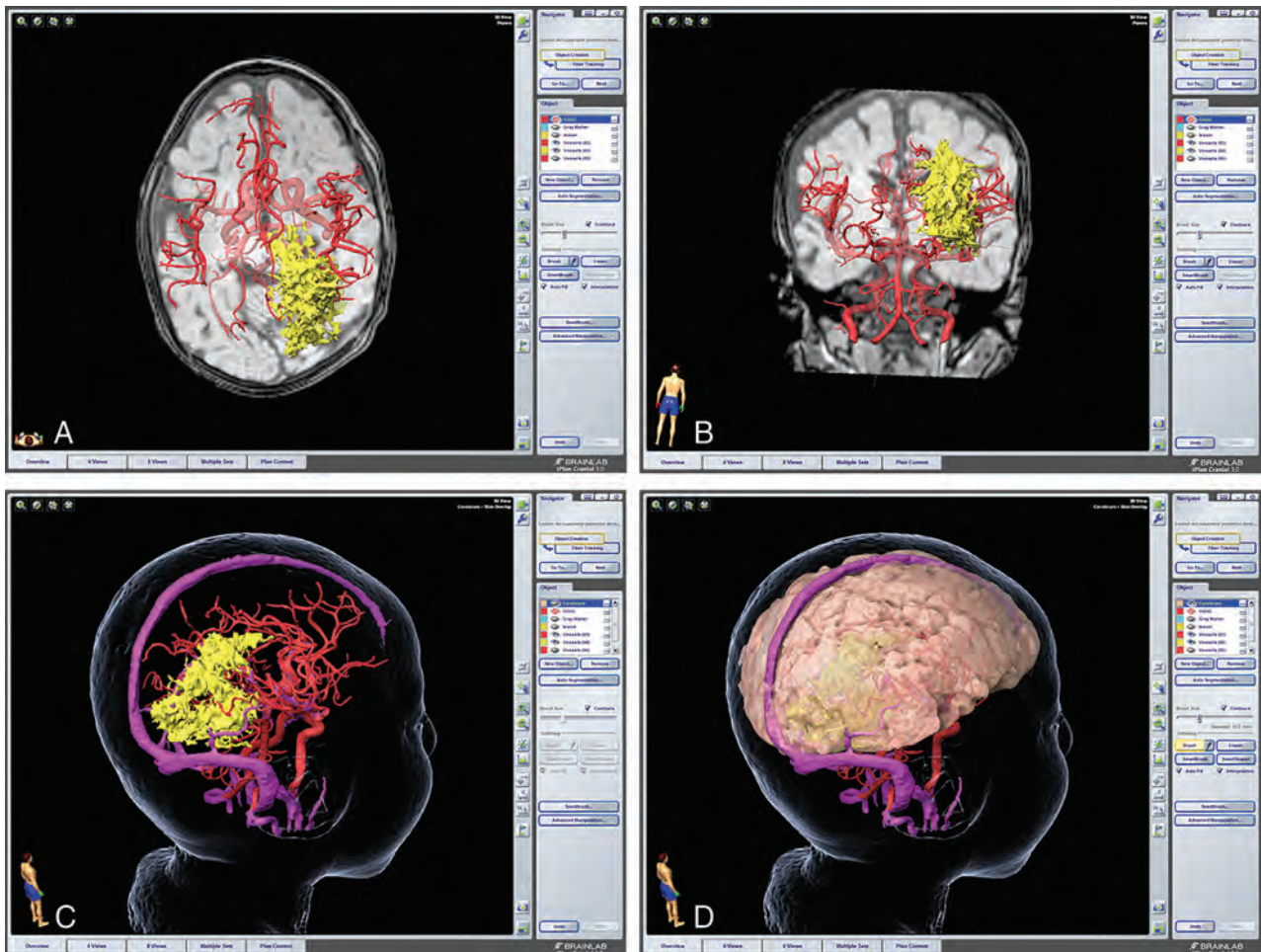


FIGURE. A and B, Axial and coronal T2*-weighted MR imaging of a patient with long-standing epilepsy due to extensive cortical dysplasia. The right parieto-occipital cortical dysplasia has been rendered in yellow, and the circle of Willis, in red on the 3D model. C and D, Transparent reconstruction of the patient's head with and without the brain where the circle of Willis and the venous sinus and vein of Labbé (in purple) are related to dysplasia. This image illustrates the surgical complexity of this dysplasia; planning the surgery took into consideration that endangering the vein of Labbé would carry the risk of venous infarction. Electrocorticography showed active spiking in the posterior cingulate gyrus, which has undergone complete resection. Final intraoperative electrocorticography showed no epileptiform activity.

REPLY:

We read with interest the letter from Dr. Valencia-Calderón. The neuronavigation system can be coupled with 7T MR images as a working examination devised to help the surgeon define the epileptogenic area without invasive recordings. Specifically, in focal cortical dysplasia, especially type I, which is mainly defined as a disorder of cortical lamination, anatomic boundaries are ill-defined and epileptogenic activity, which is poorly delimited, often requires depth electrodes for accurate mapping. In this context, the outcome of epilepsy surgery is strictly dependent on complete removal, which is more easily

achieved if 7T MR imaging is available. For low-grade gliomas, on the other hand, many suggest supramaximal resection whenever possible to prevent tumor recurrence and malignant transformation. In this context, again, ultra-high-field 7T MR imaging can also be a valid tool for neurooncologic surgical purposes. On this basis, we encourage large referral centers to seek 7T MR imaging support for elective neurosurgery.

 **R. Guerrini**

Department of Pediatric Neurology

 **F. Giordano**

Department of Neurosurgery

Children's Hospital Anna Meyer, University of Florence
Florence, Italy

 **M. Cosottini**

Neuroradiology Unit
Cisanello Hospital, University of Pisa
Pisa, Italy

<http://dx.doi.org/10.3174/ajnr.A6490>

Time to Refocus the Target in Stroke Therapy Again?



Stroke treatment has made enormous advances during the past decades. While initial research was focused on the brain parenchyma and its eventual demise, it was actually the arrival of treatments of clot that completely changed the game. Indeed, while from a basic point of view, the pathophysiology of stroke is well-investigated and partly understood enough to develop a pharmaceutical agent,^{1,2} these approaches have, until now, failed. Indeed, while the animal models were very often able to create an ideal model of stroke, the translation into the clinical setting has not met with great success for neuroprotection. However, now that imaging and revascularization have made great progress, it may be time to reassess if neuroprotection could be possible. Indeed, whether by using CT³ or MR imaging⁴ or even DSA-based techniques⁵ or even bypassing these and going directly into the catheter lab, it is possible to obtain imaging of the brain that will diagnose an ischemic event with high certitude and a short time interval. This fast and improved global brain imaging approach, together with the recent successes of interventional revascularization, shows increased rates of recovery⁶⁻⁹ within a longer therapeutic window than previously achievable.¹⁰

The combination of improved diagnostics and interventional measures could make us reassess whether the era of neuroprotective agents may come again. Indeed, while revascularization itself by interventional techniques is now the standard, the results, on the one hand, may be improved if the drugs can now be given directly into the target zone,¹¹ which could lead to new therapeutic drug trials. This means that we also have to reassess the way we conceive the penumbra or the tissue at risk.^{12,13} Indeed, from being at the beginning a metabolic event that was supposed to become the therapeutic target, the penumbral model evolved into a hemodynamically based one with new imaging technologies. This evolution coincided with the initial thrombolysis trials and led to the initial successes against the disease. However, now that we see that not just collaterals play a role in maintaining tissue vitality, we may need to additionally assess the topics of tissular fragility more with advanced imaging techniques and possibly artificial intelligence algorithms to demonstrate the potential ac-

tivity of pharmaceutical treatment. This assessment could, in the end, also facilitate treatment by offering additional therapies with wider access than is currently available to patients who have an ischemic event and do not live close to an integrated stroke center.

REFERENCES

1. Siesjö BK. **Pathophysiology and treatment of focal cerebral ischemia, Part II: mechanisms of damage and treatment.** *J Neurosurg* 1992;77:337–54 CrossRef Medline
2. Siesjö BK. **Pathophysiology and treatment of focal cerebral ischemia, Part I: pathophysiology.** *J Neurosurg* 1992;77:169–84 CrossRef Medline
3. Lövblad KO, Baird AE. **Computed tomography in acute ischemic stroke.** *Neuroradiology* 2010;52:175–87 CrossRef Medline
4. Lövblad KO, Laubach HJ, Baird AE, et al. **Clinical experience with diffusion-weighted MR in patients with acute stroke.** *AJNR Am J Neuroradiol* 1998;19:1061–66 Medline
5. Mueller A, Wagner M, Hattingen E, et al. **Flat panel computed tomography pooled blood volume and infarct prediction in endovascular stroke treatment.** *Stroke* 2019;50:3274–76 CrossRef Medline
6. Jovin TG, Chamorro A, Cobo E, et al; REVASCAT Trial Investigators. **Thrombectomy within 8 hours after symptom onset in ischemic stroke.** *N Engl J Med* 2015;372:2296–306 CrossRef Medline
7. Saver JL, Goyal M, Bonafe A, et al; SWIFT PRIME Investigators. **Stent-retriever thrombectomy after intravenous t-PA vs. t-PA alone in stroke.** *N Engl J Med* 2015;372:2285–95 CrossRef Medline
8. Goyal M, Demchuk AM, Menon BK, et al; ESCAPE Trial Investigators. **Randomized assessment of rapid endovascular treatment of ischemic stroke.** *N Engl J Med* 2015;372:1019–30 CrossRef Medline
9. Campbell BC, Mitchell PJ, Kleinig TJ, et al; EXTEND-IA Investigators. **Endovascular therapy for ischemic stroke with perfusion-imaging selection.** *N Engl J Med* 2015;372:1009–18 CrossRef Medline
10. Nogueira RG, Jadhav AP, Haussen DC, et al; DAWN Trial Investigators. **Thrombectomy 6 to 24 hours after stroke with a mismatch between deficit and infarct.** *N Engl J Med* 2018;378:11–21 CrossRef Medline
11. Shi L, Rocha M, Leak RK, et al. **A new era for stroke therapy: integrating neurovascular protection with optimal reperfusion.** *J Cerebr Blood Flow Metab* 2018;38:2073–91 CrossRef Medline
12. Astrup J, Siesjö BK, Symon L. **Thresholds in cerebral ischemia: the ischemic penumbra.** *Stroke* 1981;12:723–25 CrossRef Medline
13. Schlaug G, Benfield A, Baird AE, et al. **The ischemic penumbra: operationally defined by diffusion and perfusion MRI.** *Neurology* 1999;53:1528–37 CrossRef Medline

The article was funded by a grant from the Swiss National Science Foundation, grant No. 32003B_182382/1.

Indicates open access to non-subscribers at www.ajnr.org

<http://dx.doi.org/10.3174/ajnr.A6416>

K.-O. Lövblad

Service de Neuroradiologie Diagnostique et Interventionnelle, Département Diagnostique
Hôpitaux Universitaires de Genève
Genève, Switzerland

The Possible Role of Elastic Properties of the Brain and Optic Nerve Sheath in the Development of Spaceflight-Associated Neuro-Ocular Syndrome

We read with great interest the article recently published in the *American Journal of Neuroradiology* by Roberts et al,¹ and we appreciate the opportunity to make a comment.

The authors retrospectively analyzed brain MR imaging scans of National Aeronautics and Space Administration astronauts to quantify pre- to postflight changes in brain structure.¹ Long-duration spaceflights aboard the International Space Station, but not short-duration Space Shuttle flights, resulted in a significant increase in the percentage of total ventricular volume change (10.7% versus 0%, $P < .001$, $n = 12$ versus $n = 7$). The percentage of total ventricular volume change was significantly associated with the mission duration ($r = 0.72$, $P = .001$, $n = 19$) but negatively associated with age ($r = -0.48$, $P = .048$, $n = 19$). The authors also examined post hoc the extent to which pre- to postflight structural brain changes were associated with the development of spaceflight-associated neuro-ocular syndrome (SANS). They hypothesized that ventricular enlargement postflight would correlate with the development of SANS. However, of the 12 long-duration astronauts, the 4 astronauts with ophthalmologic changes had a smaller change in the percentage of total ventricular volume than those without SANS (12.8% versus 6.5%, $P = .02$, $n = 8$ versus $n = 4$). This preliminary result suggested that ventricular enlargement, as seen in astronauts without SANS, may not be a characteristic feature of SANS.¹ With regard to this apparently surprising finding, we would like to present an additional viewpoint.

In a recent article, Van Ombergen et al² found an increased ventricular CSF volume after long-duration spaceflights in supratentorial ventricular structures (ie, lateral and the third ventricles) and further hypothesized that the impact on the supratentorial regions is an indicator of the structural compliance and CSF reserve capacity of these ventricles acting as buffers in healthy adults. According to the authors, this might be considered a preliminary coping mechanism in space, which acts as an intermediate overflow zone for the reduced CSF resorption. They further suggested a potential link between

the brain ventricular and CSF changes and symptoms of SANS, in the sense that a larger compensatory reserve capacity in the CSF space (eg, by a greater compliance and elasticity of the ventricles) may protect against ophthalmic changes in space travelers by delaying CSF pressure buildup in the retro-orbital space. Wostyn and De Deyn^{3,4} had previously proposed a similar compensatory mechanism at the level of the optic nerve sheath. They hypothesized that astronauts with less compliant optic nerve sheaths may be more likely to develop optic disc edema, given that a greater degree of optic nerve sheath rigidity that prevents further expansion may result in more CSF pressure increase in the subarachnoid space surrounding the optic nerve. According to these 2 hypotheses, microgravity-induced ocular changes may be partially determined by the elastic properties of the brain ventricles and optic nerve sheath. Thus, the entire CSF compartment, including the dural bulges around the cranial nerves, may act as a buffer zone against the development of SANS. This view is consistent with the smaller change in the percentage of total ventricular volume experienced by astronauts with SANS, as observed in the present study by Roberts et al.¹

Disclosures: Peter Wostyn—UNRELATED: Patents (Planned, Pending or Issued): Peter Wostyn is the inventor of a pending patent application pertaining to biomarkers for spaceflight-associated neuro-ocular syndrome.

REFERENCES

1. Roberts DR, Asemani D, Nietert PJ, et al. **Prolonged microgravity affects human brain structure and function.** *AJNR Am J Neuroradiol* 2019;40:1878–85 CrossRef Medline
2. Van Ombergen A, Jillings S, Jeurissen B, et al. **Brain ventricular volume changes induced by long-duration spaceflight.** *Proc Natl Acad Sci USA* 2019;116:10531–36 CrossRef Medline
3. Wostyn P, De Deyn PP. **Intracranial pressure-induced optic nerve sheath response as a predictive biomarker for optic disc edema in astronauts.** *Biomark Med* 2017;11:1003–08 CrossRef Medline
4. Wostyn P, De Deyn PP. **Optic nerve sheath distention as a protective mechanism against the visual impairment and intracranial pressure syndrome in astronauts.** *Invest Ophthalmol Vis Sci* 2017;58:4601–02 CrossRef Medline

Ⓛ P. Wostyn

Department of Psychiatry
PC Sint-Amandus
Beernem, Belgium

Ⓛ T.H. Mader

Colonel, US Army (retired), Moab, Utah

Ⓛ C.R. Gibson

Coastal Eye Associates
Webster, Texas
KBR, Houston, Texas

Ⓛ F.L. Wuyts

Lab for Equilibrium Investigations and Aerospace
University of Antwerp
Antwerp, Belgium

Ⓛ A. Van Ombergen

Lab for Equilibrium Investigations and Aerospace
Department of Translational Neurosciences
University of Antwerp
Antwerp, Belgium

Ⓛ P. zu Eulenburg

German Center for Vertigo and Balance Disorders
Faculty of Medicine
Ludwig-Maximilians-University Munich
Munich, Germany

Ⓛ P.P. De Deyn

Department of Biomedical Sciences
Laboratory of Neurochemistry and Behavior
Institute Born-Bunge
University of Antwerp
Antwerp, Belgium

Department of Neurology and Alzheimer Research Center
University of Groningen and University Medical Center Groningen
Groningen, the Netherlands

Department of Neurology and Memory Clinic
Middelheim General Hospital
Antwerp, Belgium

REPLY:

We thank Wostyn et al for their interest in our recent article. We initially hypothesized that astronauts presenting with the spaceflight-associated neuro-ocular syndrome (SANS) would have ventricular enlargement at postflight MR imaging. Instead, we found greater percentage changes in pre- to postflight ventricular size in the astronauts without SANS. In this regard, we find the comment of Wostyn et al very interesting. The authors suggest that “microgravity-induced ocular changes may be partially determined by the elastic properties of the brain ventricles and optic nerve sheath” and that the “CSF compartment ... may act as buffer zones against the development of SANS.” In fact, we have also previously hypothesized that viscoelastic properties may contribute to the development of ventricular enlargement, which may represent a neuroadaptive response to spaceflight.^{1,2} We have made recommendations to the National Aeronautics and Space Administration (NASA) to consider the inclusion of MR elastography as a noninvasive imaging measure of brain stiffness,³ which may serve as a preflight predictor of who may be more susceptible to the development of SANS. Most important, we believe that NASA should consider the inclusion of advanced MR imaging protocols, such as MR elastography, to further explore the mechanisms underlying both the ophthalmologic changes of SANS and the structural changes to the brain experienced by astronauts on long-term missions to the International Space Station. This is particularly critical as we plan for future missions to the Moon or Mars.

We also believe that investigating the response of the intracranial compartment to the spaceflight environment may provide new insights into the understanding of CSF disorders here on Earth.² For example, it could be that patients who develop idiopathic intracranial hypertension (IIH) have less compliant brains without the ability of the ventricular system to enlarge in times of

elevated CSF pressures. As Wostyn et al have proposed for astronauts with SANS, perhaps, too, in patients with IIH, the ventricles may not act as a buffer, leading to the development of optic disc edema. This hypothesis is supported by the characteristic finding in patients with IIH of slit-like ventricles on MR imaging. We look forward to further studies of intracranial physiology during spaceflight both to ensure the safety of our space explorers and to benefit patients with disorders of CSF homeostasis on Earth.

REFERENCES

1. Roberts DR, Petersen LG. **Mischaracterization of spaceflight-associated neuro-ocular syndrome: reply.** *JAMA Neurol* 2019 Aug 12. [Epub ahead of print] CrossRef Medline
2. Roberts DR, Petersen LG. **Studies of hydrocephalus associated with long-term spaceflight may provide new insights into cerebrospinal fluid flow dynamics here on earth.** *JAMA Neurol* 2019;76:391–92 CrossRef Medline
3. Murphy MC, Huston J 3rd, Ehman RL. **MR elastography of the brain and its application in neurological diseases.** *Neuroimage* 2019;187:176–83 CrossRef Medline

 **D.R. Roberts**

 **D. Asemani**

Department of Radiology and Radiological Science

 **P.J. Nietert**

Department of Public Health Sciences

 **M.A. Eckert**

Department of Otolaryngology–Head and Neck Surgery

 **D.C. Inglesby**

Department of Radiology and Radiological Science

Medical University of South Carolina

Charleston, South Carolina

 **J.J. Bloomberg**

Neurosciences Laboratory

NASA Johnson Space Center

Houston, Texas

 **M.S. George**

Department of Psychiatry and Behavioral Sciences

Medical University of South Carolina

Ralph H. Johnson VA Medical Center

Charleston, South Carolina

 **T.R. Brown**

Department of Radiology and Radiological Science

Medical University of South Carolina

Charleston, South Carolina

<http://dx.doi.org/10.3174/ajnr.A6431>

Stroke-like Episodes in m.3243A ≥ G Carriers Need to Be Monitored by MRI Starting with the Onset of Clinical Manifestations

With interest, we read the article by Bhatia et al¹ about a retrospective study of 8 patients with genetically confirmed mitochondrial encephalopathy with lactic acidosis and stroke-like episodes (MELAS). It was found that among 31 imaging studies, performed between 2006 and 2018, forty-one lesions were “new” in 17 studies.¹ It was concluded that cortical lesions most commonly affect the primary visual, the primary somatosensory, and the primary auditory cortices.¹ The study has a number of limitations and shortcomings.

Because patients with MELAS may develop involvement of the heart,² we should know how many of these 8 patients had cardiac disease, in particular atrial fibrillation, atrial flutter, ventricular arrhythmias, cardiomyopathy, noncompaction, or heart failure. Acute cortical lesions may be due to cardiac disease, so it is crucial to know the results of cardiac investigations. We also should know the current medication.

A further shortcoming of the study is that only 15 of the 31 studies had an acute indication. The other 16 studies were follow-ups ($n = 15$) or screening ($n = 1$).¹ In contrast, 41 T2-hyperintense lesions were found in the acute stage according to Table 2, suggesting that the 16 studies without an acute indication were also included in this evaluation. This discrepancy requires clarification.

Furthermore, it is unclear whether patients with “new” lesions progressed clinically between 2 consecutive MR imaging investigations. We also should know the intervals between the previous and current MR imaging that were used for classifying a lesion as new.

Because the phenotype of MELAS and thus the phenotypic variability among the 8 patients strongly depend on the heteroplasmy rate of the m.3243A>G variant, it is crucial to know the amount of mutated mitochondrial DNA in the mitochondria in the 8 included patients. A heteroplasmy rate of only 21% in patient 2 raises doubts about the causality of the mutation.

The morphologic correlate of a stroke-like episode (SLE) is the stroke-like lesion (SLL) on imaging, best visualized on MR

imaging.³ Because patients 1, 4, and 8 experienced SLEs, we should know whether these 3 patients also showed SLLs on MR imaging and the appearance of these SLLs. SLLs typically present with hyperintensity on DWI, ADC, and PWI, but hypointensity on oxygen extraction fraction MR imaging.³ Occasionally, however, this pattern is variable, and there are SLLs that show a mixture of vasogenic and cytotoxic edema or solely cytotoxic edema in a nonvascular distribution of the lesion.

Because MELAS is characterized by lactic acidosis in the serum and the CSF,⁴ we should know the serum and CSF lactate values (determined by CSF investigation or MR spectroscopy) in the 8 included patients. Lactate levels may correlate with the severity of the MELAS phenotype.

In Table 2, the authors differentiate between “ADC prior low” and “ADC prior normal/high.”¹ However, in none of the cases is the ADC during the first week described as normal/high.¹ Only low ADC values are mentioned. This discrepancy requires clarification.

A further discrepancy concerns the SWI sequences. In the acute stage (first week), low SWI was described in none of the investigations. However, in the subacute stage (weeks 4–8), 7 investigations with low SWI were described among those with ADC prior low.¹ We should know whether low SWI was interpreted as bleeding, and bleeding occurring 4–8 weeks after onset should be explained.

We should also know whether the classifications “acute,” “subacute,” and “chronic” refer to the clinical presentation or the MR imaging findings. If these categories refer to the MR imaging findings, we should know whether changes on MR imaging were accompanied by a clinical correlate.

Not only the metabolic and angiopathic hypotheses have been proposed to explain the development of an SLL but also the epileptogenic hypothesis.

Overall, this interesting study has a number of shortcomings as outlined above, which need to be addressed before final conclusions can be drawn. SLEs in m.3243A>G carriers need to be prospectively monitored by MR imaging starting with the onset of clinical manifestations.

REFERENCES

1. Bhatia KD, Krishnan P, Kortman H, et al. **Acute cortical lesions in MELAS syndrome: anatomic distribution, symmetry, and evolution.** *AJNR AJNR Am J Neuroradiol* 2020;41:167–73 CrossRef Medline
2. Finsterer J, Zarrouk-Mahjoub S. **The heart in m.3243A>G carriers.** *Herz* 2018 Aug 20. [Epub ahead of print] CrossRef Medline
3. Finsterer J. **Mitochondrial metabolic stroke: phenotype and genetics of stroke-like episodes.** *J Neurol Sci* 2019;400:135–41 CrossRef Medline
4. El-Hattab AW, Almannai M, Scaglia F. **MELAS.** 2001 Feb 27 [updated 2018 Nov 29]. In: Adam MP, Ardinger HH, Pagon RA, et al, eds. *GeneReviews*®. <http://www.ncbi.nlm.nih.gov/books/NBK1233/>. Accessed December 10, 2019

 **J. Finsterer**

Krankenanstalt Rudolfstiftung
Messerli Institute
Vienna, Austria